Faculty of mathematics, physics and informatics,
Comenius University in Bratislava
&
Slovak physical society

17th CONFERENCE OF SLOVAK PHYSICISTS

PROCEEDINGS

Hotel Družba, Bratislava

16.-19. 9. 2009

Editor: M. Reiffers

17th CONFERENCE OF SLOVAK PHYSICISTS
PROCEEDINGS

Editor: doc. RNDr. Marián Reiffers, DrSc.

Published: Slovak Physical Society
Printed: CD – Department of experimental Physics, Faculty of mathematics, physics and informatics, Comenius University, Bratislava
Bratislava 2009

ISBN 978-80-969124-7-6
EAN 9788096912476

OPENING ADDRESS

Ladies and Gentlemen,

this year 17th Conference of the Slovak Physicists move after long time to Bratislava. Increased number of participants is the confirmation of my expectation. Therefore, it is a great pleasure for me to welcome you on behalf of the Organizing Committee of the 17th Conference of the Slovak Physicists in Bratislava. I would like to thank the local organising committee under heading of Prof. A. Plecenik from Department of Experimental Physics of Faculty of mathematics, physics and informatics of Comenius University for very good organisation of conference. I hope that the University hotel Družba will be a proper place to obtain new information about physics in Slovakia and about life of physicists in Slovakia.

The Conferences of the Slovak Physicists have a rich tradition. They are held every year. The participants of these general conferences are the scientists and teachers from the universities, institutes of the Slovak Academy of Sciences and others, working in basic or applied research. Participants are also teachers from the secondary schools and young post-gradual physicists. Programme and organising committees hope that they choose interesting invited plenary lectures with high scientific level. I expect also the interesting short lectures and poster section, too. The Conferences of the Slovak Physicists are unique opportunity for all physicists, teachers and students of the post-gradual study to give the information about their scientific and educational work and results. I would like to stress the awarding of Slovak lecturer Dr. Slavomir Tuleja by the pedagogical division of European Physical Society as outstanding European teacher. The General Meeting of the SPS connected with the election of new SPS committee, will be held through this conference.

In conclusion, I would like to thank my colleagues from the Slovak Physical Society, the members of the Organization and Program Committees, as well as other colleagues, who contributed to the organization of this conference. I would like to thank you, the participants of this Conference, mainly for your active attendance and valuable contributions. I think with satisfaction, that the 17th Conference of the Slovak Physicists will have the high scientific level, will be successful and useful for the further development of physics in Slovakia. I wish you all to spend useful and pleasant time here in Bratislava.

Marian Reiffers
President of the SPS

CONTENT

FLUCTUATIONS OF ELECTROMAGNETIC FIELD AT THE INTERFACE BETWEEN MEDIA

Ladislav Šamaj, Ladislav.Samaj@savba.sk, Institute of Physics, SAS, Dúbravská cesta 9, 845 11 Bratislava, Slovakia
Bernard Jancovici, Bernard.Jancovici@th.u-psud.fr, LPT, Université de Paris-Sud, Orsay, France

INTRODUCTION

This study is related to the fluctuation theory of electromagnetic (EM) fields, charges, and currents in systems formulated in the three-dimensional (3D) Cartesian space of points $\mathbf{r} = (x, y, z)$. The studied problem is inhomogeneous along one of the axis, say along the first coordinate x, and translationally invariant along the plane formed by the remaining two coordinates normal to x, denoted as $\mathbf{R} = (y, z)$. The model consists of two semi-infinite media (conductor, dielectric or vacuum) with the frequency-dependent dielectric functions $\epsilon_1(\omega)$ and $\epsilon_2(\omega)$ which are localized in the complementary half-spaces $x > 0$ and $x < 0$, respectively (see Fig. 1). The interface between media is the plane $x = 0$. We assume that the media have no magnetic structure and the magnetic permeabilities $\mu_1 = \mu_2 = 1$. The media and the radiated EM field are in thermal equilibrium at some temperature T, or the inverse temperature $\beta = 1/(k_B T)$ with k_B being the Boltzmann constant.

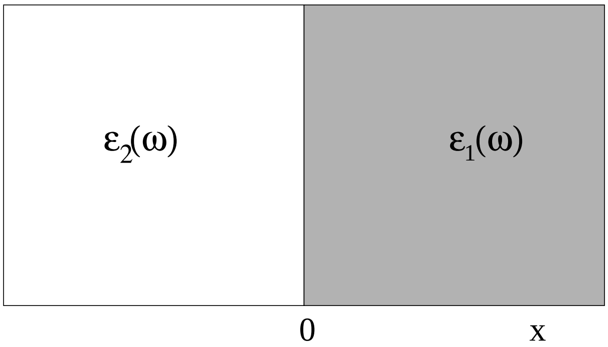

Fig. 1. Two semi-infinite media characterized by the dielectric functions $\epsilon_1(\omega)$ and $\epsilon_2(\omega)$.

The different electric properties of the media give rise to a surface charge density $\sigma(t, \mathbf{R})$ at time t and at a point $\mathbf{r} = (0, \mathbf{R})$ on the interface which must be understood as being the microscopic volume charge density integrated along the x-axis on some microscopic depth from the interface. In thermal equilibrium, this quantity fluctuates in time around its mean value, usually equal to 0. Based on the elementary electrodynamics, the surface charge density is associated with the discontinuity of the normal x component of the electric field at the interface: In Gauss units, we have

$$4\pi\sigma(t, \mathbf{R}) = E_x^+(t, \mathbf{R}) - E_x^-(t, \mathbf{R}), \qquad (1)$$

where the superscript $+$ $(-)$ means approaching the interface through the limit $x \to 0^+$ $(x \to 0^-)$. The tangential y and z components of the electric field are continuous at the interface.

The fluctuations of the surface charge density at two points on the interface, with times different by t and distances different by $R = |\mathbf{R}|$, are correlated due to the EM interactions among the charged particles forming the two media. We are interested in the (symmetrized) two-point surface charge correlation function defined by

$$S(t, \mathbf{R}) \equiv \frac{1}{2}\langle \sigma(t, \mathbf{R})\sigma(0, 0) + \sigma(0, 0)\sigma(t, \mathbf{R})\rangle^{\mathrm{T}}, \qquad (2)$$

where $\langle \cdots \rangle^{\mathrm{T}}$ represents a truncated equilibrium statistical average, $\langle AB\rangle^{\mathrm{T}} = \langle AB\rangle - \langle A\rangle\langle B\rangle$, at the inverse temperature β. With regard to the relation (1), the function (2) is related to fluctuations of the EM field on the interface between media. Although the system is not in the critical state, due to the presence of long-ranged EM forces in the media the asymptotic large-distance behavior of the surface charge correlation function (2) exhibits in general a long-ranged tail of type

$$\beta S(t, \mathbf{R}) \sim \frac{h(t)}{R^3}, \qquad R \to \infty, \qquad (3)$$

where the form of the prefactor function $h(t)$ depends on "the physical model" used. We can consider:

- Either *classical* or *quantum* mechanics. According to the correspondence principle, the two theories provide the same results in the high-temperature limit $\beta\hbar \to 0$.
- Either *non-retarded* or *retarded* regime of the EM interaction. In the non-retarded (non-relativistic) regime, the speed of light c is taken to be infinitely large, $c = \infty$, ignoring in this way magnetic forces acting on the particles. In the retarded (relativistic) regime, c is assumed finite and so the particles are fully coupled to both electric and magnetic parts of the radiated EM field.

The particles themselves are non-relativistic, classical or quantum.

It is useful to introduce the Fourier transform

$$S(t, \mathbf{q}) = \int \mathrm{d}^2 R \, \exp(-\mathrm{i}\mathbf{q} \cdot \mathbf{R}) S(t, \mathbf{R}), \qquad (4)$$

with $\mathbf{q} = (q_y, q_z)$ being a 2D wave vector. Since, in the sense of distributions, the 2D Fourier transform of $1/R^3$ is $-2\pi q$, a result equivalent to (3) is that $\beta S(t, \mathbf{q})$ has a kink singularity at $\mathbf{q} = \mathbf{0}$, behaving like

$$\beta S(t, q) \sim -2\pi h(t) q, \qquad q \to 0. \qquad (5)$$

The correlation function $S(t, \mathbf{R})$ and its long-ranged decay (3) are of importance for two reasons. Firstly, the Fourier transform is a measurable quantity by scattering experiments. The fact that $S(t, q)$ is linear in q for small q makes this quantity very different from the usual correlation functions with short-ranged decay which are proportional to q^2 in the limit $q \to 0$. The second application arises in the context of the average polarization $\mathbf{P}$ of a charged system, localized inside a domain Λ of volume $|\Lambda|$ entoured say by vacuum and exposed to a constant electric field $\mathbf{E}$. In the linear limit, we have

$$\frac{P_j}{|\Lambda|} = \sum_k \chi_{jk} E_k \qquad j,k = x,y,z, \tag{6}$$

where χ_{jk} is the dielectric susceptibility tensor. One expects that an extensive quantity like $\mathbf{P}$ divided by the volume $|\Lambda|$ tends, for a fixed temperature, to a constant in the thermodynamic limit $|\Lambda| \to \infty$, independently of the shape of the infinite domain Λ. This is not true in the case of the dielectric susceptibility tensor. It can be shown that χ_{jk} contains contributions from both short-ranged bulk and long-ranged surface charge (3) correlation functions which causes its shape dependence [1, 2]. Such a phenomenon is predicted by the macroscopic laws of electrostatics [3].

The two media configuration studied so far was restricted to a conductor, localized say in the half-space $x > 0$ with the dielectric function $\epsilon_1(\omega) \equiv \epsilon(\omega)$, in contact with vacuum of the dielectric constant $\epsilon_2(\omega) = 1$. The obtained results can be summarized as follows.

- **Classical non-retarded regime:** Let the conductor be modelled by a classical Coulomb fluid composed of charged particles with only the instantaneous Coulomb interactions. By a microscopic analysis [4], the long-ranged decay of the static (i.e. $t = 0$) surface charge correlation was found such that

$$h_{\rm cl}^{(\rm nr)}(0) = -\frac{1}{8\pi^2}, \tag{7}$$

where the subscript "cl" means "classical" and the upperscript "nr" means "non-retarded". The same result has been obtained later [5] by simple macroscopic arguments based on a combination of the linear response theory and the electrostatic method of images. Note the universal form of $h_{\rm cl}^{(\rm nr)}(0)$, independent of the composition of the classical Coulomb fluid.

- **Quantum non-retarded regime:** The quantum description of a general conductor is very complicated. A simplification arises in the so-called jellium model, i.e. a system of identical pointlike particles of charge e, mass m and bulk number density n, immersed in a uniform neutralizing background of charge density $-en$. The dynamical properties of the jellium have a special feature: There is no viscous damping of the long-wavelength plasma oscillations for identically charged particles [6]. The frequencies of non-retarded nondispersive long-wavelength collective modes, namely ω_p of the bulk plasmons and ω_s of the surface plasmons, are given by

$$\omega_p = \left(\frac{4\pi n e^2}{m} \right)^{1/2}, \qquad \omega_s = \frac{\omega_p}{\sqrt{2}}. \tag{8}$$

The dielectric function of the jellium is well described by a simple one-resonance Drude formula

$$\epsilon(\omega) = 1 - \frac{\omega_p^2}{\omega(\omega + i\eta)}, \tag{9}$$

where the dissipation constant η is taken as positive infinitesimal, $\eta \to 0^+$. The prefactor function $h(t)$ for the quantum jellium was obtained in Refs. [7, 8]. It has the nonuniversal form

$$h_{\rm qu}^{(\rm nr)}(t) = -\frac{1}{8\pi^2} \left[2g(\omega_s)\cos(\omega_s t) - g(\omega_p)\cos(\omega_p t) \right], \tag{10}$$

where

$$g(\omega) = \frac{\beta\hbar\omega}{2} \coth\left(\frac{\beta\hbar\omega}{2} \right) \tag{11}$$

and the subscript "qu" means "quantum". In the high-temperature limit $\beta\hbar \to 0$, the function $g(\omega) = 1$ for any ω and the quantum formula (10) reduces to the classical non-retarded one

$$h_{\rm cl}^{(\rm nr)}(t) = -\frac{1}{8\pi^2} \left[2\cos(\omega_s t) - \cos(\omega_p t) \right]. \tag{12}$$

For $t = 0$, we recover the classical static result (7).

The present study reviews some new results in the field [9, 10, 11]. These results concern a generalization of the formalism to contacts between all kinds of media, i.e. conductors, dielectrics and vacuum, and to the retarded regime. It turns out that, for any time t, the inclusion of retardation effects surprisingly converts the quantum results into the static classical ones.

To deal with the physical problem of such complexity, we use a macroscopic theory of equilibrium thermal fluctuations of EM field, initiated by Rytov [12] and further developed in Ref. [13]; we adopt the notation from the course by Landau and Lifshitz [14] (see Section 2). Based on Rytov's fluctuational theory, we derive in Section 3 the general formula for the surface charge correlation function between two semi-infinite media. The analysis of the asymptotic large-distance form of this formula, in both non-retarded and retarded regimes, is the subject of Section 4. We first consider the special configuration of the jellium conductor in contact with vacuum (Subsection 4.1) and then the general configuration (Subsection 4.2). Section 5 is a Conclusion.

FLUCTUATIONAL ELECTRODYNAMICS

Let us consider a non-magnetoactive ($\mu = 1$) medium with the isotropic, frequency and (possibly) position dependent, dielectric function $\epsilon(\omega;\mathbf{r})$. The coupled EM field is defined, in the classical format, by the scalar potential $\phi(t,\mathbf{r})$ and the vector potential $\mathbf{A}(t,\mathbf{r})$. In the considered Weyl gauge $\phi = 0$, the microscopic electric and magnetic fields are given by

$$\mathbf{E} = -\frac{1}{c}\frac{\partial \mathbf{A}}{\partial t}, \qquad \mathbf{B} = \operatorname{curl} \mathbf{A}. \tag{13}$$

The elementary excitations of the *quantized* EM field are described by the photon operators $\hat{A}_j$ ($j = x,y,z$) which are self-conjugate Bose operators; $\hat{A}_j(t,\mathbf{r})$ will denote the vector-potential operator in the Heisenberg picture. The construction of all types of photon Green's functions is based on the retarded Green function D, defined as the tensor

$$iD_{jk}(t;\mathbf{r},\mathbf{r}') = \langle \hat{A}_j(t,\mathbf{r})\hat{A}_k(0,\mathbf{r}') - \hat{A}_k(0,\mathbf{r}')\hat{A}_j(t,\mathbf{r}) \rangle \tag{14}$$

for $t > 0$ and equal to 0 for $t < 0$. The Fourier transform in time of the retarded Green function reads

$$D_{jk}(\omega;\mathbf{r},\mathbf{r}') = \int_0^\infty dt\, e^{i\omega t} D_{jk}(t;\mathbf{r},\mathbf{r}'). \qquad (15)$$

For media with no magnetic structure, the Green function tensor possesses the important symmetry

$$D_{jk}(\omega;\mathbf{r},\mathbf{r}') = D_{kj}(\omega;\mathbf{r}',\mathbf{r}) \qquad (16)$$

The EM fields, being in thermal equilibrium with medium, are random variables which fluctuate around their mean values obeying macroscopic Maxwell's equations. To deal with thermal fluctuations, Rytov put a classical current $\mathbf{j}(t,\mathbf{r})$ due to the thermal motion of particles into the medium [12]. This current acts as an "external force" on the vector-potential operator in the interaction Hamiltonian

$$\mathcal{H}_{\rm int}(t) = -\frac{1}{c}\int d^3r\, \mathbf{j}(t,\mathbf{r})\cdot\hat{\mathbf{A}}. \qquad (17)$$

The mean values of the components of the vector-potential operator can be expressed in terms of the retarded Green function by using Kubo's linear response in currents:

$$\frac{\bar{A}_j(\omega,\mathbf{r})}{c} = -\frac{1}{\hbar c^2}\int d^3r' \sum_k D_{jk}(\omega;\mathbf{r},\mathbf{r}') j_k(\omega,\mathbf{r}'). \qquad (18)$$

The fact that the mean value $\bar{\mathbf{A}}$ satisfies the macroscopic Maxwell equation due to the classical current $\mathbf{j}$ implies the differential equation of the dyadic type fulfilled by the retarded Green function tensor:

$$\sum_{l=1}^{3}\left[\frac{\partial^2}{\partial x_j \partial x_l} - \delta_{jl}\Delta - \delta_{jl}\frac{\omega^2}{c^2}\epsilon(\omega;\mathbf{r})\right] D_{lk}(\omega;\mathbf{r},\mathbf{r}') = -4\pi\hbar\delta_{jk}\delta(\mathbf{r}-\mathbf{r}'). \qquad (19)$$

Here, in order to simplify the notation, the vector $\mathbf{r} = (x,y,z)$ is represented as (x_1,x_2,x_3). The differential equation must be supplemented by certain boundary conditions. The second space variable $\mathbf{r}'$ and the second index k only act as parameters, the boundary conditions are formulated with respect to the coordinate $\mathbf{r}$ and the Green function $D_{lk}(\omega;\mathbf{r},\mathbf{r}')$ is considered as a vector with the components $l = x,y,z$. There is an obvious boundary condition of regularity at infinity, $|\mathbf{r}| \to \infty$. At an interface between two different media, the boundary conditions correspond to the macroscopic requirements that the tangential components of the fields $\mathbf{E}$ and $\mathbf{H} = \mathbf{B}$ be continuous. The vector potential is related to the Green function tensor via the linear response (18), and the electric and magnetic fields are related to the vector potential by (13). This is why the role of the vector components E_l, up to an irrelevant multiplicative constant, is played by the quantity

$$i\frac{\omega}{c} D_{lk}(\omega;\mathbf{r},\mathbf{r}') \qquad (20)$$

and the role of the vector component H_l is played by the quantity

$$\sum_j {\rm curl}_{lj} D_{jk}(\omega;\mathbf{r},\mathbf{r}'). \qquad (21)$$

Here, we use the notation ${\rm curl}_{lj} = \sum_m e_{lmj}\partial/\partial x_m$ with e_{lmj} being the unit antisymmetric pseudo-tensor. For our geometry in Fig. 1, the tangential components (20) and (21), which are continuous at the interface $x = 0$, correspond to indices $l = y, z$.

Eq. (18) defines $-D_{jk}(\omega;\mathbf{r},\mathbf{r}')/(\hbar c^2)$ as the tensor of generalized susceptibilities corresponding to the variable $\mathbf{A}/c$. The fluctuation-dissipation theorem tells us that the fluctuations of random variables can be expressed in terms of the corresponding susceptibilities. For the assumed symmetry (16), the theorem implies that

$$[A_j(\mathbf{r})A_k(\mathbf{r}')]_\omega = -\coth(\beta\hbar\omega/2)\,{\rm Im}\, D_{jk}(\omega;\mathbf{r},\mathbf{r}'), \qquad (22)$$

where the spectral distribution $[A_j(\mathbf{r})A_k(\mathbf{r}')]_\omega$ is the Fourier transform in time of the symmetrized (truncated) correlation function

$$\frac{1}{2}\left\langle \hat{A}_j(t,\mathbf{r})\hat{A}_k(0,\mathbf{r}') + \hat{A}_k(0,\mathbf{r}')\hat{A}_j(t,\mathbf{r})\right\rangle^{\rm T}. \qquad (23)$$

The spectral distribution of the electric-field fluctuations can be easily found by using the first relation in Eq. (13),

$$\begin{aligned}[E_j(\mathbf{r})E_k(\mathbf{r}')]_\omega &= \frac{\omega^2}{c^2}[A_j(\mathbf{r})A_k(\mathbf{r}')]_\omega \\ &= -\frac{\omega^2}{c^2}\coth(\beta\hbar\omega/2) \\ &\quad \times {\rm Im}\, D_{jk}(\omega;\mathbf{r},\mathbf{r}'). \qquad (24)\end{aligned}$$

SURFACE CHARGE CORRELATIONS

The retarded Green function tensor for the studied problem of two semi-infinite media in Fig. 1 is obtained as the solution of the dyadic differential Eq. (19) supplemented by the mentioned boundary conditions [9]. Since the system is translationally invariant in the $\mathbf{R}$-plane perpendicular to the x axis, we introduce the Fourier transform of the retarded Green function tensor with the wave vector $\mathbf{q} = (q_y, q_z)$,

$$D_{jk}(\omega;\mathbf{r},\mathbf{r}') = \int \frac{{\rm d}^2 q}{(2\pi)^2} {\rm e}^{i\mathbf{q}(\mathbf{R}-\mathbf{R}')} D_{jk}(\omega,\mathbf{q};x,x'). \qquad (25)$$

Let us define for each of the half-space regions the inverse length $\kappa_j(\omega,q)$ $(j=1,2)$ by

$$\kappa_j^2(\omega,q) = q^2 - \frac{\omega^2}{c^2}\epsilon_j(\omega), \qquad {\rm Re}\,\kappa_j(\omega,q) > 0; \qquad (26)$$

from two possible solutions for κ_j we choose the one with the positive real part in order to ensure the regularity of the Green function at asymptotically large distances from the interface. We shall only need the quantity $D_{xx}(\omega,q;x,x')$ for which the obtained results can be summarized as follows:

(i) If $x, x' > 0$,

$$D_{xx} = \frac{4\pi\hbar c^2}{\omega^2\epsilon_1}\delta(x-x') - \frac{2\pi\hbar(cq)^2}{\omega^2\epsilon_1\kappa_1}\Bigg({\rm e}^{-\kappa_1|x-x'|} + \frac{\kappa_1\epsilon_2-\kappa_2\epsilon_1}{\kappa_1\epsilon_2+\kappa_2\epsilon_1}{\rm e}^{-\kappa_1(x+x')}\Bigg). \qquad (27)$$

(ii) If $x < 0$ and $x' > 0$,

$$D_{xx} = -\frac{4\pi\hbar(cq)^2}{\omega^2}\frac{1}{\kappa_1\epsilon_2 + \kappa_2\epsilon_1}\mathrm{e}^{\kappa_2 x - \kappa_1 x'}. \qquad (28)$$

(iii) The case $x > 0$ and $x' < 0$ is deducible from Eq. (28) by using the symmetry relation (16).

(iv) If $x, x' < 0$, considering the $1 \leftrightarrow 2$ media exchange symmetry, we obtain from Eq. (27) that

$$\begin{aligned} D_{xx} &= \frac{4\pi\hbar c^2}{\omega^2\epsilon_2}\delta(x-x') - \frac{2\pi\hbar(cq)^2}{\omega^2\epsilon_2\kappa_2}\left(\mathrm{e}^{-\kappa_2|x-x'|}\right. \\ &\left. + \frac{\kappa_2\epsilon_1 - \kappa_1\epsilon_2}{\kappa_2\epsilon_1 + \kappa_1\epsilon_2}\mathrm{e}^{\kappa_2(x+x')}\right). \qquad (29) \end{aligned}$$

The symmetrized surface charge correlation function (2) is expressible in terms of the fluctuations of the symmetrized electric field xx-components by using relation (1). These electric-field fluctuations are related to the xx elements of the Green function tensor via Eq. (24). The terms proportional to $\delta(x-x')$ in Eqs. (27) and (29) can be ignored since they originate from the short-distance terms proportional to $\delta(\mathbf{r}-\mathbf{r}')$ which do not play any role in the large-distance asymptotic. Since the combination

$$\begin{aligned} & D_{xx}(0^+,0^+) + D_{xx}(0^-,0^-) - 2D_{xx}(0^+,0^-) \\ & = -\frac{4\pi\hbar(cq)^2}{\omega^2}\frac{1}{\kappa_1\epsilon_2+\kappa_2\epsilon_1}\left(\frac{\epsilon_2}{\epsilon_1} + \frac{\epsilon_1}{\epsilon_2} - 2\right), \qquad (30) \end{aligned}$$

we finally arrive at the quantum result

$$\beta S_{\mathrm{qu}}(t,q) = \int_{-\infty}^{\infty}\frac{\mathrm{d}\omega}{\omega}\mathrm{e}^{-\mathrm{i}\omega t}\mathrm{Im}\, f(\omega), \qquad (31)$$

where, in the retarded regime, $f(\omega) \equiv f_{\mathrm{qu}}^{(\mathrm{r})}$ with

$$\begin{aligned} f_{\mathrm{qu}}^{(\mathrm{r})} &= \frac{q^2}{4\pi^2}g(\omega)\frac{1}{\kappa_1(\omega,q)\epsilon_2(\omega) + \kappa_2(\omega,q)\epsilon_1(\omega)} \\ &\times \frac{[\epsilon_1(\omega) - \epsilon_2(\omega)]^2}{\epsilon_1(\omega)\epsilon_2(\omega)}. \qquad (32) \end{aligned}$$

In the non-retarded case, $f(\omega) \equiv f_{\mathrm{qu}}^{(\mathrm{nr})}$ is obtained from (32) by setting the speed of light $c \to \infty$. According to Eq. (26), the inverse lengths $\kappa_1 = \kappa_2 = q$ in this limit, so that

$$f_{\mathrm{qu}}^{(\mathrm{nr})} = \frac{q}{4\pi^2}g(\omega)\left[\frac{1}{\epsilon_1(\omega)} + \frac{1}{\epsilon_2(\omega)} - \frac{4}{\epsilon_1(\omega)+\epsilon_2(\omega)}\right]. \qquad (33)$$

ANALYSIS OF THE RESULTS

Jellium conductor in vacuum

We first considered the previously studied configuration of the jellium conductor of the dielectric function $\epsilon_1(\omega)$ given by the Drude formula (9) in contact with the vacuum of $\epsilon_2(\omega) = 1$ [9, 10].

In the non-retarded regime, using the Weierstrass theorem

$$\lim_{\eta\to 0^+}\frac{1}{x \pm \mathrm{i}\eta} = \mathcal{P}\left(\frac{1}{x}\right) \mp \mathrm{i}\pi\delta(x) \qquad (34)$$

($\mathcal{P}$ denotes the Cauchy principal value) in the representation (33), the integration over frequency (31) leads the previous result (10). This result is valid for intermediate distances R on the interface, given by the inequalities $\lambda_{\mathrm{ph}} \ll R \ll c/\omega_p$, where $\lambda_{\mathrm{ph}} \propto \beta\hbar c$ stands for the thermal de Broglie wavelength of photon and c/ω_p is the wavelength of electromagnetic waves emitted by charge oscillations at frequency ω_p.

The analysis of the frequency integral (31) with the retarded function (32) is much more complicated [9]. At specific values of ω, given by the surface-plasmon dispersion relation

$$q^2(\epsilon_1 + \epsilon_2) - \frac{\omega^2}{c^2}\epsilon_1\epsilon_2 = 0, \qquad (35)$$

the integration passes in the infinitesimal vicinity of a singularity. The final result for the small q-expansion is of the classical static type

$$\beta S_{\mathrm{qu}}^{(\mathrm{r})}(t,q) = \frac{q}{4\pi} + o(q). \qquad (36)$$

In other words, for both static and time-dependent surface charge correlation functions, the inclusion of retardation effects causes the quantum prefactor to take its universal static classical form

$$h_{\mathrm{qu}}^{(\mathrm{r})}(t) = h_{\mathrm{cl}}^{(\mathrm{r})}(0) = -\frac{1}{8\pi^2}. \qquad (37)$$

This formula is valid in the strictly asymptotic region of distances R on the interface, given by the inequality $c/\omega_p \ll R$. Note that it holds

$$h_{\mathrm{cl}}^{(\mathrm{r})}(0) = h_{\mathrm{cl}}^{(\mathrm{nr})}(0) \equiv h_{\mathrm{cl}}(0). \qquad (38)$$

This relation is of general validity due to the Bohr-van Leeuwen theorem [15, 16].

The same result (37) was derived by another (partially microscopic) method, based on the analysis of the collective vibration modes of the system [10].

General configuration

For an arbitrary configuration of the plane contact between two distinct media, the small-q analysis of the surface charge correlation function (31) was done in Ref. [11] by using general analytic properties of dielectric functions in the complex frequency upper half-plane and contour integration techniques.

We start with the simpler static case $t = 0$. The formula (31) reads

$$\beta S_{\mathrm{qu}}(0,q) = \int_{-\infty}^{\infty}\frac{\mathrm{d}\omega}{\omega}\mathrm{Im}\, f(\omega), \qquad (39)$$

where the function $f(\omega)$ is given by (32) in the retarded regime and by (33) in the non-retarded regime. For a real frequency ω, the symmetry relations $\epsilon^*(\omega) = \epsilon(-\omega)$ and $\kappa^*(\omega) = \kappa(-\omega)$ imply $f^*(\omega) = f(-\omega)$, i.e.

$$\mathrm{Re}\, f(\omega) = \mathrm{Re}\, f(-\omega), \qquad \mathrm{Im}\, f(\omega) = -\mathrm{Im}\, f(-\omega). \qquad (40)$$

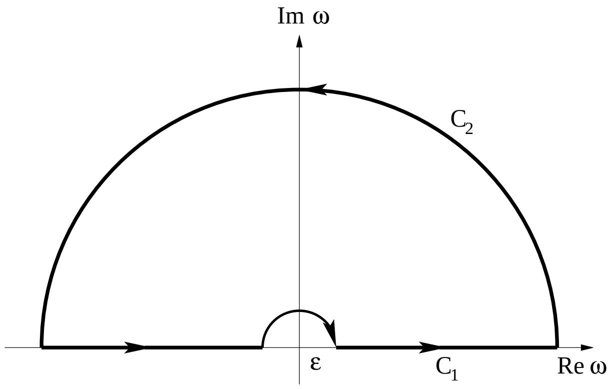

Fig. 2. The contour in the complex frequency plane for $t = 0$.

As $\omega \to 0$, $\mathrm{Im}\, f(0) = 0$ and

$$\mathrm{Re}\, f(0) = \frac{q}{4\pi^2}\left[\frac{1}{\epsilon_1(0)} + \frac{1}{\epsilon_2(0)} - \frac{4}{\epsilon_1(0)+\epsilon_2(\omega)}\right]. \tag{41}$$

Let C_1 be the path following the real axis, except it goes around the origin $\omega = 0$ in a small semicircle in complex upper half-plane whose radius ϵ tends to zero and C_2 be the closure of C_1 by a semicircle at infinity (see Fig. 2). The integration along the real axis in Eq. (39) is expressible in terms of the path integration over the closed contour $C = C_1 \cup C_2$ as follows

$$\int_{-\infty}^{\infty} \frac{\mathrm{d}\omega}{\omega} \mathrm{Im}\, f(\omega) = \pi f(0) + \mathrm{Im} \oint_C \frac{\mathrm{d}\omega}{\omega} f(\omega). \tag{42}$$

The integral over the contour C can be evaluated by using the residue theorem at poles $\{\omega_j\}$ of the function $f(\omega)$ in the ω upper half-plane bounded by C,

$$\mathrm{Im} \oint_C \frac{\mathrm{d}\omega}{\omega} f(\omega) = 2\pi \sum_j \frac{\mathrm{Res}(f,\omega_j)}{\omega_j}, \tag{43}$$

provided that $\mathrm{Res}(f,\omega_j)/\omega_j$ is real (which will be the case); Res denotes the residue. Both the retarded (32) and non-retarded (33) versions of the f-function contain $g(\omega)$ defined in (11). Since $g(\omega)$ can be expanded in ω as [17]

$$g(\omega) = 1 + \sum_{j=1}^{\infty} \frac{2\omega^2}{\omega^2 + \xi_j^2}, \qquad \xi_j = \frac{2\pi}{\beta\hbar} j, \tag{44}$$

it has in the upper half-plane an infinite sequence of simple poles at the imaginary Matsubara frequencies

$$\omega_j = i\xi_j, \qquad \mathrm{Res}(g,\omega_j) = \omega_j \quad (j = 1,2,\ldots). \tag{45}$$

Using general analytic properties of dielectric functions it was shown in Ref. [11] that, in both retarded and non-retarded regimes, these are the only poles of the f-function inside the contour C. The static correlation function (39) is therefore expressible as follows

$$\begin{aligned}\beta S_{\mathrm{qu}}(0,q) &= \frac{q}{4\pi}\left[\frac{1}{\epsilon_1(0)} + \frac{1}{\epsilon_2(0)} - \frac{4}{\epsilon_1(0)+\epsilon_2(0)}\right] \\ &\quad + F(0,q), \end{aligned} \tag{46}$$

$$F(0,q) = 2\pi \sum_{j=1}^{\infty} \frac{\mathrm{Res}(f,i\xi_j)}{i\xi_j}. \tag{47}$$

The first term on the rhs of Eq. (46), linear in q, is independent of $\beta\hbar$ and c, the q-dependence of the static function $F(0,q)$ depends on the considered (retarded or non-retarded) regime.

In the retarded case (32), we have

$$\begin{aligned}F_{\mathrm{qu}}^{(\mathrm{r})}(0,q) &= \frac{q^2}{2\pi}\sum_{j=1}^{\infty} \frac{1}{\kappa_1(i\xi_j)\epsilon_2(i\xi_j) + \kappa_2(i\xi_j)\epsilon_1(i\xi_j)} \\ &\quad \times \frac{[\epsilon_1(i\xi_j) - \epsilon_2(i\xi_j)]^2}{\epsilon_1(i\xi_j)\epsilon_2(i\xi_j)}. \end{aligned} \tag{48}$$

We are interested in the limit $q \to 0$ for which $\kappa_{1,2}(i\xi_j) \sim \xi_j \epsilon_{1,2}^{1/2}(i\xi_j)$ ($\epsilon_{1,2}(i\xi_j)$ are real). Since $\xi_j \propto j$ and $\epsilon(i\xi_j) - 1 = O(1/j^2)$ in the limit $j \to \infty$, the sum in (48) converges. This means that the function $F_{\mathrm{qu}}^{(\mathrm{r})}(0,q)$, being of the order $O(q^2)$, becomes negligible in comparison with the first term in Eq. (46) when $q \to 0$. We find the static h-prefactor associated with the asymptotic decay to be

$$h_{\mathrm{qu}}^{(\mathrm{r})}(0) = -\frac{1}{8\pi^2}\left[\frac{1}{\epsilon_1(0)} + \frac{1}{\epsilon_2(0)} - \frac{4}{\epsilon_1(0)+\epsilon_2(0)}\right]. \tag{49}$$

Since this expression does not depend on the temperature and $\hbar$, its classical $\beta\hbar \to 0$ limit is the same, i.e. $h_{\mathrm{cl}}^{(\mathrm{r})}(0) = h_{\mathrm{cl}}^{(\mathrm{nr})}(0) \equiv h_{\mathrm{cl}}(0)$ with

$$h_{\mathrm{cl}}(0) = -\frac{1}{8\pi^2}\left[\frac{1}{\epsilon_1(0)} + \frac{1}{\epsilon_2(0)} - \frac{4}{\epsilon_1(0)+\epsilon_2(0)}\right]. \tag{50}$$

This classical result was derived independently in the non-retarded regime by using the linear response theory combined with the electrostatic method of images [11]. We see that from the dielectric functions of the two media only their values at zero frequency appear; we recall that $\epsilon(0) \to i\infty$ for conductors, $\epsilon(0) = \epsilon_0 > 1$ for dielectrics and $\epsilon(0) = 1$ for vacuum. The h-prefactor is nonzero for an arbitrary configuration of different media, except for the special case of two conductors.

In the non-retarded case (33), we have

$$\begin{aligned}F_{\mathrm{qu}}^{(\mathrm{nr})}(0,q) &= \frac{q}{2\pi}\sum_{j=1}^{\infty}\left[\frac{1}{\epsilon_1(i\xi_j)} + \frac{1}{\epsilon_2(i\xi_j)}\right. \\ &\quad \left. - \frac{4}{\epsilon_1(i\xi_j)+\epsilon_2(i\xi_j)}\right]. \end{aligned} \tag{51}$$

It is evident from the asymptotic behavior $\epsilon(i\xi_j) - 1 = O(1/j^2)$ that the sum in (51) converges. The function $F_{\mathrm{qu}}^{(\mathrm{nr})}(0,q)$ is thus of the order $O(q)$ and $h_{\mathrm{qu}}^{(\mathrm{nr})}(0)$ is a complicated function of the temperature.

A more laborious analysis is needed for the time-dependent case $t \neq 0$ [11]. The final result is

$$h_{\mathrm{qu}}^{(\mathrm{r})}(t) = -\frac{1}{8\pi^2}\left[\frac{1}{\epsilon_1(0)} + \frac{1}{\epsilon_2(0)} - \frac{4}{\epsilon_1(0)+\epsilon_2(0)}\right]. \tag{52}$$

As before, the quantum time-dependent prefactor to the asymptotic decay takes, for any temperature, its classical static form (50).

CONCLUSION

Although the present study is rather technical, its main result (52) is of importance. We do not understand which are *physical* reasons that the inclusion of retardation effects causes the asymptotic decay of time-dependent quantum surface charge correlation functions to take its static classical form, independent of the temperature factor $\beta\hbar$ and the speed of light c.

This is one of the rare phenomena in the Condensed Matter physics when retardation (relativistic) effects play an essential role.

ACKNOWLEDGMENT: L. Š. is grateful to LPT for very kind invitations and hospitality. The support received from the MISGAM program of the European Science Foundation, Grant VEGA No. 2/0113/2009 and CE-SAS QUTE is acknowledged.

REFERENCES

1. P. Choquard, B. Piller, R. Rentsch and P. Vieillefosse, J. Stat. Phys. **55**, 1185 (1989).
2. B. Jancovici and L. Šamaj, J. Stat. Phys. **114**, 1211 (2004).
3. L. Landau and E. Lifshitz: *Electrodynamics of Continuous Media* (Pergamon, Oxford - 1960).
4. B. Jancovici, J. Stat. Phys. **29**, 263 (1982).
5. B. Jancovici, J. Stat. Phys. **80**, 445 (1995).
6. D. Pines and P. Nozières: *The Theory of Quantum Liquids* (Benjamin, New York - 1966).
7. B. Jancovici, J. Stat. Phys. **39**, 427 (1985).
8. B. Jancovici, J. L. Lebowitz and P. A. Martin, J. Stat. Phys. **41**, 941 (1985); erratum: J. Stat. Phys. **79**, 789(E) (1995).
9. L. Šamaj and B. Jancovici, Phys. Rev. E **78**, 051119 (2008); e-print arXiv.0807.4667
10. B. Jancovici and L. Šamaj, Phys. Rev. E **79**, 021111 (2009); e-print arXiv.0811.0295
11. B. Jancovici and L. Šamaj, Equilibrium long-ranged charge correlations at the interface between media coupled to the electromagnetic radiation, accepted for publication in Phys. Rev. E; e-print arXiv.0905.3334
12. S. M. Rytov, Sov. Phys. JETP **6**, 130 (1958).
13. M. L. Levin and S. M. Rytov: *Theory of Equilibrium Thermal Fluctuations in Electrodynamics* (Science, Moscow - 1967).
14. E. M. Lifshitz and L. P. Pitaevskii: *Statistical Physics, Part 2* (Pergamon, Oxford - 1981).
15. N. Bohr: Dissertation (Copenhagen-1911).
16. H.-J. Van Leeuwen, J. Phys. Radium **2**, 361 (1921).
17. I. S. Gradshteyn and I. M. Ryzhik: *Table of Integrals, Series, and Products* (Academic Press, London-2000).

STUDY OF COMPOSITE SYSTEMS CONTAINING MAGNETIC PARTICLES

P. Kopčanský, kopcan@saske.sk, G. Lancz, glancz@saske.sk, N. Tomašovičová, nhudak@saske.sk, M. Koneracká, konerack@saske.sk, V. Závišová, zavisova@saske.sk, Institute of Experimental Physics, Slovak Academy of Sciences, Košice and M. Múčková, M.Muckova@hameln-rds.com, hameln rds, Modra

INTRODUCTION

Magnetic fluids (MFs) are dispersions of magnetic particles in appropriate liquids. A way to prepare them is to create a stabilizing cover (by a surfactant) on the particles of a magnetic material (e. g. magnetite Fe_3O_4, maghemite γ-Fe_2O_3) and subsequently disperse them in the given liquid (water, oil, etc.). The magnetic particles can be incorporated into more complex units of colloidal or micrometric sizes, for instance, they can be encapsulated in polymeric nanospheres. As they can be driven by externally applied magnetic fields, they have got unique possibilities of applications.

The behaviour of such ferrofluids is mainly determined by their magnetic properties. Because of their small size, these magnetic colloids contain a single magnetic domain, and therefore have a permanent magnetic moment proportional to their volume. Although magnetic colloids are ferromagnetic on the molecular scale, they resemble a paramagnet on the colloidal scale. Such a system of particles does not retain any remanent magnetisation as it is superparamagnetic, i.e. the particles have no hysteresis. Due to their superparamagnetic nature, ferrofluids behave as non-magnetic fluids under conditions of zero magnetic field. Each coated particle will behave as a single domain particle and so any rotation of magnetisation is brought about both Brownian and Néel mechanisms. Thermal fluctuation are sufficient to keep the magnetisation vector of particles randomly oriented, such that the net magnetisation of the system is zero. In the presence of a magnetic field, the magnetic moment of the particles will try to align with the magnetic field direction leading to a macroscopic megnetization of the liquid. An important property of concentrated ferrofluids is that they are strongly attracted by permanent magnets, while their liquid character is preserved. The attraction can be strong enough to overcome the force of gravity.

The energy of a photon of the infrared (IR) spectrum responds to the changes in the vibrational-rotational state of molecules or atomic groups. Therefore, the IR spectrum of a sample may identify the presence of some compounds and reveal interactions between their atomic groups. A common range investigated at an IR measurement is 4000 – 400 cm^{-1}. A lot of compounds have got absorption bands in this range and can be identified for this. An IR spectrum of a sample can be collected by various measuring methods. For example, solid specimens can be mixed with KBr and pressed into a pellet, for liquid samples a ZnSe cell may be suitable. These materials cause a lower wavenumber-limit of the obtainable spectrum for their absorption (KBr ca. 400 cm^{-1}, ZnSe ca. 530 cm^{-1} when measuring in transmission mode).

We utilized IR spectroscopy to characterise the components of MFs proposed for various employments. We tried to reveal possible interactions between these components and to confirm the presence of required compounds.

MATERIALS AND METHODS

This section describes the preparation of specimens that were investigated using IR spectroscopy and also the methods of spectrum collection and data evaluation.

Spherical magnetic particles

The synthesis of the spherical magnetic nanoparticles was based on co-precipitation of Fe^{2+} and Fe^{3+} salts by NH_4OH at 60°C. To obtain Fe_3O_4 precipitate, $FeCl_2.4H_2O$ and $FeCl_3.6H_2O$ were dissolved in deionized water by vigorous stirring (the ratio Fe^{3+}/Fe^{2+} was 2:1). The solution was heated to 80°C and 25% NH_4OH was added. The precipitate was isolated from solution by magnetic decantation by washing with water. The magnetic properties were estimated by magnetization measurements using a vibrating sample magnetometer (VSM) and the size and morphology of the particles were determined by transmission electron microscopy (TEM) (Fig.1.) and atomic force microscopy (AFM) working in taping mode. The mean diameter of obtained magnetic nanoparticles was 11.6 nm.

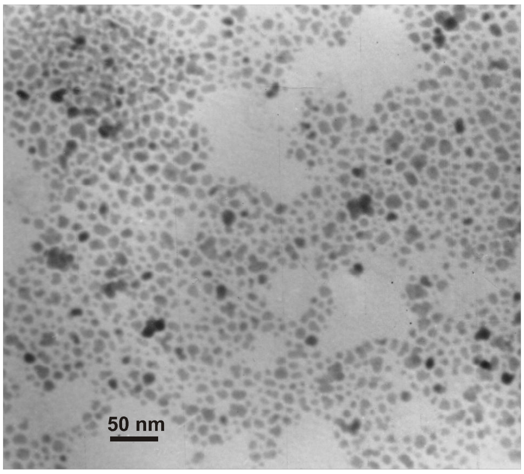

Fig.1 TEM image of the prepared spherical particles.

Rod-like magnetic particles

For some purposes, it is needed to prepare magnetic particles of non-spherical shape. In order to obtain rod-like (elongated) particles that can introduce higher anisotropy into given systems (e. g. particles to dope liquid crystals, see below), various synthetic methods are tried.

The synthesis of rod-like magnetic particles consists in the thermal decomposition of urea and subsequent hydrolysis in a water based solution containing iron(III) chloride and iron(II) sulphate [1]. According to the authors, the molar ratio Fe^{3+}: Fe^{2+} has to be kept at 2 : 1. The mechanism of synthesis can be roughly written by these equations:

$(NH_2)_2CO + H_2O \rightarrow 2\ NH_3 + CO_2$ (1)

$NH_3 + H_2O \rightarrow NH_4^+ + OH^-$ (2)

$Fe^{3+} + 3\ OH^- \rightarrow \alpha$ - FeOOH (goethite) + H_2O

$Fe^{2+} + 2\ OH^- \rightarrow Fe(OH)_2$

2 α - FeOOH + $Fe(OH)_2$ □ Fe_3O_4 (magnetite) + 2 H_2O

If these reactions take place under reflux condition, carbon dioxide is allowed to leave the reaction environment and the pH value rises continuously (equations 1 & 2). In our case, the reflux condition was changed. Various reactant amounts were checked out (Rod A, F, H). The used amounts and conditions are described below:

Rod A

0.6756 g of $FeCl_3 \cdot 6\ H_2O$, 0.3426 g of $FeSO_4 \cdot 7\ H_2O$ and 0.60 g of $(NH_2)_2CO$ were dissolved in 10 ml of deoxygenated (nitrogen-purged) water. This mixture was heated using a modified reflux apparatus with a closed condenser – the pressure was somewhat stabilised with an air pump at the beginning. Heating for 12 h with a water bath at 90 – 95 °C followed. After the cooling it was standing for 12 h – the aging process was taking place. The arisen dark reddish-brown precipitate was washed several times (at least 6 times) with deoxygenated water and dried.

Rod F

The procedure of preparation of this sample was similar as for Rod A but the molar ratio urea/iron was higher: 1.217 g of $FeCl_3$, 1.042 g of $FeSO_4 \cdot 7\ H_2O$ and 2.748 g of $(NH_2)_2CO$ were dissolved in 100 ml of deoxygenated water. The subsequent procedure (heating, aging, washing) wasn't changed.

Rod H

The procedure of preparation was also similar as for Rods A and F, but oleic acid as a new reactant was applied: 0.65 g of $FeCl_3 \cdot 6\ H_2O$, 0.32 g of $FeSO_4 \cdot 7\ H_2O$, 0.587 g of $(NH_2)_2CO$ and 0.5 ml of oleic acid were mixed with 100 ml of deoxygenated water. Sonication followed the adding of oleic acid, the subsequent procedure (heating, aging, washing) wasn't changed.

A summary is given in Table 1.

TAB. 1. Used reactant amounts for synthesis of rod-like magnetic particles

Rod sample	Fe^{2+}	Fe^{3+}	Urea	Oleic acid	H_2O
A	0.0012 mol	0.0025 mol	0.010 mol	-	10 ml
F	0.0037 mol	0.0075 mol	0.046 mol	-	100 ml
H	0.0012 mol	0.0024 mol	0.010 mol	0.5 ml	100 ml

Magnetite (spherical particles) can be simply obtained by co-precipitation from solutions of ferric and ferrous salts (e. g. iron(III) chloride and iron(II) sulphate): the water based solutions are mixed (at the molar ratio $Fe^{3+} : Fe^{2+} = 2 : 1$) and subsequently ammonia is added. The black precipitate (Fe_3O_4) is then washed with deionised water using a magnet to speed up and fasten the sedimentation of magnetite during the cleaning procedure.

Transmission electron microscopy (TEM) and scanning electron microscopy (SEM) were also used to characterise sample Rod A (SEM: JEOL 7000F microscope, TEM: Tesla BS 500 microscope).

Liquid crystal 6CHBT doped with magnetic particles

The term nematic phase of a liquid crystal (LC) refers to one of the possible phases in which the molecules have got an orientational order. Ferronematics are nematic LCs in which magnetic particles have been dispersed. They are prepared with the purpose to increase the value of anisotropy of diamagnetic susceptibility and to enhance the controllability of molecules of LCs by external magnetic fields in this way [2].

The spherical magnetite nanoparticles were used as dopants for the liquid crystal 1-isothiocyanato-4-(*trans*-4-hexylcyclohexyl)benzene (6CHBT). The precursor was the so-called magnetic paste, which was introduced into a mixture of 6CHBT and phenyl isothiocyanate (PhNCS). This magnetite-doped LC is denoted Fe_3O_4+6CHBT+PhNCS.

A typical preparation procedure of the magnetic paste: To a heated (85 °C) mixture of water solutions of iron(II) sulphate (0.055 mol Fe^{II} in 150 ml) and iron(III) chloride (54 ml, 30 wt%), ammonium hydroxide (75 ml of commercial NH_3 water solution, ca. 26 %) was added at once, during vigorous stirring. Fine magnetite particles precipitated. Oleic acid (150 ml) was added drop-wise, this addition took 20 min. The product was the magnetic gel, that was left to cool down to room temperature and then it was washed with deionised water (using a magnet to settle the gel). The redundant oleic acid was removed by washing with acetone.

The preparation of magnetic-particles-doped LC: The prepared Fe_3O_4 particles were introduced into 6CHBT by dispersing the magnetic paste. In our case, first, the LC (6CHBT) was slightly diluted with phenyl isothiocyanate (PhNCS, approx. 10 molar % of PhNCS in the resulting solution). Then, the magnetic paste was dispersed in this solution, which was heated to isotropic phase and stirred for the preparation.

Magnetic fluid for cancer therapy

MFs carrying anticancer agents have to transport the contained drug to the tumour avoiding the action of the drug on healthy tissue and minimize the side-effects in this way.

In our study, the main component of this MF were polymeric nanoparticles – nanospheres (NPs) that contained the anticancer drug Taxol (paclitaxel) and poly(ethylene glycol)/oleate-coated magnetite particles. These magnetic polymeric nanospheres (MNPs) loaded with drug were prepared by the modified nanoprecipitation method [3, 4].

The polymer used for the encapsulation was poly(lactide-*co*-glycolide) (PLGA, lactide : glycolide ratio 85 : 15, 50000–75000 g.mol^{-1}). Another important reactant was Pluronic F 68.

At the preparation of the MNPs for *in vivo* experiments, the drug was used at an amount of 5 mg of Taxol / 100 mg of PLGA 85:15.

Measurement

We carried out the Fourier Transform Infrared (FTIR) measurements using:
(**1**) KBr pellet for some solid samples and (**2**) ZnSe cell for some liquid samples (the thickness of the liquid sample can be adjusted with spacers). Both methods were applied using an Avatar 330 instrument (from Thermo Nicolet, resolution 2 cm^{-1}). (**3**) Attenuated Total Reflectance (ATR-FTIR) measurements were carried out with an FTLA2000-154 instrument (from ABB, resolution 4 cm^{-1}, ZnSe measuring window ('crystal')).

The ATR spectra were collected in two ways: (**3a**) direct measurement - dried matter of sample, (**3b**) dried matter after ethanolic extraction (see below).

One of our goals was to confirm the encapsulation of the drug in the MNPs, and the methods used for this purpose are discussed in more details.

The spectra of magnetic PLGA nanospheres (MNPs) and Taxol loaded MNPs were collected with the KBr pellet method and also using ATR-FTIR spectroscopy.

In the ATR measurement, the dried MNPs were manually pressed onto the measuring window (direct method **3a**). After measuring this kind of untreated specimen, ethanol was added to the sample and the measuring window was partially naked. In this way, a thin layer of Taxol-enriched dried matter was created in the case of Taxol loaded MNPs as the ethanol evaporated (method **3b**).

A physical mixture of Taxol and the NPs with MF (dried matter) was also measured.

The spectra collected with the Avatar instrument were mostly baseline-corrected. Smoothings of central moving average (taking the average of 15 experimental points excluded at the borders of the smoothing range) or Savitzky-Golay (2nd order polynomial, 15 points) [5] were also applied for some spectra. The samples, instrument, technique of measurement and smoothings are summarised in the following Table 2. (The spectra are mostly fitted by multiplying and shifting vertically for clarity.)

TAB. 2. Summary of methods used for obtaining the IR spectra: A – Avatar, F – FTLA, CMA – central moving average, SG – Savitzky – Golay, dried matter – direct ATR measurement of the NPs, EtOH – treatment of the sample with ethanol (extraction)

Sample	Instrument Resolution	Technique	Smoothing range [cm^{-1}]	Fig.
Oxidised Fe_3O_4	A 2 cm^{-1}	KBr pellet	none	3
Rod A			CMA 4000 - 1323	3, 4
Rod F			none	3
Rod H				3, 4
Magnetic paste		ZnSe cell, no spacer		5
6CHBT		ZnSe cell, *d* = 12 µm		
Fe_3O_4+ 6CHBT+ PhNCS				
Taxol		KBr pellet		6
MNPs without Taxol				8
Taxol loaded MNPs				
MF-NPs-Taxol physical mixture				
MNPs without Taxol (**3a**)	F 4 cm^{-1}	ATR - dried matter	SG 1805 - 600	9
Taxol loaded MNPs (**3a**)		ATR - dried matter	none	
MNPs without Taxol (**3b**)		ATR - EtOH		
Taxol loaded MNPs (**3b**)		ATR - EtOH		

RESULTS AND DISCUSSION

Characterisation of rod-like particles

Fig. 2 and 3 show the TEM and SEM images of sample A of the prepared rod-like particles.

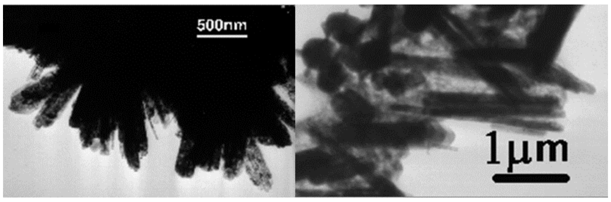

Fig. 2. TEM images of Rod A

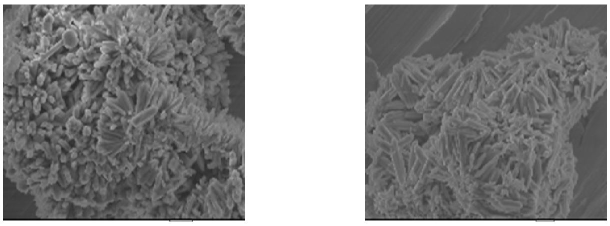

Fig. 3. SEM images of Rod A

The spectra of Rod samples are shown in Fig. 4 and 5. As a reference, a spectrum of oxidised magnetite is included in Fig. 4. The observation that the magnetite was oxidised stems from the comparison of the measured spectrum with published spectra of iron oxides [6]: there are shoulders at 629 cm^{-1} and 434 cm^{-1} that may refer to γ-Fe_2O_3.

The main component of the samples A and H is goethite. The identification was done according to the article of Weckler and Lutz [7]. The bands at ca. 800 and 900 cm^{-1} (OH librations, out-of-plane and in-plane, respectively [7]) prove the presence of goethite in all Rod samples. A significant shift of the position of the band near 400 cm^{-1} (Rod A: 415 cm^{-1}) is in agreement with a previous observation by Krehula et al [8]. Oleic acid is obvious in sample H. The absorption band at 1713 cm^{-1} refers to the stretching C=O vibration of the undissociated (COOH) carboxyl group.

Sample F is missing a typical band of goethite referring to the OH stretching mode (it is observed at 3136 cm^{-1} for sample H) and thus, it is probably partially converted. Taking into account the band at 571 cm^{-1}, magnetite could be the product of this conversion. There isn't observed a significant absorption band with a maximum absorption at ca. 1595 cm^{-1} as it is in the case of the Fe_3O_4 based magnetic paste (see Fig. 6). The presence of carboxylate (oleate) anions may be suggested by the absorption in the range ca. 1580 – 1500 cm^{-1}

Results for the magnetic paste and the 6CHBT ferronematic

The band of the magnetic paste at 1593 cm^{-1} refers to oleate anion, it is caused by the chemisorption of oleic acid on Fe_3O_4 [9]. The COOH group (not dissociated) of oleic acid is visible at 1711 cm^{-1}.

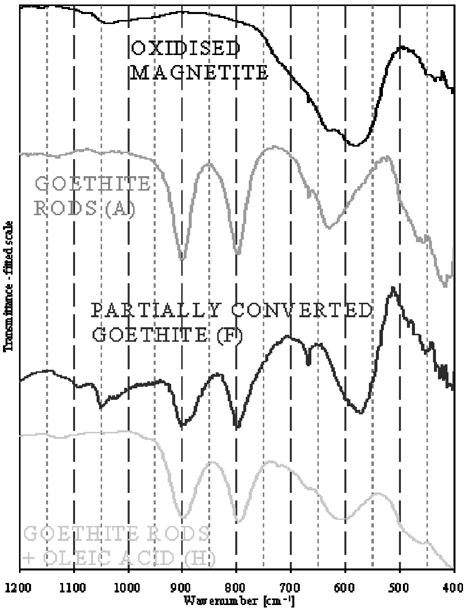

Fig. 4. Spectra of the samples Rod A (goethite), Rod F (impure goethite) and Rod H (oleic acid covered goethite). The spectrum of oxidised magnetite is also shown for comparison.

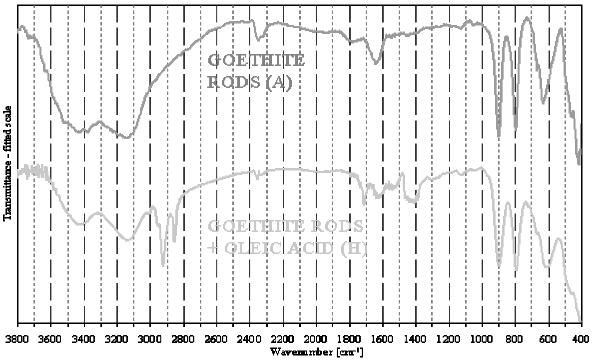

Fig. 5. The spectra of Rod A (goethite) and Rod H (goethite covered with oleic acid).

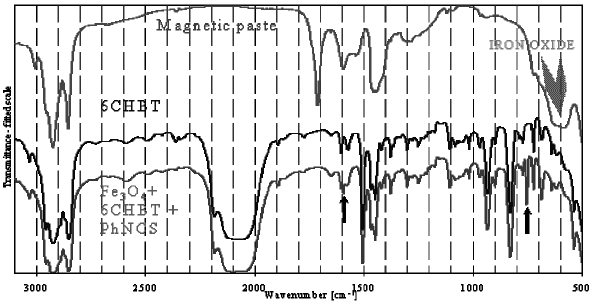

Fig. 6. Magnetite particles doped LC 6CHBT (Fe_3O_4+6CHBT+PhNCS) prepared using the magnetic paste and PhNCS. The arrows are pointing at some remarkable differences between pure LC and doped LC – the presence of PhNCS is obvious.

Examination of the anticancer magnetic nanospheres

The images of the Taxol molecule, and the Taxol-carrying MF are shown in Fig 8. As a reference for the MNPs spectra, the spectrum of Taxol in KBr is shown in Fig. 7.

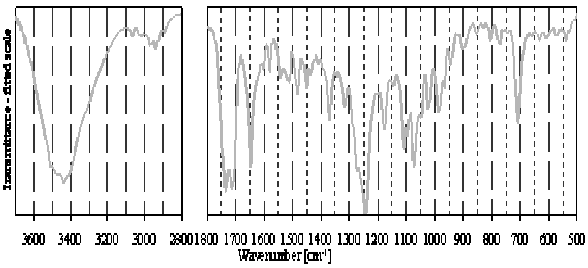

Fig. 7. The IR spectrum of Taxol collected with KBr pellet method

It should be noted, that the KBr pellet sample of Taxol loaded MNPs (Fig. 9) was prepared with a quite large amount of Taxol (40 mg / 100 mg of PLGA), probably not the whole amount of Taxol was encapsulated in the polymer matrix. There are differences between the physical mixture MF-NPs-Taxol and Taxol loaded MNPs – some absorption bands of Taxol are observed at altered wavenumbers, for example 1250 cm^{-1} for the sample of Taxol loaded MNPs, and 1242 cm^{-1} for the physical mixture.

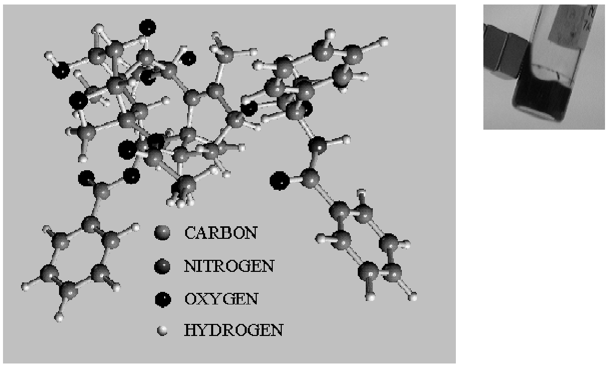

Fig. 8. Taxol loaded PLGA NPs being attracted by magnets. A model of the Taxol molecule – initial data obtained from the HIC-Up database [10], image created using the programs Moldraw [11], Molden, Gaussian, POV-Ray

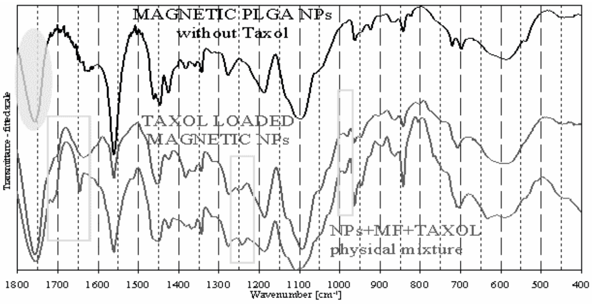

Fig. 9: Spectra of MNPs, Taxol loaded MNPs and physical mixture in KBr pellets. Some regions of obvious differences are marked with rectangles, the shaded band belongs to PLGA.

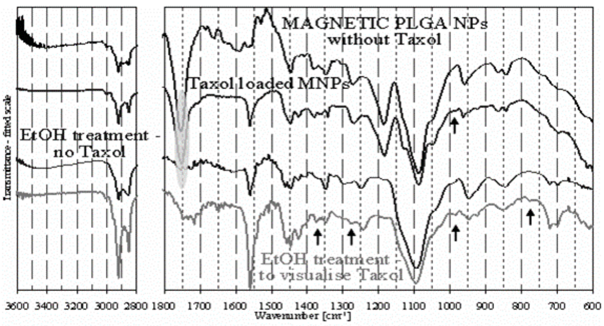

Fig. 10. IR spectra of the MNPs collected with ATR method.

Fig. 10. shows the results of ATR measurements. Comparing the spectra of Taxol loaded and Taxol-less untreated nanospheres, one can see that the manifestation of Taxol is weak – a weak absorption band is visible at 984 cm^{-1}. The difference between Taxol-less and Taxol loaded MNPs in the range 1300 – 1700 cm^{-1} is not reliable to prove the presence of Taxol in the untreated samples – the spectrum at the top had to be smoothed. (Using KBr pellet method, see Fig. 8, the band at 1562 cm^{-1} is clearly visible for the MNPs without Taxol.)

In contrast, using ethanol, Taxol is clearly visible at 1277 cm^{-1} and other wavenumbers (marked with arrows). The reason is the weak solubility of PLGA in ethanol, which allows Taxol to be extracted from the polymer matrix. In agreement with this fact, a reduction of absorption bands at ca. 1750 cm^{-1} and at 1184 cm^{-1} is observable. These bands belong to PLGA.

The presence of the drug is obvious, e. g. at 1277 cm^{-1}. The weak bands/shoulders at 1734, 1717, 1647, 1541, 1508, 1489, 1375, 777 cm^{-1} may refer to Taxol or possibly to its product with ethanol, for it undergoes transesterification in methanolic solution [12]. The band position near 777 cm^{-1} is typical for this ethanolic treatment of Taxol – it is observed for the dried matter of ethanolic Taxol solution with ATR method (not shown), whereas Taxol in KBr shows a band at 771 cm^{-1}. That is, some bands are shifted in comparison with the spectrum of Taxol in KBr.

CONCLUSIONS

Considering that magnetite has got an absorption band at ca. 580 cm^{-1}: Using a ZnSe measuring window (‘crystal’) in the ATR technique resulted in a limitation of the observed spectral range at ca. 600 cm^{-1}. Thus, magnetite, a basic component of many MFs, couldn’t be detected with this method. If ZnSe cell is used (transmission mode), this limit is extended to ca. 530 cm^{-1}, and magnetite is observable (see Fig. 6, magnetic paste).

Various reactant ratios have been checked out with the aim of preparing rod-like magnetic particles. IR spectroscopy identified the products of these attempts.

Oleic acid is a common reactant of MF-syntheses. It may be attached to the magnetic particles as a result of chemical reaction (oleate anions may arise).

The incorporation of the anticancer drug Taxol into magnetic PLGA NPs has been confirmed using IR spectroscopy. Collecting the IR spectrum of the dried magnetic nanospheres in the state in they are may not be enough to undisputedly identify Taxol in the sample, when it is present at a concentration that was used for *in vivo* experiments. To detect Taxol in the nanospheres, extraction may be needed before collecting the IR spectrum.

ACKNOWLEDGMENT: This work was supported by by implementation of the 'Cooperative phenomena and phase transitions in nanosystems with perspective utilization in nano- and biotechnology' project No. 26220120021, Funding for the operational research and development program was provided by the European Regional Development Fund. Author GL would like to thank to Jozef Uličný and Tomáš Tokár at the Department of Biophysics of P. J. Šafárik University, Faculty of Science, for the help in the obtaining of the image of Taxol molecule.

REFERENCES

1. S. Lian et al., *Solid State Communications* **129**, 485 (2004).
2. F. Brochard, P. G. de Gennes, *J. Physique* **31**, 691 (1970).
3. C. Fonseca et al., *Journal of Controlled Release* **83**, 273 (2002).
4. V. Závišová et al., *J. Magn. Magn. Mater.* **321**, 1613 (2009).
5. A. Savitzky, M. J. E. Golay, *Analytical Chemistry* **36**, 1627 (1964).
6. B. Gillot, *Vibrational Spectroscopy* **6**, 127 (1994).
7. B. Weckler, H. D. Lutz, *Eur. J. Solid State Inorg. Chem.* **t. 35**, 531 (1998).
8. S. Krehula et al., *Materials Letters* **54**, 108 (2002).
9. X. Liu et al., *J. Magn. Magn. Mater.* **306**, 248 (2006).
10. G. J. Kleywegt, T. A. Jones, *Acta Cryst.* **D54**, 1119 (1998) (CCP4 Proceedings).
11. P. Ugliengo, D. Viterbo, G. Chiari, *Z. Kristallogr.* **207**, 9 (1993).
12. S. L. Richheimer et al., *Analytical Chemistry* **64**, 2323 (1992).
13. M. Horák, D. Papoušek: Infračervená spektra a struktura molekul (Academia, Praha - 1976).

EFFECT OF NANODIMENSION ON THE PROPERTIES OF III-V FERROMAGNETIC SEMICONDUCTORS

J. Novák, eleknova@savba.sk, I. Vávra, J. Šoltýs, S. Hasenöhrl, Elektrotechnický ústav SAV, Bratislava,
M. Reiffers, Ústav Experimentálnej Fyziky SAV, Watsonova 47, Košice, FHPV PU, Prešov,
P. Štrichovanec, Instituto de Nanoscience de Aragon, Zaragoza, Spain

INTRODUCTION

The study of manganese based III-V diluted magnetic semiconductors (DMS) has attracted great interest due to their potential applications in spintronic devices. These very progressive materials are usually prepared in form of thin epitaxial layers. Molecular beam epitaxy (MBE) and metal organic vapour phase epitaxy (MOVPE) in various growth modes were used to overcome solubility and lattice mismatch limitations with aim to reach the highest possible Curie temperature (T_c). The first ferromagnetic InMnAs was successfully prepared by MBE. Magneto-transport measurements showed that InMnAs containing 1.3% Mn had a T_c close to 10K [1]. This value was very close to Tc= 35 K predicted for InMnAs by application of modified Ruderman, Kittel, Kasuya and Yosida (RKKY) theory [2]. According the RKKY theory, the ferromagnetism in III-V semiconductors is stabilised by presence of free carriers and the magnetic ions that are randomly distributed on the cation sites. A major breakthrough resulted in year 1996 when the synthesis of ferromagnetic GaMnAs with a Curie temperature of 110K was reported. This started a worldwide search for semicondustors with a Curie temperature above room temperature [3].

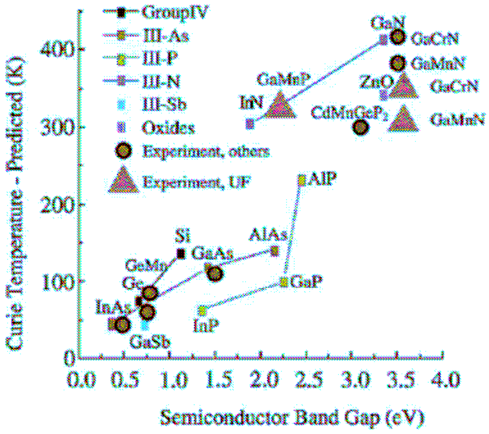

Fig. 1. Predicted Curie temperatures as a function of bandgap, along with some experimentally reported values in the literature [3].

Application of MOVPE technology lead to preparation of InMnAs with concentration of Mn ions in range of 1-15% and Curie temperature of 333K [4]. The T_c value was independent on the Mn concentration. This unexpected property was attributed to the formation of atomic scale clusters. On the other hand, the x-ray diffraction and TEM analysis proved a phase purity and presence of zincblende structure only. These experimental results indicated that ferromagnetism in InMnAs can be stabilised through other mechanism as predicted by RKKY theory. Bouzerar et al [5] proposed a model in which a room temperature ferromagnetism should be possible provided so that the probability of transition metal pair formation is enhanced. In case of GaMnAs it means that for fully correlated pair formation the T_c above 400K may be reached whereas for fully uncorrelated pairs a Tc of 180K was predicted.

The calculations of Kudrnovsky et al [6] showed that alloy is unstable with respect to segregation into related components. Two type of domains – with higher and with lower Mn content may be formatted. Size of these domains may reach several nanometers. In addition, this disorder may be supported by the presence of spinodal decomposition of the alloy. Since disorder depends on alloy preparation conditions, T_c should also strongly depend on the growth method. Especially application of the Stranski – Krastanov growth mode (i.e. technology similar to that is widely used for growth of quantum dots) may lead to the interesting results due to contemporary influence of the applied strain and limited source of material. In adition, it was found that InMnAs quantum dot can be ferromagnetic at room temperature when there is only one hole in the dot. This prediction made by Zhang depicts dependence of the Curie temperature on the dot diameter [7]. Recently, Chen et al. [8] presented properties of $In_{1-x}Mn_xAs$ quantum dots (QD) samples prepared by low temperature MBE growth. MnAs molar fraction increased from x=0.19 up to x=0.45. Microstructure analysis proved that samples with Mn content lower as x=0.38 showed zincblende structure and Curie temperature varied with x in range from 260 to 340K. The magnetic properties of QD samples with x=0.19 and 0.21 were explained as a property of InMnAs material itself without any contribution of MnAs or GaMn nanoclusters. The high T_c value for the other three samples with high Mn content was explained by the enhancement of hybridization strength between the quantum confined carriers in the dots and itinerant carriers in the valence band.

Very high T_c value for InMnAs quantum dots with relatively low Mn content of 16% was presented by Jeon et al [9]. They prepared mutiple stacked self-assembled dots with T_c as high as 400K by MBE. Similarly high T_c of 350K was reported by Holub et al [10] for InMnAs stacked dots prepared with Mn/In flux ratio of 0.15. This high T_c value was explained by the structural and magnetic disorder introduced by a random incorporation and inhomogeneous distribution of Mn atoms.

In this paper, we report the growth of $In_{1-x}Mn_xAs$ dots with low Mn content ($0<x<0.11$) by MOVPE technique. The aim of this study is to verify conclusions made by Chen that InMnAs quantum dot samples with x=0.19 and 0.21 represent properties of InMnAs material and a presence of nanoclusters may be fully ruled out. In this case, the Curie temperature of our samples should be lower in comparison to T_c values presented by Chen but they should be related to the InMnAs composition.

EXPERIMENTAL

The InMnAs structures (InMnAs layers or InMnAs quantum dots) presented within this study were grown on (100) GaAs substrates by Aixtron 200 RD equipment. At first, a set of In_{1-x} Mn_xAs single epitaxial layers with various composition was prepared with the aim to characterize material that was subsequently intended for the preparation of dots. The growth condition were optimized for growth of single phase InMnAs ternary without Mn or MnAs precipitates. All InMnAs samples under study were grown at a V/III ratio of 133. The composition of the ternary was controled by adjusting the ratio between the partial pressure of $((MeCp)_2Mn$ to TMIn. The partial pressure of $(MeCp)_2Mn$ was kept constant at a value of 3.59×10^{-2} mbar and the partial pressure TMIn was decreased. The p_{Mn}/p_{In} ratio in the gas phase increased from 0 to a maximum value of 0.582. This composition of the gas phase was used for preparation of InMnAs dots too.

STRUCTURAL PROPERTIES

The properties of InMnAs single layers were characterized by means of Van der Pauw method, transmission electron microscopy (TEM), x-ray fluorescence measurements (EDX) and commercial superconducting quantum interference device magnetometer (SQUID). All InMnAs layers (with nominal thickness of 300 nm, marked as MO996, MO997 and MO1014) were p-type with Hall hole concentration in range $3\text{-}4 \times 10^{18}$ cm^{-3} with Hall hole mobility lower as 100 cm^2/Vs. TEM cross-sectional imaging and electron diffraction analysis showed that all three InMnAs layers are pseudomorphic in relation to GaAs substrate with zincblende structure. The nominal Mn concentrations in all three epitaxial layers were determined using EDX measurements. These measurements showed that changing of p_{Mn}/p_{In} ratio in the gas phase led to an increase of Mn content in the $In_{1-x}Mn_xAs$. We prepared layers with x=0.051, 0.075 and 0.102. The Curie temperature obtained by SQUID measurements after subtraction of diamagnetic contribution of the GaAs substrate was approximately 343K. All these properties are fully in agreement with that ones published for similar materials by Blattner group [4].

The InMnAs/GaAs dot structures were prepared in the following way: The substrate was at first overgrown with two buffer layers. The first one was a high-temperature GaAs buffer layer (T_g=640 °C) and the subsequent one was a 30 nm thick low-temperature GaAs buffer (T_g=500°C). Following the buffer layers, the InMnAs 0.9 ML thick wetting layer was grown at T_g=500 °C. These samples were marked as MO998, MO1015 and MO1020.

Atomic force microscopy (AFM) study showed that the size and density of InMnAs dots depend on the Mn content. At the lowest Mn content the average dots diameter was between 20 and 30 nm and average height close to 7-8 nm. For the highest Mn content the dot average diameter increased up to 50 nm and average dot height reached 20nm. In addition, the dot density decreased from 6×10^9 cm^{-2} (for p_{Mn}/p_{In} =0.303) to 3.2×10^9 cm^{-2} (for p_{Mn}/p_{In} =0.582). AFM measurements showed a clear tendency of InMnAs dots to concentrate deposited material into lower number of dots with the larger diameter.

Detailed characterization of the microstructure and the crystalographic phase of the deposited InMnAs dots were performed by crossectional and plane TEM measurements.

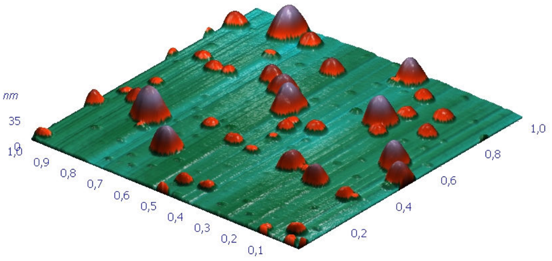

Fig.2 AFM surface scan of InMnAs dot sample with Mn content of 7.5 %.

Fig.3 depicts TEM cross-sectional view of the sample MO1015 (with the highest Mn content) in the 110 direction. Size of dots evaluated from TEM measurements is consistent to that one evaluated from AFM measurements. Some structural defects in the low temperature buffer are visible in this figure but without influence on the dot. Heterointerface between the buffer and dots is clean a nd sharp. Electron diffraction pattern indicated presence of two zincblende structures. One represents the GaAs substrate, the second one presents the zincblende structure of InMnAs dots. Electron diffraction pattern for (004) direction was used for this estimation due to its coherence with used in HRXRD charactzerization.The lattice mismatch between the dot structure and GaAs substrate was estimated to be close

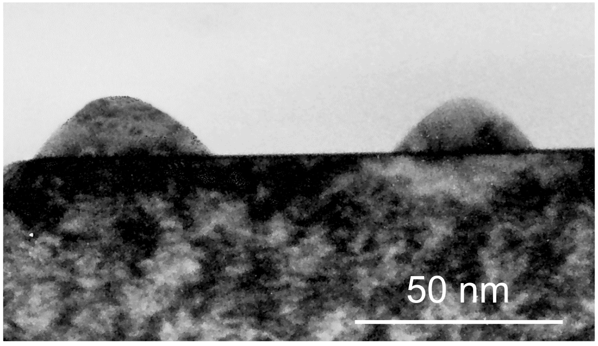

Fig.3 Cross-sectional TEM image of InMnAs dot structure prepared on low temperature GaAs buffer. Sample MO998.

to 6.6 %. It means that the lattice constant of dots is smaller as at InAs or zincblende MnAs but larger that of GaAs (see Fig.4).

A TEM plane view of the InMnAs dot is shown in Fig. 5. The moiré fringes present at this picture are typical for a plastically relaxed structure. The fringes result from the electron diffraction on the two different lattices. One lattice belongs to the GaAs substrate (or buffer layer) and the second one belongs to the relaxed material of InMnAs dots.

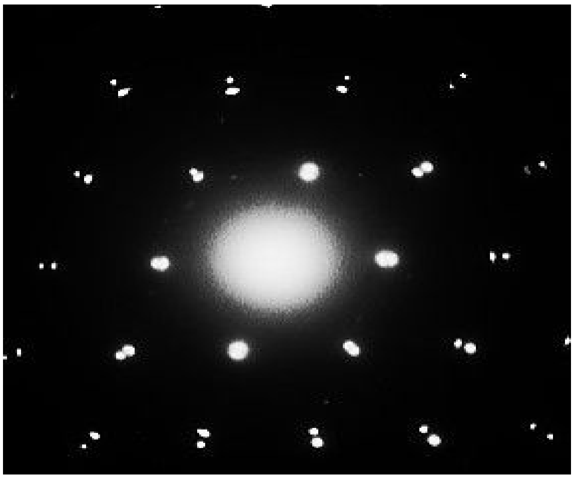

Fig.4 Electron diffraction pattern describes the presence of two zincblende structures (one for GaAs, second one for the InMnAs dot structure)

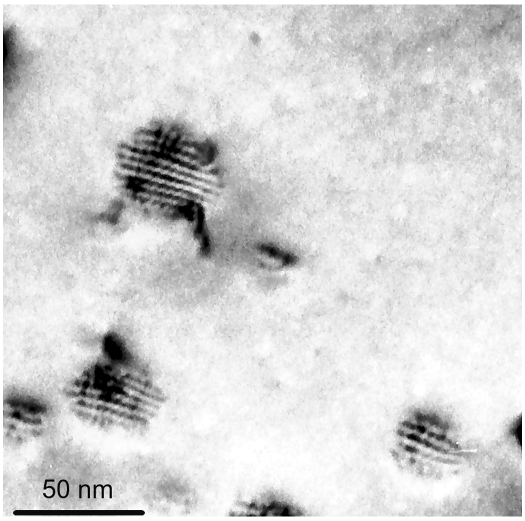

Fig.5 Plan view TEM image of InMnAs dot structure prepared on low temperature GaAs buffer. Moiree fringes indicate plastically relaxed structure

In addition, we used EDX measurement system connected with TEM machine for evaluation of InMnAs dots composition. We used dot structure showed in Fig.3. According to the spot dimension, only dots laterally larger than 50 nm were used. This experiment proved that manganese is incorporated in the dots a its average content in InMnAs was estimated as a ternary compound with a MnAs molar fraction of x=0.106. This x value obtained for dots is something higher as that one for single layer prepared under the same gas flow (x=0.102). We suppose that this small discrepancy may be caused by two various reasons. One is the use of two various EDX systems (standard for single layers and another one connected with TEM for dots). Second reason may be connected with the MOVPE epitaxial growth where the deposition of manganese may be different in case of thick epitaxial layer and very thin wetting layer for the formation of dots.

MAGNETIC PROPERTIES

The temperature dependent magnetic properties of epitaxial single layers and quantum dots were measured using a superconducting quantum interference device (SQUID) with a magnetic field in range 50-1500 Oe applied perpendiculary to the plane of the sample. After subtraction of the diamagnetic contribution of the GaAs substrate the resulting magnetization was evaluated. An example of the magnetization curves for a single epitaxial layer and the dot structure prepared at the same partial pressure ratio p_{Mn}/p_{In} =0.582 (i.e. x above 0.1) is shown in Fig.6. Sample MO1014 presents single layer and sample M01015 is sample with dots prepared under Stranski-Krastanov growth mode. A Curie temperature of 343K was estimated for all three InMnAs single layers under study. This value is very similar to that published for single epitaxial layers in [4] and it is caused by ordering of the magnetic phase in this material.

On the other hand, the Curie temperature of all three dot samples depended on the dots material composition. The Curie temperatures of 41, 53 and 123 K were estimated for x=0.051, 0.075 and 0.102, respectively.

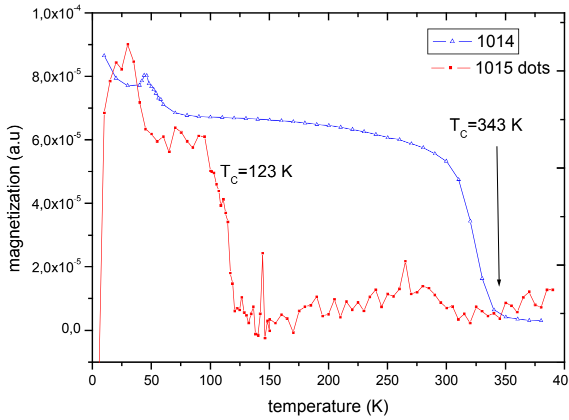

Fig.6 Comparison of magnetization curves for InMnAs single epitaxial layer (MO1014) and dot structure (MO1015) prepared from the same gas phase composition.

This Tc dependence indicates that Stranski-Krastanov growth mode enables fully another creation of the crystal structure with strong impact on the magnetic properties. It seems that in this case the InMnAs material is more uniform with very low tendency to create the ordered regions. Although the presence of ordered structure cannot be fully excluded, the magnetization measurements showed that Curie temperature of quantum dot structures depends on the composition of the ternary.

The magnetic field dependence of in-plane magnetization for all QD samples was measured in temperature interval from 2K up to 350K. All QD samples showed clear ferromagnetic hysteresis. Fig.7 shows M-H dependence of sample MO1015 (x=0.106, T_c=123K) measured at 5 and 110K, respectively. Both curves showed a clear hysteresis loops indicating the existence of ferromagnetism at both temperatures.

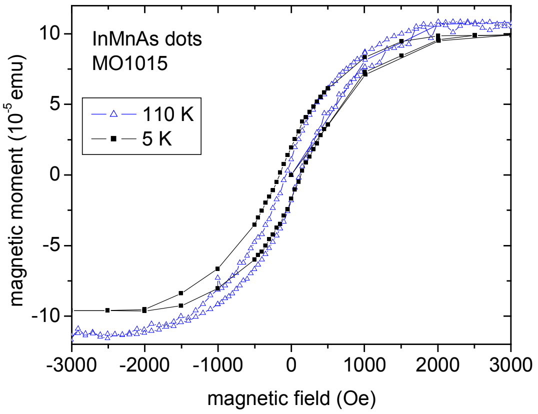

Fig. 7. Dependence of magnetization on the magnetic field for QD sample MO1015.

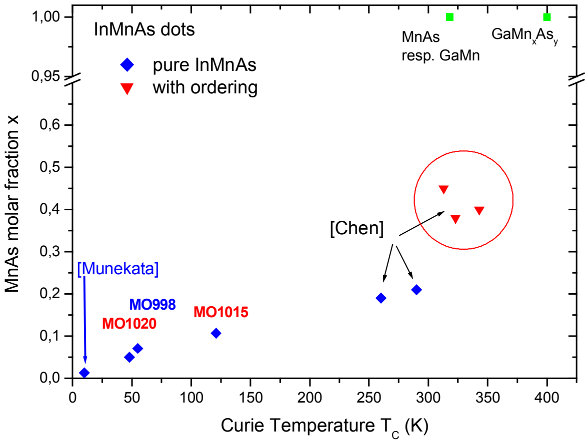

Fig. 8. Relation between Curie temperature and composition for InMnAs quantum dot structures with and without ordering

Fig.8 summarizes relation between estimated Curie temperature and material composition for our samples and it compares our results with the other published data. As follows from this figure, the QDs may be divided into two groups. The first group presents nearly linear relation between T_c and increasing Mn content in the sample. This property follows the modified RKKY predictions and may be explained as a property of pure InMnAs material without presence of ordering effect. The magnetic properties of the second group are influenced by the presence of ordered domains and consequently they show much higher T_c values as it is predicted by RKKY theory.

CONCLUSIONS

In conclusion, we prepared a set of InMnAs samples in form of epitaxial layers and quantum dot structures. EDX measurements showed that Mn content in single layers and QD structures (prepared from the identical gas phase) is the same. Structural characterization proved that InMnAs dots prepared on the GaAs substrate are pseudomorphic, relaxed and they are created in the zincblende crystallographic structure. The interface between the GaAs buffer and dot structure is sharp without inclusions or clusters.

We showed that at the certain composition of the gas phase the resulting magnetic properties may be fully different in the dependence on the growth mode used. While at single epitaxial layers the room temperature ferromagnetizm was observed, the QD structures showed clear dependence of the estimated T_c values on the composition of InMnAs ternary. This dependence is fully coherent with the dependence published by Chen [8]. Both results support the assumption that quantum dot technology allows to prepare pure InMnAs material without ordered domains. Such material is very interesting for study of the coherence between the theoretical predictions and the real properties of material.

ACKNOWLEDGMENT: This research was partially supported by VEGA Agency No. 2/6096/27 and APVV projects VVCE-0049-07 and APVV-0731-07, by VVCE-0058-07, VEGA 2/0007/09 and the CLTP as the Centre of Excellence of the SAS. The liquid nitrogen for the experiment has been sponsored by the U.S. Steel Kosice, s.r.o.

REFERENCES

1. H. Munekata, H. Ohno, S. von Molnár, A. Segmüller, L.L. Chang and L. Esaki: Phys. Rev. Lett. **63** (1989), 1849.
2. T. Dietl, H. Ohno. and F. Matsukura: Phys. Rev. **B63** (2001) 195205
3. S.J. Pearton: Materials Science and Engineering **R 40** (2003) 137–168
4. A.J. Blattner, J. Lensch and B.W. Wessels: J. Electron. Mater. **30** (2001) 1408
5. G. Bouzerar, T. Zima, and J. Kudnrovsky: Europhysics Letter 69 (2005) 812
6. J. Kudnrovsky, V. Drchal, G. Bouzerar and R. Bouzerar: Ordering effects in diluted magnetic semiconductors *Phase Transit.* **80 (**2007)333–50
7. X.W. Zhang, W.J.Fan, S.S. Li and J.B. Xia: Appl. Phys. Lett. **92** (2008) 013129
8. Y.F. Chen, J.H. Huang, W.N. Lee, T.S. Chin, R.T. Huang, F.R. Chen, J.J. Kai and H.C. Ku: Appl. Phys. Lett. **90** (2007) 022505
9. M. Holub, S. Chakrabati, S Fathpour, P. Bhattacharya, Y. Lei and S. Ghosh, Appl. Phys. Lett. **85** (2004) 973
10. H.C. Jeon, T.W. Kang and T.W. Kim, J. Cryst. Growth **310** (2008) 541

MAGNETIC PROPERTIES OF POWDER AND COMPACTED Fe, Co AND Ni BASED MATERIALS

P. Kollár[1], peter.kollar@upjs.sk, J. Füzer[1], jan.fuzer@upjs.sk, J. Bednarčík[1,2], jozef.bednarcik@desy.de,
D. Olekšáková[3], denisa.oleksaková@tuke.sk, J. Füzerová[3], jana.fuzerova@tuke.sk, R. Bureš[4], rbures@imr.saske.sk,
M. Fáberová[4], mfaberova@imr.saske.sk
[1]Department of Condensed Matter Physics, Institute of Physics, Faculty of Science, P. J. Šafárik University, Park Angelinum 9, 04154 Košice, Slovakia
[2]Deutsches Elektronen-Synchrotron (HASYLAB), Notkestraße 85, 22607 Hamburg, Germany
[3]Department of Applied Mathematics, Faculty of Mechanical Engineering, Technical University in Košice, Letná 9, 04200 Košice, Slovakia
[4]Institute of Materials Research, Slovak Academy of Sciences, Watsonova 47, 043 53 Košice, Slovakia

INTRODUCTION

Soft magnetic composites is well known group of materials suitable for various AC and DC electromagnetic applications as cores with three dimensional isotropic ferromagnetic behavior for transformers, electromotors and electromagnetic circuits, sensors, electromagnetic actuation devices, low frequency filters, induction field coils, magnetic seal systems and magnetic field shielding [1]. In some applications these composites together with bulk metallic glasses (BMG) have an ambition to replace electrical steel sheets or ferrites [1, 2].

Among the recently developed metallic glass systems, Fe-based alloys have attracted considerable attention related to their good soft magnetic properties with near-to-zero magnetostriction, high saturation magnetization, low core loss and high permeability, which render the material a potential candidate for a variety of applications such as magnetic recording heads and electronic sensors [3-5]. Amorphous Vitroperm ($Fe_{73}Cu_1Nb_3Si_{16}B_7$) alloy will transform into nanocrystalline material with optimum magnetic performances when it is annealed appropriately [6]. Amorphous Fe-Co-Si-B alloys [7] and Ni-Fe based polycrystalline materials [8] milled in high-energy planetary mill exhibit also very good properties suitable for preparation of soft magnetic bulk materials.

The composite materials consisting of small particles of ferromagnetic material (pure elements of Fe, Co, Ni or alloys based on them) isolated by an electrical insulating film exhibiting soft magnetic properties as low hysteresis losses, low eddy current losses, high permeability at low magnetic field and high saturation flux density extend possibilities this group of materials for higher frequency AC applications [9, 10].

One of the ways to prepare bulk material is compaction of powder produced by milling of amorphous or nanocrystalline ribbons [11, 12]. Ball milling technique has been successfully used to prepare many alloys in powder form, which are therefore suitable for compaction into a variety of shapes [13, 14].

The aim of this work was to investigate the structure and magnetic properties of various bulk soft magnetic materials prepared by compaction of Fe, Ni and Co based alloys with and without of resin to extend possibilities for DC and AC application.

DC AND AC MAGNETIC PROPERTIES OF POWDER CORES

Good DC soft magnetic properties required for most applications are high saturation magnetization J_S, high initial permeability μ_i, low coercivity H_c and zero magnetostriction λ_S.

The most important AC properties are power losses W_t (in J/kg) consisting of hysteresis W_h, eddy current W_e and anomalous losses W_a [15, 16]

$$W_t = W_h + W_e + W_a \,. \qquad (1)$$

The total losses of some materials determined experimentally can be separated to the components according to this theory [3, 17, 18].

The total power losses P_t (in W/kg) can be obtained by multifying (1) by frequency

$$P_t = P_h + P_e + P_a = W_h\, f + P_e + P_a \,. \qquad (2)$$

Hysteresis losses W_h (assumed to be frequency independent) can be obtained by extrapolation the total losses frequency dependence to $f = 0$.

The eddy current losses P_e can be according to [15, 16] expressed as

$$P_e = \frac{(\pi\, d\, B_m f)^2}{\beta\, \rho_R\, \rho}, \qquad (3)$$

where d is effective dimension, (for the material prepared by casting d is thickness of the sample, for laminated material thickness of the sheet), B_m is maximum flux density, f frequency, ρ_R specific resistivity, ρ density of the material and β geometrical coefficient. For rectangular cross-section perpendicular to the direction of magnetic flux is

$$\beta = \frac{6}{1 - 0.633\,(w/h)\tanh\,(1.58\; h/w)}, \qquad (4)$$

where w is width and h height of the rectangle.

MAGNETIC PROPERTIES OF NANO-STRUCTURED VITROPERM ALLOY POWDER CORES

The ribbon $Fe_{73}Cu_1Nb_3Si_{16}B_7$ – (Vitroperm 800, provided by Vacuumschmelze Hanau) exhibit after annealing leading to the nanocrystalline state zero saturation magnetostriction [6]. We believe that this property (including excellent soft magnetic properties) is crucible for preparation of soft magnetic bulk by compaction of powder prepared by milling in high energy mill, because non-magnetostrictive material is not sensitive to magnetic hardening by defects creating during milling and compaction acting as mechanical stress field sources acting as pinning centers for domain walls motion.

Two samples of VITROPERM powder were prepared by milling in RETSCH PM4000 planetary ball mill in hardened steel vials with speed of 180 rpm at a ball-to-powder mass ratio of 6:1. First sample R1 was prepared by milling at room temperature and second sample L1 at liquid nitrogen temperature (cryomilling).

All handling of the powder was done in a glove box with controlled atmosphere ($O_2 < 1$ ppm, $H_2O < 1$ ppm). The samples were consolidated at 700 MPa for 5 min at 500°C into cylinders with outer diameter of 10 mm and thickness of 3 mm. The compacts were annealed at temperatures: 500°C, 520°C, 540°C and 560°C, time of annealing was 60 min and heating rate was 10 K/min in argon.

Short-time (6h) ball-milling of $Fe_{73}Cu_1Nb_3Si_{16}B_7$ ribbons has no influence on its structure, determined by XRD analysis, and the powder remained amorphous [12]. More than 90% of powder particles milled at room temperature has the size from 50 μm to 250 μm. Cryomilled powders have larger and smaller particle sizes, from 10 μm to 200 μm [19]. The resulting particle size distribution affects the density of the compacted material, the compacted disk L1 has higher value of the density (6730 kg/m^3) than disk R1 (6709 kg/m^3).

The influence of milling conditions on resulting powder is very good visible on SEM micrographs of the samples milled at liquid nitrogen and room temperatures, Fig.1, 2.

The sample L1 consists of small flat pieces of the ribbon, while pieces of the powder R1 sample have specific form which is result of “plastic” deformation, as we assume, caused by creation of very small crystallites on the area of the sample-ball collision. There is a small free volume closed in each powder piece of the sample R1, which cannot collapse during consolidation, leading to the lower density of the compact in comparison with that for bulk of the sample L1. The low temperature during milling of the sample L1 probably prevented the creation of such free volumes by deformation.

To reduce the total losses we have studied the electrical resistivity (by the Van der Pauw method) and the magnetostriction (by means of the strain gauge method) of all bulk samples obtained with different procedures. Fig. 3 shows the influence of the milling procedures and heat treatment on the resistivity.

Fig. 1. The morphology of the L1 sample, amorphous powder cryomilled for 6 hours and consolidated at 500°C for 5 min

Fig. 2. The morphology of the R1 sample, amorphous powder milled for 6 hours and consolidated at 500°C for 5 min.

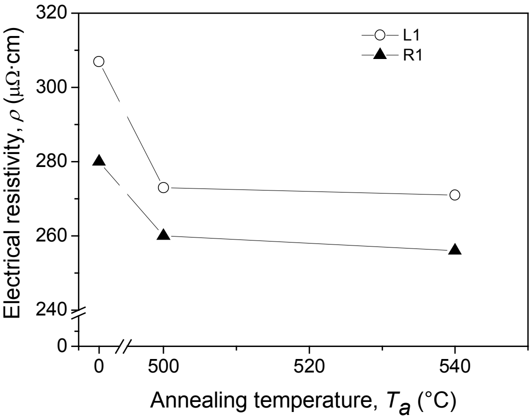

Fig. 3. Electrical resistivity as a function of annealing temperature determined by van der Pauw method.

The contact created between the particles (partially covered by adsorbed gasses and other impurities) during the compaction leads more than twice higher electrical resistivity of the compacted material compared to the same alloy in the form of the ribbon (about 115 μΩ·cm [20]). Further annealing improves this contact and the resistivity decreases with the increase of annealing temperature.

Fig. 4 shows the influence of the milling procedures and heat treatment on saturation magnetostriction.

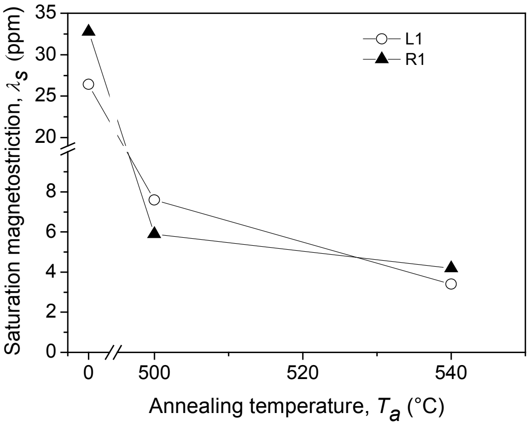

Fig. 4. Saturation magnetostriction as a function of annealing temperature determined by strain-gauge measurements.

Decreasing of the saturation magnetostriction is due to the transformation of amorphous into nanocrystalline phase and the resulting λ_S is affected by the magnetostriction of the forming nanocrystalline grains with different chemical composition. Near zero magnetostriction in nanocrystalline Fe-base alloys requires a crystalline volume fraction with negative magnetostriction in order to compensate the positive value of the amorphous Fe-based matrix [6].

The changes in the DC coercivity (measured by a Förster Koerzimat) with heat treatment were analyzed in both as-compacted and post-annealed disks, Fig. 5.

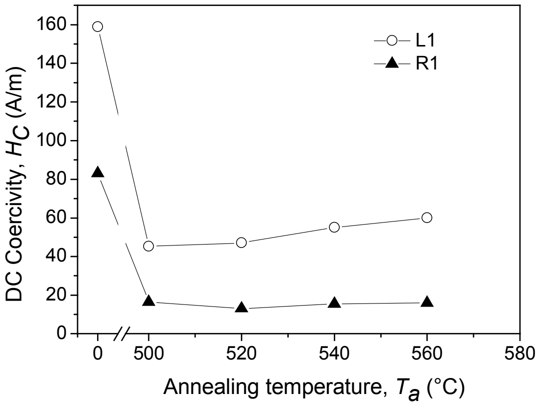

Fig. 5. DC coercivity as a function of annealing temperature determined for bulk samples.

The coercivity, H_C of the compacted samples decreases after annealing reaching a minimum value 13.0 A/m for 520°C (sample R1) and 45 A/m for 500°C (sample L1), respectively. The value of H_C depends mostly on the surface and volume pinning of magnetic domain walls. This contribution is proportional to the product of saturation magnetostriction and the amplitude of stress fluctuations [21]. Further annealing (540°C, 560°C) has no positive influence on the coercivity and values are almost slight greater with increasing of the annealing temperature.

The AC magnetic properties of the bulk samples were investigated by AC hysteresisgraph AMH 401 POD WALKER. Fig. 6 shows the core losses, P and peak permeability, μ_p as a function of frequency for L1 and R1 samples for flux density B_{max}=0.2T.

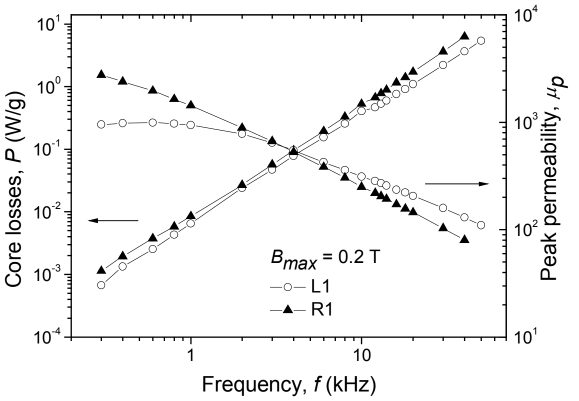

Fig. 6. Frequency dependence of the core losses and the peak permeability for sample L1 and sample R1 for B_{max}=0.2 T. The samples are after annealing at 540°C.

The frequency dependence of the peak permeability for R1 and L1 bulk samples decreases about 10 times on the continuous increase of the frequency from 300 Hz to 50 kHz. The variation of the magnetic peak permeability as a function of frequency is less pronounced for the sample L1, indicating this sample as more suitable candidates for frequency applications. The behavior of the core losses as a function of frequency for both samples is similar, regarding the nature of the electrical resistivity of the samples. The electrical specific resistivity ranges from 273 μΩ·cm for sample L1 to 256 μΩ·cm for sample R1.

For the sample L1 with w=2.56 mm and h=3.54 mm, the calculated value for β (according to eq. (4)) is 10.8366. Separation of losses eq. (2) is complicated by the fact that classical eddy current losses cannot be calculated in a reliable way. Compacted materials are not homogeneous and eddy currents are not restricted to the single sheets but may cover the full thickness or even the package of particles. If we take the largest value of d i.e. $d=h$ we obtain the value of P_e of 2.48 W/g (sample L1, f=10 kHz, B_{max}=0.2 T) which is higher value in comparison with experimentally measured total losses, P of 0.41 W/g. It is important to remark that the values obtained for the coercivity and core losses are comparable and even lower than those reported for other bulk soft magnetic materials such as Ni-Fe or Ni-Fe-Mo permalloys [15] and Fe-Nb-B-Cu alloys [22].

MAGNETIC PROPERTIES OF AMORPHOUS Co-Fe-Si-B BASED POWDER CORES

Amorphous $Co_{70.3}Fe_{4.7}Si_{10}B_{15}$ and $Co_{56}Fe_{16}Zr_{8}B_{20}$ alloys exhibit very good soft magnetic properties with good stability of permeability up to high frequencies and near-to-zero magnetostriction [23]. Their structure is relatively stable with supercooled liquid region deep under crystallization temperature [24]. These materials are also suitable for preparation of bulk samples by hot compaction of powder.

The thin ribbons of amorphous $Co_{70.3}Fe_{4.7}Si_{10}B_{15}$ and $Co_{56}Fe_{16}Zr_{8}B_{20}$ alloys were prepared by melt spinning method. The as-quenched ribbons were subsequently short time milled using a RETSCH PM4000 planetary ball mill. The milling was performed under argon atmosphere with speed of 200 rpm at a ball-to-powder mass ratio of 6:1. The milling times were chosen so that to avoid structural changes during the milling and prepare fine-grained powders. The powder consolidation into bulk samples (cylindrical discs: 10 mm in diameter and 3 mm in thickness) was done in a uniaxial hot press under argon atmosphere. During the consolidation experiments the powders were constant-rate heated at 60 K/min to the consolidation temperature, held isothermally at supercooled liquid region temperatures and pressed for 2 min using a pressure of about 900 MPa.

The bulk prepared by such a way ehibit excellent DC soft magnetic properties [25], Tab. 1

TAB. 1. The saturation magnetic polarization and coercivity of $Co_{70.3}Fe_{4.7}Si_{10}B_{15}$ and $Co_{56}Fe_{16}Zr_{8}B_{20}$ alloys in the form of ribbon, bulk and bulk annealed at 500°C.

Sample		J_S [T]	H_C [A/m]
Co-Fe-Si-B	ribbon	0.83	3
	ring	0.77	23
	annealed ring	0.77	9
Co-Fe-Zr-B	ribbon	0.88	7
	ring	0.77	13
	annealed ring	0.77	7.5

MAGNETIC PROPERTIES OF MICRO-CRYSLALLINE Fe-Ni POWDER CORES

Permalloy of the composition 81 wt% of Ni and 19 wt% of Fe, which is nonmagnetostrictive material, remains after milling single-phased material fullfitting conditions for preparation of a soft magnetic material by powder compaction [8, 15].

The powder suitable as material for compaction was prepared by mechanical milling (RETSCH PM4000 with hardened steel vials and balls) with ball-to-powder-ratio of 6:1 and with a speed of 180 rpm up to 30 h) of NiFe (81 wt% of Ni) microcrystalline ribbon obtained by melt spinning in Ar-protective atmosphere in a high-energy planetary ball mill.

The compaction of small pieces of broken ribbon with area of several mm^2 respectively of powders in the form of cylinders (diameter 10 mm, height 2.5 mm, weight approx. 2 g) was performed at a pressure of 800 MPa for 5 min at 600°C in vacuum of 5×10^{-3} Pa (in order to prevent oxidation and to remove free gases from powder before the compaction). The cylinders were annealed at temperatures between 500°C and 1200°C for 1 h.

In order to prepare ring-shaped samples suitable for AC measurements, the cylinders of bulk samples were drilled using spark plasma erosion (the diameter is 5 mm, 10 primary turns, 20 secondary turns). The losses and maximum permeability were obtained from the AC hysteresis loops traced by an AC hysteresisgraph (AMH 401 POD WALKER) in the frequency range 100 Hz–3 kHz at maximum magnetic induction of 0.2 T.

The duration of the milling of the ribbon used for preparation the bulk sample influences significantly the losses up to 5 h of milling time, when the average linear size of the powder elements is about 30 μm [8], Fig. 7.

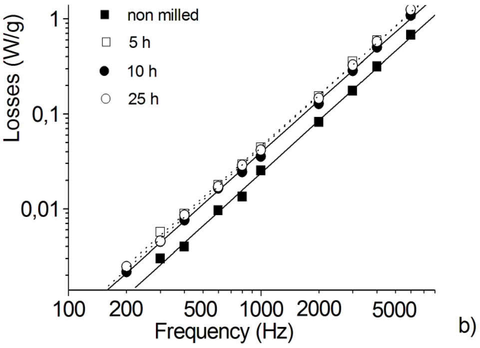

Fig. 7 Losses as a function of frequency of bulk samples prepared by compaction at 600°C of the ribbon milled for various milling times and then annealed at 1000°C.

Further decrease of the particle size of the compacted sample practically does not influence the frequency dependence of the losses, which steeply increases with the frequency due to large contribution of eddy current losses.

The peak permeability reflects moveability of the domain walls significantly [15], Fig. 8.

The domain walls motion is easy possible for longer distances in the bulk created from relatively larger pieces of the ribbon in low frequency AC magnetic field leading into larger values of peak permeability. After annealing at 1000°C is the domain walls motion much more easily (a part of pinning centers vanished) and the permeability increases. The permeability of the nontreated and at 1000 °C treated bulk prepared from the powder milled for 30 h has the some tendency, only the absolute values are smaller. The permeability of all samples decreases with the increase of the frequency.

AC MAGNETIC PROPERTIES OF Fe-BASED COMPOSITE MATERIALS

We have studied the influence of resin content on AC magnetic properties of Fe-based composite material to extend the possibility for application of composite material at higher frequency.

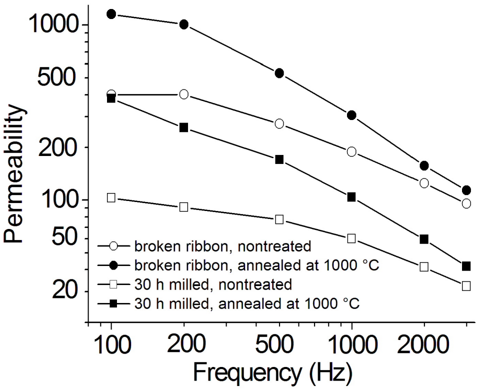

Fig. 8. Peak AC permeability of the bulk samples prepared by compaction at 600°C of the broken ribbon or ribbon milled for 30 h (before heat treatment and after annealing at 1000°C) as a function of the frequency.

For preparation of soft magnetic composite samples we used conventional powder metallurgy. Pure iron powder ASC 100.29, Höganäs AB Sweden [26] was chosen as ferromagnetic material and phenol-formaldehyde resin (Bakelite ATM) as insulator. The particles of the iron powder have spherical form and exhibit (according material producer) following particle size distribution: 50 wt. % particles have the diameter below 75 μm and 0.9 wt. % above 180 μm.

The bakelite was milled for 3 × 30 s in the knife mill to obtain the particle size below 100 μm.

Three experimental samples were prepared by mixing of 90 vol. % of iron (sample A), 80 vol. % of iron (sample B) and 70 vol. % of iron (sample C) with resin in Turbula mixer. The mixed powder was pressed in cylindrical die at the uniaxial pressure of 800 MPa to obtain compacts in the form of cylinder or ring. After that we cured the resulting product at the temperature of 165°C for 60 min. in electric furnace in air atmosphere.

Sample S is a reference material, prepared from Somaloy® 700 powder provided by Höganäs AB, Sweden by producer-developed technology (compaction at 800 MPa and heat treatment at 530 °C for 30 min in air). Outer diameter of all samples is 24 mm, inner diameter 17.8 mm and height about 3 mm.

The total losses dependencies (measured by an AC hysteresisgraph Model MATS-2010SA) as a function of maximum flux density B_m measured at the frequency $f = 10$ kHz of all samples are depicted in Fig. 9.

The values of total losses as a function of maximum flux density increase similar for samples A, B and C and less steeply than that for reference sample S. We assume that lower values of losses of the samples A, B and C are caused by lower contribution of the eddy current losses to the total losses due to higher specific resistivity of these samples (505 μΩ·m, 1330 μΩ·m and 56000 μΩ·m) in comparison with the specific resistivity of the sample S (4.579 μΩ·m).

The difference between losses vs. flux density dependences of the samples A, B and C is negligible. We can explain this effect by low contribution of the eddy current losses, which decrease with the increase of volume fraction of the resin in the composite material.

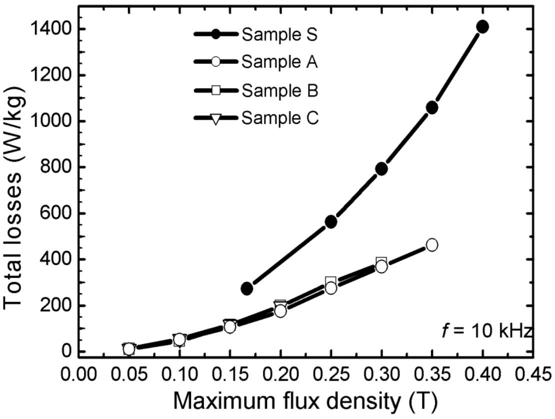

Fig. 9. Total losses P_t as a function of maximum flux density B_m measured for the sample A, B, C and S at the frequency $f = 10$ kHz.

The total losses dependencies as a function of frequency measured at the maximum flux density $B_m = 0.2$ T of all samples are depicted in Fig. 10.

The slope of total losses dependencies versus frequency of samples A, B and C is smaller than that for sample S. It is caused by lower contribution of eddy current losses of samples A, B and C, due to higher specific resistivity of the composite material. Similar tendencies have the frequency dependencies of total losses of the sample A measured at maximum flux densities B_m=0.05 T, 0.1 T and 0.2 T, Fig. 10.

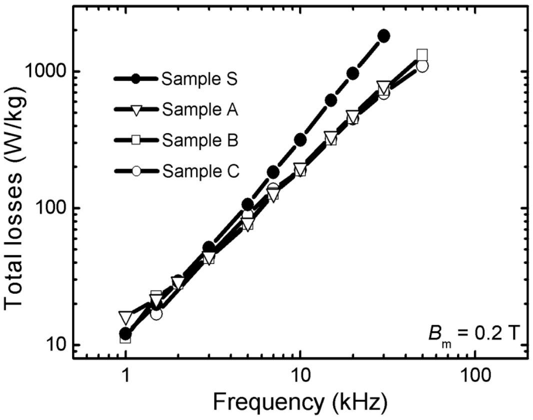

Fig. 10. Total losses P_t as a function of the frequency f for the sample A, B, C and S measured at maximum flux density $B_m = 0.2$ T.

We assume that sample A containing 90 % of iron is more suitable for application at frequencies above 1 kHz, than Sample S. The absolute values of total losses and the slope frequency dependence of total losses of composite material are lower than values for metallic compacted powder Fe-Ni based material [8].

CONCLUSIONS

By investigation of the structure and DC and AC magnetic properties of the bulk compacted materials we revealed that it is possible to prepare the material based on Fe, Co and Ni in a bulk form: cylinder or ring with excellent soft magnetic properties which are comparable with the magnetic properties of the material with the same (or similar chemical content) usually in the form of ribbon or thin sheet prepared by casting.

We can conclude that the bulk material fabricated by compaction of powder prepared by milling of soft magnetic alloys can be competitive in DC and low frequency application with bulk metallic glasses (BMG) and soft magnetic composites consisting of small particles of ferromagnetic material with insulating with possibility to replace ferrites in medium frequency applications.

ACKNOWLEDGMENT: This work was realized within the frame of the project „Centre of Excellence of Advanced Materials with Nano- and Submicron-Structure“, which is supported by the Operational Program "Research and Development" financed through European Regional Development Fund. This work was also supported by the Slovak Research and Development Agency under the contract No. APVV-0490-07 MICOMAT and by the Scientific Grant Agency of the Ministry of Education of Slovak Republic and the Slovak Academy of Sciences, project No. VEGA 1/4020/07 and No. VEGA 2/0149/09. Special thanks to Höganäs AB Sweden for providing Somaloy® powder.

REFERENCES

1. T. Maeda, H. Tyoda, N. Igarashi, K. Hirose, K. Mimura, T.Nishioka, and A.Ikegaya, SEI Tech. Rev., 60, (2005) 3–9
2. H. Chiriac and N. Lupu, IEEE Trams. Magn., 41, (2005) 3289-3291
3. T. D. Shen, U. Harms, and R. B. Schwarz Mater. Sci. Forum, 386–388, (2002) 441-446,.
4. P. Ripka,J. Magn. Magn. Mater., 320, (2008) 2466-2473
5. L. A. Dobrzanski, M. Drak, and B. Ziebowicz, J.Mater. Process. Techn. 191, (2007) 352-355,
6. G. Herzer, J. Magn. Magn. Mater., 158, (1996) 133-136
7. P. Kollár, J. Bednarčík, S. Roth, H. Grahl and J. Eckert, J. Magn. Magn. Mater. 278 (2004) 373-378
8. P. Kollár, D. Olekšáková, J. Füzer, J. Kováč, S. Roth and K. Polański, J. Magn. Magn. Mater. 310, (2007), 2609-2611
9. H. Shokrollahi, and K. Janghorban, Journal of Materials Processing Technology, 189, (2007) 1–12
10. A.H. Taghvaei, H. Shokrollahi, and K. Janghorbana, Journal of Alloys and Compounds, 481, (2009) 681–686
11. M. M. Raja, N. Ponpandian, B. Majumdar, A. Narayanasamy, and K. Chattopadhyay, Mater. Sci. Eng, 304, (2001) 1062-1065
12. J. Füzer, J. Bednarčík, P. Kollár, and S. Roth, J. Magn. Magn. Mater., 316, (2007) e834-e837
13. C. Suryanarayana, Progress in Mater. Sci., 46, (2001) 1-184
14. J. Füzer, P. Kollár, D. Olekšáková, and S. Roth, Acta Phys. Polon., A113, (2008) 59-62
15. R. M. Bozorth, Ferromagnetism, third edition, IEEE Press, Piscataway, NJ, 1993.
16. G. Bertotti, Hysteresis in Magnetism, Academic Press, San Diego, May1998.
17. H. Chiriac, N. Lupu, and M. Tibu, IEEE Trans.. on mag., 39, (2003) 2040-2042
18. R. Piccin, P. Tiberto, H. Chiriac, and M. Baricco, J. of Magn. Magn. Mater. 320, (2008) e806–e809
19. J. Füzer, P. Kollár, J. Bednarčík, C. Lathe, J. Füzerová, R. Bureš, and S. Roth, submitted for publication.
20. S. Flohrer, R. Schäfer, J. McCord, and S. Roth, Acta Mater., 54, (2006) 4693-4698
21. A. H. Morrish, The Physical Principles of Magnetism, Robert E. Krieger Publishing Company, Huntington, chapter 7, 1980.
22. J. Torrens-Serra, P. Bruna, and S. Roth, J. Rodriguez-Viejo, M. T. Clavaguera-Mora, Intermetallics, 17, (2009) 79-85.
23. S. Roth, A. R. Ferchmin, S. Kobe, in Landolt-Bornstein: Numerical Data and Functional Relationships in Science and Technology, vol III/19, ed H. P .J. Wijn: Berlin, Springer Verlag , (1994) 144
24. A. Inoue, T. Zhang, H. Koshiba, A. Makino: Journal of Applied Physics 83 (1998) 6326
25. J. Füzer, J. Bednarčík, P. Kollár, acta phys. slov. 56, (2006) 119-122
26. Product catalog: Somaloy® Metal Powders for SMC Components, URL: http://www.hoganas.se, Höganäs AB, Sweden

COATINGS FOR INDUSTRIAL APPLICATIONS

M. Mikula, ummsmiku@savba.sk, Institute of Materials and Machine Mechanics, SAS Račianska 75, Bratislava, Slovakia, B. Grančič, grancic@fmph.uniba.sk, Department of Experimental Physics, FMPI, Comenius University, Mlynská dolina, Bratislava, Slovakia, T. Roch, roch@fmph.uniba.sk, Department of Experimental Physics, FMPI, Comenius University, Mlynská dolina, Bratislava, Slovakia, I. Vávra, elekvavr@savba.sk, Institute of Electrical Engineering, SAS Dúbravská cesta 9, Bratislava, Slovakia, V. Buršíková, vilma.bursikova@gmail.com, Department of Physical Electronics MU, Kotlářska 2 Brno,Czech Republic, A. Šatka, satka@ilc.sk, Surface and Material Analysis Laboratory, ILC, Ilkovičova 3 Bratislava, Slovakia, A. Plecenik, plecenik@fmph.uniba.sk, Department of Experimental Physics, FMPI, Comenius University, Mlynská dolina, Bratislava, Slovakia, P. Kúš, kus@fmph.uniba.sk, Department of Experimental Physics, FMPI, Comenius University, Mlynská dolina, Bratislava, Slovakia

INTRODUCTION

Nowadays materials in a form of thin films and coatings are used in wide range of industrial applications. In machining industry, where improvements in the cutting rate and tool lifetime are essential, cutting surfaces are coated by wear-resistant hard coatings. Scientific research devoted to hard coatings is focused on development of novel nanostructured (nanocomposite) coatings. Several deposition techniques can be used for preparation of hard coatings with wide variety of microstructures, surface topographies, mechanical properties and good adhesions. Magnetron sputtering enables effective influencing of the coatings microstructure development by means of ion bombardment during deposition [1]. Most used hard coatings are carbide nitride and oxide coatings of transition-metals. Best-known in this group is TiN coating.

Superhard coatings are defined by extremely high hardness exceeding H>40 GPa. Typical one-phase examples are based on borides like TiB_2, ZrB_2, c-BN [2, 3]. These materials exhibit reasonably high hardness values already in the bulk form. By structure modification during growth as well as by incorporation of high residual stresses superhardness can be reached [4]. On the other side multicomponent systems like Ti-Al-N, Ti-Si-N, Ti-B-N naturally build nanocomposite structure with nanocrystallites embedded in amorphous matrix, whereby the necessary condition is the low solubility of phases [4 – 6]. In these materials dislocation mobility is considerably reduced. Grain boundary sliding is the only significant mechanism enabling deformation. Hardness of these coatings can reach values close to hardness of diamond (80 – 100 GPa) [7].

In this article we observe effects of electrical bias and substrate temperature on the structure of TiN, TiB_2 hard coatings. For TiN coatings the ion bombardment was examined as a way for full-dense structure preparation. In the case of TiB_2 coatings substrate biasing enabled manipulation of crystallinity. Significance of microstructure changes caused by bias application was evaluated with respect to hardness improvements. Effect of nitrogen addition on structure and consequently on hardness was examined for Ti-B-N coatings. Adhesion as crutial quality for application purposes was evaluated as well. Recently ReB_2 material appeared in the literature achieving the hardness of 60 GPa already in the bulk form [8]. We report on the progress which was achieved on the ReB_2 coatings preparation.

EXPERIMENTAL DETAILS

TiN, TiB_2 and Ti-B-N coatings were deposited on mirror-polished Si(001), high speed steel (HSS, ČSN 19 830) and WC+Co (Sandwik Coromant) substrates using an unbalanced d.c. magnetron sputtering from titanium (99.99%, Ø100 mm) and a stoichiometric TiB_2 (99.5%, Ø100 mm) target in Ar or Ar+N_2 (both of 99.999% purity) glow discharges. Substrates were ultrasonically pre-cleaned in acetone and isopropyl alcohol followed by Ar-plasma etching at the high substrate bias -1000V.

TiN coatings were deposited at the cathode current I_k=2.5A. The vacuum chamber was evacuated to a pressure of 2 x 10^{-3} Pa. Working gas pressure during deposition was kept on 0.6Pa (nitrogen partial pressure of 0.025Pa). TiB_2 a Ti-B-N coatings were prepared at I_k=1.5A, p_{Ar}=0.5Pa and p_{N2} in range from 0.01Pa to 0.025Pa. The target-to-substrate distance was 7 cm. The substrate bias U_s was applied in range from 0 to -300V and substrate temperature T_s was changed in tree steps: room temperature (RT – no resistive heating was applied), 300 and 700°C.

ReB_x coatings were deposited from ReB_2 target (99.5%, Ø50 mm) on mirror-polished Si(001) and austenitic steel (STN 417249) substrates in Ar glow discharges by means of unbalanced magnetron. Base pressure of the vacuum chamber was 3 x 10^{-5} Pa.

Morphology and a thickness of coatings were observed by field-emission scanning electron microscopy (FE-SEM) LEO 1550 and scanning electron microscopy (SEM) Tescan. Chemical composition of the coatings was measured by energy dispersive x-ray analysis (EDX) Oxford INCA and by glow-discharges optical emission spectrscopy (GD-OES) LECO SA-2000. Structure of the coatings was determined from a combination of x-ray diffraction (XRD) URD6 with CuKα monochromator (λ=0.15418 nm) and transmission electron microscopy (TEM) and cross-sectional TEM (XTEM) Jeol 1200EX (120kV). The measurement of universal plastic hardness H_{pl} was carried out on microhardness tester Fischerscope H100 equipped by Vickers diamond tip. Adhesion of the coatings was measured by Rockwell C indentation test (load of diamond tip = 1500N) and scratch test (uniform load increase from 0 N to 120 N on the length of 12 mm).

RESULTS AND DISCUSSION

TiN coatings

Depending on the substrate temperature used during deposition the TiN coatings exhibit various cross-section and surface morphologies (Fig. 1). TiN coatings deposited at U_S=-50V and T_S=RT have porous cone-shaped cross-section with rough surface on the other hand coatings deposited at U_S=-50V and T_S=400°C have dense and non-porous cross-section with very smooth topography of the surface (Fig. 1b).

The GD-OES concentration depth profile of TiN coatings deposited at U_S=-50V on a stainless steel substrate is in the Fig. 2a. Almost stoichiometric 1:1 concentration ratio of Ti and N can be observed along the whole coating thickness.

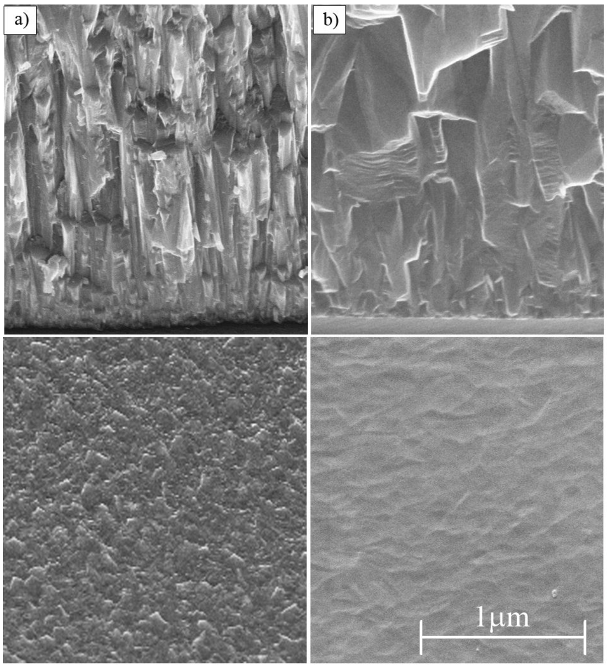

Fig. 1 FE-SEM cross-sectional and plane-view images of TiN coatings grown on Si(001) substrate at a) U_s= -50V and T_s=RT; b) U_s= -50V and T_s=400°C

Characteristic XRD pattern for TiN coatings deposited on stainless steel substrate changing substrate bias U_S in range 0V to -200V at T_S=RT (room temperature) are in Fig. 2b. Only one phase (cubic NaCl crystallographic structure) was detected with strong (200) preferred crystallographic orientation for all used substrate biases. Relatively small diffraction peaks corresponding to the crystallographic orientation (111) and (220) were detected. Increased deposition temperature didn't have observable influence on the preferred crystallographic orientation. Only the crystallites size D determined by Scherrer formula increased at higher deposition temperatures. The average crystal size in direction perpendicular to the substrate surface plane was determined to be D=29 nm for T_S=RT and D=68 nm for at T_S=400°C.

It is worth to note that in case of magnetron sputtering with balanced magnetic field, resp. in case of arc deposition it wasn't possible to obtain strong preferred (200) crystallographic orientation. Here the (111) orientation dominated regardless used deposition parameters.

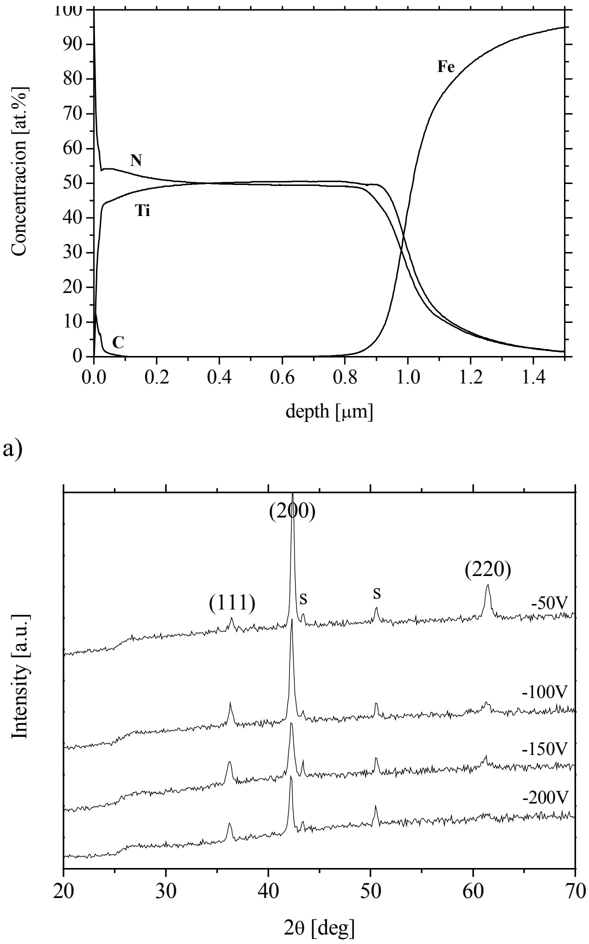

a)

b)

Fig. 2 a) GD-OES profil depth profile of TiN coating deposited on austenitic steel substrate at T_s=RT and U_s= -100V; b) XRD pattern of TiN coatings deposited on austenitic steel substrates at T_s=RT and series of U_s values.

TiB_2 and Ti-B-N coatings

Typical FE-SEM cross-sectional images of TiB_2 and Ti-B-N coatings are displayed on Fig. 3. All TiB_2 coatings prepared by magnetron sputtering with unbalanced magnetic field exhibit dense columnar morphology on the cross-section as well as smooth surface (average roughness R_a~1nm measured by AFM). Dense morphology without apparent columnar structure was observed in case of Ti-B-N coatings. EDX chemical analysis of TiB_2 coatings showed the concentration ratio B/Ti of approximately 2.1 regardless the used deposition parameters U_S, T_S. As a result of substrate biasing small amount of Ar atoms incorporated in the coating was detected. The Ar concentration increased for higher electrical bias ranging from 0.06 at.% typical for U_S=0 V up to 0.21 at.% typical for U_S=-200 V. Small amount of impurities like carbon or oxygen in total less than 3at.% was detected as well. Nitrogen concentration in Ti-B-N was determined in range 21.5 - 45 at.% depending on partial

N_2 pressure. Also for Ti-B-N small Ar and other impurities were detected (~0.7 at.% and <3 at.%, respectively).

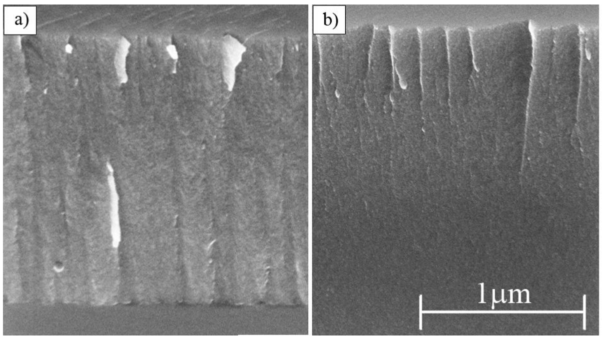

Fig. 3 FE-SEM cross-sectional images of a) TiB_2 coating deposited on Si(001) substrate at U_s = -50V, T_s = RT and b) Ti-B-N coating grown on Si(001) substrate at U_s = 0V, T_s = RT and p_{N2}= 0,025Pa.

XRD analysis of TiB_2 coatings confirmed strong influence of applied substrate bias on the coatings microstructure on all used substrate types. In the case of depositions made at U_s=0 V only strong substrate diffraction peaks could be observed. These XRD patterns for U_s=0 V are typical for amorphous or randomly oriented nanocrystalline structure with very small grain size. If the energy of ions striking the coating surface during growth was increased by applying the substrate bias TiB_2(0001) diffraction peak occurred in the spectra and its amplitude increased with substrate bias. Ion bombardment energy supported the formation of TiB_2 crystalline phase. No other crystalline phases were detected in the coatings.

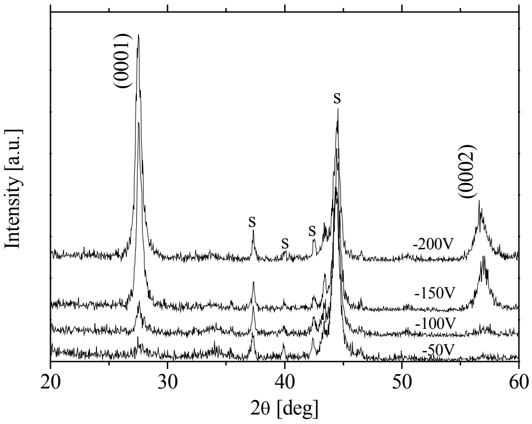

Fig. 4 XRD pattern of TiB_2 coatings deposited on HSS substrates for series of the substrate bias U_s.

Substrate temperature (T_S=300°C and 700°C) during deposition didn't cause any significant change of the coating microstructure. Also for higher substrate temperature the diffraction peak TiB_2(0001) was detected only after substrate bias application (U_S>0 V).

Using Warren – Averbach analysis of measured spectra the average crystal size in direction perpendicular to the substrate surface plane was determined to be D~13 nm. Influence of substrate bias or heating on the crystal size wasn't observed.

Transmission Electron Microscopy (TEM) enabled more detailed microstructure description in dependence on deposition conditions. Cross-sectional dark field TEM images of the TiB_2 coatings deposited at T_S=RT and for two values of substrate bias U_S=0V and U_S= -50V are in Fig. 5. By tilting the sample during observation in bright field TEM we determined that the coatings can be characterized as nanocomposite system with nanocrystals embedded in amorphous matrix. Electron diffraction from the subsurface coatings region revealed the randomly oriented TiB_2 crystalline phase for U_S= 0V.

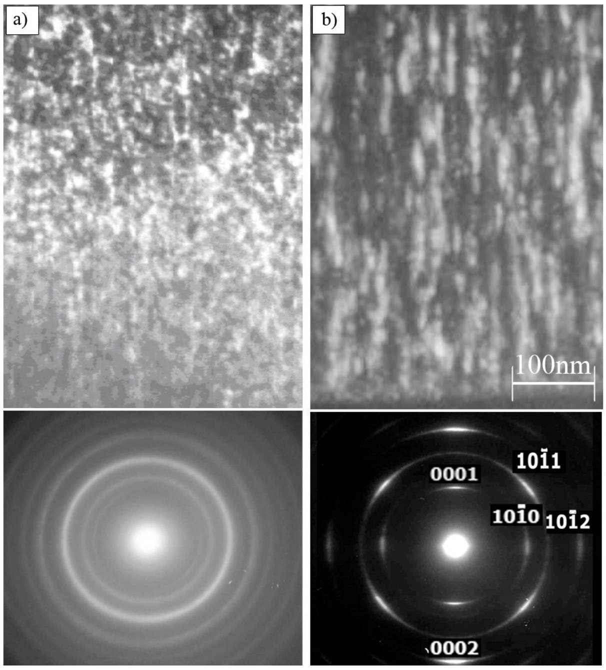

Fig. 5 Dark-field cross-sectional TEM images with corresponding SAED patterns of TiB_2 coatings deposited a) at U_s= 0V and T_s= RT; b) at U_s= -50V and T_s= RT.

In case of the coating deposited at U_S=-50V nanocrystals build fiber structure. The (0001) crystallographic planes of TiB_2 nanocrystals are oriented parallel with sample surface. During coating growth the strong preferred orientation occurred gradually within a 100 nm thick layer. Similar structure development caused by substrate bias was observed also for increased deposition temperatures T_S.

No diffraction peaks which could be associated with Ti-B-N coatings were detected in XRD spectra. Thus the Ti-B-N coatings have nanostructural character with very small crystallites or have predominant amorphous phase (Fig. 6a). The bright field TEM images taken on coatings deposited using partial N_2 pressure p_{N2}=0.01Pa revealed very small nanocrystallites (D~2nm) in amorphous matrix. By increasing the partial N_2 pressure the crystalline grain size was suppressed. The coating with highest nitrogen concentration (p_{N2}=0.025Pa) exhibited amorphous structure (Fig. 6b).

All studied TiB_2 coatings had plastic hardness H_p ~ 40 GPa what is comparing to the bulk material almost

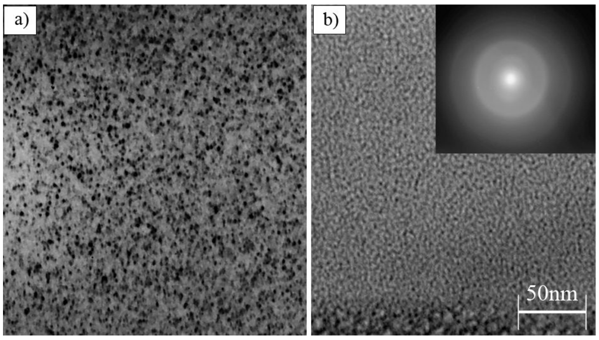

Fig. 6 a) Bright-field plane-view TEM image of Ti-B-N coating deposited at p_{N2}= 0,01Pa; Dark-field cross-sectional TEM images with corresponding SAED pattern of TiB_2 coatings deposited of Ti-B-N coating deposited at p_{N2}= 0,025Pa.

twice higher value. The increased hardness of coatings comparing to the bulk material is usually connected to different microstructure and the high residual stresses. Our coatings had residual macrostresses in orders of GPa as calculated by Stoney equation from substrate curvature [9]. Application of substrate bias especially in case of T_S=RT led to enormous increase of H_p up to value 73 GPa for U_S=-200V (Fig. 7a). In case of higher T_S no apparent influence of substrate bias on H_p value was observed. According to Ref. [9] in case of high T_S the temperature reduced the residual macrostress value and there was no observable change of microstructure. Enhanced hardness for T_S=RT can be therefore assigned with high residual macrostresses. This statement is valid for the electrical bias range from -50V to -200V. For higher values -200V to -300V the coatings delaminated during indentation and the values can be considered only as informative.

The dependence of plastic hardness of Ti-B-N coatings on load is in the Fig. 7b. It can be concluded that the nitrogen addition caused decrease of plastic hardness. The plastic hardness for p_{N2}=0.01 Pa was close to H_{pl} of pure TiB_2 but didn't reach this value.

The adhesive – cohesive behavior was evaluated by means of Rockwell C indentation as well as from scratch test (Fig. 8). After penetration into the coating–substrate system only very small cracks (not visible in the Fig. 8) were generated on the border of the indent which suggests that the TiB_2 coatings had very good adhesion. On the other hand the circular cracks (Fig. 8a) were generated close to the indent whereby their number and the area which was influenced by the cracking was growing for higher electrical bias values. We think that this circular cracking was caused by high compressive residual stresses. During indentation the substrate material was forced to pile up outside of the indent. This pile-up caused that the coating in this region was compressively pressed. After reaching certain critical value of compressive stress the coatings cracked up. Here the value of residual stress (present before indentation) could be simply added to the stress caused by indentation.

The good TiB_2 adhesion was also confirmed by scratch method, whereby on the whole scratch length no adhesive failure was observed (Fig. 8b).

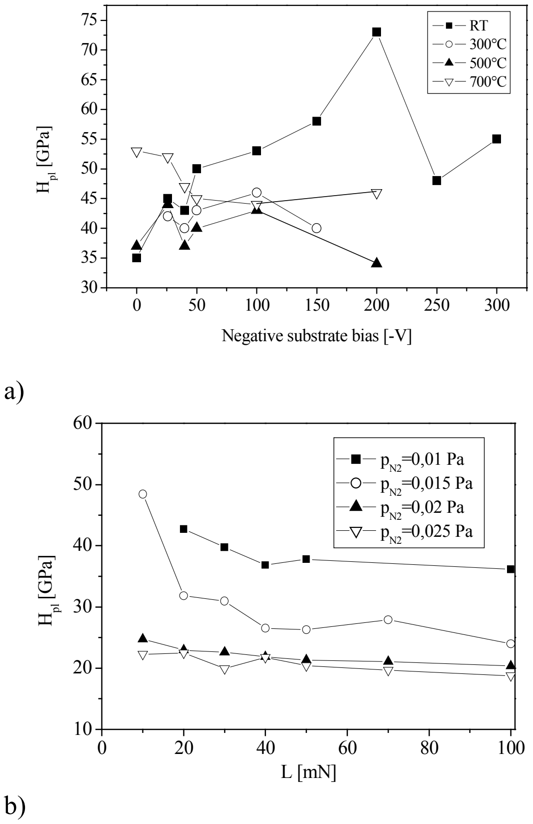

Fig. 7 a) Plastic hardness H_{pl} of TiB_2 coatings deposited on WC substrates as a function of U_S and T_S; b) H_{pl} of Ti-B-N coatings deposited on HSS substrates at different p_{N2} as a function of load L.

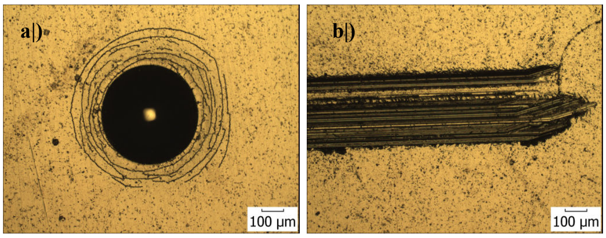

Fig. 8 a) image of the Rockwell C indent in the sample with TiB_2 coating; b) image of a scratch in TiB_2 coating deposited on HSS substrate at U_s =-150V and T_s= RT.

ReB_x coatings

Rhenium diboride is a new unique material exhibiting the hardness over 60 GPa in a bulk form [9].

Our present research is focused on preparation of ReB_2 hard coating, seeking for optimal deposition parameters. At first, we had successfully synthetized stoichiometric ReB_2 powder and then it was hot isostatic sintered to the target (Fig. 9).

Many sputtering processes with different deposition parameters were performed in order to fabricate stoichiometric ReB_2 coating. Fig. 10 shows SEM image of ReB_x coating cross-section, which exhibited a glassy, non-porous morphology.

EDX analysis confirmed B/Re concentration ratio ~1 and these ReB_x coatings degraded rapidly in the several days. The XRD analysis didn't confirm any crystalline ReB_2 phase. Consequently, the next growing coatings were doped by boron during co-deposition from ReB_2 and boron targets. These coatings were annealed at 800°C for 30 min. in vacuum.

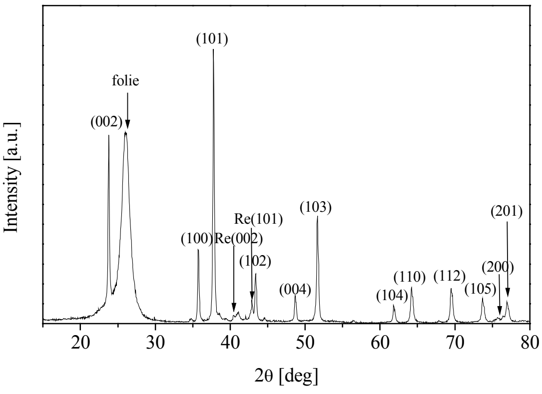

Fig. 9 XRD pattern of ReB_2 powder synthetized at Department of Experimental Physics FMPI CU.

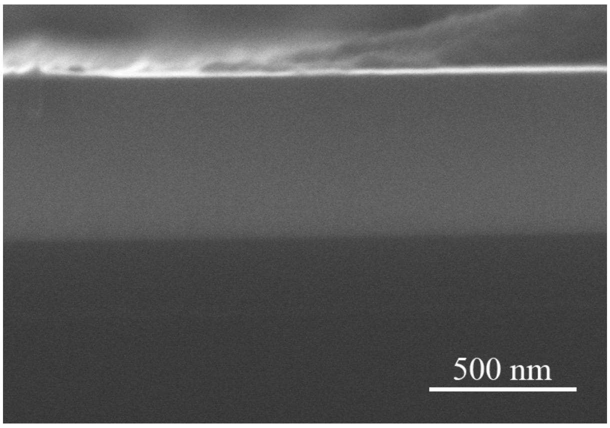

Fig. 10 SEM micrograph of a coating fracture cross-section showing the typical morphology of ReB_x coating grown on Si(001) substrate.

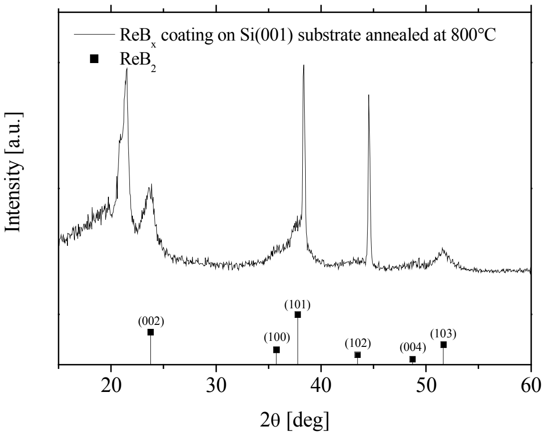

Fig.11 XRD pattern of ReB_x coating deposited on Si(001) substrate and post-depositionally annealed in vacuum at 800°C for 30 min.

The B/Re ratio of annealed coatings observed by EDX analysis increased to 2 and XRD analysis confirmed a crystalline ReB_2 phase (Fig. 11). In the next step, we propose to prepare a new ReB_x target with suitable B/Re ratio >2 and to sputter coatings without boron addition from a second target.

CONCLUSIONS

Influence of deposition conditions on the microstructure changes of TiN, TiB_2, Ti-B-N and ReB_x coatings prepared by magnetron sputtering with unbalanced magnetic field is reported. Mechanical properties of the coatings depending on a structure are also investigated.

TiN coatings with strong (200) preferred orientation were deposited as a result of intensive ion bombardment during deposition. Application of negative substrate bias U_s influenced the crystallographic orientation TiB_2 coatings. The microstructure character was changed from randomly oriented crystalline structure to very strong (0001) texture depending on value of U_s. Undesirable effect was a generation of compressive residual stresses in coatings. Relaxation of stresses occurred at increased substrate temperature during deposition, but the hardness of coatings decreased. The highest hardness (73GPa) was measured on TiB_2 coatings prepared at U_s=-200V and T_s=RT. The addition of nitrogen to operational atmosphere during deposition caused a reduction of crystalline size. Ti-B-N coatings with the highest content of nitrogen exhibited an amorphous structure. All the tested coatings exhibited good adhesion.

Furthermore we focused our research on deposition of ReB_x coatings. Stoichiometric and crystalline ReB_2 coatings were prepared by dual ReB_2 and boron target sputtering and by post-deposited annealing in vacuum.

ACKNOWLEDGEMENTS: This work was supported by APVV-0034-07 project (Hard and superhard nanocomposite coatings). The authors would like to thank Dr. Miroslav Hnatko for hot-isostatic pressing of ReB_2 target at Institute of Inorganic Chemistry Slovak Academy of Sciences.

REFERENCES

1. P. J. Kelly, R. D. Arnell: J. Vac. Sci. Technol. A 16(5) (1998).
2. P. H. Mayrhofer, Ch. Mitterer, L. Hultman, H. Clemens: Progess in Materials Science 51 (2006) 1032-1114.
3. B. Grančič, M. Mikula, Ľ. Hrubá, M.Gregor, M. Štefečka, A. Csuba, E. Dobročka, A. Plecenik, P. Kúš: Vacuum 80 (2005) 174–177.
4. R. F. Bunshah: Handbook of Hard Coatings, Noyes Publications, New York, 2001.
5. I. Petrov, P. B. Barna, L. Hultman, J. E. Green: J. Vac. Sci. Technol. A 21(5) (2003) 117 – 126.
6. S. Veprek, M. G. J. Veprek-Heijman, P. Karvánková, J. Procházka: Thin Solid Films 476 (2005) 1-29.
7. P. B. Barna, M. Adamik: Thin Solid Films, 317 (1998) 27-33.

8. H. Y. Chung, M. B. Weinberger, J. B. Levine, A. Kavner, J. M. Yang, S. H. Tolbert, R. B. Kaner: Science 316 (2007) 436-439.
9. M. Mikula, B. Grančič, V. Buršíková, A. Csuba, M. Držík, Š. Kavecký, A. Plecenik, P. Kúš: Vacuum 82(2) (2008) 278-281.

ÚPLNÉ ZATMENIA SLNKA – LABORATÓRIUM PRE VÝSKUM KORÓNY, PLANÉT, KOMÉT A TESTU ODCHYLKY SVETLA

V. Rušin, vrusin@ta3.sk, Astronomický ústav SAV, 059 60 Tatranská Lomnica

ÚVOD

Úplné zatmenia Slnka Mesiacom sú vzácnym prírodným úkazom, ktorý sa za 100 rokov vyskytne 74-75 krát. Ich vzácnosť a výnimočnosť spočíva v tom, že počas úplných zatmení Slnka sa dá pozorovať najvrchnejšia zložka slnečnej atmosféry – koróna. Počas úplných zatmení koncom 19. storočia bolo objavené hélium, emisné spektrálne čiary vysokoionizovaných prvkov, napríklad železa, čo neskôr viedlo k záveru, že koróna je veľmi horúca. Zo zakrivenia polárnych lúčov bielej koróny začiatkom 20. storočia v blízkosti pólov sa napríklad predpokladala existencia magnetického poľa na Slnku, ktoré E. Hale v roku 1908 po prvýkrát pozorovaním potvrdil. Dokonca aj prvá ejekcia koronálnej hmoty, kométa Kreutzovej skupiny, či overenie všeobecnej teórie relativity sa pozorovali počas úplných zatmení Slnka. Počas zatmení sa hľadala aj hypotetická planéta Vulkan. Dnes sa síce koróna pozoruje nielen zo Zeme, ale aj pomocou prístrojov na umelých družiacich Zeme či kozmických sondách v celom spektre elektromagnetického žiarenia, ale mnohé experimenty s vysokou rozlišovacou schopnosťou sa dajú robiť len počas úplných zatmení. Podobne, aj kométy sa pozorujú z kozmu. Aké poznatky, hlavne o slnečnej koróne máme dnes, a ktoré otázky sú nezodpovedané, sa pokúsime zodpovedať v tomto článku. Vulkan neexistuje a odchýlka svetla sa spoľahlivo meria pomocou kvazarov. Samotné úplné zatmenia slúžia na meranie rotácie Zeme.

KORÓNA

Slnečná koróna (obr. 1) - slabé bledomodré svetlo okolo tmavého Mesiaca, začala pútať veľkú pozornosť po úplnom zatmení Slnka 18. júla 1860 v Španielsku, keď na základe fotografických pozorovaní Warren de la Rue a Angelo Secchi, ktorí boli od seba vzdialení 400 kilometrov, prehlásili, že „koróna a protuberancie sú atmosférou Slnka“. Koróna od čias Keplera (pozoroval ju počas úplného zatmenia Slnka 12.10.1605) bola považovaná za atmosféru Mesiaca, i keď isté náznaky jej pozorovaní po roku 1851 (28. júla pás totality prechádzal severnou Európou) naznačovali, že tomu tak nie je.

E. Young a W. Harkness na základe spektrografického pozorovania počas úplného zatmenia Slnka 7. augusta 1869 zistili, že v spektre koróny sa nachádza emisná spektrálna čiara s vlnovou dĺžkou „okolo“ 530 nm, ktorá nemala ekvivalent v Mendelejevovej tabuľke chemických prvkov. Keď sa ani po 25 rokoch nenašiel nijaký chemický prvok, zvolil sa rovnaký postup ako v prípade chemického prvku hélia, ktoré bolo tiež najprv objavené počas úplného zatmenia Slnka 18. augusta 1868 na Slnku J. Janssenom a neskôr pomenované po gréckom bohovi Slnka Héliovi (plynné hélium na Zemi bolo objavené až v roku 1895). Emisná spektrálna čiara, ktorá bola pozorovaná v zelenej oblasti spektra dostala meno „zelená čiara“, ktoré sa používa aj v súčasnosti, a mal ju tvoriť nový chemický prvok – korónium („coronium“). Korónium malo byť ľahšie ako vodík, čo sa však nepotvrdilo.

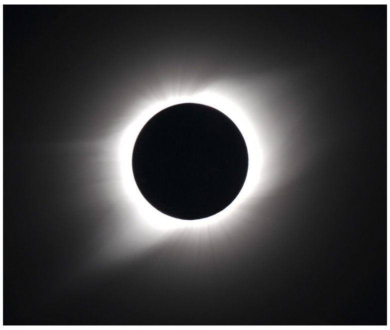

Obr. 1. „Klasická“ biela koróna dňa 1. augusta 2008 na pozorovacom stanovišti v dedine Altaj (Mongolsko). Rubinar 10/1000, EOS D 20, ½ s. (M. Druckmüller, P. Aniol, V. Rušin).

Pri určovaní hmotností korónia sa vychádzalo z nasledujúcich predpokladov: (a) prilbicovité lúče koncom 19. a začiatkom 20. storočia sa pozorovali už do vzdialenosti 10 polomerov Slnka (1 polomer = 696 tisíc km); (b) chemické zloženie koróny sa nepoznalo, ale predpokladalo sa, že svieti odrazeným svetlom. Aby takýto koronálny lúč vo svojej základni nebol veľmi jasný a deformovaný pod vplyvom gravitačnej sily Slnka, musel by obsahovať materiál oveľa ľahší ako vodík. Keďže koronálne lúče neboli ani deformované, ani vo svojich základniach extrémne jasné, korónium nemohlo byť ľahšie. Začiatkom 20. storočia fyzika slnečnej koróny prežívala veľkú krízu. Medzitým sa samozrejme už pozorovali ďalšie emisné spektrálne čiary, napríklad spektrálna čiara 637,4 nm, ktoré tiež nemali svoje miesto v Mendelejevovej tabuľke prvkov.

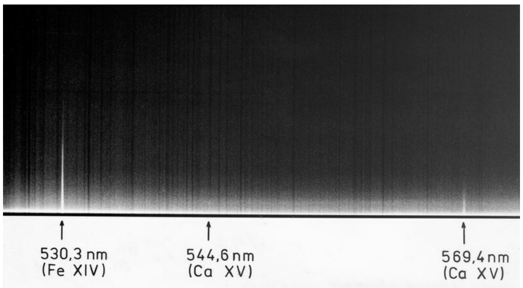

Obr. 2. Emisné spektrálne čiary koróny vo vizuálnej oblasti spektra. (Archív Astronomického ústavu SAV, Tatranská Lomnica).

Problém korónia sa podarilo vyriešiť až v 40. rokoch dvadsiateho storočia a pričinili sa o to W. Grotrian a B. Edlén, pričom k identifikácií emisných spektrálnych čiar koróny prispelo už skôr vyriešenie záhadného “nebúlia”, ktoré sa pozorovalo v spektre planetárnych hmlovín a ktorého čiary vyžarovali ionizované prvky kyslíka, dusíka, neónu a pod. a ukazovali tak, že ich výskyt spôsobuje vyššia teplota. Edlén pri svojich pokusoch s elektrickou iskrou vo vákuovom spektrografe (teplota tam bola 5×10^5 K) a Grotrian na základe teoretických výpočtov zistili, že priemerný rozdiel termov železa FeX (9,5338 nm) a FeXI (8,7025 nm), ktoré sa pozorovali v ultrafialovej oblasti spektra, je veľmi podobný vlnočtu červenej koronálnej čiary 637,4 nm a 789,2 nm. Zhoda nemohla byť náhodná, čo viedlo k záveru, že koronálne čiary vyžarujú vysokoionizované atómy známych chemických prvkov. Na základe izoelektrónovej postupnosti sa prišlo k záveru, že červená spektrálna čiara patrí deväťkrát ionizovanému železu (FeX) a odtiaľ už bol malý skok, aby sa identifikovali ďalšie emisné spektrálne čiary v koróne. Zelená čiara, ktorá patrí Fe XIV (trinásťkrát ionizované železo), bola identifikovaná v roku 1942 [1], kde sa dá detailne zoznámiť s celým postupom riešenia identifikácie emisných čiar koróny. Koróna sa tak stala zrazu veľmi horúcou – od 1 do 5 miliónov K. Jeden problém sa vyriešil a nastal ďalší problém, ktorý spoľahlivo nie je rozriešený ani dnes – mechanizmus ohrevu koróny, keďže fotosféra má teplotu len okolo 5700 K. O vysokej teplote koróny sa spočiatku pochybovalo, ale objav rádiového žiarenia Slnka po druhej svetovej vojne vysokú teplotu koróny potvrdil a dnes to potvrdzujú aj emisné spektrálne čiary koróny pozorované v extrémne ultrafialovej a röntgenovej oblasti spektra.

Dnes sa odhaduje, že vo vizuálnej oblasti spektra je okolo 28 emisných čiar. Všetko sú to tzv. zakázané čiary, čo znamená, že k ich emisii dochádza v dôsledku preskoku elektrónov z ich „vybudených“ hladín na základnú dráhu daného elektrónu, obiehajúceho okolo jadra atómu. Takéto stavy môžu nastať len v prostredí nízkej hustoty a vysokej teploty. Dovolené spektrálne čiary sa nachádzajú v EUV alebo rőntgenovej oblasti spektra.

Koncom 50-tych rokov 20. storočia sa dokončila separácia zložiek slnečnej koróny. Dnešné zloženie je nasledovné:

- Emisná koróna (E koróna) – je to vlastné žiarenie koróny. Názov je odvodený z existencie emisných spektrálnych čiar vysokoionizovaných prvkov, napríklad železa, vápnika, niklu a pod.
- Koróna spojitého spektra, elektrónová koróna (K koróna) – jej svetlo vzniká rozptylom žiarenia fotosféry na voľných elektrónoch. Keďže elektróny sa v koróne pohybujú rýchlo a rôznymi rýchlosťami, absorpčné fotosférické čiary sú rozmazané, strácajú sa. V opačnom prípade by spektrum koróny malo mať podobu spektra fotosféry. Spektrum bielej koróny, ako aj emisnej koróny, je silno polarizované.
- Fraunhoferova koróna alebo prachová koróna (F koróna). Jej svetlo nie je polarizované a spôsobuje ho rozptyl žiarenia fotosféry na prachových časticiach, ktoré sú okolo Slnka a v medziplanetárnom priestore (zodiakálne svetlo je pokračovaním F koróny). Pohyb častíc medziplanetárnej hmoty je pomalý, takže v rozptýlenom spektre sa pozorujú absorpčné čiary fotosféry.

Biela koróna, ktorá sa spravidla pri zatmeniach pozoruje najčastejšie, lebo je to najjednoduchšie pozorovanie, je vlastne súhrnom všetkých zložiek. Po objave koronografu B. Lyotom v roku 1930 [2], emisná koróna – pomocou spektrografu alebo úzkopásmových filtrov, sa dá pozorovať z vysokých nadmorských výšok aj mimo úplných zatmení Slnka. Pozorovanie emisných spektrálnych čiar koróny vo vizuálnej oblasti spektra (obr. 2) sa na Slovensku robí na Lomnickom štíte (okrem toho v USA, Ruskej federácii a Japonsku). Jediné pozorovania bielej koróny na svete pomocou koronografu a polarizácie sa robí na Mauna Loa (Havaj, USA). Kým ale pri pozorovaní emisnej koróny sa pohybujeme v priestorovom rozlíšení okolo jednej oblúkovej minúty, v bielej koróne je to menej.

Základným problémom, prečo nie je možné korónu pozorovať hocikedy, je skutočnosť, že jej svetlo v blízkosti povrchu Slnka je asi milión krát slabšie, ako svetlo fotosféry. So vzdialenosťou od Slnka jej jas prudko klesá a napríklad v dvoch polomeroch Slnka jej pokles voči okraju Slnka je o ďalšie 4 rády nižší.

V 60-tych rokoch dvadsiateho storočia sa objavili teoretické úvahy o tom, že v infračervenej oblasti spektra by sa mal zjaviť nadbytok žiarenia, ktorého zdrojom by mala byť reemisia žiarenia fotosféry na prachových časticiach okolo Slnka. Tento nadbytok žiarenia sa pomenoval sa T koróna: termálna koróna. Očakávaný nadbytok žiarenia v infračervenej oblasti spektra vo výškach okolo 4 polomerov Slnka na vlnovej dĺžke 2,2 μm, bol pozorovaný počas úplného zatmenia Slnka 12. novembra 1966 Petersonom [3].

Ďalšou zložkou koróny by mala byť S koróna: sublimačná koróna. Mali by ju tvoriť emisné rezonančné spektrálne čiary *H* a *K* jedenkrát ionizovaného vápnika (*Ca II*) s vlnovou dĺžkou okolo 396,9 a 393,4 nm, ktoré by mali vznikať sublimáciou prachových častíc vo vzdialenostiach asi 20 polomerov Slnka, keď sa po „keplerovských“ dráhach približujú k Slnku [4].

Posledné dve zložky koróny, vo všeobecnosti, nie sú vedeckou obcou veľmi prijímané. Možno sa opakuje stav, aký bol koncom 19. storočia. Trvalo tridsať rokov, kým sa akceptovala myšlienka, že koróna je súčasťou Slnka.

Dlho sa predpokladalo, že biela koróna je sféricko-symetrický útvar. Dnes vieme, že tomu tak zďaleka nie je. Biela, ale podobne aj emisná koróna je mimoriadne štruktúrovaná: od veľkých prilbicovitých lúčov, ktorých „nohy“ sú od seba zakotvené aj vo vzdialenosti viac ako 100 tisíc kilometrov, po super tenké ihlicovité, radiálne, ale aj mierne zakrivené lúče o šírke len niekoľko tisíc kilometrov (1-2 tisíc), prípadne aj menej. V základni prilbicovitých lúčov (obr. 4), ktoré sa rozprestierajú nad neutrálnou čiarou, oddeľujúcou veľkoškálové polarity magnetických polí na povrchu Slnka, sa pozoruje protuberancia/filament, a nad ňou koncentrické tmavé a svetlé slučky, ktoré formujú siločiary lokálneho magnetického poľa, kým siločiary veľkoškálových polí formujú celý prilbicovitý lúč. Pokračovaním prilbicovitého lúča v heliosfére je tzv. neutrálna vrstva (neutral sheet), ktorá oddeľuje opačné polarity magnetického poľa. Veľkoškálové prilbicovité lúče sú s veľkou pravdepodobnosťou zdrojom pomalej zložky častíc v slnečnom vetre, kým otvorené štruktúry – koronálne diery, kde siločiary magnetického poľa sú otvorené, tvoria zdroj vysokorýchlostných častíc (koronálne diery sú zároveň miesta v slnečnej koróne, kde hustota častíc a teplota je voči svojmu okoliu nižšia). Najnovšie výskumy ukazujú, že okrem klasických prilbicovitých lúčov existujú aj pseudo prilbicovité lúče [5]. To sú také lúče, ktorých „nohy“ sú zakotvené v rovnakej polarite veľkoškálového magnetického poľa, spravidla nad silným lokálnym poľom magnetickým poľom alebo jedna „noha“ takého lúča je „ukotvená“ priamo v tomto silnom magnetickom polí. Z kvalitných zatmeňových snímok bolo zistené, že tenké, radiálne orientované lúče o šírke asi 5-10 oblúkových sekúnd (alebo aj menej) sa premietajú aj do prilbicovitých lúčoch, čo vyvoláva dojem „strapatej“ koróny.

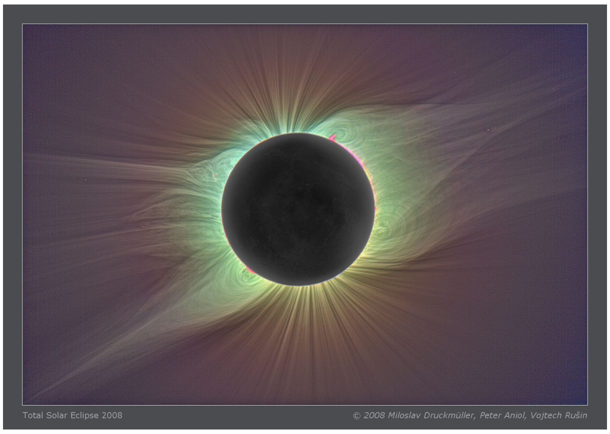

Obr. 3. Biela koróna z 1. augusta 2008 po spracovaní Druckmüllerovou metódou. Výsledný obrázok je zložený z 28 samostatných expozícií. (M. Druckmüller, P. Aniol, V.Rušin).

V oblasti pólov Slnka, hlavne okolo minima slnečnej aktivity, sa pozorujú klasické polárne lúče s hrúbkou okolo 10 tisíc kilometrov (15 oblúkových sekúnd), ktoré na zatmeňových záberoch siahajú až do výšky troch-štyroch polomerov Slnka. Z ich sklonu sa odvodila dĺžka dipólu celkového magnetického poľa Slnka, ktoré v prvom priblížení má dipólový charakter – minimálne v minime cyklu; v maxime cyklu podľa všetkých náznakov má kvadrupólový charakter. Je paradoxné, že hoci všetky štruktúry koróny formuje magnetické pole Slnka, priamo v slnečnej koróne ho nemôžeme merať. V porovnaní s povrchom Slnka je slabé (predpokladá sa, že je v intervale hodnôt 10^{-4} - 10^{-3} T), pološírka emisných spektrálnych čiar je široká – okolo 0,9 Å, takže na jeho meranie sa nedá použiť rozštep spektrálnych čiar (Zeemanov jav). Aj z tohoto dôvodu sa hľadajú emisné spektrálne čiary v infračervenej oblasti spektra koróny, pretože rozštep stúpa so štvrtou mocninou vlnovej dĺžky, a ako ukázal Judge [6], k najintenzívnejším by mali patriť: [Fe XIII] 1,0747 a 1,0798 µm; [Si X] 1,43 µm; [Si IX] 2,58 a 3,93 µm; [Mg VIII] 3,03 µm; and [Mg VII] 5,50 a 9,03 µm. Kým čiary Fe XIII sa darí vcelku dobre pozorovať aj mimo úplných zatmení, pokusy pozorovať ďalšie emisné čiary v čase zatmení nie sú až také úspešné. Ich pozorovanie je dôležité aj preto, že v horúcej koróne sa pozoruje aj „chladná“ zložka, pričom koexistencia „horúcej“ a „chladnej“ koróny sa ťažko vysvetľuje. Zatmeňové pozorovania, robené na základe farby koróny, nevedú k jednoznačným záverom o existencii „chladnej“ koróny. Z uvedeného vyplýva, že štruktúra koróny nám poskytuje informácie aj o rozdelení magnetického poľa v koróne.

Dlhodobé pozorovania bielej koróny ďalej ukázali, že jej variabilita s cyklom slnečnej aktivity sa mení a dá sa vyjadriť koeficientom sploštenia, ktorý navrhol Ludendorf a nesie jeho meno. Koeficient sploštenia sa určuje z izofót, ktoré v čase okolo maxima sú okolo tmavého mesačného disku takmer kruhové (koeficient sploštenia je nulový), kým v čase minima sú silne eliptické – hustota častíc nad pólmi je minimálne o jeden rád nižšia ako nad rovníkom (pozri obr. 3) a hodnota koeficientu je okolo 0,3.

Z vyššie uvedeného vyplýva, že celkový vzhľad bielej koróny sa s fázou cyklu slnečnej aktivity mení (obr. 4), ale ako sa jednotlivé koronálne lúče tvoria, akú majú životnosť, nie je známe.

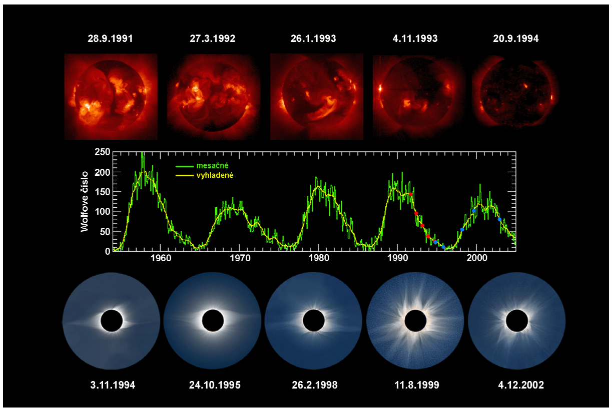

Obr. 4. Variabilita tvaru bielej koróny (dole), priebeh Wolfowho čísla (stred) a röntgenovej koróny z družice Yohkoh (hore). (Yohkoh, P. Rapavý a V. Rušin)

V poslednom období, na základe počítačového spracovania snímok bielej koróny Druckmüllerovou metódou [7], sa dajú získať extrémne kvalitné snímky bielej koróny, ktoré prinášajú svoje ovocie. Takto napríklad v roku 2006 bol na základe pozorovaní bielej koróny od Nigeru po Turecko pozorovaný výtrysk lúča v polárnej oblasti s rýchlosťou asi 70 $km.s^{-1}$. Niečo podobné sa pozorovalo z družíc [8], ale toto bolo prvé pozorovanie v bielej koróne zo Zeme. Dá sa predpokladať, a nielen z tohoto zatmenia, že máloškálová dynamika nebude pre bielu korónu ničím výnimočným. Pri inom zatmení sa zistilo, že jasné štruktúry bielej koróny sú temer identické s tými, ako sa pozorujú v spektrálnych čiarach extrémne ultrafialovej oblasti spektra [9]. Výnimočnosťou Druckműllerovej metódy je aj to, že pri vhodne zvolenom pozorovacom programe a kvalitnom počasí počas úplného zatmenia sa prilbicovité štruktúry identifikovali až vo vzdialenosti 20 polomerov Slnka, čo vlastne dokáže len C3 koronograf na kozmickej sonde SOHO. Iným dôkazom vysokej citlivosti Druckmüllerovej metódy je identifikácia plošného, intenzitne veľmi slabého útvaru počas úplného zatmenia v roku 2006 nad severným pólom Slnka. Tento útvar podľa svojho vzhľadu bol pomenovaný „záclona“ [10]. Žiaľ, doteraz sa nepodarilo vysvetliť, či je to ejekcia koronálnej hmoty alebo nárazová vlna po erupcii, alebo je to niečo, čo sme doteraz nepozorovali. Proti erekcií koronálnej hmoty alebo nárazovej vlne svedčí skutočnosť, že výška „záclony“ voči povrchu Slnka sa v priebehu 64 minút nezmenila.

Viac informácií o výskume slnečnej koróny, či už počas úplných zatmení Slnka Mesiacom alebo mimo zatmení sa dá nájsť v [11], [12] a [13].

KOMÉTY A EJEKCIE KORONÁLNEJ HMOTY

Úplné zatmenia Slnka sa do histórie zapísali aj prvým pozorovaním kométy Kreutzovej skupiny (X/1882 K1 známa aj pod menom *Zatmeňova kométa 1882*) a to pri zatmení Slnka 17. mája 1898 (obr. 5), ako aj prvým pozorovaním ejekcie koronálnej hmoty (CME) – pri zatmení 1860 v Torreblanca (obr. 6, vľavo), ktorý zakreslil nemecký astronóm W. Tempel [14]. Druhý CME v čase zatmenia bol pozorovaný 16. februára 1980 a jeho polohu vo výške asi 6 polomerov Slnka sme identifikovali na základe pozorovania bielej koróny v Indii [15]. Jeho prvá poloha bola pozorovaná v Afrike a pri porovnaní s pozorovaním v Indii bolo zistené, že jeho projektovaná rýchlosť bola 650 km s^{-1} a radí sa k priemerným rýchlostiam CME, ako boli určené na základe mnohých pozorovaní zo SOHO (SOlar and Heliospheric Observatory). SOHO bežne pozoruje CME (obr. 6, vpravo) – v minime asi jeden prípad za deň, v maxime aj šesť.

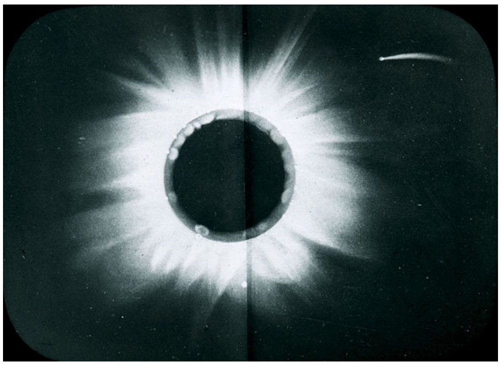

Obr. 5. Kométa Kreutzovej skupiny pri úplnom zatmení Slnka 17. mája 1882. (http://xjubier.free.fr/site_stickers/solar_corona_shape/1882_05_17_Comet.jpg).

Kométy Kreutzovej skupiny majú perihélium v extrémnej blízkosti Slnka (okolo 100 tisíc km) a veľmi často sa mnohé z nich v dôsledku vysokej teploty „vyparia“ v koróne. Meno nesú podľa nemeckého astronóma H. Kreutza (1854-1907), ktorý študoval ich dráhy. Veľké kométy Kreutzovej skupiny, napríklad kométa Ikeya-Seki (C/1965 S1), aj keď perihélium majú blízko Slnka, v jeho atmosfére sa nevyparia a v prípade ich vysokej jasnosti, sú pozorovateľné malým ďalekohľadom aj cez deň. Počet komét Kreutzovej skupiny zo SOHO presiahol už počet 6000.

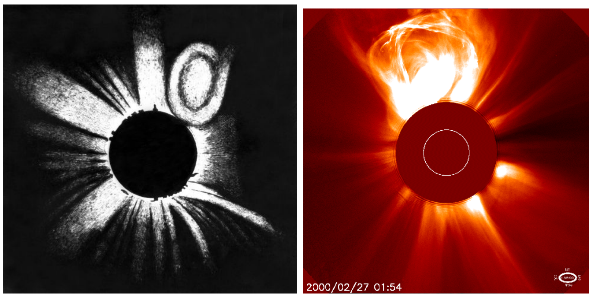

Obr. 6. Ejekcia koronálnej hmoty ako ju zakreslil W. Tempel (vľavo) a z kozmickej sondy SOHO. (Reprodukcia zo [14] a ESA/NASA/SOHO/C2).

Za zmienku stojí ešte skutočnosť, že Druckműllerova metóda spracovania obrazov je mimoriadne citlivá, o čom svedčí fakt, že na snímkach bielej koróny z 1. augusta 2008 bola na základe pozorovaní v okolí Novosibírska (Ruská federácia) a Altaja (Mongolsko) s časovým rozdielom 19 minút, identifikovaná aj kométa Kreutzovej skupiny (obr. 7) s magnitúdou len okolo 10.

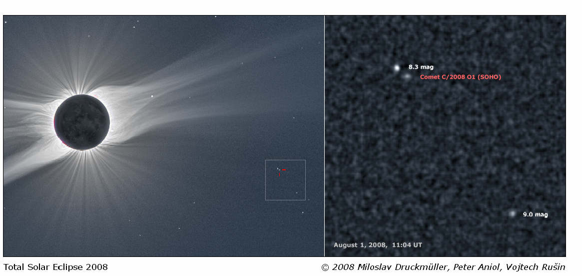

Obr. 7. Kométa Kreutzovej skupiny (na snímke vpravo), pozorovaná 1. augusta 2008. (M. Druckmüller, P. Aniol, V. Rušin).

VULKAN A VŠEOBECNÁ TEÓRIA RELATIVITY

Úplné zatmenia Slnka poskytli aj príležitosť pre výskumy, ktoré bezprostredne nesúvisia s pozorovaním koróny počas úplných zatmení, ale pri zatmeniach sa takéto experimenty robili. V podstate to boli dva druhy experimentov:

(1) hľadanie malej, hypotetickej planéty Vulkan. Vulkan mal byť k Slnku bližšie ako Merkúr a jeho existenciou sa malo dať vysvetliť stáčanie perihélia Merkúra – okolo 43 oblúkových sekúnd za storočie. Túto hypotézu predložil francúzsky matematik J. Le Vernier, ktorý ju v definitívnej verzií publikoval v roku 1859. Na základe denných pozorovaní viacerých astronómov amatérov tej doby, ktorí údajne pozorovali prechod Vulkana aj popred slnečný disk, Le Vernier vypočítal, že Vulkan by sa mal nachádzať vo vzdialenosti asi 21 miliónov kilometrov od Slnka (0,14

astronomickej jednotky = AU) s dobou obehu 19 dní a 17 hodín a sklonom 8 stupňov k ekliptike. Pri pozorovaní zo Zeme jeho najväčšia elongancia nemala byť väčšia ako 8 stupňov. Neskoršie, denné aj zatmeňové hľadania hypotetickej planéty Vulkan neboli jednoznačné potvrdené. Hypotetická planéta sa nenašla ani pri experimente z roku 1973, ktorý robili aj naši kolegovia v Nigeri. Dnes sa všeobecne predpokladá, že vo vzdialenosti okolo 0,1 AU by sa mohli nachádzať, možno aj dočasne, malé asteroidy s priemerom do 60 km, ale pozorovania nič také nepotvrdzujú. Stáčanie perihélia Merkúra vysvetlila až všeobecná teória relativity, ktorú v roku 1915 publikoval Albert Einstein a je spôsobené gravitačným poľom Slnka.

(2) Ako je známe, v roku 1905 A. Einstein, najväčší fyzik všetkých čias, nositeľ Nobelovej ceny z roku 1921 za objav fotoelektrického efektu a za zásluhy o rozvoj teoretickej fyziky, predložil špeciálnu teóriu relativity, ktorú neskôr rozšíril a zovšeobecnil. Od roku 1915 ju poznáme pod menom všeobecná teória relativity. Obe teórie zásadným spôsobom ovplyvnili vývoj astronómie, astrofyziky a fyziky vôbec, a sú základom modernej kozmológie a relativistickej astrofyziky. Základom všeobecnej teórie relativity je tzv. princíp ekvivalencie, ktorý hovorí, že gravitačné a zotrvačné sily majú rovnakú fyzikálnu podstatu a riadia sa rovnakými fyzikálnymi zákonmi. Podľa tejto teórie hmotné telesá spôsobujú zakrivenie okolitého priestoročasu, preto všetko, čo bude prechádzať v dostatočnej blízkosti okolo ľubovoľného hmotného telesa, pohybuje sa po zakrivenej dráhe. Veľkosť zakrivenia závisí od hmotnosti pôsobiaceho telesa.

Zo všeobecnej teórie relativity okrem iného vyplýva, že zakrivenie svetelného lúča pri jeho prechode v tesnej blízkosti Slnka bude okolo 1,75 oblúkovej sekundy, kým z klasickej Newtonovej teórie to malo byť len 0,87 oblúkovej sekundy [16] a [17]. Výpočty previedol sám Einstein, ktorý ako prvý na takéto zakrivenie svetelného lúča poukázal. Veľkosť zakrivenia v tom čase sa mohla dať overiť len pri úplnom zatmení Slnka Mesiacom. Polohy hviezd na snímkach, ktoré sa počas zatmenia nachádzali v blízkosti Slnka, by v porovnaní s ich polohami na snímkach, ktoré boli urobené mimo zatmenia, boli posunuté zhruba o 1,75 oblúkových sekúnd smerom od centra Slnka.

Einstein listom požiadal o preverenie svojich výpočtov amerického astrofyzika G. E. Haleho, objaviteľa mnohých astronomických zariadení, okrem iného, aj spektroheliografu a spektrohelioskopu, magnetického poľa na Slnku a riaditeľa hvezdárne na Mount Wilson, či by mohol tento efekt pri najbližšom úplnom zatmení Slnka zmerať. Hale však jeho žiadosť zdvorilo zamietol. Takýto experiment je značne náročný, pretože pozorovanie Slnka pri zatmení sa musí robiť ďalekohľadom s dostatočne dlhým ohniskom, aby bola veľká rozlišovacia schopnosť. Zorné pole oblohy, do ktorého sa premietalo Slnko počas úplného zatmenia sa muselo fotografovať neskôr v noci, najlepšie o pol roka neskôr. Okrem toho, na exponovanej snímke počas úplného zatmenia Slnka sa popri bielej koróne musia nachádzať aj hviezdy, čo znamená, správne odhadnúť expozíciu. Pri značnej variabilite svetla koróny medzi minimom a maximom slnečnej aktivity je to dosť problematické. V „preexponovanej“ koróne by svetelné stopy hviezd zanikli, pri krátkej expozícii by sa na fotografickom materiále vôbec nemuseli objaviť. Polohy hviezd na oboch platniach sa musia veľmi presne zmerať. Rozdiel v polohe hviezdy medzi normálnou nočnou polohou a „zatmeňovou“, je efekt všeobecnej teórie relativity.

Preveriť správnosť Einsteinových výpočtov o zakrivení svetelného lúča v blízkosti Slnka sa chceli pokúsiť nemeckí vedci. Zorganizovali výpravu za zatmením Slnka, ktoré nastalo 21. augusta 1914. Na ruskom území boli zadržaní a internovaní asi jeden mesiac. Zatmenie nečakalo, a tak sa nijaký experiment neuskutočnil.

Riskantný experiment s ohybom svetla počas úplného zatmenia Slnka sa pokúsil urobiť mladý a vynikajúci anglický fyzik a astronóm, sir A. S. Eddington. So svojím „relativistickým“ experimentom sa vybral pozorovať úplné zatmenie Slnka na ostrov Principe (západne od Afriky), ktoré nastalo 29. mája 1919. Eddington a jeho spoločník E.T. Cottingham tvorili jednu skupinu. Druhá dvojčlenná skupina, C. Davidson a A. Crommelin, sa vybrala pozorovať rovnaké zatmenie do Brazílie, na pozorovacie stanovište Sobral. Kým počasie v Sobrale bolo dobré, Eddingtonovi nebolo veľmi priaznivo naklonené. Ráno v deň zatmenia pršalo a Slnko cez mraky začalo byť viditeľné až po prvom kontakte (Mesiac už bol „nasunutý“ na Slnko). Mladý, ambiciózny Eddington aj cez tenkú vrstvu mrakov urobil z úplného zatmenia 16 záberov. Po pol roku svoj experiment zopakoval. Dňa 6. novembra 1919 na zasadaní Kráľovskej astronomickej spoločnosti v Londýne bolo oznámené, že odchýlka svetelného lúča pomocou dvoch experimentov v blízkosti slnečného okraja bola nameraná s hodnotami 1,61 ± 0,30 (Principe) a 1,98 ± 0,12 oblúkových sekúnd (Sobral) [18]. Opakované premeriavanie polôh hviezd na platniach zo Sobralu, ktoré bolo robené v roku 1979 potvrdilo správnosť nielen pôvodnej hodnoty zo „4-inch lens“ experimentu, teda 1,98 oblúkových sekúnd, ale pre druhý experiment „astrographic lens“ sa namerala odchýlka 1,55 ± 0,34, kým jeho pôvodná hodnota bola „len“ 0,93 oblúkových sekúnd [19]. Einsteinova všeobecná teória relativity dopadla na výbornú a aj vďaka médiám si začala raziť cestu do vedeckého a laického sveta. Dnes o správnosti všeobecnej teórii relativity, ktorá zmenila fyziku, nik nepochybuje. Prispeli k tomu jednak opakované experimenty s ohybom svetla počas úplných zatmení Slnka Mesiacom v rokoch 1922, 1961, 1973, no najmä pozorovania kvazarov v rádiovej oblasti spektra (viac ako 2 milióny). Z týchto pozorovaní vyplýva, že pozorovaná odchýlka s predpovedanou hodnotou je takmer súhlasná s presnosťou na 0,99992 ± 0,00023.

ROTÁCIA ZEME

Poloha mesačného tieňa na povrchu Zeme sa dá presne vypočítať. Rotácia našej Zeme, ako je známe sa spomaľuje (asi 1,7 milisekundy za sto rokov), následkom čoho sa mesačný tieň od vopred vypočítanej polohy posunie. Historické zatmenia Slnka tak môžu poslúžiť na výskum rotácie Zeme. Ako príklad sa uvádza úplné zatmenie Slnka z 15. apríla 136 pred naším letopočtom, o ktorom sa dá so stopercentnou istotou povedať, že prechádzalo cez Jeruzalem. Ak sa predpokladá, že rotácia Zeme by bola po celé toto obdobie konštantná ako je dnes, výpočty ukazujú, že mesačný tieň by sa musel nachádzať asi 5000 km od Babylonu na západ. Ak sa zoberie do úvahy príliv a odliv, teda sily, ktoré spomaľujú rotáciu Zeme, potom by sa mesačný tieň mal nachádzať 2000 km od Babylonu smerom na východ [24]. Dôvody pre kolísanie rotácie Zeme nie sú spoľahlivo vysvetlené, ale môžu byť vyvolané aj topením sa ľadovcov a následnou zmenou výšky hladín svetových morí a pod.

ZÁVER

Úplné zatmenia Slnka, hoci sa vyskytujú zriedkavo, v minulosti poslúžili na zásadne nové objavy: koróna, hélium, vysokoionizované prvky, ejekcia koronálnej hmoty, nový typ komét; hľadala sa hypotetická planéta Vulkan, testovala sa odchýlka svetla hviezd v blízkosti Slnka. Zo spomínaných výskumov, úplné zatmenia Slnka slúžia dnes predovšetkým alebo výhradne výskumu bielej koróny, predovšetkým jej najvnútornejšej časti, pretože jej vonkajšia časť sa pozoruje z kozmického priestoru. Vo výskume slnečnej koróny zostáva niekoľko nezodpovedaných otázok, napríklad, stupeň polarizácie, najmä v emisnej koróne, doplňovanie hmoty do koróny z povrchu Slnka, tvorba veľkoškálových prilbicovitých štruktúr a ich životnosť. Za najväčší problém súčasnej astrofyziky sa pokladá mechanizmus ohrevu koróny. Koróna má veľmi vysokú teplotu, 1-5 miliónov K, kým povrch Slnka len 5700 K. Čo teda ohrieva korónu na tak vysokú teplotu? V súčasnosti sa predpokladajú minimálne 4 mechanizmy ohrevu: (1) akustické (zvukové) vlny, ktoré generuje konvektívna zóna, (2) Alfvénove vlny alebo (3) iné typy vĺn, ktoré generujú magnetické polia. Štvrtým typom by mali byť nanoerupcie, pri ktorých sa uvoľňuje asi 6 x 10^{17} W energie. Termín nanoerupcia bol zavedený Parkerom [20], ako možný mechanizmus pre ohrev koróny, avšak doteraz nanoerupcie neboli pozorované [21]. Nanoerupcia, podobne ako erupcia, je výsledkom rekonexie magnetických polí veľmi malých rozmerov s krátkym časovým trvaním. Mali by sa vyskytovať permanentne po celom povrchu Slnka. Svoju úlohu pri ohreve koróny by mala zohrať aj disipácia elektrických prúdov v koróne, spojená s rekonexiou magnetických polí (napr. [13]). Keďže koróny sa pozorujú aj u iných typov hviezd, napr. [22], [23], problematika ich výskumu je zložitejšia.

Slnečná koróna je horúci, dynamický objekt, ktorý cez slnečný vietor zasahuje ďaleko za obežnú dráhu našej Zeme. Zem sa nachádza v slnečnej koróne a je „obklopená“ siločiarami magnetických polí zo Slnka, ktoré so sebou ťahajú častice slnečného vetra. Magnetické pole Slnka tak reaguje s galaktickým kozmickým žiarením, ktoré pre život na Zemi je veľmi nebezpečné. Dá sa len veriť, že koordinované pozorovania koróny zo Zeme, družíc či kozmických sond, nám pomôže „odhaliť“ v krátkej dobe všetky jej tajomstva a prispieť tak k lepšiemu poznaniu nielen fyziky Slnka, ale aj jeho vplyvov na Zem, ktoré sa dnes robí v rámci medzinárodného programu „Kozmické počasie“.

POĎAKOVANIE: Práca bola čiastočne podporená agentúrou VEGA č. 7012 "Výskum magnetických polí v slnečnej koróne a ich odozvy v heliosfére" a APVV, projekt LPP-0146-06 „Stretnutia s vesmírom“. Ďakujem organizátorom za pozvanie na predmetnú konferenciu a finančný príspevok na cestu.

REFERENCES

1. B. Edlén, Z. Astrophys. **22**, 30 (1942).
2. B. Lyot, Z. Astrophysik **5**, 73 (1932).
3. A.W. Peterson, Astrophys. J. **148**, L37 (1967).
4. R.A. Gulyaev, P.V.Shcheglov, Contr. Astron. Obs. Skalnaté Pleso **28** (1999).
5. Y.M. Wang et al., Astrophys. J. **658**, 1340 (2007).
6. P.G. Judge, Astrophys. J. **500**, 1009 (1998).
7. M. Druckmüller, V. Rušin, M. Minarovjech, Contr. Astron. Obs. Skalnaté Pleso **36**, 131(2006).
8. A.H. Gabriel, F. Bely-Dubau, P. Lemaire, Astrophys. J. **589**, 623 (2003).
9. J.M. Pasachoff et al., Solar Physics **238**, 261 (2006).
10. J.M. Pasachoff, M. Druckmüller, V. Rušin, M. Saniga, Astrophys. J. **665**, 827 (2007).
11. V. Rušin, M. Rybanský, Slnečná koróna (VEDA, vydavateľstvo SAV, Bratislava - 1990).
12. P. Guillermier, S. Koutchmy, Total eclipses, science, observations, myths and legends, (Springer – Praxis Publ. Ltd, Chichester, UK – 1999).
13. L. Golub, J.M. Pasachoff, The solar corona, (Cambridge University Press, Anglicko – 2009).
14. J.A. Eddy, Astron. Astrophys. **34**, 235 (1974).
15. V. Rušin, M. Rybanský, Bull. Astron. Inst. Czechosl. **34**, 257(1983).
16. A. Einstein, Ann. Phys. **340**, 898 (1911).
17. A. Einstein, Ann. Phys. **354**, 769 (1916).
18. F.W. Dyson, A.S. Eddington, C.R. Davidson, Philos. Trans. R. Soc. London, Ser. A, **220**, 29 (1920).
19. D. Kennefick, Physics Today, March 2009**,** 37 (2009).
20. E.N. Parker, Astrophys. J. **264**, 642 (1983).
21. M.J. Aschwanden, Astrophys. J. **672**, L135 (2008).
22. J.H.M.M. Schmidt, R.Wichman, Nature **412**, Issue 6846, 508 (2001).
23. E.N.Parker, In Solar and stellar coronal structure and dynamics (ed. R.C. Altrock), (Sunspot NM, USA – 1988).
24. V. Rušin, Slnko-naša najbližšia hviezda (VEDA, Bratislava -2005).

A NEW MECHANISM FOR THE PHI MESON PRODUCTION

B. Tomášik[ab], tomasik@fpv.umb.sk, E.E. Kolomeitsev[a], kolomeitsev@fpv.umb.sk
[a]Univerzita Mateja Bela, Tajovského 40, 97401 Banská Bystrica
[b]FJFI, České vysoké učení technické v Praze, Břehová 11, 11519 Praha 1

INTRODUCTION

The ϕ meson is very useful probe in experiments with relativistic nuclear collisions, that aim to study nuclear matter at large baryon densities and/or temperatures. The dominant part of its wave function is the spin-one bound state of $\bar{s}$ and s quarks. Hence, its abundance is closely related to the production of strangeness. Note that enhanced strangeness production is one of the signatures for the appearance of deconfined matter due to lower thresholds and higher available energies [1]. In order to claim an enhancement, the reference value must be well known, i.e. the expected abundance of ϕs in the hadronic system.

Nuclear collisions produce baryon-dominated matter, the dominance being stronger in collisions at lower energies. In the hadronic matter created in collisions in the SIS or AGS energy domain, i.e. $\sqrt{s_{\rm NN}}$ of the order hundreds of MeV up to a few GeV, the usually assumed processes for ϕ production are reactions $\pi N \to \phi N$. The cross-section for such a reaction is, however, small in accord with the Okubo-Zweig-Iizuka rule (OZI), which dictates the suppression of the interaction of pure $\bar{s}s$ state with non-strange hadrons. Strangeness coalescence reactions like $K\bar{K} \to \phi$, $K\bar{K} \to \phi\rho$ and $K\Lambda \to \phi N$ are also possible. Yet they are extremely unlikely (at these low energies) because of the rareness of strange hadrons in the fireball.

In addition to the mentioned processes, we propose that the ϕ meson can be produced in hadronic systems in catalytic reactions $\pi Y \to \phi Y$ and $\bar{K}N \to \phi Y$ [2]. In comparison to the coalescence reactions these processes might have higher rates because they involve only one strange species as reactant and thus are less suppressed in case of strangeness undersaturation. In addition to that, the catalytic reactions are not OZI suppressed. At the AGS energies, where kaon coalescence is practically impossible, with cross sections of the order of few millibarns they can contribute to ϕ production comparably to conventional reactions.

EXPERIMENTAL SITUATION

Abundance of the ϕ meson was measured at the SIS energies by FOPI collaboration in Ni+Ni reactions at 1.93 AGeV [3] and by the HADES collaboration in Ar+KCl reactions at 1.756 AGeV [4]. The measured yields were clearly larger than theoretical calculations from various transport models, which at these subthreshold energies operate with reactions $BB \to BB\phi$, $\pi B \to \phi B$ ($B = N, \Delta$) and even $\rho B \to \phi N$, $\pi N(1520) \to \phi N$ [5, 6, 7]. Kaons are so scarce at these energies that kaon coalescence channel is effectively inoperative.

At the SPS, the NA49 collaboration measured widths of the rapidity distributions of ϕ mesons [8]. With increasing collision energy they are found to grow faster than the widths of πs, Ks, and Λs. This contradicts the expectation that would follow from the strangeness coalescence reactions and points to a new mode of ϕ production. It must be clarified whether it requires the appearance of deconfined matter.

AN ESTIMATE OF THE CROSS-SECTIONS

We estimate the cross-sections of the catalytic reactions $\pi Y \to N\phi$ and $\bar{K}N \to Y\phi$ within a simple model in which we consider the lightest strange hadrons (K, $\bar{K}$, Y) that interact with pions and nucleons. The ϕ meson is included as a gauge boson for the local $U(1)$ symmetry associated with strangeness conservation. The lagrangian reads

$$\begin{aligned}
\mathcal{L} &= \bar{\Lambda}\left(i\,\partial\cdot\gamma+\phi\cdot\gamma-m_{\Lambda}\right)\Lambda \\
&+ \bar{\Sigma}_a\left(i\,\partial\cdot\gamma+\phi\cdot\gamma-m_{\Sigma}\right)\Sigma^a \\
&+ \frac{1}{2}\left(\partial-i\,\phi\right)_{\mu}K^{\dagger}\left(\partial+i\,\phi\right)^{\mu}K-\frac{1}{2}\,m_K^2\,K^{\dagger}\,K \\
&+ C_{\pi\Lambda\Sigma}\left(\bar{\Lambda}\,\gamma_{\mu}\,\gamma_5\,\Sigma^a+\bar{\Sigma}^a\,\gamma_{\mu}\,\gamma_5\,\Lambda\right)\partial^{\mu}\pi_a \\
&+ C_{\pi\Sigma\Sigma}\,i\,\epsilon_{abc}\left(\bar{\Sigma}^a\gamma_{\mu}\,\gamma_5\Sigma^b\right)\partial^{\mu}\pi^c \\
&+ C_{KN\Sigma}\Big(\bar{N}\,\gamma_{\mu}\,\gamma_5\,\tau_a\Sigma^a\left(\partial^{\mu}+i\,g_{\phi}\,\phi^{\mu}\right)K \\
&\qquad\qquad +\left(\partial^{\mu}-i\,g_{\phi}\,\phi^{\mu}\right)K^{\dagger}\,\bar{\Sigma}_a\tau^a\,\gamma_{\mu}\,\gamma_5\,N\Big) \\
&+ C_{KN\Lambda}\Big(\bar{N}\,\gamma_{\mu}\,\gamma_5\,\Lambda\left(\partial^{\mu}+i\,g_{\phi}\,\phi^{\mu}\right)K \\
&\qquad\qquad +\left(\partial^{\mu}-i\,g_{\phi}\,\phi^{\mu}\right)K^{\dagger}\,\bar{\Lambda}\,\gamma_{\mu}\,\gamma_5\,N\Big)\,, \qquad (1)
\end{aligned}$$

where π^a and Σ^a stand for isospin triplets of pions and Σs; isospin doublets of kaons and nucleons are $K = (K^+, K^0)$ and $N = (p, n)$. Couplings assume the values $g_\phi = 4.64$ (from $\phi \to K\bar{K}$ decay), $C_{\pi\Lambda\Sigma} = 0.63\,m_\pi^{-1}$, $C_{\pi\Sigma\Sigma} = -0.56\,m_\pi^{-1}$, $C_{KN\Lambda} = -0.7\,m_\pi^{-1}$, and $C_{KN\Sigma} = 0.4\,m_\pi^{-1}$ (from the analysis of meson-baryon interactions).

The resulting isospin-averaged cross-sections for pion-hyperon reactions are shown in Fig. 1 as functions of $\Delta s^{1/2} = s^{1/2} - s_0^{1/2}$, where $s_0^{1/2}$ is the threshold energy. Cross-sections for reactions $\pi Y \to \phi Y$ are compared with the known values of OZI suppressed reactions $\pi N \to \phi N$. Cross-sections for the catalytic reactions are up to 70 times bigger than the πN reactions. For brevity, we do not show the cross-section for the $\bar{K}N \to \phi Y$ reaction, but they are of similar magnitude.

In order to get similar or larger yields from catalytic reactions as from the conventional ones, the cross-sections should fulfill

$$\begin{aligned}
\sigma(\pi\Lambda\to\phi Y) &\gtrsim \frac{N_{\rm part}}{\langle\Lambda\rangle}\,\sigma(\pi N\to\phi N)\,, \\
\sigma(\bar{K}N\to\phi Y) &\gtrsim \frac{\langle\pi^+ + \pi^-\rangle}{2\,\langle K^-\rangle}\,\sigma(\pi N\to\phi N)\,, \qquad (2)
\end{aligned}$$

where $N_{\rm part}$ is the number of participants, and $\langle\Lambda\rangle$, $\langle\pi^+ + \pi^-\rangle$, and $\langle K^-\rangle$ stand for the average multiplic-

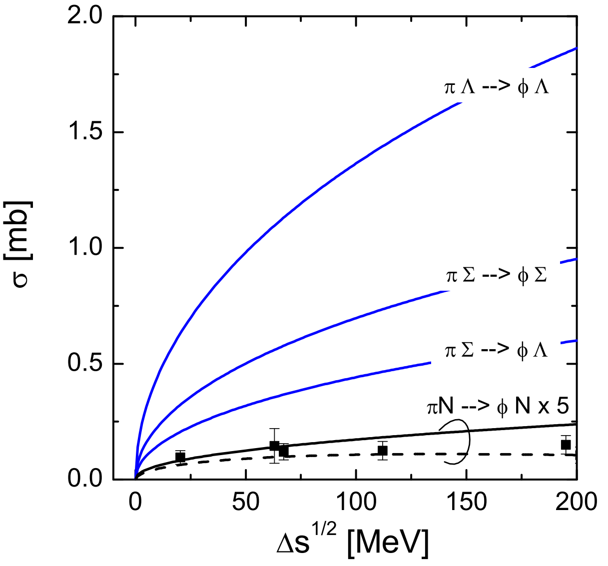

Fig. 1. Cross-sections of catalytic ϕ-producing reactions as a function of $\Delta s^{1/2}$ (see text). The data points are measurements for the $\pi N \to \phi N$ reaction, the two lowest curves are results of two different model calculations for that reaction; all are scaled by a factor of 5.

ities of lambdas, charged pions, and negative kaons, respectively. For nuclear collisions at $\sqrt{s_{\rm NN}} = 10$ GeV these estimates give minimal cross-sections about 1 mb [2]. The calculated cross-sections are well within this ball park.

PRODUCTION OF ϕ

The resulting amount of ϕs that is produced in nuclear collisions is obtained from integrating the production rates over the whole space-time history of fireball evolution. In general, the rate for reaction $ab \to cd$ is given as

$$\mathcal{R}_{ab}^{cd} = \kappa_{ab}^{cd}\, \rho_a\, \rho_b\, , \tag{3}$$

where

$$\kappa_{ab}^{cd} = \frac{\langle \sigma_{ab}^{cd} v_{ab}\rangle}{1+\delta_{ab}}\, , \tag{4}$$

is the cross-section averaged with relative velocity of the reactants over their momentum distribution. The ρs are the densities of the reactants.

Kaon and hyperon densities needed for the ϕ production rates must be calculated together with ϕ. In this calculation we parametrise the temperature and the baryon density as

$$T(t) = \frac{T_m}{(t/t_0+1)^\alpha}\, , \qquad \rho_B(t) = \frac{\rho_m}{(t/t_0+1)^{3\alpha/2}}\, . \tag{5}$$

Densities of pions and non-strange baryons are calculated according to chemical equilibrium. For kaon production we consider reactions of πN, $\pi\Delta$, $\pi\pi$, NN, and $N\Delta$. The rates for ϕ production calculated for evolution scenario $T_m = 150$ MeV, $\rho_m = 6\rho_0$, $\alpha = 0.5$, $t_0 = 10$ fm/c are shown in Fig. 2. Under these conditions, the rates for catalytic production after 2 fm/c are higher than those for $\pi N \to \phi N$ reactions.

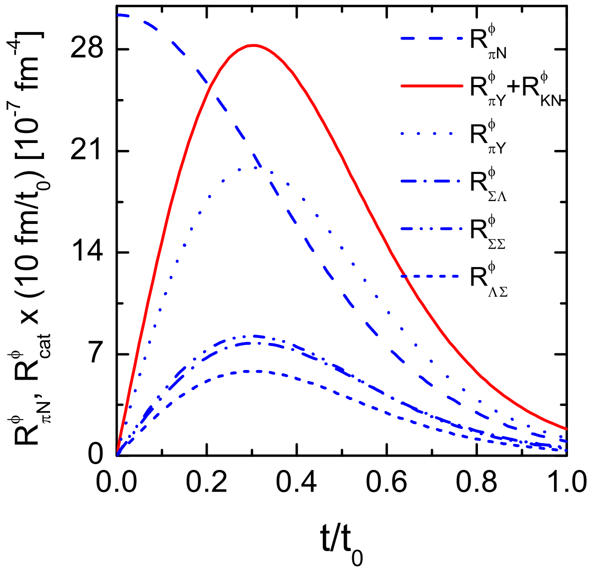

Fig. 2. Production rates for ϕ production from $\pi N \to \phi N$ reactions (dashed) and from the catalytic reactions (solid line). The contribution from reactions $\pi Y \to \phi Y$ marked by dotted line is also broken into individual channels: $\pi\Sigma \to \phi\Lambda$ (dash-dotted), $\pi\Sigma \to \phi\Sigma$ (dash-dot-dot), and $\pi\Lambda \to \phi\Sigma$ (short-dashed).

We have also looked at the widths of the rapidity distributions of ϕ at the SPS [8]. Their rise with the collision energy is much stronger than that of kaons. It could be driven by the hyperons. We estimated the widths just by assuming that they are given by the products of the distributions of the reactants. Taking into account strangeness coalescence $K\Lambda \to \phi N$ and catalytic reaction $\pi\Lambda \to \phi Y$ we obtained theoretical values for the ϕ width which agrees with data up to the collision energy of 80 AGeV.

SUMMARY

Catalytic ϕ-producing reactions may be relevant source of ϕ-mesons. The cross-sections and more precise description of fireball dynamics deserve more careful studies.

Financial support provided by VEGA 1/4012/07.

REFERENCES

1. P. Koch, B. Müller and J. Rafelski, Phys. Rept. **142** (1986) 167.
2. E. E. Kolomeitsev and B. Tomášik, J. Phys. G **36** (2009) 095104 [arXiv:0903.4322 [nucl-th]].
3. A. Mangiarotti *et al* (FOPI Collaboration), Nucl. Phys. A **714** 89 (2003).
4. G. Agakishiev *et al* (The HADES Collaboration) arXiv:0902.3487 [nucl-ex].
5. W.S. Chung, G.Q. Li and C.M. Ko, Nucl. Phys. A **625** 347 (1997).
6. B. Kämpfer, R. Kotte, C. Hartnack and J. Aichelin J. Phys. G: Nucl. Part. Phys. **28** 2035 (2002).
7. H.W. Barz, M. Zétényi, Gy. Wolf and B. Kämpfer, Nucl. Phys. A **705** 223 (2002).
8. C. Alt *et al.* [NA49 collaboration], Phys. Rev. C **78** (2008) 044907.

REALIZATION OF THE LENGTH UNIT -METRE

[1]Bartl, J., umerbart@savba.sk, [1]Ševčík, R., umersevc@savba.sk,
[1]Jacko, V., umerjack@savba.sk, [2]Fíra, R., fira@smu.gov.sk
[1]Institute of Measurement Science Slovak Academy of Sciences, Dubravska cesta 9, 841 04 Bratislava, Slovakia
[2]Slovak Institute of Metrology, Karloveska 63, 842 55 Bratislava, Slovakia

INTRODUCTION

Since 1983 is he length unit defined ***as the distance, travelled by light in vacuum during the time period of 1/299 792 458 s***. It was adopted the speed of light in vacuum be 299 792 458 m/s exactly [1] and thus uncertainties of both SI basic units (meter and second) are equal ($\sim 10^{-15}$), as far the definition is concerned.

According to the Recommendation 1 (CI-1983), the following three ways for the length unit realization are possible:

a) By means of the length l of the path travelled in vacuum by a plane electromagnetic wave in a time t; this length is obtained from the measured time t, using the relation $l = c_o.t$ and the value of the speed of light in vacuum c_o = 299 792 458 m/s;

b) By means of the wavelength in vacuum λ of a plane electromagnetic wave of frequency ν; this wavelength is obtained from the measured frequency ν using the relation $\lambda = c_o/\nu$ and the value of speed of light in vacuum
c_o = 299 792 458 m/s;

c) By means of one of the radiation from the CIPM Recommendation 1 CI-1997, whose stated wavelength in vacuum or whose frequency can be used with uncertainty shown, provided that the given specifications and accepted good practice are followed;

that in all cases any necessary corrections be applied to take account of actual conditions such as diffraction, gravitation or imperfection in the vacuum.

HELIUM-NEON LASER

Right from the start, the method "c" was the most convenient way of the length unit realisation. The invention of femtosecond comb technique at the end of last century and subsequent progressive spread of comb generators made the method "b" more accessible with increasing trend. Nevertheless, even at the present time the most preferred method is method "c", based on the list of radiations, which frequencies are sufficiently stable to fulfil the metrological criteria. The most widely used and relatively easy viable is the HeNe laser 633 nm, stabilised by the saturated absorption in iodine molecules $^{127}I_2$, having the relative standard combined uncertainty of its frequency $2,5.10^{-11}$. In general, the optical quantum generator is based upon the following principles:

- Stimulated **light emission** in the active optical medium, which is able to be kept at the **thermodynamic unbalance state**, characterized by the energy level inversion;
- **Positive optical feedback**, making possible to convert the quantum amplifier into the light generator. It is realised by placing the active medium into the Fabry-Perot optical resonator created by two mirrors. However, just part of all possible geometrical configurations lead to stable operation – the mostly used combinations are two coaxial concave mirrors or plane and concave mirror.

Frequency of generated waves ν is proportional to the energetic difference ΔW between two energetic states of neon $\nu = \Delta W/h$. In each case the spectrum of frequencies is emitted, forming the spectral line of given shape and finite width, depending on the emitting particle structure and on another external influences as well.

In the ideal case, when all external influences are eliminated to the largest possible extent, the spectral line has the minimal, the so-called **natural width**. The reason beyond its finite value is the fundamental Heisenberg uncertainty principle. In real conditions, the line is broadened noticeably comparing to its natural width, mainly due to the motion and collisions of emitting particles. However, the most determinant factor is the **Doppler broadening** because of the motion of emitting particle (source of radiation), depending on the active medium's mean temperature. Such system can be described as the system of two oscillators. The features of quantum transition determine the first oscillator. Its spectral characteristic is affected mainly by the Doppler phenomenon due to thermal motion of particles, to the detriment of elementary oscillator's radiated energy. The second oscillator is optical resonator and is characterised by its resonance features. Since the quality of optical resonators is large, their spectral width is just a few MHz. Two waves propagate inside the Fabry-Perot resonator, one falling onto the mirror and second being reflected in the opposite direction. The resultant interference depends on phases and all waves are suppressed except of those meeting the condition $\lambda_n = 2.L/n$, where L is the resonator length and n is an integer number. Just those sine waves can have zero amplitude at both mirrors. Therefore at a given resona-

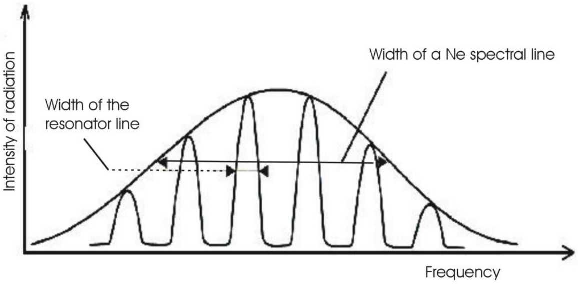

Fig. 1 Comparison of width of spectral line Ne to width of spectral line of resonator

tor length just those electromagnetic oscillations can be kept, which wavelength is given by the mentioned expression. Intervals $\Delta\nu$ between neighbouring frequencies are equal and $\Delta\nu = c/2L$. It means that the frequency of laser radiation is determined mainly by the resonator parameters (Fig.1).

ELIMINATION OF THE DOPPLER BROADENING

As follows from the Maxwell-Boltzmann law of the particles speed distribution of ideal gas, a typical speed of neon molecule at room temperature is about 400 m/s and at the frequency of radiant transition 474 THz, the chaotic motion causes Doppler's broadening of the emission frequency line of about 650 MHz (in relative form $1.37\text{x}10^{-6}$). If such light source is used for the measuring of 1 m length by interferometry, the resulting measurement uncertainty will be at least 1.37 µm, the value being insufficient in most cases. Doppler's broadening can be suppressed by the saturated absorption in vapour of some atoms or molecules. Elimination of the Doppler broadening in HeNe laser 633 nm is realised by inserting of the cell, filled up with iodine $^{127}I_2$, into the resonance cavity. The list of frequencies, corresponding to the iodine hyperfine structure, is given in supplement (Table 20) of the Recommendation 1 (CI-2002).

Absorption of photons arises only in those cases when energy of photons corresponds to energy of the iodine absorption quantum transition. When the frequency of laser beam photons differs a bit from that of iodine molecule, two opposite passing beams in resonator interact with the molecules having the velocities $\pm\, v_x$ (component in the x-axis direction, considered along the optical axis) and stimulate the transition of electrons to the higher level in those molecules moving with the mentioned velocity values. This phenomenon is expressed with two local minimums. If we tune the frequency by changing the resonator length L towards the iodine transient frequency, the local minimums shift to each other and deepen - equal to one half rate at the given speed. If the laser frequency is tuned up to the frequency of iodine transition ν_a the qualitative change takes place, because of the same molecules interact with both beams simultaneously. In such a case, the value of v_x is equal to zero. It means that the beam interacts just with those iodine molecules moving in that moment strictly perpendicularly to the optical axis and thus the Doppler's effect is suppressed. However, the second order Doppler's effect still exists, because of the large velocity values of molecules (hundreds meters per second). One of beams causes drop of excited states rate to 0.5 and the second one is not able to cause the same effect, since the rate on the basic level cannot drop under the value 0.5. Therefore no one molecule can be excited by the second beam [2], i.e. for this beam the iodine vapour is transparent. In the very close proximity of the frequency value ν_a, the absorption dips rapidly, which one can observe on the power curve as small peak.

The saturated absorption reaches its maximum at the iodine vapour pressure of 17.29 Pa. In order to get the mentioned pressure in cell, the temperature of the cell's "cold finger" must be kept at 15.0 °C. If the laser is tuned up to the absorption line, the laser frequency is stabilised by the optoelectronic feedback. The feedback is realised by the photodetector, which is placed behind the back resonator mirror. Its electric signal is amplified and filtered.

CONCLUSIONS

The realisation of the length standard in accordance with the current definition of metre has become the object of physical research in many world physical and metrological laboratories. This research contributes to development of new types of lasers of different construction. The effort of researchers is focussed to overcome the magic limit of the relative stability of frequency in orders of 10^{-14} - 10^{-15}, however in the optical domain of electromagnetic spectrum. It can be shown, that due to the second order Doppler's broadening, at the temperature of absorbing medium 15 °C the frequency stability limit lies around the level of 10^{-12}. Therefore it seems that the only way is to cool down the absorbing medium to temperatures close to 0 K (to "stop" the particles), in order to suppress the second order Doppler's effect.

At the present time, such facilities for the length unit realisation are too expensive to be used widely.

ACKNOWLEDGMENT: The authors are grateful Scientific Grand Agency of Ministry of Education of the Slovak Republic and Slovak Academy of Sciences VEGA for financial support of the project No. 2/7081/27 and Science and Technology Assistance Agency SR for financial support of the project APVT-51-012102 during the years 2002-2005.

REFERENCES

1. ČERVEŇ, I.- CHAUPKOVÁ, A.: Physical quantities and units. Bratislava, JSMF & SFS, Edičné centrum Matematicko fyzikálnej fakulty UK Bratislava 2000, 41 p. (In Slovak).
2. FÍRA, R.- NAVRÁTIL, V.: Stabilisation of laser's frequency for metrological purposes by use of saturated absorption. Metrology and testing, **6**, 1999, No. 1-2, pp. 20-24 (In Slovak).
3. LAZAR, J.- ČÍP, O.-RUŽIČKA, B.: Extended cavity semiconductor lasers in fundamental metrology. Fine Mechanic and Optics, **48**, 2003, No. 5, pp.142-145.

CALCULATION OF REPRESENTATIVE CONSTANTS IN DEVELOPED TURBULENCE

L. Ts. Adzhemyan, Loran.Adzhemyan@pobox.spbu.ru, Department of Theoretical Physics, St. Petersburg University, Ulyanovskaya 1, St. Petersburg, Petrodvorets, 198504 Russia, M. Hnatič, hnatic@saske.sk,Institute of Experimental Physics, Slovak Academy of Sciences, Watsonova 47, 040 01 Košice, Slovakia, Faculty of Sciences, P.J. Šafarik University, Moyzesova 16, 040 01 Košice, Slovakia and J. Honkonen, juha.honkonen@helsinki.fi, Department of Military Technology, National Defence University, P.O. Box 7, 00861, Helsinki, Finland

INTRODUCTION

Description of developed turbulence based on the stochastic Navier-Stokes equation in the form of an effective field-theoretic model opens new possibilities for understanding of both the Kolmogorov scaling and the deviation therefrom as well as for calculation of principal physical quantities. The renormalization-group (RG) approach with its various perturbation schemes (e.g. the famous ε expansion, see [1]), with effective analytical and numerical algorithms for evaluation of quantities involved forms a robust method, which allows to put into practice this scenario.

A specific feature of the renormalization-group approach and the ε expansion in the theory of developed turbulence is that the formal small parameter ε is not connected with the space dimension and it is determined only by the noise correlator of random forcing in the stochastic Navier-Stokes equation [2, 3]. Its physical value $\varepsilon = 2$ is not small [4, 5], hence reasonable doubts arise about the effectiveness of such an expansion. For some paramount physical quantities like the critical dimensions of the velocity field and the coefficient of viscosity the ε expansion terminates at the first term due to the Galilei invariance of the theory [2, 3]. Therefore, exact values are predicted for these quantities. However, there are other physically important quantities, viz. the skewness factor, the Kolmogorov constant and critical dimensions of various composite operators, for which the ε series do not terminate [6, 7, 8], therefore the question about the effectiveness of the expansion remains open.

Consider a quantity A calculated at the fixed point of the RG in the renormalized field theory of developed turbulence. In d dimensions it is a function of the parameters ε and d: $A = A(\varepsilon, d)$. In practice, calculations are often carried out in the ε expansion, whose coefficients for the quantity $A(\varepsilon, d)$ depend on the space dimension d

$$A(\varepsilon, d) = \sum_{k=0}^{\infty} A_k(d)\varepsilon^k. \tag{1}$$

Analysis shows that these coefficients $A_k(d)$ have singularities at dimension $d = 2$, which are not eliminated by the renormalization of the d-dimensional theory [8, 9]. These divergences manifest themselves in the form of poles in the parameter $(d-2) \equiv 2\Delta$ in the coefficients of the ε expansion $A_k(d)$, which therefore may be expressed as Laurent series of the form

$$A_k(d) = \sum_{l=0}^{\infty} a_{kl}\,\Delta^{l-k}. \tag{2}$$

Divergences in Δ may be absorbed to suitable additional counterterms, which give rise to a different renormalized field theory. Henceforth, we therefore consider the theory with two formal small parameters ε and Δ, which satisfy the relation $\zeta \equiv \varepsilon/\Delta = const$. This gives rise to the double series

$$A(\varepsilon, d) = \sum_{k=0}^{\infty}\sum_{l=0}^{\infty} \zeta^k a_{kl}\,\Delta^l. \tag{3}$$

Adzhemyan et al [7, 8] have recently proposed to improve the ε expansion of the quantity A by a special summation procedure of the double series (3). This improved ε expansion has produced values of the Kolmogorov constant and skewness factor in a notably better agreement with their experimental values than in the usual ε expansion.

In this paper we strive for the same goal by the aid of a suitably modified renormalization procedure. Instead of the minimal subtraction scheme used in [7, 8], we use the scheme with a normalization point, in which the renormalization constants are chosen by prescribing to suitable renormalized correlation functions finite values at given wave numbers. Such a calculation (*without* expansion in ε) guarantees true reproduction of terms of the minimal subtraction approach and leads to good agreement with experiment already in the one-loop approximation. ¿From the point of view of renormalization of the d-dimensional theory this approach corresponds to the inclusion in the action (see below) of an infrared irrelevant at $d > 2$ operator, which becomes relevant, when $d \to 2$.

STOCHASTIC MODEL OF DEVELOPED TURBULENCE

The statistical model of developed homogeneous and isotropic turbulence of incompressible fluid is based on the stochastic Navier-Stokes equation

$$\nabla_t\varphi_i = \nu_0\partial^2\varphi_i - \partial_i\mathcal{P} + f_i, \qquad \nabla_t \equiv \partial_t + (\varphi\partial). \tag{4}$$

Here, $\varphi_i(t,\mathbf{x})$ is transverse vector field of the fluid velocity, $\mathcal{P}(t,\mathbf{x})$ the pressure, $f_i(t,\mathbf{x})$ is the transverse external random force per unit mass and ν_0 stands for the coefficient of kinematic viscosity. The random force f mimics instabilities generated by initial and boundary conditions and it is assumed to have a Gaussian distribution with zero mean and the pair correlation function

$$D_{ij}(t,\mathbf{x};0,0) = \frac{\delta(t)}{(2\pi)^d}\int d\mathbf{k}\,P_{ij}(\mathbf{k})\,d_f(k)\,e^{\mathrm{i}\mathbf{k}\mathbf{x}}, \tag{5}$$

where $P_{ij}(\mathbf{k}) = \delta_{ij} - k_ik_j/k^2$ is the transverse projection operator and d the dimension of space. In the framework of the RG approach, the function $d_f(k)$ is assumed to have the powerlike form

$$d_f(k) = D_{10}k^{2-2\Delta-2\varepsilon} + D_{20}k^2,\, D_{i0} = u_{i0}\nu_0^3/\bar{S}_d,\, i = 1, 2,$$

where $\Delta \equiv (d-2)/2$, $\bar{S}_d \equiv S_d/(2\pi)^d$, $S_d \equiv 2\pi^{d/2}/\Gamma(d/2)$ is the surface area of the unit sphere in d-dimensional space and Γ is Euler's Gamma function. The quantities Δ, $\varepsilon > 0$ play the rôle of two formal small expansion parameters. The physical value $\Delta = 1/2$ corresponds to three-dimensional space. The physical value of the parameter ε is equal to 2 which corresponds to the energy injection by infinitely large eddies. The second quadratic term with the amplitude D_{20} was introduced to absorb the singularities, which appear in the model as $d \to 2$ (see below). The parameters u_{10} and u_{20} play the rôle of bare charges. The stochastic problem (4), (5) is equivalent to the field-theoretic model with two transverse vector fields $\{\varphi, \varphi'\}$ and the de Dominicis-Janssen action [2]

$$S = \varphi' D \varphi'/2 + \varphi'[-\partial_t \varphi + \nu_0 \partial^2 \varphi - (\varphi\partial)\varphi], \qquad (6)$$

where D is the correlator of random force (5). In (6) all necessary integrals over time and space as well as sums over vector indices are implied. Model (6) is logarithmic (i.e. the coupling constants u_{i0} are dimensionless) at $\varepsilon = 0$, $\Delta = 0$. Ultraviolet (UV) divergences appear in the form of poles in ε, Δ and their linear combinations in the correlation functions of the fields $\{\varphi, \varphi'\}$. The standard analysis of canonical dimensions supplemented by arguments of Galilei invariance shows that for $d \geq 2$ superficial UV divergences in model (6) appear only in the one-irreducible functions $\langle\varphi'\varphi\rangle_{1-\mathrm{ir}}$, $\langle\varphi'\varphi'\rangle_{1-\mathrm{ir}}$ and the counterterms are of the form $\varphi'\partial^2\varphi$ and $\varphi'\partial^2\varphi'$.

These counterterms give rise to multiplicative renormalization of the parameters ν_0 and u_{10}, u_{20} in action (6) with two independent renormalization constants for the coefficient of viscosity ν_0 and for the amplitude D_{20}. Relations between renormalized and bare parameters are

$$\bar{S}_d D_{10} = u_{10}\nu_0^3 = u_1 \mu^{2\varepsilon} \nu^3,$$

$$\bar{S}_d D_{20} = u_{20}\nu_0^3 = u_2 \mu^{-2\Delta} \nu^3 Z_{D_2}, \nu_0 = \nu Z_\nu$$

$$u_{10} = u_1 \mu^{2\varepsilon} Z_{g_1},\; u_{20} = g_2 \mu^{-2\Delta} Z_{u_2},$$

$$Z_{u_1} Z_\nu^3 = 1,\; Z_{u_2} Z_\nu^3 = Z_{D_2}\,.$$

Here, μ is the scale setting parameter, ν is the renormalized viscosity and u_1, u_2 are the dimensionless renormalized coupling constants. The amplitude D_{10} of the non-local term of the correlator of the random force is not renormalized. The renormalization constants Z_ν and Z_{D_2} are found from the condition that the one-irreducible functions $\langle\varphi'\varphi\rangle_{1-\mathrm{ir}}\big|_{\omega=0}$ and $\langle\varphi'\varphi'\rangle_{1-\mathrm{ir}}\big|_{\omega=0}$ are UV finite (are free from poles in ε at $\Delta/\varepsilon = const$).

An RG analysis of the model (6) shows the presence of an IR-stable fixed point $u_1*, u_2 \sim \varepsilon$ for small $\varepsilon > 0$ at $\zeta = const.$, which governs the infrared scaling. The parameters of this scaling – critical dimensions and universal scaling functions – are calculated in the form of series in ε. Due to the Galilei invariance of the theory the series for critical dimensions of fields Δ_φ, $\Delta_{\varphi'}$ and the frequency Δ_ω are terminated at the first order:

$$\Delta_\varphi = 1 - 2\varepsilon/3, \Delta_{\varphi'} = d - 1 + 2\varepsilon/3, \Delta_\omega = 2 - 2\varepsilon/3.$$

These formulae are exact without higher order corrections in ε and at the realistic value $\varepsilon = 2$ assume Kolmogorov values $\Delta_\varphi = -1/3$, $\Delta_\omega = 2/3$. Critical dimensions are free from singularities at $d \to 2$. However, other physical quantities like the skewness factor, the Kolmogorov constant and critical dimensions of various composite operators strongly depend on the space dimension and are expressed in the form of infinite series of types (1), (3).

In order to determine the dependence of these quantities on space dimension we have calculated the renormalization constants, infrared fixed points and scaling exponents in the one-loop approximation. In [9] the renormalization constants were calculated in the minimal subtraction (MS) scheme [only poles with respect to ε, $\Delta = O(\varepsilon)$ and their linear combinations are subtracted]. To improve the numerical performance we have used a renormalization scheme with a normalization point (NP). It is convenient to introduce normalized scalar one-irreducible functions

$$\Gamma_{\varphi'\varphi} = \frac{\langle\varphi_i'\varphi_i\rangle_{1-\mathrm{ir}}\big|_{\omega=0}}{\nu p^2(1-d)}\,, \qquad (7)$$

$$\Gamma_{\varphi'\varphi'} = \frac{\langle\varphi_i'\varphi_i'\rangle_{1-\mathrm{ir}}\big|_{\omega=0}}{\nu^3 p^2(d-1)} - \frac{u_1(\mu/p)^{2\Delta+2\varepsilon}}{\bar{S}_d} - \frac{u_2}{\bar{S}_d} \qquad (8)$$

and determine the renormalization constants from the conditions

$$\Gamma_{\varphi'\varphi}\Big|_{\substack{p=0,\\ \mu=m}} = 1\,, \qquad \Gamma_{\varphi'\varphi'}\Big|_{\substack{p=0,\\ \mu=m}} = 0\,, \qquad (9)$$

where m is an infrared cut-off. Since physical quantities – critical exponents and universal scaling functions – are independent of the renormalization scheme, the application of the RG approach to the renormalized model specified by the condition (9) leads to the same ε, Δ expansions as in [9]. Instead, we propose to use the renormalization scheme (9) *without* the ε, Δ expansion. Such a scheme reproduces correctly the leading terms of expansion in both regimes $\varepsilon \to 0\,, \Delta = const$ and $\varepsilon \sim \Delta \to 0$ simultaneously. In the former, the additional term $\varphi'\partial^2\varphi'$ is an infrared irrelevant operator in the action and the renormalization constant Z_{D_2} describes the renormalization of this additional operator.

Crucial quantities for the RG analysis are $\beta-$functions and anomalous dimensions γ defined as follows

$$\gamma_i = (\beta_1\partial_{u_1} + \beta_2\partial_{u_2}) \ln Z_{u_i}\,, \qquad i = 1, 2\,, \qquad (10)$$

$$\beta_1 = -u_1(2\varepsilon + \gamma_1)\,, \qquad \beta_2 = -u_2(-2\Delta + \gamma_2)\,. \quad (11)$$

One-loop calculation of the renormalization constants Z_{u_i} yields

$$\gamma_1 = -\frac{3(d-1)(u_1+u_2)}{4(d+2)}\,, \gamma_2 = \frac{(d^2-2)(u_1+u_2)^2}{4d(d+2)\,u_2} + \gamma_1. \qquad (12)$$

With the use of (11)and (12) the coordinates of the nontrivial fixed point $u_{1*} > 0$, $u_{2*} > 0$ are found as the solution of the equations $\beta_1(u_*) = 0$, $\beta_2(u_*) = 0$ in the form

$$u_{1*} + u_{2*} = \frac{8\varepsilon(d+2)}{3(d-1)}, u_{2*} = \frac{\varepsilon^2}{\varepsilon + \Delta}\,\frac{8(d^2-2)(d+2)}{9d(d-1)^2}\,.$$

Stability of the fixed point is determined by the sign of the real part of the eigenvalues $\omega_{\pm}$ of the matrix $\partial_j\beta_i\big|_{u=u_*}$:

$$\omega_{\pm} ** = \Delta + \frac{2\varepsilon(2d^2-3d+2)}{3d(d-1)} \pm$$

$$\pm\sqrt{\Delta^2 - \frac{4(d^2-2)}{3d(d-1)}\,\varepsilon\,\Delta - \frac{4(d^2-2)(2d^2-3d+2)}{9d^2(d-1)^2}\,\varepsilon^2}\,.$$

We are interested in the region $\varepsilon > 0$, $\Delta > 0$, in which the eigenvalues $\omega_{\pm}$ are positive. Therefore, the fixed point is infrared stable. In the regime $\varepsilon \sim \Delta \to 0$ we obtain

$$\omega_{\pm} = \Delta + \frac{4\varepsilon}{3} \pm \sqrt{\Delta^2 - \frac{4}{3}\varepsilon\,\Delta - \frac{8}{9}\,\varepsilon^2} + O(\varepsilon^2) \qquad (13)$$

which is consistent with the result of [9]. At $\varepsilon \to 0$, $\Delta = const$ it follows that

$$\omega_{-} = 2\varepsilon + \frac{2(d^2-2)}{3d(d-1)} \cdot \frac{\varepsilon^2}{\Delta} + O(\varepsilon^3)\,, \qquad (14)$$

$$\omega_{+} = 2\Delta + \frac{2(d^2-3d+4)}{3d(d-1)}\varepsilon - \frac{2(d^2-2)}{3d(d-1)} \cdot \frac{\varepsilon^2}{\Delta} + O(\varepsilon^3)\,. \qquad (15)$$

The quantity ω_{-} plays the rôle of the correction index ω in the usual ε expansion in the theory of developed turbulence, whereas ω_{+} determines the critical exponent of the infrared-irrelevant composite operator $\varphi'\partial^2\varphi'$.

The terms $\sim\varepsilon$ in (14) and (15) are reliable: for ω_{-} relation (14) reproduces the known one-loop expression [2] for the exponent ω; for ω_{+} we have checked the result by a direct calculation of the critical dimension of the composite operator $\varphi'\partial^2\varphi'$ in the usual ε expansion. Moreover, the terms $\sim\varepsilon^2/\Delta$ yield the true singular part with respect to Δ in the coefficients of ε^2: for ω_{-} it was confirmed by the pioneering two-loop calculation [6], for ω_{+} we have checked it by calculation of the critical dimension of the composite operator $\varphi'\partial^2\varphi'$ in two-loop approximation. Expression for ω in fact, correctly reproduces main singular terms of the form $\varepsilon(\varepsilon/\Delta)^k$ and all leading terms of the ε expansion, i.e. the first terms of the corresponding Laurent series (2).

Calculation of graphs with increasing number of loops in our renormalization scheme guarantees that results become more precise step by step in the sense that the number of true terms of the ε expansion and the number of singular in Δ contributions is increased: an n-loop calculation correctly reproduces first n of all coefficients $A_k(d)$ in (1), while simultaneously of the coefficients $A_k(d)$ with $k > n$ the first n terms of their Laurent series (2) will be reproduced correctly.

CALCULATION OF THE KOLMOGOROV CONSTANT AND SKEWNESS FACTOR

In the framework of the proposed renormalization scheme we have calculated the Kolmogorov constant and skewness factor.The skewness factor is defined as follows

$$\mathcal{S} \equiv S_3/S_2^{3/2}. \qquad (16)$$

In the Kolmogorov theory the third-order structure function $S_3(r)$ (determined exactly) and the second-order structure function $S_2(r)$ (in the inertial range) have the forms [10, 11]:

$$S_3(r) = -\frac{12}{d(d+2)}\,\bar{\mathcal{E}}\,r, \quad S_2(r) = C_K\bar{\mathcal{E}}^{2/3}r^{2/3} \quad (17)$$

where $\bar{\mathcal{E}}$ is the average energy dissipation rate per unit mass and C_K is the Kolmogorov constant, the value of which is not determined in the framework of the phenomenological approach. All these expressions allow to connect the Kolmogorov constant with the skewness factor:

$$C_K = \Big[-\frac{12}{d(d+2)\mathcal{S}}\Big]^{2/3}. \qquad (18)$$

Among the three quantities $S_2(r)$, $S_3(r)$ and $\mathcal{S}$ only the last one has a unique well-defined ε expansion. Thus, relation (18) may be used to determine C_K by means of the calculated value $\mathcal{S}$.

To find the RG representation of the skewness factor (16) the RG representations of the functions $S_2(r)$ and $S_3(r)$ have to be determined. Using results of calculations of the previous section we obtain the following values for the Kolmogorov constant and the skewness factor at fixed point

$$C_K = [3Q(2)/2]\,[12/d(d+2)]^{2/3}\,, \mathcal{S} = -\,[3Q(2)/2]^{-3/2}\,,$$

where in the one-loop approximation

$$Q(\varepsilon) = \left[4(d-1)/9/u_{1*}^2\right]^{1/3} \cdot \frac{u_{1*}+u_{2*}}{2}.$$

Using the last relation for $\varepsilon = 2$ we arrive at the values $C_K \approx 1.889$ and $\mathcal{S} \approx -0.308$. The values $C_K \approx 2.01$ and $\mathcal{S} \approx -0.28$ are considered the most reliable experimental values of these quantities [12]. Therefore, the suggested scheme for calculations yields quite reasonable agreement with the experiment.

CONCLUSION

The version of the RG approach used in the present paper bears certain resemblance with the well known RG method in the real space, which is widely used in the theory of critical phenomena. (it is also called the "g expansion"). In the theory of phase transitions the parameter ε has the meaning of deviation from the critical space dimension (e.g, $\varepsilon = 4 - d$ for the φ^4-model). In the framework of the g expansion renormalization constants are calculated in the form of power series in the coupling constant g directly at $\varepsilon = 1$, i.e. at real value of the space dimension $d = 3$. In the framework of the g expansion calculations are notably simplified because it is much easier to calculate finite integrals in three dimensions than to calculate integrals with singularities at $d \to 4$. This is the reason why the use of the g expansion in the theory of critical phenomena has allowed to achieve better accuracy in perturbative calculations than in the usual ε expansion.

In the present paper we have used an approach akin to the g expansion to achieve a different aim. The choice of the renormalization constants from natural normalization conditions for the response and correlation functions together with the additional renormalization of random forcing allowed to include singular in $d-2$ contributions to the coefficients in all orders of the ε expansion. This summation led to a remarkable improvement of agreement of the theoretical prediction with the experimental value of the Kolmogorov constant already in the one-loop approximation.

ACKNOWLEDGEMENTS: The work was supported by the Russian Foundation for Fundamental Research (grant No 08-02-00125a), Academy of Finland (grant No 127436), VEGA grant 0173 of Slovak Academy of Sciences, and by Centre of Excellency for Nanofluid of IEP SAS. This work was also created by implementation of the Cooperative phenomena and phase transitions in nanosystems with perspective utilization in nano- and biotechnology project no. 26220120021. Funding for the operational research and development program was provided by the European Regional Development Fund.

REFERENCES

1. K. G. Wilson, J. Kogut, Physics Reports 12, 75 (1974).
2. C. De Dominicis, P. C. Martin, Physical Review A 19, 419 (1979).
3. L. Ts. Adzhemyan, A. N. Vasil'ev, Yu. M. Pis'mak, Teoreticheskya i Matematicheskaya Fizika 57, 268 (1983).
4. L. Ts. Adzhemyan,N. V. Antonov, A. N. Vasil'ev, Uspekhy Fizicheskikh Nauk 166, 1257 (1996).
5. L. Ts. Adzhemyan,N. V. Antonov, A. N. Vasil'ev: The Field Theoretic Renormalization Group in Fully Developed Turbulence. (Gordon & Breach, London, 1999).
6. L. Ts. Adzhemyan,N. V. Antonov,M. V. Kompaniets, A. N. Vasil'ev, International Journal of Modern Physics B 17, 213 (2003).
7. L. Ts. Adzhemyan, J. Honkonen, M. V. Kompaniets, A. N. Vasil'ev, Physical Review E68, 055302(R) (2003).
8. L. Ts. Adzhemyan, J. Honkonen, M. V. Kompaniets, A. N. Vasil'ev, Physical Review E 71, 036305 (2005).
9. J. Honkonen, M. Yu. Nalimov, Zeitshrift für Physik B99, 297 (1996).
10. A. S. Monin, A. M. Yaglom: Statistical Fluid Mechanics: Mechanics of Turbulence, Vol. 2. (MIT Press, Cambridge, 1975).
11. U. Frisch: Turbulence: The Legacy of A. N. Kolmogorov. (Cambridge University Press, Cambridge, 1975).
12. K. R. Sreenivasan¡ Physics of Fluids 7, 2778 (1995).

SHAPE COEXISTENCE IN PLATINUM, GOLD AND MERCURY ISOTOPES

M. Venhart, martin.venhart@fys.kuleuven.be, Instituut voor Kern- en Stralingsfysica, K.U. Leuven, Celestijnenlaan 200D
B-3001 Leuven, Belgium

INTRODUCTION

Low-energy excitations associated with different shapes in a single nucleus (commonly referred as a shape coexistence) have been long recognized to be of critical importance in our understanding of the nature of nuclear interactions. Region in close vicinity to Z = 82 and N = 104 provide an unique field with best examples known so far - see e.g. [1, 2] and references therein. In the pioneering experiment reported in [3], the triplet of 0^+ states associated with spherical, oblate (discus) and prolate (rugby ball) shape, was identified.

EVEN-EVEN MERCURY ISOTOPES

In neutron-deficient even-even Hg isotopes the properties of weakly oblate ground-state remains rather constant with decreasing neutron number until ^{188}Hg. There the ground-state band is crossed by intruding prolate band. The prolate 0_2^+ state appears due to the excitation of a proton pair across the Z = 82 shell gap into the $h_{9/2}$ and $f_{7/2}$ orbitals minimize their energies in ^{182}Hg. However, the 0_2^+ still lie above the ground-state. The experimental systematics of known 0_2^+ states in even-even Hg isotopes is given in the upper panel of Fig. 1. The 2^+ and 4^+ are rotational states based on the 0_2^+ prolate deformed state. The 0_2^+ prolate intruder states follow the parabolic trend with minimum in close vicinity of the neutron mid-shell at N = 104. This is because of the residual quadrupole-quadrupole proton-neutron interaction. See e. g. [4] and references therein for more detailed discussion.

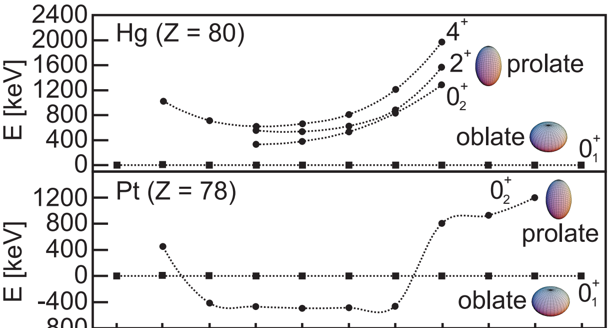

Fig. 1. Systematics of 0_2^+ states in even-even Hg and Pt isotopes. The values were taken from [5].

EVEN-EVEN PLATINUM ISOTOPES

As illustrated in lower panel of Fig. 1, the structure of even-even Pt isotopes differs from Hg. The ground-state of $^{178-186}$Pt was identified as the prolate intruder configuration. Note that even mass Pt isotopes are complicated by the mixing of strongly (prolate) and weakly deformed (oblate) states. See e. g. [2] for more detailed discussion.

ODD-MASS GOLD ISOTOPES

The structure of intruder and single-particle excitations in light gold isotopes is of particular interest. A systematic study has revealed states associated with the $s_{1/2}$, $d_{3/2}$, $d_{5/2}$ and $h_{11/2}$ proton hole configurations and the $h_{9/2}$ and $i_{13/2}$ proton particle configurations in odd-mass Au isotopes with A ≥ 185 [6]. Proton particle and hole states couple to different cores; the proton particles couple to $^{A-1}$Pt cores, while the proton holes couple to the $^{A+1}$Hg cores, resulting in distinct groups of states. The idea behind this fundamental point was demonstrated in the level scheme of ^{189}Au, where structures corresponding to the coupling with ^{188}Pt and ^{190}Hg cores were clearly observed [7].

Consequently, the presence of excited 0_2^+ state in both Pt and Hg cores naturally suggests a search for $\mathrm{j}^{-1} \otimes {}^{A+1}$Hg ($0_2^+$ prolate) and $\mathrm{j}^{+1} \otimes {}^{A-1}$Pt ($0_2^+$ oblate) states. The ^{185}Au was studied via EC/β^+ decay of the mass separated sample of ^{185}Hg and four coexisting states were identified [8]:

- $\mathrm{j}^{-1} \otimes {}^{186}$Hg ($0_1^+$ weakly oblate ground-state)
- $\mathrm{j}^{-1} \otimes {}^{186}$Hg ($0_2^+$ strongly prolate excited state)
- $\mathrm{j}^{+1} \otimes {}^{184}$Pt ($0_1^+$ strongly prolate ground-state)
- $\mathrm{j}^{+1} \otimes {}^{184}$Pt ($0_2^+$ weakly prolate excited state)

Fig. 2 gives the portion of the level scheme of the states associated with the $h_{9/2}$ proton-particle orbital. Two subsets are evident, proton-particle is coupled either to the 0_1^+ prolate or to the 0_2^+ weakly oblate ^{184}Pt core. The $13/2^-$ corresponds to coupling with 2^+ of the prolate or oblate band of the core. Higher members of the band based on the $h_{9/2}$ proton-particle structure were identified by an in-beam experiment [9]. The band was observed up to spin $49/2^-$. Note that the $5/2^-$ ground-state also arises from $h_{9/2}$ prolate intruder orbital and was interpreted as the anti-aligned rotational state localized 9 keV below the band-head. A portion of level scheme of $h_{11/2}$ proton-hole states is depicted in Fig. 3. As in the case of $h_{9/2}$ proton-particle excitations, two subsets are evident. A strongly-coupled band is expected to be based on second $11/2^-$ state [10]. This remains to be discovered, as a proof of whole interpretation. In the same way, the neighboring isotope ^{187}Au was studied [11, 12] in great detail.

The lighter Au isotopes were studied only in-beam [13, 14, 15] and via the alpha and proton decay [16]. The low-lying part of the spectrum is practically unknown, because the in-beam experiments focuss on the higher excitations and as soon as the yrast line is reached, the deexcitation proceeds only via yrast states. Non-yrast states are poorly populated. The alpha and proton decay feeds only a couple of states.

Just recently, we identified new isomeric state in ^{179}Au [17]. Isomeric with the half-life $T_{1/2} = 326$ ns decays via the internal transitions. This decay can could be employed as a powerful tag in ER–isomer tagging experiment. The band above the isomer would allow the insight into its structure. A proposal for such an experiment was already worked out by our collaboration.

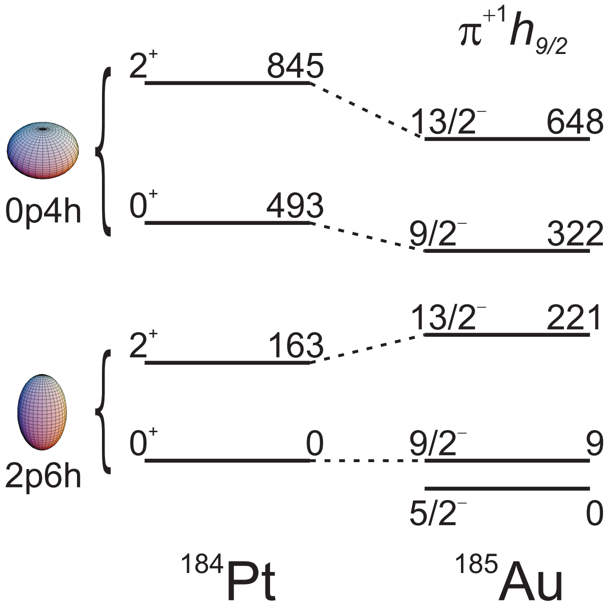

Fig. 2. Portions of the $h_{9/2}$ proton-particle bands in ^{185}Au compared to the strongly prolate and weakly oblate 0^+ and 2^+ levels in ^{184}Pt. The corresponding core-particle couplings are noted with dashed lines. Values were adapted from [8].

CONCLUSIONS

The odd-mass gold isotopes provide a prolific testing field on nuclear models. While the general picture is settled, more experimental information on ligher isotopes is necessary, especially at low excitation energy. Future experiments aimed to studies of these nuclei must envisage an efficient detection system in which both the conversion electrons electrons and γ rays could be measured. A possible way how to study lighter Au isotopes under cleaner conditions could involve the use of a mass separator, such as ISOLDE at CERN. Here we could perform detailed EC/β^+ studies of lighter Hg isotopes. According to the current yields of mercury isotopes which are presently available, the studies up to mass 179 are possible. Another experiments that might improve our knowledge on lighter isotopes would be atomic hyperfine splitting spectroscopy providing the direct spin measurement. We also expect that similar isomers as was just recently identified in ^{179}Au occurred also in neighboring isotopes. A campaign of experiments involving investigation of isomeric states is in preparation.

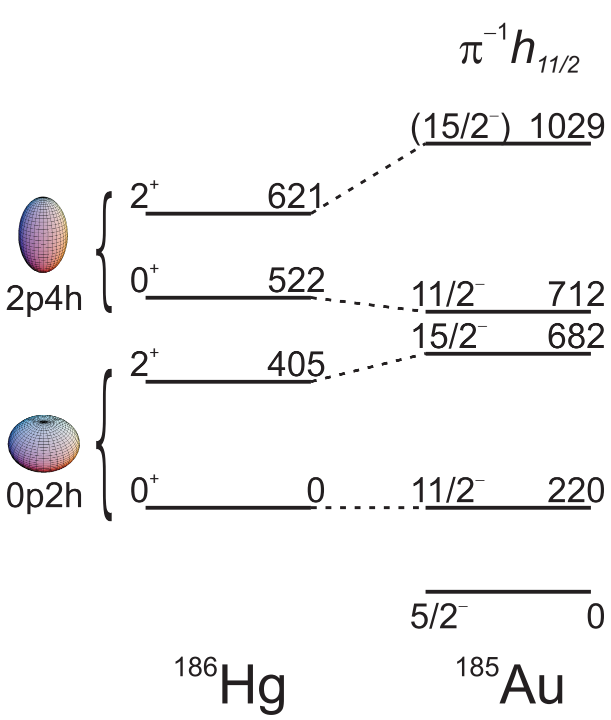

Fig. 3. Portions of the $h_{11/2}$ proton-hole bands in ^{185}Au compared to the strongly prolate and weakly oblate 0^+ and 2^+ levels in ^{186}Hg. The corresponding core-hole couplings are noted with dashed lines. Values were adapted from [8].

ACKNOWLEDGMENT: This work was supported by FWO-Vlaanderen (Belgium), GOA/2004/03 (BOF-K.U.Leuven) and the Interuniversity Attraction Poles Programme - Belgian State, Belgian Science Policy (BriX network P6/23). A fruitful discussions with J. L. Wood, A. N. Andreyev and R. D. Page are highly acknowledged.

REFERENCES

1. K. Heyde *et al.*, Phys. Rep. **102**, 291 (1983)
2. J. L. Wood *et al.*, Phys. Rep. **215**, 101 (1992)
3. A. N. Andreyev *et al.*, Nature (London) **405**, 430 (2000)
4. R. Julin, K. Helariutta and M. Muikku, J. Phys. G **27**, R109 (2001)
5. Evaluated Nuclear Structure Data File URL: `http://www.nndc.bnl.gov/ensdf`
6. M. O. Kortelahti *et al.*, J. Phys. G **14**, 1361 (1988)
7. J. L. Wood *et al.*, Phys. Rev. C **14**, (1976)
8. C. D. Papanicolopulos *et al.*, Z. Phys. A **330**, 371 (1988)
9. A. J. Larabee *et al.*, Phys. Lett. **169B**, 21 (1986)
10. W. L. Wood, private communication (2009)
11. D. Rupnik *et al.*, Phys. Rev. C **58**, 771 (1998)
12. D. Rupnik *et al.*, Phys. Rev. C **581**, R2867 (1995)
13. W. F. Mueller *et al.*, Phys. Rev. C **59**, 1999 (1999)
14. W. F. Mueller *et al.*, Phys. Rev. C **69**, 064315 (2004)
15. F. G. Kondev *et al.*, Phys. Lett. B **512**, 268 (2001)
16. G. L. Poli *et al.*, Phys. Rev. C **59**, R2979 (1999)
17. M. Venhart *et al.*, to be submitted to Phys. Rev. C

SIMPLE MODEL FOR THE DETERMINATION OF AN INDOOR RADON CONCENTRATION

Monika Műllerová, mullerova@fmph.uniba.sk and Karol Holý, holy@fmph.uniba.sk, Department Nuclear Physics and Biophysics, Faculty of Mathematics, Physics and Informatics CU, Mlynská dolina F1, 841 04 Bratislava

INTRODUCTION

The radon (^{222}Rn) is the most important natural source of radiation exposure of the population. Residential areas are the greatest source of radon population exposure. One of the topical questions, which arise during investigation of indoor radon, is correct determination of indoor radon activity concentration in house. Effort of predict of indoor radon activity concentration, using details of building, climate and parameter of subsoil, leaded to creation different models. In this contribution an approach of calculating the radon activity concentration in the work room is tested.

BEHAVIOUR OF RADON IN ENCLOSED AREAS

In simplified case, the radon activity concentration in the building is the function of two parameters: radon entry rate and air exchange rate. Both are functions of many different meteorological parameters, but from all of them the main role has the pressure difference between indoor and outdoor air. In common situations the pressure difference is dominantly caused by the indoor – outdoor temperature differences and by the wind [1].

Under the assumption of homogenous distribution of the radon inside a building, the activity concentration can be described by the equation [2]:

$$A_{in} = R/\left(V.\lambda_v\right) + A_{out} \qquad (1)$$

where: A_{in} is the indoor radon activity concentration, R is the radon entry rate, V is the volume of the room, λ_v is the air exchange rate (or the ventilation rate) and A_{out} is the outdoor radon activity concentration.

Under the assumption A_{in} >> A_{out} we get the mean ^{222}Rn activity concentration in the room:

$$A_{in} = R/\left(\lambda_v.V\right) \qquad (2)$$

On the basis of this equation we can illustrate three cases of the behaviour of the radon activity concentration in dependency on R and λ_v:

a) $R = const.$, $\lambda_v \sim \Delta T$ (ΔT is indoor-outdoor temperature difference), A_{in} is indirectly proportional to ΔT with a maximum in the afternoon and minimum during the night,

b) $\lambda_v = const.$, $R \sim \Delta T$, A_{in} is proportional to ΔT with a minimum in the afternoon and maximum during the night,

c) $R\left(\Delta T\right)$, $\lambda_v\left(\Delta T\right)$ for A_{in} we can write $A_{in} \sim R\left(\Delta T\right)/\lambda_v\left(\Delta T\right)$, A_{in} can rise or fall as a function of ΔT.

It is likewise useful to distinguish two ventilation modes in the next analysis. In balanced systems the air-exchange rate is effectively independent of the pressure difference across the building shell. A mechanical ventilation system that provides equal supply and exhaust flows is balanced. Infiltration and natural ventilation that provides only supply or exhaust are considered unbalanced ventilation modes: the air-exchange rate varies directly with the pressure difference across the building shell. In our case mechanical ventilation was not installed, because balanced ventilation component is equal zero. The unbalanced ventilation component is related to the average pressure difference across the building shell by a power-law relationship [3]:

$$\lambda_v = \lambda_{v,u} = \frac{P}{V}\left(\Delta p\right)^n \qquad (3)$$

where: $n = 0.5$ has been adopted in a commonly used infiltration model; P is the permeability coefficient of the building envelope, V is the interior volume and Δp is characteristic pressure difference, such as the mean of the absolute value, across the building envelope.

The characteristic pressure difference can be estimated as the sum of three components – those due to temperature differences, wind, and unbalanced mechanical ventilation [3]:

$$\Delta p = \frac{\rho}{2} f_s^2 \left|T_o - T_i\right| + \frac{\rho}{2} f_w^2 v^2 + \left|\Delta p_{mv,u}\right| \qquad (4)$$

where: ρ is the air density, f_s is parameter of temperature difference (stack parameter), f_w is parameter of wind speed (wind parameter), $\Delta p_{mv,u}$ is pressure difference caused by unbalanced mechanical ventilation, v is wind speed, T_i and T_o are indoor and outdoor temperatures.

SAMPLING LOCALITY AND METHODS

The radon activity concentration was measured at workroom in the office building of the FMPI of the CU in Bratislava. The room is situated at the second floor, with north-oriented windows, and is shielded against the direct influence of wind by the other parts of the building. The radon entry rate was constant during whole period of the radon concentration measurement.

For the monitoring of the radon activity concentration in indoor air the AlphaGUARD radon monitor [4] developed by Genitron was used. The monitor sensitivity is about 0.05 cpm at 1 Bq·m^{-3} of ^{222}Rn activity concentration. The background signal is lower than 1 Bq·m^{-3} [4]. The monitor can record the ^{222}Rn activity concentration, temperature, pressure and humidity of the room in 1-hour intervals.

RESULTS AND DISCUSSION

We tested a simplified parametric model describing the indoor radon activity concentration. During the radon activity measurement, the variations of the radon entry rate were disregarded. We considered only the change of the air exchange in response to changes of meteorological parameters (indoor and outdoor temperatures and wind speed). To ensure the constant radon entry rate during the period of the experiment a strong flow of radon from the soil was introduced into the observation room R_{soil}. This radon entry rate from the soil ($1.7Bq/s = 6120Bq/h$) was three and a half times greater than the radon entry rate from the building materials E. The average exhalation rate of radon from the building materials calculated by us was about 4.32 mBq·m^{-2}·s^{-1}, which represented the contribution of the radon entry rate from the building materials $0.5Bq/s = 1800Bq/h$ for our room.

From the known expression of the air exchange rate for the room we derived a simplified relationship:

$$\lambda_v = \sqrt{P_S^2 \left|T_i - T_o\right| + \left(P_W.v\right)^2} \Big/ V \qquad (5)$$

where: P_S and P_W are parameters including stack and wind parameter, T_{in} and T_o are indoor and outdoor temperature, v is wind speed and V is volume of the room.

Further, the air exchange rate can be expressed also by using measured indoor (or even outdoor) radon activity concentration. From the equation (1) for steady state condition we get the relationship:

$$\lambda_v = {R} \Big/ {V\left(A_{in} - A_{out}\right)} \qquad (6)$$

By substitution of relationship (5) into equation (6) we obtain the relationship for calculating the radon activity concentration in the room depending on the meteorological parameters in the following format:

$$A_{in} = \frac{R}{\sqrt{P_S^2 \left|T_i - T_o\right| + \left(P_W.v\right)^2}} + A_{out} \qquad (7)$$

For a short period (we have chosen the period 1.4. – 7.4.2008) we determined the parameters P_S, P_W and E (where: $R = E + R_{soil}$) from experimental data.

For unsealed room we obtained the following values $P_S = 15\ m^3h^{-1}/\sqrt{°C}$, $P_W = 23\,m^2$ and $E = 1800Bq/h$. The correlation between the air exchange rates obtained using the equations (5) and (6) is very good (R^2 ~ 0.55). Then we calculated the radon activity concentration using the parameters P_S, P_W and E and using equation (7). The measured record and the calculated indoor radon activity concentrations are shown in Fig. 1. The courses of the radon activity concentration show a good agreement (R^2 ~ 0.43) for unsealed room.

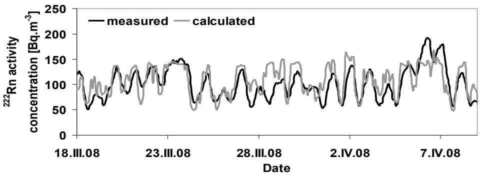

Fig. 1. The comparison of the measured record and the calculated radon activity concentrations for the unsealed room

In the next step the maintenance shaft in the room was sealed and the natural ventilation was possible only through the window leaks. For the sealed room we obtained the following values $P_S = 10\,m^3h^{-1}/\sqrt{°C}$ and $P_W = 13\,m^2$. It is clear that the dependence of the radon activity concentration on the meteorological parameters in the sealed room was reduced. Also in this case the measured radon activity concentrations show a good correlation (R^2 = 0.37) with the calculated radon activity concentrations.

CONCLUSIONS

For the description of the radon activity concentration in the room we used a simplified parametric model. The radon entry rate was considered to be constant. We considered only the change of the air exchange rate in response to changes of the meteorological parameters (indoor and outdoor temperatures and wind speed). The correlation between measured radon activity concentration and calculated radon activity concentration using the simplified model is good. We have shown that the dependence of the radon activity concentration on the meteorological parameters in the sealed room was reduced in the comparison with the unsealed room.

ACKNOWLEDGMENT: This work was supported by VEGA projects No. 1/3046/06 and No. 1/0678/09 of the Ministry of Education of the Slovak Republic.

REFERENCES

1. J. Hůlka, Radon investigations in the Czech Republic IV., 22-26 (1993).
2. UNSCEAR – Report 1982 (New York)
3. W. W. Nazaroff el al.: “Soil as a Source of Indoor Radon: Generation, Migration and Entry“, in *Radon and its decay products in indoor air,* edited by W. W. Nazaroff and A. W. Nero, New York: John Wiley and Sons – 1988, pp.
4. V. Genrich, Genitron Instruments GmbH (Frankfurt).

EFFECTIVE MEAN-FIELD PARAMETERIZATION OF THE DBHF RESULTS

K. Petrík, *kristian.petrik@savba.sk*, Institute of Physics, Slovak Academy of Sciences, Bratislava

The knowledge of the nuclear equation of state (EoS) is one of the fundamental goals in nuclear physics which has not yet been achieved. Retrieval of information on the EoS, in particular at high baryon density, is restricted to two fields of research. Concerning terrestrial systems, detailed knowledge of the EoS is important, for instance, for understanding heavy-ion collision dynamics. On the other hand, the EoS is crucial for determining the properties of one of the most exotic objects in the universe - neutron stars. Despite the fact that the physical conditions in these two contexts are quite different, it is possible to connect them, and the EoS provides the substantial concept to establish this link. Although considerable progress has been made, the EoS of dense matter remains uncertain at densities above $\simeq 3\times 10^{14}$ g/cm^3 [1]. Therefore, determining the high-density stellar matter EoS is a tremendous task. While at densities $\rho \simeq \rho_0$ ($\rho_0 \simeq 0.17$ fm^{-3} is the normal nuclear density), matter consists mainly of nucleons and leptons; at higher densities, several other species of particles are expected to appear due to the rapid rise of the baryon chemical potentials with density [2]. New exotic particles and phases alter not only the global properties of compact stars, the total mass and radius, but also the cooling evolution and the stability against the delayed collapse to a black hole. Many different model approaches predict that hyperons are present in neutron star matter around twice normal nuclear matter density. Occurrence of hyperons significantly influence the equation of state and the global properties of compact stars, hence, the calculations within hyperon star model can lead to important constraints on effective interaction. Numerous calculations have established that relativistic mean-field (RMF) models, like quantum hadrodynamics (QHD) [3], provide a reliable tool for realistic description of the bulk properties of finite nuclei and nuclear matter [4]. In addition to this successful low-energy phenomenology, these models are often extrapolated into regimes of high density and temperature to extract the nuclear equation of state. The relativistic mean field approach has been also widely used in determining total masses and radii of neutron stars [5, 6]. The QHD approach to the dense nuclear matter is therefore believed to be the eligible tool that can help us to better understand the role of EoS in the physics of compact stars. In QHD models the complicated many-body dynamics of strong interactions at low energy are contained effectively in meson-baryon coupling constants and nonlinear meson self- and cross-interactions. They represent free parameters of RMF theory. It is reasonable to retain the basic structure of QHD and provide a more direct access to many-body dynamics through adjustment of these free parameters to the more fundamental Dirac-Brueckner-Hartree-Fock (DBHF) theory.

THEORETICAL FORMALISM

The detailed dynamics of the relativistic nuclear many-body problem must be specified by choosing a particular Lagrangian density. The QHD has to be regarded as an effective field theory, where all types of hadronic couplings satisfying general symmetry requirements are to be included. In the case of nonlinear RMF model Lagrangian generally includes the nucleon field in the form of isospinor ψ, the isoscalar-scalar meson field σ, the isoscalar-vector meson field ω, the isovector-vector meson field $\boldsymbol{\rho}$, and the isovector-scalar meson field $\boldsymbol{\delta}$,

$$\begin{aligned}
\mathcal{L} &= \bar{\psi}\left[i\gamma^\mu\partial_\mu - (m_N - g_\sigma\hat{\sigma} - g_\delta\boldsymbol{\tau}\cdot\hat{\boldsymbol{\delta}}) - g_\omega\hat{\omega}_\mu\gamma^\mu - g_\rho\boldsymbol{\tau}\cdot\hat{\boldsymbol{\rho}}_\mu\gamma^\mu\right]\psi \\
&+\frac{1}{2}\partial_\mu\hat{\sigma}\partial^\mu\hat{\sigma} - \frac{1}{2}m_\sigma^2\hat{\sigma}^2 - \frac{1}{4}\hat{\omega}_{\mu\nu}\hat{\omega}^{\mu\nu} + \frac{1}{2}m_\omega^2\hat{\omega}_\mu\hat{\omega}^\mu \\
&+\frac{1}{2}\partial_\mu\hat{\boldsymbol{\delta}}\partial^\mu\hat{\boldsymbol{\delta}} - \frac{1}{2}m_\delta^2\hat{\delta}^2 - \frac{1}{4}\hat{\boldsymbol{\rho}}_{\mu\nu}\cdot\hat{\boldsymbol{\rho}}^{\mu\nu} + \frac{1}{2}m_\rho^2\hat{\boldsymbol{\rho}}_\mu\cdot\hat{\boldsymbol{\rho}}^\mu \\
&-\frac{1}{3}b_\sigma m_N(g_\sigma\hat{\sigma})^3 - \frac{1}{4}c_\sigma(g_\sigma\hat{\sigma})^4 + \frac{1}{4}c_\omega(g_\omega^2\hat{\omega}_\mu\hat{\omega}^\mu)^2 + \frac{1}{4}c_\rho(g_\rho^2\hat{\boldsymbol{\rho}}_\mu\cdot\hat{\boldsymbol{\rho}}^\mu)^2 \\
&+\frac{1}{2}\Lambda_{vv}(g_\rho^2\hat{\boldsymbol{\rho}}_\mu\cdot\hat{\boldsymbol{\rho}}^\mu)(g_\omega^2\hat{\omega}_\mu\hat{\omega}^\mu) + \frac{1}{2}\Lambda_{vs}(g_\rho^2\hat{\boldsymbol{\rho}}_\mu\cdot\hat{\boldsymbol{\rho}}^\mu)(g_\sigma^2\hat{\sigma}^2).
\end{aligned}$$

In addition to nucleon-meson interactions the Lagrangian density includes the scalar b_σ, c_σ and the vector c_ω self-interactions, and the isovector vector c_ρ self-interaction [7, 8, 9, 10]. Finally, the nonlinear cross-interactions Λ_{vv} and Λ_{vs} [11, 12] are included to modify the density dependence of the symmetry energy $a_{sym}(\rho_{\mathcal{B}})$. The field equations for this model follow from the Euler-Lagrange equations in a standard way. The resulting Dirac equation for the baryon field is

$$[i\gamma^\mu\partial_\mu - (m_N - g_\sigma\hat{\sigma} - g_\delta\boldsymbol{\tau}\cdot\hat{\boldsymbol{\delta}}) - g_\omega\hat{\omega}_\mu\gamma^\mu - g_\rho\boldsymbol{\tau}\cdot\hat{\boldsymbol{\rho}}_\mu\gamma^\mu]\psi = 0.$$

When quantized, meson equations of motion become nonlinear quantum field equations, whose exact solutions are very complicated, moreover, the coupling constants are large, so perturbative solutions are not useful. Two approximations are necessary to circumvent this problem: *relativistic mean-field approximation* in which operators of meson fields are replaced by their ground state expectation values in static and homogenous infinite matter, and *no-sea approximation* introduced by exclusion of the filled Dirac sea of negative energy states. The set of coupled equations for the baryon and meson fields can be then solved self-consistently using the iteration procedure, and the properties of the nuclear matter can be then obtained from these fields. Subsequently, from the energy-momentum tensor

$$\mathcal{T}^{\mu\nu} = \frac{\partial\mathcal{L}}{\partial(\partial_\mu\psi)}\partial^\nu\psi - g^{\mu\nu}\mathcal{L} = (\epsilon + P)u_\mu u_\nu - g^{\mu\nu}P,$$

we can calculate the energy density ϵ and pressure P, *i.e.* equation of state of asymmetric nuclear matter.

RESULTS AND DISCUSSION

The new RMF parameterization was obtained by adjusting free parameters of QHD model to fit the DBHF results for nuclear matter obtained by van Dalen, Fuchs and Faessler [13]. Furthermore, additional parameterizations were acquired using two older DBHF data calculated by Lee, Kuo, Li, and Brown [14], and Huber, Weber, and Weigel [15]. In each case the Bonn A potential was employed.

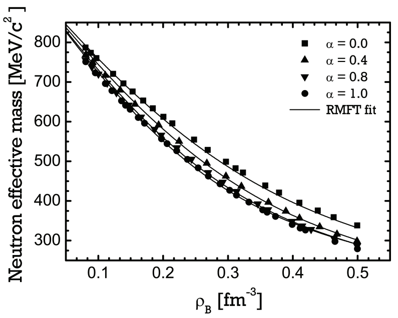

Fig. 1. Binding energy per nucleon for different asymmetries as resulted from the RMF fit (lines) to the DBHF data (symbols) of van Dalen *et al.* [13].

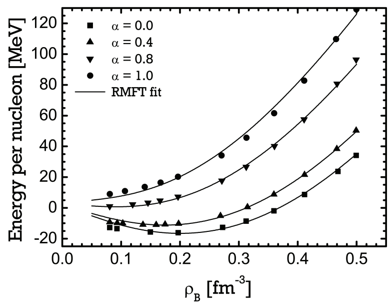

Fig. 2. Effective neutron mass for different asymmetries as resulted from the RMF fit (lines) to the DBHF data (symbols) of van Dalen *et al.* [13].

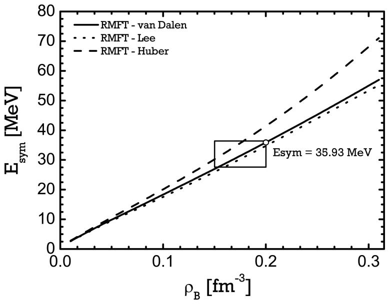

Fig. 3. Symmetry energy results given by different RMF models are compared. Saturation value of E_{sym} following from fit to van Dalen data [13] is depicted.

TAB. 1. Parameter sets resulting from fit to DBHF data of Lee [14], Huber [15], and van Dalen [13].

	Lee	Huber	van Dalen
g_σ^2	102.116	86.877	76.949
g_ω^2	146.802	108.096	100.842
g_ρ^2	9.6695	31.112	40.806
g_δ^2	-	29.499	49.3978
b_σ	0.00082	0.00316	0.00115
c_σ	0.00126	-0.00295	0.00053
c_ω	0.00520	-	-
c_ρ	-	-	-
Λ_{vv}	-	-	0.02362
χ^2/N	2.9106	4.2833	13.6029
m_σ [MeV]	550.	550.	550.
m_ω [MeV]	783.	783.	783.
m_ρ [MeV]	770.	770.	769.
m_δ [MeV]	-	980.	980.
m_N[MeV]	939	939.	939.

The DBHF binding energies per baryon for various asymmetries along with the neutron effective mass were taken as an input to the fitting procedure. Initial data were weighted correspondingly to their physical significance - uncertainties 0.3 MeV for binding energy and 5 MeV for potentials have been chosen. Value 0.3 MeV is the usual estimation which stems from macro-micro approaches to the nuclear matter, whereas 5 MeV originates from the fact that although the Hugenholtz-Van Hove's theorem is fully consistent with the mean-field model it is violated within the DBHF theory. In the process of mapping of the RMF model on this microscopic theory one should cover this fact by introducing an additional uncertainty in the potentials.

The data of Lee *et al.* and Huber *et al.* were successfully parameterized using standard RMF $(\sigma, \omega, \rho, b_\sigma, c_\sigma, c_\omega)$, in the latter case with help of δ meson. However, the van Dalen's *et al.* data could not be satisfactorily reproduced by these mean-field models. Fortunately, we have found that the use of Λ_{vv} cross-interaction in the model can solve arisen difficulties. It is due the fact that the vector ω-ρ cross-interaction directly influences the symmetry energy through the effective ρ mass. Inclusion of this term not only improved the binding energy and effective mass fit (Fig.1, Fig.2), but also it suitably reproduced the symmetry energy value - RMF model with Λ_{vv} gives $E_{sym} = 35.93$ MeV (Fig.3), which is in compliance with typical values at mean-field level.

CONCLUSIONS

In this work the relativistic mean-field theory was used to obtain an effective parametrization of the properties of asymmetric nuclear matter by adjusting it to reproduce the DBHF calculations of different groups. New parameterization was obtained through the use of van Dalen *et al.* DBHF data [13]. It has been shown that the vector ω-ρ cross-interaction is inevitable for obtaining the proper fit in the whole density range. The mean-field symmetry energy calculated within this model shows sufficient agreement with the DBHF predictions.

ACKNOWLEDGEMENT: This work has been supported in part by the VEGA Grant Agency under grant no. 2/7117/27.

REFERENCES

1. G. Bao et.al, Nucl. Phys. **A575**, 707 (1994).
2. M. Baldo et al., Phys. Rev. C **61**, 55801 (2000).
3. J. D. Walecka, Ann. Phys. (N.Y.) **83** 491 (1974).
4. B. D. Serot, J. D. Walecka, Adv. Nucl. Phys. **16** 1 (1986).
5. S. F. Ban et al., Phys. Rev. C **69**, 045805 (2004).
6. S. Lawley, W. Bentz, A. W. Thomas, Nucl. Phys. Proc. Suppl. **141**, 29 (2005).
7. J. Boguta, A. R. Bodmer, Nucl. Phys. **A292**, 413 (1977).
8. A. R. Bodmer, Nucl. Phys. **A292**, 703 (1991).
9. S. Gmuca, Nucl. Phys. A **547**, 447 (1992).
10. H. Mueller, B. D. Serot, Nucl. Phys. **A606**, 508 (1996).
11. C.J. Horowitz, J. Piekarewicz, Phys. Rev. Lett. **86**, 5647 (2001).
12. C.J. Horowitz, J. Piekarewicz, Phys. Rev. C **64**, 062802 (2001).
13. E. N. E. van Dalen, C. Fuchs, Amand Faessler, Nucl. Phys. **A744** 227-248 (2004).
14. C. H. Lee *et al.*, Phys. Lett. B 412, 235 (1997); Phys. Rev. C 57, 3488 (1998).
15. H. Huber et al., Phys. Lett. B 317, 485 (1993); Phys. Rev. C 51, 1790 (1995).

PERSISTENT CURRENTS IN PERFECT CRYSTALLINE INSULATORS: REALISTIC TIGHT-BINDING MODEL

J. Tóbik[a,b], jaroslav.tobik@stuba.sk, A. Mošková[a], elekmosk@savba.sk, M. Moško[a], elekmoso@savba.sk
[a] Elektrotechnický ústav SAV, Dúbravská cesta 9, 841 04 Bratislava
[b] Katedra fyziky, FEI STU, Ilkovičova 3, 812 19 Bratislava

Magnetic flux piercing the opening of a mesoscopic conducting ring gives rise to the persistent electron current circulating around the ring [1]. This paper discusses a realistic calculation of persistent current in a nano-ring made of the perfect crystalline insulator. We first review our results [2] obtained for a one-dimensional ring-shaped lattice with single-level lattice sites. Then we discuss a simple tight-binding model with two-level sites [3]and we eventually extend the discussion to a realistic tight-binding model [4], suitable for a ring made of the real insulator.

SINGLE-LEVEL LATTICE MODEL

Consider the circular one-dimensional ring of circumference L pierced by magnetic flux Φ. The electron wave function $\psi(x)$ in the ring obeys the cyclic boundary condition $\psi(x+L)=\psi(x)$. If we apply the Peierls transformation $\psi(x)=\varphi(x)e^{-i2\pi\frac{\Phi}{\Phi_0}x}$, magnetic flux Φ disappears from the Hamiltonian and emerges in the boundary condition $\varphi(x+L)=e^{i2\pi\frac{\Phi}{\Phi_0}}\varphi(x)$ [1]. For simplicity, below Φ labels magnetic flux in units $\Phi_0=h/e$. Assuming that the electron states of two different lattice sites are orthogonal, the lattice model of Ref. [2] can described by the lattice Hamiltonian

$$H=\sum_{n=1}^{N}\left(\epsilon {c_n}^{\dagger}c_n+\sum_{l=1}^{\infty}t_l\left(c_n^{\dagger}c_{n+l}+c_{n+l}^{\dagger}c_n\right)\right) \quad (1)$$

where N is the number of the lattice sites in the ring, ϵ is the (discrete) energy level of the site, $c_n^{\dagger}$ / c_n is the creation/anihilation operator of the particle localized at site n, and t_l is the probability amplitude of hopping over l sites. We define $c_{n+N}=e^{i2\pi\Phi}c_n$. It can be shown that the ring with N sites can be represented mathematically by an infinite 1D lattice with unit cell containing N sites which repeats periodically infinite number of times. Therefore, the ring Hamiltonian 1 contains not only the N really existing sites, but also the periodic replicas of the site, say $n+N, n+2N$, etc.. Transformation

$$a_p=\frac{1}{\sqrt{N}}\sum_{n=1}^{N}e^{-i2\pi\frac{(p+\Phi)n}{N}}c_n,\; a_p^{\dagger}=\frac{1}{\sqrt{N}}\sum_{n=1}^{N}e^{i2\pi\frac{(p+\Phi)n}{N}}c_n^{\dagger} \quad (2)$$

diagonalizes the Hamiltonian (1) as

$$H=\sum_{k=1}^{N}\left(\epsilon+\sum_{l=1}^{\infty}t_l 2\cos\left(2\pi\frac{(k+\Phi)l}{N}\right)\right)a_k^{\dagger}a_k. \quad (3)$$

We see that the single-particle eigenenergy is

$$\epsilon(k)=\epsilon+\sum_{l=1}^{\infty}t_l 2\cos(l\delta_k), \quad (4)$$

where $\delta_k\equiv 2\pi(k+\Phi)/N$. The term involving the sum over l is the hopping contribution to the energy ϵ. The discrete level ϵ thus splits into the band $\epsilon(k)$. When the band is fully filled, it emulates the valence band of the perfect crystalline insulator. Summing the energies $\epsilon(k)$ over all N available states k one finds the ground-state energy (per spin)

$$E_{tot}=N\epsilon+2Nt_N\cos(2\pi\Phi)+\cdots, \quad (5)$$

where the dots stand for the terms proportional to $t_{2N}, t_{3N}, \ldots$. The persistent current is given as [1]

$$I\propto-\frac{\partial E_{tot}}{\partial\Phi}. \quad (6)$$

In fact [2], the hopping amplitude t_l decreases exponentially with increasing l due to the exponentially decreasing wave-function overlap between the sites n and $n+l$. Using the ground-state energy (5) and keeping only the leading term ($\propto t_N$) one obtains from the formula (6) after some algebra the result $I\propto 2Nt_N\sin(2\pi\Phi)$. Thus, the persistent current in the fully-filled band is due to the (exponentially weak) hopping from a given site to the same site via a single hope around the ring. Notice now what happens in the tight-biding approximation, when $t_l=0$ for all l except for $l=1$. Obviously, the result $I=2Nt_N\sin(2\pi\Phi)$ turns to $I=0$. On the first glance, the perfectly zero current in a fully-filled band may seem to be an intuitively acceptable result, however, such result is not correct. We show in the next section, that the fully-filled band carries a non-zero persistent current also in the tight-binding approximation, if the lattice is composed of the lattice sites with two discrete levels.

TWO-LEVEL TIGHT-BINDING LATTICE

Now we consider the lattice Hamiltonian

$$H=\sum_{n=1}^{N}\sum_{i=1}^{2}\left(\epsilon^i c_n^{i\dagger}c_n^i+t^i\left(c_n^{i\dagger}c_{n+l}^i+c_{n+l}^{i\dagger}c_n^i\right)\right)+$$
$$+t^{12}\left(c_n^{1\dagger}c_{n-1}^2+c_{n-1}^{2\dagger}c_n^1+c_{n-1}^{1\dagger}c_n^2+c_n^{2\dagger}c_{n-1}^1\right), \quad (7)$$

where two localized states ($i=1,2$) with discrete energies ϵ^1 and ϵ^2 are considered at each lattice site and only the hopping between the neighboring sites is taken into account. In particular, the hopping amplitude t^i describes hopping between the state i and the same i at the neighboring site and t^{12} describes hopping from $i=1$ to $i=2$. The model (7) implicitly assumes that the states $i=1$ and $i=2$ have the same symmetry like e. g. the 1s and 2s wave functions of the hydrogen atom. Owing to this assumption the hopping events $(n,1)\to(n+1,2)$, $(n,1)\to(n-1,2)$, $(n,2)\to(n+1,1)$ and $(n,2)\to(n-1,1)$ can be described by the same amplitude t^{12}. Our conclusions are however valid also in a general case when such symmetry is absent [3].

The transformation (2) applied to c_n^i and $c_n^{i\dagger}$ allows us to rewrite the Hamiltonian (7) in the form

$$H = \sum_{k=1}^{N} \sum_{i=1}^{2} \epsilon^i + 2t^i \cos\left(2\pi \frac{k+\Phi}{N}\right) a_k^{i\dagger} a_k^i$$
$$+2t^{12} \cos\left(2\pi \frac{k+\Phi}{N}\right) \left(a_k^{2\dagger} a_k^1 + a_k^{1\dagger} a_k^2\right), \qquad (8)$$

which can be diagonalized. After some manipulations, the diagonalization procedure reduces to the diagonalization of the Hamiltonian matrix

$$\begin{pmatrix} \epsilon^1 + 2t^1 \cos(\delta_k) & 2t^{12} \cos(\delta_k) \\ 2t^{12} \cos(\delta_k) & \epsilon^2 + 2t^2 \cos(\delta_k) \end{pmatrix} \qquad (9)$$

at a fixed value of k. The resulting eigenenergies are

$$\varepsilon^{1,2}(k) = C_1 + C_2 \cos(\delta_k) \pm \qquad (10)$$
$$\sqrt{(C_1 + C_2 \cos(\delta_k))^2 + C_3 + C_4 \cos(\delta_k) + C_5 \cos^2(\delta_k)},$$

where $C_1 = (\epsilon^1 + \epsilon^2)/2$, $C_2 = t^1 + t^2$, $C_3 = -\epsilon^1 \epsilon^2$, $C_4 = -2t^1\epsilon^2 - 2t^2\epsilon^1$, and $C_5 = 4t^1t^2 - 4(t^{12})^2$. To emulate the band insulator, the parameters ϵ and t can be chosen in such way that the bands $\varepsilon^1(k)$ and $\varepsilon^2(k)$ are separated by an energy gap. If we completely fill the lower energy band, $\varepsilon^1(k)$, and let completely empty the higher energy band $\varepsilon^2(k)$, the band $\varepsilon^1(k)$ emulates the fully-filled valence band of the insulator. It should be noted, that δ_k is a continuous variable as it involves the continuous variable Φ. Therefore, the Fourier expansion of $\varepsilon^1(k)$ possesses an infinite number of Fourier terms. If we now expand $\varepsilon^1(k)$ into the Fourier series with respect to δ_k, we obtain the infinite Fourier expansion which formally resembles the result (4), except that now the origin of the Fourier coefficients is physically different. Due to this formal resemblance it is clear that the fully-occupied band $\varepsilon^1(k)$ carries a nonzero persistent current in spite of the fact that only the nearest-neighbor hopping is considered. Unlike the model of the preceding section, in this case non-zero current is due to the presence of two localized levels coupled via t^{12}.

REALISTIC TIGHT-BINDING MODEL

The realistic band structure of the infinite zinc-blend crystal like diamond or silicon can be successfully calculated [5] by means of the tight-binding model with eight localized states per primitive unit cell (per lattice site). The eight states correspond to two s-orbitals and six p-orbitals of two non-equivalent atoms in the unit cell. These eight states give rise to the valence band and conduction band separated by gap. We have coupled the tight-binding scheme of Ref. [5] with the cyclic condition $\varphi(x+L, y, z) = e^{i2\pi\Phi}\varphi(x, y, z)$ in order to describe the energy spectrum of the ring-shaped crystal. Our approach can be viewed as a "rubber-like" model depicted in the figure 1. After obtaining the energy spectrum of the ring we completely fill all available states in the valence band and we calculate the ground-state energy $E_{tot}(\Phi)$. We eventually obtain the persistent current by means of the formula (6). The resulting persistent current is presented in the figure 2 for various materials. The diamond, silicon and germanium were parametrised using the tight-binding parametrisation of Ref. [5] while indium-arsenide was parametrized following Ref. [6]. The major prediction of figure 2 is the following one. The persistent current in a ring made of the realistic band insulator decreases with L exponentially, nevertheless, a careful choice of the insulating material (say InAs) allows to achieve the persistent current of measurable value ~ 0.01nA for technologically realizable ring size ($L \sim 100$nm).

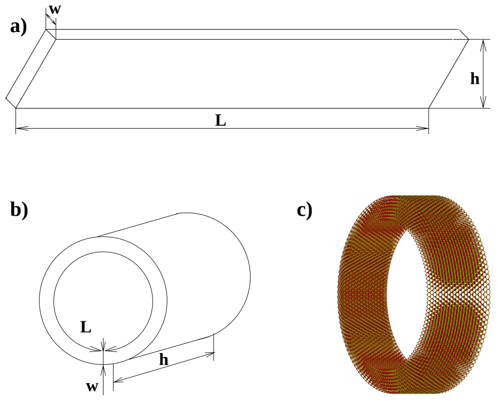

Fig. 1. Nano-ring with finite cross section in the rubber-like model. The bar depicted in the panel (a) is elastically bent to form the hollow cylinder (panel b). The panel (c) depicts the atomistic structure of the resulting ring, with $w = 8$, $h = 16$ and $L = 100$ being the number of the primitive unit cells (for zinc-blend structure) along the directions $(1,0,0)$, $(0,1,0)$, and $(0,0,1)$.

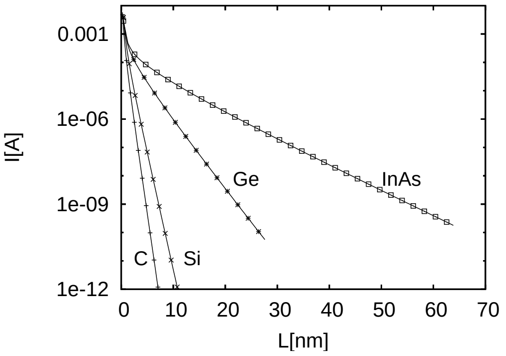

Fig. 2. Persistent current versus the ring length L for the rings made of various insulating materials listed in the figure. Magnetic flux is fixed to $\Phi = 0.25\Phi_0$.

ACKNOWLEDGMENT: This work was supported by the grants APVV-51-003505 and VEGA-1/0452/09.

REFERENCES

1. Y. Imry: Introduction to Mesoscopic Physics (Oxford University Press, Oxford, UK, 2002).
2. A. Mošková et al.,. Physica **E**, 1991 (2008).
3. A. Mošková et al., unpublished.
4. J. Tóbik et al., unpublished.
5. D.J. Chadi, M.L. Cohen, Phys. Status Solidi B **68**, 405 (1975).
6. J.P. Loehr, D.N. Talwar, PRB **55**, 4353 (1997).

HEAT CAPACITY AND POINT CONTACT SPECTRA OF THE MELT-SPUN CUBIC RECu₅ COMPOUNDS (RE – HEAVY RARE EARTHS)

S. Iľkovič, ilkovic@unipo.sk, Faculty Faculty of Sciences, University of Prešov, ul. 17.novembra 1, 081 16 Prešov, Slovakia, M. Reiffers, reiffers@saske.sk, Institute of Experimental Physics, Slovak Academy of Sciences, Watsonova 47, SK-043 53 Košice, Slovakia, Faculty Faculty of Sciences, University of Prešov, ul. 17.novembra 1, 081 16 Prešov, Slovakia, B. Idzikowski, Institute of Molecular Physics, Polish Academy of Sciences, M. Smoluchowskiego 17, PL-60-179 Poznań, Poland, J. Šebek, E. Šantavá, Institute of Physics, Praha, Czech Republic

INTRODUCTION

Limited experimental data on physical properties and crystalline electric field (CEF) configurations are available for the cubic intermetallic compounds of the *RE*Cu$_5$ (*RE* – heavy rare earths) series. It is because of the difficulty in obtaining of single-phase samples, due to the proximity of the congruently melting *RE*Cu$_5$ phase (hexagonal at high temperatures and cubic at low temperatures) [1]. One successful preparation method is melt spinning [2]. The light *RE*Cu$_5$ compounds (*RE* from La to Gd) crystallize in the simple hexagonal CaCu$_5$-type structure, while the heavy rare earths compounds exhibit the cubic AuBe$_5$-type structure [3] and hexagonal one. There are two exceptions – heavy fermion compounds CeCu$_5$ and cubic YbCu$_5$, which are quite well studied [1]. Due to the presence of rare earths in the compounds one could expect the presence of crystalline electric field (CEF) and its influence on their transport and magnetic properties.

The measurements of the temperature dependences of susceptibility and magnetization performed for cubic *RE*Cu$_5$ (*RE* - Tb, Dy, Ho, Er and Tm) between 2.1 and 300 K gave information about the magnetic ordering temperatures [4]. While the authors have been able to determine the transition temperature for TbCu$_5$ (T_N = 15 K) and DyCu$_5$ (T_C = 7 K), they concluded that the ordering at low temperatures changes with increasing atomic number from antiferromagnetic (*RE* - Tb) to ferromagnetic (*RE* - Ho, Er, Tm) and DyCu$_5$ shows metamagnetic transition as a function of temperature. Contrary, the measurement of heat capacity of TmCu$_5$ [5] showed that it is an induced moment system which does not order magnetically. CEF in TmCu$_5$ has been studied by the inelastic neutron scattering (INS) [5] but the interpretation of results is not trivial. Previously we have studied the electron-quasiparticle interaction (EQI) by point-contact (PC) spectroscopy in cubic *RE*Cu$_5$ compounds [e.g. 6, 7]. We have determined the crystalline electric field contributions to EQI and determined the CEF transition from ground state to the excited states. Moreover, we have studied heat capacity of cubic Kondo dense compound YbCu$_5$ [8]. In order to detect expected magnetic transitions at low temperatures and to estimate energy of CEF levels from Schottky effect, we performed systematic study of heat capacity measurements of *RE*Cu$_5$ in the applied magnetic field up to 9 T and in the temperature range from 0.4 to 300 K on samples prepared by melt-spinning technique.

EXPERIMENTAL

*RE*Cu$_5$ starting ingot was prepared by arc-melting using high purity elements (*RE* 99.95% or more, and Cu 99.95 %). Melt-spun cubic *RE*Cu$_5$ samples were obtained by rapid solidification of the melt on the copper wheel surface. The crystalline structure of the ribbons was examined by X-ray diffraction (XRD) using Co-Kα radiation [2]. Heat capacity measurements were performed by PPMS commercial device (Quantum Design) in the temperature range 0.4 – 300 K and in applied magnetic field up to 9T. Heat capacity was measured using the two-tau model of the relaxation method.

RESULTS

Fig. 1. shows low temperature detail of the temperature dependences of heat capacity of all cubic *RE*Cu$_5$ compounds. We observed the magnetic transitions in all compounds except YbCu$_5$ and YCu$_5$ as follows: antiferromagnetic transitions for GdCu$_5$ (T_N = 21.5 K) and TbCu$_5$ (T_N = 12.5 K), ferromagnetic for DyCu$_5$ (T_C = 6.5 K) and first time observed in heat capacity antiferromagnetic transition for HoCu$_5$ (T_N = 3 K) [9] and magnetic transition in ErCu$_5$ (T_C = 1.6 K) and TmCu$_5$ (T_C = 1.3 K). Especially, in case of TmCu$_5$ we could conclude that ground CEF level is doublet contrary to expected singlet in [5]. Moreover, in HoCu$_5$ we have seen below 1 K upturn of C(T), which is characteristic for nuclear contribution of Ho into C(T). In DyCu$_5$ we did not observed anomaly at 15 K like in susceptibility [10]. The sharpness of maxima in C(T) connected with transitions is influenced by polycrystallinity of samples.

All transitions were influenced by applied magnetic

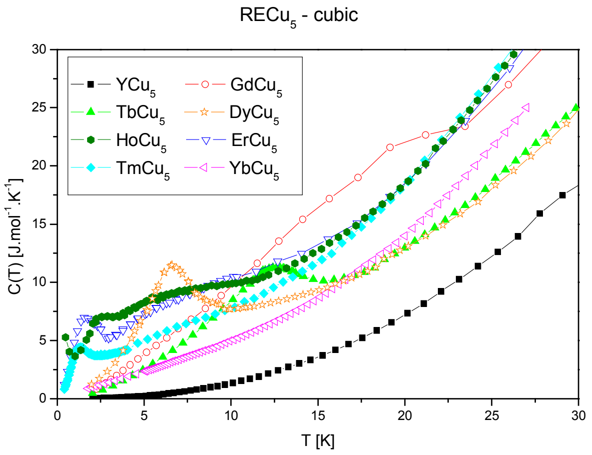

Fig. 1. Temperature dependence of heat capacity of cubic *RE*Cu$_5$ (*RE* = Gd, Tb, Dy, Ho, Er, Tm, Yb) and hexagonal YCu$_5$ in zero magnetic field.

field. In Fig. 2. we present as an example characteristic magnetic field behaviour of C(T) of $TmCu_5$ at low temperatures. One could see that magnetic field 1 T is enough to depress transition. At about 3 K appears Schottky-type maximum, which is shifted to higher temperatures with increasing magnetic field. Similar behaviour was observed in a case of $ErCu_5$ and $HoCu_5$, where 1 T is enough again to depress magnetic transition. In $DyCu_5$ the magnetic field larger than 6 T was necessary to depress transition. The maximum in heat capacity slightly decreases to lower temperatures. For $TbCu_5$ the magnetic field 9 T does not fully depressed the magnetic transition. In order to confirm the type of magnetic transition in $TmCu_5$ and $ErCu_5$, the measurements of magnetic properties are necessary.

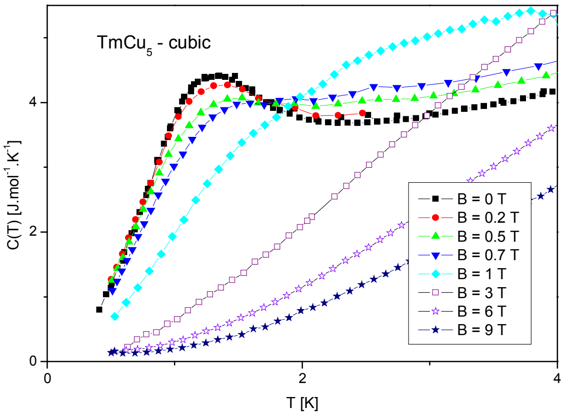

Fig. 2. Low temperature detail of magnetic field dependence of heat capacity of cubic $TmCu_5$.

In order to estimate the magnetic contributions to heat capacities and magnetic entropies, we have used the YCu_5 as non-magnetic analogue. Then Schottky contribution was fitted using standard procedure for cubic CEF to estimate appropriate energy levels. In Figure 3 and Figure 4 such characteristic results are shown for $HoCu_5$. We have used magnetic doublet as a ground state for magnetically ordered compounds. In case of $HoCu_5$ Schottky fit yielded to CEF energies 1, 1.8, 3.8, 7.4 and 7.8 meV. The CEF energies in paramagnetic state (above T_N) determined from PC spectroscopy measurement are 1, 4 and 8 meV [9], which is in a good agreement with heat capacity results. The transition from ground state to 1.8 and 3.8 meV are probably not allowed in according to selection rules. One could also see good agreement between experimentally determined entropy and theoretical limit drown in Figure 4. Quite well agreement was obtained between all CEF energy levels determined by PC spectroscopy and that determined from Schottky fit. Thus we have shown the capability of both methods for obtaining the information about CEF splitting.

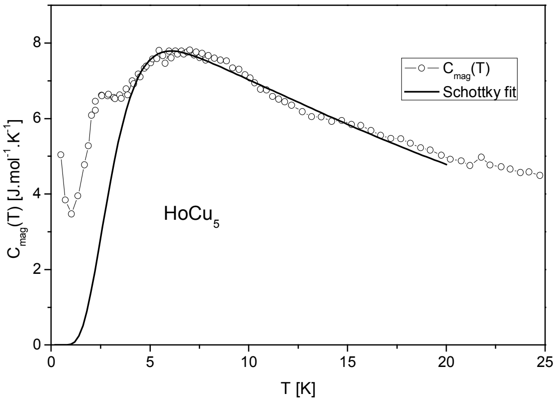

Fig. 3. Magnetic contribution to the heat capacity of $HoCu_5$ and Schottky fit.

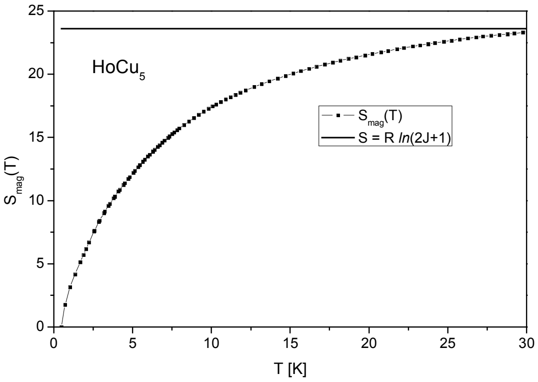

Fig. 4. Magnetic entropy of $HoCu_5$.

CONCLUSIONS

We have measured the heat capacity of cubic *RE*Cu_5 compounds and the influence of magnetic field. We observed the magnetic transitions for $TmCu_5$, $HoCu_5$ and $ErCu_5$. Determination of magnetic contribution to the heat capacity and magnetic entropy gave us possibility to estimate energy level of CEF splitting. Those results are in a good agreement with PC spectroscopy data.

ACKNOWLEDGMENT: This work has been partly supported by the COST - ECOM P16; the Slovak grant agency VEGA 2/0007/09; the Slovak Research and Development Agency under the contract No. VVCE-0058-07; the CLTP as the Centre of Excellence of the Slovak Academy of Sciences and P.J. Šafárik University. The liquid nitrogen for the experiment has been sponsored by the U.S. Steel Kosice, s.r.o.

REFERENCES

1. D. Gignoux, D. Schmitt, In: Handbook of Magnetic Materials vol **10**, ed. K.H.J. Buschow (Amsterdam, Elsevier - 1997) 239.
2. B. Idzikowski, A. Jezierski, K. Nenkov, J. Appl. Phys. **85,** 4744 (1999).
3. K.H.J. Buschow, Rep. Prog. Phys. **42**, 1373 (1979).
4. K.H.J. Buschow et al., J. Appl. Phys. **41**, 4609 (1970).
5. K. Knorr et al., J. Phys. **F9**, 645 (1979).
6. M. Reiffers, B. Idzikowski, S. Ilkovič, K.-H. Müller, Phys. Stat. Sol. (a) **196,** 286 (2003).
7. M. Reiffers et al., J. Magn. Magn. Mater. **272-276, P1,** 209 (2004).
8. M. Reiffers et al., Physica B **378-380,** 738 (2006).
9. S. Ilkovič et al., J. Magn. Magn. Mater. **242-245,** 858 (2002).
10. K. Nenkov et al., Acta Physica Polonica **A97,** 843 (2000).

CHARACTERISATION OF NOVEL MATERIALS FOR FOTOVOLTAICS AND SENSORICS WITH COMPLEMENTARY USED ELECTRICAL AND ELECTROCHEMICAL METHODS

K. Gmucová, katarina.gmucova@savba.sk, L. Chitu, livia.chitu@savba.sk, E. Majková, eva.majkova@savba.sk, V. Nádaždy, vojtech.nadazdy@savba.sk, and M. Weis, martin.weis@savba.sk, Institute of Physics, Slovak Academy of Sciences, Dúbravská cesta 9, 845 11 Bratislava, Slovak Republic

INTRODUCTION

Characterisation of materials is a research area with a high impact on the development of both the photovoltaic devices and sensors. Aimed at the improvement of device functionalities, and based on the experimentally obtained data, the properties of materials under interest can be effectively tailored. Our group has been actively working in this field. Two classes of such materials, organic semiconductor thin films and hybrid structures with incorporated nanoparticles, are in the sphere of our main interest. This paper is a short review of our recently obtained results [1-9].

Organic semiconductors offer many advantages in comparison with their inorganic counterparts, which make them particularly attractive for photovoltaic and sensor applications. The possibility to use organic semiconductors in roll-to-roll fabrication techniques, which can dramatically decrease manufacturing costs, is an important attribute for the preparation of low-cost solar cells. Similarly, the use of organic semiconductors may lead to new biosensors that are small, easily portable, inexpensive, fast, and capable of detecting low concentrations of specific analytes with high sensitivity and high selectivity. In the last decades, metalic nanoparticles with their amazing electronic, optical, and catalytic properties have attracted great interest in sensorics and photovoltaics applications, too.

EXPERIMENTAL

Let us focus on the advantages of the complementary usage of electrical and electrochemical methods in materials science. The analogy of electrical and electrochemical approaches is demonstrated in Fig. 1. A model system, cobalt nanoparticles encapsulated in organic envelope and adsorbed onto carbon microfiber, has been studied in [1]. Electro-chemical signal obtained in aqueous environment is depicted on the lower part of Fig.1. At the zero potential cobalt nanoparticles were reduced to their initial neutral state. After their redox potential was reached, nanoparticles were oxidized and voltcoulometric signal was recorded as a characteristic peak. Additional information has been obtained using a typical electrical measurement. The movement of the adsorbed nanoparticles has been demonstrated by the feedback capacitance-potential method, the related curve is depicted on the upper part of Fig. 1. To obtain this curve, sampling excitation pulses of amplitude 60 mV were applied to the microfibre, and the transient response was measured according to the rules published in [10]. From the electrochemical point of view, these pulses cause the oxidation of species nearby the carbon surface. Thus, the nanoparticles become positively charged, and are repulsed from the microfibre surface. After the trailing edge of the excitation pulse the system tends to reach the equilibrium, *i.e.*, the nanoparticles are reduced to the neutral state, their distance from the electrode surface is contracted. It does match the situation, when the measured capacitance grows. Later, we have reported a possibility to observe nanoparticle rotation movement using electrochemical methods [2,3].

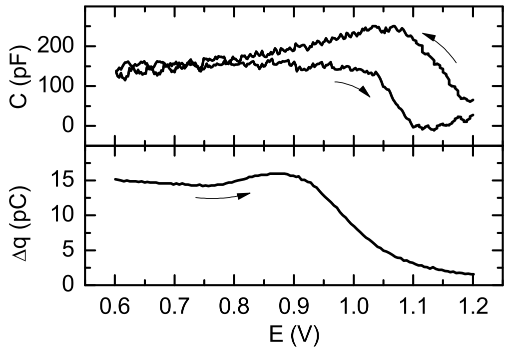

Fig. 1. Electrical and electrochemical signals from cobalt nanoparticles adsorbed on carbon fibre microelectrode. Upper part: capacitance-potential curve, lower part: voltcoulometry. Arrows indicate the course of potential change.

Another example of an appropriate application of both the electrical and electrochemical methods in material characterization refers to the improved understanding of the defect formation in pentacene. Pentacene is a polycyclic aromatic hydrocarbon consisting of 5 linearly-fused benzene rings. A first-principles study for the hydrogen- and oxygen-induced defect states in pentacene has been reported in [11]. It was shown that adding hydrogen or hydroxyl radical to a pentacene molecule forms a fourfold-coordinated carbon atom that gives rise to three charge states in the gap. Other first-principles calculations [12] of defect formation by oxygen and water molecules have shown that for both of them it is energetically favourable to enter the pentacene molecule. Generally, defects in pentacene play important role in controlling its electronic and transport properties. Therefore, their improved understanding should be implemented in the rational architectures of novel devices.

The idea to use electrochemistry for the defect characterization is based on the following analogy. While with the help of the electrical methods the activation energy either for the capture or for the emission from a defect (deep trap) is measured, electrochemical methods yield the potential at which either reduction or oxidation of species under consideration take place. Realizing that oxidation describes the loss of electrons, while the reduction describes the gain of electrons, the emission from electron traps can be regarded as an oxidation process, the capture of electrons in electron traps as a reduction process. On the contrary, for hole traps the emission of holes from hole traps can be regarded as a reduction process, the capture of holes in hole traps as an oxidation process.

We have reported observation of a metastable defect in pentacene thin film [6]. Here, charge DLTS was used as a typical representative of electrical methods – see Fig. 2. The samples were prepared by thermal evaporation of pentacene onto p^+ *c*-Si substrate, Schottky-type contacts were deposited on pentacene thin film by thermal evaporation of aluminum. Metastable defect with the associated deep level characterized by an activation energy and attempt-to-escape frequency of 0.6 eV and $5x10^{12}$ s^{-1}, respectively, was reversibly created/ removed under a negative/positive bias voltage applied to the aluminum/pentacene Schottky diode at room temperature in air. Also, annealing the sample in vacuum at 360 K removes the defect and prevents the creation of this defect by application of any bias voltage in vacuum. We assume that the above-mentioned defect is 6-pentacenequinone.

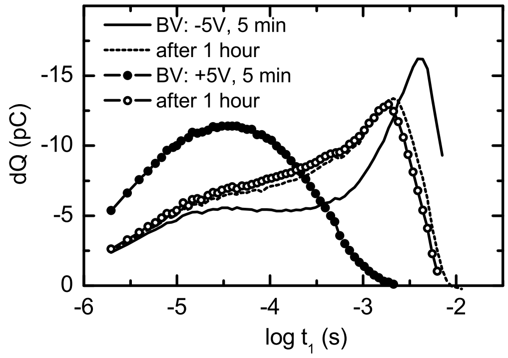

Fig. 2. Metastable behavior of pentacene thin film. After keeping the samples without any bias voltage at room temperature for 1 hour DLTS measurements yield spectra similar to as-deposited states regardless of the previous bias treatment (bias voltage +5 or −5 V).

The performance of the organic or hybrid organic/inorganic devices often depends on the environmental conditions and the endeavour to study the effect of the air (and/or humidity) exposure on the pentacene electronic properties continues unabatedly. Recently, we have published an electrochemical study of the formation of water related trap states in pentacene [7]. Metastable defects in pentacene thin films deposited onto platinum electrode have been studied in the electrochemical cell filled with various acidic and basic solutions - see Fig. 3. The redox reactions of different pentacene weak bonded defects formed in aqueous solutions with prevailing concentration of hydrogen cations or hydroxyl anions, were observed as voltammetric waves. Based on the obtained data we have suggested the assignment of the measured activation potentials to various pentacene defects marked with arrows on Fig. 3. Proceeding from -1 V to + 1 V, the following defects were observed: 6-pentacenequinone, 6-pentacenehydroquinone, 6,13-dihydropentacene, and 6,13-pentacenehydroquinone.

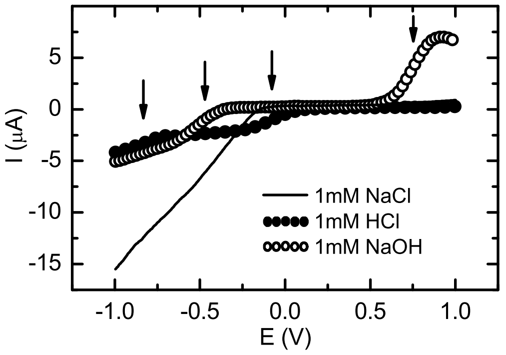

Fig. 3. Voltammetric signals of the pentacene Langmuir-Blodgett thin film modified Pt electrode immersed in 1mM solutions of NaCl, HCl, and NaOH.

More information, concerned with our research related to novel materials for photovoltaics and sensorics, and based on complementary usage of electrical and electrochemical methods, can be found in our works [1-9].

CONCLUSIONS

Various analytical techniques have to be used to study different types of material related issues. We have shown that complementary used electrical and electrochemical approach enable us to study material properties under markedly different experimental conditions, which provides a better understanding of material properties.

ACKNOWLEDGMENT: This research was supported by the projects SAV-FM-EHP-2008-01-01, APVV-0267-06, APVV-0173-06, and VEGA-2/7118/27.

REFERENCES

1. K. Gmucová et al., Anal. Sci. **21**, 1227 (2005).
2. K. Gmucová et al., ChemPhysChem **9**, 1036 (2008).
3. K. Gmucová et al., Appl. Surf. Sci. **254**, 7008 (2008).
4. M. Weis et al., Electroanalysis **19**, 1323 (2007).
5. M. Weis et al., J. Nanosci. Nanotechnol. **8**, 5684 (2008).
6. V. Nádaždy et al., Appl. Phys. Lett. **90**, 092112 (2007).
7. G. Gmucová et al., Phys. Status Solidi A **206**, 1404 (2009).
8. V. Nádaždy et al., J. Non-Cryst. Solids **354**, 2888 (2008) .
9. M. Weis et al., Collect. Czech. Chem. Commun. **74**, 565 (2009).
10. T. J. Mego, Rev. Sci. Instrum., **57**, 2798 (1986).
11. J.E. Northrup and M.L. Chabinyc, Phys. Rev. B **68**, 041202(R) (2003).
12. L. Tsetseris, and S.T. Pantelides, Phys. Rev. B **75**, 153202 (2007).

EXPERIMENTAL STUDY OF THE SPIN RELAXATION IN S=7/2 HEISENBERG ANTIFERROMAGNET $Gd_2(fum)_3(H_2O)_4.3H_2O$

L. Sedláková[a], lucia.sedlakova@upjs.sk, M. Orendáč[a], martin.orendac@upjs.sk, E. Čižmár[a], erik.cizmar@upjs.sk, A. Orendáčová[a], alzbeta.orendacova@upjs.sk, W. H. Zhu[b], Z. M. Wang[b], S. Gao[b], gaosong@pku.edu.cn
[a]Centre of Low Temperature Physics, Faculty of Sciences, P. J. Šafárik University, Park Angelinum 9, 041 54 Košice, Slovakia
[b]Beijing National Laboratory for Molecular Sciences, College of Chemistry and Molecular Engineering, Peking University, 100871, China

INTRODUCTION

In the recent years magnetic relaxation, in which the excess energy associated with electron spins in a magnetic field is transferred to the lattice, has been intensively studied both theoretically and experimentally. Mechanism of the relaxation represents considerable problem in subsequent potential tuning of dynamic properties of the magnetic materials with potential applications in magnetic cooling, data storage techniques or quantum computing.

In the present work we study relaxation properties of $Gd_2(fum)_3(H_2O)_4.3H_2O$ identified as a three-dimensional S = 7/2 Heisenberg antiferromagnet. The behavior of the relaxation time is consistent with the phonon bottleneck effect considering resonance trapping of low-energy phonons, recently proposed in Ni_{10} molecular magnets [1].

EXPERIMENTAL

The compound $Gd_2(fum)_3(H_2O)_4.3H_2O$ (fum-fumarate = $C_4H_2O_4$) was synthesized and characterized following well establish procedure [2]. The crystal structure of the sample was determined by NONIUS KappaCCD diffractometer. The alternating susceptibility studies in the temperature range from 2 to 30 K were performed using commercial SQUID magnetometer MPMS, Quantum Design. The amplitude of the alternating magnetic field was 0.3 mT. Specific heat of a powder sample in the temperature range 90 mK – 2.5 K was measured using dual slope technique in a commercial refrigerator TLE 200.

RESULTS AND DISCUSSION

$Gd_2(fum)_3(H_2O)_4.3H_2O$ (Gdfum) crystallizes in the monoclinic space group, with unit cell parameters a = 9.4793(1) Å, b = 14.7439(3) Å, c = 14.7929(2) Å. The structure is a 3D porous framework consisting Gd-fum layers further pillared by fum ligands. The basic structural unit is the Gd_2 dimer in which the two Gd^{3+} ions are bridged by two COO groups. The Gd_2 dimers are interlinked into a wavy layer parallel to *ac* plane through the first two fum ligands, then the layers are pillared by the third fum to form the 3D framework.

Specific heat of the compound was investigated in zero magnetic field below 2.5 K. Since the studied material represents magnetic insulator only magnetic and lattice subsystems will contribute to the total specific heat. The lattice contribution was subtracted using Debye approximation. Magnetic specific heat (Fig. 1) displays a peak at 0.19 K revealing the transition to magnetically ordered state. The magnitude of the exchange interaction among magnetic ions was estimated from the value of the critical temperature. Using mean-field approximation an estimate of the exchange interaction may be obtained from the equation $k_BT_c/J = 2/3zS(S+1)$, where T_c denotes the critical temperature, z stands for the number of the nearest neighbours; taking z = 6, the mean field approximation yielded $J/k_B = 2.6$ mK.

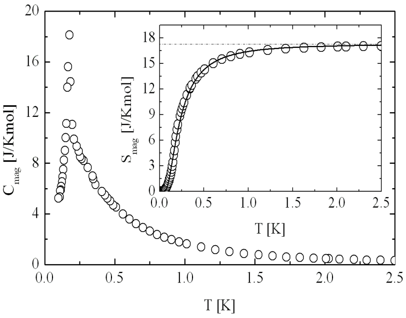

Fig. 1: Temperature dependence of the magnetic specific heat for Gdfum. Inset: Temperature dependence of the magnetic entropy for Gdfum (opened symbols), dashed line denotes the saturation value of the magnetic entropy for S=7/2 paramagnet. Full line represents the prediction for magnetic entropy for S=7/2 paramagnet with single - ion anisotropy for g=2.0 and $|D|/k_B \approx 0.24$ K.

Alternatively, using pure dipolar approach an estimation of the relative strength of the interaction between magnetic Gd^{3+} ions can be obtained by using approximation $J_{dip} = (\alpha/2)g_1g_2\mu_B^2/r^3$, where α is a constant whose magnitude depends on the orientation of the neighbouring spins, g_1 and g_2 represent their g factors, r stands for the distance and μ_B denotes Bohr magneton. For α = 2, corresponding to antiparallel orientation of spins, and average distance r_{av} = 6 Å, this approach yields the value of a through-space magnetic interaction $J_{dip}/k_B \approx 31$ mK.

Moreover, the effect of the crystal field was determinated considering the theoretical prediction for the magnetic entropy of S=7/2 paramagnet. The temperature dependence of the entropy, which was calculated numerically from specific heat data, can be reproduced using the prediction for S=7/2 paramagnet with single - ion anisotropy, for g=2.0 and $|D|/k_B \approx 0.24$ K involved (inset from Fig. 1).

Alternating susceptibility was studied from nominally 2 K to 30 K at various frequencies varying from 10 Hz to 10 kHz and magnetic fields up to 3 T. Imaginary component is characterized by the formation of a broad maximum shifting towards higher temperatures with increasing pumping frequency. Analyzing the position of the broad maximum in imaginary susceptibility, the temperature and magnetic field dependence of the relaxation time τ was constructed (Fig. 2).

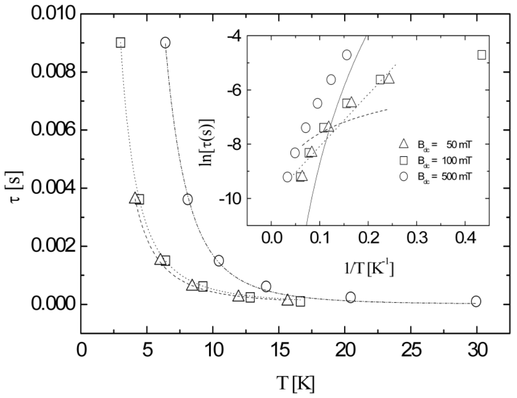

Fig. 2: Relaxation time of Gdfum as a function of the temperature at different dc fields (opened symbols). Lines represent fits of τ(T) with formula $\tau^{-1}=DT^{\alpha}$. Inset: Logarithm of the relaxation time as function of inverse temperature (opened symbols). Lines represent fits for direct (dashed line), Raman (full line), Orbach (dot line) relaxation process.

Considering the values of the characteristic parameters, single - ion approximation was adopted for the analysis of the obtained behaviour of the relaxation time. However, taking into account direct, Raman and Orbach processes representing mechanisms for the single spin relaxation, fail in the description of the experimental data (see Fig. 2, inset). The failure of the aforementioned approach suggests that the relaxation observed in Gdfum can not originate from the relaxation of a single spin to a phonon bath.

ESR experiments on diluted Gd-salts suggest the spin - lattice relaxation times of such systems are much shorter than the relaxation time in Gdfum which is of the order of milliseconds. Notably, the spin relaxation time may be greatly enhanced by the presence of a neighboring spin [3] due to the reabsorption of the emitted phonon. This may lead to the resonant trapping of the phonon associated with phonon bottleneck effect. The phonon bottleneck theory indicates that the temperature of the lattice modes interacting with the spins rise to a value approaching the spin temperature. The phonons may become “hot”, and the observed relaxation behaves as $\tau^{-1}=DT^{2}$ for $B \to 0$ [4]. The temperature dependences of the resulting relaxation times obtained at 50 mT and 100 mT were fitted using formula $\tau^{-1}=DT^{\alpha}$, the analysis yielded $\alpha=2.4$ for both sets of data in a good agreement with the value of the exponent $\alpha_{theor}=2$ predicted by the theoretical models assuming the presence of phonon bottleneck effect.

The aforementioned scenario of the relaxation time behaviour is in agreement with the investigation of the magnetic field dependence of the relaxation time. This study was performed in magnetic fields up to 3 T at selected temperatures 5 K, 10 K and 20 K and the results are presented in Fig. 3. For all temperatures the observed dependence is characterized by a broad maximum, the position of which is shifted upwards with increasing temperature. The influence of magnetic field on the resonant phonon trapping may be deduced from the relation $P(t) \sim B^{2}$ [3], where P(t) is the asymptotic probability of releasing the trapped phonon. Consequently, phonon trapping should be less effective with increasing magnetic field and thus the relaxation time due to phonon bottleneck effect should decrease with increasing magnetic field. The experimental observation of the broad maximum in τ(B) dependence becomes consistent with the sketched energy level scheme of Gd^{3+} ion (Fig. 3, inset).

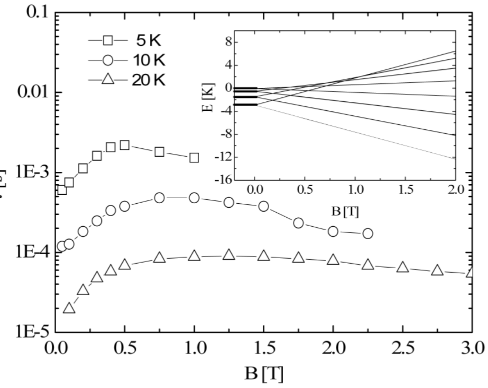

Fig. 3: Magnetic field dependence of the relaxation time of Gdfum. Inset: the energy level scheme of Gd^{3+} ion for D/k_B = 0.24 K.

As can be seen, several crossings of energy levels occur for magnetic fields from 0.4 T to 1 T. The energy level scheme reveals that below 1 T increasing magnetic field decreases the difference in energy levels making resonant phonon trapping for the corresponding energy levels more efficient. On the other hand, no such behavior may be anticipated for magnetic fields higher than 1 T where increasing magnetic field increases the separation among energy levels. As a result, a broad maximum in the magnetic field dependence of the relaxation time due to phonon bottleneck at about 1 T may be expected in accord with the experimental observation.

CONCLUSIONS

The investigation of alternating susceptibility revealed the onset of slow spin relaxation. Temperature dependence of the relaxation time indicates the presence of phonon bottleneck effect in the studied material. Characteristic parameters $v=3.89.10^{5}$cm/s, $k_0=7.4.10^{4}$ cm^{-1}, $k_0r_0<<1$ ($r_0=4.151.10^{-8}$cm is separation between spins) suggest that the resonance phonon trapping may be the fundamental mechanism of the relaxation in Gdfum. The magnetic field dependence of the relaxation time qualitatively supports the proposed scenario.

ACKNOWLEDGMENT: This work was supported by grants SK-CN-0032-07, APVV LPP-0102-06 and 973-2006CB601102. Material support of U.S. Steel is also gratefully acknowledged.

REFERENCES

1. S. Caretta et al., Phys. Rev. Lett. **97**, 207201 (2006).
2. W.H. Zhu et al., Dalton Trans. **6**, 765 (2006).
3. D.L. Huber, Phys. Rev. B **142**, 137(1966).
4. P.L. Scott et al., Phys. Rev. **127**, 32 (1962).

POLYMORPHIC STRUCTURAL TRANSITIONS IN DNA + DPPC + DIVALENT METAL CATIONS AGGREGATES

D. Uhríková[1], uhrikova@fpharm.uniba.sk, P. Pullmannová[1], pullmannova@fpharm.uniba.sk, [1]Faculty of Pharmacy, Comenius University, Odbojárov 10, 832 32 Bratislava, Slovakia, S.S. Funari, sergio.funari@desy.de, Hasylab at DESY, Notkestr. 85, D-22603 Hamburg, Germany, J. Teixeira, jose.teixeira@cea.fr, LLB CEA Saclay, 91191 Gif-sur-Yvette Cedex, France and P. Balgavý[1], balgavy@fpharm.uniba.sk

INTRODUCTION

Zwitterionic phospholipids (i.e. dipalmitoylphosphatidylcholine DPPC) in a solution of divalent metal cations spontaneously form vesicles with a positive surface charge. Cationic vesicles interact electrostatically with DNA polyanion, forming colloidal particles with an ordered internal structure. The aim of the present work is to study the phase behaviour of the DNA+DPPC mixture as a function of ions concentration and temperature. Aggregates were prepared at milimolar concentrations of divalent cations that are physiologically relevant. Two ions, calcium and zinc were chosen for the study. Aggregates prepared with biogenic ions like calcium or magnesium are potential gene delivery vehicles. The physico-chemical properties of the aggregates were documented e.g. in [1] and references therein. This contribution is focused to temperature induced polymorphic behaviour of DNA+DPPC+Zn^{2+} aggregates. The structure of the aggregates was examined using small-angle X-ray diffraction (SAXD) and neutron scattering (SANS).

EXPERIMENT

The DNA:DPPC=1:3 base/mol aggregates were prepared by interaction of short fragmented DNA (<1000 bp, Applichem, Germany) with DPPC (Avanti Polar Lipids, USA) in solution of $CaCl_2$ or $ZnCl_2$ (Merck, Germany) at different concentrations. 5 mmol/l NaCl in either redistilled water or D_2O (99.9%, Merck, Germany) were used for the preparation of solutions (pH ~ 7). SAXD experiments were performed at the soft-condensed matter beam-line A2 at HASYLAB, DESY, Hamburg. SANS experiments were performed on the PAXE spectrometer in LLB CEA France. Sample preparation as well as the data treatment is described in more details in [1, 2]. Experiments were performed at 20 and 60 °C (or 50 °C) when the lipid forms a gel (L_β) and a liquid-crystalline (L_α) phase, respectively.

RESULTS AND DISCUSSION

Hydrated phospholipids form lyotropic smectic mesophases. Two reflections of a lamellar phase (Fig. 1a) is a typical SAX diffractogram of fully hydrated DPPC. The repeat distance, d ~ 6.4 nm, is the sum of the lipid bilayer thickness, and the thickness of the water layer situated between two lamellae. Fig. 1b shows the diffractogram of DNA+DPPC aggregate prepared in 20 mmol/l Ca^{2+} in the gel phase. In addition to two reflections of the lamellar phase (d ~ 8.0 nm) we identify a broad reflection related to the regular packing of DNA strands in the water phase between the DPPC lamellae. We found the DNA-DNA distance d_{DNA} ~ 5.1 nm. The aggregate forms the condensed lamellar phase L_β^c [3]. Aggregates DNA+DPPC+ion^{2+} are formed when cations mediate DNA – DPPC binding. The binding of cations induce changes in the $P^- - N^+$ dipole conformation of the DPPC molecule. The positive side of the dipole is pushed out into the aqueous phase and, due to electrostatic interaction with the negatively charged phosphate groups of DNA, the aggregate is formed. In the L_α phase, at 60 °C (Fig. 1c), the regular packing of DNA strands is broken, and the periodicity of the lipid bilayer stacking slightly decreased, d ~ 7.6 nm. The DNA+DPPC aggregate at 20 mmol/l Zn^{2+} forms the L_β^c phase (not shown) at 20 °C. Heating the sample to the L_α phase the regular packing of the aggregate was broken, we observe no reflection in SAXD (Fig. 1d). The SANS experiments were performed with the aim to identify the observed

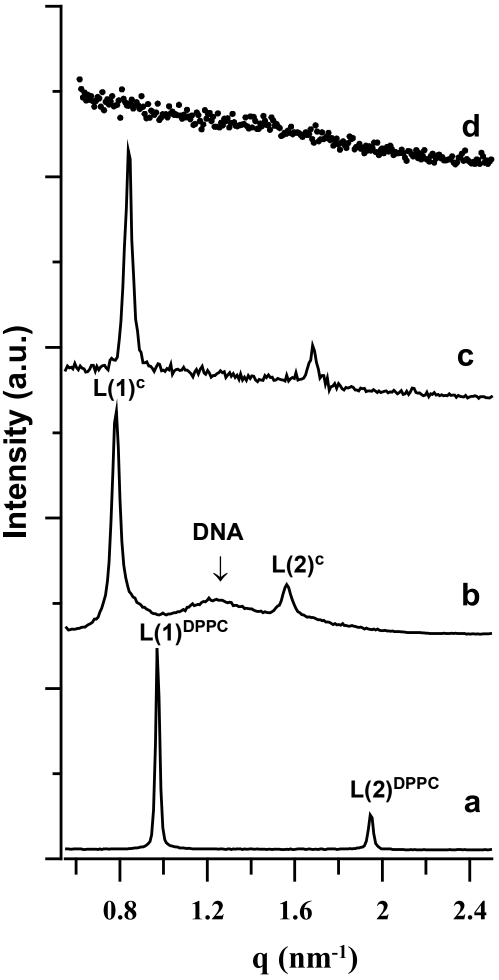

Fig. 1. SAX diffractograms of multilamellar DPPC vesicles, 20 °C (a), and DNA+DPPC aggregates in: 20 mmol/l $CaCl_2$ 20 °C (b), 60 °C (c), 20 mmol/l $ZnCl_2$ 60 °C (d).

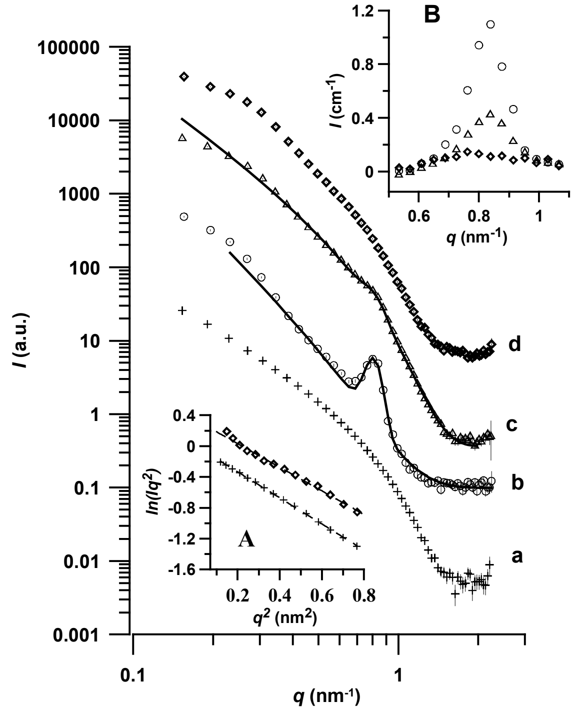

Fig. 2. SANS curves of DPPC vesicles in 20 mmol/ZnCl$_2$ (a), and DNA+DPPC aggregates in ZnCl$_2$: 5 mmol/l (b), 20 mmol/l (c), 30 mmol/l (d) at 50 °C. Inset A: Kratky-Porod plot of (a) and (d). Inset B: *S(q)*-1 extracted analytically from curves (b), (c), and (d).

structural changes.

For dispersions of monodisperse centrosymmetric particles, the SANS intensity is given by

$$I(q) = N_p \cdot P(q) \cdot S(q) \qquad (1)$$

where q is the scattering vector $q=4\pi \sin\theta/\lambda$, 2θ is the scattering angle. N_p the number density of particles, *P(q)* their form factor and *S(q)* the interparticle structure factor. Fig. 2a shows a typical SANS curve of unilamellar vesicles. Unilamelar vesicles are formed spontaneously when the surface charge is higher than 1 – 2 μC/cm^2 [4]. For unilamellar vesicles, *S(q)* is approximately equal to 1 [5], we do not observe any correlation peak. The scattered intensity can be fitted by a model of randomly oriented planar bilayers [6]. According to the Guinier approximation, at values of q large as compared with the inverse of the radii of the vesicles [7], the scattered intensity factor can be written as:

$$I(q) = Cte \cdot q^{-2} \exp(-q^2 R_g^2) \qquad (2)$$

where *Cte* is a constant and R_g is the radius of gyration of a flat bilayer. Eq. 2 is valid for finite size objects when $L^{-1} \le q \le R_g^{-1}$, where L is the largest dimension size of the object. The thickness of the two-dimensional planar sheet d_g can be obtained from R_g as $d_g^2 \cong 12\ R_g^2$. The Kratky – Porod plot ln(Iq^2) *vs.* q^2 is usually used to determine easily the radius of gyration R_g (Fig. 2, inset A). The d_g in the q range $0.34 \le q \le 1.97$ nm^{-1} are given in the Tab. 1. The thickness d_g of DPPC unilamellar vesicles prepared by extrusion is given in the Tab. 1 for the comparison [2].

Fig. 2b – d shows the SANS curves of the DNA+DPPC aggregates formed in 5 – 30 mmol/l ZnCl$_2$. The observed correlation peak with the maximum at $q \sim 0.8$ nm^{-1} indicates an organized structure due to multilamellar stacking. Part of the lipid is bound to DNA, forming a DNA+DPPC+Zn^{2+} aggregate. The observed peak is the first order reflection due to lipid bilayer stacking in a condensed lamellar phase of the aggregate, as confirmed by SAXD. To analyze the scattering profile, one must assume an interparticle structure factor *S(q)*. We imposed Gaussian shape for *S(q)*, and the form and structure factor were separated analytically. Fig. 2, inset B shows the obtained structure factors *S(q) vs. q*. Full lines in Fig. 2 represent the scattered intensities fitted by Eq. 1. With increasing concentration of zinc, the intensity of the correlation peak decreases. The SANS curve of DNA+DPPC aggregate at 30 mmol/l ZnCl$_2$ does not show any correlation peak (Fig. 2). The Kratky - Porod plot (Fig. 2, inset A) as well as data in Tab. 1 document a "dissolution" of the aggregate into DPPC+Zn^{2+} unilamellar vesicles and DNA+Zn^{2+}. The contrast between DNA+Zn^{2+} and D$_2$O at the used DNA concentration is small and thus its contribution to the SANS intensity is negligible.

CONCLUSIONS

Our experiments document structural heterogeneity of DNA+DPPC+ion^{2+} (Ca^{2+}, Zn^{2+}) aggregates as a function of cation concentration, and temperature. The observed polymorphic behaviour of aggregates results from the different size of the cations and their binding affinity due to differences in their electronic structure.

ACKNOWLEDGMENT: This work was supported by the EC under the FP6 Programme: RII3-CT-2004-506008 (IA-SFS) (HASYLAB project I-20080187 EC); by the JINR project 07-4-1069-09/2011 and by the VEGA grant 1/0292/09 to DU.

Tab. 1. Structural parameters of DPPC bilayer at 50 °C.

	c (mmol/l)	R_g^2 (nm^2)	d_g (nm)
DPPC		1.37±0.05	4.05±0.08
DPPC+Zn^{2+}	20	1.73±0.01	4.56±0.01
DNA+DPPC+Zn^{2+}	5	1.37±0.05	4.05±0.08
DNA+DPPC+Zn^{2+}	20	1.68±0.02	4.49±0.03
DNA+DPPC+Zn^{2+}	30	1.87±0.03	4.74±0.03

REFERENCES

1. D. Uhríková, A. Lengyel, M. Hanulová, S.S. Funari, P. Balgavý, Eur. Biophys. J. **36**, 363 (2007)
2. D. Uhríková, P. Pullmannová, M. Bastos, S.S. Funari, J. Teixeira, Gen. Physiol. Biophys. **28** 146 (2009)
3. J.O. Radler, I. Koltover, C.R. Safinya, Science **275**, 810 (1997)
4. H. Hauser: Phospholipid Handbook (Marcel Dekker, Inc., New York – 1993)
5. T. Nawroth, H. Conrad, K. Dose, Physica B **156&157**, 477 (1989)
6. P. Balgavý et al., Acta Physica Slo-vaca **48**, 509 (1998).
7. O. Glatter, O. Kratky: Small Angle X-Ray Scattering (Academic Press, New York – 1983)

MODELLING THE PENETRATION OF LASER LIGHT THROUGH BIOLOGICAL TISSUES

I. K. R. Haverlík, haverlik@fmph.uniba.sk, L. Šikurová, sikuroval@gmail.com;
Department of Nuclear Physics and Biophysics, Faculty of Mathematics, Physics and Informatics, Comenius University, Mlynska dolina F1, 842 48 Bratislava, Slovakia

INTRODUCTION

The role of lasers in medicine has increased dramatically over the past two decades [1]. A fundamental understanding of laser-tissue interactions is vital for the proper and appropriate use in clinical practice. The optical properties of biological tissues determine the penetration of the radiant energy from a laser source into tissue. Subsequently, the laser energy is converted into chemical, thermal, or mechanical energy and a variety of laser-tissue interactions are possible. The initial distribution of the radiant energy, however, affects the distribution and often the nature of the subsequent laser-tissue interactions. Biological tissues are characterized by absorption, scattering, reflection, refraction and diffusion of light beams [2].

LAMBERT-BEER-BOUGER LAW FOR TURBID MEDIA OF THE LASER LIGHT PENETRATION

Estimations of the laser light penetration through biological tissues are based only on one exponential function, taking into consideration the processes of absorption and Mie and Rayleigh scattering on biological molecules. These were seen insufficient for the experimentally gained data description.

So far, penetration of laser light through biological tissues along the central axis of the irradiation beam have been described by a simple exponential function, which is in accordance with the so-called modified Lambert-Beer-Bouger law for turbid media. This law can be expressed by Equation (1) where the values of spectral radiant power, P(d), obtained at the depth d below the sample surface on the central axis of the irradiation beam are determined as

$$\mathrm{P}(d) = \mathrm{P}_0 \exp\{-\mu_t\, d\}, \tag{1}$$

where P_0 is the spectral radiant power of incident radiation, μ_t is the total attenuation coefficient, depending on the scattering coefficient as well as on the absorption coefficient of the sample.

Weakening of the light beam at transition through a biological tissue is determined in Equation (1) mainly by absorption and scattering. Reflection and diffusion of light beams are included only in P_0, so only the light, outgoing from the sample is included. No doubt, multiple diffused reflection of laser light occurs insight biological samples, first of all on tissues' cells. Therefore, model of penetration of laser light through biological tissue, taking the multiple reflection of the light beam into consideration, is suggested in this report.

RESULTS

The presented model is based on the Lambert-Beer-Bouger law for turbid media and a discrete model of laser beam penetration through biological tissues [2, 3] at the same time. The model takes into consideration not only processes of absorption and scattering but also processes of multiple diffused reflection of the laser beam on biological tissues' cells.

Discrete model of the laser light penetration

Penetration of laser light through biological tissues is modelled by the basic equation:

$$\mathrm{P}(d) = \exp\{-\mu d\} \sum_{i=0}^{k} \mathrm{P}_i, \tag{2}$$

where P(d) is the radiant power of light transmitted through biological tissue, P_i is the radiant power of light after the i-th double diffused reflections, μ is the attenuation coefficient characterizing the light absorption and scattering.

Cascade model of the laser light penetration

The detailed digital cascade model of the laser light penetration through biological tissue takes into consideration the repeated reflections in each layer of the material.

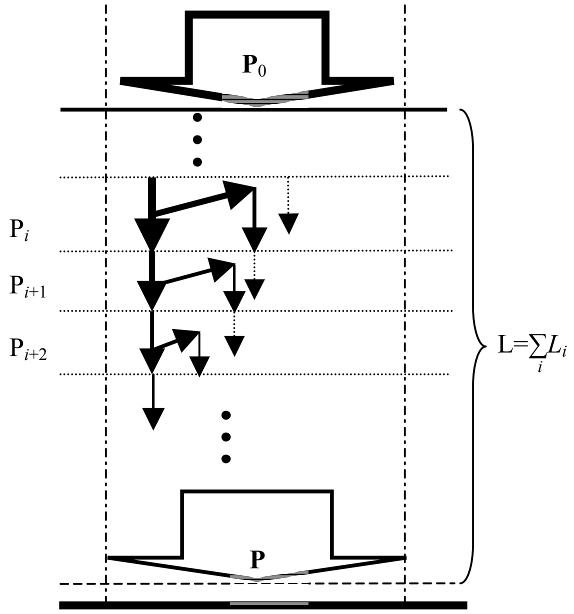

Fig. 1. Laser beam penetration through biological tissue sample - scheme of the models' basic structure.
$\mathrm{P}_i = \mathrm{P}_{i,1} + \mathrm{P}_{i,2} + \mathrm{P}_{i-1,3}$;
$\mathrm{P}_{i+1} = \mathrm{P}_{i+1,1} + \mathrm{P}_{i+1,2} + \mathrm{P}_{i,3}$;
$\mathrm{P}_{i+2} = \mathrm{P}_{i+2,1} + \mathrm{P}_{i+2,2} + \mathrm{P}_{i+1,3}$;

At the same time, it supposes the thickness of the tissue sufficient for manifestation of double reflections. Penetration of the laser beam through the i-th layer is, in this case, modelled by equation

$$\mathrm{P}_i = \exp\{-\mu L_i\} \sum_{k=0}^{m-1} \mathrm{P}_{i-1,k} + \exp\{-\mu L'_i\} \sum_{k=0}^{m-1} \sum_{j=1}^{n-k} R^j \mathrm{P}_{i-1,\mathrm{j},\mathrm{k}}, \qquad (3)$$

where L_i is thickness of the i-th layer, L'_i is the average trajectory length of a part of the laser light diffusively reflected in this layer, $j = j(i) = 1, 2, ..., n_i$; is the multiplicity of double reflections in the i-th layer, R is the reflectance factor for the relative contribution of the diffused reflection, $m = m(i)$ is the considered multiplicity of the reflection in the previous layer, $(i, j, k \in \boldsymbol{N})$: $m \le n$; $k \le n$.

The stated model was experimentally verified in the particular case of a suspension of isolated human erythrocyte membranes (ghosts) and compared with penetration of the laser beam through full blood. Excellent agreement was proved between the model and experimentally measured data.

CONCLUSIONS

The presented cascade model of processes considered in the decrease the radiant power of light in biological tissues can be used in laser dosimetry for medical application using light.

REFERENCES

1. M. Ben-David, et al., Lasers in Surgery and Medicine **40**, 464 (2008).
2. L. Šikurová, et al., Laser Physics **13**, 217 (2003).
3. I.K. Haverlík, et al., Laser Physics **13**, 222 (2003).

BESS MODEL RESONANCE AT FUTURE e^+e^- COLLIDERS

M. Gintner[1,2,3], gintner@fyzika.uniza.sk, J. Juráň[3], Josef.Juran@seznam.cz, I. Melo[1], melo@fyzika.uniza.sk,
B. Trpišová[1], trpisova@fyzika.uniza.sk
[1]Department of Physics, University of Žilina, Žilina, Slovak Republic
[2]Science and Research Institute, Matej Bel University, Banská Bystrica, Slovak Republic
[3]Institute of Experimental and Applied Physics, Czech Technical University, Prague, Czech Republic

INTRODUCTION

The still unknown mechanism of spontaneous electroweak symmetry breaking (ESB) has to take place in the Standard model of electroweak interactions (SM) in order to preserve the gauge invariance principle. The benchmark hypothesis explaining this mechanism is represented by the Higgs complex doublet scalar field of non-zero vacuum expectation value.

A number of theories alternative to the SM Higgs have been built that contain non-SM fields. Since it was highly desirable to describe their low energy phenomenology in a unified way, the effective Lagrangian formalism had been developed. This formalism was exploited also in building the BESS (Breaking Electroweak Symmetry Strongly) model (see [1] and the references therein). In the frame of this model description there appears in its particle spectrum a new boundstate - a vector ρ resonance - as a result of new strong interactions that may lie at the root of the ESB mechanism. This resonance has a form of an isospin triplet (ρ^0, ρ^+, ρ^-).

The model presented in this paper was built by modifying the BESS model. While in the BESS model considered in the literature ρ couples directly and with equal strength to the fermions of all generations, we assume that the ρ resonance, apart from the coupling to the W and Z bosons, couples directly only to the third generation of quarks - the top and the bottom quark [2],[3]. This is motivated by the extraordinary large mass of the top quark compared to the masses of other fermions. This mass is close to the ESB scale, which may suggest that the mechanism of its generation is the same as the mechanism of the strong ESB. We also added to the Lagrangian new terms that obey the model's symmetry, thereby introducing two new free parameters which relaxes the low energy constraints on the model parameters.

In this paper we study the processes $e^+e^- \to W^+W^-$, $e^+e^- \to t\bar{t}$, and $e^+e^- \to b\bar{b}$ in which the neutral ρ^0 resonance appears in the intermediate state. We did our calculations with the CompHEP program [4] which gives altogether 16 channels for the decay of ρ^0 into two particles. Out of these 16 channels only three - W^+W^-, $t\bar{t}$, and $b\bar{b}$ - give a dominant contribution to the total width of the ρ^0 for the ranges of parameters that are consistent with the low energy constraints [3]. Due to this fact we chose the three above given processes for a more detailed analysis.

RESULTS

The direct interaction of ρ with the left (t,b) doublet and the right top our model parameterizes by the coupling constants b_1 and b_2, respectively. Our results depend only on the values of these constants and the $SU(2)_V$ gauge coupling g_V since all other parameters can be expressed in terms of these three. All calculations presented here were performed for the neutral resonance of mass 1 TeV. We used no cuts.

Fig.1 depicts the total width of ρ^0 which is a function of g_V, b_1, and b_2 and is basically the sum of the partial widths of the W^+W^-, $t\bar{t}$, and $b\bar{b}$ decay channels. In the figure $\Gamma_{\rho^0}^{tot}$ is ploted as a function of g_V for several different sets of values b_1 and b_2.

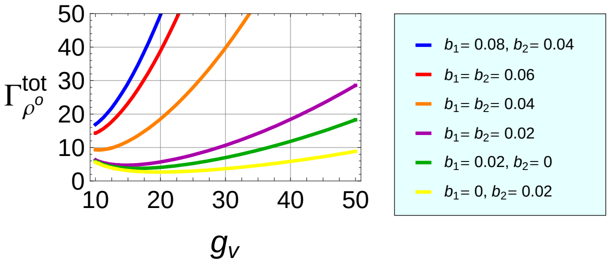

Fig. 1. The total width of the neutral ρ resonance as a function of g_V for selected sets of values b_1, b_2.

Fig.2 illustrates the effect of the initial state radiation (ISR) and beamstrahlung (BS) on the cross-sections of our processes. They show the total cross-sections as a function of the collision energy for each of the three processes for $g_V = 10$, $b_1 = 0.08$, and $b_2 = 0.04$. In this case the calculated branching ratios, *i.e* the percentage probabilities that a particular decay of the ρ^0 will occur, are 31%, 38%, and 31% for the W^+W^-, $t\bar{t}$, and $b\bar{b}$ decay channels, respectively. The total width $\Gamma_{\rho^0}^{tot}$=16.9 GeV.

The curve marked as irreducible background was obtained by effectively removing ρ^0 from the spectrum. The $R = 5$ curve represents the cross-sections we would get if the statistical significance R were equal to 5. These cross-sections were calculated using the relation

$$R = \frac{N_S - N_B}{\sqrt{N_B}}, \tag{1}$$

where N_S stands for the number of events of the signal process and N_B is the number of events of the irreducible background. We assumed the integrated luminosity 1 fb^{-1} at each collision energy. Also the curve corresponding to the SM with $M_{Higgs} = 115$ GeV, ISR and BS included, is shown.

However, to obtain a more realistic values for the cross-sections, we took into account further decay of the W bosons and the tops and the 50% efficiency of the b quark detection. All the decay modes through which the W^+W^- and $t\bar{t}$ decay are listed in Tab.1, where l stands for lepton, ν for neutrino, and j for a light jet. To each decay mode corresponds a reduction factor r with which the original cross-sections have to be multiplied [5].

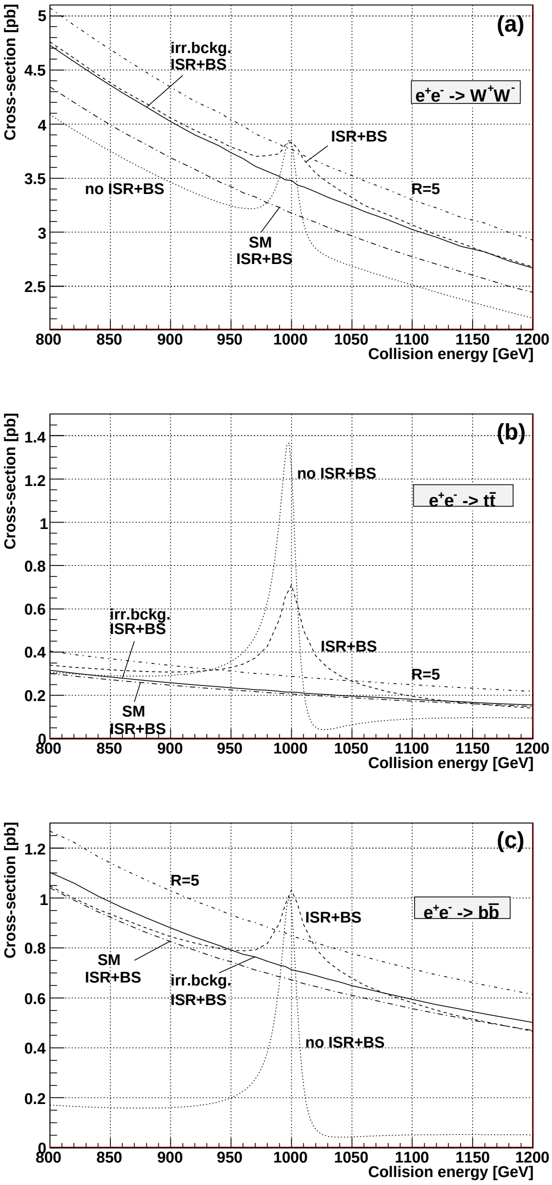

Fig. 2. Comparison of the effects of the ISR and BS on the signal for (a) $\mathrm{e^+e^-} \to \mathrm{W^+W^-}$ (b) $\mathrm{e^+e^-} \to \mathrm{t\bar{t}}$ (c) $\mathrm{e^+e^-} \to \mathrm{b\bar{b}}$. We also show the curve representing the irreducible background, the curve that corresponds to the statistical significance $R = 5$, as well as the curve that represents the SM with M_{Higgs}=115 GeV all of which include the effects of the ISR and BS.

TAB. 1. Reduction factors r, reduced chi-squared $\tilde{\chi}_o^2$ and corresponding probabilities P for various decay modes of the signal processes.

signal process	final state	r	$\tilde{\chi}_o^2$	P [%]
$\mathbf{W^+W^-}$	$l_1^+\nu_{l_1}l_2^-\nu_{l_2}$	0.0121	0.837	55.6
	$l^+\nu_l jj$	0.0704	4.870	0.0
	$jjjj$	0.4096	28.332	0.0
$\mathbf{t\bar{t}}$	$l_1^+\nu_{l_1}l_2^-\nu_{l_2}bb$	0.003025	1.089	36.7
	$l^+\nu_l jjbb$	0.0176	6.336	0.0
	$jjjjbb$	0.1024	36.863	0.0
$\mathrm{b\bar{b}}$	bb	0.25	13.738	0.0

To find out whether the deviation of our model from the SM is statistically significant, we applied the chi-squared test [6] to our data. We calculated the quantity called reduced chi-squared according to the following formula

$$\tilde{\chi}_o^2 = \frac{1}{n}\sum_{k=1}^{n}\frac{(O_k - E_k)^2}{E_k}. \qquad (2)$$

In equation (2), O_k and E_k stand for the signal cross-sections obtained using our model and the SM, respectively, that refer to the corresponding curves in Fig.2, both including the reduction by the factor r. The variable n is the number of collision energies which we took to evaluate $\tilde{\chi}_o^2$.

On the basis of the calculated $\tilde{\chi}_o^2$ we found the percentage probability $P = Prob(\chi^2 > \tilde{\chi}_o^2)$ that the χ^2 we would obtain if O_k followed the assumed distribution E_k is greater than or equal to $\tilde{\chi}_o^2$. In calculating the $\tilde{\chi}_o^2$ we chose $n = 7$ points in the interval 950 GeV-1050 GeV and used the integrated luminosity 1 fb^{-1}. The values obtained and the corresponding probabilities P are given in Tab.1.

CONCLUSIONS

The work shown in this contribution represents just first steps in studying the $\mathrm{e^+e^-}$ processes using our model. For the processes presented here more realistic conclusions can be drawn after performing deeper analysis that would include the detector reconstruction efficiencies and the study of reducible backgrounds. If the ρ resonance really exists, then in case of the $\mathrm{e^+e^-}$ processes with two particles in the final state the collider has to be able to scan the whole interval of the possible ρ masses with an appropriate scanning step in order to detect the ρ peak as our plots suggest.

REFERENCES

1. R. Cassalbuoni et al., Phys.Lett. **B253**, 275 (1991)
2. M. Gintner, I. Melo, Acta Phys. Slov. **51**, 139 (2001)
3. M. Gintner, I. Melo, B. Trpišová, Acta Phys. Slov. **56**, 473 (2006)
4. E. Boos et al. [CompHEP Collaboration], Nucl. Instrum. Meth. **A534**, 250 (2004)[hep-ph/0403113]. A. Pukhov et al.: [hep-ph/9908288].
5. M. Gintner, I. Melo, B. Trpišová, Proceedings of the 16th conference of Czech and Slovak physicists, Hradec Králové, 2008
6. J.R. Taylor, An Introduction to Error Analysis (University Science Books, Sausalito - 1997)

LEVEL CROSSING OF PARTICLE-HOLE AND MESONIC MODES IN ETA NUCLEI

E.E. Kolomeitsev[a], kolomeitsev@fpv.umb.sk, D. Jido[b], H. Nagahiro[c], S. Hirenzaki[d]
[a]Univerzita Mateja Bela, 97401 Banská Bystrica, [b]YITP, Kyoto 606-8502, Japan
[c]RCNP, Osaka University, Ibaraki, Osaka 567-0047, Japan, [d]Nara Women's University, Nara 630-8506, Japan

INTRODUCTION

The eta bound states in nuclei are intensively studied both theoretically and experimentally over the last decade. Being electrically neutral the eta meson can be bound only by strong interactions. Simultaneously, the strong interactions induce nuclear absorption of the bound eta meson. As the result the position and the width of the bound level are determined by a complicated interplay of the nuclear density distribution and the strength of the in-medium ηN interaction. The experimental proof of the existence of eta bound states could provide information on modification of meson properties in nuclear matter complimentary to that obtained from pionic and kaonic atoms.

The prominent feature of the eta meson is that the eta-nucleon system couples dominantly to the $N^*(1535)$ (S_{11}) resonance at threshold energies. The ηNN coupling is, on the contrary, much smaller than ηNN^* and πNN ones and is basically irrelevant for analyses of the ηN scattering and the threshold η production on a nucleon [1]. Therefore, the low-momentum eta meson would dominantly excite N^*–nucleon-hole $(N^* - h)$ states in nuclear medium. The difference between the eta mass and the $N^* - N$ mass gap is just 50 MeV, which is smaller than the N^* width $\Gamma_{N^*} \simeq 75$ MeV and is comparable with the depth of the attractive potential acting on the nucleon in a nucleus, $\sim 50 - 60$ MeV. Hence, one could expect the eta meson nuclear dynamics to be sensitive to modifications of nucleon and N^* properties in medium.

The question about in-medium dynamics of the $N(1535)$ resonance addresses an interesting aspects of the chiral symmetry of strong interactions. Being the lowest lying baryon with the opposite parity to the nucleon, the $N(1535)$ can be viewed as its chiral partner [2, 4]. If now the chiral symmetry is getting restored with an increasing baryon density the parity partners will become degenerate. The important implication of this picture for the eta meson physics is that the $N - N^*$ mass gap decreases in nuclear medium and at some density goes below the η mass. This changes the sign of the η meson optical potential making it repulsive at saturation density as found in [3]. The parity-doublet concept corresponds to a linear realization of chiral symmetry in terms of hadrons. In a non-linear realization the parity partner is not present in the Lagrangian as an independent degree of freedom but rather manifests itself as a pole of the scattering amplitude generated dynamically by coupled channels. So, the $N^*(1535)$ can be viewed as a $K\Sigma$ and $K\Lambda$ quasi-bound state [5]. In general the dynamically generated states could be very sensitive to in-medium modifications of the meson-baryon loops they are made of. These two different pictures for $N(1535)$ imply distinct phenomenological consequences for eta meson dynamics in the nuclear matter.

ETA-MESON MODES

The propagation of the eta meson in medium is described in terms of the Green's function $G_\eta(\omega, k; \rho) = 1/(\omega^2 - k^2 - m_\eta^2 - \Pi_\eta(\omega, k; \rho) + i\,0)$ with the self-energy $\Pi_\eta(\omega, k; \rho)$. Here ω and k denote the eta energy and momentum, ρ is the nuclear density, and m_η is the vacuum eta mass. The eta-nucleon interaction is dominated by the N^* resonance, which contribution to the s-wave scattering amplitude is defined by the Lagrangian $\mathcal{L}_{\eta NN^*} = g\left(\overline{N}\,N^* + \overline{N^*}\,N\right)\eta$, with $g \simeq 2$ from the vacuum $N^* \to \eta N$ decay. Thus, the main contribution to the self-energy of slow eta mesons is due to the excitations of N^*-nucleon-hole modes. Then, the self-energy reads

$$\Pi_\eta = \frac{g^2\,\rho\,(2\,\omega_R(k;\rho) - i\,\Gamma_{N^*}/2)}{[\omega - \omega_R(k;\rho) + i\,\Gamma_{N^*}/2]\,[\omega + \omega_R(k;\rho)]}\,. \qquad (1)$$

Here $\omega_R(k;\rho) = m^*_{N^*}(\rho) - m^*_N(\rho) + k^2/(2m^*_{N^*}(\rho))$ and the density-dependent in-medium masses of the N^* and N are denoted as $m^*_{N^*}(\rho)$ and $m^*_N(\rho)$, respectively. $\Gamma_{N^*}(\omega;\rho)$ is the in-medium N^* width determined by the N^* self-energy, $\Gamma_{N^*}(\omega;\rho) = -2\,\Im\Sigma_{N^*}(m^*_N(\rho) + \omega;\rho)$ calculated in [3]. We use the chiral doublet model [4] for the medium modification of the N and N^* masses. Accordingly, the mass difference of the nucleon and N^* is determined by the value of the chiral condensate, which roughly linearly decreases with a baryon density increase: $m^*_{N^*}(\rho) - m^*_N(\rho) = (m_{N^*} - m_N)(1 - C\,\rho/\rho_0)$ and $C = 0.2$.

The in-medium Green's function can be written as $G_\eta(\omega, k; \rho) = \sum_i \Gamma_i(k;\rho)/(\omega - \omega_i(k;\rho) + i\,0)$, where ω_i's are complex solutions of the Dyson equation $G_\eta^{-1}(\omega, k; \rho) = 0$. This equation has two solutions with a positive real part, $\omega_i(k)$, $i = 1, 2$. These solutions describe two branches of the η-meson spectrum in nuclear matter. They are shown in Fig. 1 by solid lines for $k = 0$ as functions of the baryon density. With the vanishing coupling constant g the eta-meson mode and N^*-nucleon-hole mode are decoupled and only the mesonic mode can carry the η quantum numbers. This case is depicted by the dashed lines on the left panel in Fig. 1. The modes cross each other at $\rho \simeq 0.4\,\rho_0$ for $k = 0$. The finite value of the coupling g leads to the avoided level crossing and the redistribution of the eta quantum numbers between both branches. The residua of the poles of the propagator $G_\eta(\omega, k)$ at $\omega = \omega_i$ quantify the occupation of each branch by the eta-meson quantum numbers. Note $\Gamma_1(k;\rho) + \Gamma_2(k;\rho) = 1$. The dependence of the occupation factors on the nucleon density is shown on the right panel in Fig. 1. We see that at $\rho < 0.4\,\rho_0$ the eta quantum numbers populate dominantly branch 2 and for $\rho > 0.4\,\rho_0$ branch 1. The eta-meson spectrum changes substantially if we take

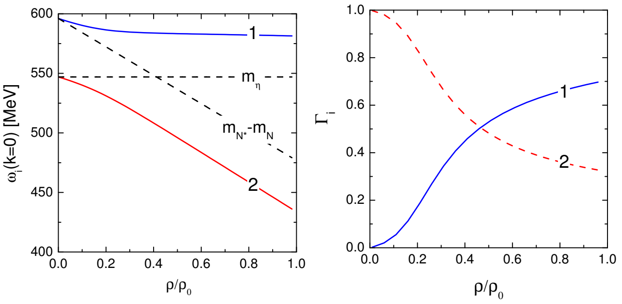

Fig. 1. The real parts of the solutions, $\omega_i(k=0)$ (left panel) and the occupations factors $\Gamma_i(k=0)$ (right panel) as functions of the baryon density.

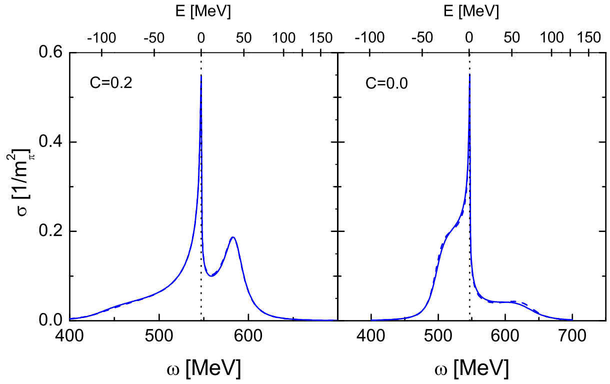

Fig. 2. The density-averaged nuclear response function (2) for $k = 0$ as a function of the eta meson energy, ω, (lower scale) and the binding energy $E = (\omega^2 - m_\eta^2)/2\,m_\eta$ (upper scale) calculated for $C = 0.2$ (left panel) and $C = 0$ (right panel). Dashed lines correspond to the constant N^* width and solid lines to the energy and density dependent width. The vertical dotted lines mark the bare eta mass value.

$C = 0$. The mass gap of branch 1, $\omega_1(k=0)$, increases now with the increasing density and that of branch 2 decreases half as strong as for $C = 0.2$. The occupation factors show that branch 2 carries now the dominant part of the eta mesons.

In order to get a feeling on the response of a nucleus to an external source with the eta-meson quantum numbers its instructive to study the spectral function averaged over the density distribution in a nucleus:

$$\sigma(\omega, k) = -\frac{4}{A}\int \mathrm{d}r\, r^2\, \rho(r) \Im\, G_\eta(\omega, k; \rho(r))\,. \qquad (2)$$

Here $\rho(r)$ is a spatial distribution of the nucleon density normalized to the total number of nucleons $A = 4\,\pi \int \mathrm{d}r\, r^2\, \rho(r)$. In Fig. 2 we plot the density-averaged nuclear response functions (2) for $C = 0.0$ and $C = 0.2$ calculated for the ^{11}B density distribution.

ETA-NUCLEUS RESONANCES

In order to understand better the bump structure of the response function shown in Fig. 2, we study poles of the eta-meson-nucleus scattering amplitude on the complex energy plane. The positions of the poles correspond to energies and widths of bound states of the eta and N^*-h modes in the nucleus. We search for non-trivial solutions of the Lippmann-Schwinger equation

$$\Psi(p) - \int_0^\infty dp'\, \frac{v_L(p, p'; \omega)\, p'^{\,2}}{\omega^2 - m_\eta^2 - p'^{\,2} + i\epsilon}\Psi(p') = 0\ .$$

existing for particular values of the binding energy $E = (\omega^2 - m_\eta^2)/(2\, m_\eta)$. The potential $v_L(p, p'; \omega)$ is given by the Fourier transform of the energy-dependent self-energy $\Pi_\eta(\omega, 0; \rho(r))$ evaluated under the local density approximation:

$$v_L(p, p'; \omega) = \frac{2}{\pi}\int_0^\infty \mathrm{d}r\, r^2 \Pi_\eta(\omega, 0; \rho(r)) j_L(pr) j_L(p'r)$$

with the spherical Bessel function $j_L(x)$.

We discuss the results obtained for $L = 0$ and $C = 0.2$. On the first Riemann sheet we find two poles at $E_1 = (-88.53 - i\,11.54)$ MeV and $E_2 = (-74.13 - i\,15.00)$ MeV, which correspond to the deepest bound η state in the ^{11}B nucleus and its first radial excitation, respectively. In the response function in Fig. 2 they manifest themselves as a small bump at about -80 MeV. On the first Riemann sheet there is another pole at $E = (6.40 - i\,0.46)$ MeV. Located above the threshold, this pole stands for a virtual state, which is not seen in the spectrum as a resonance bump but causes the cusp at the threshold. On the second Riemann sheet there is a resonance state at $E = (61.02 - i\,25.82)$ MeV, which shows up as a bump at ~ 50 MeV in the continuum region. Thus, we conclude that the structure of the response function in Fig. 2 (left panel) contains signals of the two bound, one virtual and one resonance states. For the $C = 0$ case the analytical structure changes. The attraction weakens and there remains only one bound state at $(-22.18 - i\,12.88)$ MeV on the first Riemann sheet. The other former bound state moves up and becomes a resonance at $(3.47 - i\,54.78)$ MeV on the second Riemann sheet. The other resonance state on the second Riemann sheet is located now at somewhat smaller energy $(31.91 - i\,54.79)$ MeV. The virtual state on the first Riemann sheet stays almost put at $(6.13 - i\,0.69)$ MeV.

CONCLUSION

The N^*–h contribution is important for the eta meson in nuclear matter and induces strong energy dependence of the eta self-energy. The reduction of the difference between the masses of N^* and N as a result of the medium effects leads to level crossing of the eta and N^*–h modes, and modification of the eta spectral function. The change of the spectral function will be clearly seen in formation spectra of eta nuclei [6].

REFERENCES

1. W. Grein, P. Kroll, Nucl. Phys. A **338**, 332 (1980).
2. C. DeTar, T. Kunihiro, Phys. Rev. D **39**, 2805 (1989).
3. D. Jido et al., Phys. Rev. C **66**, 045202 (2002); Nucl. Phys. A **721**, 665 (2003).
4. D. Jido et al., Nucl. Phys. A **671**, 471 (2000).
5. E.E. Kolomeitsev, M.F.M. Lutz, Phys. Lett. B **585**, 243 (2004).
6. D. Jido et al., Nucl. Phys. A **811**, 158 (2008).

ATTEMPTS TO SYNTHESIZE NEW SUPERHEAVY ELEMENTS

Š. Šáro, saro@fmph.uniba.sk, Faculty of Mathematics, Physics and Informatics, Comenius University Bratislava

INTRODUCTION

As the first accelerators allowed energetic projectiles to overcome the nuclear Coulomb barrier, isotopes of elements heavier than uranium were synthesized, first at Berkeley and later in few other laboratories. Up to now 25 heavy and superheavy elements were synthesized having together more than 260 isotopes [1]. Today it is generally accepted that the stability of transuranium nuclei is due to the shell structure of atomic nuclei. The first theoretical models from the 1960-ties and 1970-ties extremely overestimated the stabilizing effect of the predicted closed proton shell at Z = 114 and neutron shell at N = 184. The prediction of half-lives and production cross-sections for new heavy and superheavy nuclei later became more realistic but still can differ significantly from experimental data. In Fig. 1 the calculated stabilizing shell correction energy (given in MeV) is plotted versus neutron and proton number. The calculation made by P. Moller, J. R. Nix was published in 1988 [2]. The calculation gives a wide area of neutron numbers with a very high shell correction energy of 9 MeV around Z = 114 – 116.

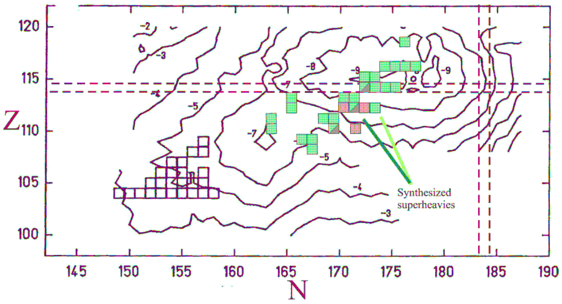

Fig. 1. Calculated shell correction energies (given in MeV) as a contour plot versus neutron and proton number [2]. The heaviest isotopes known at that time are marked with squares. The dashed lines - the position of the most proposed position of the closed proton and neutron shells at Z =114 , N = 184.

Calculation made in [3] later included more new experimental data and the shell correction energy was decreased at the supposed center of enhanced stability by about 2 MeV, from -9 MeV to -7 MeV. According to the rule of thumb the change of fission barrier by 1 MeV results in a change of cross-section by one order of magnitude, The 2 MeV drop of shell correction energy means approximately the same drop of the fission barrier. The result is a considerable decrease of the proposed stability resulting in shorter half-lives and significantly lower production cross-sections.

ATTEMPT TO SYNTHESIZE ELEMENT Z = 120

The cross-sections of cold fusion reactions, based on the double magic nucleus ^{208}Pb and neighboring ^{209}Bi fell at Z = 113 to the experimentally limiting value of 0.078 pb [10] and for Z = 114 one can expect a value about 0.01 pb or even lower. Moreover the cold fusion products lay far left from the proposed region of enhanced stability around the closed neutron shall N = 184. Using hot fusion reactions of transuranium target nuclei and double magic ^{48}Ca ions the isotopes of Z = 112, 114, 115, 116 and 118 were synthesized on cross-section levels around 0.5 – 5 pb [7].

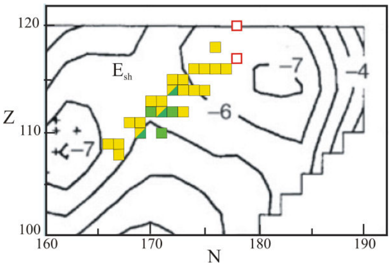

Fig. 2. Ground state shell correction energies (in MeV) calculated for the heavy and superheavy nuclei as a contour plot versus neutron and proton number [3]. Crosses - heaviest nuclei which were synthesized at the time when the plot was made. Superheavy isotopes which were synthesized later - yellow-green squares, the ongoing attempts - red squares.

All the possible combinations of transuranium nuclei with ^{48}Ca were exhausted and for new heavier elements projectiles of Z > 20 have to be used. In recent years the excitation functions of several possible target – projectile combinations were calculated for element Z = 120 [5]. The highest cross-section $\sigma(4n)_{calc} \approx 0.025$ pb should have the reaction of $^{54}Cr + ^{248}Cm \rightarrow ^{302}120^*$ at an excitation energy of E* = 43- 44 MeV [4].

In years 2007-08 an attempt was made at the kinematic separator SHIP (GSI Darmstadt) to synthesize a new element of Z = 120 using the hot fusion reaction $^{64}Ni + ^{238}U \rightarrow ^{302}120^*$. The aim of the experiment was to test the real value of the shell correction energy E_{sh} in this region, where different theoretical calculations presents broad range of E_{sh}. According to some calculations at Z = 120 a proton subshell should be closed leading to an enhanced stability. The metallic uranium target was irradiated 116 days with ^{64}Ni ions, the full dose was 2.11 x 10^{19} ions. Three excitation energies were used with an average value of 36.4 MeV. No true event was observed at the cross-section limit of $\sigma < 0.09$ pb [5] therefore very high shell-correction energy at Z = 120 can be excluded. Another possible reason of the nonobservation of ^{298}120 or ^{299}120 may be their very short half-life. Calculated alpha-decay half lives of these isotopes are close to the experimentally measurable limit (about 1 μs), namely 1.6 μs or 2.9 μs for ^{298}120 and 9.8 μs or 15 μs for ^{299}120. The calculated fission half-lives have millisecond values [6]. In Fig. 3 the measured cross-sections of hot fusion reactions used to synthesize isotopes of elements of Z = 112 – 120 and calculated cross-sections of three hot fusion reactions leading to the same isotope of element Z = 120 are presented. One can see a considerable drop in cross-section for Z = 120 compared to Z <= 118 also for the reaction ^{58}Fe + ^{244}Pu realized at Dubna.

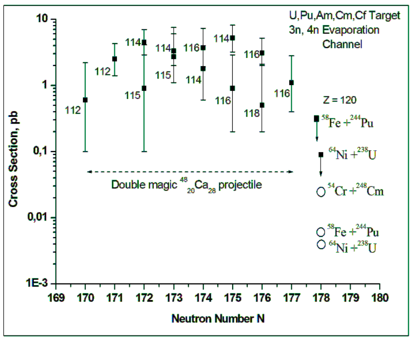

Fig. 3. Measured cross-sections of hot fusion reactions used to synthesize isotopes of elements of Z = 112 – 120 (squares), calculated cross-sections of three hot fusion reactions leading to the same isotope of element Z = 120 (hollow circles).

At present another attempt to synthesize element of Z= 120 at SHIP based on ^{248}Cm target nucleus is in preparation [8]. ^{248}Cm is one of the heaviest and most neutron reach available target nuclei. Its neutron number N = 152 has an increased shell effect. According to the latest calculations [4] the highest cross-section is proposed for the reaction of ^{54}Cr + ^{248}Cm → $^{302}120^*$: $\sigma(3n)_{calc} \approx$ 0.015 pb and $\sigma(4n)_{calc} \approx$ 0.025 pb. Because of the very low cross-section, several preparatory experiments will be made in front of the main experiment. At first the whole experimental set-up will be tested using the test experiment of ^{22}Ne + ^{248}Cm → ^{265}Sg + 5n at a known cross-section of 240 pb. As the second step the excitation function of ^{48}Ca + ^{248}Cm → ^{292}116 + 4n will be investigated. This reaction was investigated already [7] but only 2 energy positions for the 4n evaporation channel and 3 energy positions for the 3n evaporation channel were measured as it is shown in Fig. 4. The maximum of the excitation functions were not determined. More experimental points on the excitation function is necessary to determine the maximum of the cross-section and for the extrapolation of the optimum beam energy which should be used at the synthesis of the compound nucleus $^{302}120^*$. From the technical point of view considerable increase of the beam intensity on the target and increased transport efficiency of SHIP will be necessary to have a real probability to synthesize an atom of element 120.

ATTEMPT TO SYNTHESIZE ELEMENTS OF Z = 117 AND 119

According to the latest calculations made by V. Zagrebaev and W. Greiner [4] the still “missing” element of Z=117 can be synthesized at relatively high cross-section in the fusion reaction of ^{48}Ca + ^{249}Bk → $^{297}117^*$. The calculated maximum evaporation cross-sections is about 2.5 pb at beam energy $E_{c.m.}$= 212 MeV for the 3n evaporation channel and about 2.4 pb at beam energy $E_{c.m.}$= 214 MeV for the 4n evaporation channel. The successive decay nuclei are assumed to have relatively long half-lives which should help at the identification of the mother nucleus and also to investigate its chemical properties. Calculated T_α systematic for even–even nuclei for the elements of Z = 100 – 124 [9] allows to suppose that also the odd-even nucleus ^{276}117 should have a half-life above the experimental minimum (about 1 μs).

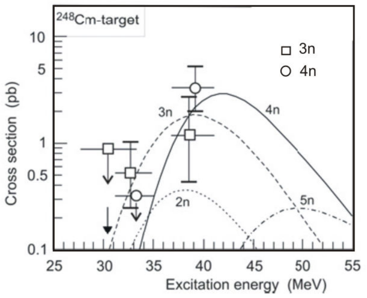

Fig. 4. Production cross sections of nuclei of Z = 116 produced in the reaction of ^{48}Ca + ^{248}Cm → $^{296}116^*$ at different excitation energies of the compound nucleus. Lines are the calculated excitation functions of the *xn*-evaporation channels. Black arrow shows the excitation energy of the compound nucleus ^{296}116 at the Coulomb barrier (B_{Bass}) [7].

At this time an experiment to synthesize element 117 is going at JINR Dubna on the gas-filled separator DGFRS, where the hot fusion reactions synthesizing elements of Z = 112, 114, 115, 116 and 118 were realized. If the synthesis of element 117 will be successful, there is the possibility to try to synthesize element 119 using the same target and ^{50}Ti ions in the reaction of ^{50}Ti + ^{249}Bk → $^{299}119^*$.

CONCLUSION

The structure and properties of the heaviest atomic nuclei are poorly understood. Their stability is based on shell structure, but the quantitative determination of the strength of this effect is unsatisfactory. To help the theory to present more reliable predictions of shell stabilizing effects more experimental data are needed, especially at higher proton and neutron numbers. The ongoing and planed experiments can give very important new data to improve our knowledge on this problem.

REFERENCES

1. J. Magil, G. Pfennig, J. Galy, Chart of the nuclides, 7th edition, (2006).
2. P. Moller, J. R. Nix, At. Data, Nucl. Data Tables **39,** 213 (1988).
3. A. Sobiczewski, K. Pomorski, Progr. Part. and Nucl. Phys., **58**, 292 (2007).
4. V. Zagrebaev, W. Greiner, Phys. Rev. C **78**, 034610 (2008).
5. S. Hofmann et al., GSI Scientific Report 2008, GSI Report 2009-1.
6. A. Sobiczewski and S. Hofmann. GSI Scientific Report 2007, GSI Report 2008-1.
7. Yu. Ts. Oganessian, J. Phys. G: Nucl. Part. Phys. **34**, R165 (2007).
8. S. Hofmann et al., unpublished, January 2009.
9. R. Smolanczuk, J. Skalski, A. Sobiczewski, Proc. Int. Workshop, Hirschegg (Austria) (1996).
10. K. Morita et al., J. Phys. Soc. Jap. 73, 2593 (2004).

NUCLEAR ISOMERS IN HEAVIEST NUCLEI

S. Antalic, Stanislav.Antalic@fmph.uniba.sk, Comenius University, 84248 Bratislava

INTRODUCTION

Around forty years ago was suggested that the 'island of stability in the sea of instability' should exists around the next double magic nucleus $^{298}114$ [1, 2]. The attempt to prove the idea for an existence of these so called 'superheavy elements' is one of the most exciting challenges in nuclear physics in last several decades. However even after many successful experiments with a production of new elements the real localisation of the next double magic nucleus and the structure of these nuclei is still opened question.

Two main methods were used for the production of new - superheavy - elements. Using the compound fusion reactions of medium mass projectiles with the lead and bismuth target nuclei were synthesized the elements up to proton numbers 112 and 113 [3, 4]. On the other hand the reactions between lighter ions, mainly ^{48}Ca, and radioactive actinide targets were employed and successfully used for the production of the elements up to $Z = 118$ [5].

Unfortunately, to obtain any information about the structure of heaviest nuclei is extremely difficult due to extremely low reaction cross-section. This is typically in the order of few picobarn or even bellow and leads to the synthesis of only very few nuclei per week. On the other hand recent developments of experimental techniques opened a door for detailed gamma spectroscopy studies in the region of trans-fermium nuclei.

Generally, two methods are applied in the nuclear structure studies. Firstly, in beam measurements using the recoil decay tagging method. In this kind of measurement γ transitions and conversion electrons (CE) are studied at the target position triggered by the implantation signal of the recoil or/and its α decay separated from the projectile beam and identified at the focal plane of separator.

Secondly, the studies of nuclear decay using the detector system at the focal plane position when α decays and conversion electrons are detected by the position sensitive silicon detector and γ transitions are registered by germanium clover detectors.

K ISOMERS

Nuclear isomers represent rich source of information about the nuclei with a very low production yield. The lifetimes above the few microseconds give us a possibility to separate such an excited nucleus after its synthesis from the primary beam and transport it into a dedicated detector system. Afterwards we could investigate either the radioactive decay of such an excited meta-stable state or its de-excitation into lower lying excited states. In this way we could localise excited states which are only very weakly populated in almost backgroundless conditions.

One of the most interesting cases is the possibility to study K-isomers in the heaviest nuclei. K-isomers are a special kind of spin-traps whose existence depends not only on the spin value but also on its orientation. Experiments aimed to investigate such phenomena provide important information on the nuclear structure of the heaviest elements and are stringent tests for the quality of nuclear models. One can obtain e.g. information on the nucleon pairing, single particle levels, or one can study properties of levels and collective excitations not observable in in-beam measurements.

For heavy and superheavy nuclei it is of special interest with the respect to the different lifetime expected for the ground-state and isomeric state of the nucleus. In some certain cases when the lifetime of the isomeric state exceeds the lifetime of the ground-state this might be important stabilization effect in the process of the superheavy element production. Such a possibility for enhancement of the stability of heavy and superheavy nuclei due to high-spin isomerism is supported also by the theory [8]. In fact two cases are known already in transfermium region. This is the case ^{270}Ds where the ground-state has a half-life of $100\,\mu$s and isomeric state around 6 ms [6]. Similar case is also the isotope ^{250}No, with the reported half-life of $43\,\mu$s for the isomeric state and $3.7\,\mu$s for the ground-state [7].

As already a classical example for the K isomer in the trans-fermium region might be considered the isotope ^{254}No where two high-K isomers were observed [9, 10]. The first isomer at the excitation energy of 1293 keV with the half-life of 266 ms and $K^{\pi} = 8^{-}$ was assigned as a two-quasi-proton state $9/2^{+}[624]_{\pi} \times 7/2^{-}[514]_{\pi}$. The second isomer with the half-life of $(198 \pm 14)\,\mu$s is assigned as a four-quasi-particle state with $K \geq 18$ and the excitation energy above 2.9 MeV [11].

In the fusion-evaporation reaction of ^{206}Pb(^{48}Ca,2n)^{252}No at SHIP separator in GSI Darmstadt a K isomer with the half-life of (110 ± 10) ms at an excitation energy of 1254 keV in the neighbouring even-even nucleus - ^{252}No - has been identified as well and assigned as the two-quasi-neutron configuration $K^{\pi} = 8^{-}$ [13].

K isomeric multi-quasi-particle states were recently observed also in odd-even nuclei in the trans-fermium region. First observed cases are the isotopes ^{253}No and ^{255}Lr [14].

DECAY OF ^{255}Lr

Besides the know single-particle isomeric state assigned to $7/2^{-}[514]$ Nilsson level, a second isomeric state decaying by γ emission was identified recently [14, 16]. According to measurement at VASSILISSA separator a half-life of (1.4 ± 0.1) ms was obtained, and from coincidences between CEs and γ rays a lower limit of the excitation energy of 720 keV was estimated [16].

In experiment at SHIP the decay properties of this isomer were measured in more detail in the reaction of ^{209}Pb(^{48}Ca,2n)^{255}Lr. In order to search for decay

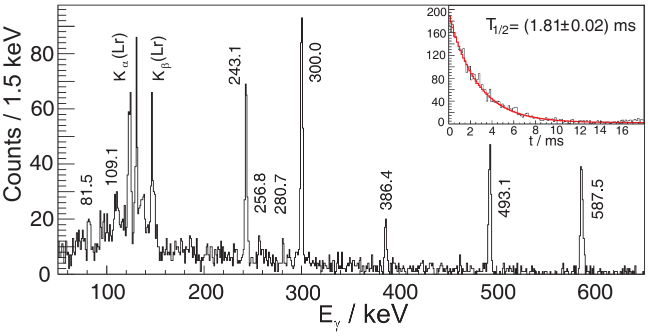

Fig. 1. Energy spectrum of γ transitions detected in coincidence with conversion electrons within a time interval 20 ms after implantation of ERs. The inset shows the time distribution of the registered CE-γ coincidences following ER implantations. Energy values are given in keV.

channels in addition to an α emission a use of CEs was made usually accompanying a cascade of electromagnetic transitions. In this case the advantage offered by the method of position and time correlation was used by searching for correlations between implanted ERs, identified by their characteristic energy and time-of-flight values, and subsequently emitted CEs, also measured with the position sensitive silicon strip detector. γ rays emitted promptly with the electrons were measured with the germanium detectors.

Energy spectrum of γ transitions detected in coincidence with conversion electrons within a time interval 20 ms after implantation of ERs is shown in fig. 1. The inset shows the decay time of the CE-γ coincidences following ER implantations. A half-life of the isomer of (1.81 ± 0.02) ms was determined, which is slightly longer than the value given in [16]. The estimated lower limit for the excitation energy of this K isomer is 1.6 MeV. Due to the un-observation of the α decay it is possible consider the lower limit for the spin of the isomer to be 21/2. However the uncertainty related with configuration hindrance of the α decay from the K isomeric state does not allow to make any final conclusion [14].

DECAY OF ^{253}No

In search of γ transitions delayed by $\approx 100\,\mu$s after ER implantations we observed a γ line of 167 keV having a half-life of $(23 \pm 3)\,\mu$s which we assigned to $5/2^+[633] \rightarrow 9/2^-$ [734] transition. This result was confirmed in the measurement with indirect production of ^{253}No via the α decay of ^{257}Rf [17]. Based on this result we located the $5/2^+[622]$ level at the excitation energy of 167 keV thus extending the systematics in N = 151 isotones up to Z = 102.

Furthermore we observed a second isomeric state in ^{253}No using the previously mentioned experimental technique of CE - γ coincidences. The lower limits for the the angular momentum and the excitation energy of this multi-quasi-particle isomeric state were tentatively evaluated to be $21/2\,\hbar$ and 1.6 MeV, respectively. The unique result obtained in this measurement is the observation of a rotational band populated in the de-excitation of the multi-quasi-particle isomer. The analysis shows small differences between the gamma transitions of the band populated by decay of the observed multi-quasi-particle isomer and the band observed in previous in-beam studies [18].

CONCLUSIONS

Besides the direct production of superheavy elements nuclear spectroscopy is a very important tool to investigate the nuclear structure of heaviest elements. Detailed spectroscopy measurements indicate a new island of isomerism in the neutron deficient region around N = 152, Z = 100. For the first time in the region of heaviest nuclei multi-quasi-particle isomeric states were studied also in odd-even nuclei. To obtain new information more detailed experiments with a significantly improved detection system have to be performed.

ACKNOWLEDGMENT: Experiments were performed in collaboration with S. Hofmann, F.P. Heßberger, D. Ackermann, B. Kindler, B. Lömmel, R. Mann, B. Sulignano (GSI, Darmstadt), Š. Šáro, B. Streicher, M. Venhart (Comenius University, Bratislava), K. Nishio (JAEA, Tokai) and M. Leino (University of Jyväskylä). This work was supported by the Slovak Research and Development Agency under the contract No. APVV-20-006205, VEGA (Project No. 1/4018/07) and by EURONS (EUROpean Nuclear Structure - Transnational Access to GSI, Contract N.RII3-CT-2004-506065).

REFERENCES

1. V.M. Strutinsky, Nucl. Phys. A **95**, 420 (1967).
2. V.M. Strutinsky, Nucl. Phys. A **122**, 182 (1968).
3. S. Hofmann *et al.*, Eur. Phys. J. A **14**, 147 (2002).
4. Morita K. Et al. Journ. Phys. Soc. Japan **73**, 2593 (2004).
5. Yu. Ts. Oganessian, J. Phys. G: Nucl. Part. Phys. **34**, R165 (2007).
6. S. Hofmann *et al.*, Eur. Phys. J. A 10, **5** (2001).
7. D. Peterson *et al.*, Phys. Rev. C **78**, 014316 (2006).
8. F.R. Xu *et al.*, Phys. Rev. Lett **92**, 252501 (2004).
9. R.-D. Herzberg *et al.*, Nature **442**, 896 (2006).
10. R.-D. Herzberg *et al.* Phys. Scr. T125, 73 (2006).
11. F.P. Heßberger *et al.*, submitted to EPJ (2009).
12. P.T. Greenlees *et al.* Phys. Rev. C **78**, 021303 (2008).
13. B. Sulignano *et al.*, Eur. Phys. J. A **33**, 327 (2007).
14. S. Antalic *et al.*, Eur. Phys. J. A **38**, 219 (2008).
15. A. Chatillon *et al.*, Eur. Phys. J. A **30**, 397 (2006).
16. K. Hauschild *et al.*, Phys. Rev C **78**, 021302 (2008).
17. B. Streicher, Ph.D. thesis, Comenius University Bratislava (2006).
18. R.D. Herzberg and P.T. Greenlees, Prog. Part. Nucl. Phys. 61, 674 (2008).

CENTRAL COLLISIONS OF RELATIVISTIC NUCLEI IN EMULSION TRACK DETECTOR

J. Vrláková, janka.vrlakova@upjs.sk and S. Vokál, stanislav.vokal@upjs.sk , P. J. Šafárik University, Košice, Slovakia

INTRODUCTION

Non-statistical fluctuations of produced relativistic particles have been studied using the method of scaled factorial moments. Such fluctuations may be use to signal the formation of a quark gluon plasma in the early stage of heavy ion interactions at high energies [1]. The experimental data of ^{208}Pb nuclei at 158 A GeV/c taken with emulsion track detector have been analysed. The results have been compared with values obtained from the other experimental data.

EXPERIMENT

The emulsion detector was irradiated horizontally by ^{208}Pb nuclei at 158 A GeV/c (experiment EMU12/CERN SPS). Experimental details can be found in [2]. The interaction of ^{208}Pb nucleus in emulsion track detector is shown in Fig. 1.

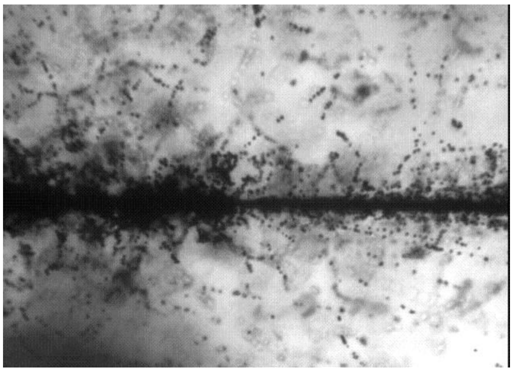

Fig. 1: The interaction of ^{208}Pb+Em at 158 A GeV/c.

In the measured interactions all charged particles were classified according to the commonly accepted emulsion experiment terminology into groups. The group of relativistic (shower) particles includes particles (with β > 0.7) produced in the interactions as well as those knocked-out from the target nucleus. The polar (Θ) and azimuthal (Ψ) emission angles of all tracks have been measured. The value of pseudorapidity

$$\eta = -\ln\left[\tan\frac{\Theta}{2}\right] \tag{1}$$

has been calculated for each relativistic particle.

ANALYSIS AND RESULTS

In this paper we present some results of the analysis of the particle fluctuations in pseudorapidity scale. A. Bialas and R. Peschanski suggested to study the dependence of factorial moment F_q, where q is the order of the moment, as a function of the bin width $\delta\eta$ [3, 4]. The intermittent behaviour should lead to a power law dependence $F_q \propto (\Delta\eta/\delta\eta)^{\varphi_q}$, φ_q > 0, $\Delta\eta$ is the pseudorapidity interval of produced relativistic particles.

The horizontal factorial moment method has been used for our analysis. Detailed description of this method can be found in [5]. The horizontal factorial moment $F_e(q)$ characterizing *eth* event is defined as

$$F_e(q) = M^{q-1}\sum_{m=1}^{M}\frac{F(n_{me};q)}{[N_e]^q} , \tag{2}$$

M is number of equal bins of size $\delta\eta$ into which the pseudorapidity interval $\Delta\eta$ has been divided, n_{me} is the number of relativistic particles in the *mth* bin, N_e is total number of relativistic particles of event. The factorial moment is given as

$$F(n_{me};q) = n_{me}(n_{me}-1)...(n_{me}-q+1) . \tag{3}$$

Vertical averaging of $F_e(q)$ gives the full form

$$F(q) = \frac{1}{E}\sum_{e=1}^{E}F_e(q) . \tag{4}$$

From the total number of 628 measured interactions of ^{208} Pb in emulsion, 64 central events with number of relativistic particles $n_s > 350$ have been selected.

The $\ln <F_q>$ dependences on $\ln M$ have been obtained by horizontal factorial moment method and some results of the analysis have been published in our previous work [6].

In our present analysis the dependences of parameters α_q and φ_q ($\ln <F_q> = \alpha_q + \varphi_q . \ln M$) on the order of factorial moments q have been studied for $\Delta\eta=0\text{-}7.4$, $M=7\text{-}74$. In Fig.2 the increasing dependences of values of slopes (φ_q) on q for two groups ($n_s > 350$, $n_s > 1000$) of Pb induced interactions in emulsion are shown. These dependences ($\varphi_q > 0$) show an evidence for the presence of intermittent behaviour or non-statistical fluctuations, the steepest dependence was observed for interactions with $n_s > 1000$.

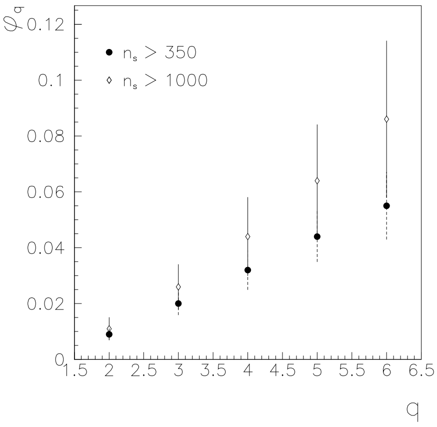

Fig.2: The φ_q dependences on q (q=2-6) for Pb +Em interactions with $n_s > 350$ and $n_s > 1000$, $\Delta\eta=0\text{-}7.4$, $M=7\text{-}74$.

The dependence of intercept parameter α_q on q for central Pb interactions is shown in Fig. 3 for $q=2\text{-}6$.

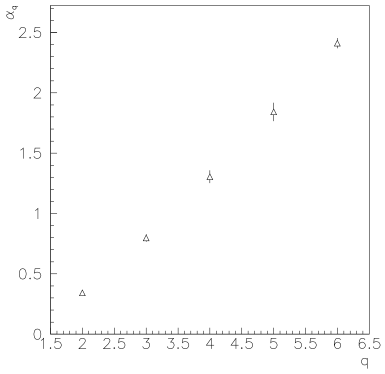

Fig.3: The α_q dependence on q (q=2-6) for Pb+Em interactions with $n_s>1000$, $\Delta\eta=0\text{-}7.4$, $M=7\text{-}74$.

For next comparison we used different experimental data obtained by the same standard emulsion method. The characteristics of used data – beam nucleus, momentum (p), bin size ($\delta\eta$) of relativistic particles and number of bins (M) are given in Tab. 1.

TAB.1. Experimental data

Beam nucleus	^{16}O	^{16}O	^{197}Au	^{208}Pb
p[A GeV/c]	60	200	11.6	158
M	6-64	8-76	4-25	7-74
$\delta\eta$	1.07-0.1	0.95-0.1	1.25-0.2	1.057-0.1

In Fig. 4 the dependences of slope (φ_q) on q for Pb+Em (events with $n_s>350$) and Au+Em ($n_s>100$) central interactions are shown. The similar dependences for Pb+Em data were published in [7].

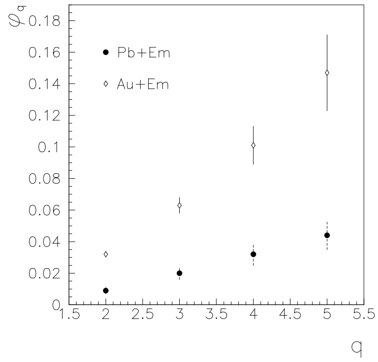

Fig.4: The φ_q dependences on q ($q=2\text{-}5$) for Pb+Em and Au+Em interactions.

The dependences of intermittency parameter (λ_q) on the order of factorial moment q for different primary nuclei have been studied. The intermittency parameter is defined as

$$\lambda_q = \frac{\varphi_q + 1}{q} \tag{5}$$

If the function λ_q on q has a minimum at a certain $q=q_c$, there would be possibility of observing a non-thermal phase transition [8, 9]. In Fig. 5 the λ_q dependences on the order of factorial moment q for different experimental data samples (see Tab. 1) are presented, but no minimum has been found. There are some hints for existence of minima at $q_c=4\text{-}5$ in [9, 10].

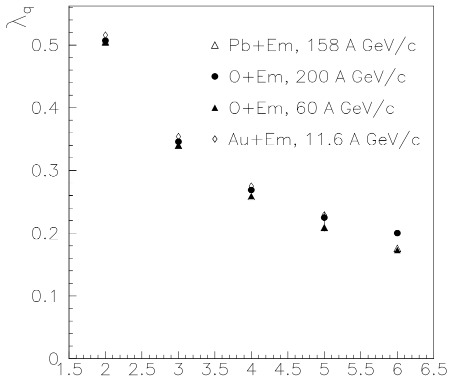

Fig.5: The dependences of intermittency parameter (λ_q) on q ($q=2\text{-}6$) for different primary nuclei.

CONCLUSIONS

Central interactions of ^{208}Pb nuclei at 158 A GeV/c taken with emulsion track detector have been analysed using the horizontal factorial moment method. An evidence for the presence of intermittent behaviour has been shown. The comparison for different primary nuclei (^{16}O, ^{197}Au) at momenta of 11.6 – 200 A GeV/c has been done. The dependences of intermittency parameter λ_q on q for different primary nuclei have been studied, but no clear minimum has been found.

ACKNOWLEDGMENT: Financial support from the Scientific Agency of the Ministry of Education of Slovak Republic and the Slovak Academy of Sciences (Grant No. 1/0080/08) is cordially acknowledged.

REFERENCES

1. M. Jacob, In Search of Quark Gluon Plasma, Springer Verlag (1985)
2. M. I. Adamovich et al., Proc. of XVII Meeting of the EMU01 col. on perspectives of the emulsion techniques in the exp. at the Nucleotron relativistic nuclear beams, May 18-20, 1999, Dubna, Russia, Eds.: V. Bradnova, N. V. Prozorova, JINR, Dubna, 2000, p.143.
3. A. Bialas, R. Peschanski, Nucl. Phys. B 273 (1986) 703.
4. A. Bialas, R. Peschanski, Nucl. Phys. B308 (1988) 857.
5. M. Blažek, Int. J. of Mod. Phys.A12 (1997) 839.
6. J. Vrláková et al., Acta Physica Slovaca 56 (2006) 83.
7. B. Wosiek, Acta Physica Slovaca 46(1996)531.
8. A. Bialas, K. Zalewski, Phys. Lett. B238 (1990) 413.
9. D. Ghosh et al., Europhys. Lett. 41 (1998) 371.
10. E. K. Sarkisyan et al., Phys. Lett. B347 (1995) 439.

LEPTON FLAVOUR VIOLATION IN MSSM

D. Plašienka, dusan.plasienka@gmail.com, T. Blažek, blazek.111@gmail.com, Department of Theoretical Physics, Faculty of Mathematics, Physics and Informatics, Mlynská dolina 842 48, Comenius University Bratislava

MSSM

Current theory of elementary particles and their interactions is known as the Standard model (SM) and it is a theory in remarkable consistency with experiments (up to 100 GeV). Despite this fact, there are theoretical motivations to study theories beyond SM. Among them, the most studied theories are those with so called supersymmetry (susy), especially the Minimal Supersymmetric Standard Model (MSSM). The motivations for susy include natural solution of the Higgs mass stability compared to the Planck scale (the hierarchy problem in the SM), unification of the running gauge couplings at high energy (10^{16} GeV) or giving us a good candidate for the universe dark matter.

The MSSM Lagrangian brings in new particles that more than double the SM particle spectrum and also many more new interactions, but no new dimensionless couplings. All of the new particles (with one exception in the Higgs sector) are partners to the SM particles and are called superpartners. To make the MSSM phenomenologically acceptable, we have to add new terms into the MSSM Lagrangian that violate supersymmetry. This is because in an exactly supersymmetric Lagrangian we obtain susy particles with the same masses as their SM partners. As far as we have not observed these particles yet, we have to assume their masses to be large and therefore add susy breaking terms into the MSSM Lagrangian. These breaking terms contain many free parameters - from over one hundred in the most general model down to less than ten in the most constrained MSSM (CMSSM). Experimental limits from non-observation flavour changing neutral currents processes are then good tools for constraining these free parameters.

LEPTON FLAVOUR VIOLATION

Lepton flavour violation (LFV) is a phenomenon in which we observe nonconservation of L_e, $L)\mu$ or L_τ. For charged leptons, such process has not been observed yet. In the SM, the individual lepton number is "accidentally" conserved. However, in the massive neutrinos extension of the SM, the LFV is premitted, but very rare. In our discussion, we will take two examples of LFV processes - $\tau \to \mu\gamma$ and $\mu - e$ conversion in nuclei.

Process $\tau \to \mu\gamma$ is permitted in the massive neutrinos extention of SM, but due to $(m_\nu/m_W)^4 \approx 10^{-40}$ dependence in the decay rate, the $\tau \to \mu\gamma$ decay channel is far beyond experimental limits (also to the far future). In case of MSSM, the situation is different. $\tau \to \mu\gamma$ process may occur via 6 types of 1-loop Feynman diagrams (Figure 1) with susy particles in loops.

After computations, the MSSM interaction Lagrangian needed for this process can be expressed in the language of the effective interaction Lagrangian

$$\mathcal{L}_{eff}^{\tau\to\mu\gamma} = \tau A^\mu e[m_\tau \sigma_{\mu\nu} q^\nu (A_L P_L + A_R P_R)]\mu$$

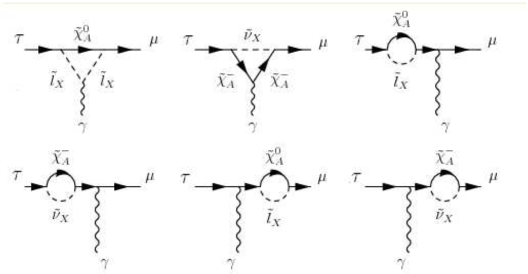

Fig. 1. Susy particles are labeled with tilda on this figure. All of the diagrams are in fact many diagrams as far as the susy particles should hold an index.

where we have computed the one particle irreducible amplitides A's

$$A_L =$$
$$\frac{i}{16\pi^2 m_{\tilde{l}}^2}\left(F_2(X)ad + \frac{m_\mu}{m_\tau}F_2(X)bc + \frac{m_{\tilde{\chi}^0}}{m_\tau}F_4(X)ac\right) -$$
$$\frac{i}{16\pi^2 m_{\tilde{\nu}}^2}\left(F_1(Y)np + \frac{m_\mu}{m_\tau}F_1(Y)mo + \frac{m_{\tilde{\chi}^\pm}}{m_\tau}F_3(Y)no\right),$$
$$A_R =$$
$$\frac{i}{16\pi^2 m_{\tilde{l}}^2}\left(F_2(X)bc + \frac{m_\mu}{m_\tau}F_2(X)ad + \frac{m_{\tilde{\chi}^0}}{m_\tau}F_4(X)bd\right) -$$
$$\frac{i}{16\pi^2 m_{\tilde{\nu}}^2}\left(F_1(Y)mo + \frac{m_\mu}{m_\tau}F_2(Y)np + \frac{m_{\tilde{\chi}^\pm}}{m_\tau}F_3(Y)mp\right).$$

In these relations, we didn't write summation over indices that should be on susy particle masses $m_{\tilde{l}}^2$ and $m_{\tilde{\nu}}^2$ and symbols $a - d$'s, $m - p$'s as well as X and Y, that all are still complicated functions of free susy parameters. Details can be found in [1] (in Slovak).

To obtain numerical results, we used one reference point in susy parameter space in the susy breaking model inspired by the Grand Unification Theory [2]. After taking these specific values of susy particle masses and mixing angles, we have made numerical analysis of matrix diagonalization (using Mathematica) and calculating the decay rate (in C++). Finally, we have obtained the result for BR($\tau \to \mu\gamma$)= 8.163x10^{-7} that is approximately one order above present experimental limit - BR($\tau \to \mu\gamma$)< 4.5x10^{-8} [3].

Thus, we have excluded this special reference point and presently we are testing other points in the model. Promising fact is that the process calculated in the MSSM gives us results approximately of the same order as the experimental limit. Whole procedure could be repeated to $\mu \to e\gamma$ process as far as the scheme is the same.

$\mu - e$ conversion in nuclei is another example of a promising process for the MSSM. It is a process $|\mu, N> \to |e>|N>$ in which muonic atom "decays" (splits) into the sharp-energy electron and ionized atom. This process can occur in MSSM via 4 types of (types of) Feynman diagrams (Figure 2) including photon, Z boson and Higgs transition, as well as the box diagrams.

The MSSM interaction Lagrangian allowing this process can be expressed as the effective Lagrangian

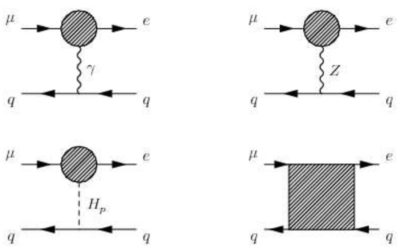

Fig. 2. First "diagram" with photon transition in fact contains sum of all diagrams from Figure 1

$$\mathcal{L}_{eff}^{\mu-e\ con} = -\frac{G_F}{\sqrt{2}}\sum_q\{[g_{LS(q)}\bar{e}_L\mu_R + g_{RS(q)}\bar{e}_R\mu_L]\bar{q}q+ \\ [g_{LV(q)}\bar{e}_L\gamma^\mu\mu_L + g_{RV(q)}\bar{e}_R\gamma^\mu\mu_R]\bar{q}\gamma_\mu q\}$$

that contains effective 4-fermionic interactions, where couplings g's are complicated functions of the free MSSM parameters and the known constants from SM [4].

The $\mu - e$ conversion is a non-trivial process in sense of the QFT because it includes initial and final states that are not typical sharp-momenta (multiparticle) states and so we cannot use standard techniques of Feynman rules to obtain the probability for it. In this case, we have the initial muon in the $1s$ bound state over nucleus and the outgoing electron is the sharp-energy continuous state in the electrostatic field of the nucleus. To obtain the conversion rate ω (1 over mean time of this event) of this process from any Lagrangian, most authors use relation introudces by Weinberg and Feinberg [5]. More precise and physically acceptable methods to deal with this problem were developed by Czarnecki [6] and further calculated by Kitano, Koike and Okada [7].

Their idea is following. For $1s$ bound muon state (and analogically for the electron state) we define creation and annihilation operators and their anticommutation relations

$$|1s>= a^\dagger_{n=1,\ j=1/2,\ \mu=\pm 1/2,\ k=-1}|0> \\ \{a_{nj\mu k}, a^\dagger_{n'j'\mu'k'}\} = \delta_{n,n'}\delta_{j,j'}\delta_{\mu,\mu'}\delta_{k,k'}$$

and then we assume that the muon field can be written (and secondary quantized) as

$$\mu = \sum_{nj\mu k}\psi^\mu_{nj\mu k}\,a_{nj\mu k}\ +\ (anti-particle\ part)$$

where n, j, μ and k are proper quantum numbers.

The muon and electron bispinor fields in the interaction Lagrangian will also change. Now, they won't be (superpositions of) solutions of the free Dirac equation, but of the Dirac equation with Coulomb potencial ϕ

$$(\gamma^\mu D_\mu + m)\psi = 0;\ D_\mu = \partial_\mu + ieA_\mu$$

written in non-standard but in this field still used conventions. In above equation $\psi \equiv \psi^\mu_{nj\mu k}$. This Dirac equation with Coulomb potencial ($\vec{A} = 0$, $\phi = Ze/r$) is completely equivalent to the equation

$$i\partial_t\psi = H\psi \\ H = \vec{\alpha}.\vec{p} + \beta m - e\phi;\ \phi = Ze/r$$

that is in fact Schrdinger equation for 4-componental ψ and 4x4 matrix Hamiltonian H. More details about theoretical background of these equations (and relativistic QM point of view) and conventions could be found in [8].

After this, we will finally use ordinary non-relativistic QM to compute ψ's. In case of muon and also electron, we will solve the system of equations [8]

$$H\psi = E_n\psi;\ J^2\psi = j(j+1)\psi \\ J_z\psi = \mu\psi;\ K\psi = -k\psi;\ K = (\vec{\sigma}.\vec{l} + 1)\beta$$

to determine (superpositions of) the eigenfunctions $\psi^{\mu,\ e}_{indices}$ for bound states of μ and continuous states for e. Superpositions of these eigenfunctions will then occur in the interaction Lagrangian. We do not have to find the complete sets of the eigenfunctions as far as we need just one wave function for the muon (the $1s$ state) and one for the electron (state with total relativistic energy $E_e = m_\mu - E^{bound}_{1s}$). This is due to the fact, that certain creation and annihilation operators will meet leaving just one wave function relevant. Even in this case, it is still a non-trivial mathematical task including substitutions, looking for solutions in power series, reccurence relations and hypergeometric functions and it is most often solved numerically [7].

Final formula for $\mu - e$ conversion could be found in [7]. Our numerical results for this process are in progress.

REFERENCES

1. D. Plašienka, Narušenie leptónového čísla v MSSM (2008).
2. T. Blazek and S.F. King, Phys. Lett. B, Muon anomalous magnetic moment and $\tau \to \mu\gamma$ in a realistic string-inspired model of neutrino masses, Physics Letters B (2001).
3. Particle Physics Booklet (2008).
4. E. Arganda, M. J. Herrero and A. M. Teixeira, arXiv:hep-ph/0707.2955v2.
5. S. Weinberg and G. Feinberg, Phys. Rev. Lett. 3 (1959) 111.
6. A. Czarnecki, W. J. Marciano and K. Melnikov, arXiv:hep-ph/9801218
7. R. Kitano, M. Koike, Y. Okada, arXiv:hep-ph/0203110
8. M. E. Rose, Relativistic Electron Theory (John Wiley, New York, 1961)

EXPERIMENTAL SEARCH FOR NEUTRINOLESS DOUBLE ELECTRON CAPTURE PROCESS OF ^{74}Se

Ivan Sýkora[1], sykora@fmph.uniba.sk, Pavel P. Povinec[1], povinec@fmph.uniba.sk, Miroslav Ješkovský[1], jeskovsky@fmph.uniba.sk, Dieter Frekers[2], frekers@gmail.com, Fedor Šimkovic[1], simkovic@fmph.uniba.sk,
[1]Department of Nuclear Physics and Biophysics, Faculty of Mathematics, Physics and Informatics, Comenius University, Bratislava, Slovakia, [2]Institut für Kernphysik, Westfälischen Wilhelms-Universität Münster, Wilhelm-Klemm Strasse 9, D-48149 Münster, Germany

INTRODUCTION

In the last decade many experiments brought important results concerning neutrino properties. The oscilations of solar, atmospheric and terrestrial neutrinos driven by a nonzero neutrino mass and neutrino mixing have been clearly confirmed. The neutrino oscillations experiments are sensitive to the squared mass differences of neutrinos and to the angles of the Pontecorvo-Maki-Nakagawa unitary mixing matrix. But, they provide no information on the absolute mass scale of neutrino masses, CP properties of neutrinos and the nature of neutrinos (Dirac or Majorana). The Majorana neutrinos are required by Grand Unified Theories (GUT) and allow processes with total lepton number violation, which are strictly forbidden within the Standard Model of electroweak interactions.

The neutrinoless double beta decay experiments look for a signal of lepton number violation. An observation of this rare process would allow to determine the Majorana nature of neutrinos, absolute neutrino mass scale and probably also to conclude about the Majorana CP violating phases.

The most frequently investigated mode of the double beta decay is a lepton number violating nuclear transition in which the charge of the nucleus is increased by two units and two electrons are emitted. Till now, other possibilities, such as double electron capture, have been less exploited. One of perspective experiments is considered a study of the neutrinoless double electron capture of ^{74}Se. A motivation for search for the ^{74}Se → ^{74}Ge (1204.2 keV) resonant transition was presented in [2].

As the atomic mass difference ΔM between ^{74}Se and ^{74}Ge is known to an accuracy of 2.3 keV (at one standard deviation), one can investigate possible resonant capture of two electrons from L shell for the transition to the 1204.2 keV level in ^{74}Ge. In 66% of cases this process will be accompanied by a cascade of two γ- quanta of 608.4 and 595.8 keV energies; in 34% of cases it will be one γ-quantum of the energy of 1204.2 keV. It has to be mentioned that the observation of these γ - quanta will provide strong evidence of neutrinoless double-electron capture because two neutrino capture is heavily suppressed (because of the extremely low transition energy) [3].

Single, and likewise double-electron capture processes leave the final daughter atom in an excited atomic state with one, resp. two inner-shell vacancies, but other-wise neutral. This inner-shell excitation has to be subtracted from the Q-value, and one may note that a capture of two K-shell electrons in ^{74}Se is not allowed for energy reasons. A double K-shell binding energy of $K^1{}_B K^2{}_B$ ~ 23 keV would have to be paid, which places the efective Q-value of the reaction below the 1204 keV excitation in ^{74}Ge near 1186 keV. For estimation this binding energy one can assume an intermediate charge of $Z = 33$ (^{74}As) for the frst capture process and $Z = 32$ (^{74}Ge) for the second. This estimate should be accurate to within a few tens of eV. Similarly, a K- and an L-shellhole places the efective Q-value at 1196.8 keV, which is about 7 keV below the nuclear level. Creating a double L-shell vacancy, however, will cost an energy of about 2.9 keV, and the efective Q-value now lies 2 keV above the 1204 keV level. This 2 keV value further coincides with the present precision, with which the mass diference is known, and one may speculate about a possible complete energy degeneracy with an atomic final state. Although such a degeneracy would present a singular opportunity, as the $0_{\nu\varepsilon\varepsilon}$ rate could now be enormously enhanced, a complete match to within a few eV would certainly be a coincidence too much to ask for.

The ECEC*(*0ν*)* transitions may be considered for three cases of electron captures [3] - 1) **-** two electrons are captured from the *L* shell. In this case, Q is equal to 1206.9 keV and three transitions are investigated, i.e. (i) to the second 2+ level of ^{74}Ge (1204.2 keV), accompanied by 595.8 keV and 608.4 keV de-excitation γ -quanta (66%), or a 1204.2 keV de-excitation γ -quantum (34%);

(ii) to the first 2+ level of ^{74}Ge (595.8 keV), accompanied by a 611.1 keV bremsstrahlung and a 595.8 keV de-excitation γ -quantum;

(iii) to the ground state of ^{74}Ge, accompanied by a 1206.9 keV bremsstrahlung γ -quantum.

2) **-** one electron is captured from the *K* shell, another from the *L* shell. In this case, Q is equal to 1197.2 keV and two transitions are investigated, i.e.

(i) to the first 2+ level of ^{74}Ge, accompanied by a 601.4 keV bremsstrahlung γ -quantum and a 595.8 keV de-excitation γ -quantum;

(ii) to the ground state of ^{74}Ge, accompanied by a 1197.2 keV bremsstrahlung γ -quantum.

3) **-** two electrons are captured from the *K* shell. In this case, Q is equal to 1185.9 keV and two transitions are investigated, i.e.

(i) to the first 2+ level of ^{74}Ge, accompanied by a 590.1 keV bremsstrahlung γ -quantum and a 595.8 keV de-excitation γ -quantum;

(ii) to the ground state of ^{74}Ge, accompanied by a 1185.9 keV bremsstrahlung γ -quantum.

EXPERIMENT

The search for the 596 keV and 608 keV γ-ray cascade in ^{74}Se was carried out using the low-radioactivity detector setup at the Department of Nuclear Physics and Biophysics of the Comenius University in Bratislava. A specially designed thin plastic container was filled with 2.5 kg of natural selenium granules. The overall density was about 1.4 g/cm^3. The natural abundance of ^{74}Se is 0.89%, which amounts to about 22 g (equiv. to 1.81x 10^{23}atoms) of ^{74}Se inside the container. For the γ-ray detection a HPGe detector and a NaI(Tl) scintillator were set up in a coincidence mode. The selenium probe was placed between the two detectors in closest geometry. The coincidence detection efficiency combines the photo-efficiency of the two detectors, the solid angle and the self-absorption of the sample.

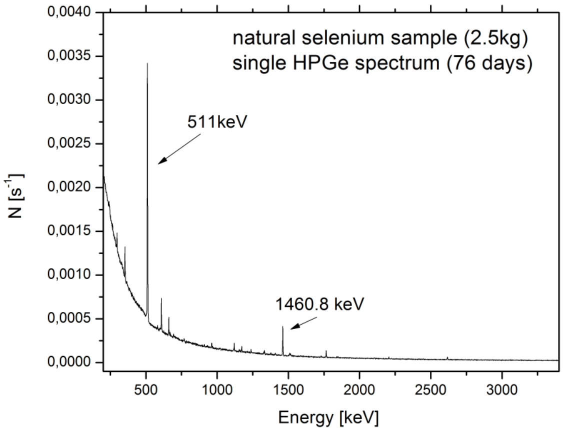

Fig.1 Single HPGe detector g-ray spectrum of the selenium sample (measured for 76 days)

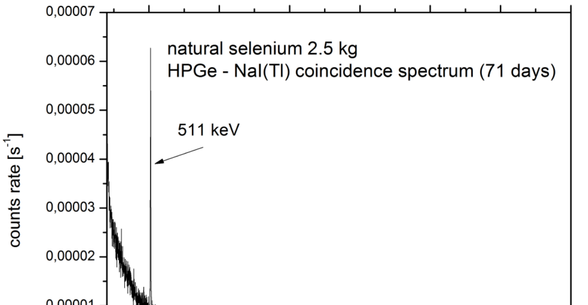

Fig.2 Coincidence HPGe-NaI(Tl) spectrum of the selenium sample (measured for 71 days)

The experiment was run over 71 days. During the coincidence measurements, also single HPGe detector γ –ray spectra were simultaneously registered. The background spectra, coincidence and single, without selenium sample were also measured during this experiment.

The single HPGe detector γ-ray spectrum is shown in Fig. 1 and the coincident spectrum is given in Fig. 2. The energy calibration was carefully performed over the entire energy region using various known γ-lines. Photon detection efficiencies were computed with the CERN Monte Carlo code GEANT 3.21 and also checked by measuring a standard of the same geometry as the sample.

RESULTS AND DISCUSSION

The present experimental result cannot not support evidence for a εε decay of ^{74}Se into the second excited state of its daughter ^{74}Ge. However, we can estimate a lower limit for the half-life on 90% confidence limit. With the data obtained from experiment, preliminary lower limit for the half-life was found to be $T_{1/2} \geq 4x10^{19}$y (90% C.L.)

This lower limit value is slightly larger than the value recently reported by Barabash *et al.* [3]

.

CONCLUSIONS

In this work we investigated double electron capture process to the second excited state of ^{74}Se by the combined method measuring coincidences between two gamma-rays and simultaneously recording single detector spectra. The coincidence method has an advantage in very good purity of the spectrum and low detection limit, but lower detection efficiency required very long counting time for obtaining sufficient counting statistics.

A follow-up experiment using larger quantities of ^{74}Se in an enriched sample is planned. However, emphasis must then be placed on the reduction of background levels, in particular on the reduction of theambient radioactivity from the radon emanation of the surrounding material as well as increasing the detection efficiency.

REFERENCES

1. Frank T. Avignone III, Steven R. Elliott, Jonathan Engel, Double beta decay, Majorana neutrinos, and neutrino mass, REVIEWS OF MODERN PHYSICS, VOLUME 80, APRIL–JUNE (2008).
2. D.Frekers, Nuclear-atomic state degeneracy in neutrinoless doble-electron capture: A unique test for a Majorana-neutrino,hep-ex/0506002v1, 1. jun 2005.
3. A.S. Barabash, Ph. Hubert, A. Nachab, V. Umatov, Search for β^+EC and ECEC processes in ^{74}Se, Nuclear Physics A 785, 371–380 (2007).

FLUCTUATIONS OF RAPIDITY DISTRIBUTIONS IN HEAVY-ION COLLISIONS

I. Melo[a], melo@fyzika.uniza.sk, B. Tomášik[b,c], tomasik@fpv.umb.sk, G. Torrieri[d], torrieri@th.physik.uni-frankfurt.de, S. Vogel[e], svogel@th.physik.uni-frankfurt.de, M. Bleicher[e], bleicher@th.physik.uni-frankfurt.de, M. Gintner[a,b], gintner@fyzika.uniza.sk and S. Koróny[b], samuel.korony@umb.sk
[a] Žilinská Univerzita, Univerzitná 1, 01026 Žilina, Slovakia
[b] Univerzita Mateja Bela, Tajovského 40, 97401 Banská Bystrica, Slovakia
[c] FJFI, České vysoké učení technické v Praze, Břehová 11, 11519 Prague, Czech Republic
[d] FIAS, Johann Wolfgang Goethe-Universität, Ruth-Moufang-Str. 1, 60438 Frankfurt, Germany
[e] Institut für Theoretische Physik, Johann Wolfgang Goethe-Universität, Max-von-Laue-Str. 1, 60438 Frankfurt, Germany

INTRODUCTION

We propose to use the Kolmogorov-Smirnov (KS) test [1, 2] to uncover non-statistical differences between events created in heavy-ion collisions within the same centrality class. These could be induced, e.g., by the fragmentation of the fireball during the phase transition from partonic to hadronic phase. Two mechanisms of the fragmentation have been suggested, each applicable in different region of the QCD phase diagram: spinodal decomposition in the first order phase transition region [3, 4] and the sudden rise of the bulk viscosity in the smooth crossover region [5].

The advantage of the KS test over other approaches which are currently in use, is that it is sensitive to any difference between the events and is not restricted to any moments of the distribution of hadrons.

THE KOLMOGOROV-SMIRNOV TEST

Let us have two events with n_1 and n_2 particles, respectively and measure the quantity x (rapidity in our case) for all particles. We ask, whether the two rapidity distributions are the same in the sense that they would correspond to the same underlying theoretical single-particle probability density, and there are no correlations between particles in one event. If so, the difference between the two events can only be due to statistical fluctuations.

To do the KS test, empirical cumulative distribution function (ECDF) for each event is constructed so that a step of the height $1/n_i$ $(i = 1, 2)$ is made on all positions of measured x's (Fig. 1). Then one takes the *maximum* vertical distance D between the two ECDFs and introduces scaled distance

$$d = \sqrt{n}D = \sqrt{\frac{n_1 n_2}{n_1 + n_2}}D. \qquad (1)$$

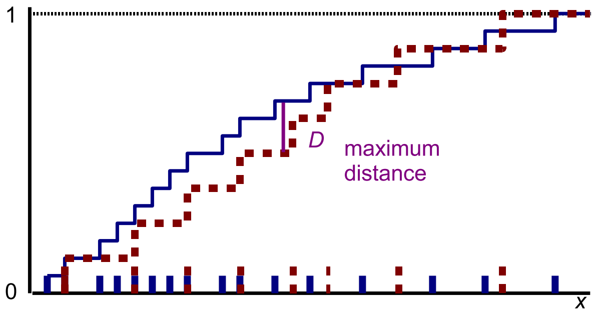

Fig. 1. Construction of the two ECDFs.

First consider a situation where all events are generated from the *same probability distribution* $\rho(x)$. We define $Q(d)$ as the fraction of event pairs with scaled distance larger than d. Theoretical calculation of this Q is presented elsewhere [6]. Note that $Q(d)$ does not depend on the shape of the underlying event distribution $\rho(x)$. It follows that the values of Q calculated for a large set of event pairs are distributed *uniformly*, provided that i) all events are generated from the *same probability distribution*; ii) within one event all particles are produced *independently* from each other. The differences (fluctuations of rapidity distributions) among events are only statistical.

Any departure from the uniform distribution of $Q's$ indicates nonstatistical differences among events. They are induced if one or both of the assumptions i), ii) are broken. For the fragmented fireball the assumption i) is broken leading to an enhanced population of low Q's (large d's). Energy and momentum conservation breaks assumption ii), which leads to a depleted population of low Q's.

To quantify the deviation from the uniform distributions of $Q's$, we introduce the parameter

$$R = \left(N_0 - \frac{N_{\text{tot}}}{B} \right) / \sqrt{\frac{N_{\text{tot}}}{B}}\,, \qquad (2)$$

where N_0 is the number of pairs in the first bin, N_{tot} is the total number of pairs, and B is the number of bins of the Q-histogram. Fireball fragmentation leads to positive R and momentum conservation to negative R.

THE FRAGMENTED FIREBALL

For testing purpose, we generate event samples with the Monte Carlo event generator DRAGON [7]. Momenta of hadrons are generated as if they were produced from a fragmented fireball. The pattern of expansion is that of the blast-wave model. Parameters of the model can be varied in order to simulate different physical situations.

Sets of 10^4 events are generated out of which we randomly choose 10^5 pairs. On them we evaluate Q and fill histograms. Recall that departure from a flat distribution indicates non-statistical differences between the events or correlations. In Fig. 2 we show the effect of fragmentation in Q-histograms. Results from a

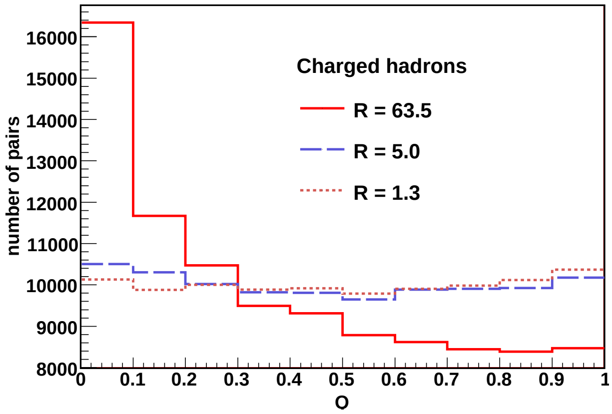

Fig. 2. Solid red lines: Q-histograms from a simulation for central Au+Au reactions at $\sqrt{s_{NN}} = 200$ GeV (RHIC) with assumed fragmentation into fragments with mean volume of 5 fm^3. Dashed blue lines: non-fragmented fireball at RHIC, dotted brown lines: non-fragmented FAIR ($E_{beam} = 30A$GeV). Rapidities of all charged hadrons are used for the KS test.

simulation with fragments are compared to two cases with direct emission of hadrons. In the histogram obtained for all charged hadrons one clearly observes that fragmentation leads to a pronounced peak at small Q. For comparison, simulations without fragments (i.e. the hadrons are emitted directly from the bulk fireball) were also studied. Naively, one would expect flat Q-histograms in these cases. However, one observes smaller peak at low Q (Fig. 2) due to correlations between hadrons from resonance decays, which actually act as small clusters. This (unwanted) correlation can be minimized by using only pions of one charge.

We have also checked that bigger droplets lead to more pronounced low-Q peak.

ENERGY AND MOMENTUM CONSERVATION

We consider energy and momentum conserving system of n stable particles and assume that all spectra are given by the phase space of this n-body system alone. We generate four-momenta of particles within their proper kinematic limits following the GENBOD algorithm [8]. Each event (n-body system) is then accepted or rejected according to its phase space weight. After we generate 10^4 events, we randomly choose 10^5 pairs of events and apply the KS test as before (Fig. 3). The multiplicity is Poisson-distributed with the mean value $n = 100$, mass of the particles $m = 0.139$ GeV/c^2 and the total energy of the system is 100 GeV. The effect four-momentum conservation is a large negative R signal (solid red line). In the next step we assume that our n particles are resonances decaying into two daughters. In this case the total four-momentum conservation effect is modified by the clustering effect (two daughters act as a cluster) which drives R to positive values and by the four-momentum conservation during the decay (negative R). The combined effect is shown as a dashed blue line. Finally, we show how the conservation effect can be removed by imposing the cut $y > 0$ on the daughters of the previous case (dotted green line).

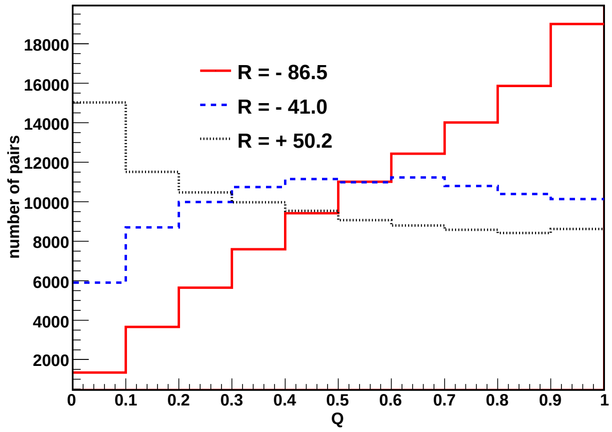

Fig. 3. Q-histograms demonstrating the 4-momentum conservation: for stable particles (solid red line), for resonances decaying into two daughters (dashed blue line), and decayed resonances with a cut $y > 0$ (dotted green line).

CONCLUSIONS

Analyzing data with the Kolmogorov-Smirnov test can provide novel insights and identify interesting effects not seen before with other methods. We showed that the fragmentation of the fireball can be clearly identified with the help of the KS technique. We also showed that the four-momentum conservation is an important effect and we offered means to separate it from the fragmentation. The influence of other processes such as fluctuations of the initial state of the fireball evolution and quantum correlations needs yet to be studied. The important message of the KS test is that it can test the usual paradigm that data from many collisions (within the same centrality class) are produced by basically identical fireballs.

ACKNOWLEDGMENT: This work was supported by VEGA 1/4012/07 (Slovakia), MSM 6840770039, LC 07048 (Czech Republic), the Helmholtz International Center for FAIR within the framework of the LOEWE program launched by the State of Hesse, and DAAD (Germany).

REFERENCES

1. A. Kolmogorov, Giornale dell' Instituto Italiano degli Attuari **4**, 83 (1933).
2. N.V. Smirnov, Mat. Sb. **6**, 3 (1939);
   N.V. Smirnov, Moscow, Bull. Univ. **2**, 3 (1939).
3. I. N. Mishustin, Phys. Rev. Lett. **82**, 4779 (1999).
4. O. Scavenius *et al.*, Phys. Rev. D **63**, 116003 (2001).
5. G. Torrieri *et al.*, Phys. Rev. C **77**, 034903 (2008).
6. I. Melo *et al.*, Phys. Rev. C **80**, 024904 (2009).
7. B. Tomášik, Comp. Phys. Comm. **180**, 1642 (2009).
8. F. James, *Monte Carlo Phase Space*, CERN 68-15.

SCHOOL EXPERIMENTS WITH HF35C ANALYZER

J. Degro, jan.degro@upjs.sk, M. Feretová, M. Leššová, UFV PF UPJŠ, Košice

INTRODUCTION

Nowadays many people use equipments working on the basis of high frequency electromagnetic fields (HF EMF) e.g. microwave owen (2.45 GHz), cordless phone (2.4 GHz) mobile phone (e.g. GSM800, GSM1900 TDMA, CDMA, AMPS, iDEN), as well as next generation technologies such as UMTS (3G) or Bluetooth and wifi [1]. We can't neither see, nor feel HF EMF. We thought about, how to make them “visible”.

In spite of the fact that professional measurements of HF EMF are demanding, and expensive, there is some possibility to do “simple” experiments in your surrounding, so “to make them visible”. For this purpose is suitable analyzer HF35C. It allows a competent assessment of high frequency exposures between 800 MHz and 2.5 GHz. This frequency range is interested from the building biology perspective. The values shown on the display of HF35C always reflect the power density *S* in μW/m^2 [1].

The goal of this article is to *present simple experiments* with HF35C, which you can realise in school, and at home. The next goal is also to *present high school project* dealing with the topic HF EMF.

EXPERIMENTAL ASSIGNMENTS

There are many possibilities, of how to use the HF analyzer. We have decided for the simple experiments in local environment of pupil in school, at home and its environment. Instructions (six) for use in practice are placed on address:
http://physedu.science.upjs.sk/degro/pokus/pokusy.html
(1)

Experiments can be divided in two groups:

a) Background:

- Determine the power density *S* of EMF outside your flat and school.
- Determine the power density *S* of EMF inside your flat and classroom.

b) In the immediate neighbourhood of equipments:

- Determine the power density *S* of EMF in the surrounding of microwave oven.
- Determine the power density *S* of EMF in the surrounding of cordless phone and mobile phone.
- Determine the power density S of EMF in the surrounding of wifi transmitter.
- Analyze the measured values of power density S and compare them with standards.

HIGH SCHOOL PROJECT

Project named “High frequency electromagnetic fields in the pupils local environment” we realised at high school of St. Nicholas in Prešov. Project had 4 periods:

- *Study* of literature.
- *Inquiry* for *status finding* of mobile phone using by pupils. (Inquiry and results are presented on address http://physedu.science.upjs.sk/degro/dotaz/dotaz.html).
- *Measurement* of *S* (μW/m^2) using HF35C.
- *Comparison* of measured results with standard values. *Presentation* of results to schoolmates.

STANDARD VALUES

Before analysis of experimental results pupils should familiarize with The Slovak National Standards [2]. Table 1 shows standard values of the power density *S* for the inhabitants and employee.

TAB. 1. Standard values of power density *S* of equipollent plane wave.

Frequency range	*S* (W/m^2) employee	*S* (W/m^2) inhabitants
10MHz <400 MHz	10	2
400MHz<2000MHz	f/40	f/200
2 GHz < 300 GHz	50	10

SOME EXPERIMENTAL RESULTS

Background - outside. At housing estate, among buildings, measured values of power density change in the range circa 10-500 μW/m^2, depending on place. Outside the school the power density *S* changes in the range circa 10-200 μW/m^2. At forest, near the town, power density changes in the range of 0.5–3.0 μW/m^2.

Background - inside flat and school. In the kitchen and sleeping room S changes in the range circa 0.1–4.6 μW/m^2, in study and classroom 0.8-19.4 μW/m^2.

In the next part we will present the measured values of *S, in the form of graphs,* in neighbourhood of microwave oven and cordless phone. Procedure of measurement is in (1).

Microwave oven

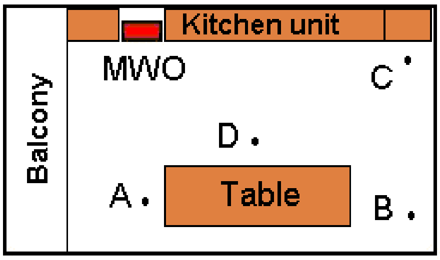

Fig. 1. *Kitchen* - ground plan (2.80 m x 4 m); A, B, C and D measuring points; MWO – microwave oven is read.

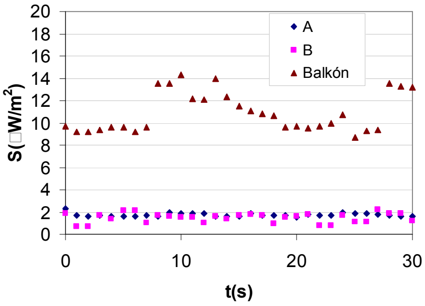

Fig. 2. Time dependences of power density *S* in the kitchen - background. Measuring points A, B, Balcony (Balkón), see fig. 1.
MWO is switched off.

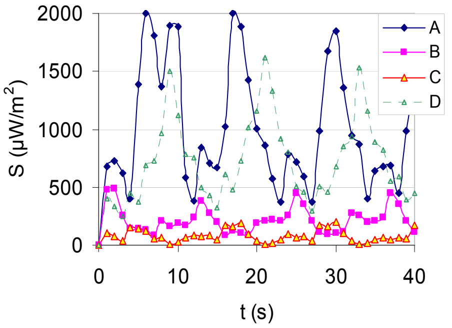

Fig. 3. Time dependences of power density *S* in the kitchen. Measuring points A, B, C, and D, see fig. 1. MWO is switched on.

Dependences of *S*(*t*) in Fig. 2. and Fig. 3. show that switched on MWO radiate HF EMF. Power density of *S* changes, in the kitchen, with time and distance from MWO. Intensities of *S,* in comparison to Slovak National Standards [2], are (in worst-case) circa 1000-times lower as reference values, but they are circa 100-1000-times higher than background. The highest radiation was in front of the MWO door, more than 2000 μW/m^2 (range of analyzer). According to SBM2008 [3] there are, in the kitchen, high and extreme anomalies of HF EMF.

Cordless phone

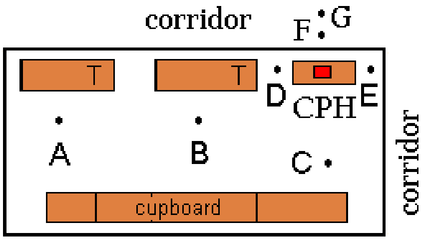

Fig. 4. *Study* - ground plan
(6,5 m x 2,5 m); A, B, C, D, E, F, and G measuring points; T – table,
CPH – cordless phone - read.

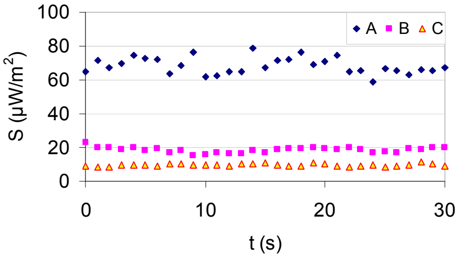

Fig. 4. Time dependences of power density *S* in study - background. Measuring points A, B, C - see fig. 4. CPH is switched off.

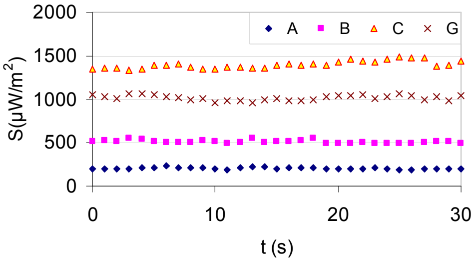

Fig. 5. Time dependences of power density *S* in study - background. Measuring points A, B, C - see fig. 4. CPH is switched on (connect to 220V), in standby mode.

Dependences of *S*(*t*) in Fig. 4. and Fig. 5. show that CPH, in standby mode, radiate HF EMF. Intensities of *S,* in comparison to [2], are circa 1400-times lower as reference values, but they are circa 25-150-times higher than background. In measuring points D and E measured radiation was higher than 2000 μW/m^2 (range of analyzer). Radiation goes through the wall, point G.

CONCLUSIONS

Presented experiments can motivate pupils to study physics and also improve their environmental thinking. They are good starting point for discussion with specialists.

ACKNOWLEDGMENT: Article was supported by project KEGA 3/5272/07.

REFERENCES

1. Instruction manual HF35C, GIGAHERTZ SOLUTIONS GMbH, D-90579 Langenzenn, Germany, www.conrad.de, (2005)
2. http://www.zbierka.sk/ Statute book no. 534/2007
3. BAUBIOLOGIE MAES /Institut für Baubiologie + Ökologie/, SBM-2008, Holzham, Deutchland

PHYSICAL PENDULUM – THE TOOL FOR RESEARCH OF A RIGID BODY ROTATIONAL MOTION, FOR SURVEY OF INFLUENCE OF VARIOUS FORCE FIELDS

M. Kladivová, maria.kladivova@tuke.sk, Ľ. Mucha, lubomir.mucha@tuke.sk, Department of Physics, Faculty of Electrical Engineering and Informatics, Technical University of Košice, Park Komenského 2, 042 00 Košice, Slovakia and
S. Iľkovič, ilkovic@unipo.sk, Department of Physics, Faculty of Humanities and Natural Sciences, Prešov University in Prešov, 17 novembra 1, 080 01 Prešov, Slovakia

INTRODUCTION

The rigid body dynamics is a part of physics, which is very important for understanding other parts of physics. However, it is not very good accepted by schoolchildren and students. The main problem is with an acceptation of physical quantities: torque, angular momentum, moment of inertia. This paper presents a simple experiment with physical pendulum for survey and study some features of a rigid body motion [1].

The pendulum is a topic suitable for primary and secondary schools and also for undergraduate [2]. It is full of potential for learning about physics, and the relationships between sciences, mathematics, and technology [3]. These possibilities can be important in realization of a new process of education started now in elementary and secondary school education in our country. At the same time the experiments with pendulum are very simple and cheap; therefore they are also often used in work with talented youth in courses and competitions [4, 5].

THEORY

Physical pendulum is a rigid body that can oscillate about a fixed horizontal axis passing through any pivot point other than its center of mass [6, 7, 8]. If the pivot joint is frictionless, the equation of motion is

$$I\alpha = -mga\sin\varphi, \qquad \alpha = \frac{\mathrm{d}^2\varphi}{\mathrm{d}t^2}, \tag{1}$$

where φ is a displacement angle, I is moment of inertia of the rigid body about the axis of rotation, a is the perpendicular distance from pivot axis to the center of mass. For small φ ($sin\varphi \approx \varphi$, in radians) the body will execute simple harmonic motion and the period of the physical pendulum can be obtained from the Eq. (1)[1]

$$T = 2\pi\sqrt{\frac{I}{mga}}. \tag{2}$$

The moment of inertia about the pivot axis can be found using the parallel axis theorem

$$I = I_0 + ma^2. \tag{3}$$

I_0 is the moment of inertia about the center of mass. Scheme of used physical pendulum – a thin uniform rod of length L with additional mass Z – is depicted in the in the Fig. 1a). A typical dependence period versus position O of the pivot axis on the rod for this pendulum is depicted in the Fig. 1b)[2]. The x_T on the x-axis is a position of the center of mass T of the pendulum. The reduced length l of the physical pendulum, i.e. the distance between two possible parallel axis of the rotation with the same period but in general at different distance from the center of mass T is, as can be seen in the Fig. 1b)

$$a_1 + a_2 = l. \tag{4}$$

For the reduced length l using the condition $T_1 = T_2$ it is possible to prove

$$l = \frac{I_1}{ma_1} = \frac{I_2}{ma_2}, \tag{5}$$

where I_1 a I_2 are the moments of inertia for two possible pivot points, which can be obtained from Eq. (3). (The period of a simple pendulum of length l is the same as the period of physical pendulum of reduced length l as follows from the Eqs. (2, 5)).

EXPERIMENT

Laboratory tasks:
1. To measure the dependence $T(x)$ of the period of physical pendulum on the position x of the pivot axis.
2. To determine the position of the center of mass.
3. To determine the moment of inertia with respect to the axis passing through the center of mass.
4. To determine the gravitational acceleration.
5. To determine the position of the pivot axis, for which the period is the shortest.

All experimental results were obtained using only the measured dependence $T(x)$. Following parameters of the physical pendulum were given: m_r – the rod mass, m_Z – the mass of nut Z, L – the rod length, x_Z – distance of nut position from the rod end A. These values enabled students to calculate all asked output and compare experimental results with them.

Result processing:
1. The measured $T(x)$ is depicted in the Fig. 1c).
2. Using symmetry of this graph it is possible to determine position x_T of the center of mass (see Fig. 1b)). For instance, it is possible to determine position of pivot axes for minimal period. The center of mass T is exactly in the middle between them. Obtained value can be verified immediately by searching equilibrium point of pendulum and also by calculation of the center of mass. Due to the pendulum geometry a simplified formula can be used $x_\mathrm{T} = (m_\mathrm{r}\frac{L}{2} + m_\mathrm{Z}x_\mathrm{Z})/(m_\mathrm{r} + m_\mathrm{Z})$.
3. The distance between pivot points for minimal period is the minimal reversible length $l_\mathrm{min} = a_{1\mathrm{min}} + a_{2\mathrm{min}}$ ($a_{1\mathrm{min}} = a_{2\mathrm{min}}$) of a physical pendulum as can be seen in the Fig. 1b). The moment of inertia about the center of mass can be evaluated using the graphi-

---

[1] For secondary school students the Eq. (2) can be obtained using the law of energy conservation [9, 8].

[2] Character of the dependence $T(x)$ and the Eqs. (4, 5) are general and valid for an arbitrary shape of physical pendulum.

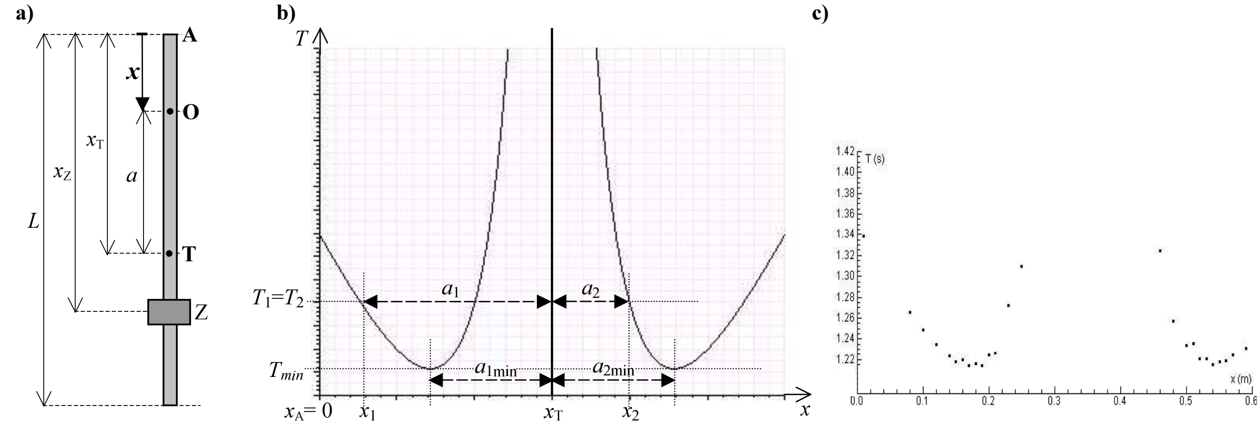

Fig. 1. a) Scheme of the pendulum used in experiment. b) A typical theoretical $T(x)$. c) An experimental $T(x)$.

cally obtained value $l_{\rm min}$ and Eq. (5)[3].

$$I_{0\rm nam} = (m_{\rm r} + m_{\rm Z}) \left(\frac{l_{\rm min}}{2}\right)^2. \tag{6}$$

(The moment of inertia I_0 can be evaluated also from an arbitrary reversible length $l = a_1 + a_2$ obtained from the graph (see Fig. 1b)) using Eqs. (3, 4, 5).) The obtained value I_0 can be proved using formula $I_0 = \frac{1}{12} m_{\rm r} L^2 + m_{\rm r} \left(x_{\rm T} - \frac{L}{2}\right)^2 + m_{\rm Z} \left(x_{\rm Z} - x_{\rm T}\right)^2.$

4. To determine the gravitational acceleration g – this is a problem solved by method of reversible pendulum. Using the graphically obtained value of the period $(T_{1\rm min} + T_{2\rm min})/2$ and $l_{\rm min}$ the gravitational acceleration g can be obtained using and Eqs. (2, 3, 4, 5)

$$g = \frac{l_{\rm min}}{\left(\frac{T_{1\rm min} + T_{2\rm min}}{4\pi}\right)^2}. \tag{7}$$

(An arbitrary $l = a_1 + a_2$ and corresponding T obtained from $T(x)$ can be used for evaluation of g.)

5. The last task is a standard theoretical problem solved by undergraduates. Solving problem for finding extremes of period T (see Eq. (2)) as function of distance a it can be find that the distance $a_{\rm min}$ corresponding to the minimal period of oscillations is

$$a_{\rm min} = \sqrt{\frac{I_0}{m}} = R_0 = \frac{l_{\rm min}}{2}. \tag{8}$$

The experimentally obtained $a_{\rm min}$ can be compared with calculated one using theoretically evaluated I_0.

CONCLUSIONS

The presented experiment is suitable for all levels of education. For elementary school it is possible to observe period of oscillations as function of a pivot axis position. For this purpose it is appropriate to use an unsymmetrical planar object. Pupils found out that axes with the same period site on a circle, which centre is on the axis through the centre of mass. They can conclude that point of application of gravitational force is in the centre of mass and do not depend of a shape of body. Secondary school students can measure the proposed laboratory practical. Furthermore it is possible to obtain minimal periods for various position of a nut and conclude that periods of oscillations are smaller if mass of pendulum is close to the center of mass. Students can also use a simple pendulum to obtain some of reduced lengths of physical pendulum and prove the Eq. 4. Obtained dependence $T(x)$ can be used in mathematical applications: analyze of function, using of mathematical software. Observations of pendulum motion can be used also in other subjects as biology [10], programming, informatics, and technical subjects. For undergraduates and talented youth this experiment can be extended by observation and interpretation of influence of other force fields [5, 11, 12, 13].

ACKNOWLEDGMENT: This work was supported by the Slovak Research and Development Agency under the contract No. LPP-0067-07 "Scouting and education talents in physics by physics competitions on the elementary and secondary schools".

REFERENCES

1. http://web.tuke.sk/feikf/FEI/FEI_ped.html
2. P. Horváth, OMFI **35**, 43 (2006).
3. M. R. Matthews, C. Gauld, A. Stinner: The Pendulum (Springer, 2005).
4. http://fpv.uniza.sk/fo/ 45/AI/7(2003), 47/AIII/ex.(2006), 49/BI/7(2007).
5. http://www.jyu.fi/tdk/kastdk/olympiads/ 27 IPhO 1996 (Oslo): Experimental Problems
6. D. V. Sivuchin: Mechanika (Nauka, Moskva - 1974).
7. Z. Horák, F. Krupka: Fyzika (SNTL, Praha - 1976).
8. http://fyzika.jreichl.com/
9. http://fo.cuni.cz/index.php?file=25&who=ucitel Harmonické kmity mechanických soustav
10. http://sciencelinks.jp/j-east/article/ 200702/000020070206A1001784.php
11. M. I. Gonzáles et al., Eur. J. Phys. **27** 257 (2006).
12. Y. Kraftmakher, Eur. J. Phys. **28** 1007 (2007).
13. C. Gauld Sci. Educ. (Dordr.) **13** 811 (2004).

---

[3] In practice the searched parameter is a minimal radius of gyration $R_0 = \sqrt{I_0/m} = l_{\rm min}/2$, where m is a total mass [7].

PROPAGTION OF IMPULSE IN ELASTIC MEDIA

I.Tunyi, geoftuny@savba.sk, Geophysical Institute SAS, Dubravska cesta 9, 845 28 Bratislava, D.Krupa, krupa@savba.sk, Institute of Physics SAS, Dubravska cesta 9, 845 11, Bratislava

INTRODUCTION

Paper represents didactic approach to apprehension of mechanical disturbance transmission in elastic media based on the theory of density changes caused by shock wave. It is aimed for students in the university first physics course.

DISPLACEMENT PROPAGATION IN STRING

Let as assume one-dimensional space in the form of an infinite string with density ρ, elasticity modulus E and the cross-section S. Let an impulse force $\boldsymbol{F}$ act on it as shown in Fig. 1.

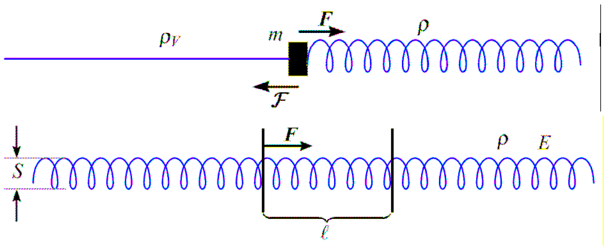

Fig.1: Displacement propagation in string

The force $\boldsymbol{F}$ compresses the stressed part of the string. We may consider the increased density as the body of mass m. Further, the stressed part of the string we may consider as volume of thinner density ρ_V, where $\rho_V << \rho$ (Fig. 1.)

The body m moves into the unstressed part of the string under the influence of F. The moving body in its wake leaves not only the reduced mass density, but also the force $\boldsymbol{F}$ generated by the tension in the stressed part of the string. This may mean that each moving body leaves behind a space with reduced mass density.

Let the force $\boldsymbol{F}$ act on the slice l of the string; let the time interval during which the force is acting be t (Fig. 2.).

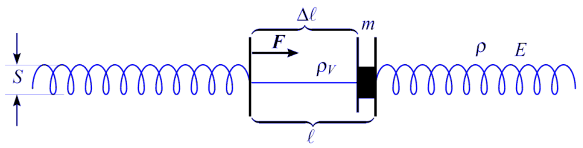

Fig.2: Force acting

The force $\boldsymbol{F}$ compresses the slice l, the length of the slice becomes $l - \Delta l$. On the decrement Δl the string will acquire the density ρ_V (Fig. 2.).

The force $\boldsymbol{F}$ acting on l during the time interval t represents an impulse imparted to the segment Δl. Note that it was the segment Δl, from which the body m was assembled, i.e. $m = \rho S\,\Delta l$. Thus,

$$\boldsymbol{Ft = mv} \tag{1}$$

The force F is governed by the Hooke's relation,

$$F = E\,S\,\frac{\Delta l}{l} \tag{2}$$

Rearranging,

$$\frac{l}{t} = v \tag{3}$$

$$E\,S\,\frac{\Delta l}{l}\,t = \rho\,S\,\Delta l\,v \tag{4}$$

we get

$$v = \sqrt{\frac{E}{\rho}} \tag{5}$$

It follows that an impulse signal propagates with the constant speed through the string, regardless of the magnitude of the impulse force which is a well known fact. The propagation of the front of the shock wave is the solved problem (Fig.3., [1]).

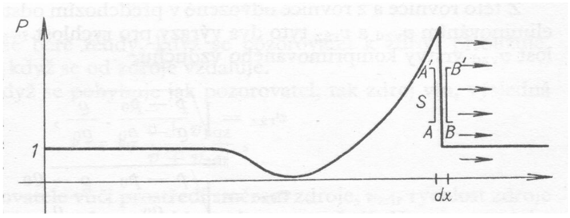

Fig. 3: Propagation of shock wave

The signal propagates also in the opposite direction along string as the motion of the thinner density volume. Applying the same procedure, let us consider this situation. Maintaining the speed v, certain amount of the mass of density ρ_V moves the distance dx through the cross-section S in the time interval dt. In the same time interval a decrement in density $(\rho_V - \rho)$ moves the same distance dx through the same cross-section S. By the conservation of mass

$$(\rho_V - \rho)\,S\,dx = \rho_V\,S\,v\,dt \tag{6}$$

it follows that

$$(\rho_V - \rho)\,\frac{dx}{dt} = \rho_V\,v \tag{7}$$

The expression dx/dt represents the speed of the front of the diluted wave. Introduce the notation $v_A = dx/dt$. Then

$$v_A = \frac{\rho_V}{\rho_V - \rho}\,v \tag{8}$$

CONCLUSION

Since the difference ($\rho_v - \rho$) is negative it follows from Eq. 8. that the thinner wave (also the breaking wave) is propagating in the direction opposite to the action of the impulse force ***F*** with the modified speed v_A

REFERENCES

1. Karjakin N.I., Bystrov K.N., Kirejev P.S., Přehled fyziky, SNTL, Praha 1970, pp. 131.

PRESENT STATE OF PHYSICS EDUCATION AT SECONDARY SCHOOLS IN SLOVAKIA

Peter Demkanin, demkanin@fmph.uniba.sk, Faculty of Mathematics, Physics and Informatics, Comenius University in Bratislava

In the last few years radical changes are done in the physics education in Slovakia. The basic document ruling the content and goals of physics education has been developed and authorised in the parliament as a part of National Curriculum (ŠVP), the implementation of the external final exams in physics has been stopped, work on a new series of textbooks has been initiated. All these changes are done very quickly in time pressure, without broad enough discussion and without allocation of necessary resources. This article brings some of the parameters of these changes and prognoses some consequences.

BASIC PARAMETERS OF ŠVP

National Curriculum is the basic document ruling the goals and content of the education pupils from ISCED0 (nursery schools) to ISCED3 (secondary education). Physics is introduced as compulsory subject in ISCED2, grade 6 (age of pupils 12) and finishes in ISCED3, grade3 (age of pupils 18). ŠVP allocated some time for optional subjects, in ISCED2 50 week-hours (out of 242), in ISCED3 30 (out of 124), what is often presented as the main positive of this curriculum. This curriculum is compulsory, so all specializations of lower secondary schools and most popular secondary schools – gymnazium must be done only within this document. The ŠVP does not rule the final exams. Hours mentioned in this article and ŠVP means 45 min lessons.

PHYSICS IN ŠVP

Physics as compulsory subject has allocated 10 week-hours as in table 1.

TAB. 1. Physics in ŠVP

grade	6	7	8	9	1	2	3	4
physics	1	1	2	1	2	2	1	0
optional	6	6	6	6	4	4	7	15

Table 1 presents also allocation for optional subjects. Some of these week-hours can be allocated to physics (by the management of the school, or in some bigger schools by the pupils). Even if schools allocate some of the optional week-hours to physics, we still see radical reducing of this subject. The allocation before reform is presented in table 2.

TAB. 2. Physics before reform

grade	6	7	8	9	1	2	3	4
physics	2	2	2	2	3	3	2	2
optional	0	0	0	0	0	0	2	2

Such radical changes and also quite obsolete curriculum issued in necessity to prepare the physics curriculum in new format.

EMPIRICAL COGNITION OF PUPILS IN ŠVP

Firstly, we sow the high pressure to physics content. Teachers used to teach content based curriculum could not easily adapt to teaching less content in less time. Also teaching in allocation 1 hour per week in majority schools does not allow teach double lessons usually used for pupil’s physics experiments. So we decided to allocate some hours in gymnazium for pupil’s experimentation. We allocated 40 hours (out of 150 hours) for a direct pupil’s work on physics empirical cognition (including planning of experiments, assembling apparatus, measurement, presentation of the outputs, but excluding data processing writing reports and teacher’s demonstrations). These experiments are not allocated to a content. This part of curriculum is focused to pupil’s competences and teacher (in few planning experiments pupil) will match these hours to a content. This allocation is compulsory, but each teacher/school can fill it up with the most favorite experiments taking into consideration the equipment available and specialization of the school.

CONTENT IN ŠVP

So we had 110 hours for content based curriculum. Of course we still need to develop the basic and subject related competences of pupils within these hours. This was the most difficult (and we hope never ending) work. What is absolutely clear, we need to have in this content a cross section of contemporary physics available on secondary school level of understanding, we should have content to high level comparable with the rest of world, we should go deep enough to develop subject competences, and we must not be too strict in formulations to keep enough space for textbooks authors and teachers/schools specialization. On the other hand we should be strict enough to allow national comparison of schools/pupils educational results. Within this frame we sow that in not possible to adapt previous content to these circumstances. So we prepared new form, based on our previous research in this field. The content has been divided into 7 sections as in tab. 3.

TAB. 3. Physics content in ŠVP

Measurement and experiments - theory	4
Force and movement	18
Energy around us	18
Electricity and magnetism	20
Properties of liquids and gases	15
Oscillations and waves	15
Electromagnetic radiations and subatomic particles	20

If we are comparing the previous and new content, we see that some content is new. Here I bring it only in some points:
- using of proper number of digits;
- planning of pupils experiment, defining of a problem, stating a hypothesis;
- linearization of a diagram;
- energy of food;
- energy in our body;
- energy in housing, travelling, industry;
- conduction, convection and radiation of heat;
- Doppler effect;
- role of research in physics in society;
- physical base of information, digital technology.

The physics is taught on a completely new level now. Before this reform physics (as also other subjects) in gymnazium was taught in focus to final exams for full four years. Now the preparation for final exams should last only two years, should be deeper and more focused. Should be done in more homogenous groups of pupils (all pupils in group should be interested in final exam in physics or in entrance tests for universities in physics). So each student should be offered physics 5 hours per week in two years before final exams in physics. But, as I have mentioned in this article, final exams are still not ruled in correlation with ŠVP.

AGREE OR DISAGREE ?

Reading these lines we could imagine, that some progress has been done in physics education in Slovakia. Of course all people dealing with physics part of curriculum tried to do as well as possible. Still I absolutely can not agree with the present state. Here are the main points of disagreement:
- the number of hours allocated for physics is extremely low in comparison with previous state and also in comparison with educational systems in other countries;
- the curriculum for final exams and allocation of hours for preparation for final exams are not ruled;
- evaluation of educational results is not developed, there is no external assessment of pupils in physics;
- the system for continuous development of the curriculum is not established;
- the system of investment to equipment necessary for physics education is not developed (majority of schools have it on the level almost zero);
- there is no system for in-service teacher training (some has been done in this field, but only on very general level);

POTENTIAL CONSEQUENCES

The physics education set by this reform clearly leads to lowering the level of physics education as a part of compulsory general education in Slovakia. The level of physics education is even before this reform quite low, the real curriculum is much lower than declared curriculum (clearly seen in external tests "monitor" some years ago), but still we see that the level goes down and technical universities will see new, much less educated students in few years (from the year 2013).Not to be so pessimistic, here are some possibilities to foster physics education. Here are some of them:
- develop the rules for final exams – clearly set the number of hours for preparation for final exam in the last two years of study and set the curriculum for the final exam deep and large enough;
- motivate the pupils to study physics in the last two years by technical universities (e.g. by the rules for accepting new students, entrance exams);
- foster the role of physics, image of physicist and physics education in general society;
- utilize all available resources for out of school physics and technical education (technical clubs, science clubs, interactive science museums);
- as soon as possible gain relevant data from schools to be able clearly present the disagreement between declared role of science education and the attainable role within the rules set by this reform (this we can have in 2013 when first students studying within these rules will be on universities).

REFERENCES

1. MŠ: Štátny vzdelávací program, www.minedu.sk.
2. EC, Education and Training 2010: http://ec.europa.eu/education/policies/2010/et_2010_en.html.
3. EC, Science and Society: http://ec.europa.eu/research/science-society/home_en.cfm.
4. International Baccalaureate: www.ibo.org.
5. UNESCO: http://portal.unesco.org/education/en.
6. EC: European Report on the Quality of School Education, 2002 Brusel.
7. OECD: Assessing Scientific, Reading and Mathematical Literacy, PISA 2006.
8. Eurydice: Key competencies, Brusseles, European Comission, 2002.
9. P. Demkanin: Inovácia prírodovedného vzdelávania – dôvody a cesty, In: Inovácie v prírodovednom vzdelávaní, FMFI UK, Bratislava, 2006.
10. P. Demkanin: Effective use of ICT in Physics Education, Didfyz 2006, UKF Nitra, 2007.
11. V. Koubek et al.: Vyučovanie fyziky a všeobecné vzdelanie, FMFI UK Bratislava, 2005.
12. V. Lapitková et al., Obzory matematiky, fyziky a informatiky 2 (2005) 39.
13. P. Demkanin,, S. Chalupková, 16th Conference of Czech and Slovak Physicists, MAFY, Hradec Králové, 2009 S. 351-360.
14. P. Demkanin: Zmeny vo fyzikálnom vzdelávaní na Slovensku-realita, alebo ilúzia, Didfyz 2008, Nitra, 2009.
15. P. Demkanin, Obzory matematiky, fyziky a informatiky 2 (2008) 54.
16. P. Demkanin et all., Effective use of ICT in science education, University of Edinburgh, 2008.
17. J. Pišút: Zmeny fyzikálneho vzdelávania-dôvod a cesty, DIDFYZ 2006, UKF, Nitra,2007.

THE USE OF OUT-OF-SCHOOL KNOWLEDGE IN PHYSICS EDUCATION

S. Chalupková, chalupkova@gmail.com, FMFI UK, Mlynská dolina, Bratislava

INTRODUCTION

The human being is learning throughout his whole life. He gains the knowledge from the early childhood. When somebody says the word education, the most of adults think of education at school. But when the child comes to school for the first time, he isn't like tabula rasa. We can't say he knows nothing. He grows up surrounded by parents, friends, is influenced by mass media. He takes with the knowledge and information, he develops later and uses in daily life. Today's student has many opportunities to be educated. He can (and under some age he must) attend school, he can choose groups; he can join to the work of different clubs. At home there is television and internet is being the normal part of everyday life of a common family.

NONFORMAL A INFORMAL LEARNING

Education takes its courses not only at school, but also in groups, clubs, or independently of any institution. We speak of education formal, which takes place at school, nonformal and informal learning. Nonformal learning is provided by different groups, clubs. It is intentional activity, which is being repeated, but it is not so strictly limited by such rules like at school. Human gains also information unawares and this kind of education is called informal learning. All three types of learning have its unsubstitutable place and they must be complemented together [1, 2]. But does the student use out-of-school information at school education? Does he realize it? But what is more important, does the teacher realize the great informational potential of out-of-school activities of his students? Does he use what the students deal with in a free time activities?

European Commission (EC): Directorate - General for Education and Culture is concerned with the problem of different types of education. The programme is called Education and Training 2010 [3] and it was approved in 2002. The main goal of the programme is to fulfill the demand: the economic of European countries must be developed dynamically and it must be based on knowledge. EC defined five basic benchmarks, which have to be fulfilled until 2010. Nonformal and informal learning arise under lifelong learning, which still doesn't reach the needed percentage value of european population and it is one of assessing benchmarks.

In major form Directorate-General for Research is concerned with the development of nonfomal and informal learning and its connections on formal education within the frame of 6th and also 7th Framework Programme for Research and Technological Development. It's the main tool of European Union for research funding in Europe. The programme is planed for period 2007 – 2013. The aim of the programme is the development in 5 areas to be the European Union the leader in. The one of the areas, Capacities, is focused on research potential, regions of knowledge, but also the status of science in society. The part Science in Society aims to connect professionals with no formal science learning. But it needs to support science education at every school grade, in all forms. The students should be curious and interested in discovering nature laws. The question is why the European Union spends a lot of money on Science in Society? What are the benefits for citizens or researchers? Science and technology influence our lives a lot. There is the need to talk about pros and cons of science research and its progress. The society should be more interested in research, in a form of various discussions. The human must decide well, e.g. in a question of global warming or when it's talked about the construction of new power plant.

What are the possibilities for out-of-school activities for Slovak student (concerning with physics)? When we take an example of a student from foreign country, e. g. Denmark with high degree of development of other forms of learning, the Slovak student should feel some kind of shortage for no formal learning. Slovak no formal physics learning offers for student the following: Physics Olympiad, Young Physicist Tournament, Physics Postcard Seminar. There are always some good and willing teachers, who devote their time to young students interested in physics. Also the non-physical activities contribute to development of physical thinking. For example the diving, flying, modeling courses, the older drivers' school. Unfortunately there are only few examples of such opportunities in Slovakia. Also the musical instrument play can influence knowledge from physics positively. Internet, the great phenomenon of 21st century, offers unlimited chances for informal learning. The same is valid for television. It brings many foreign channels, also with the programs devoted to science. Student watches a documentary film, or scientific discussion maybe randomly, maybe goal-directed. Mainly students from Bratislava (but not only them) like the serial stories "mythbusters". The aim of the program is to talk about normal phenomena from daily life, but they want to overturn some myth. The press brings the other source of physics information. From the field of physics there is really the shortage. We can mention the magazine Quark. It popularizes the science for common people in a popular form. The family and friends play very important and unsubstitutable role in a life of each person. Family influences the choice of free-time activities and thus it contributes to gaining knowledge by different ways.

CONTEXTUAL LEARNING

If we include the students' knowledge obtained by nonformal and informal learning at school, the education will gain contextual character. The taught phenomenon is set in a real situation, which the students are familiar with, or they can meet it, or it can interest them somehow.

The Slovak physics teachers strive with big problem at high schools: how to engage the students. They must show that physics isn't separated from daily life. The opposite is true. Physics is everywhere. The contextual learning is one of many ways how to attract the students. Students will be more interested in physics if the taught phenomena are interesting and comprehensible for them. Motivational effect is a great positive of contextual learning [4].

APPLICATION OF OUT-OF-SCHOOL KNOWLEDGE

But how can a teacher use what the student knows from no formal learning? R. Brozová made small investigation between "normal" people (they didn't study science). She was interested in experiences from physics education at school. One example was very nice. It was a story of 35 year old women, with liberal education. The goal of the investigation was to find out what was the respondents' relationship to science and to physics particularly. Respondent remembered only one "bright point". She taught her schoolmates about sound with the help of the violin play. As the length of the string was changing, the high of the tone changed too and everyone heard it. The common teacher can join his students to the learning process actively. There are many different ways how to do that. I will try to show how to use the out-of-school knowledge of gymnasium' students at school. The teacher can use knowledge of one student – expert in a given area. The student parachutist can contribute to the explanation of a free fall. His schoolmates believe him more than the same says teacher. Maybe the other students want to be an expert in other field too. That should increase the interest of students to require the knowledge usable at school.

Teacher can make use of short few minutes' discussions at the beginning of physics lesson. The information doesn't need to be related directly with physics. There could be some interesting information in mass media which is somehow interesting also for students. For example the mentioned construction of power plant: yes or no? In the class there are always the students for and against and we can discuss.

We can show students that they know a lot, because everything is somehow related. Teacher can use what the most of the class knows. Or he can point out the misconceptions they have about something.

All methods are important. We can join them and use anytime. They will fill up few seconds, minutes. Or they can accompany the explanation of whole physics topic.

PRACTICAL DEMONSTRATION

I tried to test the use of out-of-school knowledge with the 3rd year students of Gymnázium Jura Hronca in Bratislava. The students wrote pretest as a first step before talking about sound. I wanted to know how they are informed about sound, ultra-, and infrasound. Questions were various. They were related to musical instruments. Other questions concerned physiology of hearing, supersonic aircrafts and utilization of ultrasound in medicine and traffic. I have chosen the students – experts in the problem spoke during the lesson. Students didn't know how I choose them to answer the question, or to talk about something.

Next I created the contextual material with problems from every day life. In this group of students there were only 5 girls, so I concentrated on context of musical instruments (more popular between boys). The topic sound was taught contextually and the stress was putted on musical instruments. Later we talked also about human hearing, but only in a shortened version. We talked about decibels and sound inaudible for human then. It was nice that there were involved more students actively on running of lesson. Mainly the weaker students could show that they know also important physics information. Although they didn't know the math behind, they could be helpful for others, because they have practical experiences. Boys were engaged more in guitar play (there were 5 guitar players in that class). Girls were interested more in connection between physics and biology. The students could use the information they gained purposeful, or unknowingly. They could connect physical phenomena with common situations from their lives or from situation seen in a television.

CONCLUSIONS

When we want to use this kind of activation of students, we must know them. But it needs a lot of time from teacher. He must prepare the whole topic. He must know what is "in" to attract students' interest. In a given specimen there were only 5 girls. The situation can differ with different number of girls and boys, because the interest depends a lot on gender. Overall feeling from my investigation: maybe students had sense of playing. They were more talking than writing notes, but maybe this will make greater impression on them, like the example of R. Brozova's investigation.

ACKNOWLEDGMENT: Preparation of this paper was supported by the Grant UK: Kontextuálny prístup k téme zvuk s biomedicínskymi aplikáciami, G-09-239-00.

REFERENCES

1. Demkanin,P.: Zmeny vo fyzikálnom vzdelávaní na Slovensku - realita, alebo ilúzia, (Didfyz 2008, Nitra - 2009).
2. Demkanin,P.: Poznámky k cieľom fyzikálneho vzdelávania (Obzory matematiky, fyziky a informatiky, 2, 2008, s. 54-62).
3. EC (European Commission): *Education and training 2010*. (Brusel, 2002).
4. Bennett, P.: Teaching and learning science. (Continuum, London - 2003).

THE ROLE OF COMPLEX EXPERIMENTS IN THE EDUCATION OF SCIENCE

F. Kundracik, kundracik@fmph.uniba.sk, Faculty of Mathematics, Physics and Informatics, Comenius University, Bratislava, M. Plesch, plesch@savba.sk, Institute of Physics, Slovak Academy of Sciences, Bratislava, Z. Dzirbíková, Faculty of Natural Sciences, Comenius University, Bratislava, P. Kubinec, 1st Private Gymnasium Bajkalská, Bratislava, R. Dörnhöferová, EUREA, NGO, Bratislava

INTRODUCTION

The education of sciences in the Slovak school system was divided into separate subjects (Physics, Biology and Chemistry) for a long time. The result of such a separation is that students often take these subjects as separate disciplines. The natural connections between physics, chemistry and biology are weakened in such an educational model. Analogous situation is in physics education, where its parts (Mechanics, Electricity, Optics, …) are learned in different parts of the school year. If you are learning optics, you have to solve problems from optics. Complex tasks including more parts of physics are not commonly used in elementary and high schools.

One way how to show the connection between disciplines mentioned above is to use experiments including all biological, chemical and physical methods of investigation.

Such experiments are used also in some competitions designed for students, namely International Junior Science Olympiad (IJSO) and International Young Physicist's Tournament (IYPT) and can be effectively used in the education process.

IJSO

International Junior Science Olympiad (IJSO) is a competition designed for talented students from upper grammar (and equivalent) schools in the Slovakia, which are interested in science (mathematics, physics, chemistry and biology).

The competition has more stages. The first stage is done at home. Students have to perform an experiment covering physics, chemistry and biology and write a report (especially these experiments are suitable also for the educational purposes and their description can be downloaded from the Slovak webpage of named competition [1]). According to their results, best 30 solvers are invited to participate in the national round, where they have to solve theoretical tasks from all fields of science. Best 10 students reach the last selective stage, where finally six students are selected. These students participate in the international competition and have the opportunity to represent the Slovak republic in a foreign country. Slovakia is participating successfully from the origin of the competition (2004).

In the next text we present two experiments used in the first stage of IJSO competition.

Anthocyans – magic dyestuffs

This experiment was used in 2009. The aim of this experiment is to introduce antocyans in the red cabbage, to explain the term "pH" in more detailed form and to explain ox/redox reactions during the electrolysis.

Biological part of the experiment.

Students have to find (using magnifying glass and/or microscope) where in the cabbage the anthocyans are located. They have also to wet the specimen with vinegar and soda and observe a colour changing of cabbage. Students also have to search many databases and find, why anthocyans are useful for the cabbage and for the human body.

Solution: anthocyans are mainly located in the outer part of leaves, but not in the layer of cells located exactly on the surface. In cells are anthocyans distributed evenly in whole cytoplasma (they ar not in a vacuole) – see Fig.1.

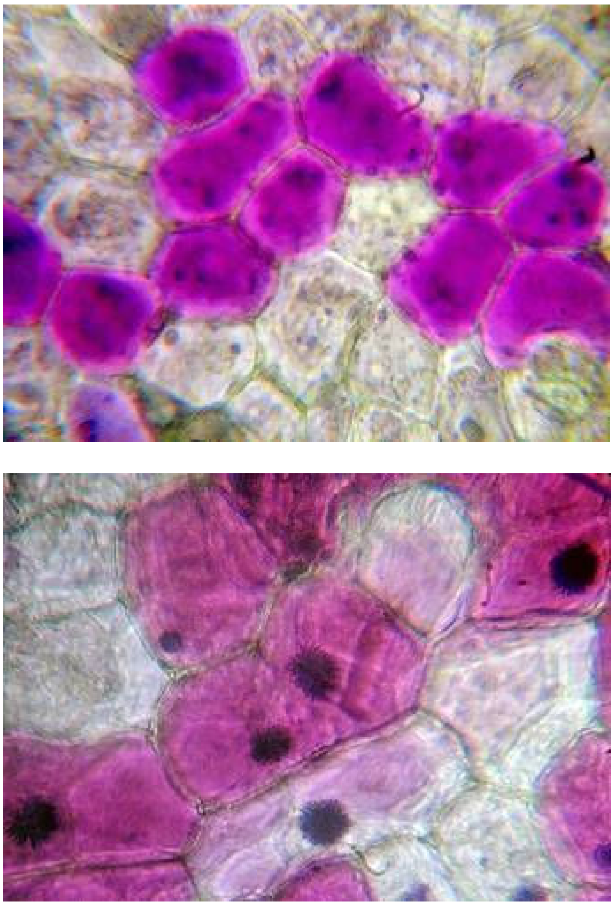

Fig.1. Cabbage cells coloured by anthocyans

Adding of the vinegar changes the colour from violet to red. Adding of the soda results in a green-coloured specimen.

Chemical part of the experiment

Firstly, the term "pH" is explained and pH of a standard vinegard solution (pH = 3) and of saturated soda solution (pH = 11) is given. Students have to prepare (by 1:10 dilution) solutions having pH = 3, 4, 5, 6, 7, 8, 9, 10 and 11. Students also have to prepare (by boiling of the cabbage in the water) concentrated solution of the anthocyans. This solution will be used as a pH indicator. Students will add a small amount of this indicator into prepared set of basic/acidic solutions and observe the colour.

Solution: The colour changes from red (pH = 3) through rose (pH = 5), violet (pH = 7), blue (pH = 9), green (pH = 10) to green-yellow (pH = 11) - see Fig.2.

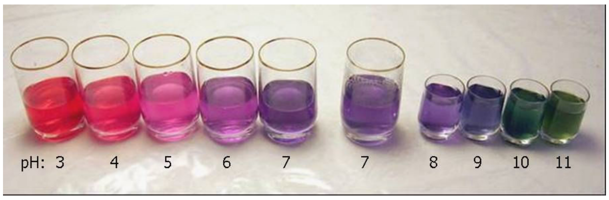

Fig.2. pH-dependence of the colour of anthocyans

Physical part of the experiment

Prepared pH indicator can be used for the visualisation of pH-changes during electrolysis of a salt water (NaCl solution). Students have to prepare an NaCl solution and an experimental setup for the electrolysis. The setup is very simple, it uses only a standard battery, graphite electrodes (from a pencil) and a soaked paper tissue as a salt bridge (Fig.3).

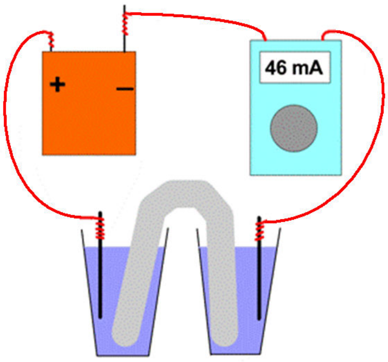

Fig.3. Schematic experimental setup for the electrolysis

Students have to observe and explain the changes in the colour of salt water with added cabbage juice in the cathodic and anodic glass.

Solution: The real experimental setup is shown in Fig.4. Near the cathode a strong colour change to green colour can be observed. After ca 30 minutes of the electrolysis the colour indicates pH = 11 (change 11 – 7 = +4). Near the anode only slight colour change is observed and after 30 minutes the pH is 5 (change 5 – 7 = -2). The explanation of these results is simple. At the cathode, each Na^+ ion is neutralised and immediately reacts with water producing NaOH (base) and easily observable gas H_2. Cathodic region is after the electrolysis basic. At the anode, Cl^- ions leave the solution in form of the gaseous Cl_2 after the neutralisation (can be easily observed and smelled). Theoretically, in the anodic region no change in pH should be observed. In the reality, part of Cl_2 is dissolved in the water building acidic compounds. But the corresponding decrease of pH is much smaller than the pH increase near the cathode.

Fig.4. Real experimental setup for the electrolysis

Fermentation

"Fermentation" is another experiment covering biology, chemistry and physics. Students have to measure (in a very simply way) the CO_2 production during the fermentation of a sugar caused by the leaven. Physics is covered by volume measurement of the gas and the volume recalculation to standard conditions (0 ^{o}C). The chemistry is covered by the calculation of moles of CO_2 produced and of moles/mass of sugar digested by leaven.

IYPT

International Young Physicist's Tournament (IYPT) is a physical competition for high school students. Each year 17 mainly experimental and complex problems, covering more fields of physics, are published. The problems are solved by teams (one school builds usually one team). At the competition, the team have to present the solution of the problem and to defend the solution (another team has a role of the opponent). More information about IYPT tasks can be found on Slovak YPT webpage [2].

ACKNOWLEDGMENT: This work was supported by APVV grant agency under contracts LPP-0179-09 and LPP-004-06.

REFERENCES

1. http://www.ijso.sk
2. http://www.tmfsr.sk

METEOROLOGICAL STATION

G. Barčiaková, gabika.barciakova@gmail.com, FMFI UK, Mlynská dolina,Bratislava

INTRODUCTION

Weather is an obvious thing for each of us. Forecasters deal with weather; let us say physics of atmosphere. Weather affects the people and their activities. It is the result of the Earth's movement around the Sun. In former times people forecasted weather by the behaviour of animals, which were getting ready for a change. In modern times we observe weather through satellites that record different textures of clouds. By these we know how to predict the weather for the next few days.

If somebody will ask us what the weather will be, we know what he is asking for. Our reply is usually: it will be sunny, cloudy, rainy or snowy.

If we were watching the forecast on television, it tells us approximately how many degrees centigrade will be, if the pressure will rise or not. Sometimes we can even predict bio-forecast. This is the only information which we can hear from the weather forecast. Not everyone can explain the predictions. TV news doesn't explain what it means, why the pressure and temperature are changing. Weather forecast consists of a number of natural physical phenomena, which we can explain. Only few of us remember these from the school, the others have never understood what the teacher said [1].

PROJECT: METEOROLOGICAL STATION

It is very important to bring to pupils the closer connection between theory and ordinary life. This is one of the main points of reform of physics education in this time. (see. e.g. [2,3,4]) One of the projects, which we can explain practically, is construction of weather stations. When we have data from more weather stations, we are able to prepare a weather forecast. Meteorological satellites or balloons help to predict the weather. The students' task is to build a meteorological station with gauges which observe and record weather results. During the construction of the gauges, which they need for measuring of weather, school children are getting technical skill. This project develops geographic, mathematical and physical skills.

This project is easier to be done in summer months (may, june), when it's possible to have physics classes for four hours a day (for example during the school leaving exams). You can build this meteorological station in two days. On the first day discuss the plan of observation with the pupils, tools required or how to make them. Pupils will choose the tools which they will need for construction. In the next four hours they will construct their own gauges. Good advice is to divide the children in to groups of four and every group will construct their own station. At the end of measuring let the groups discuss and compare their results.

WHERE TO PLACE METEOROLOGICAL STATION

The meteorological station should be placed in an open field, exposed to rain and wind. Find a covered place for the gauges, to protect them against the sun and rain. The stand should be a minimum of one meter above the ground. The instrument for measuring the wind should be placed higher to avoid obstacles. Other instruments can be placed lower. Put the station in the field, where there are no effects from trees, buildings, because they will affect the final results and amount of rainfalls, direction and speed of wind.

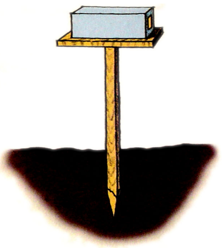

Fig. 1 Meteorological station blueprint

Meteorological station blueprint

Create your placing map. Use blank paper and draw the map of space, which you will use for placing a station. Note down the height and distance of the trees, buildings and other barriers, which are higher than one meter. Create the map with all points of the compass and note down all data, which can affect the measuring.

How to make the stand for the meteorological station

Wooden bar (as stand) fix solidly into the ground, use wooden board which will be exposed to wind and rain and place it on the top of the wooden bar. Fix the cardboard box on top of the board and make sure it is open to allow air through from both sides. Use adhesive tape to make a box waterproof.

Gauges

Shuttle anemometer: wind speed instrument. Pupils build anemometer using protractor, fibres and little balls. When it is windy, fibre on the protractor will change the angle and by this angle you can define speed of wind. Pupils from primary school get the wind speed from tables, but older students must calculate the speed of wind themselves.

Conical flask: calibrated bottle for the capturing of rainfall. Make from a bottle neck the filler to prevent condensation. At the end of observation, we determine whether it is an acid or base using the pH paper sticks. Record your results in accordance of your day or week depending on type of conical flask.

Wind indicator: wind direction instrument. It must be placed in the field, so it can turn with the wind. Indicator has to have wind rose, so pupils will be able to identify wind direction.

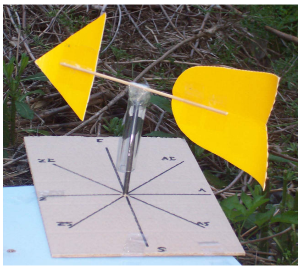

Fig. 2 Wind indicator

Thermometer: Use the laboratory or indoor thermometer for temperature measuring.

Moisture meter: instrument assigned on finding out the atmospheric humidity. Make your own measuring scale. When the air is humid, the hair will extend and indicate approximately to 100% humidity. If the air is dry, hair will shorten and approximately to 0% humidity. We can find out even 50% humidity on a measuring scale and we can compare values with commercial hygroscope.

Barometer: measuring pressure instrument. We know two kinds of commercial barometers. (Aneroid, mercury barometer). You can make your own barometer, from this you can find out, if the air pressure increases or decreases throughout the day, when the barometer was installed.

Fig. 3 Barometer

Dust glass: use it for measuring amount of dust elements in the air.

Dust strap: it is for capturing dust and dust elements in the air, when is windy.

Visibility: every day check the weather even by free eye. Most of us can already determine what the visibility is and what the clouds like in the sky are. For example, when we see dark, dense and local clouds, we suspect that storms will come here or somewhere around. We can predict which clouds will cover sunlight for the whole day, and which will disappear in some time.

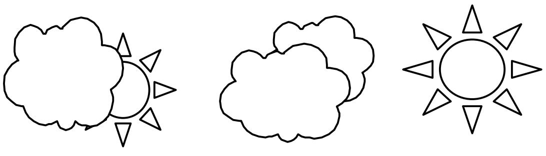

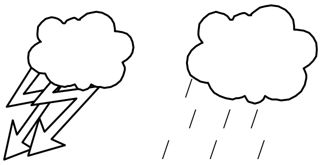

Fig. 4. Different weather situations

TAB. 1. Table for recording weather values, which pupils measure in one day.

Date	Wind direction	Wind speed (m/s)	Rainfalls (ml)
12. 6.	W-E	2,5	7

Atmospheric humidity	Air pressure	Temperature (°C)	Visibility
70	1011	21	good

CONCLUSIONS

Pupils will start to observe the nature and during that, they will learn to measure and work with the tools. This project develops geographic, mathematic and physics knowledge. In choosing the area for placing the meteorological station, mind the space to avoid distorted results of observation. Instruments we used are just our examples and construction. If the pupils are more creative, they will find more other ways. After the instruments are finished and placed somewhere around the school area, pupils should be recording the changes measured by the instruments every day, and marking these changes in the table. Together with their own recordings pupils should watch TV weather-forecast. At the final discussion they will present their own observations and explain measuring differences if they recorded some.

ACKNOWLEDGMENT: Preparation of this paper was supported by the Grant UK: Fyzika aktívne a hravo.

REFERENCES

1. V. Lapitková, E. Brestenská: Fyzika pre 8. ročník špeciálnych základných škôl (Bratislava: Expol - 2003)
2. Demkanin,P.: Zmeny vo fyzikálnom vzdelávaní na Slovensku-realita, alebo ilúzia, Didfyz 2008, Nitra, 2009
3. Demkanin,P.: Poznámky k cieľom fyzikálneho vzdelávania, Obzory matematiky, fyziky a informatiky, 2, 2008, s. 54-62
4. Lapitková, V., Pišút, J.: Obsah a metódy vyučovania príodných vied – stav a trendy, Nitra, Obzory matematiky, fyziky a informatiky 2/2005, str. 39-49.

EDUCATIONAL PRODUCT „IONIZING RADIATION AND RADIATION PROTECTION“

O. Holá, olga.hola@stuba.sk, Institute of Physical Chemistry and Chemical Physics, Faculty of Chemical and Food Technology, Slovak University of Technology, Radlinského 9, 812 37 Bratislava, Slovak Republic
K. Holý, holy@fmph.uniba.sk, Department of Nuclear Physics and Biophysics, Faculty of Mathematics, Physics and Informatics, Comenius University, Mlynská dolina F-1, 841 04 Bratislava, Slovak Republic

INTRODUCTION

The upcoming multimedia e-book „Ionizing radiation and radiation protection“ will be the output of the grant project: „Multimedia programme of education in the field of ionizing radiation and radiation protection“. The part of the multimedia component of this electronic book is presented in our contribution. First of all it deals with the set of video-films about radioactivity, about the usage of ionizing radiation in research and medicine, as well as video from the field of radiation protection. As far as the multimedia part of the mentioned e-book is concerned, it obtains the further video-films as well as presentations and posters related to this issue.

This paper also deals with an application of this educational product, not only in pedagogical process on the high schools and colleges, but as information or promotional materials for general public.

MULTIMEDIA PROCESSING

Shooting of video-clips took place on the working place of the first author – on the Institute of Physical Chemistry and Chemical Physics of Faculty of Chemical and Food Technology (FCHFT) and on Oncological Institute of Holy Elizabeth (OIHE) and Medicine Faculty (MF) of UC in Bratislava.

Processing of video-clips was done by means of software Pinnacle Studio. The own figures and photos, graphs or power-points pages with mathematical deductions were also used. The soundtrack to films consists of the original sound background, shading, and voice-over of author or experts. Parameters of the individual films are:

1. **Roentgen rays and roentgen diffractometer**

Direction, camera: doc. RNDr. Oľga Holá, PhD.
Script, voice-over: doc. RNDr. Oľga Holá, PhD.,
Expert adviser: doc. Ing. Jozef Kožíšek, CSc.
Characteristics: (720 x 576) pixels, compression: XVID, Duration: 8:58 min

2. **Usage of roentgen rays in medical diagnostics**

Direction, camera, script: doc. RNDr. Oľga Holá, PhD.
Voice-over: doc. RNDr. Oľga Holá, PhD., doc. MUDr. Viera Lehotská, PhD.
Expert advisers: doc. MUDr. Viera Lehotská, PhD., Ing. Erzsébet Füri
Characteristics: (640 x 480) pixels, compression: XVID, duration: 13:23 min

3. **Modern display techniques in radiology and nuclear medicine**

Direction, camera: doc. RNDr. Oľga Holá, PhD.
Script: doc. RNDr. Oľga Holá, PhD., Ing. Erzsébet Füri
Voice-over: doc. RNDr. Oľga Holá, PhD., doc. MUDr. Viera Lehotská, PhD.
Expert advisers: doc. MUDr. Viera Lehotská, PhD., Ing. Erzsébet Füri
Characteristics: (640 x 480) pixels, compression: DIVX, duration: 17:52 min

4. **Nuclear medicine – free sources in diagnostics and therapy**

Direction, camera: doc. RNDr. Oľga Holá, PhD.
Script: Ing. Erzsébet Füri, doc. RNDr. Oľga Holá, PhD.
Voice-over: doc. RNDr. Oľga Holá, PhD.
Expert advisers: Ing. Erzsébet Füri, doc. MUDr. Izabela Makaiová, PhD.
Characteristics: (640 x 480) pixels, compression: DIVX, duration: 12:51 min

5. **Ionizing radiation and radiation protection in medicine**

Direction, camera, script: doc. RNDr. Oľga Holá, PhD.
Voice-over: doc. RNDr. Oľga Holá, PhD.
Expert adviser: Ing. Erzsébet Füri
Characteristics: (640 x 480) pixels, compression: DIVX, duration: 10:42min

CONTENT OF VIDEOFILMS

The first of mentioned video-films deals with the origin of bremsstrahlung and characteristic radiation and explains principles of X-ray apparatus and roentgen diffractometer (Fig. 1).

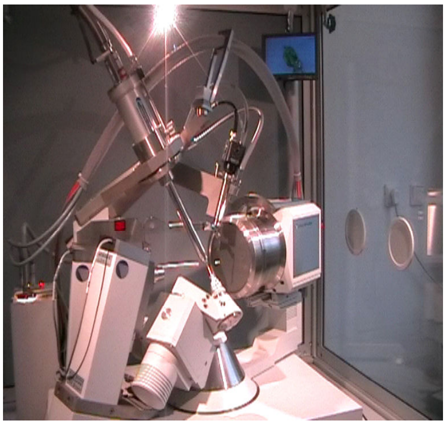

Fig. 1. Roentgen diffractometer

In the next two films we are passing through departments of the Radiological clinic and we are guided by head physician. We are acquainted with the digital medicine roentgen apparatus, sciascope (Fig 2.), mammograph (Fig 3.), and dental roentgen.

Fig. 2. Sciascope

Fig. 3. Mammograph

We visit also departments with modern depictive apparatuses as computer tomograph (CT) and its up-to-date colleague „multislice CT“. Video - film introduces also such modern techniques that do not work with ionizing radiation but they are inseparable diagnostic means at the complex medical examination of patients. These are workplaces of „magnetic resonance imaging“ (MRI) and ultrasonography.

In the video – film from the Clinic of Nuclear medicine we are acquainted with the preparation of radiopharmaceuticals – open radioactive sources that are applied to patients before their medical examination. Then we visit workplaces of scintigraphy, single photon emission tomography (SPECT) and state-of-the-art – department of the positron emission tomography (PET) (Fig. 4).

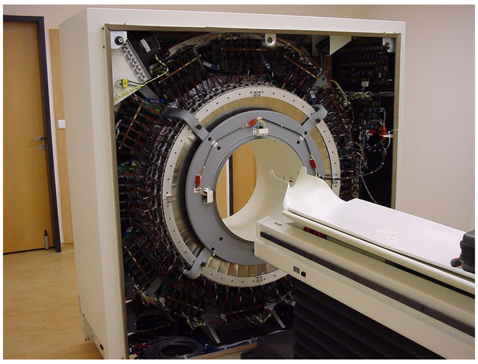

Fig. 4. PET camera

In the last of the presented video-films we explain physical principles of ionization and excitation. The basic aims and principles of the radiation protection are declared. Active and passive means of radiation protection used in medicine are mentioned. For example manipulation cells (Fig.5) and boxes, protecting shields, transport and storage containers, protective aprons, etc.

Fig. 5. Manipulation cell

APPLICATION

The set of video – films whole, or the individual films can be used as an educational product at the high schools, as well as in lectures or laboratory exercises at colleges and universities. In many subjects related to ionizing radiation, radiation protection, radioecology, radio-pharmacy, biomedicine chemistry and physics, which are lectured at various faculties with natural science, medicine, health care or technical orientation, there these video films should be applied. Nowadays they have been used as supplementary educational materials in subject “Radiation protection” and also for bachelor project at FCHFT. Some of the mentioned video – films were given free of charge as a study material to teachers who will be using them in education.

CONCLUSIONS

The use of video at the lecture enables to capture student’s attention and evoke their imaginations. The other approach to the same subject matter can be used. Moreover by means of video we can demonstrate such effects or unique equipments that we can not show directly on lecture.

In conclusion we can say that the use of the video films in teaching-learning process generally, leads to the improvement of its quality.

ACKNOWLEDGMENT: The video-film making was supported by Cultural and Educational Grant Agency of Ministry of Education of Slovak Republic (KEGA project 3/3062/05). Our acknowledgment belongs also to management of OIHE and MF UC and to all experts, who contributed to creation of videos.

SCHOLA LUDUS THEORY OF TEACHING AND LEARNING

K. Teplanová, katarina.teplanova@fmph.uniba.sk , SCHOLA LUDUS centre for support of science education and non-formal lifelong science education at the Faculty of Mathematics, Physics and Informatics Comenius University, Mlynská dolina, 842 48 Bratislava

INTRODUCTION

SCHOLA LUDUS theory of teaching and learning (TL) is an original pro-science theory based on 1. Authentic Pedagogy, 2. Thinking Based-Learning, and 3. Cognitive Constructivism [1]. This paper presents brief highlights of the complex SCHOLA LUDUS theory and its comprehensive supports for effective pro-science teaching and learning.

SCHOLA LUDUS TL

SCHOLA LUDUS Teaching accepts three stages of learning: 1. Learning by unawareness (with a matter). 2. Learning by thematization (of the matter). 3. Learning by awareness (over the matter). The meaning of the matter is during the TL process changing. The matter can represent a physical system/process as well as concepts, models or theories.

The process of SCHOLA LUDUS teaching is in agreement with Vygotsky´s conception of teacher's scaffolding with respect to learner's zone of proximal development [2] while learning process should result in conceptual changes within the learner's individual pre-scientific conceptions, and in personal development regarding his/her pro-scientific mental and crafts skills.

SCHOLA LUDUS TL THINKING

Any TL process is considered as a thinking process. A significant part of learning is based on imitation of teacher's thinking patterns, and on teacher-learners thinking intrusion that results in a mutually interwoven common thinking frame. Hence the TL process depends significantly on skills of teachers´ thinking and thinking is more than teachers´ logic or cleverness.

Thinking can be taught and learnt. Effective thinking is supported by specially designed thinking tools and mental exercises. Learners can learn different techniques enabling effective usage of mental tools and acquire useful skills necessary for effective operations with mental tools.

TL frame for pro-scientific thinking includes mental tools and techniques for systematic development of thinking skills based on serious creativity [3] and on complexity as is understood in modern science.

TL SERIOUS CREATIVITY

Serious creativity represents a way of well-disciplined thinking process with respect to the focus and concept of the thinking process, the currently applied mental tool, and the duration stated for respective parts of the thinking process. The goal of serious creativity is to create / discover / solve / establish etc. something that is 1. novel and 2. useful. At learning process the useful novelty relates to aware progress of learning that is measured by conceptual change and practice.

Creative thinking is the more effective the more we take aim of harmonious development of all types of thinking (resp. all multiple intelligences [4])- verbal, visual, motion, mathematical etc.

A basic assumption for creativity is the lateral thinking [3]. Lateral thinking is an eminent feature of mind and can be systematically developed by specially designed mental tools and techniques. As basic tool for development of lateral thinking is considered humor. To basic mental tools for serious creativity belong provocative operation [3], a tool called OKAMIH and thought experiment [1].

OKAMIH: FOCUS – CONCEPT (– ANALYSIS) – IDEAS (– INFORMATION) – VALUES

OKAMIH is the Slovak acronym for an universal basic mental tool on thought process that consists of a chain of highlights: Focus – Concept (– Analysis) – Ideas (– Information) – Values.

OKAMIH as a SCHOLA LUDUS mental tool is substantial at any thought process, at developing TL materials as well as during realization of any stage of TL cycle (see below). It serves as tool for formal input or output of a thought process and also for assessment of thought development. Highlights in OKAMIH record the way of thinking and the respective progress of the thought process.

The content of OKAMIHs learning at any stage of TL cycle can differ from those for teaching.

Effective usage of OKAMIH means to keep thought discipline, e.g. to consider at once only to one focus via the chosen concept, to create ideas relevant to the respective couple of focus and concept, and afterwards to create from several values a decision towards future.

Hence, for example, formal outputs from several parallel thought processes are values that we can take into consideration in parallel. In addition, by OKAMIH we got genesis of the respective values. This is also why an effective usage of OKAMIH is one of the requirements for serious creativity.

TL COMPLEXITY

Complexity constitutes a comprehensive thinking approach. - Any object in the complexity frame is considered as a model of a complex dynamic system and/or a part of the complex system that is in mutual interaction with other parts of the same system.

For a TL conception of complexity there are obligatory outer features and inner interactions of the respective object including assumptions under which the model is considered and conditions at which the respective processes occur.

Complexity approach is about non-linearity, and also about probability and uncertainty, and questions of order and chaos. SCHOLA LUDUS intention is to introduce complexity even on lower secondary school level. A necessary assumption to master complexity within TL process at any level is application of parallel method [1].

The parallel method is applied principally in all fields of TL. It takes advantage from lateral thinking, and accelerates individual and collective thinking - stimulate learners to recognize aspects, attributes, functionality, essence and role of a key case.

Any TL process realized in the frame of a TL cycle is established on parallel cases. Also learners' ideas, sketches, models etc. can be used as parallel cases within a TL cycle.

SCHOLA LUDUS TL CYCLE

TLC represents the basic unit of the SCHOLA LUDUS pro-science teaching and learning. Educational conception of a TLC consists of 0+6 stages.

0. Pre-action. First experiences with matter as ordinary reality. Learners don't know the object of teaching. During action they recognize something that is extraordinary.

1. Describing. Simple description of the observed system/process, its features, details, phases of development as they are seen / felt / understood. – Definition of the problem.

2. Mapping. Finding different aspects of respective complex physical system. Classification of features within an aspects. – Definition of the field of the problem.

3. Modeling. Complex study of simplified reality. Building up functional models, realizing real and / or thought experiments. – Definition of potential of the problem with respect to deeper understanding the field.

4. Abstracting. Abstracting physical conditions of the system. Generalization. – Definition of general concepts, laws and conceptions.

5. Embedding. The findings of previous stages are put into the original context and/or learners´ scientific pre- and/or mis-conceptions. – Definition of the acquired conceptual change and novelty.

6. Appropriation. Changing current learning into operational knowledge. By solving a top case of TLC learners acquire awareness that possession of the respective knowledge has a personal potential for him/her. Commonly, the top case does not relate to the key case.

The key case, the respective parallel cases and the top case are indivisible parts of a TLC design. The role of the key case is to attract and motivate, the role of parallel cases is to stimulate, the role of the top case is to open horizons. The attractive key case is applied systematically at each level of the TLC as a reference case of parallel cases. The top case can be treated also as a key case of another teaching-learning cycle.

SCHOLA LUDUS TL THEORY IN PRACTICE

Any TLC should be supported by a TL frame - a table containing sketches of the respective key case, sets of parallel cases and the top case / cases of the TLC. The TL frame is considered as a strong tool for both, teachers and learners. It represents a TL synopsis. It helps to keep focus and time disciplines. It can be used as a base for tests. On the base of TL frame a teacher can decide for appropriate TL methods. By help of TL frame can learners formulate OKAMIHs etc.

To apply SCHOLA LUDUS theory in schools, teachers can decide between three main strategies of SCHOLA LUDUS authentic learning by play: spontaneous, directed and great creation and of variety of mostly non-formal procedures, let mention a very specific form of creative discovery workshop [1].

CONCLUSIONS

The SCHOLA LUDUS pro-science theory of TL is suitable for any TL subject, is applied at any current SCHOLA LUDUS programs for schools, teachers and public [5-8]. The challenges are - new programs and education. As the theory rises from eminent features of reality and applies creative-complexity thinking it seems to become also a tool for change of chliche: "We need Mathematics in order to develop thinking …" to "We need physics with pro-science TL to understand the world."

ACKNOWLEDGMENT: The author thanks to all former and current members of the SCHOLA LUDUS Project Group for their confidence in SCHOLA LUDUS TL theory, their enthusiastic realization of educational programs in style of SCHOLA LUDUS and huge effort for theory validation and dissemination of programs.

REFERENCES

1. K. Teplanová: Ako transformovať vzdelávanie: Stratégie a nástroje SCHOLA LUDUS na… (Metodicko-pedagogické centrum v Bratislave, Bratislava - 2007).
2. L. S. Vygotsky: Mind in society: The development of higher psychological processes (Harvard University Press, Cambridge, MA - 1978).
3. E. de Bono, Serious Creativity (HarperBusiness, USA-1992).
4. H. Gardner: Dimenze myšlení: Teorie rozmanitých inteligencí (Portál, Praha – 1999).
5. T. Bene, K. Teplanova, I. Bazovsky, GIREP Conference 2004 Proceedings: Teaching and Learning Physics in New Contexts (University of Ostrava – 2004).
6. M. Bazovsky, K. Teplanova, GIREP Conference 2004 Proceedings: Teaching and Learning Physics in New Contexts (University of Ostrava – 2004).
7. K. Teplanova, M. Matejka, GIREP - EPEC Conference 2007 Selected Contributions : Frontiers of Physics Education (Zlatni rez, Rijeka – 2008).
8. D. Šimunová, 17. Conference of Slovak Physicists (Slovak Physical Society, Bratislava – 2009).

SIGNIFICANCE OF SOLID DIGITAL RECORD IN LEARNING PROCESS BY SCHOLA LUDUS

M. Zelenák, mzelenak@gmail.com, K. Teplanová, teplanova@fmph.uniba.sk,
M. Matejka, miso.matejka@gmail.com

INTRODUCTION

Digital records that differ in one or more physical parameters can serve as an excellent base for study of complex processes /identification of system elements and their interaction, physical conditions, stages of progress, dominance of physical effects, etc./, deepening of elementary physical terms of school physics and improvement of complexity creative thinking as per educational programme by SCHOLA LUDUS. All the above is subject to suitably selected and recorded series of complex processes.

PHOTO AND VIDEORECORDS AT SCHOLA LUDUS TEACHING AND LEARNINIG

Fig. 1 shows conventional use of a pair of photos to approach a relatively slow process. The value of the above can be both informative and motivating.

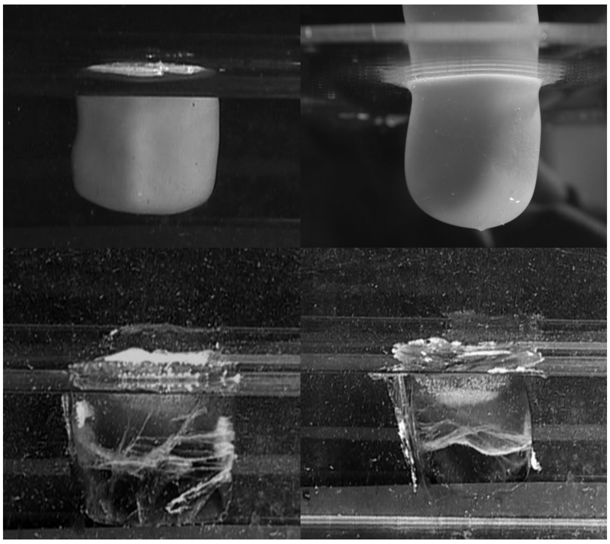

Fig. 1 Frozen oil /top/ and ice /bottom/ melting in water at t=0 and t=20 minutes. “Did you expect…?!“

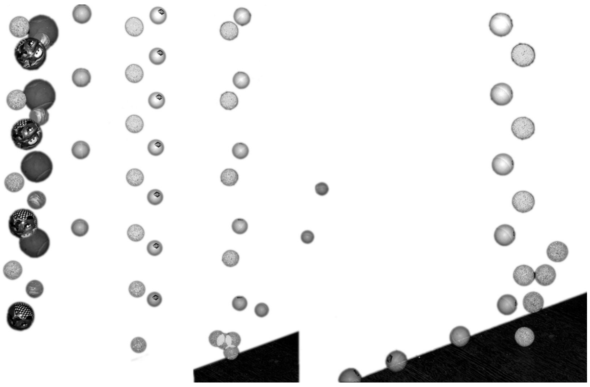

Fig. 2 Parallel falling of balls

Pictured balls (Fig. 2) represent several physical processes that can be used in very simple but sophisticated way: What can you see? What kind of physical process is recorded? Can you deduce any physical relation? Are some of these records an evidence of …? Are these processes mutually dependent or independent? What about the starting conditions? And what about the current conditions at fall and at collision/accident?

HAMMER AND CENTRE OF MASS

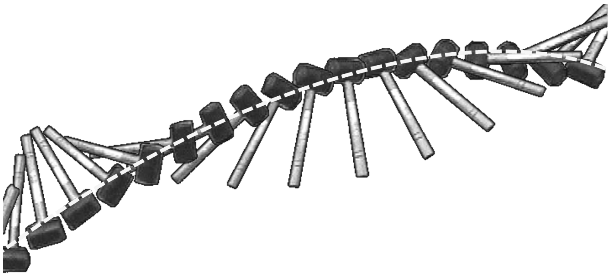

Fig. 3 Hammer’s centre of mass

Fig. 3 illustrates centre of mass of rotating non-homogeneous object in motion; in this instance the object is a hammer. To figure such an action, it is adequate to use stroboscopic shooting or videorecording, however, if the later is used it needs to be further edited in suitable bitmap editor, e.g. The Gimp, Adobe Photoshop. The first method requires special photo equipment – stroboscopic flash or light projector. The advantage of using this method is relatively simple post-processing. Apart from post-processing of videorecording being highly time consuming, several different software are required for editing compared to the other above mentioned method. Fig. 3 can be used in learning process by tutors for better illustration and consecutive understanding of behaviour of centre of mass in motion by students. The mergence of individual pictures into one seems to be crucial for overall topic understanding as more phases of subject’s motion (thrown rotating hammer in this case) can be seen in a single picture.

BOUNCING BALLOONS

Parallel method is largely adopted in Educational programmes by SCHOLA LUDUS. As shown in Fig. 4, adequately selected snapshots are presented next to each other in such a way, that this might evoke questions similar to the following, if seen few first cases: Why isn’t the empty balloon on the picture deformed? Can it be deformed at all? Are the changes after rebound so quick that they can’t be recorded? Furthermore, pictures can be selected in order to answer questions like these:

What was the order the pictures were shot in? (Fig. 5) Can you reconstruct the real process development?

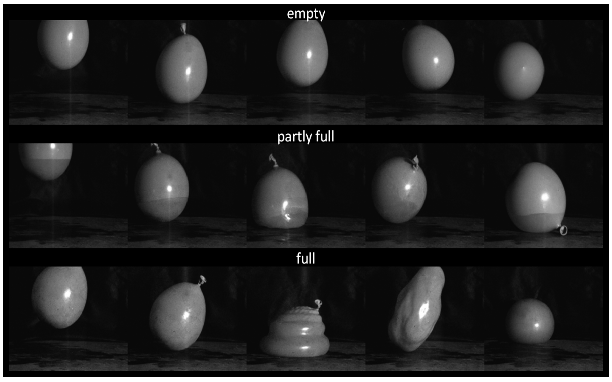

Fig. 4 Parallel visualization

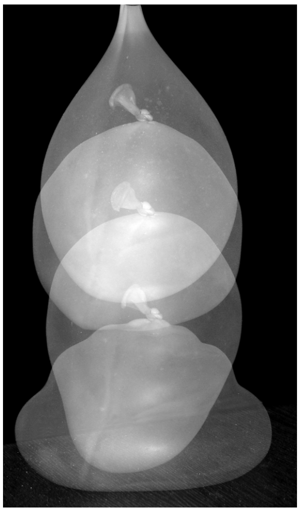

Fig. 5 Stroboscopic shooting

TIME-LAPSE IN MELTING

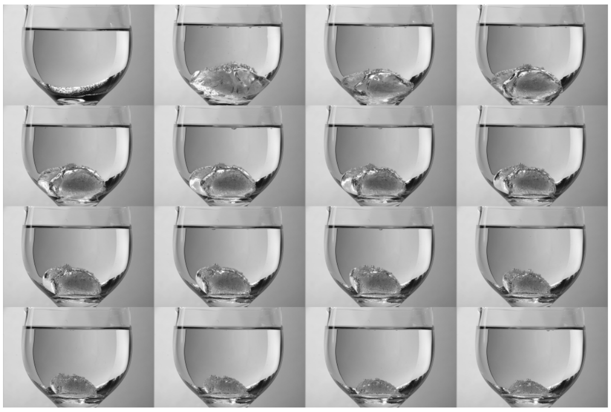

Fig. 6 Time-lapse in melting

Fig. 6 shows snapshots taken by time-lapse photography. The images taken by camera at the specific time intervals are converted to the video. This causes for observed processes to be speeded-up several times in comparison to the reality. This technique is useful when shooting slow processes such as crystallization, clouds movement, the growth of plants, etc. The final video then offers speeded up insight into observed action in return for a relatively small data space needed for high definition. Using the following formula it can be easily calculated how many times the video will be accelerated in comparison with real process.

$$AV = PVFR \cdot FI \qquad \text{(I)}$$

Acceleration Video /AV/ shows how many times is scene accelerated. Projection Video Frame Rate /PVFR/ is in EU countries 24 or 25 s^{-1}. Frame Interval /FI/ represents time between frames taken by photo camera.

Fig. 7 Various exposure times

Fig. 7 presents application of various exposure times to visualize intensity of fire/flame radiation. Long exposure time /the frame on left/ shows that flame is much more concentrated on the right side than in the middle of fire. Unlike on pictures taken with short exposure time /right frame/, many details are lost when using longer exposure time. To sum it up, to illustrate the direction of movement and group/object properties long exposure time is befitting. On the other hand, short exposure time captures the shape of objects in detail.

CONCLUSIONS

All the examples referred to in this article were prepared for SCHOLA LUDUS educational programmes and can be effectively used in different ways at any stage of SCHOLA LUDUS teaching and learning cycle for motivation, description, mapping, modelling, abstracting, imbedding as well as for appropriation [3].

Also, there are many non-formal possibilities how to use solid digital records to gain pupils and students for physics, e.g. by competitions – pupils capture records of attractive processes and provide their explanation [4] or cartoon physical jokes prepared on the base of records including original physical context [5].

REFERENCES

1. K. Teplanová: Ako transformovať vzdelávanie: Stratégie a nástroje SCHOLA LUDUS na komplexné a tvorivé poznávanie a učenie. 1. vyd. (Metodicko-pedagogické centrum, Bratislava – 2007).
2. M. Matejka, D. Šimunová, M. Zelenák: How can I draw it!? (Science on stage, Berlin - 2008).
3. K. Teplanová, in Proceedings of 17. Conference of Slovak Physicists (Slovak Physical Society, Bratislava – 2009).
4. E. Bagno et al.., Phys. Educ. 42 (2007) 45.
5. The SCHOLA LUDUS competition “Carton Physics Jokes”, http://www.scholaludus.sk/OFV/propozicie-e.htm.

WHY AND HOW TO TEACH PHYSICS AT TECHNICAL UNIVERSITIES

V. Kaššáková, viera.kassakova@stuba.sk, S. Minárik, stanislav.minarik@stuba.sk and J. Miština, juraj.mistina@ucm.sk

INTRODUCTION

Physics is an integral part of engineering education. However, there are some reports which indicate that in some engineering schools physics has lately either become a simple tool for specific engineering courses, or it is treated as a subject of low priority. We strongly hold the view that negligence in physics training will inevitably result in poor understanding of engineering subjects. In this paper we have introduced some recent trends in teaching physics to engineering undergraduate resulting in negative attitudes of general public, school managements and students as well. We try to illustrate it on the current state at the Faculty of Materials Science and Technology of The Slovak University of Technology in Trnava. In recent times, increased aversion to the subjects of natural sciences at every degree of the educational system can be seen. The only subject that has been tolerable among the general public, is mathematics. Although pupils and students have frequent problems with the acquirement of its content, in the consciousness of people is to hold that mathematics is needed in life and therefore it is considered natural that the foundation of it should be gained by everyone. In other science subjects such as physics, chemistry, biology, such awareness is lacking. It is not rare to meet with the view that to learn the fundamentals of science the person must be gifted, and therefore those subjects should not be taught to all children. The most frequent objection of parents to teaching science is to claim "...What will the knowledge of these subjects be for in real life? “. And in such a negative environment, a new generation is growing up. Unfortunately, currently we can meet such a phenomenon, that the people presenting in media their antagonism to science, showing off their poor results from these subjects, but emphasizing, that, in spite of the fact, they are successful earners and excellent people, are becoming idols of the generation. So, when young people decide how to orient their field of study, humanities clearly prevail. Only in the event of failure on the humanities-oriented study, the faculties of technical universities are considered. And again, the interest focuses primarily on the managerial and economy-oriented programs, or programs aimed at IT. And so the cycle of problems is repeated. Again, there is the emerging problem of physics, which is one of the subjects at the faculties of technical universities, making troubles and contributing to some unpopularity of technical studies.

PHYSICS AS A PART OF GRADUATE PROFILE

The problem of teaching in university technical education is global. The fact that scientific and mathematical skills are necessary for professional success in engineering professions is universally acknowledged. Why at technical universities to teach the subject that causes problems to most students, the subject reasoning in the lack of interest of secondary school graduates in programs with physics as one of compulsory subjects? Why to force future engineers or managers of technical disciplines to deal with the subject with which the majority of graduates will not meet anymore? These are the most common issues encountered by the majority of teachers providing instruction of physics or a basic course in physics at the University faculties. Even many professional colleagues, teachers of other subjects, often encourage students in their "theories" about uselessness of physics learning. It cannot therefore wonder that managements in many faculties of technical universities have decided to “attract” studies by simpler and more popular alternatives, such as reducing lessons in science, therefore in physics, too. In some faculties, testing was introduced only in a written form. The aim of each faculty of technical university is to prepare their graduates at the highest quality for professional practice. To fulfil this task is from year to year more and more difficult. A few years ago it was unthinkable that the applicant – the secondary school graduate did not know the difference between the linear and quadratic function, or to express relationship between two related variables by mathematical equation. Similarly, it can be heard that the third side of general triangle can be directly calculated using Pythagorean Theorem, or using goniometric functions. It is also true that at the bachelor degree of higher education you can now meet students, who a few years ago - when the secondary school graduates were enrolled to university studies on the basis of entrance examinations – did not even dream on university study. So in the university lecture halls, students who were purposefully prepared for higher education throughout the secondary school years can meet those students who came to the university simply “to try”. There is a large group of students who think that they are prepared for further education, but in fact they are only able to learn the prescribed curriculum, without having an idea of what actually are they learning about. Although for several decades of talk about replacing of memorising educational system by a system of understanding and comprehension, the conventional method of memorizing still prevails. A student who wishes to learn, it is often not able to, because the amount of new information to be acquired is so large that simply the semester is too short time to do it. If we consider the impact of the new environment, the need to become familiar with the new system of study without the teacher’s leadership (as it was in secondary school), these facts can call a chaos in student’s mind. The information from "experienced" older students can add up to the initial disorientation of most freshmen. Science subjects are often included in the first or second semester of bachelor degree, thus in the period when fresh university student is experiencing the greatest crisis of adaptation. How to do the students best handle the intermediate term, to be able to achieve those key issues of physics needed for further education, that they can rely upon them to deal with specific subjects?

- First, physics is necessary to be taught by qualified people and thus are familiar with it. It is quite sad that there are such cases when physics is taught by people, who graduated in physics related science – what, according to a part of the faculty management, is a sufficient qualification for admission to the Physics Department and teaching physics . It is not enough, that they are mastering physics, but they must try to pass on their enthusiasm to students. It should be realised that some students are interested in understanding lectured issues. In regard to the insufficient foundation from secondary school, undergraduates also need support and empathy of the teacher. It has to be considered that the bachelor degree is currently open to the broad masses of graduates of all types of secondary schools.
- From the beginning of teaching the "Physics" subject, students have to identify clear and understandable rules. Students will respect the rules only if they find they cannot be bypassed. But this requires a consistent approach from all teachers. The student was, is and will always be creative in order to outfox, circumvent the rules and to ensure the success s/he is willing to do the impossible.
- It is necessary to carefully consult the content and purpose of teaching curricula of particular branches of study and to align the objective of teaching the foundations of the theory of physical cognition. The knowledge content that a student has to learn must be judiciously chosen so that students have a clear association to the specific subject. To be obvious why they have to deal with a certain issue of physics, it should be pointed at what technical problem or phenomenon the knowledge is used for.
- Given that students admitted to the bachelor degree do not have the same knowledge level, it is needed, by the various supplementary lectures and courses, to allow those students who are interested in, to obtain the missing parts of the subject matter. Some years ago, the Faculty of Materials Science and Technology in Trnava sometime allowed students to choose from several optional compulsory subjects. One of them was the subject "Introduction to University Physics". It is a pity, that the subject, instead, there was preferred simpler alternative, and the subject has no longer being taught. Students thus have lost the opportunity of completing the necessary knowledge of the most elementary foundations of physics.
- Testing has to be organized so that students can demonstrate the awareness and depth of knowledge of the prescribed subject matter. It is not possible just to identify what a student knows at a mass written examination (all at once there are tested 100 to 120 students), where a few supervising teachers are unable to guarantee fair conduct of examinations. It is necessary to find out to what extent a student achieved the subject matter knowledge that can help him understand the theory of specific subjects. Students have to be tested in both written and oral forms. They should demonstrate the ability to communicate verbally on physical problems and should be able to articulate by using mathematical tools. But unfortunately, regarding the fact already mentioned - a very low knowledge level of secondary school graduates – that part of examination cannot be today considered a priority.

Although this may not be exactly the most popular act, but the consistency and requiring compliance with the study criteria should return to technical universities. It is striking that today most technical universities struggle with financial problems and so priority for funding is the number one. This problem influences all tertiary education. But if we allow that scrambling for funds will become prevalent in education, then we lose the opportunity to be a part of the countries, which can be proud of educated people.

INTERDISCIPLINARY APPROACH

Although it seems to be a secondary issue, but not only the physics departments, teachers of physics and faculty management can contribute to breaking the negative image of physics. There is a significant reserve seen in social science and humanities. The humanities subjects like philosophy of technology, history of technology, i.e. should bring more physics issues into their curricula, especially those they would "humanise" the view on physics as an impersonal, sterile, useless and outmoded subject. Their role should consist in finding mutual connections with other subjects, understanding its impact on the progress of humanity and pointing out the importance of its applications in everyday life of modern society. The good example from our workplace is cooperation of the Physics Department with the Department of Professional Language Communication. The teaching staff included several issues into the subject syllabus that can positively influence the students' approach to physics. For example, students develop projects on history of science, inventions and discoveries, where they can in a creative way search for, sort and evaluate sources, develop various outputs which they present developing their communication skills and competencies in foreign language realising physics in different "angle".

CONCLUSIONS

Teaching physics is challenging task. With the right positive attitude physics is becoming a tool that can students teach how to use the concepts of physics, in order that they may learn how to think like a scientist or engineer. And a "brain pool" of physics teachers, faculty managements and teachers of other subjects should be willing to consider new forms and new approaches for the process of education to improve the public perception of physics as a useful, interesting, and above all comprehensible human activity.

SCHOLA LUDUS CREATIVE-DISCOVERY WORKSHOP IN FORMAL AND NONFORMAL EDUCATION

V. Haverlíková, haverlikova@fmph.uniba.sk, M. Hodosyová, hodosyova@fmph.uniba.sk, SCHOLA LUDUS – Centre for Support of Science Education and Non-formal Lifelong Science Education, Faculty of Mathematics, Physics and Informatics, Comenius University, Bratislava, Slovakia

INTRODUCTION

Creative-discovery workshop (CDW) SCHOLA LUDUS is based on learning by pupils' own discovering. It is based on authentic learning by playing [1] as a strategy led to gaining serious experiences, knowledge and competencies. The SCHOLA LUDUS learning cycle is applied [1, 2].

Description of workshop "Modeling the sound propagation" depicts benefits of the CDW to the development of key universal and physics subject competencies and pupils' conceptions.

STRUCTURE OF CREATIVE-DISCOVERY WORKSHOP

1. *Assignment of the problem* - action with the key case and its description. The key case is usually attractive demonstration – real and therefore always a complex process – or a provocative statement. The key case motivates. It is a reference case. It can be introduced e.g. by provocative problem task, short skit or a video-recording.
2. *Looking for answers, solution* – mapping and modeling of parallel cases. Parallel cases are for example pupils' conceptions about the process, suggestions of a solution, or several different demonstrations of the same process. [1]
   The teacher drags pupils in her/his own "exemplar" thinking process – manages the development of pupils' learning process through questions, through her/his own contributions to hypothesizing, experimenting, modeling, etc..
3. *Evaluation of results* – includes abstraction, defining discovered concepts, formulating of the knowledge, setting bounds to its validity, embedding the new knowledge into existing structures, consciousness of the thinking progress and investigation of a top case as an application of gained knowledge in new context.

Thought-out alternation of individual and team work, small group and whole class discussions keeps pupils active and allows developing their cognitive, communicational, inter- and intrapersonal competencies.

CREATIVE-DISCOVERY WORKSHOP "MODELING THE SOUND PROPAGATION"

Modeling in school physics

Modeling as thinking process is declared in the state educational program - Physics for lower secondary education as one of developed physics subject competencies. Teaching physics is based on modeling and investigation of models. But in reality pupils cannot recognize, when they work with model and when they work with physical reality, in what condition is the model valid, what are limits of models' application. Even many upper secondary students think that everything that they learn in science lessons is real and accurate. This is why they are not able to recognize observation and theory, resp. model. [3]

To improve understanding of the term model and develop the modeling ability are two of the main goals of the CDW "Modeling the sound propagation".

Description of the creative-discovery workshop "Modeling the sound propagation"

CDW "Modeling the sound propagation" consist of two main parts: Introduction to modeling and Modeling the sound propagation. Required time refers to one/two lessons variant of CDW.

1. *Introduction to modeling* (8 / 15 minutes)

The key case = paper airplane

Action: Throwing a paper airplane

Description: What is this? Is it really an airplane? What are common and different signs of paper and real airplane?

Parallel cases = a castle dummy, cords with bells as a model of the laser object protection (example from a movie), a bag as a model of the corrival in sports training.

Mapping: What similarities and differences can we identify among parallel cases (models and originals)?

Modeling: Discussing attributes - signs, bounds and processes in selected models and originals.

Abstracting: What can be neglected, when and why? - Abstraction and idealization in process of models' creation (key case, parallel cases).

Embedding: Why we use models? Various criteria – finance, size, safety, accessibility, simplification, repeatability, slowdown/speed up processes etc.

Top case = sound propagation

Valuation: Let's try to create our own models!

2. *Modeling the sound propagation* (35 / 65 minutes)

The key case = Ball model as a provocation

Action: Throwing a ball in different conditions.

Description: Observing principles of balls' motion.

Parallel cases = waves on the string, waves on the water surface, movement of the spring (Fig.1) and string net (Fig.2)

Fig.1 Spring model

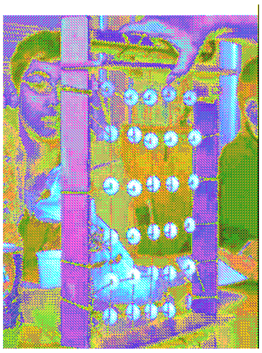

Fig.2 String net model

Mapping: Comparison proceeding of the ball model and the sound propagation (direct experimentation and discussing everyday experience).

Modeling: Comparison of parallel cases and the sound propagation, look for assigning components and bonds in the original and selected models.

Abstracting: Summarization of sound propagation patterns.

Embedding: Formulation of models' limitation. Formulation of advantages, disadvantages and limits of investigated models. Looking for the "best" model according to selected attributes.

Top case = "My own model"

Valuation: Suggestion of pupils' own models, mutual presentation of results, recommendation on particular models' improvement.

Benefit by the CDW "Modeling the sound propagation"

Addresses of the CDW "Modeling the sound propagation" can gain new facty knowledge and acquire or develop universal as well as subject competencies:

1. Facty knowledge

Knowledge about sound propagation:

- sound propagate in all directions;
- sound can be reflected, transmitted or absorbed by the barrier;
- sound propagate in gases, liquids and solids;
- material medium is required for sound propagation;
- pitch, loudness and tone quality;
- harmful effects of the sound.

Knowledge about modeling – understanding the relation original – model.

2. Developed competencies

Information: to chose appropriate information, apply gained information in problem solving.

Cognitive: to compare similarities and differences of two objects – the original and the model, fluency, flexibility, originality, redefinition, elaboration (I try to suggest a better model, improve my own model to stand the proof).

Interpersonal: team working, coordination.

Communication: to present information (clear and logic expressions), to hear comments, suggestions and questions, dispassionate argumentation.

Personal: assertiveness, enforce my own opinion in an appropriate way, accept a critic, self-motivation (I can be initiative, I am able to discover new knowledge).

Subject: to formulate the problem or question, to formulate hypothesis and verify them, to observe physical phenomena; design simple experiment and realize it; to sight analogies and utilize them; to model one process whit another; to be able find deficiencies in argumentation.

The creative-discovery workshop "Modeling the sound propagation" in formal and non-formal education

The creative-discover workshop "Modeling the sound propagation" was verified in condition of non-formal education (30 children aged 9-14, participants of summer camp SCHOLA LUDUS: Experimentáreň) and in conditions of formal school conditions (18 pupils aged 14-15, Alexander Dubček lower secondary school in Bratislava). Methodical sheet for teachers and pupils worksheets were prepared and used in school education.

Concepts of a model and modeling in context of physical education were strange to pupils at the beginning of the CDW. After the part "Introduction to modeling" pupils were able to work with selected models. They accepted provocative Ball model of the sound propagation and advised its' advantages and disadvantages. Comparison of selected models and everyday experience about sound propagation eventuated in discovering and formulation of basic properties of sound and principles of sound propagation. Form of creative-discovery workshop allowed teacher to detect and overcome pupils' misconceptions.

The sharpest differences were shown in testing of selected models of the sound propagation and in suggestion of pupils' own models. Better results were achieved by children in summer camp, nevertheless they were younger. Pupils' comparison of models and reality was insufficient; they didn't suggest any suitable model. This can be explained by abundant experience with active learning methods among summer camp participants. Furthermore many participants took part in the summer camp repeatedly. In camp one animator works with group of five children. Pupils are not used to formulate their own conceptions and change them actively. It is not enough to learn active only in one workshop per year. To change learning approach requires long-term systematic effort.

CONCLUSION

Discovery-creative workshop is at the top of active learning and teaching forms with regard to the demands imposed on teachers. But, at the same time, CDW is at the top of learning forms directed by pupils. Pupils learn in their own tempo – CDW is therefore a form suitable for slower pupils, for pupils with diagnosed learning disturbance, as well as for talented pupils. CDW allow active involving of pupils with problem behavior; everybody can access the task appropriately to her/his own abilities.

A crucial point of the creative-discovery workshops can be a possibility that pupils may handle mistaken solution. This risk is minimal if the teacher expects misconceptions and use them as advantage in order to understand how science occurs. Pupils should understand that even negative experimental result, shift the scientist towards.

REFERENCES

1. K. Teplanová: Ako transformovať vzdelávanie: Stratégie a nástroje SCHOLA LUDUS na komplexné a tvorivé poznávanie a učenie (Metodicko-pedagogické centrum, Bratislava – 2007)
2. K. Teplanová, in Contributions of 17. Conference of Slovak Physicists (Slovak Physical Society, Bratislava – 2009).
3. http://www.project2061.org/publications/bsl/online/index.php (5.9.2008)

CENTRE OF MASS IN MOTION - CONCEPTION AND REALIZATION OF A SCHOLA LUDUS EDUCATIONAL PROGRAMME

M. Matejka, miso.matejka@gmail.com, K. Teplanová, teplanova@fmph.uniba.sk, M. Zelenák, zelenak@fmph.uniba.sk

INTRODUCTION

A typical SCHOLA LUDUS programme is a complex educational module consisting of four complementary parts, each one of important function within the entire educational process:

- Interactive science theatre/show as a motivating activity with respect to a subject to be learned,
- Interactive exhibition as an activity stimulating to experimentation,
- Creative-discovery workshop for development of creative and complexity thinking skills and building systematic knowledge,
- Game-competition as a complex assessing activity.

Educational conception and realization of SCHOLA LUDUS programmes are based on theory of teaching and learning [1, 2 and 3]. The goal of SCHOLA LUDUS is to form complex teaching-learning units focused on chosen basic physical concepts including current science topics supported by modern technology and applications. In past years, we have prepared and realized educational modules centred on different topics, such as surface tension, Archimedes principle, motion and its visualization, sound and centre of mass [4].

In this contribution we present briefly the conception and realization of the creative-discovery workshop on “Centre of Mass in Motion” module addressed to secondary schools. Shortcuts of basic SCHOLA LUDUS educational concepts are as follows:

- CDW (Creative-Discovery Workshop)
- TLC (Teaching and Leaning Cycle)
- KC (Key Case)
- PC (A set of Parallel Cases)
- TC (Top Case).

CONCEPTION

A CDW [3] is a core activity of a SCHOLA LUDUS programme dedicated to students´ conceptual changes. The design of CDW is based on SCHOLA LUDUS TLC [2]. The KC of TLC on “Centre of Mass in Motion CDW” - motion of a strongly inhomogeneous symmetric box in the air is applied systematically in each level of TLC. The stages of the TLC are following:

1. Description:
   The box is thrown repeatedly (KC) - observation, drawing and description of the KC strange motion.
2. Mapping:
   Observation and sketching of motion of similarly thrown bodies: the strong inhomogeneous box, a perfectly homogeneous box and a rubber hammer (PC) (Fig. 1). Are body motions similar in some way? What are the differences?
3. Modelling:
   Observation and sketching of trajectories of the inhomogeneous box points – its corner, geometric centre and a specific point (centre of mass) (PC). Specific point trajectory is similar to a bullet’s trajectory but it is definitely not the geometric centre trajectory (Fig. 2). What kind of special point is it?
4. Abstracting:
   Solving the mass distribution of the inhomogeneous box. Comparing the trajectory of the inhomogeneous box centre of mass with a bullet and its centre of mass trajectory (PC). Can we represent the motion of a body by its centre of mass motion?
5. Imbedding:
   Dealing with the stroboscopic photographs of balls, a hammer and a pen motion in the air (PC) (Fig. 3) [5] - compound motion. A moving body can spin around its centre of mass and move itself “straight” at the same time. A decomposition of the body compound motion with respect to its centre of mass is valuable when describing/understanding and/or predicting/constructing the system behaviour. Let us use concept of compound motion to a system of several bodies, like a system of Earth-Moon-Sun!
6. Appropriation:
   Students’ appreciation of compound motion is gained by dealing with the Earth and the Moon around the Sun motion (TC). Students´ task is to sketch, step by step, in this order:
   - Trajectory of the centre of mass of Earth-Moon system around the Sun,
   - Trajectory of the Moon around the Sun and
   - Trajectory of the Earth around the Sun.

Having in mind the concept of the centre of mass students get a surprising result – the Earth is “waving” around the Sun (Fig. 4)! Of course, the scaling is not correct but the effect is present and sometimes also very important, e.g. at spacecraft navigation.

REALIZATION

All series of parallel cases are demonstrated by a facilitator. He or she throws objects repeatedly in a way of projectile motion. Students observe/deal with the processes and draw the pictures of them into their work sheets (See examples in Fig. 1, 2 and 4), formulate their own findings and conclusions.

Realization of the TLC on centre of mass in motion is supported with multimedia presentation including sequential pictures and slow motion video recordings of rubber hammer in the air and animation of Earth-Moon motion around the Sun.

CONCLUSIONS

During the CDW realization, students effectively understand the centre of mass as an outstanding physical point of the body/system of bodies with respect to its motion, as a representative point of the body “straight”

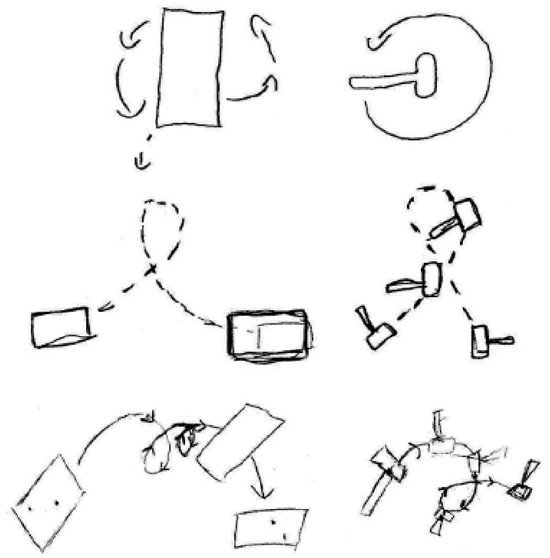

Fig. 1. Example of three students' drawings of homogeneous box and rubber hammer motion in the air (mapping level of TLC). Different motion visualizations.

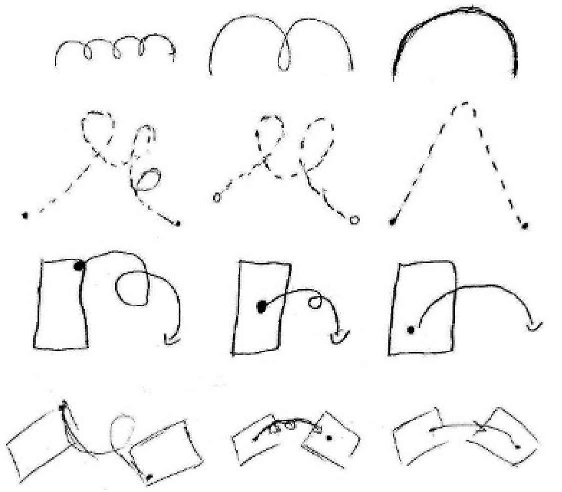

Fig. 2. Example of four students' drawings of trajectory shapes of inhomogeneous box corner, geometric centre and centre of mass (modelling level of TLC). Different trajectory visualizations.

motion, and a point around which the body rotates. In this way, students deepen their basic concepts of translation and rotation motion towards the complex motion based on the relationship between body motion trajectory and its centre of mass motion trajectory.

In addition, students are improving their pro-scientific thinking, developing their systematic creative cognition skills (by making use of analogies and models), visual thinking skills (by making their own sketches, understanding photo sequences), etc.

ACKNOWLEDGMENT: TLC described above was realized in a form of CDW as a part of educational module focused on the concept of centre of mass for more than 1000 students, 20 teachers and 11 secondary schools from Trenčín and Kolárovo thanks to financial support of European social fund, project „Veda hrou", ITMS: 11230310150.

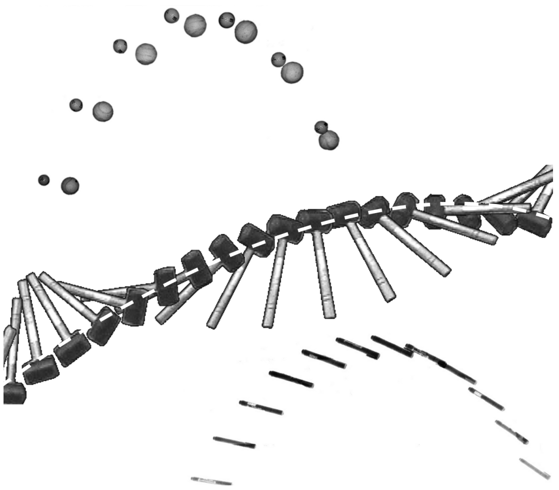

Fig. 3. Example from multimedia presentation. Stroboscopic photographs of balls, a hammer and a pen motion in the air (embedding level of TLC).

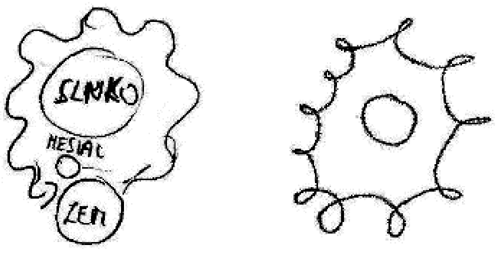

Fig. 4. Top Case problem solution. Example of students' drawings.

REFERENCES

1. K. Teplanová, Ako transformovať vzdelávanie: Stratégie a nástroje SCHOLA LUDUS na komplexné a tvorivé poznávanie a učenie (Metodicko-pedagogické centrum v Bratislave, Bratislava – 2007).
2. K. Teplanová, in Contributions of 17. Conference of Slovak Physicists (Slovak Physical Society, Bratislava – 2009).
3. K. Teplanová, M. Matejka, Selected Contributions from GIREP-EPEC Conference 2007, 158 (Zlatni Rez, Rijeka - 2008).
4. M. Matejka, Final Monitoring Report of European Social Fund project, ITMS: 11230310150 (FMFI UK, Bratislava – 2008).
5. M. Zelenák, K. Teplanová, M. Matejka, in Contributions of 17. Conference of Slovak Physicists (Slovak Physical Society, Bratislava – 2009).

DYNAMIC OF THE OUTER RADIATION BELT RELATIVISTIC ELECTRONS DURING MAGNETIC STORM ON DECEMBER 15, 2006

M.Slivka, slivka@kosice.upjs.sk,, Institute of Experimental Physics SAS, Watsonova 47, 04001 Košice, Slovakia

INTRODUCTION

The outer electron radiation belt is populated by relativistic electrons, strongly enhanced following some geomagnetic storms. These ~1 MeV electrons are called killer electrons, because they represent a serious potential hazard to orbiting satellites, space stations and humans in space.

In this paper we investigated relativistic electrons with energies 0.07 - 3.5 MeV, during strong magnetic storm occurred on December 15, 2006 (Dst = -146 nT), measured on “Universitetskiy – Tatiana” micro satellite. A more detail description of the apparatus measuring the energetic particles can be found in [1].

DATA ANALYSIS

The “Universitetskiy – Tatiana” micro satellite was launched on January 20, 2005 into a circular orbit with an inclination ~83^o and the initial altitude about 1000 km. In this paper we have used electron data with energies >70 keV, 0.3 - 0.6 MeV, 0.6 – 0.8 MeV and >3.5 MeV for monitoring relativistic electron dynamic.
Trapped radiation is described by particle fluxes as function of energy and of the geomagnetic co-ordinates L and B. The L is radial distance of the field line from the axis at the geomagnetic equator and B is the magnetic field strength. For correct comparison we selected the orbits when satellite crossed the same line in L-B space. This comparison is possible only with one day step.

We analyzed time interval between December 9 and 29, 2006. In this period was solar activity on low level on the beginning and increased to high levels on 13 December due to major flare of an X3/4B at 02.40 UT located at W21 and on 14 December due to another major solar flare of an X1/SF at 22.15 UT located at W31. Activity decreased to very low levels during 15-17 December with occasional B-class flares from region 930 [2]. This period was characteristic by strong magnetic storm on December 15. Two weak magnetic storms, first before this storm on December 12 with Dst=-41 nT and second one just after it on December 18 with Dst=-36 nT and with very long recovery phase till December 29 were observed.

Fig. 1 shows radial profiles of relativistic electron fluxes (0.3-0.6 MeV) measured on “Universitetskiy – Tatiana” micro satellite in the time of 15 December geomagnetic storm. The main phase of this storm started on December 14, 2006 (23.00UT). The radial profiles of relativistic electrons in the Fig.1a show their position and fluxes just during main phase of weak magnetic storm on December 12 (02-04 UT) and on the end of this storm (Dec.14) when the 0.3-0.6 MeV electron flux was F_e ~ 8.10^4 1/cm^2.sr.s and their maximum position L_{max}=4.7 R_E. This value is about one order higher in compare with this value during low geomagnetic activity interval (Dec. 10). After this, in the beginning of the main strong storm phase, decreased the electron fluxes about two orders to the value F_e=10^3 1/cm^2.sr.s (Fig.1b –Dec.15) and then they increased to the value about 5. 10^3 1/cm^2.sr.s during the first part of recovery storm phase (Dec. 16) and we can see also the shift of the maximum position from L_{max}=4.7 R_E on Earthward direction to L_{max}=3.5 R_E. This value is in good agreement with the relation between the maximum storm amplitude and position of maximum electron fluxes proposed by Tverskaya [4]: $|Dst|_{max}$= 2.75 x 10^4 / $L_{max}{}^4$.

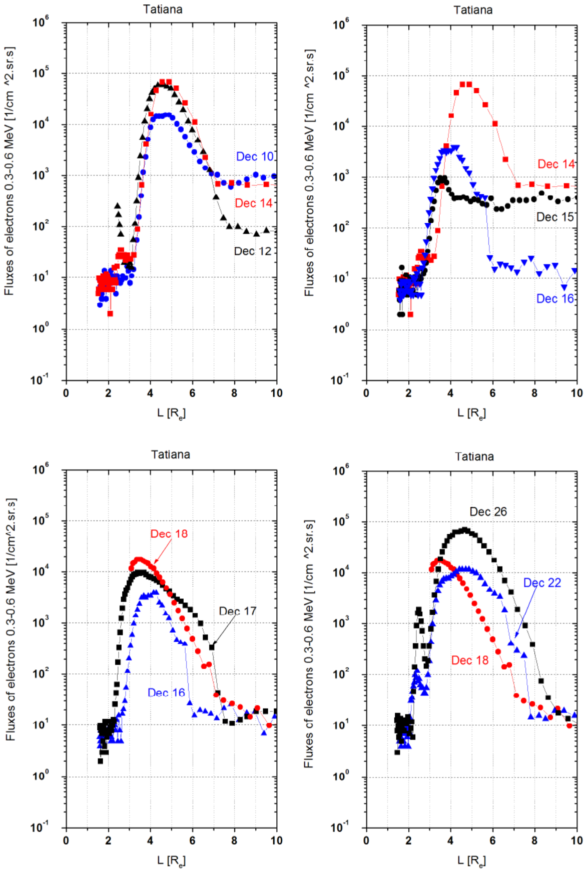

Figure 2. The radial profiles of relativistic electron fluxes (0.3-0.6 MeV) measured on “Universitetskiy – Tatiana” micro satellite in the time of 15 December 2006 geomagnetic storm.

The increase of electron fluxes continued during all recovery phase and they reached values F_e ~ 2.10^4 1/cm^2.sr.s on December 17 (See Fig.1c). During next weak storm on December 18 the position of electron maxima was till December 20 in region with L_{max}=3.5 R_E and during second part of weak storm recovery phase it return to the pre-storm position (L_{max}=4.7 R_E) on December 26 (see Fig.1d).

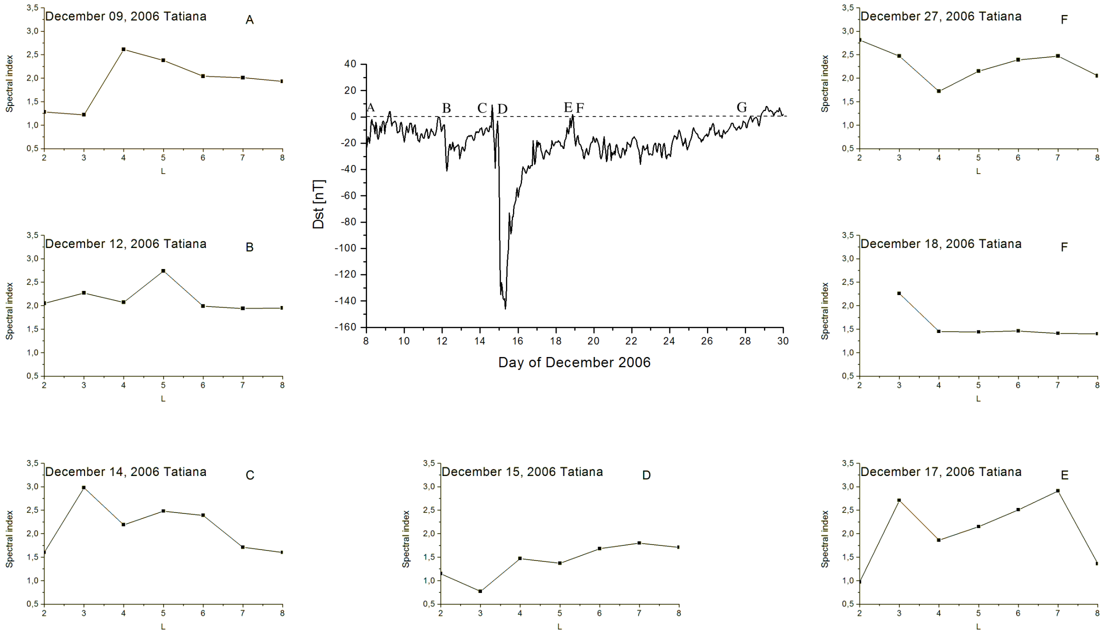

Figure 2. The behavior of spectral indices versus L parameter dependences for rather phases of December 15, 2006 geomagnetic storm.

Using data with energies 0.07 – 3.5 MeV we constructed energy spectra of relativistic electrons in outer radiation belt region. Figure 2 shows the behavior of spectral indices γ versus L parameter dependences for rather time intervals of December 2006. The behavior of this storm is pointed by time dependence of Dst index and by capital letters A, B, C, D, E, F and G are sign posted electron spectral indices for rather L. From this figure we can see that during weak storm times between December 8 and 13 (A, B) and also during the initial phase of strong storm on December 14 we observed more soft electron energy spectra (C). During main December 15, 2006 storm phase we observed harder energy spectrum of relativistic electrons (D). The same hard spectra we observed during the main phase of next weak storm on December 18 (F). During recovery storm phases of these two storms (E resp. G) the energetic spectra of relativistic electron were again softer. These results are in good agreement with these obtained for the same storm by Tverskaya et al. [3] according GLONASS satellite measurements.

CONCLUSIONS

It is evident that the dynamic of relativistic electrons during strong magnetic storms time can be characterized by four phases mentioned before in paper [5] according our research of severe magnetic storms on May 15, 2005 with Dst= -256: P1. rapid decrease of electron fluxes during the main phase of the storm; P2. rapid increase of electron fluxes at the beginning of recovery storm phase; P3. radial shift of electrons maximum earthward into the slot region during first part of the recovery phase; P4. return of the electrons maximum to the pre-storm position during the second part of the recovery phase.

It is only one difference between these two storms. The May 15, 2006 storm was single magnetic storm and the return of the electron maximum to the pre-storm position was realized during its recovery phase. The December 15, 2006 magnetic storm hasn't one step character and therefore the next weak storm on December 18, when the electron maximum was situated on L_{max}~3.7 R_E, caused the deceleration of its return to the pre-storm position till December 26. This shows that also the weak storm can influence on relativistic electron dynamic if it follows after strong one. On the other hand December 12, 2006 weak magnetic storm increased about one order the fluxes of relativistic electron but didn't change the position of their maximum.

During the main storm phase the electron flux shows spectral hardening in comparison with others storm phases. This is valid not only for strong December 15 storm but also for weak magnetic storm on December 18, 2006. The energy spectra behavior on the different L isn't the same. These testify to different mechanism of electron acceleration in these regions. Also the fluxes of electrons in lower energy channels changed more during December 15 magnetic storm time in comparison with higher one's.

ACKNOWLEDGEMENTS: The author thanks Dr. I.N.Myagkova from MSU Moscow for "Universitetskiy – Tatiana" micro satellite data. This work was supported by the VEGA Grant agency; project 2/7063/27.

REFERENCES

1. V.A. Sadovnichy et al., Cosmic Res. Abstr., **6**, 04226, (2004).
2. Space weather Highlights 11-17 December 2006.
3. L.V.Tverskaya et al., Geomagnetizm i Aeronomiya, **48**, 6, 751, (2008).
4. L.V.Tverskaya, Geomagn. Aeron., **26**, 864, (1986).
5. M.Slivka, K.Kudela, S.N.Kuznetsov, Proc. of 15-th Conference of Slovak Physicists, Stará Lesná 2006, editor: M.Reiffers, 85, (2006).

STUDY OF RADIO EMISSIONS AT MICROWAVE RANGE PRECEDING TO THE LARGE FORBUSH DECREASES

V.S.Prokudina, prok@sai.msu.ru, Sternberg Astronomical Institute, Moscow State University. Moscow 119992, Universitetskij pr. 13, Russia
M.Slivka, slivka@upjs.sk, K.Kudela, kkudela@upjs.sk, Institute of Experimental Physics SAS, Watsonova 47, 04001 Košice, Slovakia

INTRODUCTION

The object of this paper is the study of peculiarities of solar flares at microwave radio range for the events preceding to the large Forbush decrease (FD)[a]. It is known that FD is observed after the solar flares and caused by the disturbances at solar wind[b] during the spreading of coronal mass ejections (CME)[c] , magnetic clouds (MC)[d] and interplanetary shocks (IPS)[e] to the Earth. The questions about the relationship between the FD, CME and geomagnetic storms (GS)[f] are discussed at various publications [1-7]. The ejection of the plasma from the solar flares is the main condition for the increase of the density at the solar wind, if we may judge from the observation of CME, and hence that is important for the manifestation of FD.

We suppose, that the solar microwave radio bursts from the solar flare may be another important parameter, connected with plasma ejection, in addition to CME. According to statistical analysis of microwave bursts and CME, 60-84% of halo CME with velocity v>1000 km/s correlated with microwave bursts at frequency f = 2-20 GHz and the flux F >1000 units (10^{-22} W/m^2 .Hz) [8].

ANALYSIS OF OBSERVATIONAL DATA

We considered the flares with the large microwave bursts at the frequency f=15.4 GHz and the fluxes F_{max}>1000 units during 1998-2005 and compared it with the observations of Forbush decreases. At the Table 1 are given the most interesting data about FD (date, decrease at %) [9,10] and for the solar flares (date, importance in X ray and in optic, coordinate, flux at the f=15.4 GHz F_{max} and active region) [11]. The data about CME and solar wind are contented at SOHO and ACE catalogues [12,13]. Figure 1 shows two of the largest Forbush decreases, namely on August 26, 1998 and on October 29, 2003 at two different neutron monitors.

It is noticed that the flares were of M and X classes and accompanied by the radio bursts of II and IV types at metric radio range (it means the propagation of the shocks and plasma ejection through corona), and also by CME with large velocities v>1000 km/s [12]. From the analysis of data we may conclude, that at the majority of the flares, preceding to FD, is observed the large microwave bursts with F_{max} >1000 units, more over, at several cases the flux F_{max} was of 3-4 orders more than usual.

It is known, that at famous events: VIII. 1998, X-XI.2003., VII.2000, II-IV.2001, I.2005 and XI.2004 were observed very large Forbush decreases with values from 10% to 20%. At all these events the flux of microwave radio bursts during the flares reach the extreme values $F_{max}=10^4 - 5.10^4$ units (see the Table 1). As a rule, the flux F_{max}>1000 units coincided with the events FD ~3-4%.

As the correlation between hard X-Ray (HXR)[g] and microwave emission exists, it is not surprised, that during large FD the power HXR were observed, if we consider the data from [14,15].

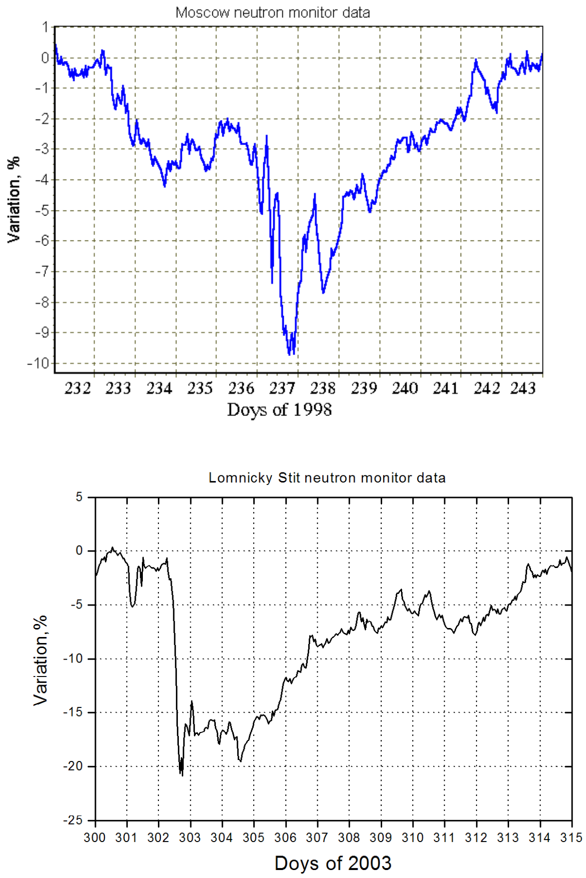

Fig.1. The Forbush decreases, measured on August 26, 1998 by Moscow neutron monitor (a) and on October 29, 2003 by Lomnicky Stit neutron monitor (b).

But it is important to say about several exclusions at our results. At first, the FD events with small microwave fluxes were observed, that may be explained by existence of corotating interaction regions (CIR)[h]; and second, on the contrary, large microwave bursts without the power FD existed. So the question about the conformity of FD and microwave bursts require the special analysis of solar wind, CIR and geomagnetic effects.

CONCLUSION

During the solar flares, preceding to the Forbush decrease (>3-10%) were observed the large microwave bursts at f =15.4 GHz with values $F_{max} > 10^3$-10^4 units.

Because the radio bursts caused by the ejection of solar plasma and energetic particles and determined the disturbances of solar wind, it may be the useful parameter, also as CME, at the study of Forbush effect and its foresight.

ACKNOWLEDGEMENTS: This work was supported by the VEGA Grant agency; project 2/7063/27.

Table 1. The list of the solar flares with microwave bursts for large FD events.

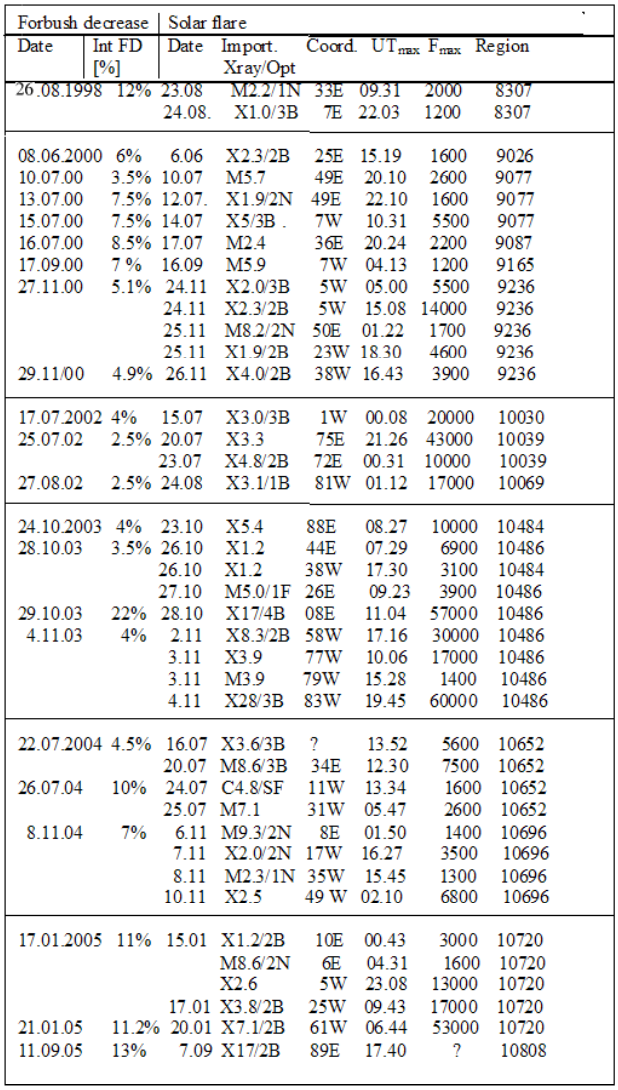

Forbush decrease		Solar flare					
Date	Int FD [%]	Date	Import. Xray/Opt	Coord.	UT_{max}	F_{max}	Region
26.08.1998	12%	23.08	M2.2/1N	33E	09.31	2000	8307
		24.08.	X1.0/3B	7E	22.03	1200	8307
08.06.2000	6%	6.06	X2.3/2B	25E	15.19	1600	9026
10.07.00	3.5%	10.07	M5.7	49E	20.10	2600	9077
13.07.00	7.5%	12.07.	X1.9/2N	49E	22.10	1600	9077
15.07.00	7.5%	14.07	X5/3B .	7W	10.31	5500	9077
16.07.00	8.5%	17.07	M2.4	36E	20.24	2200	9087
17.09.00	7 %	16.09	M5.9	7W	04.13	1200	9165
27.11.00	5.1%	24.11	X2.0/3B	5W	05.00	5500	9236
		24.11	X2.3/2B	5W	15.08	14000	9236
		25.11	M8.2/2N	50E	01.22	1700	9236
		25.11	X1.9/2B	23W	18.30	4600	9236
29.11/00	4.9%	26.11	X4.0/2B	38W	16.43	3900	9236
17.07.2002	4%	15.07	X3.0/3B	1W	00.08	20000	10030
25.07.02	2.5%	20.07	X3.3	75E	21.26	43000	10039
		23.07	X4.8/2B	72E	00.31	10000	10039
27.08.02	2.5%	24.08	X3.1/1B	81W	01.12	17000	10069
24.10.2003	4%	23.10	X5.4	88E	08.27	10000	10484
28.10.03	3.5%	26.10	X1.2	44E	07.29	6900	10486
		26.10	X1.2	38W	17.30	3100	10484
		27.10	M5.0/1F	26E	09.23	3900	10486
29.10.03	22%	28.10	X17/4B	08E	11.04	57000	10486
4.11.03	4%	2.11	X8.3/2B	58W	17.16	30000	10486
		3.11	X3.9	77W	10.06	17000	10486
		3.11	M3.9	79W	15.28	1400	10486
		4.11	X28/3B	83W	19.45	60000	10486
22.07.2004	4.5%	16.07	X3.6/3B	?	13.52	5600	10652
		20.07	M8.6/3B	34E	12.30	7500	10652
26.07.04	10%	24.07	C4.8/SF	11W	13.34	1600	10652
		25.07	M7.1	31W	05.47	2600	10652
8.11.04	7%	6.11	M9.3/2N	8E	01.50	1400	10696
		7.11	X2.0/2N	17W	16.27	3500	10696
		8.11	M2.3/1N	35W	15.45	1300	10696
		10.11	X2.5	49 W	02.10	6800	10696
17.01.2005	11%	15.01	X1.2/2B	10E	00.43	3000	10720
			M8.6/2N	6E	04.31	1600	10720
			X2.6	5W	23.08	13000	10720
		17.01	X3.8/2B	25W	09.43	17000	10720
21.01.05	11.2%	20.01	X7.1/2B	61W	06.44	53000	10720
11.09.05	13%	7.09	X17/2B	89E	17.40	?	10808

REFERENCES

1. K. Kudela, R. Brenkus, J. Atm.Sol.-Ter. Phys., **66**, 1121, (2004).
2. K. Kudela, M.Storini, J. Atm. Sol-Ter. Phys., **67**, 907, (2005).
3. S.C. Kaushik, A.K.Shrivastava, H.M.Rajput, Proc. 29 ICRC, Pune, **2**, 151, (2005).
4. R.F.Penna, A.C.Quillen, J.Geophys.Res., **110**, A09S05, doi:101029/2004JA010912, (2005).
5. S.O.Ifedili, Earth Planets Space, **58,** 5, 659, (2006).
6. S.W.Kahler, G.M.Simnett, Proc. 29th ICRC, Pune, **2**, 267, (2005).
7. Su Yeon Oh, Lu Yi, Y.H.Kim, J.Geophys.Res., **113**, AO1103, (2008).
8. Brian I. Dougherty, H.Zirin, K.Hsu, Statistical Correlation between Solar Microwave Bursts and Coronal Mass Ejections, Preprint, (2006).
9. http://helios.izmiran.rssi.ru/cosray/events.htm
10. http://sgd.ngdc.noaa.gov/sgd/
11. http://www.swpc.noaa.gov/ftpdir/indices/
12. http://cdaw.gsfc.nasa.gov/CME_list
13. http://lasp.colorado.edu/space_weather/dsttemerin/archive/dst_years.html
14. http://hesperia.gsfc.nasa.gov/hessidata
15. Chik-Yin-Lee, H.Wang, Solar Phys., **195**, 149, (2006).
16. http://en.wikipedia.org/wiki/

---

[a] Forbush decrease (FD) is a rapid decrease in the observed cosmic ray intensity following a CME [16].

[b] Solar wind (SW) is a stream of charged particles and plasma continuously ejected from the Sun.

[c] Coronal mass ejection (CME) is an ejection of material from the solar corona.

[d] Magnetic Cloud (MC) is a transient events observed in the SW.

[e] Interplanetary shock (IPS) is a non-linear plasma wave generated by plasma flow in interplanetary space.

[f] Geomagnetic storm (GS) is disturbance or fluctuation in the Earth's outer magnetosphere, usually caused by streams of charged particles (plasma) given off by solar flares.

[g] Hard X-ray (HXR) is X rays with energies > 10 keV.

[h] Corotating interaction region (CIR) is region of compressed plasma at the interface between fast and slow SW flows.

SPIN HALL EFFECT – SPIN POLARISATION INDUCED BY SPIN-ORBIT INTERACTION AND BY INTERNAL MAGNETIC FIELD

František Horvath, frantisek.horvath@gmail.com, Peter Bokes, peter.bokes@stuba.sk, Lucia Kičínová,
kicinova.lucia@gmail.com, Jaroslav Tóbik, jaroslav.tobik@stuba.sk
Slovak University of Technology, Faculty of Electrical Engineering and Information Technology, Ilkovičova 3,
812 19 Bratislava

INTRODUCTION

In the spin Hall effect (SHE) observed in 2D samples (Fig. 1) “spin-up” electrons are deflected to the one side of the sample and “spin-down” electrons are deflected to the opposite side. No magnetic field is required to produce the SHE. Theoretical studies predicted the SHE originating from asymmetries in scattering for up and down spins, which is referred to as an extrinsic SHE. The SHE offers a promising method with which to spatially separate electron spins without external magnetic field [1].

In this paper we study the influence of edge potential on spin polarisation and the effect of the internal magnetic field induced by current and its possible enhancement of the polarisation in the presence of paramagnetic substrate. We assume the sample is without impurities [2, 3].

2D MODEL OF THE SAMPLE

We studied the spin polarisation in 2D sample, which is schematically shown in Fig. 1. Electron current flows in *y* direction and electrons with opposite spins in *z* direction are accumulated on the sample opposite edges in *x* direction respectively. The sample is infinite in the *y* direction and in the *z* direction electrons are confined within the sample.

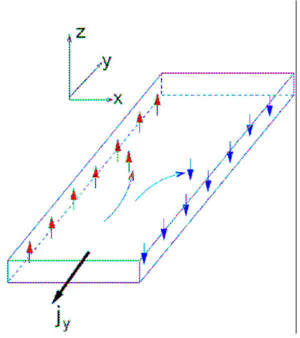

Fig. 1. 2D sample. Electron current flows in *y* direction and electrons with opposite spins in *z* direction are accumulated on the sample edge in *x* direction.

Tab. 1. Typical magnitudes of electrons density (*n*), current density (*j*), step in confining potential energy (V_1), spin-orbit coupling (λ_0) and the Fermi energy (E_F) in SI and a.u.* units.

	SI	a.u.*
N	1.04×10^{12} cm^{-2}	1.0
J	2.8×10^{-6} A/µm	0.01
V_1	2.72 eV	229
λ_0	4.6×10^{-10} m	5.53×10^{-4}
E_F	35.28 meV	3.01

For all the reported quantities we use the effective atomic units (a.u.*). Typical magnitudes in SI and a.u.* units used are presented in Tab.1.

The Schrödinger equation for the x-dependent part of the wavefunction for this model is:

$$\left(-\frac{1}{2}\frac{\partial^2}{\partial x^2}+V(x)+U_\sigma(x)\right)\chi(x)=\varepsilon\chi(x)\,, \qquad (1)$$

where $\varepsilon = E - k_y^2/2$ and k_y is a quantum wave number in y direction, $V(x)$ is potential energy from sample edges that confines electrons within the sample and $U_\sigma(x)$ is a small correction, which is spin-dependent and essential for the appearance of the spin polarisation. In the following we will consider two different physical mechanisms responsible for the spin-dependent potential.

SPIN SEPARATION BY SPIN-ORBITAL INTERACTION

In case of spin-orbit interaction the term $U_\sigma(x)$ is $V_{SO}(x)$, which has simple form

$$V_{SO}(x) = -\lambda\sigma_z \frac{dV}{dx} k_y\,, \qquad (2)$$

where σ_z is Pauli matrix, $\lambda = -10^6 \times \lambda_0$ for GaAs [4].

We computed the spin polarisation only for one edge of the sample with the model potential shown in Fig. 2.

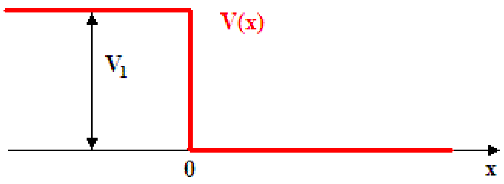

Fig. 2. Dependence of potential on the left edge of the sample.

The spin polarisation is obtained as a difference between the densities of "spin up" and "spin down" electrons. The latter is computed directly from the wavefunctions fulfilling Eq. 1. The other parameters specifying the presented calculation are: total bulk electronic density n =0.958 and the current density j=0.05. The resulting spin polarisation, shown in Fig.3, shows a pronounced maximum of the spin-down electrons near the left edge of the sample.

The magnetization per unit length of the sample (in *y* direction) is obtained by integration,

$$M = \int dx\,[n_\uparrow(x) - n_\downarrow(x)]\,. \qquad (3)$$

Its dependence on the current density at constant electron density n = 0.958 is in Fig. 4. We see that magnetization grows linearly with the current density with the slope dM/dj = -5.5x10^{-4}, in agreement with previous theoretical work [6]. Furthermore, in [2] it has been found that the magnetization is independent of the electron density.

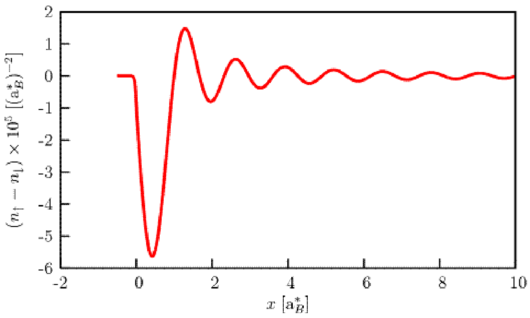

Fig. 3. The spin polarisation in x direction exhibits Friedel-like oscillations near the left edge of sample.

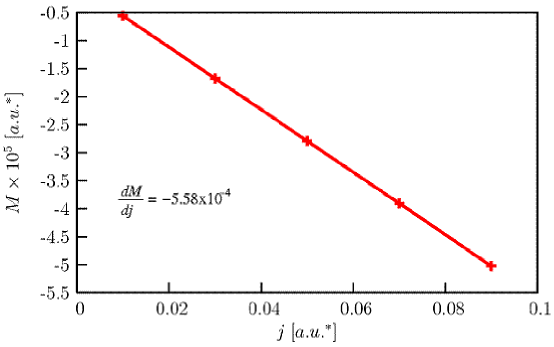

Fig. 4. Evidently linear dependence of the magnetization on the current density (electron density n = 0.958).

SPIN SEPARATION BY INDUCED MAGNETIC FIELD

Here, the source of the spin-dependent potential energy is the magnetic field induced by the current in the sample. Since the field has large extent, we have considered both edges of the sample with the total width in the x direction $100a_B$*.

We have computed the current density directly from the eigen-functions of the Schrödinger equation (for the details see [3]) which subsequently gave the induced magnetic field according to the relation [5]

$$B_y(x') = -\frac{\mu_1}{2\pi}\left(\int \frac{j(x)}{(x-x')}dx + \frac{\mu_2-\mu_1}{\mu_1+\mu_2}\int \frac{j(x)}{(x-x')}dx\right),$$

where the magnetic permeability μ_2 accounts for the paramagnetic substrate. For $\mu_2 \to \infty$ the magnetic field is at most twice as large as in the case without the paramagnetic substrate. Therefore, the presence of the substrate has no significant influence on the polarisation.

Magnetic field imposes spin-dependent potential energy in the Schrödinger equation (Eq. 1), $U_\sigma(x) = \pm\mu_B B$, (its value in a.u.* is ~ 10^{-6}). We have computed the difference in the electron density in the x direction for electrons with opposite spins using perturbation method, Fig. 5, with j = 0.05. Since both edges were used, we see both – the “spin-down” electrons dominant near the left edge of the sample, as well as the “spin-up” electrons dominant near the right edge of the sample. Similarly to the case with the spin-orbit interaction (Fig. 3), the Friedel oscillations are visible. Polarisation caused by the induced magnetic field is of the same order as polarisation caused by spin-orbit interaction.

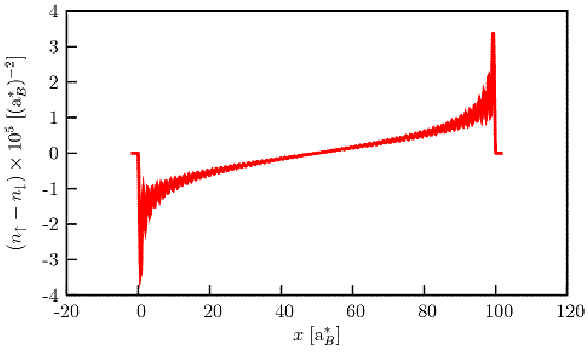

Fig. 5. Difference of electron density in x direction for electrons with opposite spins by sample width 100 a_B* due to current-induced magnetic field.

CONCLUSIONS

We have studied the influence of the edge potential on spin polarisation. The calculated magnetization corresponds to 1 uncompensated spin per 20 000 electrons. The spin polarisation caused by the induced magnetic field was 1 uncompensated spin per 25 000 electrons. Hence the polarisation caused by the induced magnetic field is comparable with polarisation induced by spin-orbit interaction. The presence of paramagnetic substrate has marginal influence on the polarisation.

ACKNOWLEDGMENT: We acknowledge the support of Slovak Grant Agency VEGA (Project No. 1/0452/09).

REFERENCES

1. V. Sih, Y. K. Kato, D. D. Awschalom, Physics World **18**, 33 (2005).
2. Horváth, F.: Spinový Hallov jav – indukcia spinovej polarizácie spin-orbitálnou interakciou. Bratislava: FEI STU, 2009. Master Thesis.
3. Kičínová, L.: Spinový Hallov jav - indukcia polarizácie vnútorným magnetickým poľom. Bratislava: FEI STU, 2009. Master Thesis.
4. H. A. Engel, B. I. Halperin, E.I. Rashba, Phys. Rev. **95**, 166605 (2005).
5. D. Mayer, J. Polák: Metody řešení elektrických a magnetických polí, Státní nakladatelství literatury, Praha 1983.
6. P. Bokes, F. Corsetti and R. Godby, Phys. Rev. Lett. **101**, 046402 (2008).

THE INFLUENCE OF AN EXTERNAL PARALLEL MAGNETIC FIELD ON A NANOPARTICLE GRATING CREATED IN A MAGNETIC FLUID

C. Musil, J. Štelina,stelin@fel.uniza.sk Department of Physics, University of Žilina, Univerzitná 1, 010 26 Žilina, Slovakia, P. Kopčanský, M. Timko, Institute of Experimental Physics, Slovak Academy of Sciences, Watsonova 47, 043 53 Košice, Slovakia

INTRODUCTION

In this article are presented the results of a study of the influence of an external magnetic field oriented in the direction of the interference patterns and lying in their plane on a nanoparticle grating created by means of an interference field set up by two crossed coherent Ar laser beams. The experiment was realized on the magnetic fluid $CO_{0.5}Zn_{0.5}Fe_2O_3$ by using an optical beam of an Ar laser with $\lambda = 488$ nm whose absorption in studied liquid is $\alpha_a \approx 0.075\ \mu m^{-1}$. Adequate absorption is important for the creation of a temperature and consecutively of a nanoparticle grating. The diffraction on this grating is used for study of the kinetics of the nanoparticles in them.

EXPERIMENTAL

The usual arrangement of the experimental setup for the interference of two crossing Ar beams was used [1], [2] (Fig.1).

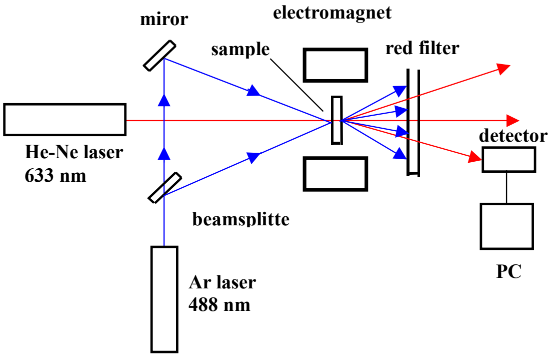

Fig. 1. The basic scheme of the apparatus used for the study of the nanoparticle kinetics in the dispersion fluids.

The light energy was supplied into the grating by means of one of the two beams, which created the nanoparticle grating. The influence of by this way supplied energy into the grating was presented in the past [3, 4], and we can see it in Fig.2.a and Fig.2.b.

Beside that the setup was supplemented by two electromagnets driven by a direct-current element. In this way the regulation of the magnetic induction B in the grating was made possible.

EXPERIMENTAL RESULTS

A sample of the magnetic liquid ($CO_{0,5}Zn_{0,5}Fe_2O_3$) was placed in the cell that was about 65 μm thin. The interference nanoparticle grating was created by means of crossing of two coherent Ar laser beams with $\lambda = 488$ nm and power of 11 mW /mm^2 (Fig. 1). This grating was during its decay illuminated by one of the two laser beams and the magnetic field parallel to the grating patterns was present, too (Fig. 3).

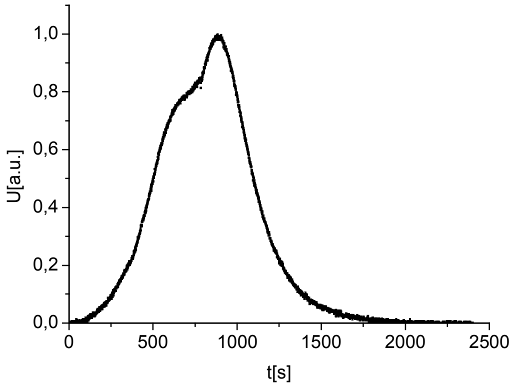

Fig. 2a. The time dependence of the rise and decay of the nanoparticle grating without additional lighting.

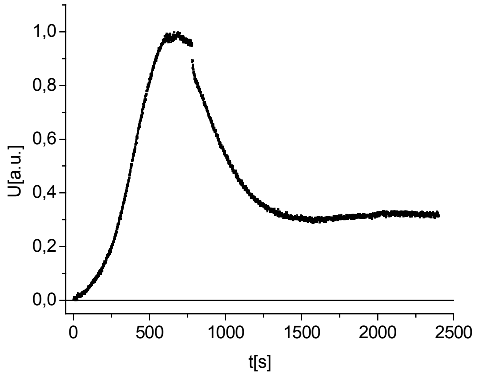

Fig. 2b. The time dependence of the rise and decay of the nanoparticle grating with additional lighting of 6 mW/mm^2.

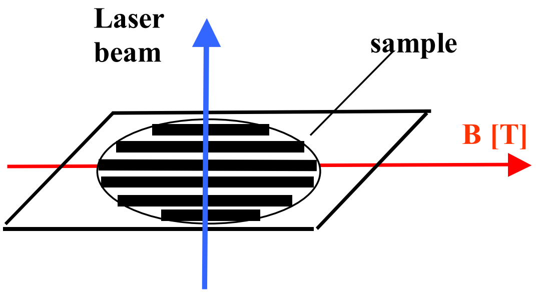

Fig.3 The relative position of the laser beam, the magnetic induction vector and nanoparticle grating

We present the time dependencies of the decay of the created nanoparticle grating that were recorded by means of the intensity of the first diffraction maximum of the diagnostic beam at $\lambda = 632$ nm from He-Ne laser (Fig. 4). In Figs. 4a, 4b, 4c, 4d are shown the time

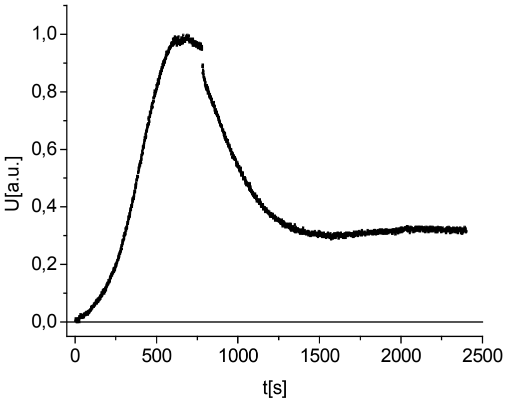

Fig. 4a. The decay of the grating at B = 8 mT

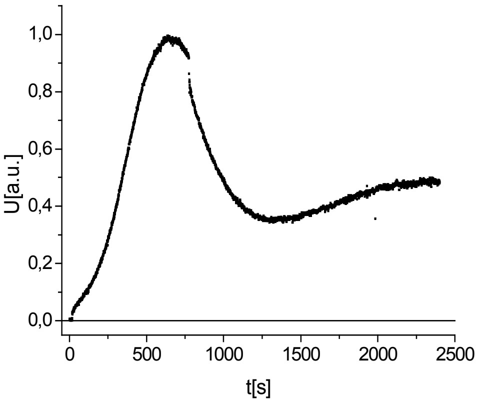

Fig. 4b. The decay of the grating at B = 16 mT

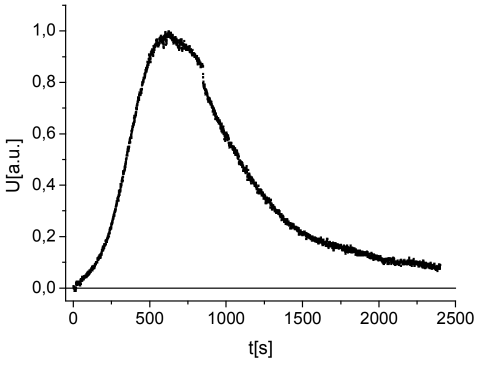

Fig. 4c. The decay of the grating at B = 24 mT

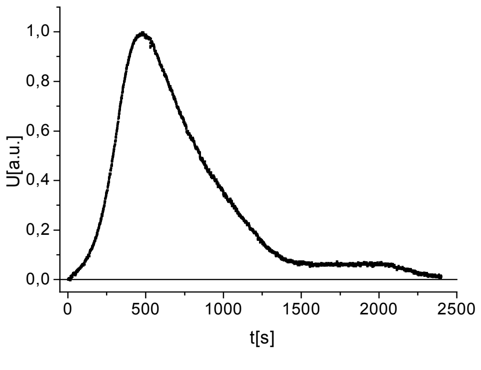

Fig. 4d. The decay of the grating at B = 30 mT

dependencies of the first maximum of the signal from the decaying nanoparticle grating when the magnetic field B is applied.

CONCLUSIONS

As was discovered in the past, the additional lighting with a suitable wavelength, i.e. such wavelength that is absorbed in the sample and that induces the rise of a suitable temperature gradient between the strips of the grating, can stabilize the grating or eventually make it of a better quality. But if at the same time a magnetic field is applied in the direction of the strips of the grating and in their plane, a better quality of the grating is observed at first. When the value of the magnetic field is above 12 mT, the stabilizing effect of the additional lighting is removed (Fig. 4d).

REFERENCES

1. A. Mezulis, E. Blums, A. Bourdon, G. Demouchy: Proceeding of the Fourth International PAMIR conf. on MHDDTM, Presquile de Giens, France, 781 (2000).
2. J. Štelina, C. Musil, M. Držík: Proceedings of the 13th International Conference on applied Physics of Condensed Matter (2007) 88.
3. J. Štelina, C.Musil, J. Braciník, P. Kopčanský, M. Timko, L. Tomčo**:** Proceedings of the 12th International Workshop on APCOM, Malá Lučivná (2006) 256.
4. C. Musil, J. Štelina, P. Kopčanský, M. Timko**:** 15th conf. of Slovak physicists, Stará Lesná,11. –14. 9. 2006.

CALCULATIONS OF THE BINDING ENERGIES OF MAGNESIUM ISOTOPES IN THE FRAMEWORK OF THE RELATIVISTIC MEAN-FIELD THEORY

J. Leja, jozef.leja@stuba.sk, Faculty of Mechanical Engineering, Slovak University of Technology, Bratislava
Š. Gmuca, gmuca@savba.sk, Institute of Physics, Slovak Academy of Sciences, Bratislava

INTRODUCTION

The paper deals with the calculations of the binding energies of even-even magnesium isotopes from proton drip-line nucleus ^{20}Mg to neutron drip-line nucleus ^{40}Mg. The calculations have been performed in the framework of the relativistic mean-field theory with four different parameterizations.

THE RELATIVISTIC MEAN-FIELD THEORY

The model [1] starts from a Lagrangian density (1) including nucleon field, isoscalar-scalar σ-meson field, isoscalar-vector ω-meson field, isovector-vector ρ-meson field and electromagnetic field.

$$\begin{aligned}
L = {} & \overline{\psi}_i \left(i\gamma_\mu \partial^\mu - M\right)\psi_i + \\
& \overline{\psi}_i \left[g_\sigma \sigma - g_\omega \gamma_\mu \omega^\mu - g_\rho \gamma_\mu \vec{\tau}.\vec{\rho}^\mu - e\gamma_\mu \frac{(1-\tau_3)}{2} A^\mu\right]\psi_i + \\
& + \frac{1}{2}\partial_\mu \sigma \partial^\mu \sigma - \frac{1}{2} m_\sigma{}^2 \sigma^2 - \frac{1}{4} O_{\mu\nu} O^{\mu\nu} + \frac{1}{2} m_\omega{}^2 \omega_\mu \omega^\mu + \\
& - \frac{1}{4}\vec{R}_{\mu\nu}\vec{R}^{\mu\nu} + \frac{1}{2} m_\rho^2 \vec{\rho}_\mu \vec{\rho}^\mu - \frac{1}{4} F_{\mu\nu} F^{\mu\nu} + \\
& - \frac{1}{3} b_\sigma \sigma^3 - \frac{1}{4} c_\sigma \sigma^4 + \frac{1}{4} c_\omega \left(\omega_\mu \omega^\omega\right)^2 \qquad (1)
\end{aligned}$$

The masses M, m_σ, m_ω, m_ρ, the coupling constants g_σ, g_ω, g_ρ, and the selfinteraction constants b_σ, c_σ, c_ω, are the free parameters of the model.

The field equations follow from the Euler-Lagrange equations in a standard way. Two approximations are necessary for their solution.

- **The mean-field approximation** introduced by replacing the field operators for mesons and electromagnetic fields by their expectation values.
- **The no-sea approximation** realized by exclusion of the filled Dirac sea of negative energy states.

The nucleon spinor can by written in standard form (2).

$$\psi_i(r,z,\varphi) = \frac{1}{\sqrt{2\pi}} \begin{pmatrix} f_i^+(r,z) e^{i\left(\Omega_i - \frac{1}{2}\right)\varphi} \\ f_i^-(r,z) e^{i\left(\Omega_i + \frac{1}{2}\right)\varphi} \\ i g_i^+(r,z) e^{i\left(\Omega_i - \frac{1}{2}\right)\varphi} \\ i g_i^-(r,z) e^{i\left(\Omega_i + \frac{1}{2}\right)\varphi} \end{pmatrix} \zeta_i \qquad (2)$$

The ζ_i represents the isospinor and quantum number Ω_i is the eigenvalue of operator J_z.

The components of nucleon spinor obey the set of Dirac equations (3-6).

$$\left(M^* + S + V_0\right) f_i^+ + \partial_z g_i^+ + \left[\partial_r + \frac{\left(\Omega_i + \frac{1}{2}\right)}{r}\right] g_i^- = \varepsilon_i f_i^+ \qquad (3)$$

$$\left(M + S + V_0\right) f_i^- - \partial_z g_i^- + \left[\partial_r - \frac{\left(\Omega_i - \frac{1}{2}\right)}{r}\right] g_i^+ = \varepsilon_i f_i^- \qquad (4)$$

$$\left(M + S - V_0\right) g_i^+ + \partial_z f_i^+ + \left[\partial_r + \frac{\left(\Omega_i + \frac{1}{2}\right)}{r}\right] f_i^- = -\varepsilon_i g_i^+ \qquad (5)$$

$$\left(M + S - V_0\right) g_i^- - \partial_z f_i^- + \left[\partial_r - \frac{\left(\Omega_i - \frac{1}{2}\right)}{r}\right] f_i^+ = -\varepsilon_i g_i^- \qquad (6)$$

The S and V_0 denote scalar and vector potentials calculated from scalar and vector fields (7, 8).

$$S = g_\sigma \sigma \qquad (7)$$

$$V_0 = g_\omega \omega_0 + g_\rho \tau_3 \rho_0^{(3)} + e\frac{(1-\tau_3)}{2} A_0 \qquad (8)$$

The meson fields and electromagnetic field obey the Klein-Gordon equations (9-12).

$$\left(-\frac{1}{r}\partial_r r \partial_r - \partial_z^2 + m_\sigma^2\right)\sigma = -g_\sigma \rho_S - b_\sigma \sigma^2 - c_\sigma \sigma^4 \qquad (9)$$

$$\left(-\frac{1}{r}\partial_r r \partial_r - \partial_z^2 + m_\omega^2\right)\omega_0 = g_\omega \rho_V + c_\omega \omega_0^3 \qquad (10)$$

$$\left(-\frac{1}{r}\partial_r r \partial_r - \partial_z^2 + m_\rho^2\right)\rho_0^{(3)} = g_\rho \rho_I \qquad (11)$$

$$\left(-\frac{1}{r}\partial_r r \partial_r - \partial_z^2\right) A_0 = e\rho_P \qquad (12)$$

The source terms of Klein-Gordon equations are the scalar density (13), the vector density (14), the isovector density (15) and the proton density (16).

$$\rho_S = 2\sum_{i>0}\left[\left(\left|f_i^+\right|^2 + \left|f_i^-\right|^2\right) - \left(\left|g_i^+\right|^2 + \left|g_i^-\right|^2\right)\right] \qquad (13)$$

$$\rho_V = 2\sum_{i>0}\left[\left(\left|f_i^+\right|^2 + \left|f_i^-\right|^2\right) + \left(\left|g_i^+\right|^2 + \left|g_i^-\right|^2\right)\right] \qquad (14)$$

$$\rho_I = 2\sum_{i>0}\tau_3\left[\left(\left|f_i^+\right|^2 + \left|f_i^-\right|^2\right) + \left(\left|g_i^+\right|^2 + \left|g_i^-\right|^2\right)\right] \qquad (15)$$

$$\rho_P = 2\sum_{i>0}\frac{(1-\tau_3)}{2}\left[\left(\left|f_i^+\right|^2 + \left|f_i^-\right|^2\right) + \left(\left|g_i^+\right|^2 + \left|g_i^-\right|^2\right)\right] \qquad (16)$$

The expression for the total energy (17) can be derived from Lagrangian density.

$$E = \sum_i \varepsilon_i - \frac{1}{2}\int \left(g_\sigma \sigma \rho_S + g_\omega \omega_0 \rho_V + g_\rho \rho_0^{(3)} \rho_I + e A_0 \rho_P \right) d^3x + \\ - \int \left(\frac{1}{3} b_\sigma \sigma^3 + \frac{1}{4} c_\sigma \sigma^4 - \frac{1}{4} c_\omega \omega_0^4 \right) d^3x \qquad (17)$$

The pairing correlations have been introduced using the BCS theory [2] and the pairing energy and the centre of mass correction have been included into the total energy.

PARAMETERIZATIONS

Four different Lagrangian parameterizations have been used for our calculations.

- **NL-BA** [3] is new parameter set dealing with a fit to a large body of observables related to ground-state properties of selected doubly-magic nuclei covering a wide variation of isospin. The predicted properties of nuclear matter indicate improvement for the incompressibility coefficient while the symmetry energy remains practically the same as in the other parameterizations.
- **NL4** [4] is parameter set obtained by minimizing the root-mean-square deviations of the macroscopic part of binding energies of 142 spherical even-even nuclei from the values obtained with the Lublin-Strasbourg Drop model. The new parameters reproduce also the radii of these nuclei with accuracy comparable to that obtained with NL1 and NL3 sets.
- **TM2** [5] is a parameter set very suitable for light nuclei. It includes a non-linear ω-meson selfinteraction term in addition to the non-linear σ-meson selfinteraction terms, the necessity of which is suggested by the relativistic Brueckner-Hartree-Fock theory of nuclear matter.
- **TMA** [6] is a parameter set which interpolates TM1 and TM2 parameter sets with very week mass dependence. These parameter sets were invented to describe ground state properties of heavy (TM1) and light (TM2) nuclei. We may interpret this mass dependence as a mean to effectively express the quantum fluctuations beyond the mean-field level or the softness of the nuclear ground states in deformation, pairing and alpha clustering in light nuclei.

RESULTS

Calculated binding energies have been compared with the data taken from the atomic mass evaluation AME 2003 [3]. The differences between calculated and experimental binding energies are plotted in Fig. 1.

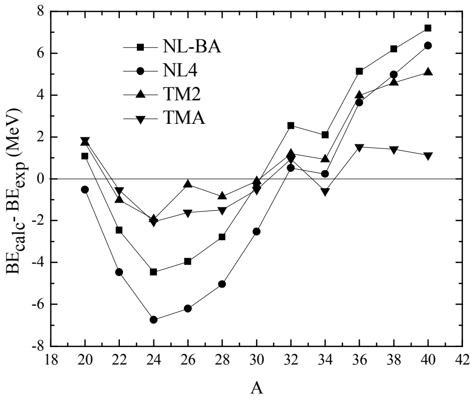

Fig. 1. The differences between calculated and experimental binding energies of magnesium isotopes

The results obtained with the NL-BA and the NL4 parameterizations are similar. Both parameterizations predict low binding energies around the N=Z nucleus ^{24}Mg and high binding energies in the neuton-rich region. TM2 predicts equivalent result in the neutron rich region but binding energies around the N=Z nucleus are calculated with good precision. The values obtained with the TMA parameterization around the N=Z nucleus are as good as the TM2 results. The situation in the neutron rich region is gratifying. TMA is the only parameterization which predicts binding energies of heaviest magnesium isotopes close to experimental values.

CONCLUSION

The comparison of calculated binding energies with experimental results shows two possibilities to improve the model predictions.

- **To introduce ω-meson selfinteraction term** which is important in the N=Z region.
- **To use mass dependent parameter set** which predicts acceptable values also for the heaviest magnesium isotopes.

REFERENCES

1. J. D. Walecka: Theoretical Nuclear and Subnuclear Physics (World Scientific, Singapore - 2004).
2. P. Ring, P. Shuck: The Nuclear many-Body Problem (Springer, New York - 1980).
3. Š. Gmuca, Proc. 2nd Int. Conf. Fission and Properties of Neutron Rich Nuclei, St. Andrews, Scotland, June 28-July 3, 1999, 75, World Scientific 2000.
4. B. Nerlo-Pomorska, J. Sykut, Int. Jou. Mod. Phys. **E13**, 75 (2004)
5. Y. Sugahara, H. Toki, Nucl. Phys. **A579**, 557 (1994).
6. Y. Sugahara: Doctor Thesis (Tokyo Metropolitan University, Tokyo – 1995)
7. G Audi et al., Nucl. Phys. **A729**, 337 (2003).

SPECIFIC PARTIAL AREA OF CHOLESTEROL IN MONOUNSATURATED DIACYLPHOSPHATIDYLCHOLINE BILAYERS

J. Gallová, gallova@fpharm.uniba.sk, Faculty of Pharmacy, Comenius University, 832 32 Bratislava, SR, D. Uhríková, uhrikova@fpharm.uniba.sk, Faculty of Pharmacy, Comenius University, 832 32 Bratislava, SR, N. Kučerka, Norbert.Kucerka@nrc.gc.ca, Canadian Neutron Beam Centre, National Research Council, Chalk River, Ontario K0J 1P0 Canada, J. Teixeira, jose.teixeira@cea.fr, Laboratoire Leon Brillouin (CEA-CNRS), CEA Saclay, Gif Sur Yvette Cedex, F-91191 France and P. Balgavý, balgavy@fpharm.uniba.sk, Faculty of Pharmacy, Comenius University, 832 32 Bratislava, SR

INTRODUCTION

Phospholipid bilayer is a basic structural element of cell membranes. Polar groups of phospholipids are located at the lipid - water interface, nonpolar acyl chains are in the interrior of bilayer to avoid contact with water. Different kinds of proteins are more or less embeded into the bilayer. The function of these proteins depends on physicochemical properties of the lipid bilayer. Cholesterol (CHOL), a ubiquitous component of mammalian cell membranes, plays an important role as a modulator of the structural and dynamical properties of the bilayer. If the phospholipid bilayer is in a liquid - crystalline state, CHOL (A) increases the conformational order of phospholipid acyl chains, thereby increasing bilayer thickness (ordering effect) and (B) decreases the surface area occupied by phosphatidycholine molecules on the lipid - water interface (condensing effect). These effects were verified by different experimental methods for bilayers consisting of saturated acyl chains but are less documented for acyl chains containing double bonds.

In this work, the effect of increasing concentration of CHOL on the bilayer thickness and area per molecule at water-lipid interface was studied by a small angle neutron scattering (SANS). Unilamellar liposomes made of monounsaturated diacylphosphatidylcholines (diCn−1PC, n=14, 18, 22) were used as an appropriate model of lipid part of biological membranes.

EXPERIMENT

diCn−1PC was co-solubilized in chloroform with an appropriate amount of CHOL. The chloroform was then evaporated under a stream of nitrogen gas followed by vacuum pumping. The lipid film was then dispersed in D_2O at a total lipid concentration 10 g/l. After homogenization, unilamellar liposomes were prepared by the dispersion extrusion through polycarbonate filter with pores of 50 nm diameter.

The SANS measurements were performed on the PAXE spectrometer located at the end of the G5 cold neutron guide on the Orphée reactor (Laboratoire Léon Brillouin, CEA Saclay, France). The experiments were performed with the sample to detector distance of 1.77 and 5.07 m and the neutron wavelength of λ=0.6 nm. The sample temperature was 30.0±0.1°C. The acquisition time for one sample was 30 min.

The normalized SANS intensity $I_{exp}(Q)$ in cm^{-1} units as a function of the scattering vector modulus $Q=4\pi\sin\theta/\lambda$, where 2θ is the scattering angle, was obtained as described in detail in [1]. An example of data is shown in Fig. 1, together with the best fits as obtained using an advanced evaluation model of lipid bilayer as a three-strip structure with a triangular shape of the probability distribution of polar head groups [2]. The volumetric data used in the analysis are the same as in [3]. The model's mathematical description [2] allows to evaluate the lateral area A_{UC} (surface per unit cell consisting of one diCn−1PC molecule and a particular fraction of CHOL) and the total thickness d_{TOT} while the polar region thickness is constrained to d_H=1 nm [2].

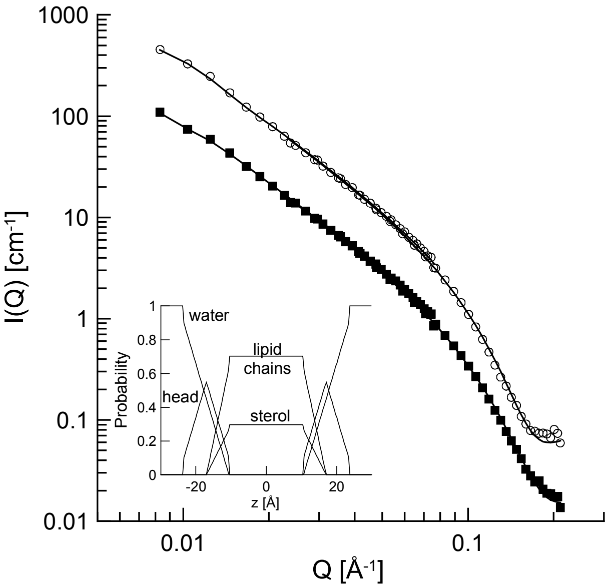

Fig. 1. Experimental SANS data obtained from unilamellar vesicles prepared from pure diC14−1PC bilayers (■) and those containing 33 mol% of CHOL (□). Scattering curves are shifted vertically for clarity of presentation. Solid lines correspond to the best fits. The volume probability distributions is shown in the inset as a dependence on the distance *z* from the bilayer centre.

RESULTS

To estimate the magnitude of the condensing effect, one has to calculate independently the areas per diCn−1PC molecule, a_{PC}, and CHOL molecule, a_{CHOL}, using known values of A_{UC}. According to [4], specific partial areas for diCn−1PC and CHOL as a function of CHOL molar fraction $X=N_{CHOL}/(N_{CHOL}+N_{PC})$ were defined

$$a_{CHOL}(X)=\left(\frac{\partial A(X)}{\partial N_{CHOL}}\right)_{N_{PC}} \qquad a_{PC}(X)=\left(\frac{\partial A(X)}{\partial N_{PC}}\right)_{N_{CHOL}} \qquad (1)$$

where *A* is the whole surface of phospholipid bilayers,

N_{CHOL} and N_{PC} are the numbers of CHOL and diCn−1PC molecules in the sample. It was shown [4] that

$$\frac{A(X)}{N_{PC}} = A_{UC} = a_{PC}(X) + \frac{X}{1-X} a_{CHOL} \qquad (2)$$

The example of the concentration dependence of A_{UC} for diC14−1PC is in the Fig 2. A_{UC} depends linearly on the molar ratio CHOL : diCn−1PC for all phosphatidylcholines studied. As follows from this fact and Eq. 2, specific partial areas a_{PC} and a_{CHOL} are constant and do not depend on the concentration of CHOL in the diCn−1PC bilayer. They represent real areas of CHOL and diCn−1PC at lipid – water interface. Their values are listed in Tab. 1. Thereby we have shown that CHOL does not condense the area occupied by diCn−1PC molecule at lipid – water interface.

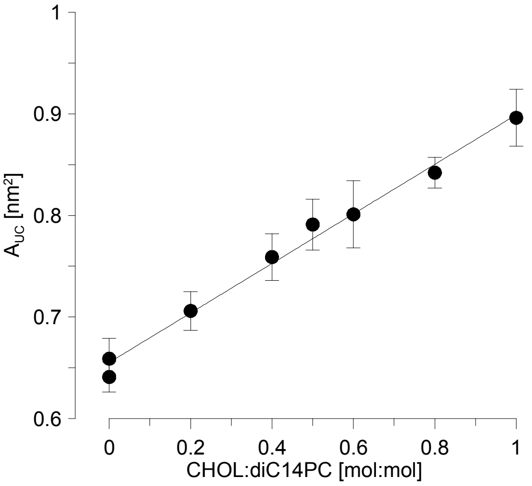

Fig. 2. Dependence of A_{UC} on the molar ratio of CHOL to diC14−1PC.

The area for diC18−1PC is in excellent agreement with [5]. Similarly as in [6], the area of diC18−1PC is larger than those for shorter and longer diCn−1PC.

TAB. 1. The partial-specific area of CHOL and diCn−1PC (n=14, 18, 22)

	a_{CHOL} [nm^2]	a_{PC} [nm^2]
diC14-1PC	0.246±0.010	0.652±0.005
diC18-1PC	0.234±0.007	0.673±0.003
diC22-1PC	0.259±0.014	0.634±0.008

Similar a_{CHOL} value (0.27 nm^2) was determined at high CHOL concentration as X approached 0.5 in diC16−0PC with saturated acyl chains [4]. Of course, for $X \leq 0.1$, a_{CHOL} was negative, what indicated a strong condensing effect of CHOL on diC16−0PC [4].

Different results regarding CHOL condensing effect were obtained by several other authors (see [7] for citations) who assume that the area per CHOL molecule in phospholipid bilayer does not depend on the lipid type and is the same as in CHOL monolayer (0.39 nm^2).

The ordering effect of CHOL on diCn−1PC acyl chains is manifested by the increase in the bilayer thickness (Fig. 3). These results are in agreement with [3].

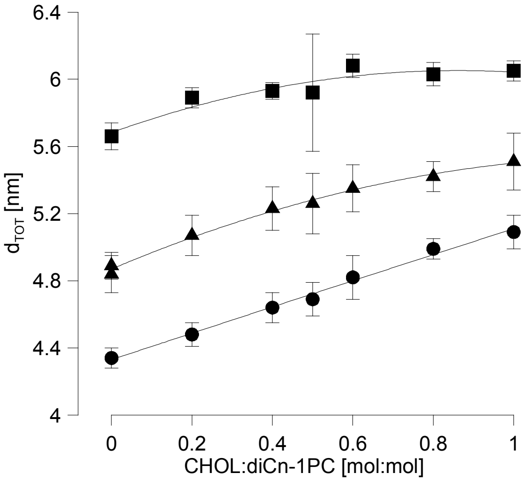

Fig 3. Dependence of A_{UC} on the molar ratio of CHOL. diC14−1PC (●), diC18−1PC (▲), diC22−1PC (■).

CONCLUSIONS

Cholesterol occupies cca 0.25 nm^2 at the interface of diCn−1PC bilayeyr and aqueous phase.

The condensing effect of CHOL on the surface of diCn−1PC at lipid - water interface is negligible.

The increase of diCn−1PC bilayer thicknes with increasing CHOL content proves the ordering effect of CHOL.

ACKNOWLEDGMENT: This work was supported by the European Commission through the Access Activities of the Integrated Infrastructure Initiative for Neutron Scattering and Muon Spectroscopy (NMI3), supported by the European Commission under the 6th Framework Programme through the Key Action: Strengthening the European Research Area, Research Infrastructures, Contract N0:RII3-CT-2003-505925, by the Dubna JINR 07-4-1069-09/2011 project and by the VEGA 1/0295/08 grant.

REFERENCES

1. N. Kučerka, D. Uhríková, J. Teixeira, P. Balgavý, Acta Facult. Pharm. Univ. Comenianae **50**, 78 (2003).
2. N. Kučerka, J.F. Nagle, S.E. Feller, P. Balgavý, Phys. Review E **69**, Art. No. 051903 (2004).
3. N. Kučerka, J. Pencer, M.P. Nieh, J. Katsaras, Eur. Phys. J. E **23**, 247 (2007)
4. O. Edholm, J.F. Nagle, Biophys. J. **89**, 1827 (2005).
5. N. Kučerka, J.F. Nagle, J.N. Sachs, S.E. Feller, Pencer J., A. Jackson, J.Katsaras, Biophys. J. **95**, 2356 (2008).
6. J. Karlovská, D. Uhríková, N. Kučerka, J. Teixeira, F. Devínsky, I. Lacko, P. Balgavý, Biophys. Chem. **119**, 69 (2006).
7. T. Róg, M. Pasenkiewicz-Gierula, I. Vattulainen, M. Karttunen, Biochim. Biophys. Acta **1788**, 97 (2009).

CHARACTERIZATION OF ZNO FILMS PREPARED BY THERMAL OXIDATION OF METALLIC ZN FILMS

Tomáš Kondela, Gamal A. M. Amin*, Ján Greguš, Miroslav Zahoran, Tomáš Roch, Faculty of Math., Physics and Informatics, Comenius University, Mlynská dolina, 842 48 Bratislava, Slovak Republic
*NCRRT, 29-Nasr City, Cairo, Egypt

INTRODUCTION

In the last decade, with growing importance of nanoscience, zinc oxide (ZnO) has attracted much attention of engineers, because of its large potential in various kinds of applications, such as gas sensors, nano–lasers, photoluminescence devices etc. This material is a candidate essential for developing the technologies for next generation computing, communication, bio-imaging, because of ability to integrate nanoelectronics and nanophotonics on it. This is due to its semiconducting and piezoelectric properties and large scale configuration of nanoobjects, as nanobelts, nanospirals etc.[1] In the photoluminescence (PL) spectra of ZnO the excitonic near band edge emission (UV) and defect related visible emission parts can be commonly distinguished. The UV band is due to excitonic recombination but the mechanism for visible emission is still discussed. Main candidates to explain the origin of this PL are intrinsic defects such as zinc vacancies and/or extrinsic impurities like Cu [1]. In this paper the variation of photoluminescence spectra of ZnO thin films on annealing temperature was studied to better understand the origin of this PL.

EXPERIMENTAL

Samples were prepared by thermal oxidation of metallic zinc films. Zinc (5N) was evaporated in a vacuum chamber on sapphire or silicon substrate at standard pressure (~ $2x10^{-3}$Pa) and then we input the samples into quartz oven with continuous flow of oxygen (5N) gas. After that, samples were thermally annealed at several temperatures from 400 ºC to 900 ºC for 1 hour. The film surface was analyzed by Scanning Electron Microscope (SEM, TESCAN REM VEGA TS 5136) and structural properties were studied by X-ray diffraction (XRD, URD – 6 with generator IRIS M4). Photoluminescence of ZnO films were investigated using grating monochromator with high resolution (<1A°) at room and liquid nitrogen temperatures, respectively. As an excitation source HeCd (10mW) cw laser was used.

RESULTS AND DISCUSSION

Structural properties

XRD spectra of ZnO films are shown in Fig. 1. Films are prepared by thermal oxidation in pure oxygen atmosphere at 550, 650 and 750 ºC. Metallic zinc was completely oxidized to form hexagonal polycrystalline ZnO layer. As we can see the spectra show three dominant diffraction corresponding to (100), (002), (101) orientation and (102) diffraction of ZnO film. With increasing temperature no additional diffraction was observed, but direction (100) becomes more intense. It may be related to the grain size increasing and orientation to preferred direction. Grains are clearly visible in Fig. 2(d). According to article [2] the intensity of peaks should increase with increasing size of grains but we only observed (100) enhancement of intensity. Figure 2 shows SEM images of the as evaporated zinc film and ZnO films prepared by annealing at temperatures 500, 700 and 900 ºC. After the zinc is evaporated on the surface of substrate and thermal oxidation started, significant changes of surface's morphology begin. In Fig. 2 the evolution of hexagonal grains can be observed. As evaporated Zn surface on

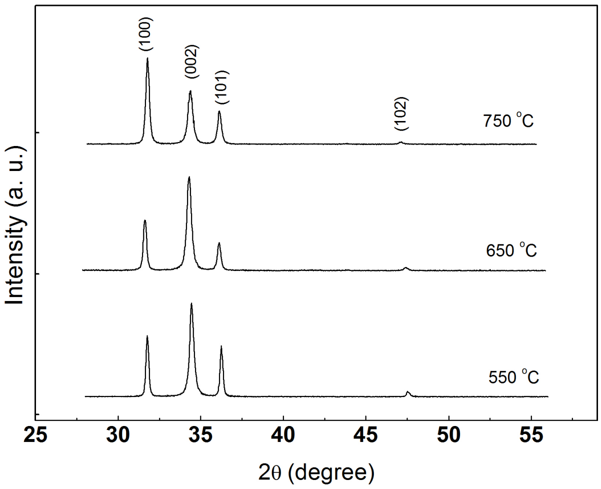

Fig.1 XRD spectra of ZnO samples prepared at temperature 550, 650 and 750 ºC

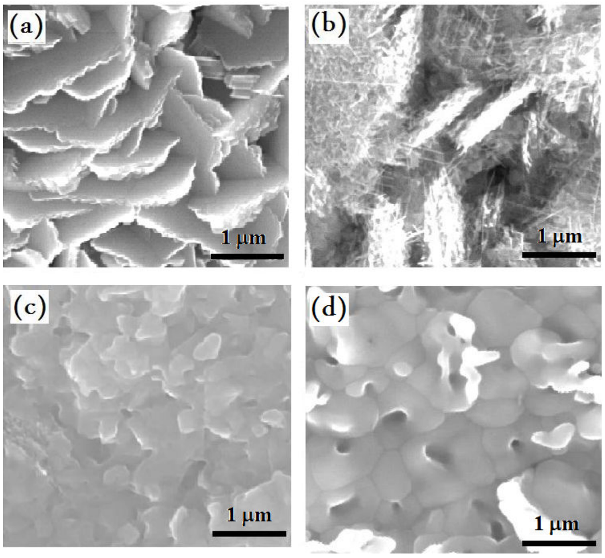

Fig. 2 SEM surface images of the (a) as evaporated zinc film and ZnO films formed under various temperatures: (b) 500, (c) 700 and (d) 900 ºC.

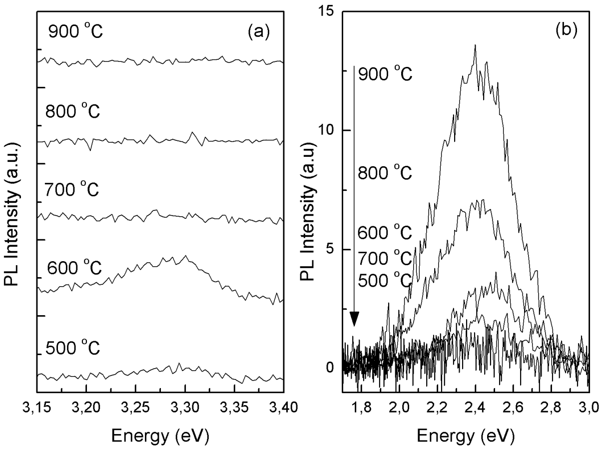

Fig. 3 (a) Near band edge and (b) green band PL spectra of ZnO samples annealed at different temperature measured at 300 K.

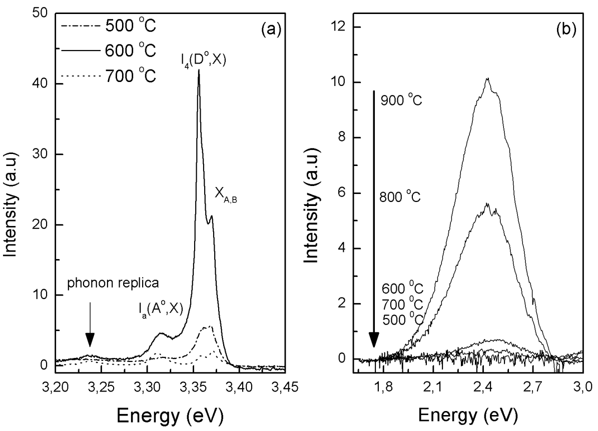

Fig. 4 (a) Near band edge and (b) green band PL spectra of ZnO samples annealed at different temperature measured at 80 K.

Fig. (2a) - annealed to 500 °C (Fig. 2b) shows presence of nanofibers which disappear at higher annealing temperature (Fig. 2c, d). With increasing temperature these “nanofibers” start to melt and grains are appeared on the surface. For films oxidized at temperature 700 °C (Fig. 2c), grains agglomerate together, so grain boundaries aren’t so distinguishable. At the temperature of 900 °C (Fig. 2d) grains become larger (from several tens of nanometers to 1 μm). Boundaries are clearly visible and form rod-like structures.

Optical properties

Room temperature near band edge PL and green band PL spectra of ZnO samples annealed at different temperature are shown in Fig. 3. These outcomes are similar with other reports [2, 3], but in our samples only at temperature 500 °C and 600 °C (Fig. 3a) near band edge photoluminescence (at about 3.27 eV) was observed. Origin of UV emission peak is from free exciton emission [1]. With increasing annealing temperature peak intensity starts to grow but above 700°C disappears. This does not agree with results of Wang et al. [2, 3] where UV emission is visible at annealing temperature in range 320 – 1000 °C but correspond to the temperature at what on our samples the nanofibers disappear (Fig. 2c). Possible explanation is that they reach better crystal quality as we and in our case the main contribution to PL spectrum is from “nanofibers”. Energy of green band emission is located in range from 2.41 to 2.48 eV (Fig. 3b). The intensity of emission increases with increasing annealing temperature, but not linearly. Spectrum corresponding to annealing temperature 600 °C is stronger than film annealed at 700 °C. The origin of green band emission is discussed in relation to copper impurities and native point defects such as V_{Zn} [1]. For better understanding of recombination process in ZnO film, we conducted low temperature PL measurements (at 80K). Results are shown in Fig. 4. Gap related PL was observed only at low annealing temperature (Fig. 4a). PL spectrum of each film consists of several peaks which have been assigned to free exciton (3.37 eV, $X_{A,B}$), donor-bound exciton (3.35 eV, (D^o,X)), acceptor-bound exciton (3.31 eV, (A^o,X))[4] and longitudinal optical phonon replica. Free exciton peak, which is dominant at temperature 300 K starts decreasing when temperature drop down and another peaks revealed. Annealed temperature has significant influence at overall intensity and at intensity of donor-bound exciton. Energy difference between bound exciton and free exciton at 80 K are 20 meV and 60 meV for donors and acceptor, respectively. These indicate that donors are shallow impurities and acceptor deep impurities [4]. Figure 4(b) shows green band of ZnO samples, as we see before (Fig. 3b) and the intensity show similar behavior as at room temperature.

CONCLUSION

ZnO films were prepared by annealing metallic zinc films at temperature from 500 to 900 °C. Samples show polycrystalline hexagonal structure. PL spectra are composed of near band edge UV emission and defect related emission band. UV emission appears only at samples annealed at temperature below 700 °C. This is discussed in connection to presence of ZnO nanofibers. As annealing temperature increased (above 700 °C) the defect related “green” band PL become dominant.

REFERENCES

1. H. Morkoç and Ü. Özgür: Zinc Oxide Fundamentals, Materials and Device Technology (Wiley-VCH, Weinheim, 2009).
2. Y.G. Wang, S.P. Lau, H.W. Lee, S.F. Yu, B.K. Tay, X.H. Zhang and H.H. Hng: J. Appl. Phys., **94** (2003) 1.
3. Y.G. Wang, S.P. Lau, X.H. Zhang, H.W. Lee, S.F. Yu, B.K. Tay, and H.H. Hng, Chem. Phys. Lett., **375** (2003) 113.
4. V.A. Fonoberov, K.A. Alim, and A.A. Balandin: Phys. Rev. B **73** (2006) 165317.

DIELECTRIC PERMITTIVITY OF YTTERBIA-STABILIZED ZIRCONIA CRYSTALS MEASURED AT HIGH FREQUENCIES

M. Hodas, Department of Experimental Physics, Comenius University, Bratislava
F. Kundracik, kundracik@fmph.uniba.sk, Department of Experimental Physics, Comenius University, Bratislava
M. Hartmanová, maria.hartmanova@savba.sk, Institute of Physics, Slovak Academy of Sciences, Bratislava
E.E. Lomonova, General Physics Institute, Russian Academy of Sciences, Moscow, Russia

INTRODUCTION

Zirconia (ZrO_2), due to its high dielectric constant, is a promising candidate for replacement of SiO_2 in MOS structures in microelectronic devices. It is well known, that adding of a trivalent oxide, such as yttria (Y_2O_3) or ytterbia (Yb_2O_3), can influence the phase composition (and dielectric constant) of the crystal. Depending on the amount of trivalent oxide, monoclinic, tetragonal or cubic phase can be stable at room temperatures. In this work ZrO_2 crystals with various concentration of Yb_2O_3 were investigated.

For microelectronic applications the dielectric constant in MHz-GHz frequency range is an important parameter. However, classical methods, such as C-V measurements or systems based on RLCG-meters or impedance analyzers, are usually designed for frequencies up to 1 – 10 MHz. At higher frequencies the parasitical inductance (connected with the length of the wires) becomes crucial.

We present a method of dielectric permittivity measurement based on Agilent E5062A network analyzer working in the frequency range of 300 kHz – 3 GHz.

SAMPLE PREPARATION

Single crystals of ZrO_2 + x. Yb_2O_3 (x = 1.50, 2.50, 3.30, 6.40, 11.10 and 13.80 mol%) were prepared by the directional solidification of melt using the direct rf melting in a cold container (skull-melting technique). The crystals were grown using the “Kristall-407” equipment at 10 mm/h growth rates. The dimensions of crystals obtained are dependent on the filling volume as well as on the composition and they are varied in the range of 15 – 60 mm in the length and 5 – 20 mm in the diameter. Samples with thickness of ~1 mm (cutted-of perpendicularly to the crystal axis) were used for dielectric measurements.

In dielectric measurements, Ag-paste was applied and dried at room temperature. Conducting Ag-electrodes built a capacitor filled with the sample.

METHOD OF THE IMPEDANCE ANALYSIS

The main problem at high-frequency measurements is connected with the length of the contacting wires, which is comparable with the wavelength of signals used. As a result, resonance effects at higher frequencies are observed and simple evaluation methods are not applicable.

To overcome this problem, we modelled the wired sample as a lossless guideline (model of wires) terminated by a pure capacitance load (model of the sample) - see figure 1. The lowest resonance frequency of the system presented in figure 1 is given by the capacity of the sample and the inductance of the connecting wires. Such an approximation can be valid for frequencies below the lowest resonance frequency only, as the impedance at the resonance frequency depends strongly on the energy losses not involved into the model.

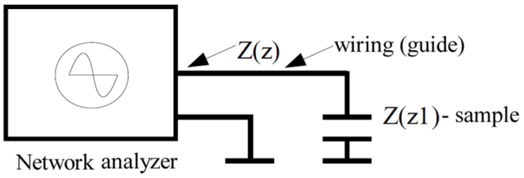

Fig. 1. Impedance model of a wired sample

Using this model we were able to calculate [1] the capacity from the measured impedance, *Z*(*z*):

$$C=\frac{\frac{Z(z)}{Z_V}tg\beta(z-z_1)-1}{\omega Z_V tg\beta(z-z_1)+\omega Z(z_1)} \qquad (1)$$

where the impedance of the guide, Z_v, and the length of the guide, z-z_1, are free parameters and have to be estimated, the wave number β is known at given frequency ω.

RESULTS AND DISCUSION

Capacity obtained from the model

Typical frequency dependence of the imaginary part of the measured impedance is shown in figure 2. The resonance at frequencies near 1 GHz is clearly visible.

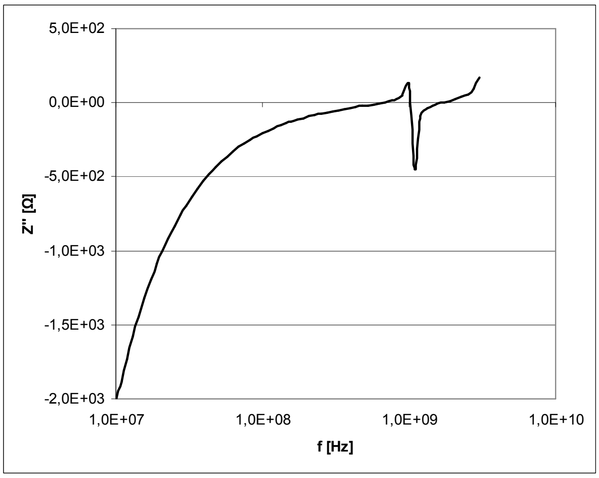

Fig. 2. Typical measured frequency dependence of the imaginary part of the impedance with resonance visible

To calculate the capacity from the imaginary part of the impedance using equation (1) we need to find both free parameters – the wave impedance of the guide (wires), Z_v, and the length of the guide (length of the wires), $l = z\text{-}z_1$. The length of the guide influences dramatically the lowest resonance frequency of the system. So, in the first step, one can set the impedance of the guide to 50 Ω (equal to the impedance of the generator) and find the optimal length of the wire (the resonance frequency corresponds to the observed one). Figure 3 demonstrates how the calculated capacity depends on the chosen length of the guide. In the case of the optimal value the low-frequency part of the resonance peak is most suppressed.

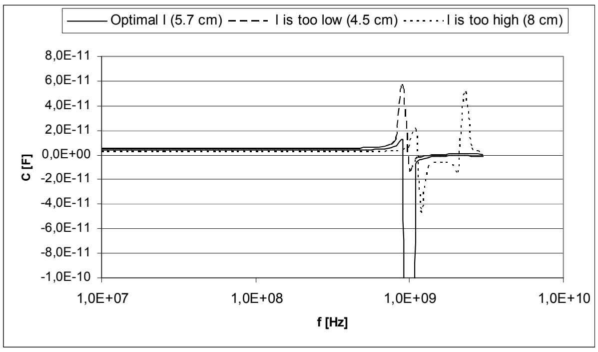

Fig. 3. Finding optimal length of the guide, $l = z\text{-}z_1$

In the next step, the impedance of the guide has to be found. In the figure 4 can be seen the influence of the impedance, Z_v, on the calculated frequency dependence of the capacity. In cases the impedance is not optimum, the left part of the resonance peak is not suppressed, or is over-suppressed.

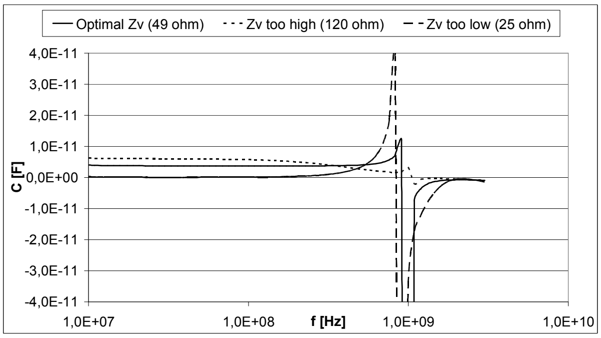

Fig. 4. Finding optimal impedance of the guide, Z_v

Both previous steps have to be repeated, but the procedure converges usually fast.

As mentioned above in the previous section, our model is not valid at resonance frequencies because of neglecting of losses. However, at lower frequencies (up to 500 MHz in our case), where the inductance of the wires dominates, our model should give proper values of the capacity of the sample.

Dielectric permittivities at 100 MHz

Dielectric permittivities of all the samples measured at 100 MHz are shown in Figure 5 and are in good agreement with the measured ones at 20 kHz [2].

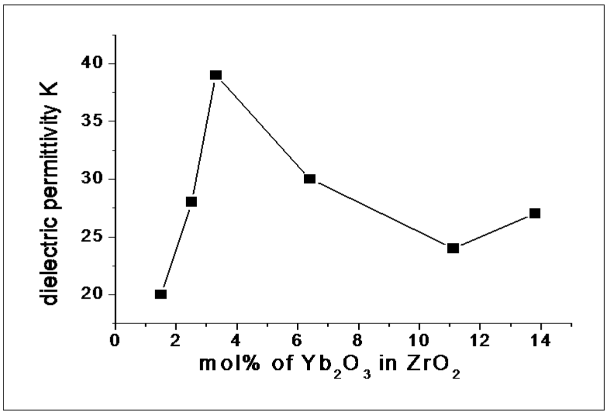

Fig. 5. Dielectric permittivities of the samples measured at 100 MHz as a function of the Yb_2O_3 content

The highest dielectric permittivity K = 39 shows the sample containing 3.3 mol% of ytterbia and having mixed monoclinic-cubic phase composition. This value is as high as the highest ones measured for tetragonal phase of pure zirconia (30-40, [3]). This sample seems to be the most interesting candidate for application in MOS structures.

CONCLUSIONS

The permittivity of investigated ytterbia-doped zirconia single crystals with various concentrations of ytterbia was measured using a network analyser. To suppress resonance effects at higher frequencies (caused by the inductance of the wires) a quide-model was introduced. Using this model the capacity can be evaluated up to frequencies near the resonance frequencies (depending on the capacity of the sample, 500 MHz in our case).

The highest dielectric permittivity K = 39 was found for the zirconia crystal doped with 3.3 mol% of ytterbia. Such a material seems to be interesting candidate for applications in microelectronics.

ACKNOWLEDGMENT: This work was partially supported by the research grant No. 2/7119/27 of the Slovak Grant Agency (VEGA).

REFERENCES

1. A. Tirpák: High frequency electronics (Comenius University, Bratislava, 2001, ISBN 8022316318).
2. F. Kundracik et al.: Dielectric properties of $Yb_xZr_{1-x}O_{2-x/2}$ solid solutions (8th Conference on Solid State Chemistry, Bratislava, Slovak republic, July 6-11, 2008, Book of abstracts, p.139).
3. H. R. Huff, D. C. Gilmer.: High Dielectric Constant Materials: VLSI Mosfet Applications (Springer-Verlag, 2005, ISBN 3540210814).

POSSIBILITIES OF HIGH DENSITY LIPOPROTEIN DETECTION BY SUPPORTED BILAYER LIPID MEMBRANE

L. Vojčíková, e-mail: leavoj@central.medic.upjs.sk
University of P.J.Šafárik, Medical Faculty, Department of Medical Biophysics, Tr. SNP 1,040 66 Košice, Slovak Republic

INTRODUCTION

To overcome membrane complexity model membrane systems are used. The models enable to study the membrane physical parameters under the controlled conditions from biophysical point of view. An interesting application of the model membrane from medical point of view is the research of interaction relevant molecules with membranes.

Cholesterol as an amphipatic lipid is a major constituent of plasma lipoprotein also. Trygliceride and cholesterol ester are insoluble in the water environment of the plasma and are solubilized by their incorporation into lipoproteins. Associating nonpolar lipid with amphipatic lipids and proteins to make water miscible lipoproteins solves this. Lipoproteins transport free cholesterol in the circulation. There are several different lipoprotein species found in plasma but their basic structures are similar. We concern on high density lipoproteins (HDL, or α-lipoproteins). Cholesterol and phospholipid are the predominant lipids in LDL and HDL. HDL concentrations are inversely related to the incidence of coronary atherosclerosis, possibly because they reflect the efficiency of cholesterol scavenging from the tissues. Coronary atherosclerosis correlates with a high plasma LDL:HDL cholesterol ratio. The high levels of HDL have a protective effect. HDL cholesterol levels are now included in suet guidelines and low levels (< 0.9 mmol/l) are regarded as an important coronary heart disease (CHD) risk factor. Conversely, a high HDL cholesterol concentration (>1.6 mmol/l) is regarded as a negative risk factor [1].

MATERIAL AND METHODS

In 1989, a simple and novel method was reported for the formation of self-assembled BLMs on solid substrates (s-BLM), which possessed the desired dynamic properties and the requisite mechanical stability [2]. Lipid membranes deposited on solid supports represent a relatively biocompatible structure for the development of new types of electrochemical sensors and biosensors with fast response times (in the order of a few seconds) and high sensitivity (i. e. nanomolar detection limits). The technique of formation of s-BLMs is based on the interaction of an amphiphilic molecule with a nascent metallic surface.

The detection of high density lipoprotein was studied by means of the supported bilayer lipid membrane (s-BLM) [3]. Supported bilayer membranes were prepared using the technique described in [4]. The experiments were performed using Universal Electrochemical Interface, IM6, Zahner elektrik, Germany that included a potentiostat / galvanostat and personal computer. The electrical parameters of s-BLM can be measured by alternating current voltage 50 mV-amplitude sine wave and 10 000 Hz was applied to the electrode. For this measurement were used two platinum Teflon coated electrodes immersed in bathing solution. The working electrode is covered with s-BLM whereas reference electrode has a naked tip. For experiments the IM6 / Thales - software was used. All biophysical experiments were carried out in a conventional two electrodes system under room temperature (23 ± 0.5 °C). The bathing solution contained the reduced solution (0.14 M NaCl, 0.005 M KCl, 0.0025 M $CaCl_2$, 0.025 M $NaHCO_3$, 0.0012 M NaH_2PO_4, 0.001 M $MgCl_2$, pH = 7.2 - 7.3). Hanks solution mimics ionic composition and concentration of electrolytes the blood for the potential using s-BLM as the base for biosensors. The trice-distilled water was used in the preparation of all aqueous solutions. High density lipoprotein from human blood plasma was received from Biochemical Laboratory of University Hospital in Košice. The determination of HDL was performed with standard procedures using diagnostic kit purchased from Human Co, Germany according to [5]. After reaching a membrane steady state we detected the added lipoprotein in the range of low concentrations (< 0.9 mmol/l). We consider the s-BLM to be in a steady state if the mean value of electrical parameters did not change in an hour more then 0.5%.

EXPERIMENTAL RESULTS

In our previous paper [4] we studied the influence of high density lipoprotein (concentration range $1x10^{-1}$ - $5.5x10^{-1}$ mmol/l) on electrical parameters of s-BLM after one addition of lipoprotein into solution. The magnitude of change was related to membrane steady state values of electrical parameters. The investigation of the lipoprotein effect on electrical properties of the same s-BLM after gradual addition of lipoprotein into solution was the aim of the present work. We concentrated on the lower critical concentrations ($0.5x10^{-2}$ - $4x10^{-2}$ mmol/l) from medical point of view. For the same supported lipid bilayer membrane sample we measured the dependence of membrane resistance difference on concentration of lipoprotein. In response to every addition of high density lipoprotein, the resistance increased and the capacitance decreased.

On the Fig. 1 is demonstrated the dependence of ΔR on concentration of lipoprotein, as ΔR is the difference of between membrane resistance after addition of HDL R_{HDL} and membrane steady state resistance R without HDL:

$$\Delta R = R_{HDL} - R \qquad (1)$$

The lipoprotein partly lipophilic character enables an adsorption on s-BLM surface and therefore membrane resistance gradually increases.

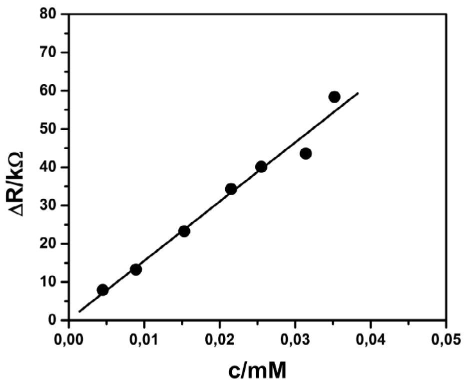

Fig. 1 Dependence of membrane resistance difference on the high density lipoprotein concentration.

Concerning the structural character of the lipoprotein, that is partly water soluble and partly lipid soluble, high density lipoprotein manifests hydrophobic behaviour too as it contains many lipids. As a consequence HDL is able to settle the interior of lipid bilayer.

The observed dependence ΔC on concentration of high density lipoprotein, where ΔC, contrary to ΔR, is the difference between steady state membrane capacitance without lipoprotein in solution and membrane capacitance after addition of HDL C_{HDL}:

$$\Delta C = C - C_{HDL} \qquad (2)$$

ΔC suggest significant changes of membrane structure. It is generally known that some properties of planar lipid bilayers, such as thickness can be determined by the measurement of transmembrane capacitance.

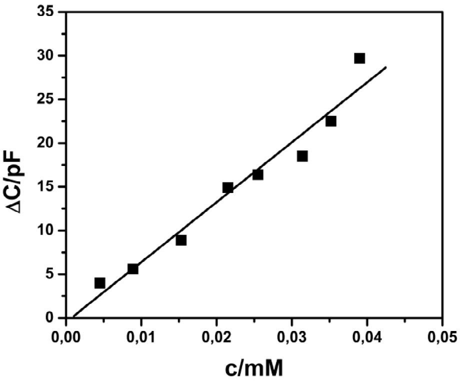

Fig. 2 Dependence of membrane capacitance difference on the high density lipoprotein concentration.

Modified thickness of membrane after addition of lipoprotein illustrates changed values of membrane capacitance, as shown on the Fig. 2. This experimental observation completed our previous results [4,6]. The results accord with our suppositions that HDL saturates hydrophobic region of membrane with cholesterol and consequently membrane thickness is extended.

The obtained dependencies of membrane electrical parameters enable the assumption that s-BLM can operate like HDL biosensor.

CONCLUSIONS

The s-BLMs are modified by HDL lipoprotein from human blood. The detail experimental study of the changes of the membrane resistance and capacitance after gradual addition of low concentrations of HDL supports our suggestion from previous experiments that high density lipoprotein modifies hydrophobic part of lipid bilayer.

The HDL - membrane fusion upraises with increasing concentration of lipoprotein in the studied range of low concentrations ($0.5\text{x}10^{-2} - 4\text{x}10^{-2}$ mmol/l), which is reflected in the higher values of electrical resistance.

The enlarged range of the studied concentrations ($0.5\text{x}10^{-2}$ - $2.5\text{x}10^{-1}$ mmol/l) completed the high concentration range from previous studies by the lower concentrations of HDL.

Our concentration analysis has confirmed that the sensitivity of supported lipid bilayer membrane for the lipoprotein detection is sufficient.

ACKNOWLEDGMENT: This work was supported in part by a Cultural and Educational Grant of Ministry of Education of Slovak Republic No 3/5153/07.

REFERENCES

1. D.J. Betteridge, J.M. Morell: Lipids and coronary heart disease, (Chapman & Hall Medical, London 1998).
2. H. T. Tien, A. Ottova: Membrane biophysics as viewed from experimental bilayers lipid membranes. Membrane Science and Technology Series 5, (Elsevier, Amsterdam, 2000).
3. J. Sabo, A. Ottova., G. Laputková, M. Legiň, L. Vojčíková, H. T. Tien, Thin Solid Films **306,** 112, (1997).
4. L. Vojčíková, J. Sabo, 14. Konferencia slovenských fyzikov, Zborník príspevkov, Smolenice 93, (2005).
5. T. Gordon, W.P. Castelli, M.C. Hjortland, W.B. Kannel, T.R. Dawber: Am. J. Med. **62,** 707 (1977).
6. L. Vojcikova, A. Ottova, H. T. Tien, J. Sabo, Bratislava Medical J. **107,** 4, 179 (2006).

RESISTANCE SWITCHING EFFECT ON $YBa_2Cu_3O_{7-x}$/Ag PLANAR JUNCTIONS

T. Plecenik, plecenik@gmail.com, DEP PMPI UK, Mlynská Dolina, 842 48 Bratislava, Slovakia, M. Tomášek, milan.tomasek@gmail.com, DEP PMPI UK, Mlynská Dolina, 842 48 Bratislava, Slovakia, M. A. Belogolovskii, bel@kinetic.ac.donetsk.ua, DIPE NASU, 83114 Donetsk, Ukraine, J. Noskovič, jaroslav.noskovic@gmail.com, DEP PMPI UK, Mlynská Dolina, 842 48 Bratislava, Slovakia, M. Gregor, maros.gregor@fmph.uniba.sk, DEP PMPI UK, Mlynská Dolina, 842 48 Bratislava, Slovakia, M. Zahoran, zahoran@fmph.uniba.sk, DEP PMPI UK, Mlynská Dolina, 842 48 Bratislava, Slovakia, T. Roch, roch@fmph.uniba.sk, DEP PMPI UK, Mlynská Dolina, 842 48 Bratislava, Slovakia, M. Kubinec, milan.kubinec@fmph.uniba.sk, DEP PMPI UK, Mlynská Dolina, 842 48 Bratislava, Slovakia, M. Španková, elekmspa@savba.sk, IEE SAS, Dúbravská cesta 9, 841 04 Bratislava, Slovakia, Š. Chromik, elekchro@savba.sk, IEE SAS, Dúbravská cesta 9, 841 04 Bratislava, Slovakia, P. Kúš, peter.kus@fmph.uniba.sk, DEP PMPI UK, Mlynská Dolina, 842 48 Bratislava, Slovakia, A. Plecenik, plecenik@fmph.uniba.sk, DEP PMPI UK, Mlynská Dolina, 842 48 Bratislava, Slovakia

INTRODUCTION

High-speed and large capacity nonvolatile memories are crucial for information technology. Several alternatives to currently used data storage devices are thus studied to obtain new generation of more powerful nonvolatile memories with improved performance. One of the most promising candidates in this field are resistive random access memories (ReRAM) based on resistive switching, i.e. reversible changes of resistance, usually induced by an electric field [1,2]. This phenomenon was firstly observed on high-temperature superconducting cuprates [3] and later on many NIN (normal metal – insulator – normal metal) systems. Research in this field is mainly focused on simple two-component oxide NIN systems and there is just a few studies of devices based on more-component oxides. In all cases, the mechanism of the resistive switching is believed to be related to redistribution of oxygen vacancies within the oxide barrier. However, details of this mechanism are still debated even in the simplest systems.

In this paper we present measurements of current-voltage characteristics of planarized and unplanarized $YBa_2Cu_3O_{7-x}$ (YBCO)/Ag junctions in temperature range from 100 to 300 K. For planarized junctions, nonvolatile reversible resistive switching is observed.

EXPERIMENTAL

Measurements had been done on epitaxial *c*-axis oriented 200 nm thick YBCO thin films deposited on single-crystalline $LaAlO_3$ substrates by dc magnetron sputtering from a stoichiometric ceramic target at temperature of 815 ˚C, oxygen pressure of 240 Pa, and sputtering power of 4.5 W/cm^2. After the deposition the films were annealed in oxygen atmosphere (10^4 Pa) at 500 ˚C during 30 minutes and than cooled down to room temperature at a rate of 15 ˚C per minute. Surface of the resulting films was than cleaned for 10 minutes in ion gun with Ar ion energy of 500 eV and beam current of 20 mA. 100 μm wide YBCO micro-strips forming the lower electrodes were than prepared by optical lithography and consequent Ar ion beam etching. In the case of planarized samples, 200 nm thick SiO_2 layer was than deposited by vacuum evaporation before photoresist removal. In the next step, upper electrodes formed by 5, 10 and 15 μm wide Ag strips were fabricated by lift-off photolithography and vacuum evaporation.

Current-voltage (I-V) characteristics were measured in standard four-contact setup with Keithley 220 Programmable Current Source and Keithley 2000 multimeter. Low temperature measurements were done in transport He Dewar container.

RESULTS AND DISCUSSION

Typical I-V curves measured at 300 K are shown on fig. 1. For planarized junctions, where the oxygen diffusion takes place only in c-axis of the YBCO film and the diffusion coefficient is small, two branches corresponding to high-resistive state (HRS) and low-resistive state (LRS) are clearly visible. In the initial state the junction is always in HRS and switches to LRS when negative electric field of sufficient intensity is applied. The junction than remains in the LRS until electric field of positive polarity and critical intensity is applied. This is in contrast with I-V curves of the unplanarized junctions, where oxygen diffusion is also possible in the ab-plane.

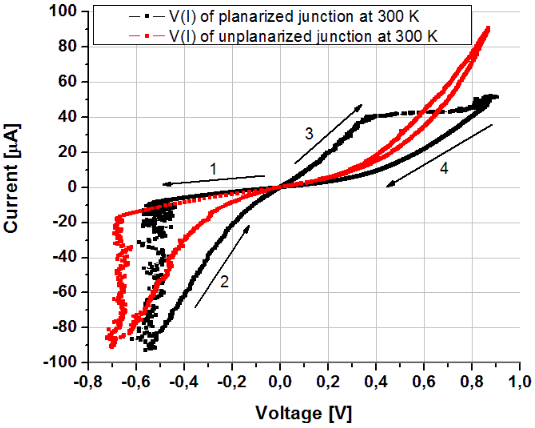

Fig. 1. Typical I-V curves of planarized (black) and unplanarized (red) junctions measured at 300 K.

In this case the junction also switches to LRS at negative electric fields, but gradually returns back to HRS when the electric field is decreased back to zero.

With decreasing temperature the critical electric field necessary to switch the junction from HRS to LRS and back is increasing (fig. 2). Also, at low temperatures the transition from HRS to LRS and back is much sharper (fig. 3). This is probably caused by the fact that at low temperatures the oxygen ion diffusion caused by thermal fluctuations is suppressed.

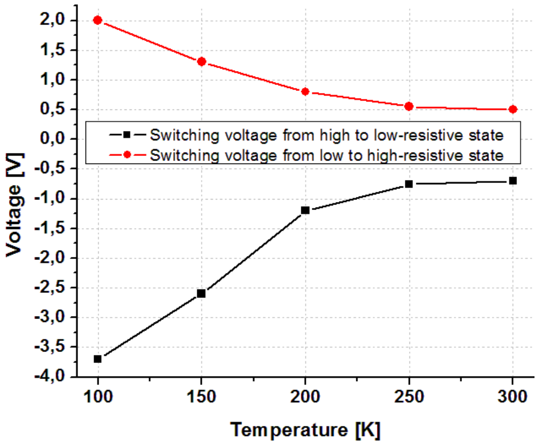

Fig. 2. Critical voltage required to switch junction from HRS to LRS (black curve) and back (red curve) as a function of temperature.

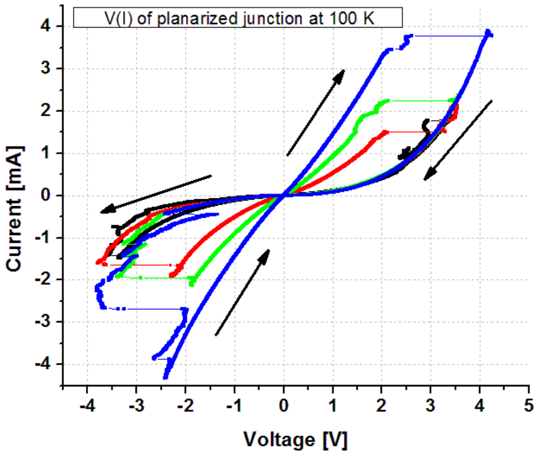

Fig. 3. Typical I-V curves of planarized junctions measured at 100 K.

From the transport measurements presented here and differential conductance measurements presented in our other work [4] we assume that the resistive switching effect on our samples is most probably related to the oxygen ion diffusion in the YBCO film within nanometer-scale proximity to the YBCO/Ag interface. In HRS the YBCO/Ag interface is strongly degraded with high concentration of oxygen vacancies, while in the LRS the oxygen ions are forced to take their regular positions within the YBCO structure and thus restore its conducting (or superconducting below T_c) properties.

CONCLUSIONS

Current-voltage characteristics of planarized and unplanarized YBCO/Ag planar junctions had been measured within 100 – 300 K temperature range. For planarized junctions, hysteretic I-V curves with two branches corresponding to HRS and LRS were observed. With decreasing temperature the critical voltage required to switch the junction between the HRS and LRS is increasing and the transitions from HRS to LRS and back are getting sharper.

ACKNOWLEDGEMENT: This work was supported by the Slovak Research and Development Agency under the contract Nos. VVCE-0058-07, APVV-0034-07, APVV-0432-07 and LPP-0176-09.

REFERENCES

1. R. Waser and M. Aono, Nat. Mater. **6**, 833 (2007).
2. A. Sawa, Mater. Today **11**, 28 (2008).
3. A. Plecenik et al., Physica C **301**, 234 (1998).
4. T. Plecenik et al., Current-Induced Resistance Switching in Yttrium-Based Cuprate Films, submitted to Phys. Rev. B (2009).

MEASUREMENT OF RESISTANCE SWITCHING EFFECT ON $YBa_2Cu_3O_{7-x}$ THIN FILMS BY CRYOGENIC SCANNING TUNNELING MICROSCOPE

M. Truchly, martin.truchly@gmail.com, DEP PMPI UK, Mlynská Dolina, 842 48 Bratislava, T. Plecenik, plecenik@gmail.com, DEP PMPI UK, Mlynská Dolina, 842 48 Bratislava, J. Noskovič, jaroslav.noskovic@gmail.com, DEP PMPI UK, Mlynská Dolina, 842 48 Bratislava, M. Tomášek, milan.tomasek@gmail.com, DEP PMPI UK, Mlynská Dolina, 842 48 Bratislava, M. Španková, elekmspa@savba.sk, IEE SAS, Dúbravská cesta 9, 841 04 Bratislava, Š. Chromik, elekchro@savba.sk, IEE SAS, Dúbravská cesta 9, 841 04 Bratislava, P. Kúš, peter.kus@fmph.uniba.sk, DEP PMPI UK, Mlynská Dolina, 842 48 Bratislava, A. Plecenik, plecenik@fmph.uniba.sk, DEP PMPI UK, Mlynská Dolina, 842 48 Bratislava

INTRODUCTION

In the last years, complex transition-metal oxides had been widely studied, as they offer many possibilities for various potential applications as well as basic research. Among others, reversible resistance switching induced by electrical field recently attracted significant attention as it may form a basic element of nonvolatile resistive random access memories (ReRAM), which are believed to be the most promising candidates for the new generation of memories with improved performance characteristics [1,2]. Although high-temperature superconducting cuprates were the first materials where this phenomenon was observed [3], research in this area is mainly focused on simple two or three-component oxides. However, even in the simple systems the mechanism of the resistance switching is still not completely understood.

In this paper we present local measurements of current-voltage characteristics of $YBa_2Cu_3O_{7-x}$ (YBCO) thin films by cryogenic Scanning Tunneling Microscope (STM). In contrast with other studies, where such measurements were done on relatively large planar YBCO/metal junction, we show that the effect of resistive switching can be observed also locally on nanometer-scale junctions realized by an STM tip.

EXPERIMENTAL

The resistance switching measurements were done on epitaxial *c*-axis oriented YBCO films prepared by dc magnetron sputtering [4]. Cryogenic scanning tunneling microscope (STM) from NT-MDT Company in Oxford Instruments Optibath SXM cryostat was used to measure current-voltage characteristics in temperature range from 77 to 300K. PtIr wire was used as STM tip. During measurements the STM tip was grounded and the sample was biased from an internal STM voltage supply. Maximum voltage that can be applied is +/- 10 V and maximum measurable tunneling current is 50nA. Topography measurements were done in constant current mode, where the sample-tip voltage was 1 V and tunneling current (set-point) was set to 1 nA. The current-voltage (I-V) characteristics were measured in the same setup within 1 second. During this time, the STM feedback was turned off and the tunneling current was measured as a function of the sample-tip voltage.

RESULTS AND DISCUSSION

STM topography of the YBCO thin film surface used in our measurements is shown on fig. 1. From the bad quality of the topographic image and its nature we assume that the SPM tip was most probably in direct contact with the surface. We suppose that this is caused by the fact that the degraded YBCO thin film surface plays the role of the tunneling barrier between the sample and the STM tip due to its insulating character and substitutes the sample – tip separation at selected voltage and tunneling current. Consequently, we assume that the STM tip was in direct contact with the sample also during the measurements of the current-voltage characteristics, forming direct YBCO/PtIr junction of nanometer scale.

I-V characteristics had been measured as a function of temperature (fig. 2) and highest applied voltage (fig. 3). Considerable hysteresis caused by switching from high to low-resistive state and back is visible on all curves where the maximum applied voltage was above 1.5 - 2 V. We assume that this effect is caused by diffusion of oxygen ions and consequent change of resistance of a nano-scale region of the YBCO film at the YBCO/PtIr STM tip interface.

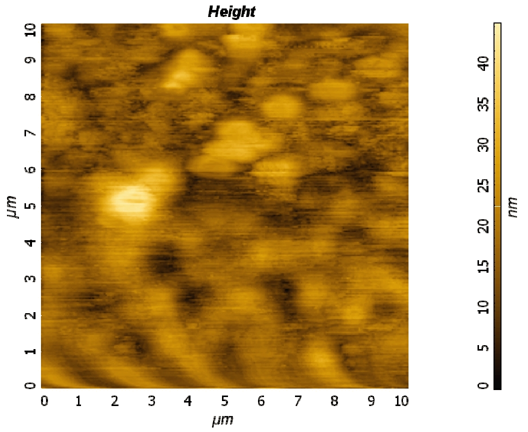

Fig. 1. 10x10 µm STM image of the YBCO thin film

Temperature dependence of the current-voltage characteristics measured from -8 to +8 V (curves 1, 2) and back (curves 3, 4) from room temperature down to 77 K is shown on fig.2. One can see that the resistance of the low-resistive state (curves 1, 2) doesn't considerably change within stated temperature interval, while the resistance of the high-resistive state (curves 3, 4) is clearly increasing with decreasing temperature, what is typical for real tunnel junctions. Thus, the hysteresis is larger at lower temperatures.

Dependence of the I-V characteristics on the maximum applied voltage measured at 77 K is shown on fig. 3. For low voltage ranges up to 1.5 – 2 V, no or very low hysteresis is visible as the electric field is insufficient to cause oxygen ions drift. When higher voltages are applied, there is clear hysteresis visible while its size is increasing with increasing voltage range. In contrast with the temperature dependence, in this case the resistance of the high-resistive state doesn't significantly change, while the resistance of the low-resistive state decreases with increasing highest applied voltage. This is in agreement with our expectations, as the high-resistive state is the initial state of the junction and is expected maintain its resistance despite of applied positive voltage. On the other hand, resistance of the low-resistive state is expected to decrease with increasing of the highest applied voltage as more and more oxygen ions are forced to return to their regular position within the YBCO structure.

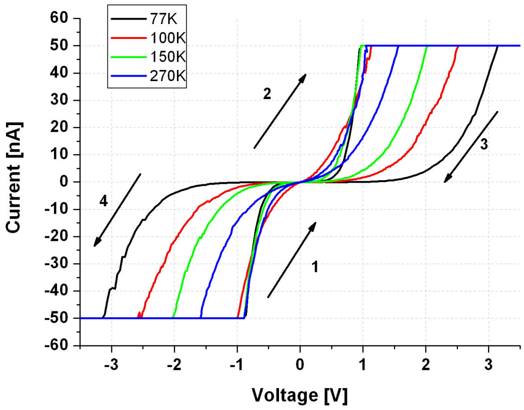

Fig. 2. Temperature dependence of the current-voltage characteristics of the YBCO – PtIr STM tip contact.

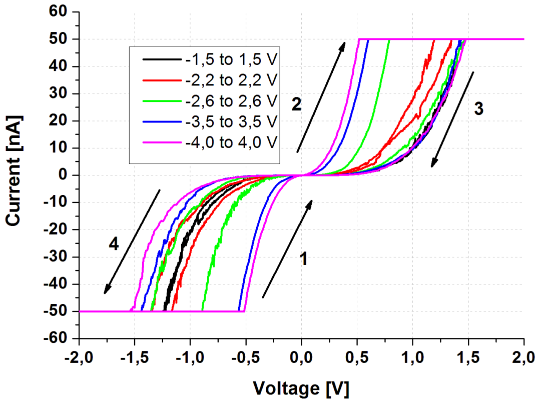

Fig. 3. I-V characteristics of the YBCO – PtIr STM tip contact measured for various voltage ranges

CONCLUSIONS

To conclude, I-V characteristics of c-axis oriented YBCO/PtIr STM tip contacts had been measured in temperature range from 77 to 300 K and hysteretic behavior related to resistive switching caused by oxygen ion migration was observed. This effect has been studied as a function of temperature and applied voltage range. It has been shown that the resistance of the high-resistive state is increasing with decreasing temperature and the resistance of the low-resistive state is decreasing with increasing of the highest applied voltage. Our measurements also show that the resistive switching effect can be observed also locally on nanometer-scale junctions realized by an STM tip, giving space for possible miniaturization of ReRAM devices to nanometer-scale.

ACKNOWLEDGEMENT: This work was supported by the Slovak Research and Development Agency under the contract Nos. VVCE-0058-07, APVV-0034-07, APVV-0432-07 and LPP-0176-09.

REFERENCES

1. R. Waser and M. Aono, Nat. Mater. **6**, 833 (2007).
2. A. Sawa, Mater. Today **11**, 28 (2008).
3. A. Plecenik et al., Physica C **301**, 234 (1998).
4. T. Plecenik et al., Current-Induced Resistance Switching in Yttrium-Based Cuprate Films, submitted to Phys. Rev. B (2009).

FRAGMENTATION OF VALINE BY ELECTRON IMPACT

J. Kočišek, kocisek@yahoo.com, D.Kubala, kubala@neon.dpp.fmph.uniba.sk, Š.Matejčík, matejcik@fmph.uniba.sk

The gas phase electron impact ionization of Valine has been studied in crossed electron-molecule experiment built in Department of Experimantal Physics, CU Bratislava [1]. The main components of experimental setup - Quadrupole Mass Analyzer (QMA) and Trochoidal Electron Monochromator (TEM) alow us not only to study mass spectra of produced fragment ions but also to precisely determine activation energies for particular reaction channels.

After detail electron attachment study [2] we continue our investigation of Valine molecule in present electron impact study. While electron ionisation mass spectra of Valine is known [3] the proposed mechanism of EI reaction have not been experimentally prooft. In presented study, the most intense fragmentation channels were subjected to further analysis. Ionization energy of molecule was acquired from energy dependent ionization yield measured for parent ion m/z=117. Afterwards activation energies for selected particular reaction channels have been determined from near threshold measurements of electron energy dependent relative ionization cross sections.

Presented data are in demand for many fields of chemistry, physics and medicine concerning basic research on molecular level. Especially we would highlight their importance for computational chemistry of amino acids and explanation of several important processes in living organisms.

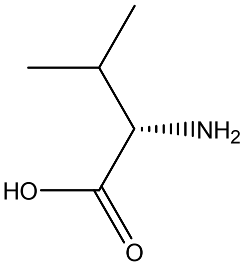

Fig. 1. Valine molecule. Simple 2D model.

MATERIALS AND METHODS

The experimental setup used was build to study reactions of single molecule with electron of defined energy. To study such type of reaction single collision conditions in reaction region need to be assured. This condition is achieved by vacuum low pressures in reaction region. Vacuum pressure is necessary also for function of other components these are set in high vacuum chamber (pressures <2^10-9mbar). Schematic representation of high vacuum part of experimental setup is on Fig[XX]. In reaction region beam of neutral molecules, produced by effusive molecular beam source, is colliding with electrons of defined energy (FWHM<200meV) produced by trochoidal electron monochromator. Reaction products are than mass spectrometrically selected using quadrupole mass analyzer and detected on secondary electron multiplier type detector.

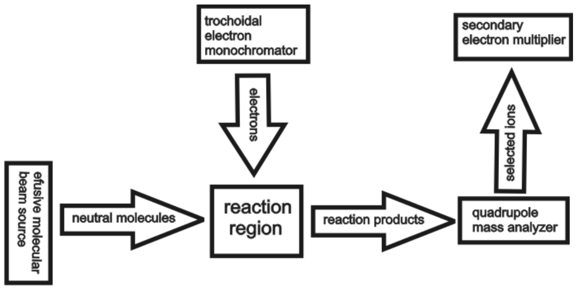

Fig.2. Schematic representation of in vacuo parts of used experimental setup.

In case of gas samples, simple capilary is used to produce molecular beam, in case of solid aminoacid, a modification of inlet system has to be done. Simple representation of cut through used molecular beam source is on Fig. 3.

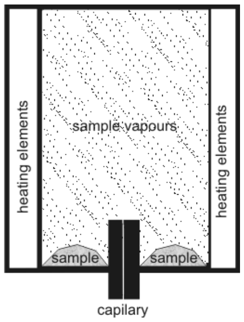

Fig. 3. Cut through heated capillary inlet used for neutral molecules beam formation in present experiment.

Small amount of sample is placed in metal container and heated by tungsten/ceramic heating elements. Sample vapours than pass through capillary into reaction region. The Precise temperature control is needed to provide enough vapor pressure for experiment and prevent sample decomposition. In case of Valin molecule temperature of capillary was kept at around 180°C.

Two modes of apparatus operation are possible. In first the energy of electrons is set constant and defined m/z region is scanned using QMA - mass spectras at defined electron energy are obtained. In second mode the m/z ratio is set constant and energy is tuned through defined region – electron energy dependent ion yields for selected reaction channels are obtained. Detailed description of experimental setup can be found in [1].

As sample Merck L-Valine for biochemistry grade, purity >99% was used.

RESULTS AND DISCUSSION

Mass spectrum measured at 70eV using quadrupole mass spectrometer is shown on Fig.3.

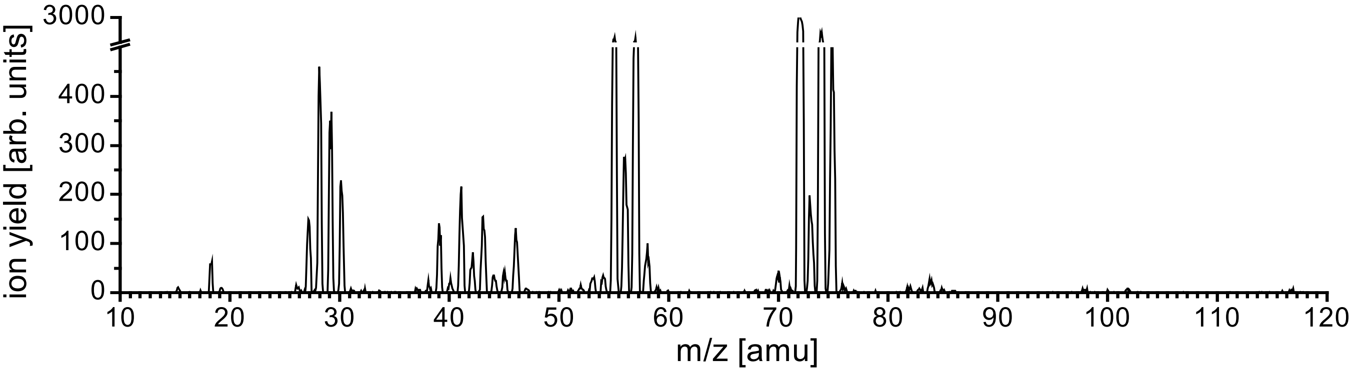

Fig. 3: Electron ionization mass spectra of Valine at incident electron energy 70eV

The electron energy ion yields for selected ionic fragments were measured in near threshold region to obtain apperence energies. The final values of appereance energies for selected channels are than summarized in Tab.1 together with assigned ionic fragments.

The ionisation energy of molecule is found to be 9.06+/-0.16. In comparison to formerly published value of ionisation energy from PES experiments [4] our value is higher. It can be due to high detection time of our experiment and resulting low signal of M$^+$ cation which is subject of further fragmentation.

Table 1: Activation energies (AE) of selected ionic fragments and their relative intensities (RI) in mass spectra.

m/z	Assigned cation	RI%	AE(eV)
117	M$^+$	0.19	9.06+/-0.3
102	(M-CH3)$^+$	0.21	11.5+/-0.3
75	NH$_2$CHC(OH)OH$^+$	14.2	10+/-0.3
73	[M-COOH]$^+$	4.35	9.2+/-0.3
72	[M-COOH]$^+$	100	9.3+/-0.3
58	C$_2$H$_4$NO$^+$	2.51	11.2+/-0.3
57	C$_2$H$_3$NO$^+$	26.1	11.7+/-0.3
56	[M-NH$_3$-COOH]$^+$	7.6	12+/-0.3
55	[M-NH$_3$-COOH]$^+$	27.8	12.2+/-0.3
46	CH(NH$_2$)OH$^+$	3.3	12.2+/-0.3
45	Cooh+	1.1	11.49+/-0.07
44	CH$_2$CHNH$_3$$^+$	1	10.5+/-0.3
43	CH$_3$CNH$^+$	4.85	11.5+/-0.3
41	C$_3$H$_5$$^+$	6.15	12.8+/-0.3
39	C$_3$H$_3$$^+$	4.44	15+/-0.3
29	C$_2$H$_5$$^+$/HCO$^+$	10.9	12.45+/-0.18
28	CNH$_2$$^+$	12.9	13.2+/-0.3
18	NH$_4$$^+$/H$_2O^+$	1.9	11.1+/-0.3

The main reaction channel is formed via cooh group dissociation and formation of C$_4$H$_{10}$N$^+$ cation. The m/z=73 is than assigned to its isotope what is confirmed by both mass and electron energy dependent ion yields.

The activation energies for all fragmentation channels are in good agreement with previous description of Junk and Svec [3], and provide good experimental confirmation of proposed reaction pathways.

Actually the computational experiment is prepared to give final description of electron ionisation of valine.

CONCLUSIONS

The activation energies for several electron ionisation channels of valine have been measured. We confirm experimentally the formerly proposed fragmentation pathways. The experimental values of activation energies than provide needful input for further computational analysis.

ACKNOWLEDGMENT: This work was supported by the Slovak Research and Development Agency under the contract LPP-0143-06.

REFERENCES

1. Stano, M. et al; J. Phys. B: At. Mol. Opt. Phys 2003.,36, , 261
2. Papp, P.; J. Chem. Phys. 2006, 125, 204301
3. Junk G., Svec H.; J. Am. Chem. Soc. 1963, 85, 839
4. Jochims H.-W. et al.; Chemical Physics 2004, 298, 279

TRANSPORT PROPERTIES OF ULTRATHIN INTERFACES BASED ON $Al/AlO_x/Al$

M. Diešková, miroslava.dieskova@gmail.com, P. Bokes, peter.bokes@stuba.sk, Department of Physics, Faculty of Electrical Engineering and Information Technology, Slovak University of Technology in Bratislava

INTRODUCTION

Metal/insulator/metal (MIM) tunnel junctions have a wide range of applications in electronics (single electron tranzistor[1], superconducting quantum bits[2], etc.). Recently it has been shown that ultrathin $Al/AlO_x/Al$ tunnel junctions can be used for strain sensing in low-dimensional nanostructures[3].

Electronic devices with dimension of few atomic layers have attracted a growing interest in last few years. Ultrathin interfaces between aluminium electrodes based on AlO$_x$ used as a basis for construction of Josephson junctions represent such structures. Functionality of these nanostructures critically depends on their transport properties.

The minimal estimated thickness in case of $Al/AlO_x/Al$ interfaces conforms to two oxygen layers. This experimental observation was in agreement with ab initio calculations of oxidized (111) surface of aluminium[4]. The height of effective potential barrier that is induced by presence of insulator has a strong and systematic dependence on its width. Both of these parameters have a direct relevance to the transport properties of the interface when modeling transport as a simple tunneling through square barrier and the dependence of the transmission spectra of ultrathin interfaces on the oxidation have been measured [5][6].

To fully understand these observations and to complement the complex problem of AlO_x interfaces it is necessary to perform an extensive computational study on the correspondence between the structure and transport processes in the interface from the first principles.

GEOMETRIC CHARACTERIZATION

Two geometric realizations of ultrathin $Al/AlO_x/Al$ interfaces, asymmetric a symmetric structure[7] are in the center of our interest. First of them (see Fig. 1) consists of chemisorbed oxygen ($O2$ atoms in Fig. 1) bounded to a full (111) layer of Al surface atoms ($Al3$ atoms). Above this oxygen there is situated a 2/3-filled Al layer ($Al2$).The 2/3-filled Al layer ($Al2$) with full oxygen layer ($O1$) and 1/3-filled Al ($Al1$) are forming an oxide AlO_x with stoichiometry $x = 1.0$ (O_{oxide}/Al_{oxide}). A width of the interface is defined as the vertical distance between the first non-bulk Al layer ($Al1$) and the last bulk-like layer ($Al3$), therefore $d = 4.53$Å. Chemisorbed oxygen layer is missing in case of symmetric structure (see Fig. 1) and AlO_x oxide conforms $Al2$ layer, $O1$ oxygen layer and $Al1$ layer, that is also the mirror plane of the oxide (see Fig. 1). Due to the sharing of 1/3-filled layer the overall stoichiometry is $x = 1.2$. The width of the interface is $d = 6.12$Å.

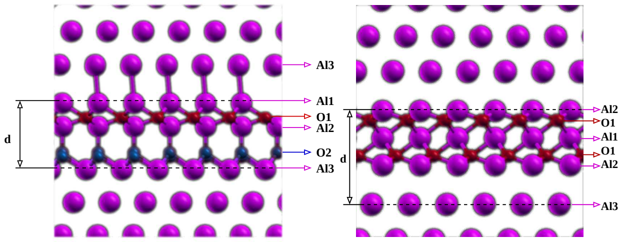

Fig. 1. Asymmetric and symmetric structure (side view).There are three types of Al layers (violet) on substrate with surface orientation (111). First type is $Al1$, 1/3-filled Al layer; second one is $Al2$, 2/3-filled Al layer, hexagonal structure without the centers; and the third type is $Al3$, full (111) layer, i.e bulk aluminum with orientation of surface (111). $O2$ atoms is a chemisorbed oxygen (only case of asymmetric structure, blue) bounded as well as $O1$ atoms (red) to a full (111) bulk aluminum $Al3$.

TRANSPORT CALCULATION

Within the approximation of non-interacting electrons transport properties can be described by Landauer approach[8]. The Landauer formula represents a connection between conductance $\mathcal{C}$ and transmission function $\mathcal{T}(E_F)$, which evaluation requires to have electronic structure of the considered system, which can be obtained from the first principles calculations.

$$\mathcal{C} = \frac{2e^2}{h}\mathcal{T}(E_F) \tag{1}$$

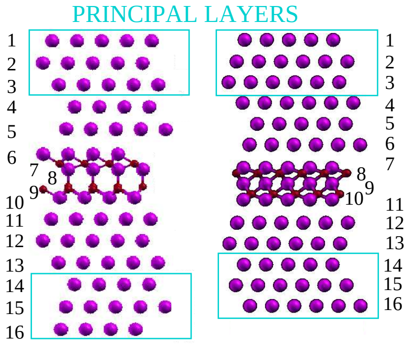

Fig. 2. Conductor region of asymmetric and symmetric structure. It contains principal layers that also conform semi-infinite leads by periodic repetition.

Calculation method combines ground state first-principles calculation of electronic structure (Density Funcional Theory (DFT) calculation based on plane-wave representations [9]), determination of the maximally localized Wannier functions (WFs) and transport calculation using a real-space Green's function formalism based on the Landauer approach. Bloch orbitals, that are delocalized in real space, can not be used directly for transport calculation due to their infinite etent. For this purpose they have to be transformed to localized functions. The most natural choice are maximally localized Wannier functions. This method is implemented in the computational package WanT [10].

Particular calculation can be divided in five main parts: calculation of electronic structure (i); splitting up the structure into three parts: conductor (C) connected to left (L) and right (R) semi-infinite leads that are constructed of periodically repeated principal layer (ii) (Fig.2); comparing of local electronic structure in order to have almost the same WFs in leads and conductor by checking the projected density of states (PDOS) (iii); finding well localized WFs (iv); and finally calculation of transport properties (v).

Finally we evaluated the two-terminal transmittance of the asymmetric and symmetric structure that is in agreement with the local density of states PDOS (v). PDOS also helps us to anticipate transport properties.

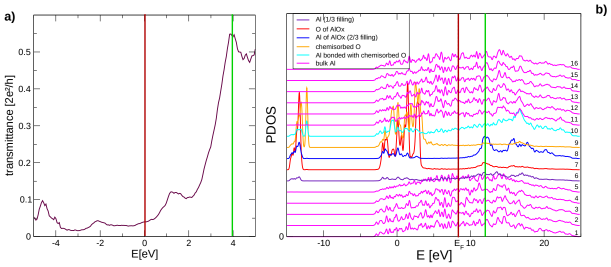

Fig. 3. (a)Two-terminal transmittance of asymmetric structure and (b) PDOS for all layers in conductor. Red line is a Fermi energy and green line represents maximum of transmittance (a). Small value of transmittance on Fermi level (a) coresrponds to a tunneling regime on E_F (b), $4eV$ above E_F there is a maximum of transmittance (a) and maximum of PDOS in 2/3 filled Al layer (b).

Both asymmetric and symmetric structure have a small value of transmittance on Fermi level that corresponds to a tunnelling regime of transport in the interface as we can see in Fig.3 and Fig.4. In case of asymmetric structure there is a maximum of transmittance $4eV$ above Fermi energy (Fig.3). On the contrary symmetric structure has a maximum $3.5eV$ below E_F, which is in agreement with PDOS calculation, there are presented states in the interface (Fig.4). According to these results we can assume two different kind of transport processes: electron mediating tunnelling in asymmetric structure and hole mediating tunnelling in symmetric structure. Due to a differences the line shape of the nearest resonances we can expect different temperature conductance dependencies, which is under our current investigation.

CONCLUSIONS

In conclusions, we have presented transport calculation of asymmetric and symmetric structure, two different arrangements for Al/AlO$_x$/Al interfaces using methodology that combines Density Functional Theory and Green's function method based on the Landauer formulation of the electronic transport within the framework of the maximally localized Wannier functions implemented in a computational package WanT. Based on our calculations we can suppose two different processes of transport for asymmetric and symmetric structure.

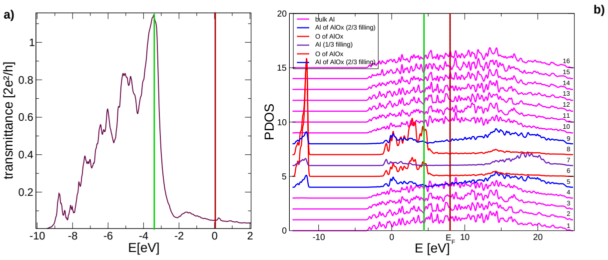

Fig. 4. (a)Two-terminal transmittance of symmetric structure and (b) PDOS for all layers in conductor. Red line is a Fermi energy and green line represents maximum of transmittance (b). Small value of transmittance on Fermi level (a) corresponds to tunnelling regime on E_F (b), $3.5eV$ below E_F there is a maximum of transmittance (a) and maximum of PDOS in interface Al (b).

ACKNOWLEDGMENT: We would like to thank Andrea Ferretti for useful discussions. The work has been performed under the Project HPC-EUROPA++ (RII3-CT-2003-506079), with the support of the European Community - Research Infrastructure Action under the FP6 Structuring the European Research Area Programme, and under Slovak grant agency VEGA (Project No. 1/0452/09).

REFERENCES

1. H.Grabert and M. Devoret, eds., *Single Charge Tunneing: Coulomb Blocade Phenomena In Nanostructures*, NATO ASI SERIES (Plenum, New York, 1992).
2. M. H. Devoret and J. M. Martinis, Quant. Info. Proc **3**, 163 (2004).
3. P. J. Koppinen, J. T. Lievonen, M. Ahlskog, and I. J. Maasilta, arXiv:0906.4234v1 [cond-mat.mes-hall] (2009).
4. D. R Jennison, A. Bogicevic, Surface Science **464**, 108 (2000).
5. K. Gloos, P. J. Koppinen, and J. P. Pekola, J. Phys.:Condens. Matter **15**, 1733 (2003).
6. W. H. Rippard, A. C. Perrella, F. J. Albert, and R. A. Buhrman, Phys. Rev. Lett. **88**, 046805 (2002).
7. M. Diešková, M. Konôpka, and P. Bokes, Surf. Science **601**, 4134-437 (2007).
8. M. Koentopp and K. Burke, Phys. Rev. B **73**, 121403 (2006)
9. F. Nogueira, A. Castro, and M. A. L. Marques, A Tutorial on Density Functional Theory, in Lecture Notes in Physics: A Primer in Density Functional Theory, Springer (2002).
10. www.wannier-transport.org.

MAGNETIC PROPERTIES OF $[Ni(en)(H_2O)_4]SO_4 \cdot 2H_2O$ – S = 1 QUANTUM MAGNET

R. Tarasenko, robert.tarasenko@gmail.com, A. Orendáčová, alzbeta.orendacova@upjs.sk, I. Potočňák, ivan.potocnak@upjs.sk, M. Kajňaková, marcela.kajnakova@upjs.sk, M. Orendáč, martin.orendac@upjs.sk, A. Feher, alexander.feher@upjs.sk, Centre of Low Temperature Physics of SAS and P.J. Šafárik University, Park Angelinum 9, 041 54 Košice, Slovak Republic and K. Tibenská, katarina.tibenska@tuke.sk, Technical university in Košice, Letná 9, 042 00 Košice, Slovak Republic

INTRODUCTION

Two-dimensional (2d) frustrated spin systems have attracted much attention since they can exhibit unconventional magnetism [1]. Recently, we studied magnetic properties of a molecular magnet $Cu(en)(H_2O)_2SO_4$ (en = ethylenediamine) which is a representative of the S = 1⁄2 spatially anisotropic triangular lattice [2]. The specifity of this material is based on the fact that the magnetic lattice is formed of unconventional exchange bridges supported by hydrogen bonds (HBs). The present work is devoted to the experimental study of magnetostructural correlations of nickel(II) analogue of $Cu(en)(H_2O)_2SO_4$, a potential representative of an S = 1 spatially anisotropic triangular lattice characterized by the competition between quantum fluctuations, geometrical frustration and single-ion anisotropy.

EXPERIMENTAL DETAILS

$[Ni(en)(H_2O)_4][SO_4] \cdot 2H_2O$ (NEHS) has been synthesized in the form of blue prisms from an aqueous solution of nickel sulphate and en in stoichiometric amounts. X-ray single crystal studies revealed that the structure of the compound is already known and was published in the work [3]. NEHS crystallizes in the monoclinic system with the unit cell parameters 9.523 x 12.185 x 11.217 Å^3. The crystal structure of the compound is build of $[Ni(en)(H_2O)_4]^{2+}$ cations, $[SO_4]^{2-}$ anions and two water molecules comprising basic structural units (Fig. 1). The units are mutually connected by a large number of HBs forming a three-dimensional crystal structure. Considering magnetic orbitals of Ni(II) ion in octahedral surroundings, the magnetic system can be viewed as a 3d array of coupled S = 1 triangular layers formed within *bc* plane (Fig. 2).

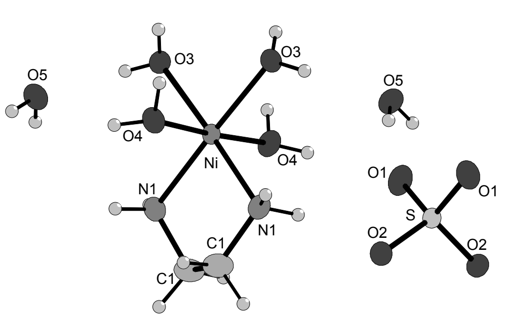

Fig. 1. Structural unit of NEHS.

Specific heat measurements of 7 mg single crystal have been performed on a commercial PPMS system. Magnetic susceptibility studies of a powder sample with a mass of 130 mg have been performed in a commercial SQUID magnetometer.

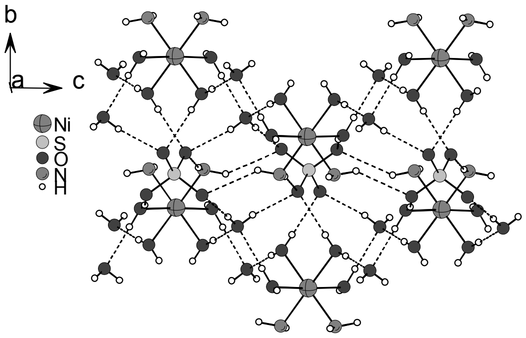

Fig. 2. Projection of the crystal structure into the *bc* plane. The hydrogen bonds are presented by dashed lines.

RESULTS AND DISCUSSION

The specific heat was experimentally studied in zero magnetic field in the temperature range from 1.8 to 30 K. The behaviour of the data is dominated by a round anomaly at 4.4 K and a monotonic increase is observed at higher temperatures (Fig. 3). Since NEHS represents a magnetic insulator, the total specific heat, C_{tot}, is determined by the phonon contribution, C_{ph} and magnetic subsystem, C_{mag}. For a quantitative analysis of magnetic specific heat, the lattice contribution has been subtracted. The standard procedure based on the finding of a temperature region where the approximation $C_{mag} \approx a/T^2$ and $C_{ph} \approx bT^3$ works, provided overestimation of the lattice contribution, thus, a higher term has been introduced in the phonon specific heat, $C_{ph} \approx bT^3 + cT^5$.

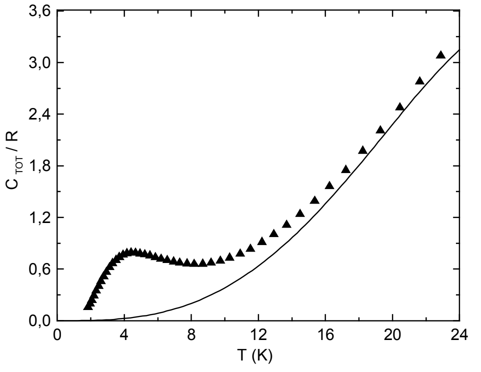

Fig. 3. Temperature dependence of NEHS specific heat in zero magnetic field (triangle). The solid line represents a lattice contribution.

The fitting procedure performed in the range from 12 to 20 K yielded the estimation of coefficients, a =

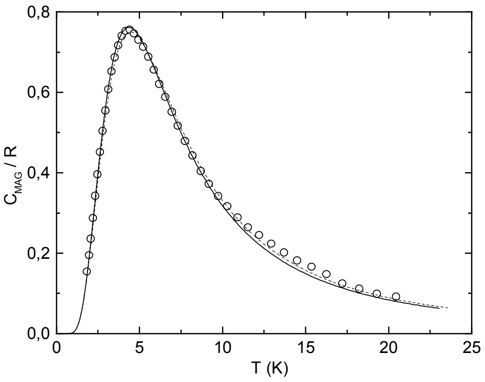

Fig. 4. Temperature dependence of magnetic specific heat of NEHS (circle). Solid and dashed lines represent the $S = 1$ paramagnet with $E/D = 0$, $D/k_B = 11.6$ K and $E/D = 0.1$, $D/k_B = 11.6$ K, respectively.

312 J K/mol, $b = 0.00345$ J/(K^4 mol) and $c = -2.7.10^{-6}$ J/(K^6 mol). Assuming 9 vibrating groups in the NEHS molecule, the Debye temperature $\Theta_D \approx 170\pm5$ K has been evaluated from the b coeffcient. The rather low value of Θ_D reflects a softness of the structure resulting from the low-energetic hydrogen bonds providing intermolecular contacts.

The analysis of the crystal structure suggests that the hydrogen bonds also support the formation of unconventional exchange paths mediating exchange coupling between $S = 1$ spins. Considering the elongation of local octahedral surroundings of Ni(II) ion, uniaxial single-ion anisotropy can be expected to control magnetic properties of NEHS. Following the approach applied in Ref. [4] for heteroleptic complexes, we estimated the effective elongation of the octahedron $D_{structure} \approx 14$ pm which corresponds to the single-ion anisotropy parameter $D/k_B \approx 12$ K while in-plane anisotropy parameter, E/k_B, related to the rhombic distortion of the octahedron, has been neglected. After subtracting the lattice contribution, the magnetic entropy was calculated from the magnetic specific heat data in the region from 1.8 K to 20 K. A standard extrapolation was employed in the interval from 20 K to $T \rightarrow \infty$, while missing specific heat data below 1.8 K have been extrapolated by an exponential decrease as expected for the systems with dominant single-ion anisotropy effects. The good agreement between the experimental value $S = 9.56 \pm 0.50$ J/(K mol) and the theoretical entropy $R\ln(2S + 1)$ for spin 1 indicates the absence of a phase transition to the ordered state below 1.8 K. Consequently, in the first approximation, the magnetic specific heat data have been analyzed within a simple model of a spin 1 paramagnet with energy levels split by a crystal field described by D and E parameters in the spin Hamiltonian $H = DS_z^2 + E(S_x^2 - S_y^2)$. The best agreement was found for the easy-plane model with $E/D < 0.1$ and $D/k_B = 11.6 \pm 1.5$ K (Fig. 4).

Magnetic susceptibility has been measured in the temperature range from 1.8 to 300 K in the field 10 mT. The susceptibility has been corrected for the contribution of core diamagnetism which was estimated using Pascal constants $\chi = -179.1 \cdot 10^{-6}$ emu/mol. The data in the whole temperature range are well characterized by a theoretical prediction for $S = 1$ paramagnet with $g = 2.07$ and $D/k_B = 11.6$ K (Fig. 5). It should be viewed that the excellent agreement between the parameters obtained from the specific heat and susceptibility analysis supports our assumptions about the dominant influence of crystal field on the magnetic properties of NEHS.

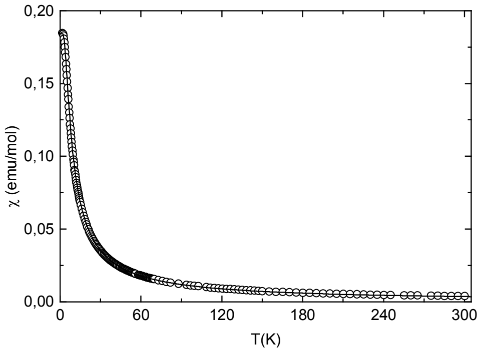

Fig. 5. Temperature dependence of the magnetic susceptibility of powdered NEHS. The solid line represents the teoretical prediction of susceptibility of powdered sample for the system with dominant effect of crystal field with $g = 2.07$ and $D/k_B = 11.6$ K.

CONCLUSION

Analysis of experimental data clearly demonstrates the dominant effect of crystal field on the magnetic properties. The analysis confirmed that the compound can be treated as a spin 1 single molecule magnet with nonmagnetic ground state. In the near future, further experiments will be performed to estimate the strength of intermolecular exchange coupling. The interplay of geometrical frustration, single-ion anisotropy and suffciently large magnetic fields is expected to introduce interesting quantum effects at temperatures comparable with the strength of magnetic correlations.

ACKNOWLEDGMENT: This work was supported by VEGA grants 1/0078/09, project APVV-006-07, ESF RNP program HFM and ERDF EU (European Union European regional development fond) grant, under the contract No. ITMS26220120005. Material support from US Steel DZ Energetika is greatly acknowledged.

REFERENCES

1. G. Misguich, C. Lhuillier: Frustrated Spin Systems (Ed. H.T. Diep, World Sci., Singapore - 2005)
2. M. Kajňaková et al., Phys. Rev. B **71**, 014435 (2005).
3. P.C. Healy et al ., Australian J. Chem. **37**, 921 (1984).
4. R. Ivaniková et al., Polyhedron **25**, 3261 (2006).

NEGATIVE IONS IN N_2/CH_4/AR PLASMA - A SIMULATION OF TITAN'S ATMOSPHERE CHEMISTRY

G. Horvath, gabriel.horvath@fmph.uniba.sk, M. Zahoran, S. Matejcik, Department of Experimental Physics,
Comenius University, Mlynska dolina F-2, 842 48 Bratislava, Slovakia, Y. Aranda-Gonzalvo, Plasma & Surface
Analysis Division, Hiden Analytical Ltd., 420 Europa Boulevard, Warrington WA5 7UN, United Kingdom
N. J. Mason, Department of Physics and Astronomy, The Open University, Walton Hall, MK7 6AA, Milton Keynes,
United Kingdom

INTRODUCTION

The recent Cassini space mission to Saturn and the release of its Huygens probe onto its largest moon, Titan, has led to a wealth of data on the atmospheric and surface composition of Titan, presenting us with a set of unexpected (and fascinating) results including the observation of hydrocarbon lakes – the first liquid 'seas' on a solar system body outside the Earth; and the observation of anions in the upper atmosphere (ionosphere) [1]. The dense atmosphere of Titan is mostly composed of N_2 with a few percent of CH_4. The most important minor compounds detected by Cassini Huygens are nitriles believed to be formed by as a result of dissociation of nitrogen and methane either by solar induced photolysis or by electron impact and hydrocarbons [2]. Charged particles, originating from the Saturnian magnetosphere, can accumulate on droplets within the clouds of the Titan's troposphere. Neutralization of these charged particles leads to corona discharges inducing chemical reactions [2].

Probably because the three-body electron attachment to radicals [3, 4] is negligible at high altitude and because aerosols were not expected to be present above ~500 km, the presence of negative ions in Titan's upper atmosphere had not postulated before the Cassini-Huygens mission. Therefore it came as a surprise when Cassini detected numerous negative ions in Titan's upper atmosphere [5, 6], observations that Vuitton *et al* have sought to explain in a new model of the chemistry in Titan's upper atmosphere [1, 7].

EXPERIMENTAL SET-UP

The apparatus used in these experiments is shown schematically in Figure 1. A simple negative point-to-plane corona discharge was formed by using a stainless steel needle aligned opposite the sampling entrance of a HPR60 (Hiden Analytical Ltd.) Molecular Beam Mass Spectrometer (MBMS), [reference: Y. Aranda Gonzalvo et. al., JVST A 24 (3) 2006]. The distance between the needle and the planar electrode was 8 mm. To hold the needle to front of the MBMS a stainless steel chamber was made. A voltage was applied between the needle (high voltage) and the entrance of the MBMS (ground electrode) creating a discharge with a constant volume of 80 cm^3. Charged particles created in the discharge were sampled through the small sampling orifice (0.2 mm diameter) of the MBMS. The present experiments were performed using a N_2(88%)/Ar(8)/CH_4(4%) mixture at a pressure of 350 Torr and ambient temperature, 20 ◦C. A mixing ratio was prepared and introduced into the reactor using MKS flow controllers. The total flow rate used (flow rate on the reactor inlet + pumping speed of the sampling orifice) were 800 $cm^3.min^{-1}$. The point electrode was powered by a Spellman HV source whose output was measured using a HV probe combined with a digital multi-meter. The discharge current was measured using a Fluke milliampmeter. A 5 MΩ resistor was connected in serial to the discharge in order to stabilize the corona.

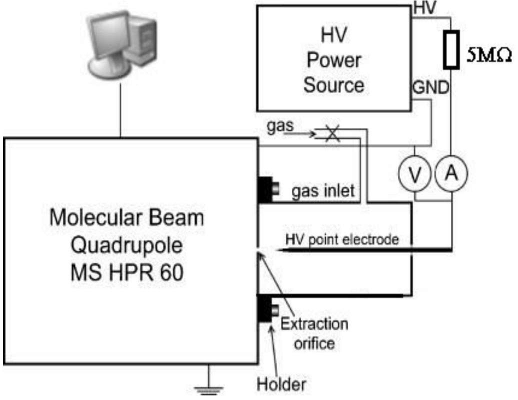

Fig. 1. A schematic diagram of the experimental apparatus.

EXPERIMENTAL RESULTS AND DISCUSSION

All the experiments were performed in a 'quasi-flowing' regime with the gas mixture being introduced into the discharge chamber through a needle valve whilst the orifice into the mass spectrometer acted as the gas outlet. Mass spectra were recorded after allowing a suitable time for the discharge to stabilize. Stable conditions in the discharge were assumed when the relative yield of detected anions reached a constant value. The relative yield Y_r of ions having a mass per charge smaller than 100 amu was calculated from the measured absolute yield of ions *i*-type in spectra Y_i by the formula

$$Y_r = \frac{Y_i}{\sum_i Y_i} \times 100(\%) \qquad (1)$$

Typical mass spectra of negative ions obtained at 0.8 mA for different flow rates (reactor pressure) are shown in Figure 2. The abundances of ions having mass more than 100 AMU were negligible. Anion mass spectra have been measured for six selected discharge currents currents in range of 0.2 up to 0.8 mA. Seven dominant anions (masses 26, 40, 41, 41, 46, 50, 65) were observed in the spectra. In addition several identified (masses 64, 66 and 74) and unidentified negative ions (masses 79, 80, 82, 83, 91 and 92) were measured albeit with typical abundances 0.2–1.5 %.

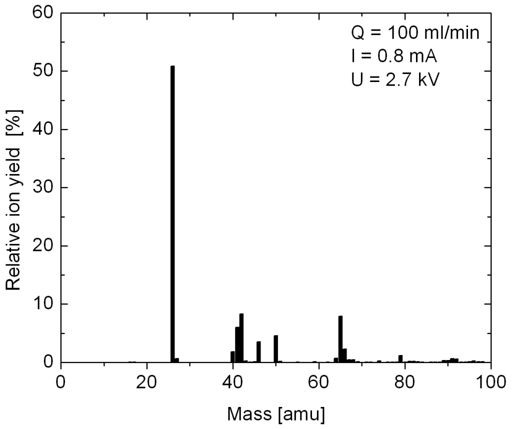

Fig. 2. Mass spectra of negative ions extracted from the discharges.

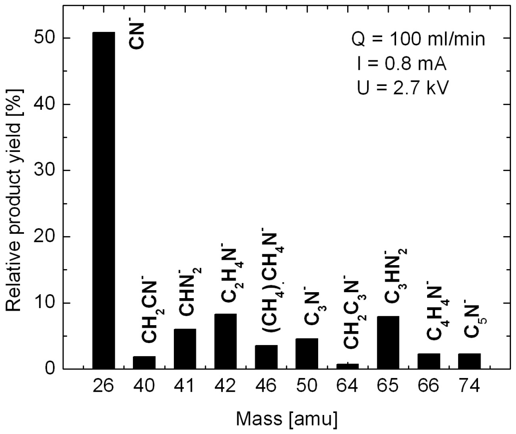

Fig. 3. Relative abundances of the most dominant anions formed in negative corona discharge.

Identification of such unidentified negative ions will require some additional experiments so will not be discussed further. Most of the dominant ion peaks could be ascribed to monomers but one species has been found in cluster form (Figure 3).

According to [1] negative ions are expected to be mostly deprotonated neutrals. For this reason we do not consider closed-shell molecules such as CH_3CN^-, $C_2H_2^-$ or HCN^- to be possible negative ion candidates. Another relevant thermodynamic constant is the gas phase acidity of the molecule AH, which characterizes the ability of the molecule to lose H+ by reactions

$$AH \rightarrow A^- + H^+ \qquad (2)$$

$$AH + B^- \rightarrow A^- + BH\,. \qquad (3)$$

Species containing the cyano (CN, C_3N) or the ethynyl (C_2H, C_4H, C_6H, C_8H) group have a very high electron affinity (≥ 3eV) [1]. As it can be seen in Figure 2, the detection of CN^-, CH_2CN^-, C_3N^-, CH_2CN^- and C_5N^- anions provides good evidence of the presence of HCN, CH_3CN, HC_3N and HC_5N neutrals that have already been detected by others and the Cassini flyby [1, 8, 9].

An important disagreement with Cassini's data and experimental measurements is that no hydrocarbon chain ions have been identified in our experiment. The absence of $C_{2n}H^-$ in the spectra can be explained by relatively fast proton transfer reactions, leading to an increase in the yield of N^-bearing ions and fast recombination of reactive $C_{2n}H^-$ anions [10, 12]) in the drift region of corona discharge

$$C_2H^- + HCN \rightarrow CN^- + C_2H_2 \qquad (4)$$

$$C_2H^- + HC_3N \rightarrow C_3N^- + C_2H_2 \qquad (5)$$

$$C_2H^- + HC_5N \rightarrow C_5N^- + C_2H_2 \qquad (6)$$

Thus the C_2H_2 neutral detected in our earlier measurements made in coaxial corona discharge [12] leads to the formation of CN^-, C_3N^- and C_5N^- anions rather than C_2H^- production. The formation of cluster anions in low-power discharges has been reported by several authors. The rapid decrease in abundance of anion at mass 46 with increasing power is a typical phenomenon of clustering where the higher electric field breaks up the weak Van der Walls bonds. The negative ion at mass 46 has therefore been identified as $(CH_4).CH_4N^-$ anion. Masses 41, 42, 65 and 66 have been tentatively identified as CHN_2-, $C_2H_4N^-$, $C_3HN_2^-$ and $C_4H_4N^-$ anions respectively but their origin needs further investigation.

CONCLUSIONS

The mass spectra of negative ions formed in a negative $Ar/N_2/CH_4$ corona discharge, operating at a pressure 350 Torr and room temperature, are very complex and have revealed many ionic species that have not been observed in previous studies. Detection of CN^-, CH_2CN^-, C_3N^-, CH_2CN^- and C_5N^- anions and the surprising absence of hydrocarbon radical anions have raised new questions about the dependence of negative ion chemistry on the discharge type.

ACKNOWLEDGMENT: This research project was supported by: The Slovak Grant Agency, VEGA 1/1267/04, VEGA 1/0051/08, project SK-CN-0029-07, ESF COST Action CM0601, CM0805 and EIPAM.

REFERENCES

1. V. Vuitton, Planet. Space Sci. in press (2009).
2. S. Vinatier, Icarus **188**, 120-138 (2007).
3. G. J. M-Cuberos, Geoph. Res. Lett. **27**, 1351 (2000).
4. E.L.O.Bakes, Icarus **157**, 464-475 (2002).
5. A.J. Coates, Geophys. Res. Lett. **34**, L22103 (2007).
6. J. H. Waite, Science. **316**, 870-875 (2007).
7. V. Vuitton, Philosophical Transactions of the Royal Society A, doi:10.1098/rsta.2008.0233 (2009).
8. A. Ricard, Plrmt. Spuw Sci. **43**, 41-46. (1995).
9. R. N-Gonzalez, Adv. Space Res. **19**, 7, 1121 (1997).
10. G.I Mackay, J. Phys. Chem. **80**, 2919-2922 (1976).
11. C. Barckholtz, Astrophys. J. **547**, L171 (2001).
12. G. Horvath, Plasma Sources Sci. Technol. **18** (2009) 034016.

CONSTRUCTION OF LABORATORY PULSED MAGNET

M. Figura[1,2], figura@saske.sk, M.Zentková[1], M. Mihalik [1], A. Zentko [1], J. Lešinský [3]
[1]Institute of Experimental Physics SAS, Watsonova 47, 040 01 Košice
[2]Faculty of Humanities and Natural Sciences, University of Prešov, ul 17. novembra, Prešov
[3]Grammar school Exnárova 10, 040 22 Košice

INTRODUCTION

Pulsed magnets play an important role in high magnetic fields science, because they can generate much higher magnetic fields when than DC magnets. The main disadvantage of this type of magnets is connected with the small working area - they tend to have very small bores (10-20 mm), and they work only for short periods of time (10 to 100 ms). Pulsed magnets are resistive magnets using material capacity and strong current source for work in extreme conditions. By providing access to fields far higher than those accessible using steady-state magnets, pulsed magnets offer opportunities for new discoveries that can take research in new directions. Primary task of our work was construction of a source of pulsed electric current – capacitor bank. In the second step we constructed magnetic coil and tested whole system.

EXPERIMENTAL AND RESULTS

Capacitor bank. Pulses are created by the fast discharging of a system of condensers directly connected to the magnetic coil. This process is accompanied by release of huge amount of energy. The heart of generator is capacitor bank consisting from 6 condensers with total capacity 12 mF chargeable up to 500 V. Schematic drawing of the capacitor bank is shown in Fig.1. Utilized SNAP-IN condensers are especially suitable for pulsed sources and can stand shortcut currents (Fig.2). We used capacitor bank as the source of DC current for magnetic coil. A tyristor was used to discharge condensers and switch on the current between 2000A and 5000 A flowing to magnetic coil.

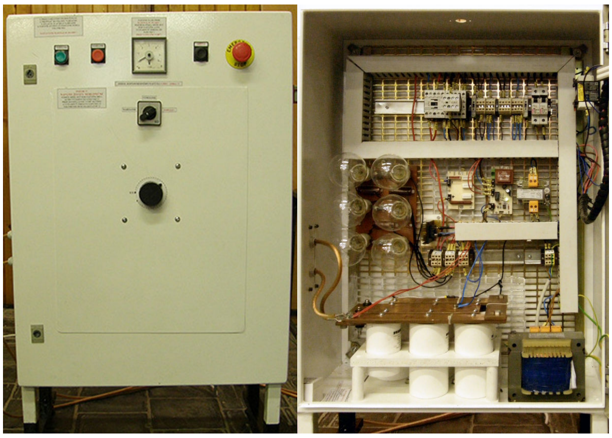

Fig.2. Capacitor bank with condensers – front panel (left-hand side) and interior (right-hand side; condensers are white cylinders in left lower corner).

The massive copper leads (8 mm thick) sunk in liquid nitrogen serve for cooling of the thyristor. Gret's bridge serving as suitable rectifier was mounted on a block of cooler and to the electric circle. It is connected by fast clamps. Proper function of the tyristor was controlled by a driver. The time of pulse for closure of the thyristor was set by triggering circuit to 10 ms. Thyristor closures the part of circuit in 10 ns. Set of 6 bulbs (above condensers – Fig.2.) serves for emergency discharging of the capacitor bank.

Magnetic and pick-up coils. From the geometric parameters of the magnetic coil and the current introduced to the coil we can estimate magnetic field generated inside the coil. For our experiment we used a set of magnetic coils which length *l* varied between 200

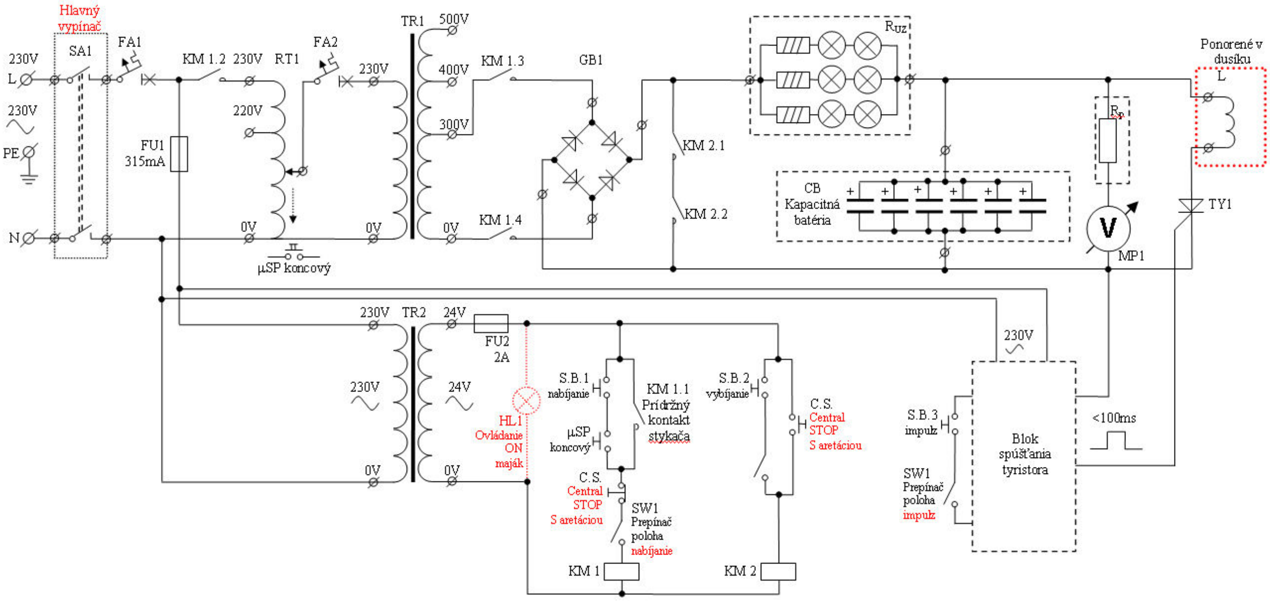

Fig.1. Schematic drawing of the capacitor bank.

and 250 mm with outer diameter close to 12 mm. Coils are produced from copper wire with typical diameter was d = 0.32 covered with cotton or isolated varnish. Pick-up coil with 80 threads is twisted on a plastic straw with inner diameter of 6 mm. The pick-up coil is separated from the magnetic coil by an isolated contracted layer (black). The magnetic coil itself consists of three layers of threads (80 – 75 – 70) isolated by the contracted layer. We tested magnetic coils fixed by epoxy resin or just without any fixation. The resistivity of magnetic coil is 0,241Ω at the temperature of liquid nitrogen. A set of tested coils is shown in Fig.3.

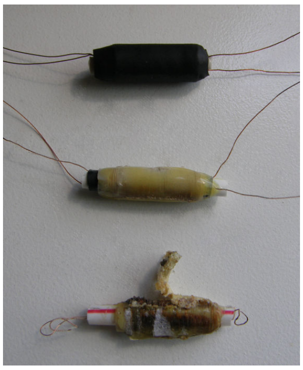

Fig.3. Set of tested coils: i.) magnetic coil covered by contracted isolated tape; ii.) magnetic coil fixed with epoxy resin; iii.) destructed coil.

As can be seen from this figure the fatigue stresses in high-field pulsed magnets often lead to dramatic failures and to destruction of the coil.

Measurements. The voltage on magnetization coil and the pick-up coil were measured by two channel 125 MHz digital oscilloscope. Experimental set up of experimental equipment is shown in Fig.4. Both coils are cooled by liquid nitrogen. Magnetic coil is connected to A channel and pick up coil is connected to B channel of the oscilloscope. The typical evolution of voltage on both coils is shown in Fig.5. We are going to focus on exact measurement of the current in magnetic coil and to analysis of voltage on pick up coil. In the circuit of magnetic coil a by-pass resistor was connected. The set of coils was tested without any sample or on $La_{0.66}Ca_{0.33}(Co_{0.06}Mn_{0.94})O_3$ ceramic.

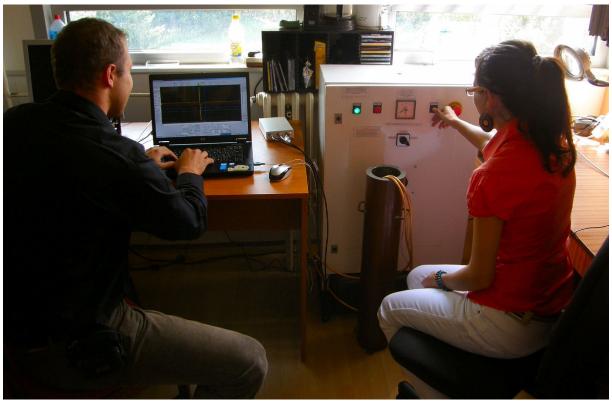

Fig.4. Experimental set up consists of the capacitor bank, magnetic and pick-up coils which are placed in liquid nitrogen, massive in let copper wires, digital oscilloscope and a computer.

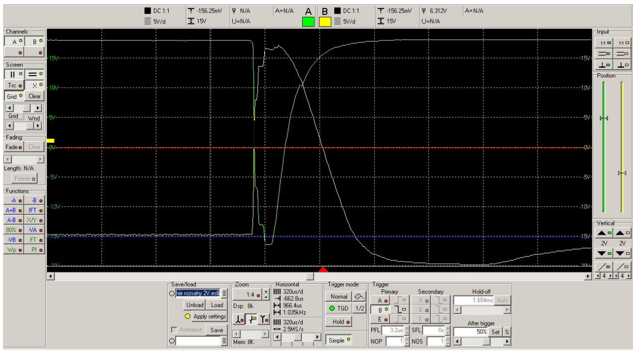

A: DC 1:1, 5V/d, -156.25mV, 15V, N/A, U=N/A, A=N/A
B: DC 1:1, 5V/d, -156.25mV, 15V, 6.312V, U=N/A, A=N/A
Zoom: 1:4, Dsp: 8k, Mem: 8K
Horizontal: 320us/d, -662.8us, 966.4us, 1.035kHz, 320us/d, 2.5MS/s
Hold-off: 1.654ms
PFL: 3.2us, SFL: 0s, NOP: 1, NOS: 1
After trigger: 50%
Save/load: nie rozsahy 2V.esb

Fig.5. Process of voltage change on magnetic and pick-up coil.

CONCLUSIONS

We constructed a capacitor bank capable to generate 10 ms current pulses up to 2000 A. The capacitor bank was tested on a set of magnetic and pick-up coils. The signal on magnetic and pick-up coil was monitored by a digital oscilloscope. The determination of exact generated magnetic field and analysis of signal in pick-up coil are in progress.

ACKNOWLEDGMENT: Presented work was supported by the projects LPP-00-30-06 “Scientific incubator for pupils and students” and LPP-0270-09”Science–user friendly”.

CHARACTERIZATION OF MICROHOLLOW CATHODE DISCHARGE IN Ar

M. Klas, klas@fmph.uniba.sk , M. Stano, stano@fmph.uniba.sk, S. Matejčík, matejcik@fmph.uniba.sk
Department of Plasma Physics, Comenius University, Mlynská dolina, Bratislava 842 48

INTRODUCTION

In present time exists deep scientific and technological interest to generate homogenous plasma processes at high pressure. The Microhollow cathode discharges (MHCD) is a promising technique to generate high pressure glow plasma [1]. MHCD structures consist of metallic electrodes with a hole in the center separated by an insulator. The range of the discharge operating pressure depends of cathode hole diameter D and thickness of the insulator according to Allis-White similarity law. In present work we study DC characteristics of the MHCD discharge as a source of uniform, nonequilibrium plasma at high pressure with relatively low breakdown voltage [2, 3]. The MHCD are very promising for various applications like a ozone generation, plasma chemistry, generation of UV radiation a.o. We are interested for MHCD as an ion source for the Ion mobility spectrometer (IMS) [4].

EXPERIMENTAL SETUP

These MHCD structure was prepared by deposition of Cu electrodes on both sides of the ceramic (Al_2O_3 96%) film. The Cu electrodes have been made by vacuum evaporation technique. A ceramic insulator was chosen for a suitable thermal and electric properties and a low sputtering coefficient that enables a longer lifetime. The hole with a diameter of 1,2mm was drilled mechanically. The discharge current of the MHCD was limited to 0.2 mA and discharge current was measured by a 1 kΩ resistor.

RESULTS AND DISCUSSION

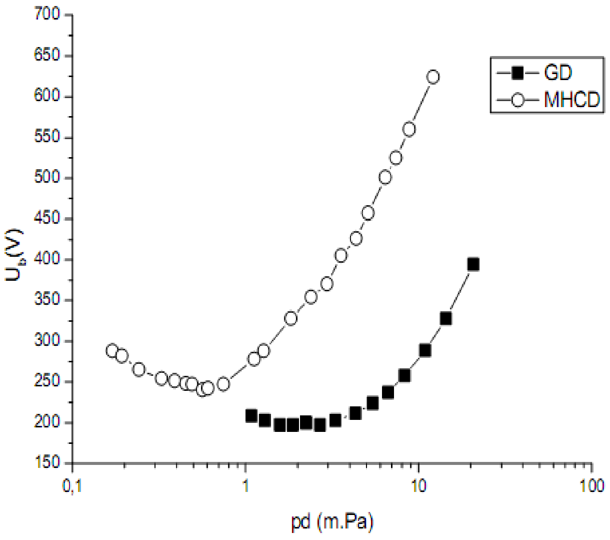

Fig. 1. Paschen curve for MHCD in Ar and Paschen curve of Ar from Reizer [5].

In the present work we have measured the breakdown voltage of the MHCD structure as a function of the Ar pressure in a limited pressure range 3-200 mbar. The measured curve is presented in a form of a Paschen curve in the Fig. 1. Present data are compared with Paschen curve of Ar of ordinary planar discharge tube published in Reizer [5]. The minima of the Paschen curves are mutually shifted due to a different mechanism of ignition and different shapes of electrodes used in the experiments.

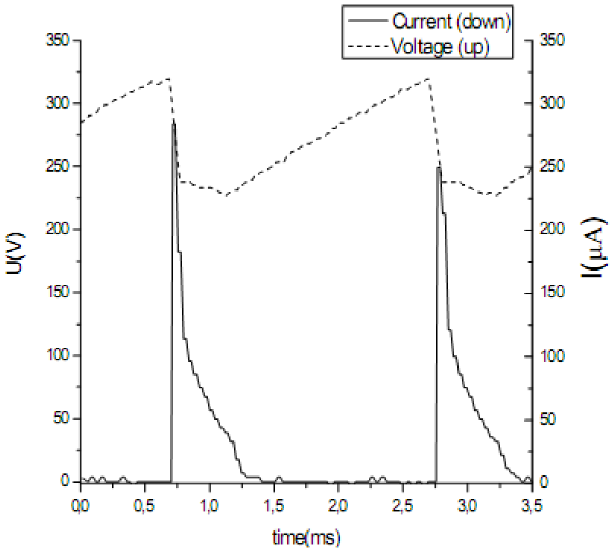

Fig. 2. Discharge course for time, p=30mbar

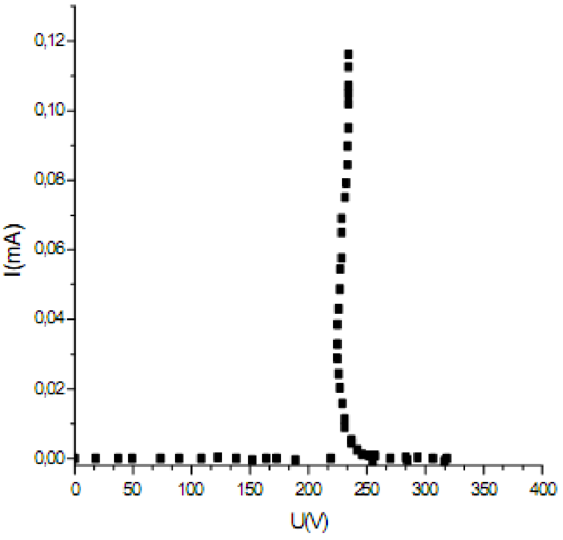

Fig. 3. Volt ampere characteristic of MHCD, p=30mbar

In the Fig. 2 the time dependence of the discharge voltage and discharge current of the MHCD is presented. We have observed a self pulsing character of the MHCD type DC discharge. This self pulsing regime (according to [6]) occurs between the abnormal glow regime where the plasma is confined in side of the hole (low current) and the normal glow regime where the plasma expand (high current).

In Fig. 3 the current voltage characteristics of discharge measured at p=30 mbar is shown. The breakdown occurred at appr. 315 V and the discharge was stabilized at app. 230V where the DC I-V characteristic has the character of a glow discharge.

CONCLUSIONS

In this experiment we have measured the DC characteristics of MHCD. The DC characteristics of the MHCD are very promising for it application as an source of the ions in IMS spectrometer. In near future we plan investigations of the MHCD at atmospheric pressure by means of optical and electrical diagnostic techniques in order to measure ion density, electron temperature, electron density, voltage current characteristics of the discharges and the electron energy distribution function of the discharge.

ACKNOWLEDGMENT: This work was supported by the Slovak grant agency VEGA project Nr. VEGA-1/0051/08.

REFERENCES

1. K.H.Schoenbach, A.El-Habachi, W,Shi, and
2. M.Ciocca, Plasma Sources Sci. Technol. 6, 468 (1997)
3. Ch. Penache, Phd thesis, Study of High-Pressure Glow Discharges Generated by Micro-Structured Electrode (MSE) Arrays, University Frankfurt am Main, (2002).
4. A. Brauning, Demian , O. Hohn , T. Jahnke and C. Penache “Microstructure electrodes: A new multipurpose plasma source,” GSI Scientific Report, pp. 114 (2001).
5. Beegle, L. W.”,A High-Pressure Hollow Cathode Discharge Source for Ion Mobility Spectrometers for In-Situ Detection of Organic Molecules on Mars“,Lunar and Planetary Science XXXII (2001).
6. Yuri P. Raizer, “Gas Discharge Physics”, SpringeVerlag Berlin Heidelberg New York (1997).
7. Xavier Aubert et al, Analysis of the self-pulsing operating mode of a microdischarge, Plasma Sources Sci. Technol. , 16 23-32 (2007).

THIN-LAYER BOLOMETRIC STRUCTURES

[1] V. Jacko, umerjack@savba.sk, [2] P. Schlosser, peter.schlosser@gmail.com, [2] T. Roch, roch@fmph.uniba.sk
[2] M. Zahoran, miroslav.zahoran@fmph.uniba.sk, [2] P. Kúš, kus@fmph.uniba.sk,
[2] A. Pleceník, plecenik@fmph.uniba.sk, [3] Š.Haščík, elekhasc@savba.sk,
[1] Institute of Mesurement Science, Slovak Academy of Sciences, Dubravska cesta 9, 841 04 Bratislava, SK
[2] Faculty of Mathematics, Physics and Informatics, Comenius University, Mlynská dolina 842 48 Bratislava, SK
[3] Institute of Electrical Engineering, Slovak Academy of Sciences, Dubravska cesta 9, 841 04 Bratislava, SK

INTRODUCTION

Microbolometric structure on base of thin layers is the basis of infrared imaging systems. Infrared cameras found wide application in many areas such as science, technology, protection of property and also in the army. It has succeeded thanks to a decreasing price of these devices. Research on new materials creates conditions for easier and more reliable production of array, but also for the sole elements. The contribution concentrates on the properties of vanadium oxide layers. These were applied to the GaAs substrate with specific characteristics. The main task was to optimize the technological processes for the desired properties of the layer, repeatability, and time stability.

PREPARATION OF VO_x LAYERS

The technology of the vacuum magnetron sputtering was used for the preparation of the layers. Magnetron was powered by direct current. A special vacuum apparatus was evacuated with the use of turbo-molecular pump, thin layers were deposited in the presence of argon and oxygen. Oxygen and its application has been a limiting factor determining the final characteristics of a created layer.

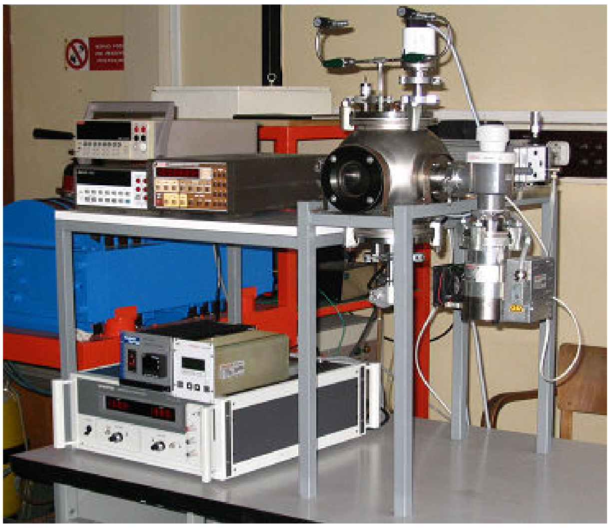

Fig. 1. Experimental apparatus

It was prepared by several groups of samples on substrates of GaAs, Si and AlGaAs. The main target was to monitor the dependence of electrical resistance on temperature and the resistance value at 25 °C. The thickness of prepared layers was measured and the chemical and structural composition of some selected samples was examined.

THICKNESS OF THE DEPOSIT LAYERS

We used SEM to measure the thickness. The following picture shows a sample cross-section. The thickness of Vox layer is approximately 220 nm.

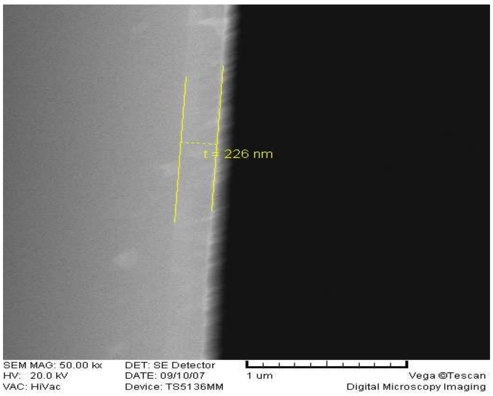

Fig. 2. SEM micrograph of a VO_x layer on silicon wafer (cross – section)

ELECTRICAL RESISTANCE, AND ITS DEPENDENCE ON TEMPERATURE

These parameters are interconnected and therefore the change of technology simultaneously affects the resistance of the sample at 25 °C and its dependence on temperature. These parameters are influenced by a controlled quantity of oxygen during the preparation of the layers. The results of the measurements are shown in Fig. 3.

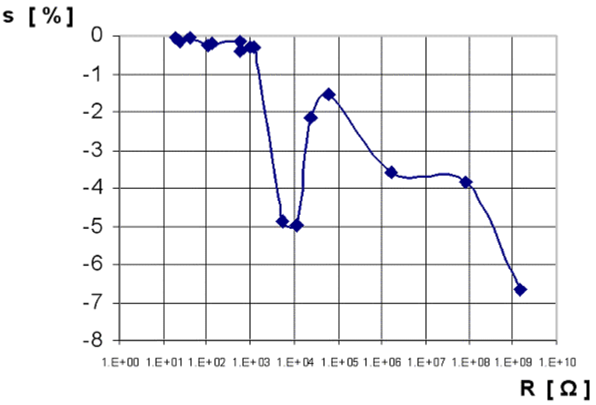

Fig. 3. Dependence of **s** vs. **R**

Electrical resistance samples in the range of hundreds of ohms to tens of kilo-ohms are interesting for practical application. The picture shows that in this range there are interesting parameters of the samples with electrical resistance of approximately 10kΩ and steepness of dependence of electrical resistance at a temperature of up to **s** = -5%.

BOLOMETER CONSTRUCTION

The thin membrane AlGaAs was used as an experimental construction. We made a simulation of its thermodynamic properties by a computer program "COMSOL MULTIPHYSICS".

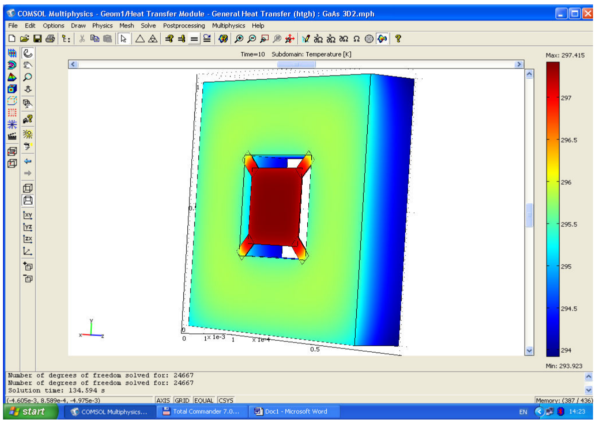

```
Number of degrees of freedom solved for: 24667
Number of degrees of freedom solved for: 24667
Solution time: 134.594 s
```

```
(-4.605e-3, 8.589e-4, -4.975e-3)
```

Fig. 4. Model structure

The figure represents the steady-state temperature ratios after irradiation. Duration of exposure was 10s. The intensity was 100W/m^2. Time constant was τ = 0.35 s. The surrounding of the membrane was filled with air. After the execution of the calculations we studied the possibility to simplify the proposed structure and to reduce the number of technological operations.

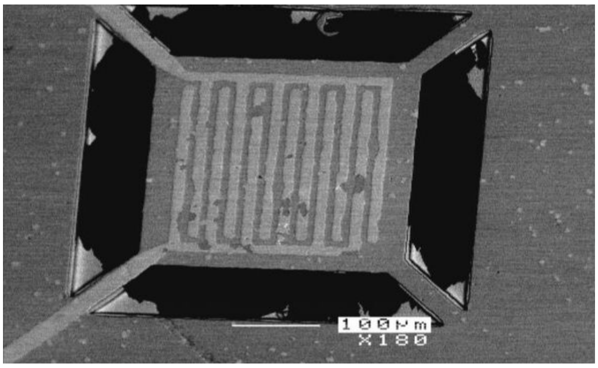

Fig. 5. Experimental sample

There is the appearance of the actual membrane with the electrodes shown in Fig.5. You can see a group of defects on the sample. We made an analysis of model membranes without carrier bridges and analysis of the membrane without holes. In the surroundings there was vacuum or diluted gas. The curves in Fig. 6 represent the obtained results. It's a graph of temperature distribution along the cross section of the membrane. The cross section was oriented across the middle of the membrane. The blue curve represents the model membranes placed freely in space. The second curve represents the model which has the membrane around the perimeter connected to the substrate. In a compact membrane model, without holes, responsivity is lower but the technology of the membrane is much easier. Bolometer system could be placed in the middle of the membrane and would have about 100 µm in average. The calculation shows that this model is the alternative for practical use. The responsivity will be lowered by about 40 %. The time constant of temperature increase on the sample also changes, as shown in Fig. 7.

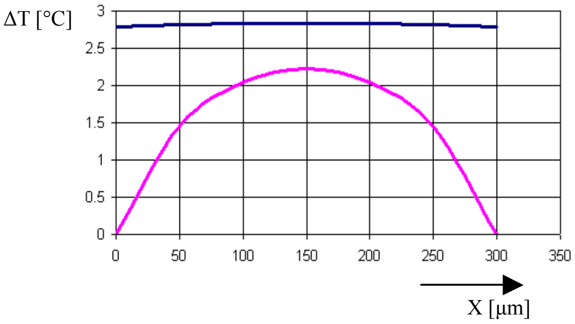

Fig. 6. Distribution of temperature on membrane

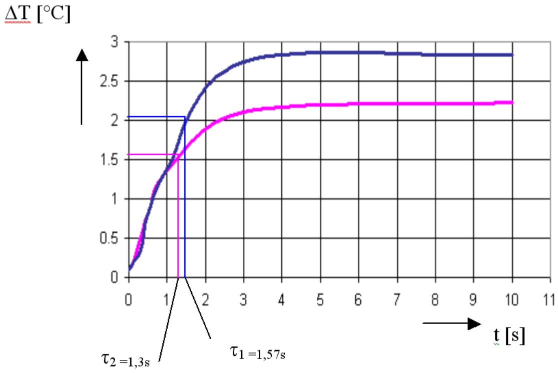

Fig. 7. Comparison of time constants

CONCLUSIONS

An experimental device suitable for preparation of thin layers of Vox has been constructed. The layers were prepared with steepness of electrical resistance depending on temperature in a wide range of values up to -6.8 % per ºC. The samples with resistance of kilo-ohm units are suitable for the implementation of micro-bolometers and they reached the values of up to -5 % / °C. An analysis of thermodynamic properties of the structure, to which the membrane layer was applied, was made. In the case of a single bolometer, it is possible to simplify the construction of the membrane and thus accelerate and simplify the production of experimental bolometers.

CALCULATION OF THE ION MOBILITY USING MOLECULAR DYNAMICS

J. Matúška, matuska@neon.dpp.fmph.uniba.sk, M. Kučera, kucera@neon.dpp.fmph.uniba.sk, M. Stano, stano@neon.dpp.fmph.uniba.sk, Department of Experimental Physics, Comenius University Bratislava, Mlynská dolina F2, 84248 Bratislava, J. Urban, urban@fmph.uniba.sk, Department of Nuclear Physics and Biophysics, Comenius University Bratislava, Mlynská dolina F2, 84248

INTRODUCTION

Ion mobility spectrometry is an ion separation method based on the fact that different ions have different drift velocities as they drift in a drift gas in a weak electric field. IMS has many advantages. The main is that ion mobility spectrometer can operate at atmospheric pressure, but the main disadvantage is poor or inaccurate database of the ion mobilities.

This problem can be solved by the Molecular Dynamics. Molecular dynamics is based on the classical newton mechanics of the studied system. The differential equation of the motion are solved by numerical integration. The number of particles (atoms, molecules, ions) in the model system is limited only by performance of the computer. The known trajectories can be used to calculate diffusion coefficient for selected ion. The mobility of the ion in buffer gas is obtained using the Einstein equation for diffusion coefficient.

The Ion mobility spectrometer on Department of Experimental Physics of Comenius University is used to analyze ions produced in corona discharge at atmospheric pressure. One of the last studied subject was ion formation in the negative corona discharge in the O_2N_2 mixtures in the nitrogen drift gas.

NUMERICAL MODEL AND CALCULATIONS

Numerical model consisted from 100 molecules of the studied ion and 100000 molecules of the buffer gas. The edge of the simulated cell was 745 angstroms long. The volume of the simulated cell was chosen to obtain atmospheric pressure by the temperature 300 K. We have used NVE ensemble to preserve system energy and volume. Calculation was performed in program DL POLY 3.09. Molecular bonds and long range potential of the atoms were calculated by universal fortified developed by Rappé [1]. We studied the evolution of the system for 20 ns.

Result from program DL POLY 3.09 was time dependence of the mean square displacement.In Fig. 1 is show the dependence of the mean square displacement (MSD) on the time for NO_3^- ion. The dependence has quadratic and linear part. The slope of the linear part of the dependence define a diffusion coefficient:

$$D = \frac{1}{6}\frac{\Delta MSD}{\Delta t} \tag{1}$$

where ΔMSD means change of the mean square displacement during the time interval Δt. Using Einstein equation obtain mobility of the ion:

$$\mu = \frac{Dq}{kT} \tag{2}$$

where q is charge of the ion, k Boltzmann constant and T temperature.

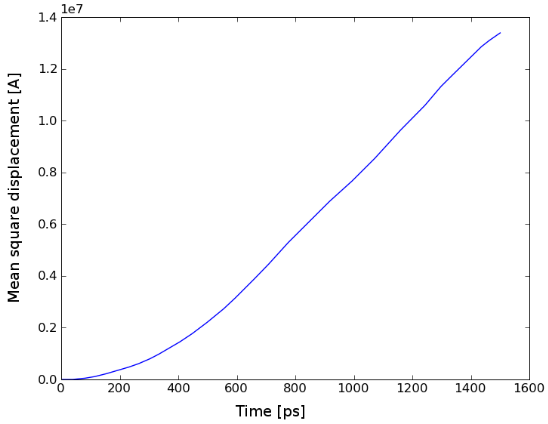

Fig. 1. Dependence of the mean square displacement on time. NO_3 ion in N_2.

RESULTS

Negative corona discharge fed by O_2/N_2 mixture produces various negative ions. The NO_3^- has been reported to be the dominant anion produced in negative corona in dry air [2]. We have used the described calculation to determine the mobility NO_3^- in nitrogen. The calculated mobility NO_3^- ion in nitrogen is 2.43 $cm^2V^{-1}s^{-1}$.

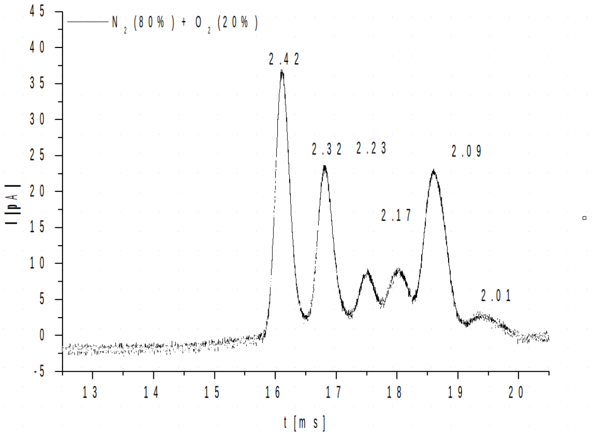

Fig. 2. Ion mobility spectrum obtained from negative corona discharge in N2/O2 mixtures. Drift gas is nitrogen. Reduced mobilities are in cm^2V1s1

We have compared this result with experimental measurement. The Fig. 2 shows mobility spectrum of ions formed by negative corona in the air-like N_2/O_2 mixture. The ions were separated in nitrogen drift gas. The reduced mobility of the dominant ion is 2.42 $cm^2V^{-1}s^{-1}$. This is in good agreement with calculated mobility of NO_3^- in nitrogen. We therefore assume that dominant ion observed in the spectrum in the Fig. 2 corespond to NO_3^-.

CONCLUSIONS

We have calculated mobility of the NO_3^- in nitrogen. We have been able to identify dominant ion produced in negative corona discharge in the N_2/O_2 mixture observed in ion mobility spectrum.

REFERENCES

1. A.K. Rappe, C.J. Casewit, K.S. Colwell, W.A. Coddard III and W.M. Skiff, J. Am. Chem. Soc. **114**, 10024-10035 (1992).
2. K. Nagato, Y. Matsui, T. Miyata, T. Yamauchi, Int. J. Mass Spectrom. **248**, 142 (2006).

IMPROVING SENSITIVITY OF ION MOBILITY SPECTROMETRY USING PULSED ION EXTRACTION FROM CORONA DISCHARGE ION SOURCE

M. Kučera, kucera@neon.dpp.fmph.uniba.sk, M. Stano stano@fmph.uniba.sk, Š. Matejčík matejcik@fmph.uniba.sk
Faculty of Mathematics, Physics and Informatics, Mlynská dolina F2, 84248 Bratislava

INTRODUCTION

Ion Mobility Spectrometry (IMS) is an analytical method based on separation of ions according to their mobilitity. The ions are separated at ambient pressure as they drift in through a gas in a weak electric field. The velocity $\boldsymbol{v}$ of a drifting ions is proportional to electric field $\boldsymbol{E}$ and a constant K called the mobility:

$$v = \boldsymbol{K}.\boldsymbol{E} \qquad (1)$$

Because of its fast response, sensitivity and small construction the IMS is often used as a small portable detector of trace gases in air [1]. The main applications include detection of explosives and narcotics. The IMS can also be used for medical and environmental applications.

The IMS consists of the ion source, the reaction region, the shutter grid and the drift tube. In the present work the ion source was realized by a negative corona discharge in a point to plane geometry. Typical current in the discharge is few µA.

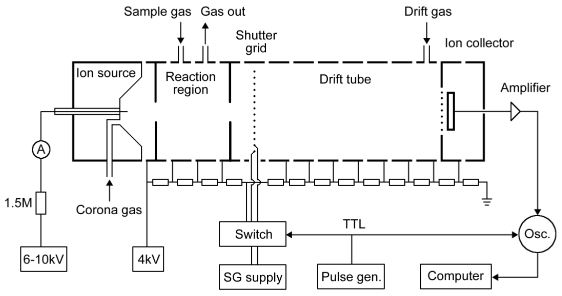

Fig. 1: Schematic view of the ion mobility spectrometer.

One of the most important parameters of IMS is its sensitivity. It is given mostly by the ion current arriving to collector on the end of drift tube. Typical value of ion current on the collector with permanently open shutter grid is approximately 500 pA. This is roughly 4 orders of magnitude lower than ion current in the discharge. It is obvious that most of ions produced by the ion source do not arrive to collector but are lost on the way. It has been shown that significant loss of ions occures at the corona grid [2]. It has been found that the ratio of ion current on collector $I_{\text{collector}}$ and ion current in the discharge I_{corona} is approximately proportional to the ratio of electric field behind E_2 and in front of corona grid E_1.

$$\frac{I_{collector}}{I_{corona}} \approx \frac{E_2}{E_1} \qquad (2)$$

In the present work we investigate the possibility of increasing $I_{collector}$ by a pulsed increase of electric field behind the corona grid E_2.

EXPERIMENT

The work was performed on a home made ion mobility spectrometer [3]. The corona discharge is realized between a point electrode made of a thin tungsten wire (∅ 100 µm) and a brass apperture with 5 mm diameter covered by a fine Ni mesh. Reaction region is ended by another apperture (∅ 6mm) covered by the same type of the mesh. The length of reaction region is 35 mm and the drift tube length (shutter to collector) is 111 mm.

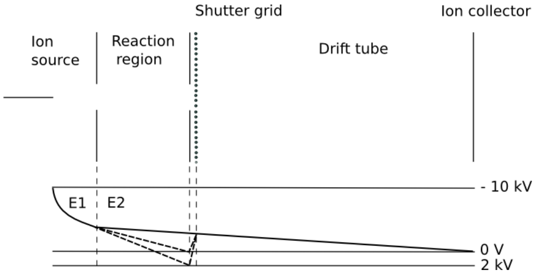

Fig 2: Schematic view of the electric field in the IMS

Figure 2 displays the electric potential along the spectrometer. Solid line presents standard electric field. This field is considered to be homogeneous along the whole spectrometer except of the ion source. Its value is 270 V/cm. Dash line presents electric field during the pulsed ion extraction. Field E_2 behind the corona grid is increased for a few milliseconds. This results in increased ion current to reaction region. In this situation, however, no ions can reach the shutter grid because field between the end of reaction region and the shutter grid has an opposite direction. The field is returned back to its original status and ions which are present in reaction region drift to the shutter grid. The opening of shutter grid is delayed by Δt after returning field E_2 to its original status. The time sequence of pulsed increase of E_2 and opening of shutter grid is shown on the figure 3. The E_2 can be increased up to 1900 V/cm.

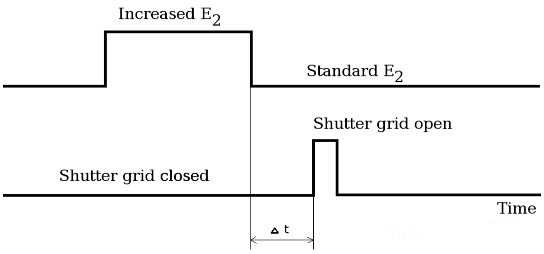

Fig. 3: Time sequence of pulsed ion extraction and opening of shutter grid.

RESULTS

Performance of the setup has been tested using the oxygen gas. Negative corona in O_2 forms single type of ions O_3^- with reduced mobility 2.55 $cm^2V^{-1}s^{-1}$ [4]. Figure 4 shows spectra obtained with different values of E_2 during the pulsed amplification and with the standard electric field.

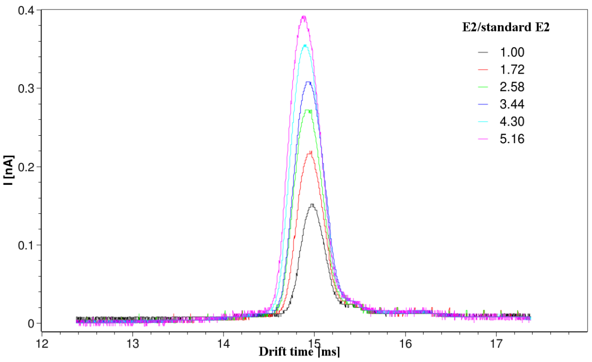

Fig. 4: Spectra with different values of E_2

Figure 5 shows dependence of ion current on delay Δt. The ions need about 1 ms to pass from reaction region to shutter grid. If the delay is shorter no ions are present on the shutter when it opens and therefore no ions are transmitted. At about 1.5 ms delay the shutter transmits ions which were at the end of reaction chamber when the field E_2 was returned to the standard value. The intensity of these ions is the highest. With further increase of the delay the ions from other parts of reaction chamber (more distant from the shutter) arrive. Intensity of those ions continuously decreases. We explain this decrease by spreading the ion beam due to the space charge. If Δt exceeds 6 ms the ions pass whole reaction chamber at standard field E_2. The intensity of ions is the same as in the standard setup without pulsed amplification of E_2.

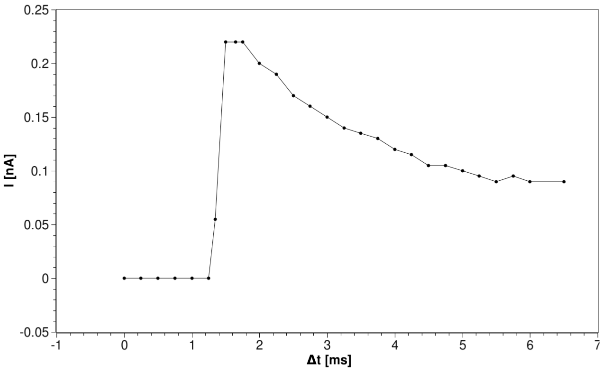

Fig. 5: Dependence of ion peak intensity on the delay Δt

Present dependence was obtained using one type of ions. If ions with other mobility were used the same dependence although with different time scale Δt would be obtained. The maximum amplification for ions with lower mobility would appear at longer Δt for ions with higher mobility at shorter Δt.

CONCLUSIONS

Signal intensity and thus sensitivity of IMS can be increased by a pulsed increase of electric field behind the corona grid. Signal intensity can be controlled by the magnitude of increased electric field. However, signal intensity strongly depends on time delay of opening the shutter grid. The amplification is the best for ions present on the end of reaction region in the moment of end of pulsed increase of electric field. Strong discrimination effects are therefore expected and it seems that a wide range spectra will need to be acquired in segments. The use of this technique for standard measurements in IMS is therefore questionable.

ACKNOWLEDGMENT: This work was supported by the VEGA grant agency, project number 1/4017/07.

REFERENCES

1. G.A. Eiceman: Ion Mobility Spectrometry (CRC Press, Boca Raton, 2005).
2. M. Tabrizchi, T. Khayamian, N. Taj, Review of Scientific Instruments **71**, 2321 (2000).
3. M. Stano, E. Safonov, M. Kučera, Š. Matejčík, Chem. Listy **99**, 1234 (2008).
4. R.M. Snuggs, D.J.Volz, J.H. Schummers, D.W. Martin, E.W McDaniel, Phys. Rev. A **3**, 477 (1971).

MAGNETIC AFTER-EFFECT OF COMPLEX SUSCEPTIBILITY IN AMORPHOUS FERROMAGNETS

J. Kravčák, jozef.kravcak@tuke.sk, Department of Physics, FEEI, TU Košice, Park Komenského 2, 042 00 Košice, Slovakia

INTRODUCTION

In a demagnetized amorphous ferromagnet the most probable positions of the 180° domain walls (DWs) are determined by the static pinning potential $E_0(x)$ (x is a DW displacement). When an external ac magnetic field $H(t)=H_0\exp(\mathrm{i}\omega t)$ with small amplitude $H_0<H_{cr}$ is applied the DW remains bounded in a potential well where it is forced to move periodically $x(t)=x_0\exp[\mathrm{i}(\omega t-\delta)]$ with a phase lag δ. As in the demagnetized state, the displacement of the 180° DW x is connected with the magnetization: $M(t)=2M_S\,x(t)$ (M_S is saturated magnetization), the complex susceptibility has to be introduced: $\chi = M(t)\,/\,H(t) = \chi_0\exp(-\mathrm{i}\delta) = \chi_1 - \mathrm{i}\chi_2$ (χ_0 is an amplitude of the susceptibility).

Due to an alignment of mobile atomic pairs within DWs parallel to the direction of local magnetization the additional stabilization of DWs occurs. The magnetic after-effect (MAE) of complex susceptibility $\chi=\chi_1-\mathrm{i}\chi_2$ is related to the additional stabilization potential $E_S(x,t)=E_S(x).G(t)$, separated to $E_S(x)=\alpha x^2/2$, for small $x<d$ (d is a DW thickness) and to time relaxation function $G(t)$. The MAE of the complex susceptibility χ is usually expressed as a change of its reciprocal value (reluctivity) $r = 1/\chi = r_1 + \mathrm{i}\,r_2$: $\Delta\,r(t)= (r(t)-r(t_1))/r(t_1)$ at time interval from t_1 to t_2 after demagnetization [1].

THEORETICAL BACKGROUND

It is well known that the moving DW exhibits an inertia. The mass of the DW can be derived from the angular momenta of the spins forming the wall [2]. Let us consider the equation of motion for 180° DW :

$$m\frac{\mathrm{d}^2x}{\mathrm{d}t^2}+\beta\frac{\mathrm{d}x}{\mathrm{d}t}+\alpha x = 2\mu_0 M_S H\,, \qquad (1)$$

where m is the mass of the DW per unit area, β the damping coefficient, α the restoring coefficient. The term $2\mu_0 M_S H$ on the right side of the Equation (1) represents the pressure acting on the 180° DW.

When an external magnetic field $H(\,t\,) = H_0\exp(\mathrm{i}\omega\,t)$ is applied with a small amplitude H_0 less than critical H_{cr}, the solution of (1) can be found: $x(t)=x_0\exp[\mathrm{i}(\omega t-\delta)]$ with amplitude

$$x_0=\frac{2\mu_0 M_S H_0/m}{\sqrt{\left(\omega_0^2-\omega^2\right)^2+(\beta/m)^2\,\omega^2}} \qquad (2)$$

and with the phase lag δ expressed as loss factor

$$\tan\delta=\frac{\beta\omega/m}{\omega_0^2-\omega^2}\ . \qquad (3)$$

The obtained amplitude of the 180° DW displacement (2) exhibits a resonance close to angular frequency $\omega=\omega_0$ ($\omega_0^2=\alpha/m$) if DW damping mechanism is weak (β_1–β_3 in Fig. 1). In case of strong DW damping (β_4–β_6 in Fig. 1) we expect monotonous decrease of the amplitude (2) with angular frequency. Substitution of $x(t)=x_0\exp[\mathrm{i}(\omega t-\delta)]$ and (2) into the expression for the magnetization: $M(t)=2M_S\,x(t)$ yields the complex susceptibility $\chi = M(t)\,/\,H(t) = \chi_1 - \mathrm{i}\chi_2$ with real and imaginary part

$$\chi_1(\omega)=\frac{\chi_S\,(\omega_0^2-\omega^2)}{(\omega_0^2-\omega^2)^2+(\beta/m)^2\omega^2}\ , \qquad (4a)$$

$$\chi_2(\omega)=\frac{\chi_S\,(\beta/m)\omega}{(\omega_0^2-\omega^2)^2+(\beta/m)^2\omega^2}\ , \qquad (4b)$$

where $\chi_S = 4\mu_0 M_S^2/m$ states for static susceptibility (Fig. 2).

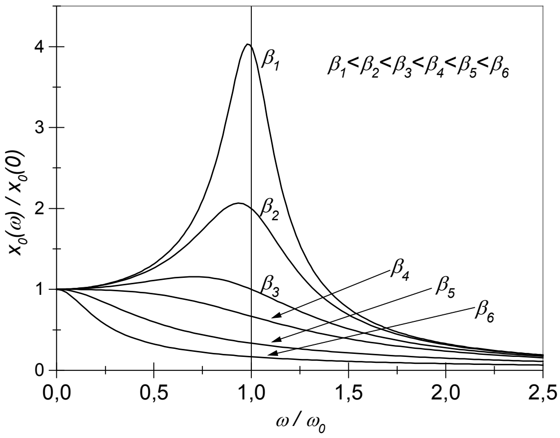

Fig. 1. Resonance of the amplitude x_0 of the 180° DW displacement for decreasing damping coefficient β.

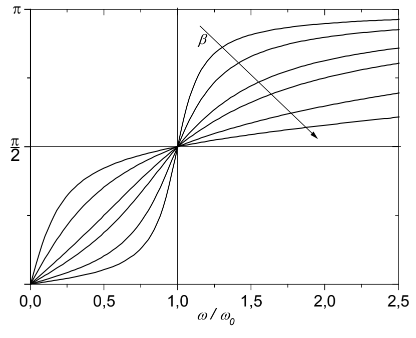

Fig. 2. The angular frequency dependence of phase lag δ of the DW displacement for decreasing damping coefficient β.

MEASUREMENTS AND DISCUSSION

Near zero magnetostrictive Co-based amorphous alloy in as-cast state with the coercivity H_c=0.6 Am^{-1} was used in experiments. The real χ_1 and imaginary χ_2 dependence on frequency of applied magnetic field with $H_0<H_{cr}$ was measured (Fig. 3). The MAE was measured between t_1=30 s and t_2=300 s after demagnetization [3]. Equation (4a) shows that the MAE of the real part of the reciprocal susceptibility $\Delta\,r_1(t)=(r_1(t)-r_1(t_1))/r_1(t_1)$ (Fig.4a) represents time development of the restoring

coefficient α (in frame of $\omega_0^2=\alpha/m$), that is a steepness of the potential well with bounded DW. Equation (4b) displays that the MAE of the imaginary part of the reciprocal susceptibility $\Delta r_2(t)=(r_2(t)-r_2(t_1))/r_2(t_1)$ (Fig. 4b) represents time development of the damping coefficient β. There are many damping mechanism affecting DW motion described in literature [2,4], e.g. eddy currents, interaction of diffusing pinning centres with the moving DW. In presented theoretical background the viscous character of damping is emphasized. As the eddy current damping is significant in a conductive ferromagnet then the resonance DW motion can not be observed. The amplitude MAEs dependences (Fig. 4) can be divided into the three intervals:

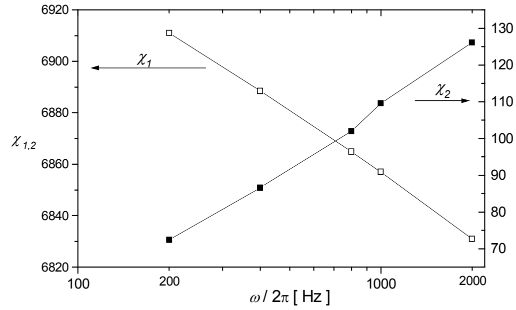

Fig. 3. Real χ_1 and imaginary χ_2 part of susceptibility dependence on frequency of the driving field with $H_0 < H_{cr}$.

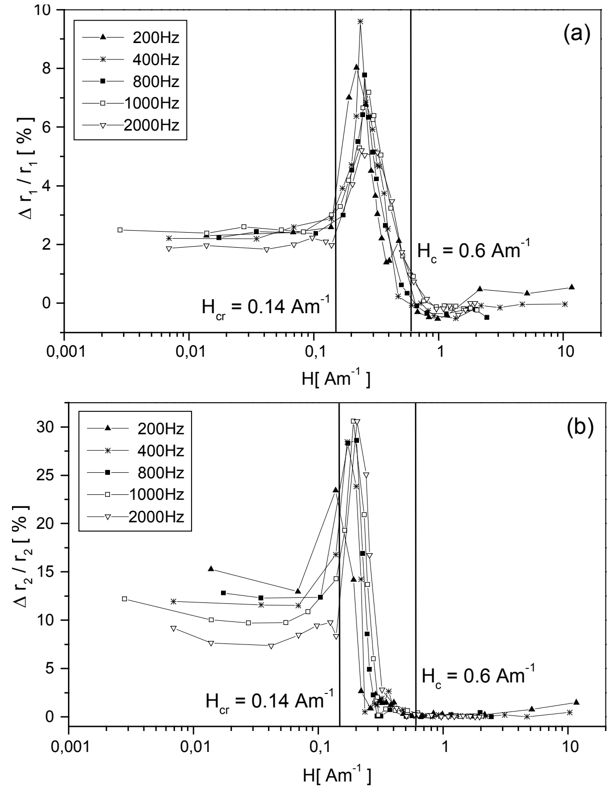

Fig. 4. MAE dependence of the real part (a) and imaginary part (b) of the reciprocal susceptibility (reluctivity) $r = 1/\chi$ on the amplitude of the driving field. The critical amplitude H_{cr} and coercivity H_c are displayed.

1) $H_0<H_{cr}$, when the DWs remain bounded in a potential well and their stabilization occurs due to reorientation of moveable atomic pairs [1]. The real part MAE (Fig. 4a) is almost constant at given frequencies, i.e. DW displacement amplitude x_0 is small.

2) $H_{cr}<H_0<H_c$, sharp peaks are observed in both MAEs. The imaginary part MAE (Fig. 4b) indicates a start of irreversible Barkhausen jumps of DWs to neighbouring potential wells. Damping coefficient β rapidly increases with the eddy currents induced by the long range DW jumps. But on the other hand partially DWs stabilization further continues as it shows the real part MAE dependence.

3) $H_c<H_0$, total destabilization of domain structure, domains expand and DWs are vanishing. Both MAEs are close to zero.

CONCLUSIONS

Complex magnetic susceptibility allows us to separate magnetic processes in amorphous ferromagnets: 1) reorientation of moveable atomic pairs in DWs and 2) eddy currents induced during reversible and irreversible DWs movement. MAE of the real part of complex susceptibility reflects time dependence of the restoring coefficient α connected with the stabilization of domain walls due to reorientation of moveable atomic pairs. MAE of the imaginary part shows development of the damping coefficient β. The resonance DW motion can not be observed in conductive ferromagnets owing to strong damping caused by eddy currents induced during reversible periodic movement of domain wall in a potential well.

ACKNOWLEDGMENT: This work has been partially financed by Department of Physics, FEEI TU Košice Projects and Slovak Scientific Grant Agency VEGA Project No. 1/0076/09.

REFERENCES

1. H. Kronmüller, Phil. Mag. B **42**, 127 (1983).
2. S. Chikazumi: Physics of Magnetism (Wiley, Florida - 1984).
3. J. Kravčák et al., Acta Physica Polonica A **113**, 43 (2008).
4. G. H. J. Wantenaar et al., J. Magn. Magn. Mat. **89**, 13 (1990).

MEASUREMENT OF ELECTRON DRIFT VELOCITY IN GASES

M. Stano, stano@fmph.uniba.sk, M. Kučera, kucera@neon.dpp.fmph.uniba.sk and Š. Matejčík, matejcik@fmph.uniba.sk, Department of Experimental Physics, Comenius University, Mlynska dolina F2, 842 48 Bratislava

INTRODUCTION

Electron transport parameters are of fundamental importantce for understanding properties of electrical discharges and electrical fenomena in gases in general. These parameters include mobility, diffusion coefficient, drift velocity or electron energy distribution function (EEDF). For many gases like nobel gases as well as mixtures used in nuclear physics gaseous detectors these coefficients have been carefully studied. On the other hand little experimental work was done concerning electron transport coefficients in dry air and even less is known about those in the humid air [1]. Better knowledge of these parameters is necessary to understand conditions in the Earth's upper atmosphere where transient luminous events as blue jets, sprites and elves have been observed [2].

In the present work we report about basic test and calibration measurements performed on a home made instrument. Electron drift velocity was measured in N_2 and Ar gas. In addition, we have studied influence of small admixtures of N_2 on electron drift velocity in Ar. Admixtures of molecular gases in noble gases are known to have strong influence on electron transport coefficients and EEDF. Discharges in noble gases are also known to be significantly influenced by such admixtures or impurities.

EXPERIMENT

The work was performed on an experimental setup schematicaly shown on the Figure 1. The device is an ion mobilitity spectrometer [3] and for present work it was equipped with faster pulse generator as well as acquisition electronics.

Free electrons are obtained from a corona-like discharge in a point-to-plane geometry. In a non-electronegative gas and with negative voltage applied to the tip electrode the current in the discharge is conducted by electrons. The electrons enter a drift tube of fixed length 111 mm in short 1 μs pulses controlled by an electronic shutter.

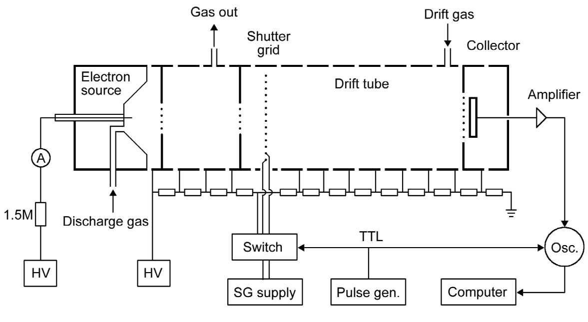

Fig. 1. Schematic view of apparatus.

Electron current is measured at the end of drift tube, it is amplified by a current/voltage amplifier (amplification 10^6, 200 kHz bandwidth) and registered by an oscilloscope. Drift velocity is calculated from electron drift time over drift tube. All measurements have been performed at ambient temperature and pressure at electric field from 33 to 363 V/cm. Reduced electric field *E/n* was in the range from 0.13 to 1.5 Td. Gas mixture used as drift gas was prepared by MKS mass flow controllers and was kept constant 500 ml/min. Discharge used as electron source was fed by 200 ml/min N_2 or Argon with 5% content of N_2. Purity of N_2 was 5.0 and purity of Ar was 4.6.

RESULTS

The electron drift velocity was measured in nitrogen and argon at ambient pressure at different electric fields. Figure 2 shows electron current on collector as a function of drift time. Measurement was performed in N_2. Decrease of electric field results in longer drift time and also to lower electron current intensity. For determination of drift time 1 μs was substracted from the peak maximum to take shutter opening pulse width and rise time of amplifier into account.

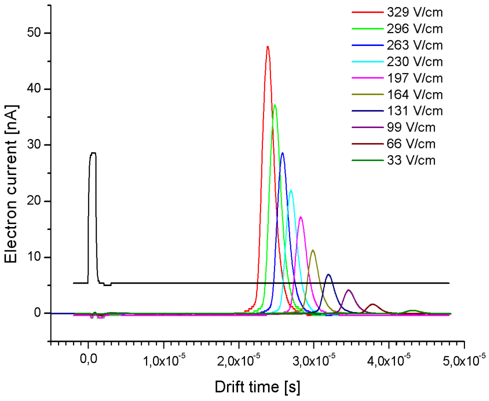

Fig. 2. Electron current measured on collector at different electric fields in N_2 drift gas. Black line is the shutter control signal.

Figure 3 shows electron drift velocity in N_2 and Ar as a function of reduced electric field *E/n*. Present results are compared with results by Pack et al [4]. We observe a good agreement in the case of N_2. However, present data show higher drift velocity in Ar as those by Pack et al.

Figure 4 shows electron drift velocity in Ar as a function of nitrogen admixture concentration. The concentration of N_2 was varried in the range 0.1% to 2%. We observe that electron drift velocity in Ar is strongly increased with N_2 admixture. The electron drift velocity at 1 Td is more than doubled and at 1.5 Td it is more than tripple compared to that the pure Ar at 1% N_2 content.

Electron transport coefficients in argon are very

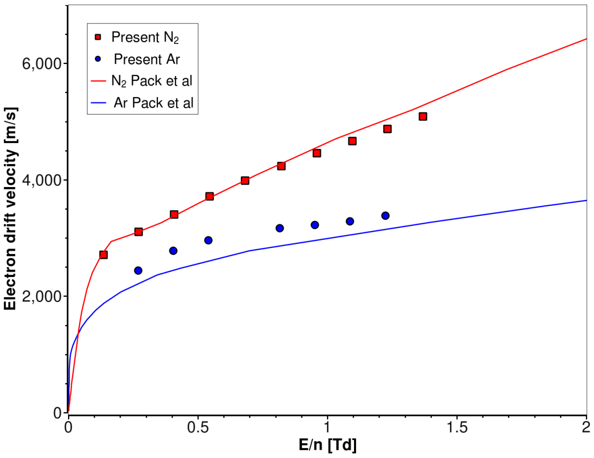

Fig. 3. Electron drift velocity in pure N_2 and Ar as a function of *E/n*

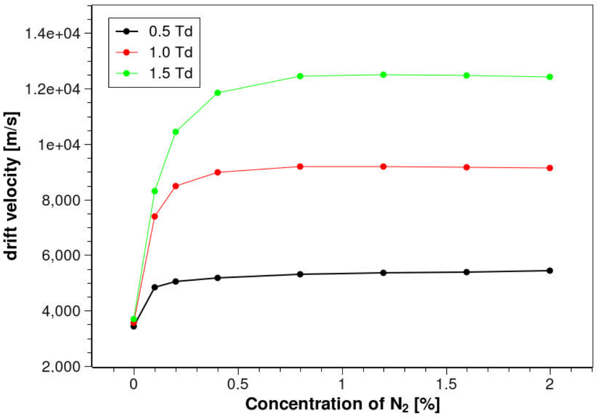

Fig. 4. Electron drift velocity in Ar with admixtures of N_2.

sensitive to impurities of molecular gases. The reason is the profound minimum in the collisional cross section at about 0.2 eV electron energy. This is known as Ramsauer-Thowsend effect. The electrons exceeding this energy in pure Ar loose their energy effectively by collisions with molecular gas, nitrogen in this case. As a result the argon gas becomes nearly transparent for electrons and electron drift velocity is significantly increased.

We assume that small impurity also led to higher values of electron drift velocity measured in the pure Ar. Present measurements were performed using Ar with purity 4.6. This corresponds to about 40 ppb impurity, mostly nitrogen. This should not influence drift velocity in Ar-N_2 mixture where N_2 concentration was much higher.

CONCLUSIONS

Good agreement of electron drift velocity in pure N_2 with previously published data lets us assume that present method is satisfactory for studied range of *E/n*. We have observed that electron drift velocity in Ar is signifficantly increased with admixture of N_2. We therefore assume that increased values of electron drift velocity measured in the pure Ar were also caused by impurities of small molecular gases.

Present range of *E/n* is limited mostly by the fixed pressure (atmospheric) at which the instrument can be operated. The measurements would be more useful if the range of *E/n* could be extended. It would also be more convenient if another type of electron source independent on the gas type, for example photoemmision, could be used.

ACKNOWLEDGMENT: This work was supported by the Vega grant agency, project number 1/4017/07.

REFERENCES

1. F. J. Gordillo-Vázquez and Z. Donkó, Plasma Sources Sci. Technol **18**, 034021 (2009).
2. E. R. Williams, Physics Today **54**, 11, 41 (2001).
3. M. Stano, E. Safonov, M. Kučera, Š. Matejčík, Chem. Listy **102**, 1414 (2008).
4. J.L.Pack and A.V.Phelps, Phys. Rev. **121**, 798 (1961).

ANALYSIS OF MOVEMENT OF MAGNETIC NANOPARTICLES IN INHOMOGENEOUS MAGNETIC FIELDS FOR CELL SEPARATION, DRUG TARGETING AND GENE THERAPY

A. Krafčík, andrej.krafcik@gmail.com, M. Babincova, babincova@fmph.uniba.sk and P. Babinec, babinec@fmph.uniba.sk, FMFI UK Bratislava, Mlynská dolina F1, 842 48 Bratislava, Slovakia

INTRODUCTION

Sources of magnetic field with high gradient together with magnetic micro/nanoparticles have a perspective application e.g. in targeting compounds or cells, their separation as well as in other scientific fields not only in biotechnology and biomedicine.

The efficiency of gene transfer systems is usually limited by two obstacles. The first one: only insufficient amount of administered gene vector can reach surface of target tissue. Second difficulty is diffusion of gene vector as common plasmids through cellular cytoplasm and its nuclear uptake. Application of the principle of magnetic force targeting of gene vectors with bonded magnetic nanoparticle, called magnetofection, results in a dramatic improvement of the gene delivery in several cell line [1]. Magnetic field is able to increase the probability of transfection of cell membrane of targeted cells by magnetic nanoparticle with joint effective compound.

First step to required applications needs looking for convenient magnetic force arrangement and size of magnetic particles first by simply theoretical modeling in the sense of magnetostatics.

MAGNETIC PARTICLE IN MAGNETIC FIELD AND VISCOUS AMBIENT

We have studied trajectories of magnetic nano/microparticles of magnetite (Fe_3O_4) with radius 50 nm to 10 μm in fluid media with viscosity of water and air in with us designed high gradient magnetic fields. Movement was described by Newton's equation of motion, where we consider only magnetic force $\mathbf{F}_m$ as well as Stokes drag force $\mathbf{F}_s$ acting on moving spherical particle in viscous ambient. Magnetic force acting on particle was determined by effective dipole moment method, where the particle is replaced by equivalent point dipole moment localized in the centre of particle. Its value depends on magnitude of intensity of applied field, rising from model based on selfdemagnetization and magnetic saturation of magnetite particles according Furlani and Ng [2]:

$$\mathbf{F}_m = \mu(\mathbf{m}_{p,eff}.\nabla)\mathbf{H}_a \quad (1)$$

$$\mathbf{m}_{p,eff} = V_p f(H_a)\mathbf{H}_a \quad (2)$$

$$f(H_a) = \begin{cases} 3 & H_a < M_{sp}/3 \\ M_{sp}/H_a & H_a \geq M_{sp}/3 \end{cases} \quad (3)$$

where: $\mathbf{F}_m$ – magnetic force, μ – permeability of ambient, $\mathbf{m}_{p,eff}$ – magnetic dipole moment of particle, $\mathbf{H}_a$ – intensity of applied magnetic field, V_p – volume of particle, M_{sp} – saturation magnetization of magnetite.

Viscous drag force of fluid ambient acting on moving spherical particle was determined by Stokes

$$\mathbf{F}_s = -6\pi\eta R_p(\mathbf{v}_p - \mathbf{v}_f) \quad (4)$$

where: μ – viscosity of fluid ambient, R_p – particle radius, $\mathbf{v}_p$ and $\mathbf{v}_f$ particle velocity and velocity of flowing fluid (zero in our calculations), respectively.

Ordinary differential equations (ODEs) describing movement of magnetic particle in magnetic field and viscous ambient obtained from mentioned above, were solved numerically by ODE solver in Matlab (The MathWorks, 2004) for every particle separately. In this work we have considered two sources of magnetic field. In the first case it was ideal wire quadrupole, which consist of four parallel infinite wires arranged to the edges of square with currents in opposite direction, which drive magnetic field defined analytically from Biot-Savart-Laplace law. The second one was cylindrical Halbach array, or octapolar magnet, which magnitude of magnetic field intensity was calculated numerically by finite element method (FEM) by software FEMM (David Meeker, 2008). Permanent magnets in FEM analysis were represented by NdFeB magnets with magnetic energy product 37 MG.Oe.

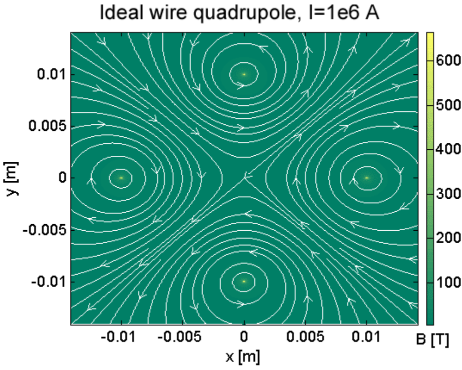

Fig. 1. Magnetic flux density and flux density lines of ideal wire quadrupole driven by current 10^6 A in transversal plane.

Calculations were done for initial position for every particle in random location inside the center of cavity of magnetic field sources and stopped after it reached its margin, initial velocities of particles were zero. Dependencies of mean capture time of given size of particles on their radius for both magnetic field arrangements and both fluid media are shown on Fig. 2 and Fig. 5. Also the dependence of mean capture time on driving current in the case of ideal wire quadrupole is shown (Fig. 3).

As we can see microparticles were captured relatively fast, instead of small nanoparticles, which majority was attracted in rather long time. There are shown similar capture times for motion of magnetite particles of same sizes in the analytically described magnetic field of ideal high-current wire quadrupole driven by current in about 5000 A (Fig. 3) [3] and in the field of cylindrical Halbach array.

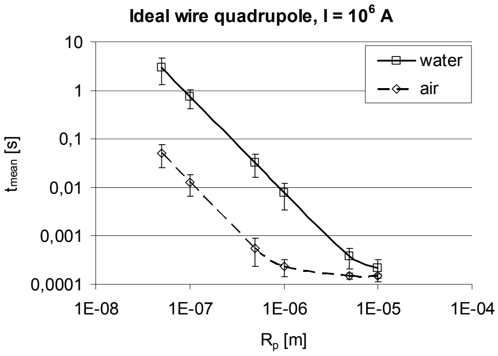

Fig. 2. Dependence of mean capture time of the magnetite particles on their radius (calculations were done for radii: 5×10^{-8}, 10^{-7}, 5×10^{-7}, 10^{-6}, 5×10^{-6} and 10^{-5} m) in the field of ideal wire quadrupole driven by current 10^6 A for two different fluid media: water and air.

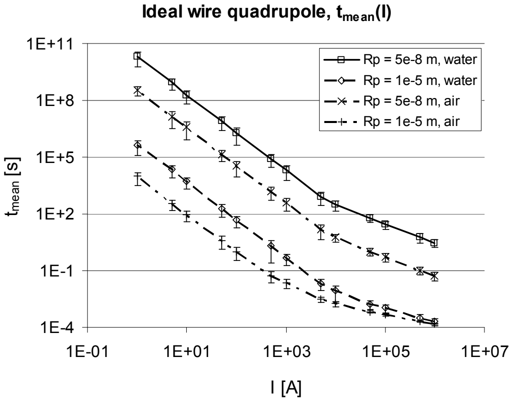

Fig. 3. Dependence of mean capture time of the magnetite particles on the driving current of ideal wire quadrupole, for small (with radius 50 nm) and large (radius 10 µm) particles in the water and air as fluid media.

Capture time needed to attract magnetic micro particles, on which can be bonded target cells, as well as nanoparticles with potentially bonded effective compounds are sufficiently short in both arrangements, or could be shortened by modification of size of particles, magnitude of magnetic field by replacing permanent magnets by pulsed electromagnets, or change geometrical scales, i.e. decrease capture time by shortening the movement trajectory.

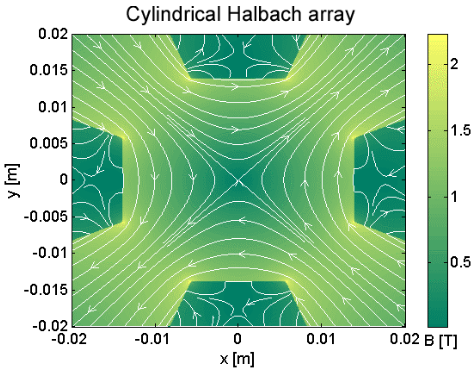

Fig. 4. Magnetic flux density and flux density lines in the cavity of cylindrical Halbach array, transversal plane.

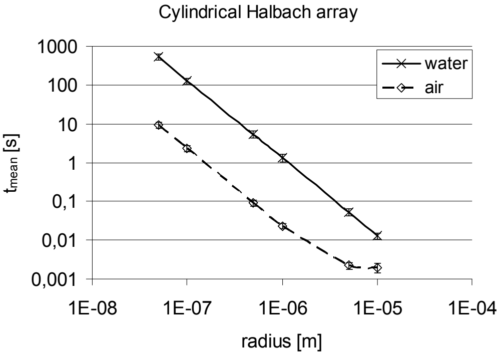

Fig. 5. Dependence of mean capture time of the magnetite particles on their radius (calculation were done for radii: 5×10^{-8}, 10^{-7}, 5×10^{-7}, 10^{-6}, 5×10^{-6} and 10^{-5} m) in the field of cylindrical Halbach array for water and air as fluid media.

CONCLUSIONS

A new possibility for a cell separation, drug targeting, and magnetofection utilizing high gradient quadrupolar magnetic field created by a short high current electric pulses as well as by cylindrical Halbach array has been described. Analyzing trajectories of magnetic nanoparticles as well as microparticles we have found that the mean capture time is sufficiently short, and the biomedical applications of such a system are feasible [4].

REFERENCES

1. F. Scherer, M. Anton, U. Schilinger, J. Henke, C. Bergeman, A. Krüger, G. Gänsbacher, C. Plank, Gene Ther **9,** 102 (2002).
2. E.P. Furlani, K.C. Ng, Phys. Rev. E **73**, 061919 (2006).
3. A. Krafcik, M. Babincova, P. Babinec, Optoelectron. Adv. Mater – Rapid Commun. **3**, 226 (2009).
4. M. Babincova, V. Altanerova, C. Altaner, C Bergemann, P. Babinec, IEEE Transactions on Nanobioscience **7**, 15 (2008).

BROWNIAN MOTION WITH A NONLINEAR FRICTION

V. Lisý, vladimir.lisy@tuke.sk, J. Tóthová, jana.tothova@tuke.sk, Department of Physics, Faculty of Electrical Engineering and Informatics, Technical University of Košice, 042 00 Košice

INTRODUCTION

There are many important situations when the damping constant in the Langevin equation depends on the velocity of the Brownian particle (BP) [1 - 5] as it is encountered, for example, in models of active motion of biological objects. For such motion the linear Stokes law does not apply and the friction force on the particle is described by various functions nonlinearly depending on the velocity. In the present contribution we consider the case when this force is given by a power law function $\sim\upsilon^{a}$. The diffusion coefficient of the particle, D_{eff}, is calculated for arbitrary constants a, including the negative ones, as a function of the intensity of the white noise driving the particle. In particular, interesting cases are considered when D_{eff} does not depend on the noise intensity at all, or when it even decreases with the increase of the noise. The Langevin equation is discussed also as a noise generator and the problem of designing a generator with desired properties of the colored noise is addressed.

LANGEVIN EQUATION WITH NONLINEAR FRICTION

Last year the scientific community celebrated 100 years from the publication of famous work [6]. In this work, Langevin devised a very successful description of Brownian motion (BM) (in his own words, "infinitely more simple" than Einstein's). As distinct from Einstein who derived and solved a partial differential equation for the probability density of a BP, Langevin used Newton's second law and incorporated in it a random force driving the particle. The obtained ordinary differential equation gave rise to the theory of stochastic processes and is now widely used to describe Markov (memoryless) processes in different fields of physics, chemistry, electrical engineering, biology, and even in finance and social sciences [7].

The Langevin equation describing the BM of a particle with the mass m is

$$m\dot{\vec{\upsilon}} = -\gamma\vec{\upsilon} + \sqrt{2D}\vec{\xi}\left(t\right), \tag{1}$$

where $\vec{\upsilon}\,(t) = \dot{\vec{x}}(t)$ is the particle velocity, the resistance force during the particle motion is the Stokes friction force proportional to $\vec{\upsilon}$, and the irregular impulses from the surrounding molecules are described by the (white) noise force $\sim \xi(t)$ with the properties

$$\left\langle \vec{\xi}(t) \right\rangle = 0\,, \; \left\langle \xi_i(t)\xi_j(t') \right\rangle = \delta_{ij}\delta(t-t')\,. \tag{2}$$

The noise intensity $D = k_BT\gamma$ (k_B is the Boltzmann constant, T is the temperature and γ the friction coefficient). Equation (1) is easily solved with the properties (2). As distinct from the Einstein formula for the mean square displacement (MSD) of BP, which is valid only for "infinite" times t, this solution predicts the particle behavior for any t. Note however that this solution has (as concerns BM) a very limited applicability. In fact, it is true only for heavy particles in a low-density environment (such as dust particles in a gas) at short times, or alternatively at long times, when it is not necessary since the Einstein theory is valid. The first generalization of (1) to a non-markovian process was done in the hydrodynamic theory of BM (for a review see [8]). Here we shall consider another generalization of (1), which is connected with the class of problems called the nonlinear BM: it consists in the use of nonlinear friction forces instead of the Stokes one linearly depending on the velocity. We consider the case when γ is replaced by the function $\gamma(\upsilon) = \gamma\upsilon^{2\alpha}$.

Various modifications of (1) during the past 20 years were used to describe the motion of living objects – molecular motors, flocks of animals, etc. In these works, a typical choice is the Rayleigh-Helmholtz friction $\gamma\left(\upsilon\right) = \upsilon^2 - \upsilon_0^2$, which is interesting because of the fact that at $\left|\upsilon\right| < \upsilon_0$ the friction acts as an energy pump. Another generalization, studied e.g. in [2 - 4], is for a d-dimensional (d = 1, 2, 3) system with

$$\gamma\left(\upsilon\right) = \gamma\upsilon^{2\alpha}\,, \tag{3}$$

where γ and α (= 0, 1, 2, 3) are constants. The Langevin equation thus becomes

$$m\dot{\vec{\upsilon}} = -\gamma\upsilon^{2\alpha}\vec{\upsilon} + \sqrt{2D}\vec{\xi}\left(t\right). \tag{4}$$

Other choices of the friction force can be found in [5].

In the mentioned work [3], the diffusion coefficient of the particle is given the main attention. D_{eff} can be calculated from the MSD of the particle,

$$D_{\text{eff}} = \lim\nolimits_{t\to\infty} \frac{1}{2dt}\sum_{j=1}^{d}\left\langle \left[x_j\left(t\right) - x_j\left(0\right)\right]^2 \right\rangle, \tag{5}$$

or using the velocity autocorrelation function (VAF)

$$D_{\text{eff}} = \frac{1}{d}\int_0^{\infty} d\tau \left\langle \vec{\upsilon}\left(t\right)\vec{\upsilon}\left(t+\tau\right) \right\rangle. \tag{6}$$

Knowing D_{eff} is important not only for the description of various kinds of nonlinear BM, e.g., in physics and biology [1 - 5], but also for designing colored-noise generators [3]. Indeed, while the force $\xi(t)$ describes the noise with equal amplitudes of any frequency component of the force spectrum, equation (4) can be regarded as a noise generator with very different properties. In such a generator, the "diffusion coefficient" D_{eff} corresponds to the noise intensity of the "velocity" υ. It is of particular interest to know the properties of this noise and its dependence on the system parameters D, γ, and m. The purpose of the work [3] was to show that

$$D_{\text{eff}} \sim D^{\beta}\gamma^{\beta'}m^{\beta''}. \qquad (7)$$

This was achieved by a quite complicated way using the solution to one-dimensional case of (4) found in [2] and the dimensional analysis for higher dimensions d = 2 and 3. It has been found that in all these situations

$$\beta = \frac{1-\alpha}{1+\alpha},\quad \beta' = -\frac{2}{1+\alpha},\quad \beta'' = \frac{2\alpha}{1+\alpha}, \qquad (8)$$

but the prefactor in the relation for D_{eff} (7), which depends on d, is known only in the 1d case; the higher dimensions are studied numerically. The most remarkable result, as pointed out in [3], was the finding that D_{eff} for the cubic force ($\alpha = 1$) does not depend on the noise intensity D at all (as seen from (8), $\beta = 0$ in this case). Here we use that eq. (4) is in fact governed not by three but only by two parameters, e.g., γ/m and D/m^2. If M, L, and T stay for mass, length, and time, respectively, then, using that the dimension of $\gamma\upsilon^{2\alpha}$ is M/T and D_{eff} has the dimension L^2/T, $(D) = (M^2L^2/T^3)$ and $(\upsilon) = (L/T)$, one easily finds from the expression

$$D_{\text{eff}} \sim \left(\frac{\gamma}{m}\right)^{x}\left(\frac{D}{m^2}\right)^{y} \qquad (9)$$

the following relations for the coefficients x and y:

$$x = -\frac{2}{1+\alpha},\ y = \frac{1-\alpha}{1+\alpha}\quad (\alpha \neq -1), \qquad (10)$$

$$x = 4/3,\ y = -1\quad (\alpha = -1),$$

so that the dependence of D_{eff} on the model parameters exactly corresponds to eqs. (7) and (8) with the coefficients β found for α = 0, 1, 2, and 3 [3]. Here, the dependence of D_{eff} on α is determined for *arbitrary* α immediately from the simple dimensional consideration. In particular, the interesting case (mentioned but not touched in [3]) when α is negative is also solved. While in [3] the question has been opened whether here the system shows normal diffusion at all, now it is seen that the answer is not. For $\alpha > 1$ and $\alpha \leq -1$ one observes that the diffusion coefficient of the BP *decreases* with the increase of the Langevin noise. “The exciting and unexplored problem” of the power-law friction is covered by the solution (10) as well.

To finish with this type of the nonlinear Langevin equation note that it is appropriate to study this equation in the dimensionless form. It has been also done in [3] in numerical simulations: the graphs for dimensionless D_{eff} as a function of D have been calculated for α = 1, 2, 3, and $d = m = \gamma = 1$. To work with dimensionless variables, one has to define the characteristic units for the mass (μ), distance (ρ), and time (τ). Then, measuring the mass, distance and time in these units, the form of (4) remains the same but all the quantities become dimensionless. Let us choose these units as those characteristic for a typical micrometer-sized BP at room temperatures in water, assuming the validity of the Stokes friction force. That is, $\mu = (4\pi/3)\cdot 10^{-15}$ kg and $\rho = 10^{-6}$ m. Taking $\tau = m/\gamma$ to be the relaxation time for the BP, the characteristic unit will be $\tau = (2/9)\cdot 10^{-6}$ s. This time corresponds to the choice $m = \gamma = 1$ in [3]. As to the noise intensity and diffusion coefficient expressed in the units for a typical BP, $\mu^2\rho^2/\tau^3$ and ρ^2/τ, respectively, we have the dimensionless $D = D_{\text{eff}} = (1.38/9\pi)\cdot 10^{-6}D^*$, where $D^* = T/(300\text{ K})$ and T (K) is the temperature. Thus, $D^* = 1$ yields the values for the typical BP at 300 K (recall that the dimensional $D_{\text{eff}} = k_BT/\gamma$ and $D = k_BT\gamma$). Note that the simulations [3] are carried out in the region of D (from 10^{-2} to 10) that is exceedingly far from that for a real BP (for such a particle the temperatures in [3] are from about $6\cdot 10^{7}$ to $6\cdot 10^{10}$ K). Due to this the behavior of the simulated BP cannot be compared at all with the behavior of the typical particle.

CONCLUSIONS

The Langevin equation can be considered as a generator of the colored noise. If this equation is used to describe the Brownian motion of particles, the noise is represented by the particle velocity υ and its properties, in particular, the dependence on frequency, are determined by the VAF of the particle. We have described an example in which the BP produces a colored noise. Instead of the Stokes friction a force proportional to $\upsilon^{2\alpha}\vec{\upsilon}$ is used; this choice is inspired by some actual models of Brownian motors [3]. The resulting Langevin equation is hard to solve. It is however possible to obtain some properties of the intensity of the generated noise (the diffusion coefficient D_{eff}) using a simple dimensional analysis. So, it can be shown that for the cubic dependence of the force on υ the noise intensity does not depend on the intensity of the white noise D driving the particle. In some cases D_{eff} even decreases with the increase of D. Since the nonlinear Langevin equation is difficult to solve analytically, numerical solutions for different friction forces are of great interest. Also, considering this equation as a colored noise generator, an interesting inverse problem of designing a generator with desired properties of the noise arises. The work in these directions is now in progress.

ACKNOWLEDGMENT: This work was supported by the Agency for the Structural Funds of the EU within the project NFP 26220120021, and by the grant VEGA 1/0300/09.

REFERENCES

1. P. Reimann, Phys. Rep. **361**, 57 (2002).
2. B. Lindner, New J. Phys. **9**, 136 (2007).
3. B. Lindner, J. Stat. Phys. **130**, 523 (2008).
4. W. Ebeling, L. Schimansky-Geier, Eur. Phys. J. Special Topics **157**, 17 (2008).
5. M. Tokuyama, Physica A **387**, 4015 (2008).
6. P. Langevin, C. R. Acad. Sci. Paris **146**, 530 (1908).
7. W. T. Coffey, Yu. P. Kalmykov, J T. Waldron: The Langevin Equation. With Applications to Stochastic Problems in Physics, Chemistry and Electrical Engineering (World Scientific, Singapore - 2004).
8. V. Lisy, J. Tothova, arxiv:cond.mat/0410222 (2004).

SPIN-ECHO NMR SIGNAL FROM CONFINED BROWNIAN PARTICLES IN FLOW

J. Tóthová, jana.tothova@tuke.sk, V. Lisý, vladimir.lisy@tuke.sk, Department of Physics, Faculty of Electrical Engineering and Informatics, Technical University of Košice, Park Komenského 2, 042 00 Košice

INTRODUCTION

After the Hahn's discovery, the NMR spin echoes are extensively used in the studies of relaxational and diffusive properties of fluids and solids. The Brownian particle mobility is easily determined from spin-echo measurements in gradient magnetic fields. However, the original interpretation of such experiments fails in the case of small samples, as first shown by Woessner (for a review see [1]). At present, the interest to solutions of the generalized Bloch-Torrey (BT) equations that take into account boundary conditions for spins moving in a restricted volume increases in connection with the increased interest in the description of processes on microscales and below. Our contribution gives a description of the simple spin-echo experiment on a fluid sample of Brownian particles confined between two nearby plates. The characteristic diffusion time to cross the sample is much smaller than the NMR relaxation times and smaller than the interval between the applied rf pulses. We thus have a problem of restricted diffusion of spins, an approximate solution to which was first given by Robertson [2]. We have recovered this solution by a different way and extend it to the presence of laminar flow between the plates.

RESTRICTED DIFFUSION

From the pulse methods which have found numerous applications in structural, relaxation, diffusion and other properties of fluids and solids, various variants of the spin echo are the most popular. This method is frequently used not only in physical, chemical and biological investigations but is an important part of imaging methods in medicine [3]. The spin echo belongs to the most accurate methods used to determine the diffusion coefficients D of nuclear spins. If the spins during the experiment diffuse in a region much smaller than the whole system, the classical BT theory yields known answers [1]. So, if H_z is a projection of the static magnetic field that creates macroscopic magnetic moment along the axis z and $G = \partial H_z / \partial z$ is a constant gradient of the field, then D can be determined measuring the spin-echo amplitude $F(2\tau, G)$ in the time 2τ after the first 90° rf pulse (τ is the time interval between the 90° and 180° pulses),

$$D = -\frac{12}{(\gamma G)^2 (2\tau)^3} \ln\left[\frac{F(2\tau,G)}{F(2\tau,0)}\right], \qquad (1)$$

where γ is the gyromagnetic ratio. However, if the mean time $\sim a^2/D$ (a is the characteristic size of the sample) for the nucleus to cross the sample is smaller or comparable to τ and the relaxation time, the effects of restriction on the diffusion reveal in the dependence of the apparent (determined using (1)) diffusion coefficient on τ. A more correct use of the BT phenomenology requires the account for boundary conditions for magnetization. It was found [1] that the magnetization decay in conditions of restricted diffusion is smaller than in unbounded media. Partially it is due to an effective averaging of the field gradient as a result of the intense motion of spins between the walls. These investigations were realized in a number of works where the restricted diffusion was studied in different geometries [1]. NMR often serves also as a tool to study fluid flow [3, 4]. However, theoretical analysis of such observations is not satisfactory. A few papers dealing with solutions of the Bloch equations generalized to take into account macroscopic flow in the sample ignore diffusion and its possible restricted nature [5]. In the present work, both these effects are studied within the Bloch-Torrey-Stejskal phenomenology.

BLOCH-TORREY-STEJSKAL THEORY FOR SPIN ECHO

We come from the equation for the sample magnetization in incompressible fluids [6],

$$\frac{\partial \vec{M}}{\partial t} + \left(\vec{\upsilon}\nabla\right)\vec{M} \qquad (2)$$
$$= \gamma \vec{M} \times \vec{H} - \frac{M_x \vec{i} + M_y \vec{j}}{T_2} - \frac{M_z - M_0}{T_1}\vec{k} + D\Delta\vec{M} \ ,$$

where $\vec{\upsilon}$ is the flow velocity, T_1 and T_2 are the longitudinal and transversal relaxation times, and $\vec{i}, \vec{j}, \vec{k}$ stay for unit vectors in the laboratory frame. The external magnetic field consists of a strong static field $H_z = H_0 + Gz$ and a much weaker high-frequency field $\vec{H}_1$, which is perpendicular to the axis z. This field oscillates with the resonance (Larmor) frequency $\omega = \gamma H_z$, i.e. $H_{1x} + H_{1y} = H_1 \exp(-\mathrm{i}\omega t)$. Due to a small gradient G the x and y components of the field should also depend on the coordinates in order to satisfy the condition $\operatorname{div}\vec{H} = 0$, but this dependence gives rise to fast oscillating terms in (2), which can be neglected [7]. Equation (2) is written in the laboratory frame, which is chosen so that the xy plane is parallel to the boundary planes and the axis z intersects them in the points $-h$ and h. We rewrite this equation for the quantity $M = (M_x + \mathrm{i}M_y)\exp(-t/T_2 - \mathrm{i}\omega t)$

$$\frac{\partial M}{\partial t} + A\upsilon(z)\frac{\partial M}{\partial x} + i\alpha z M = \left(\frac{\partial^2}{\partial x^2} + \frac{\partial^2}{\partial z^2}\right) M \ , \qquad (2)$$

where $A = h\upsilon_0/D$, $\alpha = \gamma G h^3/D$, υ_0 is the mean velocity in the cross section yz, and the flow is laminar, i.e. $\upsilon(z) = (3/2)(1 - z^2)$. The length and time are measured in the units h and h^2/D, respectively, and M in $\mathrm{i}M_0$ (the initial value of magnetization). The boundary conditions (assuming that the normal diffuse flows are zero at the boundaries) are $\partial M/\partial z = 0$ at $z = \pm 1$ and Eq. (2) must be solved with the initial conditions after the action of the rf pulses at $t = 0$ (90° pulse) and $t = \tau$ (180° pulse): $M(x, z, 0_+) = 1$, $M(x, z, \tau_-) = M^*(x, z, \tau_+)$, since the pulses rotate the magnetization in the plane perpendicular to the axis x. Here the time of duration of the pulses is neglected and the subscripts - and + are for the time moments immediately before and after the pulses. The origin of the coordinates is in the beginning of the coil creating pulses and detecting the NMR signals. The fluid moving in the x direction comes to the point $x = 0$ with the initial value of magnetization, $M(x = 0, t) = 0$. The problem is now fully formulated. Its solution for M is not known but if we are interested in finding the observed signal, we can proceed as follows.

To find the registered signal in the time 2τ, we have first to calculate the mean of M_y in the cross section,

$$F(x,t) = \frac{1}{2}\int_0^1 \left[M(x,z,2\tau) + M^*(x,z,2\tau)\right]dz \qquad (3)$$

and then to integrate (3) over the coil length L. The equation for the mean M (denoted by m) is found by integrating (2). We solve it by the method of successive approximations, when in the first step $M = m$. The resulting equation for $\Phi = M - m$ must be solved with the conditions $\Phi(x, z, 0) = 0$ and $\partial\Phi/\partial z = 0$ at $z = \pm 1$. The solution is substituted to the equation for m. Then, the obtained equation is to be solved with the initial conditions after the pulses. Fortunately, there is no necessity to solve this task twice, after each of the pulses [2]. Using the Fourier transformation (FT)

$$\varphi_k = \exp(k^2 t)\int_{-\infty}^{\infty} dx\, M \exp(-ikx) \qquad (4)$$

and expanding φ_k in functions $\Psi_n(z)$ orthogonal in the interval (0, 1),

$$\varphi_k = \sum\nolimits_{n=0}^{\infty} a_{nk}(t)\Psi_n(z), \qquad (5)$$

the FT of the searched signal is determined by only one coefficient a_{0k}:

$$F_k(2\tau) = (1/2)\left[a_{0k}(2\tau) - a_{0k}^*(2\tau)\right], F_{k0} = M_0(k). \qquad (6)$$

The appropriate functions Ψ_n are $\Psi_n(z) = (1 - \delta_{n0}/2)^{1/2} \cos[\pi n(z + 1)/2]$. By this way we find $F_k(2\tau)$ in the Fourier space, transform the result to $F(2\tau, x)$, and after the integration over x from 0 to 1 the resulting echo signal is obtained. The result is expressed through error functions and series and is rather bulky, so that we do not give it here. We only show the limit of small and large τ. In the former case (in dimensional quantities) $\tau << (2h/\pi)^2/D$, and the predicted signal is

$$F(2\tau) \approx 1 - \frac{2}{3}(\gamma G)^2 D\tau^3 - \frac{2}{L}\left(\frac{2\tau D}{\pi}\right)^{1/2} - \frac{2}{L}\left(\frac{2\tau^5 D}{\pi}\right)^{1/2}\left(\frac{\upsilon_0}{h}\right)^2. \qquad (7)$$

The first two terms correspond to the well-known equation (1) and the last two ones describe the effect of bounded diffusion and flow. The restriction on diffusion leads to a slower relaxation than in unbounded medium. This can be explained by the averaging of the dephasing influence of the field gradient, due to intense motion of the particles. In the opposite limit $\tau >> (2h/\pi)^2/D$ that corresponds to strongly restricted diffusion we have

$$F(2\tau) \approx \exp\left(\frac{-4\gamma^2 G^2 h^4}{15D}\right)\left[\frac{a}{\tau^{1/2}} + \frac{b}{\tau^{3/2}} + \ldots\right], \qquad (8)$$

where the coefficient a in the most important term in [...] is given by

$$\frac{1}{a^2} = 8\pi D\left[1 + \frac{2}{105}\left(\frac{\upsilon_0 h}{D}\right)^2\right]. \qquad (9)$$

Note that in the absence of flow these limits agree with the solution by Robertson [2]. Our result for arbitrary τ if $\upsilon_0 = 0$ analytically differs from that found in [2] but in the region of the validity of Robertson's approach the two results are quantitatively very close. An advantage of our approach is in its applicability to different, not only for the spin echo, pulse sequences.

CONCLUSIONS

Diffusion NMR is widely used as a non-invasive probe in a multitude of applications ranging from characterization of solutions to inferring microstructural features in biological tissues. In many situations the studied samples are such small that during the experiment the diffusing particles interact with the sample boundaries. In addition, a macroscopic flow of the material can be present. We have described the effects of both these phenomena on the NMR signal detected in the most frequently used pulse method, the NMR spin echo. Our work thus extends the well known Robertson's work, where the restricted diffusion was studied for the first time. The used solution allows generalizing the results obtained for spins diffusing in a fluid flowing between two plates to other geometries and can be examined in standard experiments.

ACKNOWLEDGMENT: This work was supported by the Agency for the Structural Funds of the EU within the project NFP 26220120021, and by the grant VEGA 1/0300/09.

REFERENCES

1. D. S. Grebenkov, Rev. Mod. Phys. **79**, 1077 (2007).
2. B. Robertson, Phys. Rev. **151**, 264 (1966).
3. P. A. Rinck, in: Magnetic Resonance in Medicine, Chap. 14 (Blackwell Scientific, Oxford - 2003).
4. S. Stapf, S.-I. Han: NMR Imaging in Chemical Engineering (Wiley, Weinheim - 2006).
5. O. B. Awojoyogbe, Physica A **339**, 437 (2004).
6. E. O. Stejskal, J. Chem. Phys. **43**, 3597 (1965).
7. N. M. Pomerancev, Usp. fiz. nauk **65**, 87 (1958).

DSC STUDY OF TAXOL LOADED POLYMER NANOSPHERES

A. Juríková, akasard@saske.sk, K. Csach, J. Miškuf, M. Koneracká, V. Závišová, P. Kopčanský, G. Lancz, N. Tomašovičová, M. Timko, Institute of Experimental Physics, Slovak Academy of Sciences, Košice, Slovakia, M. Múčková, Hameln rds a.s., Modra, Slovakia

INTRODUCTION

Magnetic nanoparticles encapsulated with drug into biocompactible polymer have potential applications in the field of magnetic drug targeting. Drug targeting is defined as selective drug delivery to specific physiological sites, organs, tissues or cells where drug's pharmacological activities are required. In principle, a drug distributes in the whole body when it is injected in the blood, and the drug that is distributed to sites other than the therapeutic sites may cause toxic side effects. Magnetically controlled drug targeting is one of the various possibilities of drug targeting. This technique is based on binding a selected anticancer drug with magnetic fluids into a pharmacologically stable formulation. The drug can be dissolved, entrapped, encapsulated or attached to nanoparticles and depending upon the method of preparation, nanoparticles, nanospheres (NPs) or nanocapsules can be obtained. Magnetic polymer NPs, made from organic and inorganic components, have unique characteristics due to the specific properties of the blend. The constituents of a magnetic polymer NPs play different roles: the polymer matrix acts as a shell, reservoir, and vehicle for the active component, whereas magnetite is the component that makes targeting possible by external magnetic field manipulation. Although nanoparticles can be formulated from a wide variety of natural and synthetic polymers, biodegradable polymers such as poly(D,L-lactide-*co*-glycolide) (PLGA) and polylactides (PLA) are especially suitable for subtained drug delivery applications due to their biodegradable nature and biocompactibility with cells and tissue [1]. Paclitaxel (Taxol®, TAX), an important anticancer drug, has been chosen for encapsulation to the polymer because of its significant role against a wide range of tumours (breast cancer, ovarian carcinoma, lung cancer, head and neck carcinomas) [2].

Thermal analysis methods are very useful tool in the characterization NPs and interactions in polymer–drug systems [3]. Differential scanning calorimetry (DSC) can be used to calculate the solubility of the drug in the polymer, an important parameter which influences the drug encapsulation and release from NPs [1, 4]. The aim of the work was to prepare Taxol loaded magnetic and non–magnetic polymer NPs, to characterize their thermal properties and determine the drug solubility drug in prepared PLGA NPs.

EXPERIMENTAL

Taxol was obtained from Indena company. PLGA polymer with D,L-lactide to glycolide ratio of 85:15, molecular weight of 50–75 kg.mol^{-1} and the glass transition temperature of 50°C, and Pluronic F68 used as a stabilizating agent, were purchased from SIGMA company. Poly(ethylene glycol) (PEG) with molecular weight of 1 kg.mol^{-1} was supplied by Merck. Magnetite (Fe_3O_4) was prepared by co-precipitation of ferric and ferrous salts in an alkali aqueous medium [5]. To prepare stable colloidal suspension of magnetic particles, sodium oleate as a first surfactant was used to prevent their agglomeration. PEG as a second surfactant was added to the system magnetite–sodium oleate to improve biocompatibility of magnetic material.

The modified nanoprecipitation method [6] used for entrapment magnetic fluid (MFPEG) and anticancer drug Taxol into PLGA polymer nanospheres was described in more details in [7]. After the sphere formulation, the thermal behaviour of the prepared NPs was characterized by DSC measurements were performed using Perkin Elmer DSC 7 calorimeter at the rate of 10°C/min up to 250°C in the flowing nitrogen atmosphere. We intended to determine the solid-state solubility of the drug in the polymer at the drug melting temperature by measuring the enthalpy change of melting of the free drug (not incorporated into the polymer) in dried NPs with variable Taxol loading.

RESULTS AND DISCUSSION

Magnetic and non–magnetic PLGA NPs of the spherical shape and the mean diameter of 200–250 nm loaded with different input amounts of encapsulated Taxol were prepared. Their morphology and size distribution are described in more details in [7].

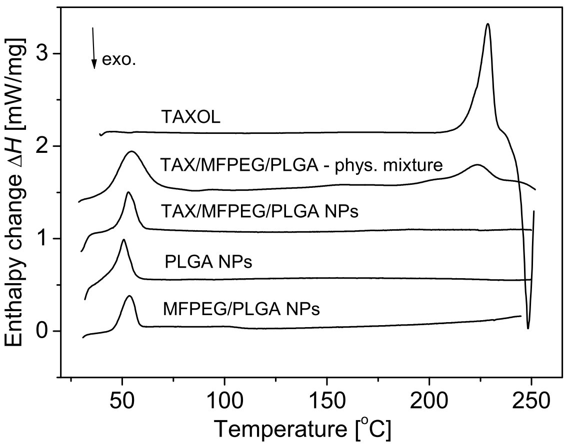

Fig. 1. DSC thermograms of prepared PLGA composite nanospheres, the physical mixture and pure Taxol.

Typical DSC curves of pure Taxol, physical mixture of Taxol and magnetic PLGA NPs, Taxol loaded magnetic PLGA NPs (TAX/MFPEG/PLGA NPs), blank PLGA NPs and magnetic particles loaded PLGA NPs (MFPEG/PLGA NPs) are in Fig. 1. As can be seen we observed no significant peak in the temperature range of 70–250°C for blank PLGA NPs as well as for MFPEG/PLGA NPs and TAX/MFPEG/PLGA NPs. The endothermic melting peak of pure Taxol (228°C) is only observed in the thermogram of the physical mixture and it is slightly shifted to a lower temperature (224°C). Therefore, it could be concluded that Taxol in NPs was in an amorphous or disordered crystalline phase of molecular dispersion or a solid solution state in the polymer matrix after the production [3]. The glass transition temperature T_g of PLGA polymer was not influenced by the preparation procedure.

Figures 2 and 3 show DSC traces of the dried non-magnetic and magnetic PLGA NPs, respectively, with variable amounts of the added drug up to 37.5 wt% ($m_{TAX}/(m_{TAX}+m_{PLGA})$). In these thermograms, endothermic peak I (around 55°C) refers to T_g of PLGA. Endothermic peak III (around 110°C) appeared in Taxol loaded magnetic NPs is associated with used MFPEG encapsulated to polymer NPs. At the melting temperature of Taxol, the observed endothermic process (peak II) corresponds to the melting of the residual undissolved drug. Values of melting enthalpy ΔH_m for both types of NPs were plotted as a function of Taxol loading percentage $m_{TAX}/(m_{TAX}+m_{PLGA})$ in Fig. 4. The X-axis intercept provided by linear regression of the data, yielded a value of TAX in PLGA at 14.9 wt% for the non-magnetic NPs. That means, when the drug was bound by the NPs, it was possible to bind a maximal amount of about 17 mg of Taxol into 100 mg of the used polymer without excess observed by DSC. However, there was a limitation by the colloidal stability. The collected data for the magnetic NPs samples gave higher ability of comprising Taxol. If we took the assumption that TAX was incorporated in PLGA and only these two components have to be taken into account, the data analysis gives a result of 17.5 wt%, what is 21.2 mg TAX/100 mg PLGA. This higher value in comparison with non–magnetic NPs might be a result of the presence of the surfactants (PEG, sodium oleate) in the used magnetic fluid.

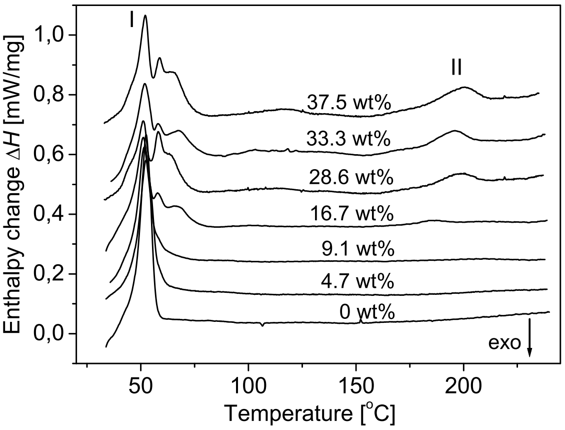

Fig. 2. DSC traces of non-magnetic PLGA NPs loaded with indicated input portions of Taxol.

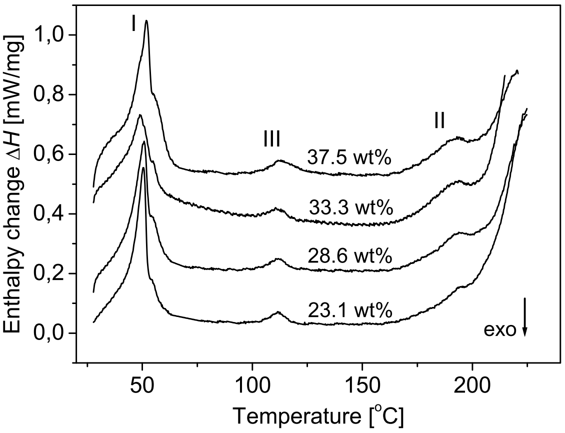

Fig. 3. DSC traces of magnetic PLGA NPs loaded with indicated input portions of Taxol.

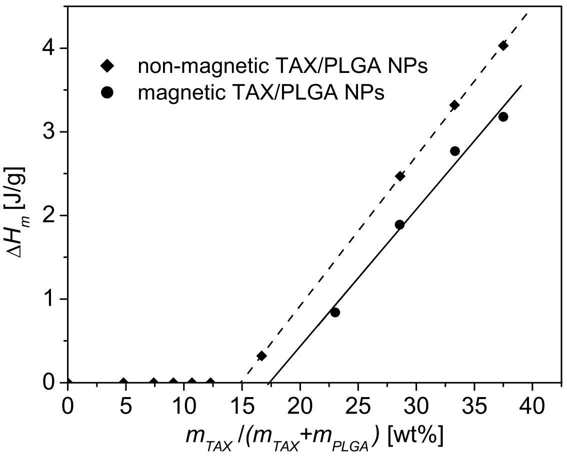

Fig. 4. The relationship between TAX loading and the enthalpy change of melting of Taxol for non-magnetic and magnetic NPs.

In conclusion, non–magnetic and magnetic PLGA nanospheres with variable loadings of Taxol were succesfully prepared and characterized. DSC measurements of non-magnetic NPs gave an estimation of Taxol loading capacity at 17 mg of Taxol into 100 mg of PLGA, although such dispersions were not stable colloids. Higher loadings without excess drug might be achievable in Taxol loaded magnetic NPs dispersions that were more stable. The results confirmed incorporation of magnetic particles and drug in the PLGA polymer.

ACKNOWLEDGMENT: This work was created by implementation of the "Cooperative phenomena and phase transitions in nanosystems with perspective utilization in nano- and biotechnology" project no. 26220120021. Funding for the operational research and development program was provided by the European Regional Development Fund.

REFERENCES

1. J. Panyam, D. Williams, A. Dash et al., J. of Pharm. Sci. **93**, 1804 (2004).
2. C. Fonseca, S. Simoes and R. Gaspar, J. of Controlled Release **83**, 273 (2002).
3. C. Dubernet, Thermochimica Acta **248**, 259 (1994).
4. F. Theeuwes, A. Hussain and T. Higuchi, J. of Pharm. Sci. **33**, 427 (1974).
5. V. Závišová, M. Koneracká, O. Štrbák et al., J. Magn. Magn. Mater. **311**, 379 (2007).
6. H. Fessi, F. Puisieux, J.P. Devissaguet et al., Int. J. Pharm. **55**, R1 (1989).
7. M. Koneracká, M. Múčková, V. Závišová et al., J. of Physics: Condensed Matter **20**, 204151 (2008).

INFLUENCE OF OUTER ELECTRODE MATERIAL ON OZONE PRODUCTION IN COAXIAL NEGATIVE CORONA DISCHARGE FED BY OXYGEN

J. Országh[1,2], orszagh@fmph.uniba.sk, G. Horváth[1,2], Š. Matejčík[1], [1]Department of Experimental Physics, Comenius University, Mlynská dolina F-2, 842 48 Bratislava, Slovakia, N.J. Mason[2], [2]Department of Physics and Astronomy, The Open University, Walton Hall, MK7 6AA, Milton Keynes, United Kingdom

INTRODUCTION

The "electric odour", observed by Van Marum when oxygen was passing trough electric spark in 1785, has been later (1839), identified by Ch. F. Schönbeim as a new chemical compound named ozone [1]. A few years later in 1857 Werner von Siemens has designed first device for ozone production that was using electrical discharge currently known as dielectric barrier discharge or silent discharge [2]. Almost from those times ozone is widely used chemical compound.

Ozone has many industrial applications such as disinfection of certain bacteria in food and water. It can be also used in the food industry for surface hygiene. It can be also used for increasing the shelf life of products, e.g. by reducing the microbial populations in fruits [3] or rapid decomposition [4].

On the other hand the ozone production is in many cases inappropriate and should be suppressed. Typical cases can be indoor air cleaning precipitators or copy machines where increased ozone concentration in air could be harmful for people. One of the approaches is to use appropriate wire electrode material such as silver [5].

In this study we are proceeding to the next step. The goal was to examine the influence of outer electrode ageing on the ozone production and find out how much time does it need to produce stable amount of ozone.

EXPERIMENT

The reactor was composed of cylindrical wire-to-cylinder system of electrodes. Two outer electrodes with the same dimensions (diameter 1.6 cm and length 6.5 cm) were used in the experiment. One was made of stainless steel and the other one of brass. The inner electrode was always made of stainless steel wire with diameter of 0.125 mm.

First the outer electrode was mechanically cleaned to remove the layer of oxides from its surface. The reactor have been filled by pure oxygen and closed. Then the negative corona discharge was generated in the reactor. The voltage on the electrodes was constantly 5.4 kV. During 1 hour exposition the time dependence of UV light absorption, discharge current and reactor temperature has been observed. After the measurement the reactor was filled by pure oxygen again. The experiment was repeated 5 times in a row without changing or cleaning the electrodes. After this set of expositions the brass electrode was found to be covered by greenish layer of oxides. On the other hand the steel electrode surface did not show any visible changes. Especially the influence of this oxidation on ozone concentration was studied. The experiments have been carried out at atmospheric pressure and ambient temperature. The ozone concentration was calculated from UV absorption data by Lambert-Beer formula using the ozone absorption cross section in Hartley band [6].

RESULTS AND DISCUSSION

The oxidation of the steel electrode had little systematic effect on the ozone concentration. On the other hand in case of brass electrode systematic diminishing of ozone concentration is evident. However, during the first exposition the ozone concentration diverted towards lower values after a few minutes (see Fig. 1.).

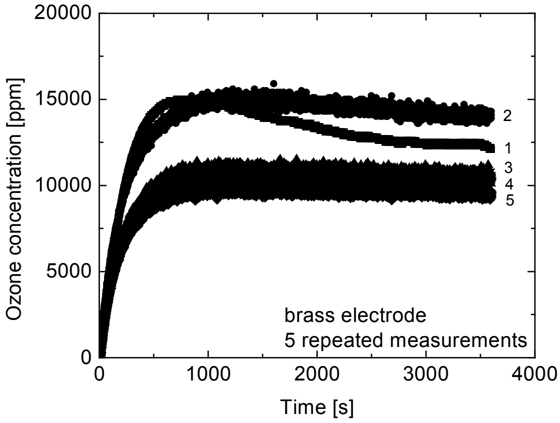

Fig. 1. Time dependence of ozone concentration for brass electrode (5 repeated measurements).

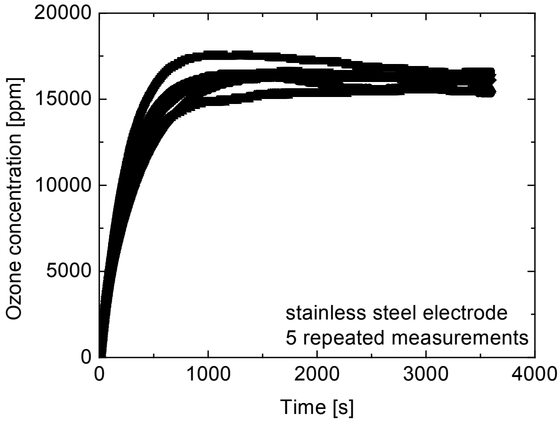

Fig. 2. Time dependence of ozone concentration for steel electrode (5 repeated measurements).

It seems that the more oxides are created on the surface the less ozone is produced. Overall ozone concentration was higher in steel electrode (Fig. 2.).

The time dependence of discharge currents (figure not shown) shows that despite of different ozone concentration these are comparable in all the regimes.

Despite the fact that input energy was comparable in all the experiments the ozone concentrations were different. Hence we can suggest that the changing properties of electrode surface are responsible for changes in ozone concentration.

The process of ozone generation is relatively simple. The oxygen atoms are produced by oxygen molecule dissociation. Ozone molecule is then formed by subsequent association three body reaction of oxygen atom with two oxygen molecules reaction.

Moreover the oxygen atoms $O(^1D)$ can be formed by electron impact. This process is two times faster as the process, however in pure oxygen $O(^1D)$ atoms have to be deexcited in reaction with another oxygen molecule and then they can contribute to ozone generation.

On the other hand ozone decomposition is a set of various processes. Generally they can be divided into homogeneous (in the volume of the gas) and heterogeneous (in contact with reactor walls). Ozone is decomposed both in the glow region of the discharge and in the drift region. The homogeneous reactions are independent on electrode material and surface so we will concentrate on heterogeneous processes.

The heterogeneous decomposition of ozone molecules on the surface of the outer electrode

$$O_3 + \text{wall} \longrightarrow O + O_2 \qquad (1)$$

The rate constant of this process depends on the type of material from which the wall is made and on the dynamics of electric wind transporting ozone molecules through the discharge gap. Simple qualitative analysis shows the differences between various electrode materials. Let ΔN be the number of ozone molecules decomposed on the unit length of the outer electrode per second. This can be calculated if we presume that ozone molecules in thin layer at the outer electrode are transported to the wall by thermal movement. Then $\Delta N = \frac{1}{4}\gamma.n.v_s.2\pi R$, where γ is the probability that ozone molecule is decomposed, n is the concentration of ozone in the discharge gap (we presume for simplicity that there in no gradient in ozone concentration in the discharge gap) and v_s is the mean thermal velocity of ozone molecules determined by temperature. The rate of ozone depletion is then

$$\frac{dn}{dt} = -\frac{\Delta N}{V} = -\frac{\Delta N}{\pi.R^2} = -\frac{1}{2}\frac{\gamma.v_s}{R}n \qquad (2)$$

The decrease of the rate of the heterogeneous decomposition is evident from (2). Values of coefficient γ are different even for various types of steel $4x10^{-7}$ – $4x10^{-9}$. For brass it is $0.2x10^{-4}$ [7]. Based on these facts it is possible to suggest that rate constant of process (1) for brass electrode should be higher than for steel electrode. It is in correspondence with experimental results where the ozone concentration was higher in steel electrode.

CONCLUSION

The experiments were performed in coaxial DC corona discharge in static regime at constant voltage. It was found that overall ozone concentration was higher if the electrode made of stainless steel has been used. The brass electrode was oxidising faster and the lower values of ozone concentration have been observed experimentally. It was explained that ozone is being decomposed in the volume of gas as well as in contact with the electrode wall. As the homogeneous decomposition processes are not affected by the electrode material the differences in ozone concentrations have to be most likely caused by differences in oxidation of steel and brass electrode.

Acknowledgments: This research project was partially supported by, UK/381/2009, UK/407/2009, ESF projects COST CM0601 and CM0805, VEGA 1/4017/07, the UK Royal Society for a Joint International project and the Leverhulme Trust.

REFERENCES

1. 1.R.S. Stolarski, Proceedings of International Ozone Symposium, Basel, Switzerland, 41 (1999).
2. J.D. Skalny, N.J. Mason, T. Mikoviny, Romanian Reports in Physics **54**, 117 (2002).
3. M.B.H. Najafi, M.H.H. Khodaparast, , Food Control **20**, 27 (2009).
4. R. Chand, D.H. Bremner, K.C. Namkung, P.J. Collier, P.R. Gogate, Biochemical Engineering Journal **53**, 357 (2007).
5. A. Yeiha, A. Mizuno, IEEE/IAS Conf. Proc. (2005).
6. R.R. Huffman, Canad. J. of Chem. **47** 1823 (1969).
7. V.V. Lunin, M.P. Popovich, S.N. Tkachenko: Fizicheskaja chimija ozona. (Izd. Moskovskogo Universiteta, Moscow – 1998).

RESONANT ENERGIES OF IONS ANALYZED BY MASS SPECTROMETRY COMPARED WITH CALCULATED REACTION ENERGIES

P. Papp, papp@fmph.uniba.sk, D. Kubala, J. Kočíšek, Š. Matejčík, Department of Experimental Physics, Faculty of Mathematics, Physics and Informatics, Comenius University, Mlynská dolina F2, 842 48 Bratislava

INTRODUCTION

Both experimental and theoretical studies on Dissociative Electron Attachment (DEA, equation 1) have been performed to several amino acids: previously to valine ($C_5H_{11}NO_2$) [1], in this work to leucine (Leu), isoleucine (Ile) ($C_6H_{13}NO_2$) and serine (Ser) ($C_3H_7NO_3$).

$$P + e^- \rightarrow (P^-)^\# \rightarrow (P-X)^- + X \qquad (1)$$

Standard quantum chemical methods are used to optimize the ground state geometries of fragmentation products and compute the Reaction Energies (RE) of the suggested fragmentation schemes. These could be then compared with the experimental Resonant Energies (ResE) which specify the upper threshold for the computed RE.

EXPERIMENT

The crossed electron-molecule beams apparatus equipped with quadruple mass-spectrometer and trochoidal monochromator was used to study the DEA to gas-phase Leu, Ile and Ser amino acids. The maximal energy resolution of this apparatus built at Comenius University [2] is 50 eV, however the measurements were performed with energy resolution 250 eV (due to the low dissociative cross sections of most of the ionic fragments). Molecules were evaporated to the reaction area at the temperature ~ 420 K (Ser) and ~ 440 K (Leu and Ile). In this experiment either the colliding electron energy is set to constant and the ionic mass/charge (m/Z) ratio intensities are measured; or at constant m/Z one can get the electron energy dependent ion yields. All these information are coupled only with the ionic fragments, it is not possible to obtain any information about the neutral products of DEA reactions. Therefore theoretical methods can be used to get more detailed information on the products.

In general, the DEA spectra of Leu, Ile and Ser have many common features with previously studied aliphatic amino acids (glycine, alanine and valine). Most abundant channel is characteristic with low energy resonance at about 1 eV, higher resonances are present at around 5 eV and 8 eV. We detected at least eleven anionic fragment channels for Leu and Ile; and more than 15 for Ser. No signal was detected for the parent ions as they are unstable with an extra electron and fragmentation or detachment is followed.

THEORY

We include two different quantum chemical methods in our theoretical calculations: **1.** Density Functional Theory (DFT) for reasonable fast geometry optimisations of parent molecules, their possible conformers and all ionic and neutral products. **2.** B3LYP functional [3] combined with 6-311++G(2df,2pd) basis set (with a reasonable number of diffuse and polarisation functions) was used in our studies. Thermo-chemistry calculations are necessary to be performed to include the thermal corrections and exclude any Transition States.

After building up an appropriate fragmentation scheme on DFT level of theory, all the parent and fragment molecules are re-calculated with G3MP2 method [4]; ab initio complex energy calculation consisting of Hartree-Fock (HF) and second order perturbation theory (MP2) optimizations, thermo-chemistry calculations, QCISD(T) correlation energy calculation and finally estimation to infinitely large basis set with inclusion of thermal and empirical corrections. This is another non-expensive way how to obtain more reliable results comparing to experiment but concerning the energies and not the geometries as for B3LYP.

PARENT MOLECULES

We have selected several different conformers of Leu [5] (Fig. 1 first line), Ile [6] (Fig. 1 second line) and Ser [7] (Fig. 2) amino acids from previous theoretical works. We would like to include in our calculations all possible low-energy geometries of parent molecules that can easily fragment to molecules like NH_3, CH_4, H_2O.

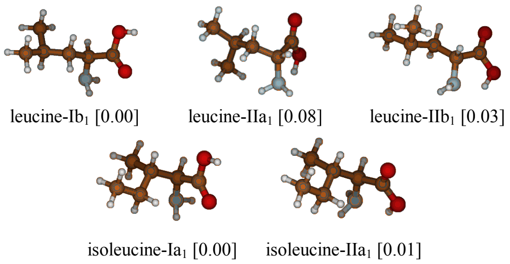
leucine-Ib$_1$ [0.00] leucine-IIa$_1$ [0.08] leucine-IIb$_1$ [0.03]

isoleucine-Ia$_1$ [0.00] isoleucine-IIa$_1$ [0.01]

Fig. 1. Conformers of Leu and Ile amino acids considered in our studies. In parenthesis are the G3MP2 relative energies [eV]. Carbons are brown, nitrogen blue, oxygens are red and hydrogens are white.

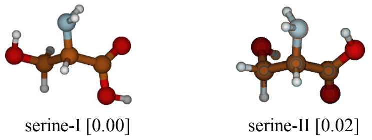
serine-I [0.00] serine-II [0.02]

Fig. 2. Two main low-energy conformers of Ser amino acid considered in our studies. In parenthesis are the G3MP2 relative energies [eV].

FRAGMENTED IONS

As for similar amino acids studied so far we expected the low energy resonance typical for $(P-H)^-$ negative ion formation to be the most abundant (spectrum of energies on Fig. 3 and Fig. 4). More detailed look at the structure of an arbitrary amino acid gives us the following fragmentation schemes: via COOH group, via NH_2 group, via side-chain group R.

There are 13 hydrogen atoms in Leu and Ile and 11 in Ser; this could lead to many possible ways of fragmentation. However fragmentation via COOH group is typical for amino acids and energetically most favorable. Tables 1 and 2 give the comparison of experimental ResE with the RE at G3MP2 level. The calculated energy of carboxylic O-H bond rupture is thus in good agreement with experimental ResE.

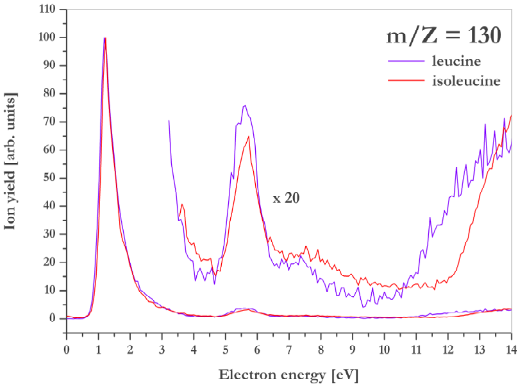

Fig. 3. The electron energy dependent ion yield spectrum of dehydrogenated Leu (blue) and Ile (red).

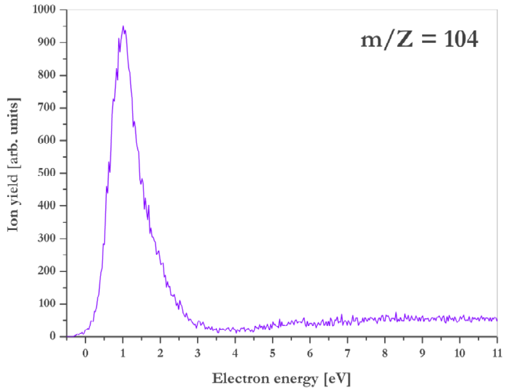

Fig. 4. The electron energy dependent ion yield spectrum of dehydrogenated Ser.

Other low energy resonances cannot be depicted here but are listed in tables 1 and 2, however these are lower in intensities as those on Fig.4 and 5. These are mostly coupled with fragmentations via NH_2 group. This can be seen for ions 115 in Leu and Ile and ion 89 in Ser, although there are really close to ResE (or higher) we still did not consider here the error bars for experiment or possible geometrical rearrangement of ionic product. The same path can be assigned to ions 114 (Leu and Ile) and 88 (Ser) that are produced via NH_3 dissociation. While leucine-IIb$_1$ and isoleucine-IIa$_1$ were considered because of the existence of COO-H$\cdots$$NH_2$ interaction and thus easier way of NH_3 creation, in serine-I the side-chain hydrogen atom is coupled to the NH_2 and this fragmentation leads to good agreement with the resonance at 1.3 eV. However if we consider one H atom shift from the C_β to C_α we can still get a good agreement (1.48 eV). Additional H atom dissociation can be observed from COOH (1.06 and 1.07 eV for m/Z 87) or from C_β (1.15 eV).

On the other hand if we do not consider production of NH_3 and we take two neutral radicals NH_2 and H as products together with $(P\text{-}NH_2\text{-}H)^-$ ions of Leu or Ile, we have a good description of higher energy resonance at 5.2 eV for m/Z 114. Bond breaks associated with carboxylic group can lead also to this higher energy resonance by dissociation of OH neutral form Leu or Ile. The same result is in agreement with the resonance at 8.3 eV in m/Z 87 of Ser fragment that is produced via CO-OH bond brake and simultaneous C_α hydrogen dissociation. Moreover production of H_2O (either from side-chain OH or carboxylic OH and C_α hydrogen) with the same ionic product instead of two neutrals can access a low energy resonance of this channel (0.35; 1.46 and 1.57 eV reaction energies). Finally we found only one path coupled with side-chain fragmentation of Leu and Ile that describes the higher energy resonance at 5.3 eV of m/Z 115 ion. Carboxylic hydrogen and simultaneous one CH_3 radical dissociation can lead to production of two different Leu and Ile residual ions $(P\text{-}CH_3\text{-}H)^-$ with RE 4.88 and 4.91 eV, resp.

TAB. 1. Experimental ResE and calculated RE of Leu and Ile fragmentation to $(P\text{-}X)^-$ ion + X neutral.

m/Z	ion	Resonant Energies [eV]	G3MP2 [eV]	
			leucine	isoleucine
130	$(P\text{-}H)^-$	1.23; 5.6; 7.5	1.14	1.10
115	$(P\text{-}NH_2)^-$	1.7; 5.3	1.68	1.72
	$(P\text{-}CH_3\text{-}H)^-$		4.88	4.91
114	$(P\text{-}OH)^-$	1.5; 5.2; 8.0	4.00	3.98
	$(P\text{-}NH_2\text{-}H)^-$		4.84	4.86
	$(P\text{-}NH_3)^-$		0.18	0.22

TAB. 2. Experimental ResE and calculated RE of two Ser conformers fragmentation to $(P\text{-}X)^-$ ion + X neutral.

m/Z	ion	Resonant Energies [eV]	G3MP2 [eV]	
			serine-I	serine-II
104	$(P\text{-}H)^-$	1.1	0.92	0.85
89	$(P\text{-}NH_2)^-$	1.3	1.45	1.59
88	$(P\text{-}NH_3)^-$	1.3	0.69; 1.48	-
87	$(P\text{-}NH_3\text{-}H)^-$	1.3; 8.3	1.06; 1.15	1.07
	$(P\text{-}H_2O)^-$		0.35; 1.46	0.35; 1.57
	$(P\text{-}OH\text{-}H)^-$		6.57	6.68

ACKNOWLEDGMENT: This work was supported by the Slovak grant agency VEGA project Nr. 1/0558/09.

REFERENCES

1. P. Papp et al., J. Chem. Phys. **125**, 204301 (2006).
2. M. Stanoet al., J. Phys. B: At. Mol. Opt. Phys. **36**, 261 (2003).
3. C. T. Lee et al., Phys. Rev. B **37**, 785 (1988).
4. L. A. Curtiss et al., J. Chem. Phys. **109**, 7764 (1998).
5. E. J. Cocinero et al., ChemPhysChem. **8**, 599 (2007).
6. A. Lesarri et al., J. Am. Chem. Soc. **127**, 12952 (2005).
7. S. Gronert, R. A. J. O'Hair, J. Am. Chem. Soc. **117**, 2071 (1995).

ANALYSIS OF RUMANOVA METEORITE ^{26}Al CONCENTRATION USING COINCIDENCE GAMMA-RAY SPECTROMETRY

Ivan Sýkora[1], sykora@fmph.uniba.sk, Pavel P. Povinec[1], povinec@fmph.uniba.sk, Vladimír Porubčan[2], porubcan@fmph.uniba.sk and Miroslav Ješkovský[1], jeskovsky@fmph.uniba.sk , [1]Department of Nuclear Physics and Biophysics, [2] Department of Astronomy, Physics of the Earth and Meteorology,Faculty of Mathematics, Physics and Informatics, Comenius University, Bratislava, Slovakia

INTRODUCTION

Interactions of cosmic-ray particles with terrestrial (e.g. atmosphere, earth surface) and extraterrestrial (e.g. meteorites, lunar surface) objects can produced cosmogenic radionuclides, which enable to study origin and characteristics of target objects, as well as temporal and spatial variations of cosmic rays. Beside other techniques (e.g. Accelerator Mass Spectrometry), gamma-spectrometry is advantageous to use for analysis of radionuclides when they decay by emission of gamma-rays, cascade gamma-rays or by emission of positrons.

Low-level gamma-ray spectrometry enables to carry out analyses of radionuclides at very low-level concentrations without any physical or chemical destruction of samples. Due to an excellent energy resolution and a high efficiency, large volume Ge detectors have been widely used in the low-level gamma-ray spectrometry.

Necessity to partially reduce the detector background due to the hard component of cosmic radiation in a ground level laboratory requires the use of anticoincidence and/or coincidence (when cascade gamma-quanta or positrons is emitted) arrangements of the detectors.

EXPERIMENTAL

The HPGe-NaI(Tl) coincidence spectrometer was used for measurement of ^{26}Al concentration in meteorite samples. The measurements were carried out in a low-level shield built in gamma-ray laboratory of he Department of Nuclear Physics and Biophysics of the Comenius University Bratislava.

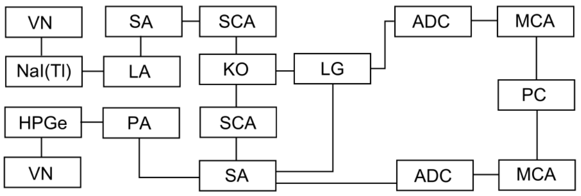

Fig. 1. Block schema of the electronics used for the HPGe-NaI(Tl) spectrometer. VN – high voltage power supply, SA – spectroscopic amplifier, SCA – single channel analyzer, PA – preamplifier, LA – linear amplifier, KO – coincidence circuit, LG - linear gate, ADC – analog to digital converter, MCA – multichannel analyzer.

The outer dimensions of the shield were 1.5x1.5x2 m^3. The shield consists of the following layers (from the outside to the inside): 10 cm of lead, 10 cm of electrolytic cooper, 10 cm of polyethylene with boric acid, 0.1 cm of electrolytic copper, 0.1 cm of cadmium and 1 cm of perspex. On the top of the shield, a layer of 12 cm of iron is added. The inner dimensions of the shield are 0.80x0.90x1.72 m^3.

For further decrease of the detector background an extra copper shield (12x20x30 cm3) has been inserted inside the large shield [2]. The shield is equipped with HPGe detector produced by PGT Europe with 70 % relative efficiency (270 cm^3 sensitive volume) and 10 cm in diameter and 10 cm long NaI(Tl) detector for coincidence measurements (Fig. 1.)

The meteorite sample was found in 1994 near the village Rumanová in Slovakia. The meteorite consisted of one piece of 4.3 kg stone with density of 3.53 g/cm^3. The Rumanová meteorite is of H5 chondrite type with dominant minerals such as enstatite, olivine, kamacite, taenite and troilite. The exposure age in the cosmic space was estimated to be about 7 million years, and the K-Ar age of about 4.3 billion years.

One piece of the broken meteorite sample (980 g) was analysed as a bulk sample. Later a 1 cm thick slide was cut, which was then divided into cubes of approximately 1,5x1,5x1,5 cm^3 of about 16 g (Fig. 2). These subsamples were then analyzed in the coincidence gamma-ray spectrometer.

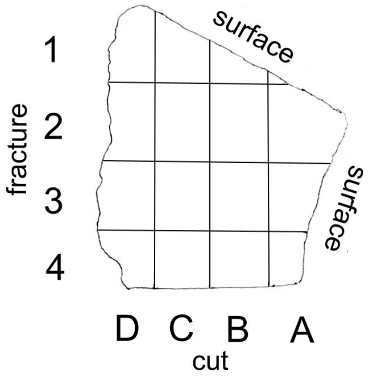

Fig. 2. Slide of the Rumanová meteorite with subsample positions.

The efficiency calibration was carried out using bulk and cube mock-ups with similar physical and chemical characteristics as the original meteorite sample. A Monte Carlo code has also been used for the calculation of the spectrometer efficiency.

RESULTS

The main target nuclei for ^{26}Al production in the Rumanová meteorite are Fe (21.2 weight %), Si (18.2 weight %), S (1.8 weight %), Al (1.03 weight %), Ca

(0.85 weight %) and Mn (0.22 weight %). The gamma-ray spectrum of the bulk meteorite sample is presented in Fig. 3. Both annihilation (511 keV) and characteristic (1809 keV) peaks are well visible in the spectrum. The coincidence gamma-ray spectrum of the A3+A4+B3+B4+C3+C4+D3+D4 subsamples is shown in Fig. 4.

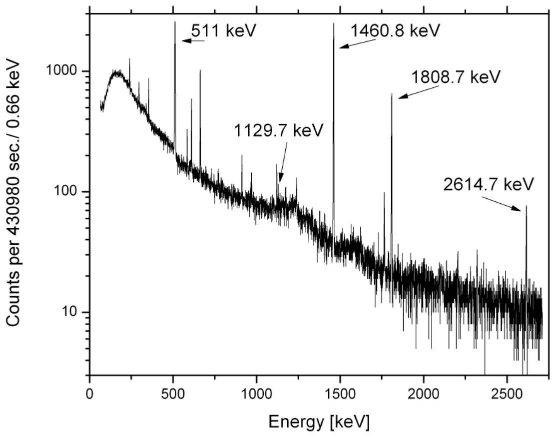

Fig. 3. Single HPGe gamma-spectrum of the meteorite bulk sample.

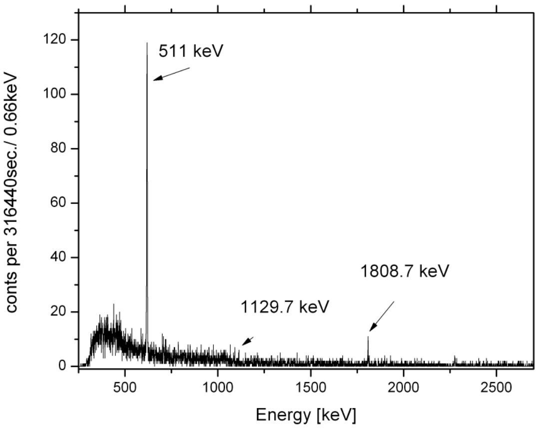

Fig. 4. HPGe-NaI(Tl) coincidence gamma-spectrum of subsamples A3,A4 - D3,D4 .

The mass activities of ^{26}Al in subsamples and in the bulk sample are presented in Tab. 1.

Table 1. Mass activity of ^{26}Al in the meteorite bulk sample and subsamples.

Sample	Weight [g]	Activity [Bq/kg]
A3+A4	19.3 + 13.6	1.45 ± 0.24
B3+B4	17.1 + 20.5	1.16 ± 0.26
C3+C4	17.7 + 21.8	1.06 ± 0.26
D3+D4	14.6 + 19.1	0.62 ± 0.11
Meteorite	980	0.817 ± 0.026

The results show that there is a little variation between the ^{26}Al activities in surface subsamples and those taken from the interior of the meteorite [3]. This is due to small size of the meteorite, as the hadron cascade did not have enough space to develop in the meteorite. A preliminary comparison of measured mass activities of ^{26}Al with Monte Carlo simulations carried out for the Estacado chondrite suggests that an exposure radius of the Rumanová meteorite was ≤ 30 cm.

CONCLUSIONS

The obtained mass activities of ^{26}Al in the Rumanová meteorite are in good agreement with similar measurements in Příbram, Saratov [4] and Estacado [5] meteorites. All these meteorites belong to chondrites, type H5, and therefore the observed agreement can be well understood.

Single and coincidence gamma-ray spectrometers have proved to be useful for measuring low concentrations of natural and anthropogenic radionuclides in meteorite samples. Because of the large inner volume of the constructed low-level shield it is possible to carry out these measurements nondestructively even for large volume samples. The coincidence gamma-ray spectrometry is especially suitable for low-level analysis of positron (^{22}Na, ^{26}Al) and cascade gamma-ray (e.g. ^{60}Co) emitters.

The ^{26}Al analyses carried out in subsamples of the Rumanová chondrite have shown differences within a factor of two between samples located in the surface and the interior of the meteorite. The obtained results suggest a small exposure size of the meteorite (the approximate radius was around 10 cm).

REFERENCES

1. Lal D.: Hard rock cosmic ray archaeology: Space Science Reviews 14 Num. 1, p. 3 (1972)
2. Sýkora I., Ješkovský M., Janík R., Holý K., Chudý, M., Povinec P.P.: Low-level single and coincidence gamma-ray spectrometry: Journal of Radioanalytical and Nuclear Chemistry 276 No.3,. s. 779–787 (2008)
3. Povinec P.P., Sýkora I., Porubčan V., Ješkovský M.: Analysis of ^{26}Al in meteorite samples by coincidence gamma-ray spectrometry: Journal of Radioanalytical and Nuclear Chemistry , inprint (2009)
4. Sýkora I., Ďurčík M., Staníček J., Povinec P.P. in: Rare Nuclear Processes, P. Povinec, Ed), World Scientific, Singapore, p. 321 (1992)
5. Masarik J., Chochula P., Povinec P.P. in: Rare Nuclear Processes, P. Povinec, Ed), World Scientific, Singapore, p. 228. (1992)

RADIOACTIVITY OF BRATISLAVA ATMOSPHERE

Ivan Sýkora, sykora@fmph.uniba.sk, Miroslav Ješkovský, jeskovsky@fmph.uniba.sk, Karol Holý, holy@fmph.uniba.sk, and Andrej Kováčik, andrejkvk@gmail.com, Department of Nuclear Physics and Biophysics, Faculty of Mathematics, Physics and Informatics, Comenius University, Bratislava, Slovakia

INTRODUCTION

Dominant source of atmospheric radioactivity is radon and its daughter products and cosmogenic radionuclide ^{7}Be. ^{7}Be is mainly produced in stratosphere and the upper troposphere. Measurement of this radionuclide at ground level can be used for tracking of stratospheric/tropospheric folding events. Isotope ^{210}Pb is long-lived daughter product of ^{222}Rn. It is interesting especially from the radio-hygienic point of view.

The aerosols radioactivity study in Department of Nuclear Physics of Faculty of Mathematics, Physics and Informatics of Comenius University Bratislava were realized in the period 1981-1995 in month intervals [1]. The continuation of study of atmospheric radioactivity started again in 2001 year but this measurements didn't have full periodic character. Since the end of the year 2003 in Bratislava locality the atmospheric aerosols radioactivity sampling with a week periode in the Department of Nuclear Physics and Biophysics has been started.

The activity concentration of ^{7}Be, ^{210}Pb, ^{137}Cs and ^{40}K radionuclides in aerosol samples was periodically investigated. At present, the aerosols are collected using high volume sampler (~ 80 m^{3}/hod.) and trapped by nitrocellulose filters with 0.85 µm diameter of gaps (PRAGOPOR 4). Radioactivity of the exponed filters is measured in low level background shield with HPGe detector [2].

EXPERIMENTAL

At present, the aerosols are collected using high volume sampler with the flow rate about 80 m^{3}/h at the height of 2.85 m above ground. The sampling site is on the meteorological station close to our university. The special nitrocellulose membrane filters (PRAGOPOR 4) with 0.85 µm holes with the approximate 100 % collection efficiency are used. The filters are changed once a week and during each sample period is about 11 000 m^{3} of air pumped. Corrections for air temperature and atmospheric pressure are applied to evaluate right volumes of pumped air.

Radioactivity measurement of the exposed filters is performed by standard gamma-ray spectrometry with two HPGe detectors (EG&G Ortec 51370/20-P with Be window and PGT IGC65-DI 845 with relative efficiency 69%) placed in low-level background shields. Corrections for radioactive decay to the mid-collection period were applied on the measured values. The total relative uncertainty of the method is about 3 %. For ^{137}Cs and ^{40}K activity concentration measurement are 4 one-week samples accumulated to a month sample and determined with about 10 % relative uncertainty.

RESULTS AND DISCUSSION

Average value of ^{7}Be concentration within observed period was 2.4 mBq.m^{-3}. Average concentration of ^{210}Pb was found as 0.8 mBq.m^{-3}. Activity concentrations of ^{7}Be and ^{210}Pb show typical seasonal variations. ^{7}Be concentrations appeared to be higher in spring and early summer (Fig.1) and opposite trend (with higher concentrations in winter months) was observed for ^{210}Pb (Fig.2). The activity concentration of anthropogenic ^{137}Cs in ground level atmosphere is at level about 0.6 µBq.m^{-3}. Mean activity concentration of primordial ^{40}K in aerosols reach low values round about 5 µBq.m^{-3}. A mean aerosol mass concentrations of about 30 µg.m^{-3} was also determined during the period of measurements.

The ^{7}Be/^{210}Pb activity ratios are presented (Fig.3) and correlation study has been carried out between the meteorological factors and concentrations of studied radionuclides (Tab. 1).

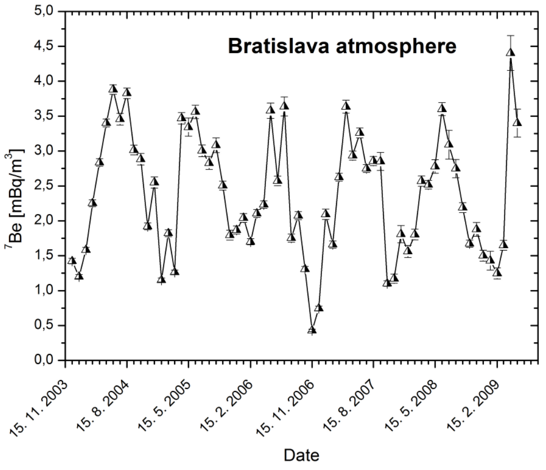

Fig. 1. Temporal variations of the ^{7}Be activity concentration in low–level air of Bratislava.

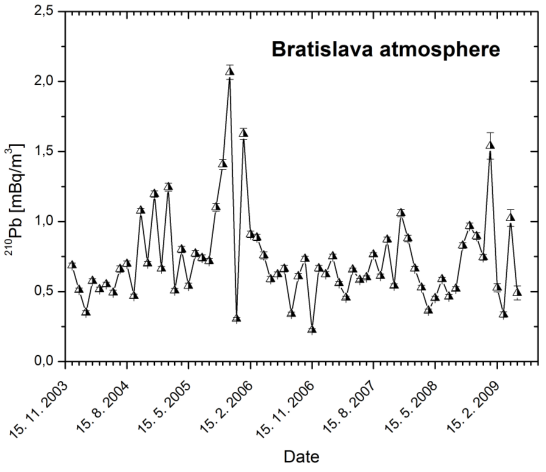

Fig. 2. Temporal variations of the ^{210}Pb activity concentration in low–level air of Bratislava.

The only significant correlation was found between the ^{7}Be concentration and air temperature. Weak negative correlations are observed for ^{7}Be with humidity and cloudiness. The values of ^{7}Be/^{210}Pb concentration ratio varied from 0.98 to 7.88, exhibit the summer maxims and winter minimums. It is caused by higher intensity of vertical convection of air in summer season. This convection brings to ground level rich air with cosmogenic nuclides from upper layers and hereby removing the elements of terrestrial origin. The observed mean values of concentrations can be considered as representative at ground level air in our geographical region [2], [3], [4].

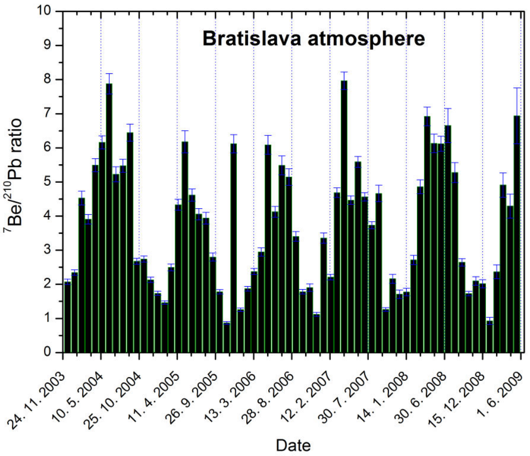

Fig 3. Temporal variations of ^{7}Be/^{210}Pb concentration ratio.

Table 1. Linear correlation coefficients between activity concentrations of ^{7}Be and ^{210}Pb and selected meteorological parameters.

Radionuclide	Temperature	Pressure	Humidity	Precipitation	Cloudiness
^{7}Be	0.70	-0.17	-0.55	0.18	-0.44
^{210}Pb	-0.25	0.32	0.35	-0.20	0.05

The aim of our environmental radioactivity monitoring is to study the transport processes between troposphere and ground-level atmosphere. For this purpose was developed one-dimensional differential model of vertical distribution of ^{7}Be concentration in atmosphere [5]. This model was derived from continuity equation, which describe the vertical diffusion of the substance. Vertical mixing in the troposphere and stratosphere, the radioactive decay, wet deposition as well as gravitational sedimentation are physical processes considered in the model. Activity concentration of ^{7}Be and deposition ^{7}Be in precipitation were used as input data for calculation of scavenging coeficients and coeficients of turbulent difusion, that provide information about vertical profile of concentration ^{7}Be.

CONCLUSIONS

Since the December 2003 a continuous monitoring of ^{7}Be and ^{210}Pb weekly concentrations in the low–level atmosphere has been carried out in Bratislava (Slovakia). In month period has been measured the concentration of ^{137}Cs and ^{40}K in atmospheric aerosol. The observed average values in this paper are in good agreement with data reported in literature for similar continental locations. The typical pattern of seasonal variations was observed for ^{7}Be and ^{210}Pb activity concentrations. The pronounced maxima in spring/summer for ^{7}Be and inverse trend for ^{210}Pb with the highest values in winter were measured. The correlation between ^{7}Be concentration and air temperature was found.

REFERENCES

1. Sýkora I., Merešová J., Ješkovský M., Holý K.: Variation of Bratislava atmosphere aerosols radioactivity, In: International Conference on Environmental Radioactivity : From Measurements and Assessments to Regulation , Vienna : IAEA, 2007. - S. 291 (IAEA-CN-145) (2007)
2. Sýkora I., Ješkovský M., Janík R., Holý K., Chudý, M., Povinec P.P.: Low-level single and coincidence gamma-ray spectrometry: Journal of Radioanalytical and Nuclear Chemistry 276 No.3,. s. 779–787 (2008)
3. Todorovic D., Popovic D., Djuric G., Radenkovic M.: ^{210}Pb in ground-level air in Belgrade city area. Atmospheric Environment 34, s.3245-3248 (2000)
4. Todorovic D., Popovic D., Djuric G., Radenkovic M.: Be-7 to Pb-210 concentration ratio in ground level air in Belgrade area. Journal of Environmental Radioactivity 79, s.297-307 (2005)
5. Hötzl H. and Winkler R.: Activity Concentrations of ^{226}Ra, ^{228}Ra, ^{210}Pb, ^{40}K and ^{7}Be and their Temporal Variations in Surface Air. Journal of Environmental Radioactivity 5, s.445-458 (1987)
6. Šimon J., Merešová J., Sýkora I., Ješkovský M., Holý K.: Modeling of temporal variations of vertical concentration profile of ^{7}Be in the atmosphere: Atmospheric Environment 43 Issue 12, s. 2000-2004 (2009)

EFFECT OF MAGNETIC NANOPARTICLES ON PHAGOCYTIC AND METABOLIC ACTIVITY OF HUMAN LEUKOCYTES

A. Dzarova*, dzarova@saske.sk, M. Dubnickova**, dubnickova@fpharm.uniba.sk, M. Timko*, timko@saske.sk, P. Kopcansky*, kopcan@saske.sk, V. Zavisova*, zavisova@saske.sk, A. Sprincova*, herman@saske.sk, *Institute of Experimental Physics, Slovak Academy of Sciences, IEP-SAS, Watsonova 47 Kosice, Slovakia, ** Departments of Cell and Molecular Biology of Drugs, Faculty of Pharmacy, Comenius University, Bratislava, Slovakia

INTRODUCTION

The applications of nanoparticles in nanomedicine impose strict requirements on the particles physical, chemical and pharmacological properties, including chemical composition, granulometric uniformity, crystal structure, stability of magnetic properties, surface structure, adsorption properties, solubility and low own toxicity [1]. The important factors, which determine the biocompatibility and toxicity of magnetic microspheres, are the magnetically responsive components such as magnetite, iron, nickel, NdFeB or Sm-Co, the size of the particles, their matrix substance and the coating used. Iron oxide particles seem to be generally well tolerated [2].

Nanotechnology makes use of the special surface properties of extremely small particles. In this rapidly growing field, many different materials are produced for a multitude of diverse applications. Possible adverse health effects of these materials however are so far scarcely investigated and are therefore a special task of toxicology. Although strategies for risk emphasize the fact that on the cellular, subcellular and molecular levels interactions between nanoparticles and target cells are relevant for the induction of possible adverse health effects, but these are still poorly understood.

The objective of this study is to test effects of volume concentrations of two different kinds of magnetic particles (synthetic magnetic particles and magnetosomes- bacterial magnetite nanoparticles) on human leukocyte activities *in vitro*. We have studied phagocytic and metabolic activity of human leukocytes.

EXPERIMENTAL SECTION

In our experiment we have used two types of nanoparticles: the chemically synthesized nearly spherical magnetite nanoparticles prepared by co-precipitation method and biological magnetic particles (magnetosomes) prepared by the biomineralization process from magnetotactic bacteria.

The synthesis of the spherical magnetic nanoparticles was based on coprecipitation of Fe^{2+} and Fe^{3+} salts by NH_4OH at 60°C. To obtain a Fe_3O_4 precipitate, $FeCl_2{\cdot}4H_2O$ and $FeCl_3{\cdot}6H_2O$ were dissolved in deionized water by vigorous stirring (the ratio $[Fe^{3+}]$: $[Fe^{2+}]$ was 2:1). The solution was heated to 80°C and 25% NH_4OH was added. The precipitate was isolated from solution by magnetic decantation.

Bacterial magnetosomes were synthesized by biomineralization process from magnetotactic bacteria *Magnetospirillum sp.* strain AMB-1. This bacteria is a Gram-negative α - *proteobacterium* that is more oxygen-tolerant and easier to grow on a large scale. The detailed description of cultivation of magnetotactic bacteria and isolation of magnetosomes is given in our previous contribution [3]. Techniques for the isolation and purification of magnetosome particles from *Magnetospirillum* species are based on combination of centrifugation and the magnetic separation. In our experiment the 500 mg bacterial magnetite could be acquired from a 2000-mL culture of *Magnetospirillum* sp. AMB-1. These isolation and purification procedures leave the surrounding membrane intact and magnetosome preparations are apparently free of contaminating material. Owing to the presence of the enveloping membrane, isolated magnetosome particles form stable, well-dispersed suspensions in water solution of HEPES (4-(2-hydroxyethyl)-1-piperazineethanesulfonic acid).

In this paper K is control sample, M sample of leukocytes with magnetosomes of concentration: 0,1, 1, 10, 20 µg/ml, MP sample of leukocyte with synthetic magnetic nanoparticles of concentration: 0,1, 1, 10, 50 µg/ml. Human leuocytes from 6–8 healthy volunteers (OHT-Derer‘s Hospital, Bratislava, Slovakia) were isolated and purified by HistoPaque-1077 (Sigma, USA). In the next step, they were cultivated for 18 h exposed to concentrations of synthetic magnetic particles and magnetosomes-bacterial magnetite nanoparticles according to Bukovský et al. (1998) [4]. Control samples contained human leucocytes that were not affected by modulators.

The phagocytic activity was determined as percentage of the phagocytosing cells; the phagocytic index was calculated as the average number of engulfed *S. faecalis* for 100 phagocytes. For the both data we used 100 phagocytes per coverslip. Particular results showed the influence of synthetic magnetic particles as well as magnetosomes on the response of nonspecific immunity of human leukocytes *in vitro*. The results are presented as means of experimental values ± standard deviations and as relative activities (%). Statistical comparisons were made based on repeated measurements (4–6 parallels) by Student’s t test; a value $p < 0.05$ was regarded as statistically significant. We have gradually tested the influence on the process of phagocytosis, the metabolic activity in leukocyte, whereupon lyzozyme activity is organized into oxygen-independent mechanisms of micro-organism and peroxidase activity into oxygen-dependent one. The both of this activity belong to nonspecific immunity.

In our experiment we observed the cell (leukocyte) count in dependence on concentration of nanoparticles during the 18 hours incubation in RPMI-1640 with 10% fetal bovine serum under the 5% CO_2 at 37˚C. Our experiment confirms the results obtain by Häfeli (1999) [2]. The control incubation of the cells with $FeCl_3$

solutions showed a small effect on cell growth. At concentrations below 5 μg/ml, no toxicity was seen. Iron concentrations between 10 and 2000 μg /ml showed lymphoma cell survival of about 80±20%. Higher iron concentrations led to complete cell kill. The human prostate cells were more susceptible to iron than were the lymphoma cells. Their cell viability between 10 and 500 μg /ml was in the 60±20% range, decreasing then rapidly to no survival at the 10000 μg /ml iron concentration. Depending on the size and the materials used to prepare the magnetic microspheres, different paths of toxicity are expected [2].

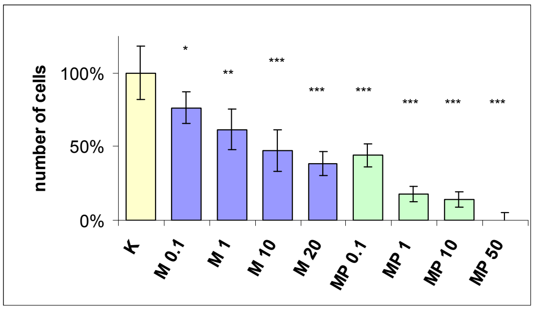

Fig. 1: Number of leukocytes for incubation in CO_2 at 37°C, n = 10.

The phagocytic activity is expressed as percentage of the phagocytosing cells of all phagocytes and also as phagocyte index, which is the number of the cells *S. faecalis* engulfed by one phagocytic cell. Phagocytosis (phagocytic activity and phagocyte index) was suppressed in all samples what means, that in the case of phagocytic activity as a mechanism nonspecific immunity, the immunosuppression was demonstrated.

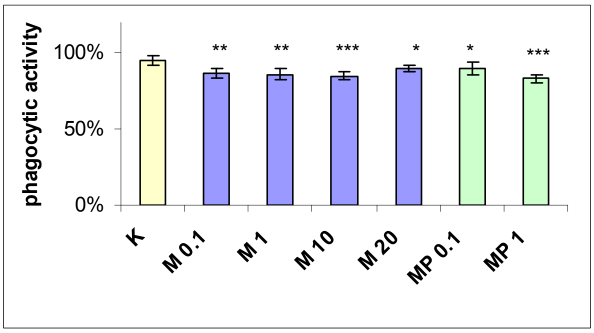

Fig.2: Number of phagocytosing cells from 100 phagocytes, n = 6.

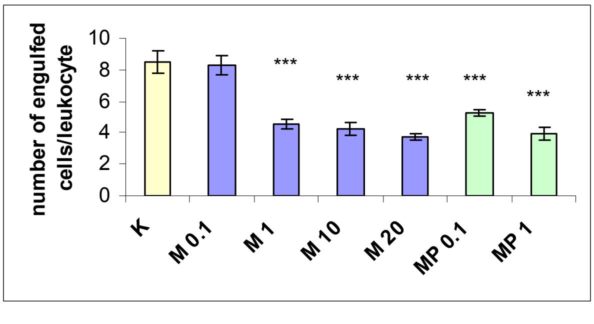

Fig. 3: Number of engulfed cells per one leukocyte, n = 6.

The phagocytes of MP samples at concentrations 10 and 50 μg/ml could not be observed the on coverslip (not showed) (Fig.2, 3). These structures of nanoparticles and magnetosomes were enabled avoidance of phagocytosis.

CONCLUSIONS

The both tested samples (nanoparticles- synthetic magnetic nanoparticles and magnetosomes) lysed (killed) leukocyte cells during incubation. From obtained results follow that spherical nanoparticles are more aggressive material than magnetosomes and their using is unavailable for this type of the test mainly for the concentration 10 and 50 μg/ml as a consequence their toxicity.

The sample concentration of 0,1 μg/ml is for both samples practically not effective. From obtained result we can conclude that leukocyte activity decreases with growing concentration for the synthetic magnetic particles and samples with higher that concentrations of 10 μg Fe_3O_4 /ml are not suitable as a consequence of their toxicity.

Magnetosomes begin to influence leukocyte activity at the concentration of 1 μg/ml and this influence grows with increasing concentration up to 20 μg/ml. At the metabolic activity the effect is changing from inhibition to stimulation.

With respect of obtained results for metabolic activities of human leukocyte, we can say that magnetosomes are more suitable for biological applications that magnetic particles.

ACKNOWLEDGMENT: This work was created by implementation of the "Cooperative phenomena and phase transitions in nanosystems with perspective utilization in nano- and biotechnology" project no. 26220120021 funded by European Community, ERDF – European regional development fund and by VEGA projects 7055, 0056, 0038, 0077.

REFERENCES

1. O.A. Kuznetsov, N.A. Brusentsov, A.A. Kuznetsov, N.Y. Yurchenko, N.E. Osipov, F.S. Bayburtskiy, JMMM **194,** 83-89 (1999).
2. U.O. Häfeli, G.J. Pauer, JMMM **194**, 76-82 (1999).
3. M. Timko, A. Dzarova, V. Zavisova, M. Koneracka, A. Sprincova, P. Kopcansky, J. Kovac, A. Szlaferek, I. Vavra Magnetohydrodynamics Journal **3** 44 (2008).
4. M. Bukovský, D. Mlynarčík, H. Koščová, Farm. Obzor **57,** 59–68 (1998) (In Slovak).

MAGNETIC CHARACTERIZATION OF TAXOL LOADED MAGNETIC PLGA NANOSPHERES

M. Koneracká, konerack@saske.sk, N. Tomašovičová, P. Kopčanský, V. Závišová, G. Lancz and J.Kováč, Institute of Experimental Physics, Slovak Academy of Sciences, Košice, Slovakia, M. Múčková, Hameln rds a.s., Modra, Slovakia, M. Fabián, Geotechnic Institute, Slovak Academy of Sciences, Košice, Slovakia

INTRODUCTION

Magnetically controlled drug targeting is one of the various possibilites of drug targeting and allows the concentration of drugs at a defined target site, away from the reticular endothelial system (RES) with aid of a magnetic field (using an internally implanted permanent magnet or an externally applied field). Depending on the application, the particles then release the drug or give rise to a local effect (for exaple hyperthermia with magnetic NPs). Typically, the intended drug and magnetic fluids are formulated into a pharmacologically stable nanosphere fomulation. A wide spectrum of synthetic and natural polymers is available for nanosphere formulation, but their biocompatibility and biodegradability are the major limiting factors for their use in the drug delivery system. Poly(lactide-co-glycolide) (PLGA), from the ester family, has been widely used for the controlled delivery of drugs due to its early use and approval as a compatible biomaterial in humans [1]. Taxol, as important anticancer drug, has been chosen for encapsulation to the polymer for its significant role against wide range of tumors (breast cancer, ovarian carcinoma, lung cancer, head and neck carcinomas and acute leukemias)[2]. As mentioned above, among the ways to control the targeting specificity is to use the magnetic particles and magnetic fluid respectively as drug carrier. For this purpose, a magnetic particles must fulfill the several requirements. One of them is superparamagnetism. Superparamagnetism in drug delivery is necessary because once the external magnetic field is removed, magnetisations disappears (negligible remanence and coercitivity) and thus agglomeration (and the possible embolization of capillary vessels) is avoided. The purpose of the present work is to investigate the structure, magnetic characteristics, and magnetisation mechanism of Taxol loaded magnetic PLGA nanospheres.

EXPERIMENTAL

The synthesis of NPs loaded with drug Taxol and magnetite particles was carried out modifying the nanoprecipitation method reported in the past [3]. The mixture of the drug and the polymer with a volatile organic solvent (acetone) was added drop by drop to a water based mixture of the magnetic fluid and the stabilising surfactant Pluronic under appropriate stirring to allow complete evaporation of the organic solvent at room temperature. A turbid nanospheres suspension (PLGA/TAX/MFPEG NPs) was formed. Synthesis of naked PLGA nanospheres was the same as described above with exception that no magnetic particles and Taxol were added to the water and organic phase, respectively. Magnetic fluids (MFPEG) used in the experiments were prepared method described in paper [4].

Scanning electron microscopy (SEM, JEOL 7000F microscope) was used to observe the morphology and surface characterization (shape, distribution, aggregation) of Taxol loaded magnetic PLGA composite nanospheres. The hydrodynamic size of the nanospheres was determined by PCCS technique (photon cross correlation spectroscopy, Nanophox, Sympatec GmbH, Germany). A SQUID magnetometer (VSM, Lake Shore Cryotronics, Inc, OH) was employed to measure the magnetic properties of the Taxol loaded magnetic polymeric nanospheres at the temperature from 4.2K to 300K .

RESULTS AND DISCUSSION

The TAX/MFPEG/PLGA NPs sample analysed by SEM showed a spherical shape in geometry (Fig.1). The surface was primarily smooth, although some roughness could be identified in certain areas of some spheres.

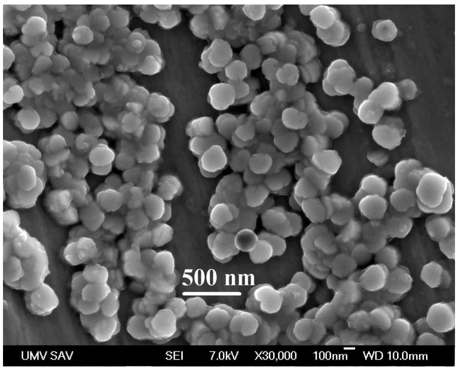

Fig. 1. SEM image of synthetised Taxol loaded magnetic PLGA NPs.

The mean diameter of all magnetic PLGA samples were about 235 nm and the results were in good agreements with results obtained from the PCCS technique (Fig.2). To confirm encapsulation of magnetic particles in to polymer matrix, the physical mixture of naked PLGA NPs and MFPEG were also analysed by PCCS (the inset in fig.2) and compared with the size distribution of MFPEG loaded PLGA NPs. We can hypothetize, that the presence 1 maximum (D = 232 nm) in PLGA/MFPEG NPs in comparison with the existence of 2 maximum (D= 66 nm for pure MFPEG and D= 195 nm for pure PLGA NPs) in case of physical mixture, validate the encapsulation magnetite in polymer matrix.

A suitable criterion for the occurrence of the superparamagnetism includes at least two requirements [5]. First, the magnetisation curve must show no hysteresis. Second, this dependence for the sample must be temperature dependent to the extent that curves

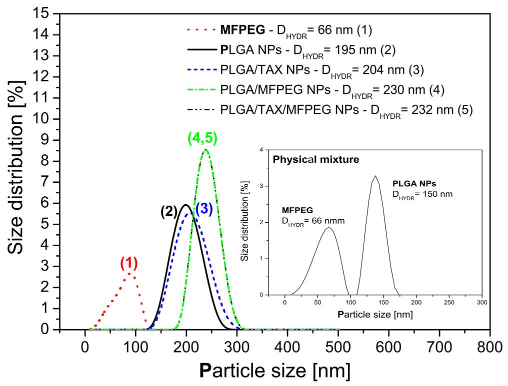

Fig. 2. The particle size distribution of PLGA composite NPs and pure MFPEG. The inset shows size distribution of physical mixture of naked PLGA NPs and MFPEG.

measured at different temperatures T must approximately superimpose when plotted against H/T. In order to test whether the sampe fulfills the requirements mentioned above, the magnetic properties of PLGA/TAX/MFPEG NPs have been made using a SQUID magnetometer.

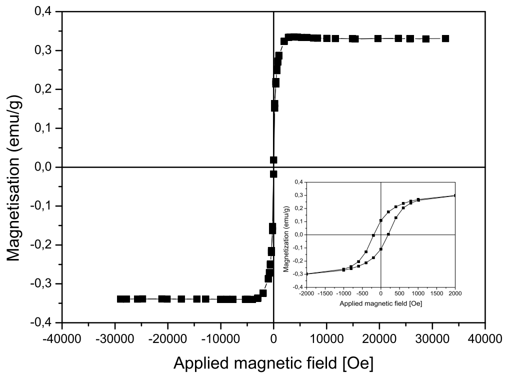

Fig. 3. Magnetisation curve as a demonstration of superparamagnetic behaviour of of TAX/MFPEG/PLGA NPs at room temperature. The inset shows hysteresis loop at T=10K.

The hysteresis loop measured at T = 300K for the PLGA/TAX/MFPEG NPs is shown in Fig.3. As seen in the figure, the magnetisation curve exhibited neither remanence nor coercivity showing that magnetite crystals have a superparamagnetic behaviour with a saturation magnetisation M_s of 0.33 emu/g which is lesser then the saturation magnetisation of pure MFPEG (5.6 emu/g) as shown in our previous paper [4]. This fact can be explained by the presence of non magnetic PLGA shell at the magnetite surface. At the sample temperature of 10 K (inset in fig.3), a symmetric hysteresis loop is observed with a remanence of 3.6 emu/g and coercitivity of 200 Oe, indicating the ferromagnetic nature of nanospheres at a low temperature. In order to test, whether the sample PLGA/TAX/MFPEG NPs fulfills the second requirements of superparamagnetism, its magnetisation M has been measured as a function of magnetic field at different temperatures range 50 - 300K. The Fig.4 shows the measured magnetisation curves plotted as a dependence of $M(T)/j_s = f(j_s H/T)$, where $j_s = M_s(T)/M_s(0)$. As seen in this figure, all the experimental points obtained for temperatures $T \geq$100K lies on practically one curve. The experimental points of magnetisation curves have been fitted to the Langevin function resulting in the solid-line curve shown in Fig.4b. Since the fit is really very good we can say that the Taxol loaded magnetic PLGA NPs exhibits superparamagnetic behaviour at temperatures suitable for biomedical applications.

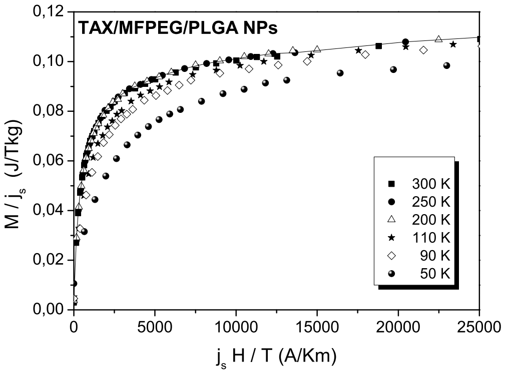

Fig. 4. Magnetisation curves vs magnetic field at different temperatures.

The results obtained showed that the methodology selected in this work allowed the formation of nanometric Taxol loaded magnetic PLGA NPs. These composite NPs were nearly spherical in shape with a mean diameter 232 nm, which is a relevant size for intravenous administration. The magnetic measurements confirmed superparamagnetic behaviour of composite PLGA sample at room temperature and the saturation magnetisation of sample $M_s = 0.33$emu/g was used to determine the weight percent magnetite in the NPs as 22%w/w. The prepared magnetic labeled PLGA NPs with incorporated Taxol are excellent candidates for the controlled release because of their suitable response to the external magnetic field.

ACKNOWLEDGMENT: This work was created by implementation of the "Cooperative phenomena and phase transitions in nanosystems with perspective utilization in nano- and biotechnology" project no. 26220120021. Funding for the operational research and development program was provided by the European Regional Development Fund.

REFERENCES

1. D. E.Perrin and J. P.English, Handbook of Biodegradable Polymers, Harwood Academy Publishers, Amsterdam 1997, p.1.
2. C. Fonseca, S. Simoes and R. Gaspar, J. of Controlled Release **83**, 273 (2002).
3. H. Fessi, F. Puisieux,J.P. Devissaguet et al., Int. J. Pharm. **55**, R1 (1989).
4. M. Koneracká, V. Závišová, M.Timko et al., Acta Physica Polonica A **113**, 595 (2008).
5. C. P. Bean and J. D. Livingston, J. Appl. Phys. **30**, 120S (1959).

EFFECT OF MAGNETIC NANOPARTICLES ON THE AMYLOID AGGREGATION OF LYSOZYME

A. Bellova*, ada.bellova@gmail.com, E. Bystrenova**, e.bystrenova@bo.ismn.cnr.it, M. Koneracka*, konerack@saske.sk, J. Bagelova*, bagelova@saske.sk, D. Fedunova*, fedunova@saske.sk, V. Zavisova*, zavisova@saske.sk, P. Kopcansky*kopcan@saske.sk, F. Valle**, valle@bo.ismn.cnr.it, F. Biscarini**, biscarini@bo.ismn.cnr.it and Z. Gazova*, gazova@saske.sk,
*Institute of Experimental Physics, Slovak Academy of Sciences, IEP-SAS, Watsonova 47 Kosice, Slovakia,
**Institute for Nanostructured Materials Studies, The National Research Council, ISMN-CNR, via Gobetti 101, I-40129, Bologna, Italy

INTRODUCTION

Protein misfolding and aggregation in general and amyloidogenesis in particular are of growing interest as scientists recognize their role in devastating degenerative diseases such as Alzheimer´s and Parkinson´s disease. Protein and peptide aggregation into mature amyloid fibrils is a multistep process iniciated by conformational changes with samplings of prefibrillar intermediate amyloidogenic aggregates, such as oligomers, protofibrils, pores, amylospheroids, and short fibrils [1]. Magnetic particles ranging from the nanometer to micrometer scale are being used in an increasing number of medical applications. The important properties of magnetic particles for medical applications are nontoxicity, biocompatibility, injectability, and high level accumulation in the target tissue or organ. Magnetic nanoparticles offer attractive and versatile applications in the field of biotechnology, such as DNA and RNA separation, cell separation, drug delivery system (DDS), magnetic resonance imaging (MRI), and hyperthermia [2]. Recent work suggests that nanoparticles may provide a novel mechanism for the onset of amyloid diseases. It was observed that several types of nanoparticles (NP-copolymer particles of 70 and 200 nm [3], thiol-linked nanoparticles [4], 16 nm hydrophilic polymer-coated quantum dots [5], 16 nm cerium oxide particles, multiwalled carbon nanotubes of 6 nm diameter [6], TiO_2 nanoparticles [7]) can significantly enhance the rate of a protein aggregation process, called fibrillation, which results in smaller proteins assembling into fibrous strands (fibrils). All of these particles were found to increase the rate of fibrillation by shortening the lag phase, consistent with the view that nucleation is a surface-assisted process [3]. It was also shown, that the gold nanoparticles protected with triethyleneglycol induce photothermal ablation of Aβ peptide aggregation [8] and the fluorinated nanoparticles and hydrophobic teflon nanoparticles inhibit Aβ amyloid polymerization [9].

In this work, we investigate the ability of electrostatically stabilized magnetic nanoparticles of Fe_3O_4 to affect the amyloid aggregation of lysozyme, as a prototypical amyloidogenic protein. We investigate the interaction of nanoparticles with lysozyme by a combination of spectroscopic (ThT assay) and microscopy techniques (AFM).

EXPERIMENTAL SECTION

The magnetic nanoparticles (NPs) were prepared by co-precipitation method [10]. The mean hydrodynamic diameter of these particles (D_{HYD} = 26 nm) was determined by photon cross correlation spectroscopy (PCCS, Nanophox, Sympatec GmbH). The magnetic properties were estimated by magnetization measurement using a SQUID magnetometer. The saturation magnetization value I_S was 1.3 mT and prepared particles were superparamagnetic without a hysteresis at room temperature. Superparamagnetism is necessary due to the prevention of particle agglomeration (and then embolization of capillary vessels) after removing of external magnetic field.

The morphology of the magnetic nanoparticles was investigated by atomic force microscopy with NT-MDT microscope in semicontact mode in air [11, 12].

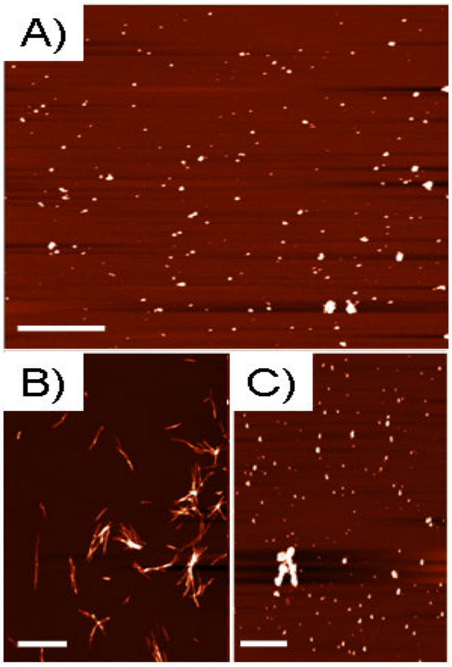

Fig. 1: AFM images of (A) Fe_3O_4 nanoparticles (NP), (B) lysozyme amyloid fibrils L_A (10 μg/ml) and after incubation with Fe_3O_4 NPs with L_A: NPs ratio equal to 1:1. Scale bar is 1 μm for all images.

From typical AFM image of magnetic nanoparticles (Fig. 1A) follows that nanoparticles have nearly spherical shape.

The potential of the magnetic NPs to inhibit formation of lysozyme amyloid aggregates or to destroy pre-formed lysozyme amyloids were tested in vitro by ThT fluorescence assay. ThT has a low fluorescence quantum yield in solution which increases considerably when bound to amyloid fibrils. The hen egg white lysozyme was chosen as model amyloidogenic protein exploiting the fact that ability to form amyloid aggregates is a generic property of proteins.

The NP concentration dependence (in the range 0.015 mg/ml to 2.5 mg/ml) of the relative ThT fluorescence intensity for the depolymerization experiments at fixed protein concentration (10 µM corresponding to 0.147 mg/ml) incubated overnight with NPs are shown in Figure 2. In the depolymerization experiment the decrease follows a sigmoidal decay of concentration (Fig. 2). A similar dependence was observed in the case of inhibition experiment (data not shown). From these profiles the values of the DC50 and IC50 were calculated. The values are equal to 163.25 g/ml and 654.56 µg/ml, respectively.

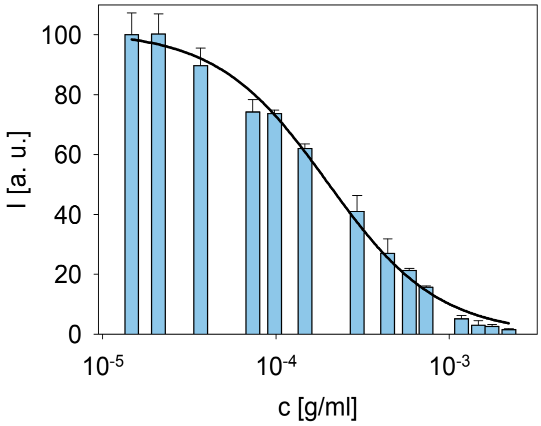

Fig. 2: Nanoparticle-induced depolymerization of lysozyme aggregates at increased nanoparticle concentration detected by ThT assay. The curve was obtained by fitting of the average values by non-linear least-square method with the equation Logistic, 3 Parameter.

The fluorescence intensities observed for NPs alone or in presence of ThT were negligible in the range of concentration explored.

In order to rule out fluorescence quenching from mechanisms other than depolymerization or inhibition (for instance, quenching from the NPs), the morphology and size of the deposits from the incubated solution were investigated by AFM. For the lysozyme solution incubated without NPs, the typical morphology of amyloid fibrils is shown in figure 1B. For lysozyme aggregates incubated overnight with NPs (L_A: NPs = 1:1), the reduction of the fibrils is observed (Fig. 1C). These AFM data are in agreement with ThT fluorescence measurements.

CONCLUSIONS

This study outlines the significant reduction of lysozyme amyloid aggregation by magnetic Fe_3O_4 nanoparticles. It was found that incubation of NPs with amyloid aggregates leads to decreasing of the aggregate size by depolymerization of amyloid structures. The NPs also inhibit lysozyme aggregation. An important finding is fact, that our NPs do not promote amyloid aggregation as it is usually observed for complexes of proteins with NPs. While further investigations are essential to clarify the role of magnetic nanoparticles in inhibiting or preventing lysozyme fibrillation, we believe that our results are important for the rational design of potential therapeutics for amyloidoses.

ACKNOWLEDGMENT: This work was created by implementation of the ”Cooperative phenomena and phase transitions in nanosystems with perspective utilization in nano- and biotechnology” project no. 26220120021. Funding for the operational research and development program was provided by the European Regional Development Fund.

REFERENCES

1. R. M. Murphy, Biochim. Biophys. Acta Biomembranes **1768**, 1923 (2007).
2. F. Y. Cheng, et al., Biomaterials **26**, 729-738 (2005).
3. S. Linse, et al., PNAS **104**, 8691-8696 (2007).
4. T. Cedervall, et. al., PNAS **104**, 2050-2055 (2007).
5. T. Liedl, S. Keller, F. C. Simmel, J. O. Radler, W. J. Parak, Small **1**, 997-1003(2005).
6. J. D. Holmes, et al., Chemistry **9**, 2145-2150 (2003).
7. W-H. Wu, et al., Biochem. Biophys. Res. Comm. 373, 315-318 (2008).
8. R. C. Triulzi, et al., Colloids and Surfaces B: Biointerfaces 63, 200-208 (2008).
9. S. Rocha, et al., Biophysical Chemistry 137, 35-42 (2008).
10. R. Massart, IEEE Trans Magn **17**, 1247-1248 (1981).
11. M. Timko, et al., Indian journal of engineering and materials sciences **11**, 276-282 (2004).
12. M. Cavallini, et al., J. Phy. Condens. Matter, 204144 (2008).

THE DC AND AC DIELECTRIC PROPERTIES TRANSFORMER OIL BASED MAGNETIC FLUID.

L. Tomčo*, ladislav.tomco@tuke.sk, K. Marton**, karol.marton@tuke.sk, M. Timko*, timko@saske.sk, P. Kopčanský*, kopcan@saske.sk, M. Koneracká*, konerack@saske.sk, *Faculty of Aeronautics, Rampová 7, 041 21 Košice, Slovak Republic **Faculty of Electrical Engineering and Informatics, Technical University, Letná 9/A, 041 20 Košice, Slovak Republic, ***Institute of Experimental Physics, Slovak Academy of Sciences, Watsonova 47 Kosice, Slovak Republic,

INTRODUCTION

The insulation fluids in power transformers perform two main functions – insulating and cooling. The highly refined mineral oils (transformers oils), typically used as insulating fluids [1], have low thermal conductivity and thus perform low-efficiency cooling. It has been shown that the heat transfer in electromagnetic devices can be substantially improved by using magnetic fluids [2] consisting of nanosized magnetic particles suspended in transformer oil.

The aggregation of magnetite particles in magnetic field produced by the transformer windings influences the magneto-dielectric behavior and the dielectric breakdown strength of a transformer oil based magnetic fluid.

The motivation of this work was to study the effect of magnetic particles concentration in magnetic fluids (MFs) on the permittivity, conductivity and dielectric breakdown strength of studied magnetic fluids,

EXPERIMENTAL METHOD

For the experiments we have used magnetic fluids with magnetite particles coated with oleic acid as a surfactant dispersed in transformer oils TECHNOL 4000 and ITO 100. The volume concentrations of magnetic particles were in the range Φ = 0.0025-0.02, with corresponding saturation magnetizations I_s= 1–8 mT. The lognormal particles size parameters were D_v = 8.6nm and standard deviation σ = 0.15 obtained by means of Chantrell et al [3] technique from VSM magnetization measurements. For the observation of agglomeration processes a drop of magnetic fluid was sandwiched between two parallel glass cover slips with the thickness d = 20μm and placed normal to the optic axis of the microscope. The optical microscope was equipped with a video camera. Helmholtz coils parallel to the magnetic fluid film plane produced a magnetic field of up to 50 mT. Dielectric breakdown strength measurements were carried out using appropriate shaped electrodes of a uniform gap of electric field-Rogowski profile [4]. The size of the electrodes was approximately 1.5 cm in diameter with the possibility to change the distance between electrodes in range of 0.1-1mm. The generating circuits generated high voltages up to 10 kV. Two permanent NdFeB magnets with sizes 5x5x0.3 cm produced the external magnetic field up to 50mT and the magnetic field was approximately uniform in measured gap of electric field. Experimental set up is on fig.1. Each point of dielectric breakdown strength of the magnetic fluid was measured seven times and the maximum and minimum values were omitted in the calculation of its mean value according to the rules of high voltage techniques [4]. The experimental error of determination of dielectric breakdown strength was ±4%.

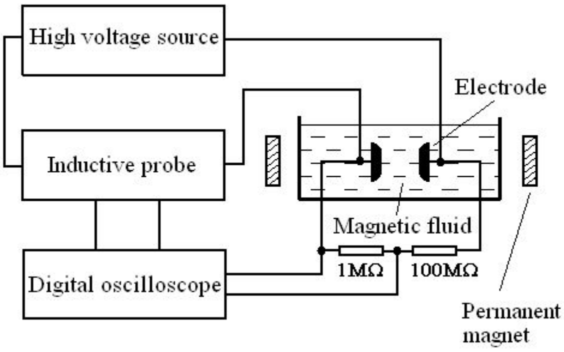

Fig.1. Experimental set up.

RESULTS AND DISCUSSION

Measurements showed that concentration of nanoparticles (Fe_3O_4) in magnetic fluid influences not only relative permittivity of magnetic fluid but their electric conductivity too. The aggregation of magnetic particle was observed by optical and electron microscope (Fig.2). From this figure we can see that magnetite nanoparticles create chain oriented in magnetic field direction.

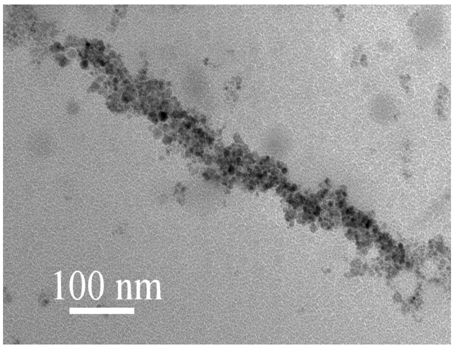

Fig.2. The magnetic particles aggregation in MF with volume concentration of nanoparticles $\Phi = 0.015$

The influence of magnetic particles concentration of magnetic fluids on their permittivity is illustrated on fig.3. It is evident, that permittivity of MFs increases with the increase of their concentration.

Fig.4 shows dependences conductivity of MFs on magnetite particles concentration. The conductivity naturally increases with the increase of magnetite particles concentration and it is dependent on direction of applied magnetic and electric field.

Figures 5 and 6 illustrate the dependencies of the AC and DC dielectric breakdown strength on the distance between the electrodes for concentration $\Phi = 0.0025$ and various orientations of external magnetic field. In both cases the AC and DC dielectric breakdown strength reaches its highest values at the **H⊥E** orientation. The decrease of the dielectric breakdown strength E with increasing d was observed for all studied cases.

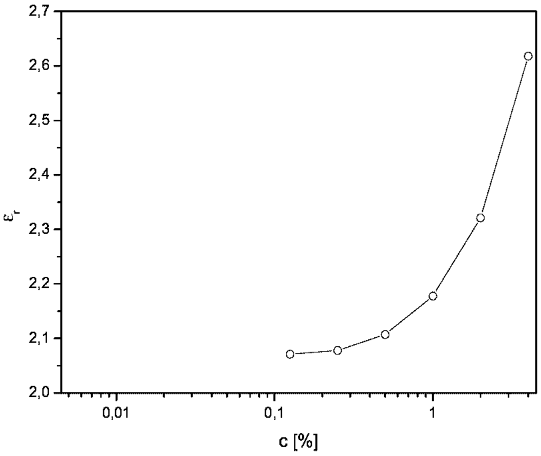

Fig.3. The influence of volume concentration of magnetic particles on relative permittivity of MFs

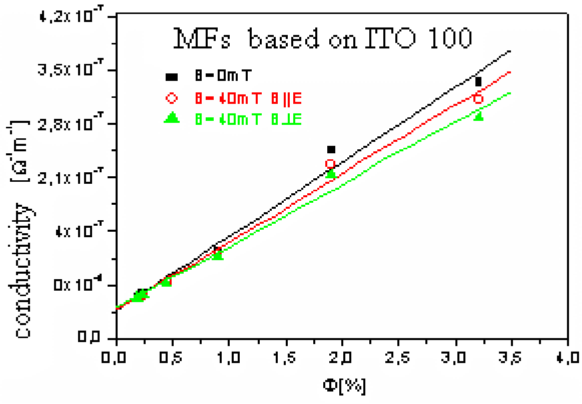

Fig.4. The dependence of magnetic fluids conductivity on magnetic particles volume concentration.

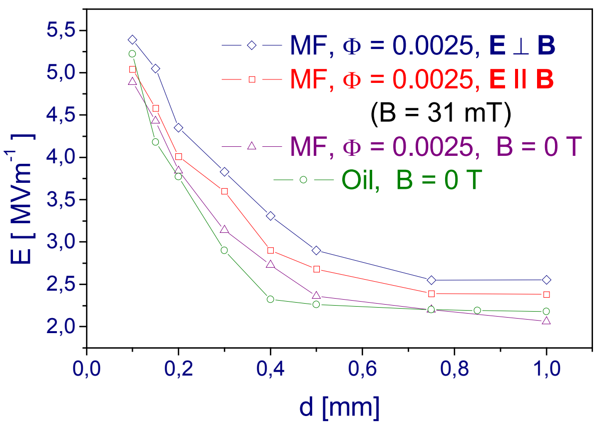

Fig. 5. The AC dielectric breakdown strength vs. distance between the electrodes for concentration Φ=0,0025.

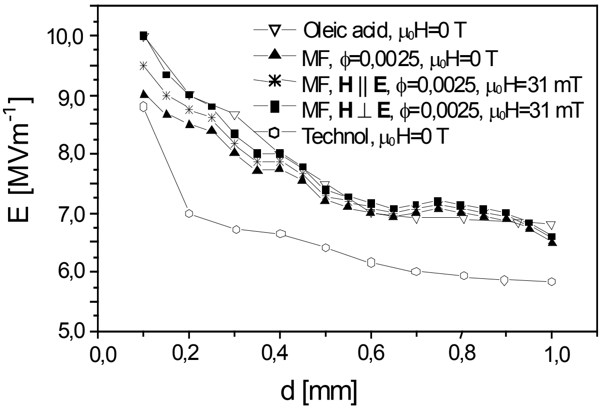

Fig.6. The DC dielectric breakdown strength vs. distance between the electrodes for concentration Φ=0,0025

The measurements showed clearly that dielectric properties of magnetic fluid with $\Phi = 0.0025$ (I_S=1mT) are better (DC) or not worse (AC) than those of the pure transformer oil.

CONCLUSIONS

To conclude it can be said that the level of magnetic nanoparticles volume concentration of MFs significantly influences their permittivity and conductivity. The field induced aggregation of magnetic particles can significantly change the dielectric breakdown strength of magnetic fluids if the sizes of the aggregates are comparable with the distance between the electrodes of the measured gap. The observations of the DC and AC dielectric breakdown strengths of pure transformer oil and transformer-oil based magnetic fluids showed that studied magnetic fluids, if their volume concentration of magnetic particles Φ<0.01 (I_S<4 mT), have better or not worse dielectric properties than pure transformer oil. Regarding to the better heat transfer, provided by magnetic fluids, their application in power transformers may lead to the improvement of the operation of these devices.

ACKNOWLEDGMENT: The authors wish to thank for the support to the R&D operational program Centre of excellence of power electronics systems and materials for their components. The project is funded by European Community, ERDF – European regional development fund.

REFERENCES

1. H.G.Erdman, Electrical Insulating Oils STP 998 (ASTM Publication, Philadelphia-1996).
2. K.Raj, A.Chorney, Indian J. Eng. Mater. Sci. **5,** 372, (1998).
3. R.W.Chantrell, J.Popplewell, S.W. Charles, IEEE Trans. Mag. **14**, 975, (1978).
4. E. Kuffel, W.S. Zaeungl, High Voltage Engineering Fundamentals (Pergamon Press, Oxford – 1984).

THE TRANSFORMER PAPER IMPREGNATED BY MINERAL OIL BASED MAGNETIC FLUID AND DIELECTRIC PROPERTIES

M. Timko*, timko@saske.sk, P. Kopčanský*, kopcan@saske.sk, M. Koneracká*, konerack@saske.sk, K. Marton**, karol.marton@tuke.sk, L. Tomčo***, ladislav.tomco@tuke.sk, , * Institute of Experimental Physics, Slovak Academy of Sciences, Watsonova 47 Kosice, Slovak Republic, **Faculty of Electrical Engineering and Informatics, Technical University, Letná 9/A, 041 20 Košice, Slovak Republic, *** Faculty of Aeronautics, Rampová 7, 041 21 Košice, Slovak Republic

INTRODUCTION

The interesting possibility of magnetic fluids application is their using in distributional transformers and later in power transformers for transmissive systems above 110 kV. The important requirement for such application was to determine electric parameters magnetic fluids based on transformer oil. That is why our previous research was devoted to study relative permittivity, coefficient of dielectric losses, conductivity and electric stability of magnetic fluids based on transformer oil ITO 100 at different orientations of applied electric and magnetic fields in the region of weak electric fields ($E < 10^6$ V/m). The observations were carried out in DC and AC electric fields at combined electric and magnetic fields. The results of these experiments were published in papers [1], [2] and [3].

The goal of this work was to study basic properties of transformer paper impregnated by magnetic fluid. Such insulator system consists of transformer oil, oleic acid, magnetic nanoparticles and transformer paper. Insulator system with transformer paper used in technology of transformer production has given number of paper layers. These layers create system of capacitors that are connected in series. In such systems there dominate migration polarization and polarization of layered materials.

EXPERIMENTAND RESULTS

The three kinds of *n*-layered insulator systems were studied:

- transformer paper with thickness $8,5.10^{-5}$ m (n =1,…,15),
- transformer paper impregnated by transformer oil ITO 100,
- transformer paper impregnated by magnetic fluid based on transformer oil ITO 100 with volume concentration of magnetite nanoparticles particles of 0,24% (MF1) and 3,21% (MF2).

Transformer paper was impregnated in liquid medium (pure transformer oil and magnetic fluids) during 24 hours. The planar electrodes system of circular shape was used in experiments. The system was placed into vessel made from Perspex (methyl methacrylate). Layers of pure transformer paper and transformer paper impregnated by both pure transformer oil and magnetic fluid were put between electrodes. Measurements were carried out by high precision apparatus for measurement of capacitance at frequency of 800 Hz and at temperature of 22 ^{o}C. Electric field intensities were in region of weak electric fields ($E < 10^6$ V/m). The value of applied magnetic field induction was 40 mT, while homogeneous magnetic field was oriented parallel and perpendicular opposite to orientation of electric field intensity.

The dependence of capacity of used insulator system on number of layer is illustrated in figure 1. Displayed courses for all materials show non-linear (quasi-hyperbolic) decay of capacities, what supports assumption written in previous part.

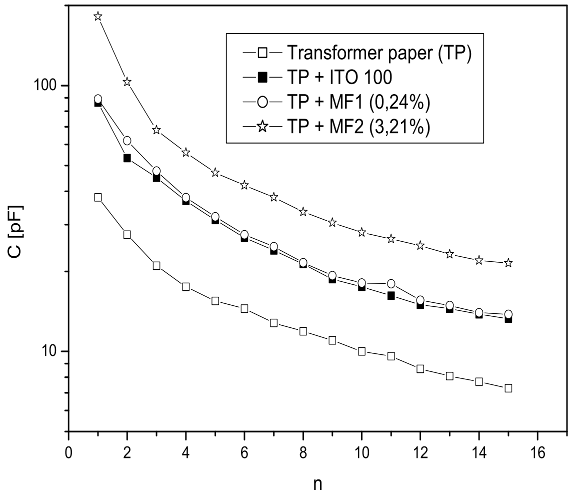

Fig.1. Dependence capacity of capacitor on number of insulator layers for different insulators (pure transformer paper and transformer paper impregnated by pure transformer oil ITO 100 and by two kinds of magnetic fluids).

The impregnant contribution to relative permittivity of transformer paper after 24 hours impregnation can be seen in table 1.

TAB. 1. Dependence insulator relative permittivity on impregnant.

Insulator	Transformer paper (TP)	TP + ITO 100	TP + MF1	TP + MF2
Relative permittivity	1.16	2,63	2.72	5.56

Relative permittivity of transformer paper impregnated by MF2 is almost 5 times bigger than it is for pure paper.

Clear effect of magnetodielectric anisotropy was observed for transformer paper impregnated by MF2, what is illustrated in fig.2. Fig.2 shows, that applied magnetic field influences polarization of insulator system in electric field. It is caused by fact that impregnant consists of monodomain magnetite particles. These particles are sensitive on combined electric and magnetic field, what influences on vector of polarization

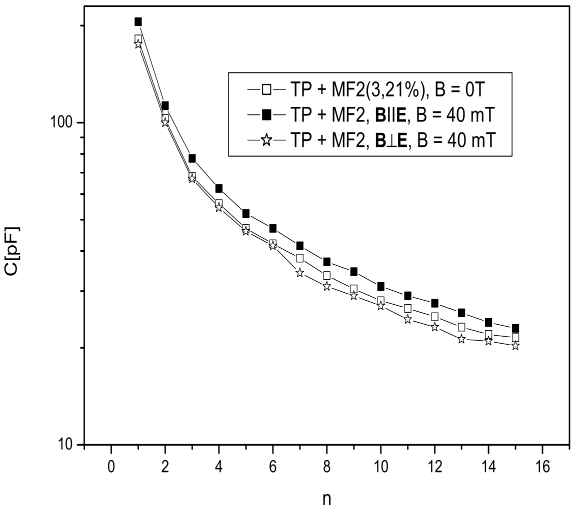

Fig. 2. The dependence of capacity (*C*) on number of insulator layers (*n*) at different orientations of magnetic and electric fields (E || B and E ⊥ B) for transformer paper impregnated by magnetic fluid with volume concentration of magnetite nanoparticles of 3,21%

P and so vector **D** too ($\mathbf{D} = \varepsilon_o.\varepsilon_r.\mathbf{E}+\mathbf{P}$).

Magnetite particles or only their magnetic moments can rotate in combined electric and magnetic fields. This movement is depend on mutual orientation of vectors **B** and **E**. As a consequence the decrease of capacity, ie relative permittivity of insulator system was detected for mutual perpendicular orientation of **B** and **E** and the increase for parallel orientation of the same vectors.

CONCLUSION

The observation of three types of insulator systems (pure transformer paper, transformer paper impregnated by pure transformer oil and by magnetic fluid) shows that the biggest relative permittivity was for system consisting of transformer paper and magnetic fluid with volume concentration of 3,21%, ie relative permittivity increases with the increase of volume concentration of magnetite particles in magnetic fluid that was used as an impregnant. The next experiments showed that permittivity of insulator system consisting of pure transformer paper and impregnated transformer paper naturally depends on number of paper layers. The magnetodielectric effect was found to be dependent on magnetite nanoparticles concentration in magnetic fluids and it increases with the increase of magnetite nanoparticles concentration.

The next work will be devoted to measurement of dielectric losses, relative permittivity and observation of magnetodielectric effect isulator systems containing magnetite nanoparticles in strong electric fields ($E \approx 10^7$ V/m) and stronger magnetic fields ($B \approx 4$ T).

ACKNOWLEDGMENT: The authors wish to thank for the support to the R&D operational program Centre of excellence of power electronics systems and materials for their components. The project is funded by European Community, ERDF – European regional development fund. This work was supported by the Slovak Academy of Sciences, in the framework of CEX-NANOFLUID, Project SAV-FM-EHP-2008-01-01, MNT-ERA Net 2008-022-SK, projects VEGA 0077, APVV 0173-06 and 0509-07 too.

REFERENCES

1. K. Marton, L. Tomčo, P. Kopčanský, F. Herchl, M. Timko and M. Koneracká, The review from international conference X. Sympozjum EUI ´05 „Problemy eksploatacji ukladów izolacyjnych wysokiego napiecia“, PRZEGLAD ELEKTROTECHNICZNY-KONFERENCJE 3 (2005) 161-164 Krynica (2005).
2. K. Marton, L. Tomčo, P. Kopčanský, F. Herchl, M. Timko and M. Koneracká, The review from international conference XI. Sympozjum EUI ´07 „Problemy eksploatacji ukladów izolacyjnych wysokiego napiecia“, PRZEGLAD ELEKTROTECHNICZNY-KONFERENCJE, Dodatek A (2007) A1-A3 Krynica (2007).
3. K. Marton, L. Tomčo, F. Herchl, R. Cimbala, M. Koneracká, P. Kopčanský and M. Timko, The review from conference Nové smery v diagnostike a opravách elektrických strojov a zariadení, ŽU Faculty of Electrical Engineering, Žilina-Zuberec, pp.3-9E (2008).
4. K. Marton, The review of scienfitic works on TUKE, pp.171-181, Košice, Vol.1, ALFA, Bratislava (1976).

STRUCTURAL PROPERTIES OF BORON THIN FILMS PREPARED BY MAGNETRON SPUTTERING

A. Pidík, andrej.pidik@fmph.uniba.sk, Department of Experimental Physic, FMPI, Comenius University, Mlynská dolina, Bratislava, Slovakia, J. Noskovič, jaroslav.noskovic@fmph.uniba.sk, Department of Experimental Physic, FMPI, Comenius University, Mlynská dolina, Bratislava, Slovakia, T. Roch, roch@fmph.uniba.sk, Department of Experimental Physic, FMPI, Comenius University, Mlynská dolina, Bratislava, Slovakia, M. Mikula, ummsmiku@savba.sk, Institute of Materials and Machine Mechanics, SAS Račianska 75, Bratislava, Slovakia, T. Plecenik, tomas.plecenik@fmph.uniba.sk, Department of Experimental Physic, FMPI, Comenius University, Mlynská dolina, Bratislava, Slovakia, A. Plecenik, plecenik@fmph.uniba.sk, Department of Experimental Physic, FMPI, Comenius University, Mlynská dolina, Bratislava, Slovakia, P. Kúš, kus@fmph.uniba.sk, Department of Experimental Physic, FMPI, Comenius University, Mlynská dolina, Bratislava, Slovakia

INTRODUCTION

Magnesium diboride (MgB_2) is two-gap superconductor with many interesting properties, like the remarkably high transition temperature Tc~39 K, large coherent length, high current density and very low material cost. For widespread applications of MgB_2, deposition of high quality MgB_2 films and formation of superconducting device structures are very important key technologies. MgB_2 thin film fabrication process was reported by Kang soon after discovering superconductive properties of MgB_2 in 2001 [1].

We show study of MgB2 sputtering method from two magnetrons on non-heated substrates. Initial MgB precursor layer is amorphous and must be annealed in order to obtain superconducting MgB_2 layer [2]. After ex-situ annealing the films reached transition temperature $T_c \sim 34$ K. Annealing process appears to be the most critical fabrication step [3]. Here we present our initial study of structural properties of MgB_2 thin films and their correlation to preparation parameters and other properties.

EXPERIMENTAL DETAILS

MgB precursor thin films were grown in the chamber, where non-tilted Mg and B targets are mounted parallel, as shown in Fig.1.

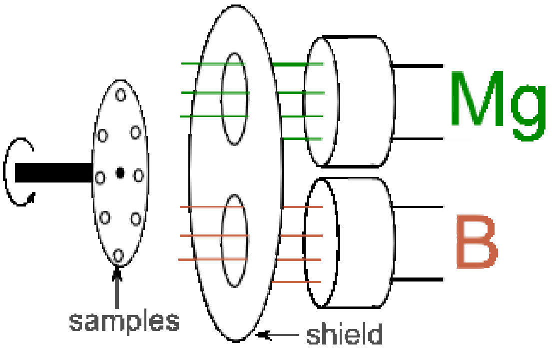

Fig. 1 Scheme of deposition chamber

The magnesium was deposited by DC magnetron sputtering and boron was deposited using AC magnetron sputtering with DC power in the range of 1.45 – 1.7 W/cm^2 and with constant AC power of 16.5 W/cm^2, respectively. The samples were located off-center on a circular sample holder which was rotated in front of two shutters of two magnetrons. In this way Mg and B were deposited sequentially only during sample position in front of corresponding magnetron. The Ar pressure during deposition was kept constant at the value of 0.7 Pa.

After deposition the MgB precursors were annealed ex situ in high vacuum chamber for 3 minutes in Ar atmosphere at 10^{-4}Pa in temperatures ranging 600-720°C. The samples have been partially dry etched by neutralized Ar 500eV ions using PLATAR KLAN-53M ion source, in order to smooth the surface and decrease the layer thickness to final value below 100nm.

RESULTS AND DISCUSSION

The transport properties of superconducting MgB_2 thin films strongly depend on annealing temperature and time. Our samples obtained transition temperature T_c ranging from 29 to 34 K and transition width was less than 2 K as documented by Fig. 2.

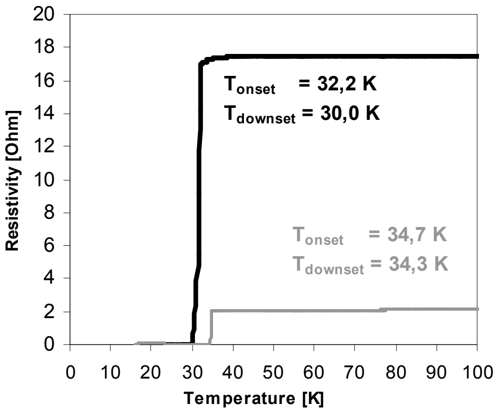

Fig. 2 Resistivity vs. Temperature characteristic

Because of relatively thin layer and low scattering yield we were not able to observe any MgB_2 peak pattern in standard Bragg-Brentano geometry of x-ray diffraction. Therefore we have tried grazing incidence geometry with the fixed incidence angle $\omega=2°$ and scanning along 2θ in the range of 25-55° Fig. 3 shows the measured data with (011) MgB_2 peak overlapped with MgO (002) peak. The nominally most intense MgB_2 and MgO lines are very weak here in our spectrum, because of small layer thickness. The other reflections originate in substrate.

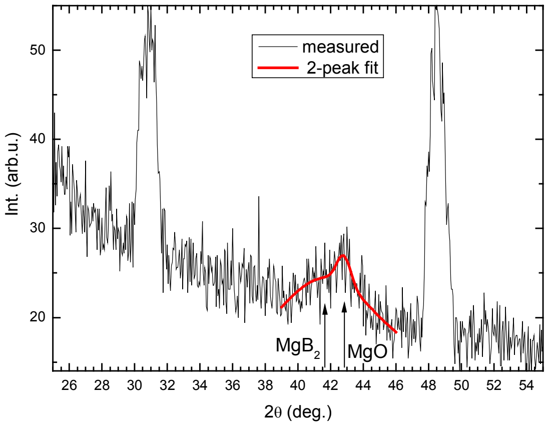

Fig. 3. Grazing incidence diffraction of MgB_2 thin layer.

The MgO presence indicates partial oxidation of very active magnesium, which happened before annealing of precursor and afterwards partially on the top MgB_2 surface too. The spontaneous oxide formation accounts for immediate annealing step after precursor deposition.

Fig.4 shows the atomic force microscopy (AFM) image of the as-grown MgB precursor and Fig. 5 shows the AFM image of the sample after annealing and partial dry etching steps. The surface topography of the as-grown sample is very rough with mean square roughness of about 50nm showing large grains of vertical size up to 400nm. The annealed and dry etched sample is smoothed down to 11nm roughness and the large grains disappeared.

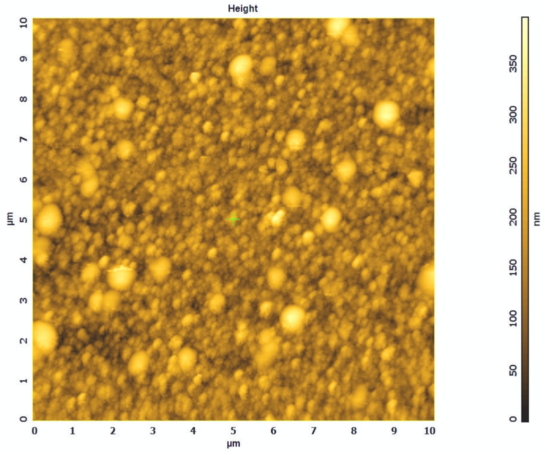

Fig. 4. AFM image with area of 10 µm x 10 µm of the as-grown MgB2 thin film surface.

We have measured x-ray reflectivity of the same as-grown precursor sample. Because of high roughness it was not possible to observe thickness fringes.

The estimate of mean square roughness is on the order of 100nm and thickness is 300nm+/-100nm. The density of the precursor layer is around 1.7g/cm^2 instead of MgB_2 bulk 2.6g/cm^2, which points to the higher roughness and porosity of the precursor.

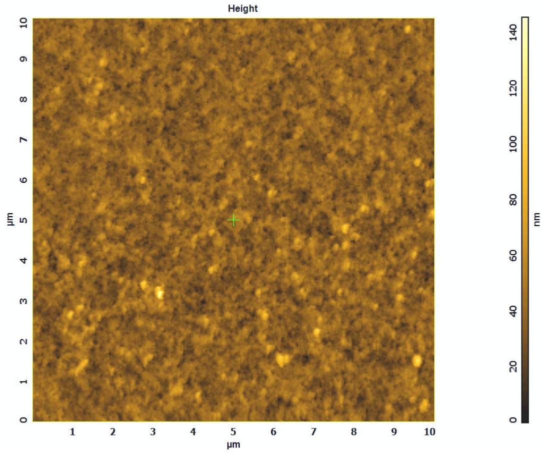

Fig. 5. AFM image with area of 10 µm x 10 µm of the annealed and 30 minutes ion etching MgB2 thin film surface.

TAB. 1. EDX measurements

	Mg	**B**	**Al**	**O**	**C**
Sample 1	2.54%	12.97%	27.63%	52.54%	4.32%
Sample 2	5.03%	11.00%	29.80%	51.10%	3.07%
Sample 3	2.80%	18.00%	26.34%	49.73%	3.13%

Chemical compounds of MgB_2 layers were measured by energy dispersion x-ray analysis (EDX). Measurements had relatively large inaccuracy, caused mainly by detector energy window, which strongly suppress the boron line. EDX data in Tab. 1 show the presence of Mg and B, with strongly varying Mg/B ratio. Aluminum and oxygen signal comes mainly from substrate and certain carbon contamination is also presented. Slightly higher oxygen content is due to MgO presence in top layer.

In conclusion, our complementary Auger measurements in future should eliminate the problem of low boron sensitivity in EDX.

ACKNOWLEDGMENT: This work was supported by Comenius University Grant 6-09-247-00, the Slovak Scientific Grant Agency Grant No. 1/0096/08, the Slovak Research and Development Agency under the contract No. APVV-0432-07, No. VCCE-005881-07, ERDF OP R\&D, Project CE QUTE ITMS 262401022, and via CE SAS QUTE. The authors would like to thank doc. Miroslav Zahoran for helpful discussion on EDX.

REFERENCES

1. W.N. Kang, H.J. Kim, E.M. Choi, C.U. Jung, S.I. Lee, Science 292 (2001) 1521.
2. R. Mičunek, et.al., Physica C 435 (2006) 78–81
3. J. Noskovič , et.al., 17KSF (2009) poster 75

PREPARATION OF SUBMICROMETER STRUCTURES USING ELECTRON BEAM LITHOGRAPHY

P. Durina, durina.pavol@gmail.com, Department of Experimental Physics, FMFI, Comenius University in Bratislava, Mlynska dolina F2, T. Roch, roch@fmph.uniba.sk, Department of Experimental Physics, FMFI, Comenius University in Bratislava, Mlynska dolina F2, M. Stefecka, stefecka@biont.sk, BIONT a.s., Karloveská 63, 842 29 Bratislava, I. Kostic, Ivan.Kostic@savba.sk, Institute of Informatics SAS, Dúbravská cesta 9, 845 07 Bratislava, P. Kúš, kus@fmph.uniba.sk, Department of Experimental Physics, FMFI, Comenius University in Bratislava, Mlynska dolina F2, A. Plecenik, plecenik@fmph.uniba.sk, Department of Experimental Physics, FMFI, Comenius University in Bratislava, Mlynska dolina F2

INTRODUCTION

As it is regular in microelectronics, dimensions of structures in today's sensor research are also reaching in the submicrometer and nanometer range. Thin films of materials with suitable properties are processed using various lithographic methods into desired sensoric structures [1,2]. Especially superconductor devices based on weak links and very sensitive chemical detectors necessitate submicrometer spacing of contacts. In this paper we present our initial development of submicrometer comb structure in platinum contact layer for the next TiO_2, MgB_2 and other sensoric material devices. In few micrometer narrow bridges prepared by photolithography, comb structures of narrow contacts (or in other point of view meanders) have been fabricated using EBL technique.

EXPERIMENT

Owing to inevitable usage of insulating substrate material, we have used single side polished sapphire Al_2O_3 because of its excellent insulating properties. Thin platinum film of 20 nm thickness was deposited by DC magnetron sputtering on the Al_2O_3 substrate. On top of Pt layer positive photoresist AZ 6624 was spin-coated using 4000 rpm for 1min in order to obtain 2 μm resist thickness. Before exposure sample with the resist layer was baked on hotplate at 95 °C for 2 minutes. Photoresist was exposed for 35 sec using JUB 2104.16 mask aligner using UV wavelength of $\lambda = 365$ nm. After exposure the sample was annealed on hotplate at 105 °C for 2 min. Subsequently photoresist was developed in developer AZ 400K for a period of 70 sec. Next, the developed structure was dry etched using electrically neutralized Ar ions generated in ion gun PLATAR at $5x10^{-3}$Pa Ar working pressure for a period of 5 min. The energy of bombarding Ar atoms was 500 eV and neutralizing current 20 mA. Fig.1a shows the contacts structure with three narrow bridges in Pt layer fabricated in this process. Fig.1b shows the detail of one of the bridges.

On the structure of platinum contacts 15nm of gold layer was deposited using DC magnetron sputtering. Gold layer is necessary because of undesirable charging effects during electron beam lithography process on insulating Al_2O_3 substrate. Cumulating charge of impinging electrons must be drained via gold thin layer and top contact in the EBL sample holder, otherwise charge electric field would cause deformation of electron beam path and deformation of the exposed structures shape.

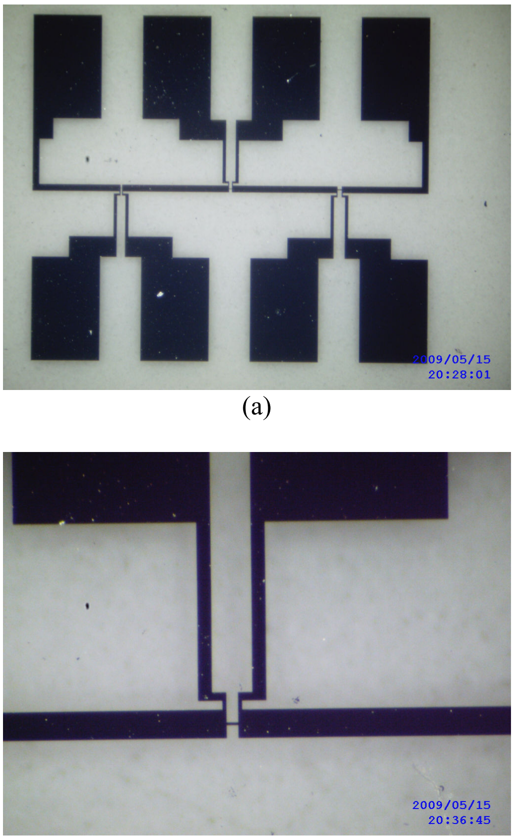

(a)

(b)

Fig. 1. (a)Contacts structure with three bridges in platinum produced by photolithography and dry etching processes (b) Detail of the platinum bridge

On all samples PMMA positive electron beam resist ARP 679.04 - 950K of the thickness of 500nm was spin coated at 2000rpm for 2min on top of Au layer. Before exposure e-beam resist was prebaked at 85 °C for the duration of 60 sec. EBL process of submicrometer comb structures in narrow Pt bridges was performed on Tescan Vega II SBH equipment using accelerating voltage 30 kV, beam current I = 20 pA and exposure dose in range of 200 - 7500 $\mu C/cm^2$. Exposed resist was developed in diluted developer MIBK (*Methyl isobutyl ketone*) : IPA (*Isopropyl alcohol*) in the ration of 1:3 for 60 sec. After EBL the structure was dry etched for 12 min using ion source Platar. We have used Ar pressure of $5x10^{-3}$Pa with the energy of 400 eV and beam current 15mA. Comb structure was dry etched through Au and Pt layers down to the substrate, Fig.2.

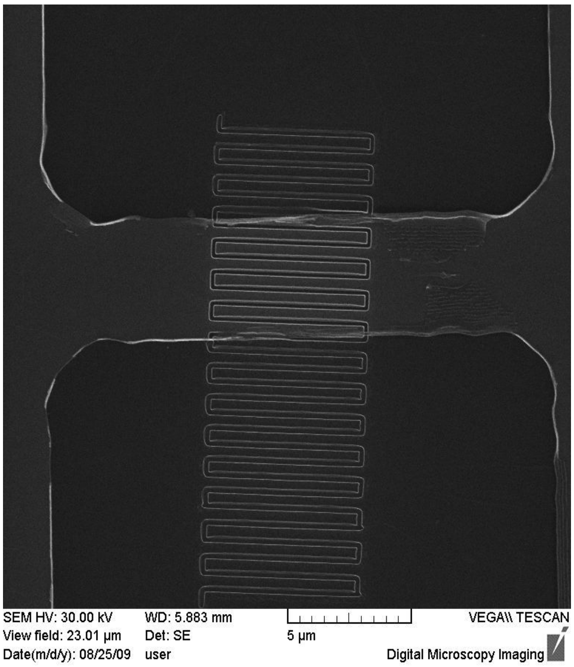

Fig.2. Comb structure formed in platinum bridge using EBL. Magnification 5000x

RESULTS AND DISCUSION

For EBL process it was necessary to determine optimal exposure dose *Q*, the value at which the whole resist thickness is overexposed and the exposed line width is minimal. Tests for finding optimal *Q* value were performed on Si substrate at first and on Al_2O_3 next. Fig. 3 shows dependence of line width d of meander (comb structure) on exposure dose value for both substrates. The results show the line width of meander structure by equal exposure doses is higher on Si substrate as compared to widths for Al_2O_3 substrate. Dashed line represents line widths at doses by which the entire resist thickness was not yet exposed through. Difference in line widths for two different substrates is caused due to higher electron back scattering of silicon (Z=14) and therefore more electrons expose resist along wider line. Based on measured data in Fig.3 we have set optimal exposure dose Q = 1450 µC/cm^2 for our comb structure in platinum bridge on Al_2O_3 substrate. For Si substrate we have set optimal dose Q = 1150 µC/cm^2.

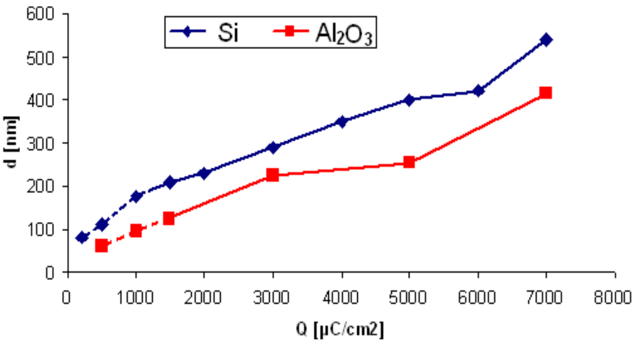

Fig.3. Line width d vs. exposure dose Q dependence for Si and Al2O3 substrates.

CONCLUSIONS

For the fabrication of metallic comb structures on Al_2O_3 substrates for testing transport properties of sensoric materials it was necessary to tune the parameters of EBL. Most important was the determination of optimal exposure dose exposure Q = 1450 µC/cm^2 for e-beam resist ARP 679.04 with the thickness of 500 nm. We have observed the line widths on Si substrates were wider than on Al_2O_3 at the same exposure conditions. Optimal exposure dose in case of Si substrate was Q = 1150 µC/cm^2. In next research we optimize EBL for other types of resists and other submicron structure patterns.

ACKNOWLEDGMENT: This work was supported by the Slovak Scientific Grant Agency, Grant No. 1/0096/08, the Slovak Research and Development Agency under the contract No. APVV-0432-07 and No. VCCE-005881-07, ERDF OP R\&D, Project CE QUTE ITMS 262401022, and via CE SAS QUTE.

REFERENCES

1. Schlosser P., Vargová, M., Kubinec, M., Haščík, Š., Roch, T., Plecenik, A.,Plesch, G., Hotový, I., 14th International Conference on Applied Physics of Condensed Matter : Proceedings, Bratislava : Slovenská technická univerzita, 2008 S. 199-202.
2. Schlosser Peter, Vargová Melinda, Roch Tomáš, Plecenik Tomáš, Maheľ Michal, Plesch Gustáv, Plecenik Andrej, 8th Conference on Solid State Chemistry. - Bratislava : SAS, 2008. - S. 263.

MAGNETO-OPTICAL PROPERTIES OF MAGNETITE NANOPARTICLES PREPARED BY VARIOUS PROCESSES

A. Dzarova*, dzarova@saske.sk, D. Jamon**,Damien.Jamon@univ-st-etienne.fr, M. Timko*, timko@saske.sk, F. Royer**, Francois.Royer@univ-st-etienne.fr, P. Kopcansky*, kopcan@saske.sk, F. Choueikani**, J.J. Rousseau**, jean.jacques.rousseau@univ-st-etienne.fr, H. Gojzewski***, gojzewsk@mpip-mainz.mpg.de *Institute of Experimental Physics, Slovak Academy of Sciences, IEP-SAS, Watsonova 47 Kosice, Slovakia, ** Laboratoire Dispositifs et Instrumentation en Optoélelectronique et Microondes-EA3523, Université Jean Monnet, 21 Rue Paul Michelon, 42023 Saint Etienne cedex 2, France, ***Max Planck Institute for Polymer Research, Ackermannweg 10, 55128 Mainz, Germany

INTRODUCTION

Magnetic fluids (or ferrofluids) are colloidal dispersions of nanosized magnetic particles in a carrier liquid. Isotropic in zero field, this hybrid medium acquires an optical anisotropy when a magnetic field is applied. This anisotropy is circular in Faraday's longitudinal configuration (magnetic field direction parallel to the light beam) and linear in Voigt configuration (magnetic field direction perpendicular to the light beam). In this report, we are interested in the circular anisotropy, studying the influence of the nanoparticle preparation process on the Faraday Rotation (FR). When linearly polarized light is passed through a ferrofluid cell in a longitudinal applied field, its polarisation rotates. The angle of rotation γ_F depends on the field intensity [1]. The origin of this effect doesn't seem to be linked to the particles anisotropy axes orientation but better to the orientation of the magnetic moments of the particles in the applied field (*H*) direction. It is justified by measurements of FR on nanoparticles doped silica gel matrix and by dynamic measurements on magnetic fluids. Thus the curve $\gamma_F = f(H)$ is similar the magnetization curve. At low volume fraction Φ of particles up to a few percents, the saturation level is proportional to Φ [2].

In this paper, we have studied the optical and magnetooptical properties of magnetic fluids prepared from magnetite nanoparticles prepared by chemical co-precipitation method and biomineralization process of magnetotactic bacteria magnetosome), respectively.

EXPERIMENTAL SECTION

Magnetic fluids exhibit linear or circular optical anisotropy under the influence of a magnetic field. These anisotropic media generate two effects: the magneto-optical birefringence and dichroism, which introduce respectively a phase shift Δ and a difference of absorption (related to an angular parameter ψ) between optical waves polarized along eigenpolarizations of the material. These eigenpolarizations are linear (along orthogonal axis x and y) or circular (along opposite circular senses + and -) for linear or circular anisotropic media, respectively. In our case, linear effects are obtained with a magnetic field direction which is perpendicular to the light beam, whereas circulars effects need a longitudinal magnetic field (Faraday Rotation and Ellipticity). The anisotropic media may be haracterized completely by the two ellipsometric angles Δ and ψ linked to the ratios:

$$\frac{t_x}{t_y} = \tan\psi \exp(i\Delta) \tag{1}$$

where t_x and t_y are transmission coefficients of the eigenpolarizations. Birefrigence Δn and dichroism Δk are linked to ellipsometric angles Δ and ψ. For an incident linear polarization, whatever its azimuth, the elliptic polarization at the output of the sample is characterized by its inclination γ in relation to the incident linear polarization azimuth and its ellipticity angle ε (for $\varepsilon<10°$) given by

$$\Delta = 2\gamma \tag{2}$$

$$\tan\Psi = 1 + 2\varepsilon \tag{3}$$

In our experiment we have used two types of nanoparticles: the chemically synthesized nearly spherical magnetite nanoparticles prepared by co-precipitation method and biological magnetic particles (magnetosomes) prepared by the biomineralization process from magnetotactic bacteria.

The synthesis of the spherical magnetic nanoparticles was based on coprecipitation of Fe^{2+} and Fe^{3+} salts by NH_4OH at 60°C. Bacterial magnetosomes were synthesized by biomineralization process from magnetotactic bacteria *Magnetospirillum sp.* strain AMB-1. The detailed description of cultivation of magnetotactic bacteria and isolation of magnetosomes is given in our previous contribution [3].

The magnetization properties of the prepared aqueous suspensions were measured by SQUID magnetometer of Quantum Design. The morphological properties and the size of magnetosomes were estimated by Transmission and High-Resolution Transmission Electron Microscopy measurements using FEI Tecnai F20 S-TWIN (Philips Corp.) transmission electron microscope (TEM) working at the accelerating voltage of 200 kV. The crystalline structures were characterized by the high-resolution transmission electron microscopy (HRTEM). The crystalline phase identification of magnetosome and synthetic magnetite particles were carried out by X-ray diffraction (XRD) with Co Kα radiations with the wavelength $\lambda = 0.17903$nm.

The XRD powder diffraction peaks of synthetically prepared nanoparticles and those prepared by mineralization (magnetosome) fit well the standard Fe_3O_4 reflections. This fact reveals that both the magnetic nanocrystal within the magnetosome and the chemically synthesized nearly spherical magnetic nanocrystals consist of magnetite. Representative HRTEM and TEM (inset) images of studied magnetosomes nanoparticles deposited on carbon-coated copper grid are shown in Fig. 1. The HRTEM image shows the clearly resolved lattice fringes of magnetosomes nanocrystals. The interplanar spaces are calculated by FFT (Fast Fourier Transform) to be about 0.49 nm and 0.26 nm, corresponding to *d* (lattice plane distance) values of (111) and (311) planes, respectively. This lattice plane distances can be indexed as face-centered cubic (fcc) Fe_3O_4.

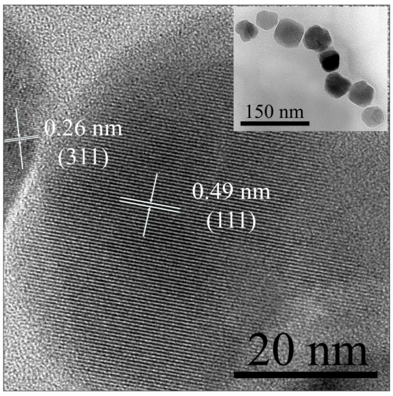

Fig. 1: HRTEM and TEM (inset) images of the magnetosomes nanoparticles

Magnetization measurements of the prepared magnetosomes suspension were carried out by SQUID magnetometer of Quantum Design.. The curve of field dependence of magnetization at 293 K exhibited the remanence and coercivity of 7.1 emu/g and 71 Oe, respectively, what is higher as for monodomain magnetite particles. This fact can connected with fact that the mean diameter (34 nm) is larger than critical size for transition from superparamagnetic to ferromagnetic behaviour.

Linear effects such as birefringence and dichroïsm obtained with a transversal field very interesting and show that magnetosomes suspensions require a very low field magnitude to be well oriented: around 20 Oe compared to 300 Oe for “classical spherical particles”. If we assume that a magnetosome is an optical anisotropic element, bearing an effective magnetic moment whose easy magnetization axis is aligned with the chain direction, we can calculate a normalized dichroism using Langevin orientation theory. The result is reported on figure 2. To do the calculation we have used the following formula $\Psi = \Psi_S \, . \, (1\text{-}3.L(\xi)/\xi)$, with $\xi = (m_S.V.H)/(k.T)$, $m_S = 320000$ A/m. The magnetic volume V has been calculated assuming 12 nanoparticles of diameter 37nm.

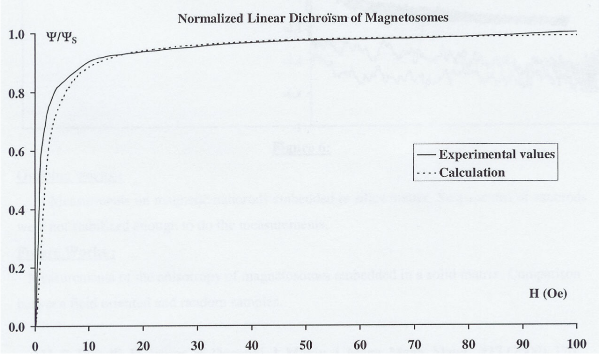

Fig. 2: Normalized linear dichroism if magnetosomes.

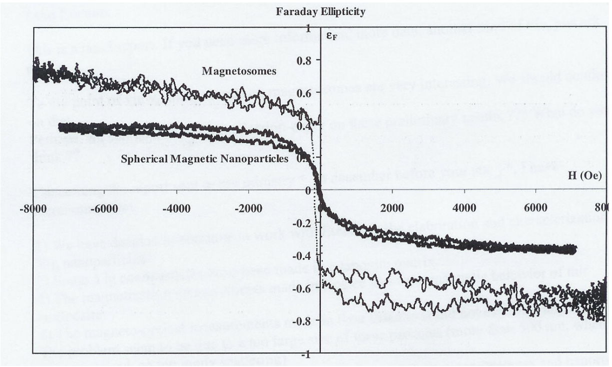

Fig. 3: Faraday eleipticity for chemically synthesized nanoparticles and magnetosomes, respectively.

The good agreement between the calculation and the experimental data is interesting even if we haven’t taken into account a size distribution. Faraday ellipticity (circular anisotropy) of magnetosomes and classical particles are plotted on fig. 3. This figure confirms that a very low field is required to orientate magnetosomes.

CONCLUSIONS

Magnetooptical and optical experiments are performed on magnetite nanoparticles prepared by chemical coprecipitation method and by biomineralization process of magnetotactic bacteria AMB-1, respectively. The obtained results from magnetooptical study confirm that very low field is required to orientate magnetosomes. Magnetosome act as an optical anisotropic element with easy magnetization axis aligned to chain direction. Faraday rotation curves are described by orientation Langevin theory. The good agreement between the calculation and the experimental data is interesting even if we haven’t taken into account a size distribution.

ACKNOWLEDGMENT: This work was created by implementation of the "Cooperative phenomena and phase transitions in nanosystems with perspective utilization in nano- and biotechnology" project no. 26220120021 funded by European Community, ERDF – European regional development fund and APVV 0173-06.

REFERENCES

1. H.W. Davies, J.P. Leweellyn, J. Phys. **13**, 2327 (1980)
2. N.A. Yusuf, I. Abu-Alarayesh, A.A. Rousan, H.M. El-Ghanem, IEEE Trans. Magn. **26**, 2852 (1990)
3. M. Timko, A. Dzarova, V. Zavisova, M. Koneracka, A. Sprincova, P. Kopcansky, J. Kovac, A. Szlaferek, I. Vavra Magnetohydrodynamics Journal **3** 44 (2008).

POSSIBILITIES OF MONITORING OF PROTEIN FLUORESCENCE IN ORGANISMS

L. Mesková, livia.meskova@gmail.com, FMFI UK, L. Šikurová, sikurova@fmph.uniba.sk;
Department of Nuclear Physics and Biophysics, Faculty of Mathematics, Physics and Informatics, Comenius University, Mlynská Dolina, Bratislava

INTRODUCTION

Biological tissues show autofluorescence due to the endogenous fluorophores. Fluorophores are primarily structural proteins, namely collagen, which is in bodies of mammals in the highest share. Proteins are composed of aminoacids, from which tryptophan is the most intensively fluorescent [1]. Our work is aimed at monitoring of the endogenous fluorophores of lungs of rats of Wistar Kyoto strain by fluorescence spectroscopy while emission spectra of spontaneously hypertensive and healthy subjects are compared.

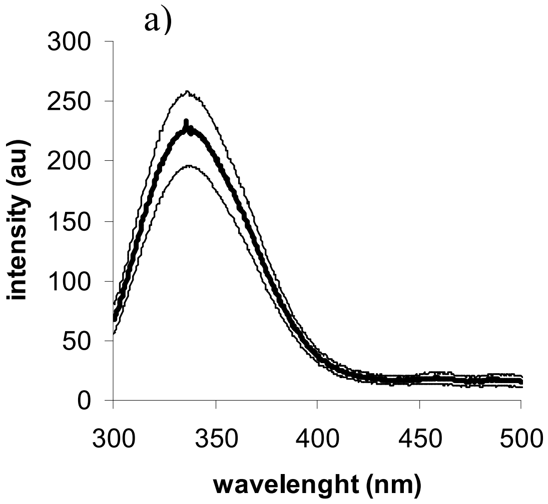

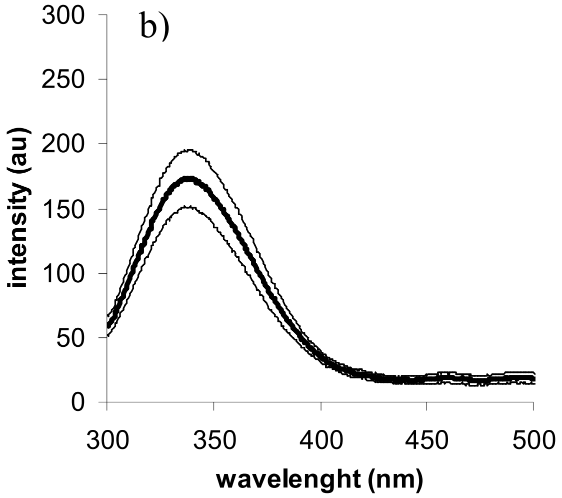

Fig. 1 Fluorescence emission spectrum of lungs of rats of Wistar Kyoto strain at excitation 280 nm. The mean values of the fluorescence intensity (n=5) are illustrated by the heavy line, the thin lines represent the 95 % confidence interval (figure for the central tendency, which provides information on the 95 % probability of occurrence of the real mean for the whole population). a) Emission fluorescence spectrum of the control sample of lungs of healthy rats of Wistar Kyoto strain. The emission maximum belongs to wavelength 336.5 nm. b) The emission spectrum of the sample of spontaneously hypertensive rats of Wistar Kyoto strain. The emission maximum belongs to wavelength 338 nm.

MONITORING OF LUNGS USING EXCITATION WAVELENGHT OF 280 NM

The wavelength of 280 nm is the excitation maximum for tryptophan, that is why we used it for monitoring of its presence in the lungs. Emission maxima at excitation 280 nm were in the range of interval 335.5 – 338.5 nm, which is the evidence of tryptophan presence. We traced the tryptophan fluorescence spectra in the range from 310 to 500 nm for lungs of 5 rats of Wistar Kyoto strain as the control sample (Fig. 1.a) and for lungs of 5 spontaneously hypertensive rats of Wistar Kyoto strain (Fig. 1.b). We constructed graphs of the mean of the fluorescence intensity for both groups. The results were subject to the two sample t-test to verify the difference in intensity of the tryptophan of the lungs of the control samples and spontaneously hypertensive samples. We found out that this difference is significant: $P < 0.025$. Amount of tryptophan is lower in case of the lungs of spontaneously hypertensive subjects than that for the control samples.

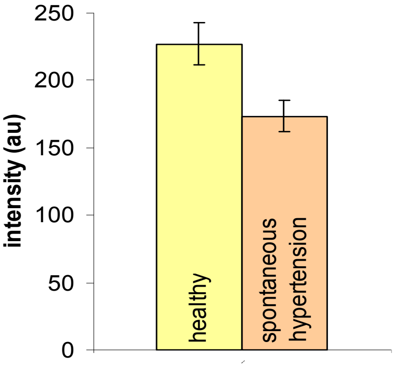

Fig. 2 The graph compares the fluorescence intensity of the control sample of lungs of healthy rats of Wistar Kyoto strain (left column) and of the sample of lungs of spontaneously hypertensive rats of Wistar Kyoto strain (right column) at excitation 280 nm. The mean wave lengths of the fluorescence maxima, which are illustrated in this graph, were found from the data in Fig. 1, a, b. The mean fluorescence maximum of the control sample belongs to the emission wavelength 336.5 nm and the mean fluorescence maximum of the investigated sample belongs to the emission wavelength 338 nm. Standard errors ($n = 5$, $P < 0.025$) are represented in the graph.

MONITORING OF LUNGS USING EXCITATION WAVELENGHT OF 325 NM

The excitation maximum 325 nm corresponds to collagen and elastin, while their emission maxima range around the wave lengths of 400 nm. We found 3 emission maxima for both investigated groups at excita-

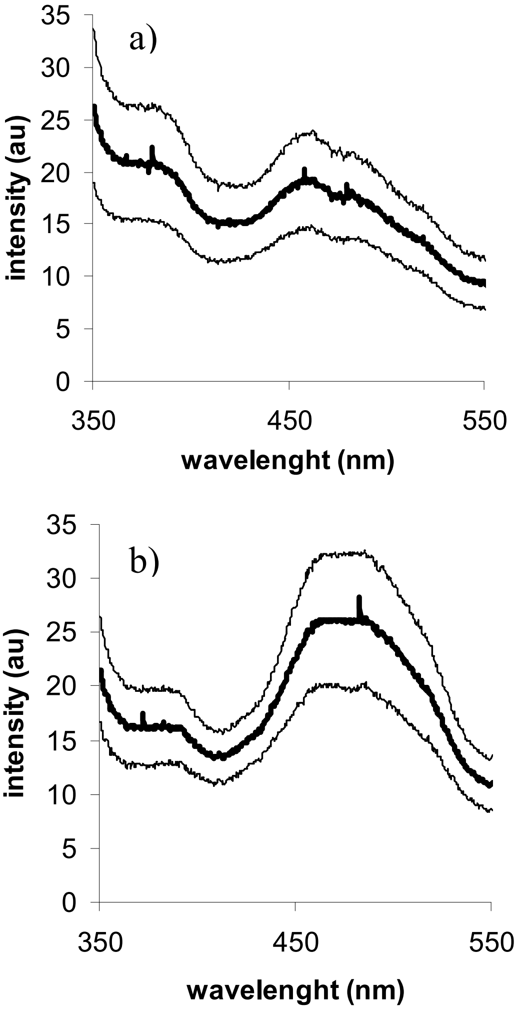

Fig. 3 Fluorescence emission spectrum of lungs of rats of Wistar Kyoto strain at excitation 325 nm. The mean values of fluorescence intensity (n=5) are illustrated with the heavy line, the thin lines represent the 95 % confidence interval (figure on the central tendency, which provides information on the 95 % probability of occurrence of the real mean of the whole population). a) Emission fluorescence spectrum of the healthy control sample of lungs of rats of Wistar Kyoto strain. The first emission maximum belongs to wavelength 378.5 nm, the second emission maximum to 362.5 nm and the third emission maximum to wavelength 485 nm. b) Emission spectrum of the sample of lungs of spontaneously hypertensive rats of Wistar Kyoto strain. The first emission maximum belongs to wave length 382.5 nm, the second emission maximum to 470.5 and the third emission maximum to wavelength 485 nm.

tion 325 nm (Fig.3). The first maximum ranges in interval from 366.5 to 380.5 nm for the control sample and it ranges in interval from 368.5 to 386 nm for the investigated sample of lungs of spontaneously hypertensive rats. The second fluorescence maximum occurs in scope 460 – 470 nm. The third maximum, visible in the graph, is in range of interval 479 – 486.5 nm for the control sample and it is within interval 483 – 486.5 nm for the investigated sample. The results were subject to the two sample t-test. There was no statistically significant difference approved for the first as well as the second fluorescence maximum, while the significant difference ($P < 0.044$) was approved for the third fluorescence maximum for the samples of lungs of healthy rats (control sample) and those of the spontaneously hypertensive rats. The third emission maximum corresponds to the reduced coenzyme Nicotinamide adenine dinucleotide (NADH) [2].

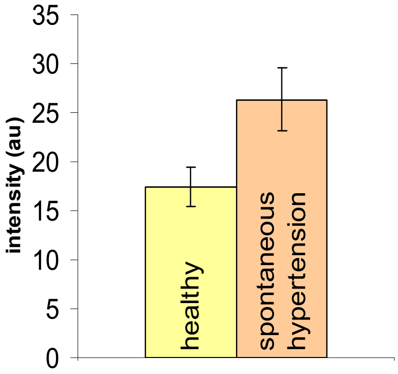

Fig. 4 The graph compares the intensity of the fluorescence of the control sample of lungs of Wistar Kyoto strain (left column) and of the investigated sample of lungs of spontaneously hypertensive rats of Wistar Kyoto strain (right column) at excitation 280 nm in the third emission maximum. The mean wave lengths of the fluorescence maxima, which are illustrated in this graph, were found from the data in Fig. 3, a, b. The mean fluorescence maximum of the control as well as of the hypertensive sample belongs to the emission wavelength 485 nm. Standard errors ($n=5$, $P < 0.044$) are represented in the graph.

CONCLUSIONS

We are able, by analysis of emission spectra, to compare quantitatively the amount of fluorophore in the traced sample in comparison to the control sample. We found out that, in the sample from spontaneously hypertensive rats, approximately by 24 % less tryptophan, that is also less proteins, occurs in comparison to the control sample. However, changes in intensity of collagen fluorescence were not observed. It was simultaneously proved that there is approximately by 36 % more NADH in the traced sample of lungs of spontaneously hypertensive rats in comparison to the control sample.

REFERENCES

1. Ramanujam N., 2000 – Fluorescence spectroscopy in vivo, Encyclopedia of Analytical Chemistry, John Wiley & Sons Ltd., Chichester
2. Lakowicz J. R., 2006 – Principles of fluorescence spectroscopy 3rd. Ed., Springer, New York

FLUORESCENT MEASUREMENT OF HYPERCHOLESTEROLEMIA-INDUCED CHANGES IN MITOCHONDRIA

M. Zvarík[1)], zvarikmilan@gmail.com, L. Šikurová[1)], sikuroval@gmail.com, O. Uličná[2)]
[1)] Department of Nuclear Physics and Biophysics, FMFI UK, Mlynská dolina F1, 842 48 Bratislava, Slovakia
[2)] Laboratory of Pharmacobiochemistry, Third Department of Internal Medicine, Faculty of Medicine, Comenius University, Bratislava, Slovakia

INTRODUCTION

The mitochondrion is a membrane-enclosed organelle found in most eukaryotic cells. Mitochondria are involved in a range of processes, such as supply of cellular energy, signalling, cellular differentiation, or cell death. Therefore, they are also likely to play a role in several human diseases. In the present contribution we study mitochondrial alterations induced by hypercholesterolemia [1,2] and its treatment by atorvastatin [3] (Fig. 1).

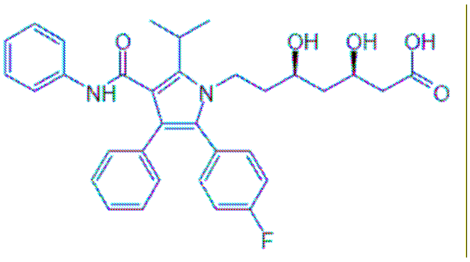

Fig. 1. Atorvastatin

MATERIALS AND METHODS

Mitochondria were isolated from livers of healthy and hypercholesterolemic adult male Wistar rats [4]. The isolation procedure was performed at 4 ºC and the isolated mitochondria were diluted to the final concentration of 12.5 mg/ml in a buffer solution. Mitochondria from four groups of animals were studied: (i) healthy animals; (control group), (ii) hypercholesterolemic animals; (iii) and (iv) hypercholesterolemic animals treated by two doses of atorvastatin, 10 and 80 mg/kg/day. Each group consisted of 7 rats. Hypercholesterolemia was induced by feeding rats diets containing an excess of cholesterol.

Alterations in mitochondria were studied with the Thiadicarbocyanine tribromide (TCBr) fluorescent probe purchased from Genolite Biotek [5,6] (Fig.2). Using fluorescence spectroscopy, fluorescence intensity changes at the 667 nm fluorescence peak of the probe with excitation at 630 nm were measured at 22 ± 1°C with a Perkin Elmer LS 45 luminometer. The probe was incubated with a suspension of mitochondria for 30 minutes, when fluorescence of TCBr reaches the plateau. ($c_{(mit)} = 0,25$ mg/ml, $c_{(TCBr)} = 5$ µmol/l) (Fig.3). Results obtained from hypercholesterolemics groups were compared with control group and statistical significance was evaluated using paired t-test.

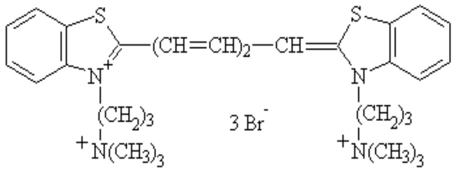

Fig. 2. Thiadicarbocyanine tribromide (TCBr)

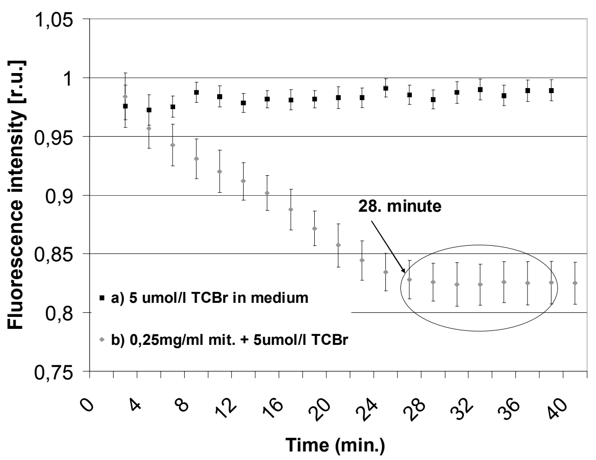

Fig. 3 Time dependence of 667 nm-fluorescence intensity of TCBr a) without presence of mitochondria, b) in presence of mitochondria. The data are expressed as the means ±SD of 7 independent experiments.

RESULTS AND DISCUSSION

The fluorescence data showed a significant decrease ($p<0.01$) in fluorescence intensity at 667 nm of the probe TCBr in mitochondria obtained from rat liver with induced hypercholesterolemia (ii) as compared to control group (i) (Fig. 4, 5). The decrease in TCBr fluorescence intensity relates to pathological changes in mitochondrial membrane caused by hypercholesterolemia. Application of 10 mg/kg/day of atorvastatin to the hypercholesterolemic rats (iii) induced further decrease ($p<0.01$) in fluorescence intensity of TCBr. This low dose of atorvastatin is probably insufficient for suppression of pathological processes in hypercholesterolemic mitochondria. After treatment of higher atorvastatin dose 80 mg/kg/day, we observed an increase in fluorescence intensity of TCBr in samples (iv) compared to hypercholestorelemic mitochondria (ii), what was probably caused by protective effects of atorvastatin (80 mg/kg/day). However, always remains a significant decline ($p<0.01$) in 667 nm-fluorescence intensity of TCBr in the treated samples (iv) compared to control group (i).

CONCLUSIONS

We found significant differences between controls and the three hypercholesterolemic groups. The diffe-

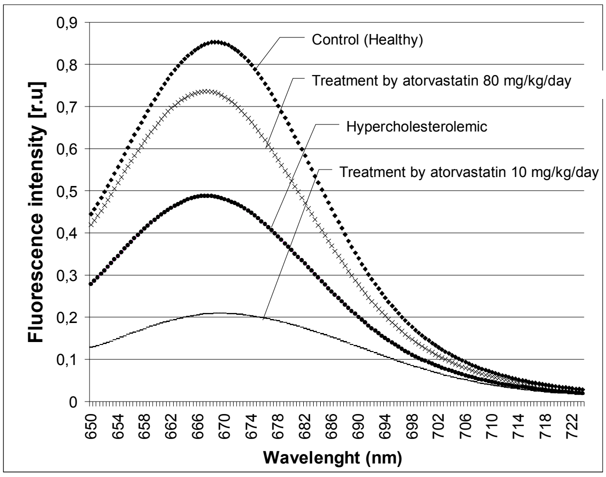

Fig. 4 Fluorescence spectrum of TCBr in mitochondria obtained from liver of healthy rats (control group), hypercholesterolemic rats; and hypercholesterolemic rats treated by two doses of atorvastatin, 10 and 80 mg/kg/day.

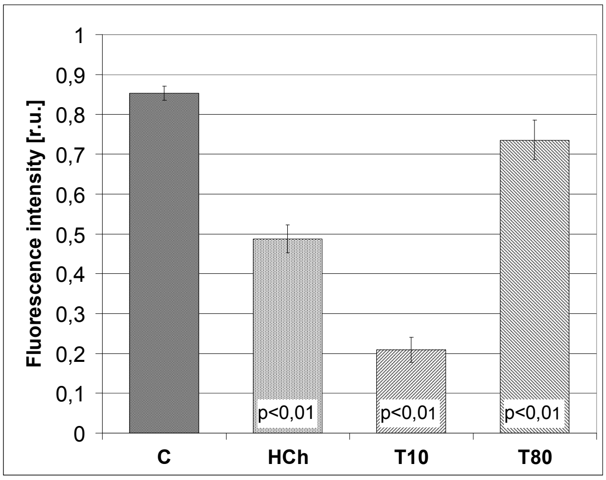

Fig. 5 Fluorescence intensity of TCBr at 667 nm in mitochondria suspension. (*C* - healthy animals (control group); *HCh* - hypercholesterolemic animals; *T10, T80*- hypercholesterolemic animals treated by two doses of atorvastatin, 10 and 80 mg/kg/day excitation 630 nm; emission 667 nm; temperature 22 ± 1°C). The data are expressed as the means ± SD of 7 independent samples experiments. Significant differences ($p<0.01$) between controls and hypercholesterolemic groups were found.

ren differences are an indication of a mitochondrial dysfunction or disorder in hypercholesterolemia, and are removed by atorvastatin treatment (80 mg/kg/day).

Our findings offer a new insight into hypercholesterolemia-induced alterations in mitochondria.

ACKNOWLEDGMENT: This work was supported by the research from the Grant UK/403/2009.

REFERENCES

1. Knight-Lozano CA, et al., Circulation **105**, 849–854 (2002).
2. Yao P.M., Tabas I., J. Biol. Chem. **276**, 42468–42476 (2001).
3. Law MR, Wald NJ, Rudnicka AR., BMJ. **326**, 1423-1427 (2003).
4. Lehninger A. L., Carafoli E., Rossi C. S., Adv. Enzymol. Relat. Areas Mol. Biol. **29**, 259—320 (1967).
5. Ferko M., Habodászová D., Waczulíková, I., Mujkošová J., Kucharská J., Šikurová Ľ., Ziegelhöffer A., Changes associated with functional remodeling of mitochondrial membranes in acute diabetic heart: Presence of endogenous protective mechanisms. In Tribulová N. Okruhlicová Ľ. Potential therapeutic targets in cardiovascular and other diseases. Bratislava: Veda, ISBN 13: 978-80-224-0942-1; ISBN 10: 80-224-0942-1, 8-10 (2006).
6. Zhao Ch., Nguzen T., Ming Boo L., Hong T., Espiritu C., Orlov D., Wang W., Waring A, Lehrer I.R, Antimicrob. Agents Chemother **45**, 2695-2702 (2001).

STUDY OF INFLUENCE THE STRETCHING ON THE MOLECULAR DYNAMICS IN POLYPROPYLENE FIBRES BY NMR SPECTROSCOPY

L. Ševčovič, ladislav.sevcovic@tuke.sk, Ľ. Mucha, lubomir.mucha@tuke.sk, Department of Physics, Technical University of Košice, Park Komenského 2, 041 20 Košice, Slovakia

INTRODUCTION

The NMR linewidths in solids like isotactic polypropylene (PP) are predominately an expression of the dipolar interaction between magnetic nuclei. Molecular motion can average out some of the dipolar interaction and the resonance line narrows. This change occurs when the frequency of the molecular motion is of the order of the linewidth, typically 10–100 kHz. The spin-lattice relaxation time T_1 is sensitive to molecular motion containing a component at about the NMR frequency. Proton NMR relaxation experiment has, therefore the potential to study both of the relaxations to provide information on the type of motion, its activation energy and its correlation time function.

There are several papers dealing with relaxation properties of the partially crystalline PP by using the pulsed NMR techniques [1–3]. A lot of investigators [3, 4] analyzed the broad-line NMR spectrum. A structure of a semicrystalline PP is frequently interpreted as a three-regional model of polymers, i.e. regions corresponding to the crystalline, intermediate and amorphous fractions, respectively. Both the molecular mobility and relaxation depends not only on temperature, but also on the molecular composition of macromolecular chains and on their spatial structure. In partially crystalline polymers the rise of crystallinity which can arise from stretching, results usually in the shift of glass temperature T_g to the higher temperatures.

EXPERIMENTAL

In this study we present proton NMR measurements of the T_1 relaxation time and second moment M_2 of the spectra in the temperature range 200–400 K for five kinds of stretched PP fibres made from isotactic PP marked as Tatren 430 and produced by Slovnaft Bratislava. The sample denoted as PP/293/1 is a starting non-stretched fibre. The samples denoted as PP/293/4 and PP/398/4 are fibres stretched at temperatures 293 K and 398 K at drawn ratio $\lambda = 4$, respectively.

RESUTS AND DISCUSION

The temperature dependences of the second moment were estimated according to the formula [5]

$$M_2(T) = M_{2\mathrm{ht}} + \frac{2}{\pi}(M_{2\mathrm{lt}} - M_{2\mathrm{ht}}) \,\mathrm{arctg}\left[\gamma\,\tau_\mathrm{c}\sqrt{M_2(T)}\right], \tag{1}$$

where γ is the gyromagnetic ratio of resonanting nuclei, $M_{2\mathrm{lt}}$ and $M_{2\mathrm{ht}}$ refer to the second moment at temperatures below and above the transition range (the low and the high temperature plateau of M_2), respectively. The correlation time, τ_c, for corresponding molecular motion, may be expressed according to Arrhénius formula

$$\tau_\mathrm{c}(T) = \tau_0 \exp\left(\frac{E_\mathrm{a}}{RT}\right), \tag{2}$$

where τ_0 is the correlation time at infinite temperature, E_a is the activation energy and R is the gas constant. The temperature dependence of the second moment M_2 for both non-stretched and stretched PP fibres and for the stretched fibres with $\lambda = 4$ for two different stretching temperatures (293 K and 398 K) is shown in Fig. 1. The second moment takes up the values of about $16 \cdot 10^{-8}$ T^2 at the temperatures below 270 K. It is known that the CH_3 side-group rotations and rigid main chains are responsible for this value. The decrease of the second moment could be ascribed to the motion of segments of PP chains in the non-crystalline regions. The molecular motions in this temperature region are referred to β-relaxation process. The second moment plateau above this temperature region shows that the segmental motions of macromolecular chains in non-crystalline part of PP are completely released.

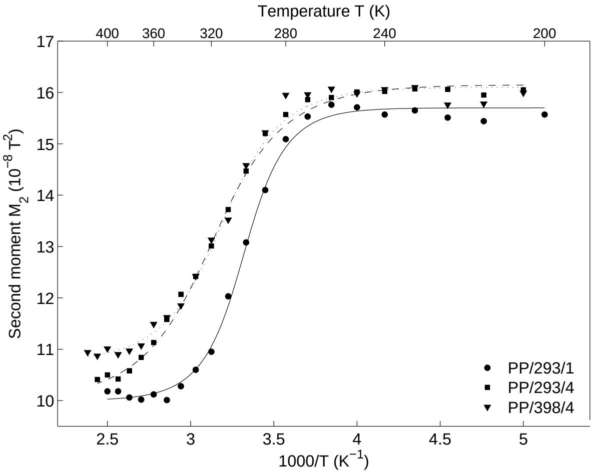

Fig. 1. Second moments M_2 in set of polypropylene samples versus temperature. The lines represent line calculated according to Eqs. (1) and (2)

The dependence log plot of T_1 on $10^3/T$, is displayed in Fig. 2. Simple small molecules typically have Debye-like relaxation while polymers often exhibit complex relaxation behaviour which cannot be characterized by a single-exponential correlation time [1]. To describe a system with a distribution of correlation times one can use the non-symmetrical modified Fuoss-Kirkwood (mFK) distribution developed by Schneider [6]. The mFK distribution, particularly suitable for an account of the temperature dependences of the rate of spin-lattice relaxation $1/T_1$ with different slopes on the low and high temperatures sides of the minimum, was considered in our calculation.

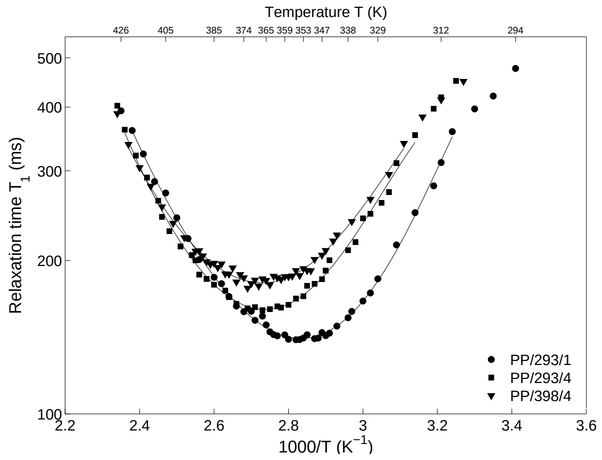

Fig. 2. Spin-lattice relaxation times T_1 versus reciprocal temperature. The solid lines represent the best fit (with the lowest χ^2). The fit was carried out using an implementation of the Large-Scale and Medium-Scale algorithms supplied by MATLAB with built-in function `lsqcurvefit` that solves any least square fitting for a small number of parameters

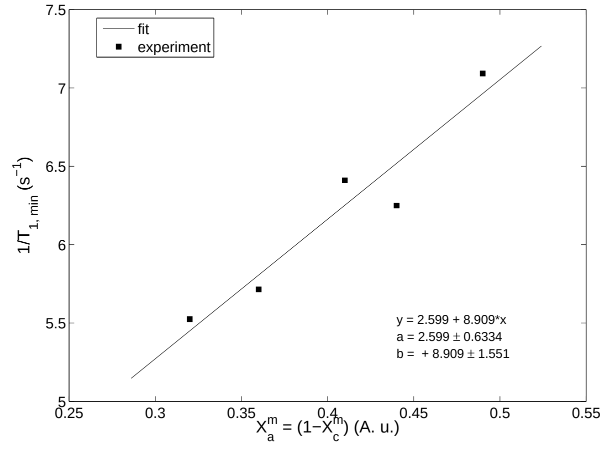

Fig. 3. The approximate linearity of $1/T_{1,\mathrm{min}}$ versus $(1 - X_c^m)$ implies that the spins in the crystalline region are coupled by spin-diffusion mechanism to the amorphous region which acts as an ensemble of relaxation centers. It is expected that the proportion of the non-crystalline region correlates with the relaxation rate

Using the mFK distribution the dependence of the spin-lattice relaxation rate $1/T_1$ on the correlation time τ_c is expressed by the equation

$$\frac{1}{T_1} = C\left(\frac{\alpha+\beta}{2\,\omega_0}\right)\sin\left(\frac{\alpha\pi}{\alpha+\beta}\right)\left[\frac{(\omega_0\tau_c)^\alpha}{1+(\omega_0\tau_c)^{\alpha+\beta}}+\frac{2\,(2\,\omega_0\tau_c)^\alpha}{1+(2\,\omega_0\tau_c)^{\alpha+\beta}}\right] \tag{3}$$

in which C is the relaxation constant. According to [1] the constant C is the fraction of the second moment M_2 of the dipolar couplings that are fluctuating and characterized by a correlation time τ_c, ω_0 is the circular resonant frequency and α and β are parameters of the mFK distribution ($0 < \alpha, \beta \leq 1$; β characterizing the distribution width in the low temperature region where $\omega_0\tau_c \gg 1$). It can be seen that at $\alpha = \beta = 1$ Eq. (3) converts to the Bloembergen-Purcell-Pounds' expression, i.e. to the isotropic motional model [7]. The constant C for homogeneous solids should be equal to that part of the Van Vleck second moment of the NMR absorption line that is being averaged by motions of the resonant particles. This constant will be reduced in heterogeneous solids by the fraction of spins taking part in the motion [1]. The spin-lattice relaxation times have their minimal value $T_{1,\mathrm{min}}$ when the condition

$$\omega_0\tau_c = 0.62\left(\frac{\alpha}{\beta}\right)^{\frac{1}{\alpha+\beta}} \tag{4}$$

is fulfilled. The T_1 spin-lattice relaxation times have the minimum assuming the magnetic dipole-dipole interaction between proton-pair system to be the predominant relaxation mechanism, τ_c is correlation time of the molecular motion and ω_0 is the circular resonant frequency $\omega_0 = \gamma B_0$. That means in our case ($f_0 = 30\,\mathrm{MHz}$) that, e.g. for sample denoted PP/293/1, the segmental motions of the PP chains in the non-crystalline region appear when the correlation time τ_c has the value about $0.63 \cdot 10^{-9}\,\mathrm{s}$ at temperature where the T_1 minima are observed. The minima observed in the temperature dependences are related to the well known β-relaxation process that is related to a segmental motion of macromolecular chains in the non-crystalline regions of the polymeric materials.

CONCLUSIONS

We have found out that the stretching of the isotactic polypropylene fibres results in the decrease of the chain mobility in the amorphous regions. The increase of the relaxation times $T_{1,\mathrm{min}}$ lead to increase of C, which correlates with polymer crystallinity. Significant differences in the $\ln T_1$ vs. $10^3/T$ plots for different fibres were observed in the high temperature region. The activation energy, estimated from CW and pulsed NMR measurements for corresponding molecular motion in the temperature range where β-relaxation is dominant, is lower for the stretched PP fibres than that for non-stretched PP fibre. We assume that the activation of the molecular motion is an Arrhénius process. Experimental results show that the differences in the nuclear relaxation behaviour are closely related to the structural changes (crystallinity and orientation) caused by the stretching process at different temperatures.

REFERENCES

1. V. J. McBrierty, K. J. Packer, Nuclear Magnetic Resonance in Solid Polymers, CPU, Cambridge, 1993.
2. C. Hedesiu, D. A. Demco, K. Remerie, B. Blümich, V. C. Litvinov, Macromol. Chem. Phys. 209 (2008) 734–745.
3. V. J. McBrierty, D. C. Douglass, D. R. Falcone, J. Chem. Soc., Far. Trans. II 68 (1972) 1051.
4. D. Olčák et al., Polymer 26 (1985) 1455.
5. G. R. Murray, J. S. Waugh, J. Chem. Phys. 29 (1958) 483.
6. H. Schneider, Journal of Polymer Science: Part B: Polymer Physics, 29 (1991) 1171.
7. N. Bloembergen, E. M. Purcell, R. V. Pound, Physical Review 73 (1948) 679–712.

MoC SUPERCONDUCTING THIN FILMS FOR CPW RESONATOR AND PHASE SLIP QUBITS

M. Trgala, marian.trgala@fmph.uniba.sk, Dpt. of Exp. Phys., Comenius University, 84215 Bratislava, M. Leporis, leporis@biont.sk, Dpt. of nanotechnology, BIONT, a.s., Karloveska 63, 84229 Bratislava, T. Plecenik, tomas.plecenik@fmph.uniba.sk, Dpt. of Exp. Phys., Comenius University, 84215 Bratislava, P. Neilinger, pavol.neilinger@fmph.uniba.sk, Dpt. of Exp. Phys., Comenius University, 84215 Bratislava, M. Grajcar, grajcar@fmph.uniba.sk, Dpt. of Exp. Phys., Comenius University, 84215 Bratislava, P. Kus, kus@fmph.uniba.sk, Dpt. of Exp. Phys., Comenius University, 84215 Bratislava, A. Plecenik, plecenik@fmph.uniba.sk, Dpt. of Exp. Phys., Comenius University, 84215 Bratislava

INTRODUCTION

Recent experiments have shown that a superconducting high quality coplanar waveguide (CPW) resonator can be coherently coupled to a superconducting quantum two-level system [1]. The resonator can be used as i) quantum bus for superconducting qubits, ii) dispersive qubit read-out and iii) as a coupling element for individual qubits. CPW resonators have several advantageous properties. Their distributed elements construction allows better microwave properties than lumped element resonators which suffer from uncontrolled stray inductances and capacitances. They can be strongly coupled to superconducting qubits with coupling energies which cannot be achieved for atoms in optical resonators. On the other hand, the intrinsic quality factor is limited to ~10^6 which is much lower than for optical resonators. There is an experimental evidence that the quality factor is limited by two levels systems located in the surface layer of the CPW [2]. It was shown empirically that a residual surface resistance of superconducting resonators scales as the square root of the specific resistivity in the normal state. Resently, a new type of superconducting qubit, so called phase slip qubit, has been proposed [3]. Since the quantum phase slip can only be observed in materials close to the superconductor-insulator transition, which exhibits relatively high specific resistivity, it is not clear whether the decoherence will be suppressed as expected by authors in [3]. By measurement of the quality factor of the CPW resonator made from the same material as phase slip qubit, one can study the dissipative processes which influence decoherence time. Therefore we have designed and simulated CPW resonator build on MoC thin layer with resonance frequency 2.5 GHz and estimated quality 40 000. Our long term aim is a measurement of the resonator quality factor on the thickness of MoC thin film. With decreasing thickness there is a superconductor-insulator transition of MoC thin film due to Anderson localization [4]. Measurement of the losses of superconducting materials nearby the insulator state can provide valuable information whether such materials are suitable for quantum devices [3].

PREPARATION OF MoC THIN FILMS

MoC thin layers were prepared by reactive magnetron sputtering. The apparatus consists of deposition chamber, magnetron and Mo target (Mo 99.95%, Kurt J. Lesker) with 2.00” diameter and 0.125” thickness powered by stabilized dc source, vacuum system cascade with rotary vacuum pump producing pressure at about 7x10^{-1} Pa, turbomolecular vacuum pump (Pfeiffer TMH 261 type) and saturation system with nitrogen gas. The pressure is measured with commercial vacuum meters Pfeiffer Vacuum PKK 251 and D 356. The chambers ultimate vacuum is 1x10^{-6} Pa. Sputtering is realized in mixture of Ar and acetylene gas. The gas flow is regulated by needle valves. The sample holder, made from ceramic heater (boralectric heater,), allows regulation of the sample temperature up to 1200 ˚C. A calibrated resistor PT 100 is used as thermometer.

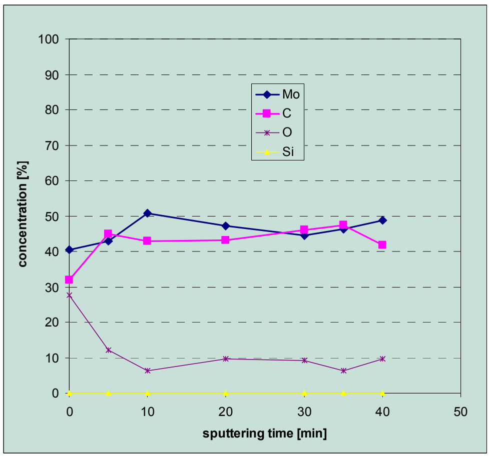

Fig. 1 Concentration profile of Mo, C and oxygen as a function of sputtering time

The samples of Moc layers are prepared on one-side polished silicon and single crystal sapphire substrate. Every single sample substrate was cleaned before deposition in ultrasonic washing machine with acetone, isopropylalcohol and distilled water. After the cleaning process the samples were placed on the sample holder and the chamber was pumped down to pressure 1x10^{-5} Pa and the sample was heat to 400-500 ˚C for 5-10 minutes to degasify its surface. In next step the sample temperature was degreased to room temperature and the partial pressure of acetylene and Ar gas was set to 4x10^{-3} – 9x10^{-3} Pa and 4x10^{-1} – 9x10^{-1} Pa, respectively. The discharge current was stabilized to 200 mA. The deposition rate was optimized and the best results were obtained for the rate 1-2 nm/min.. Deposition time was chosen to be 5 minutes which gives the thickness of the sputtered MoC thin film 50 nm. After the deposition the chamber was filled with N_2 gas up to atmospheric pressure. Concentration profile of Mo, C and oxygen is shown in Fig. 1.

RESULTS

The deposition process was optimize in order to achieve smooth thin film with high critical temperature T_c. The T_c was measured by four-point measurement of resistance (Fig. 2) as well as by non-contact ac susceptibility measurement (Fig. 3). Our samples show critical temperatures from 4.3 K to 7 K.

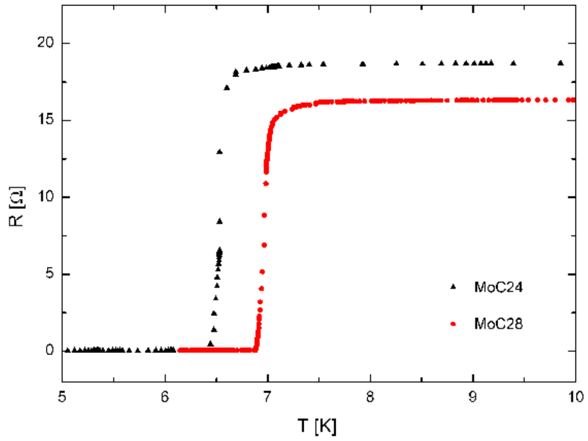

Fig. 2 Contact measurement of MoC layer, T_c at about 6.5 K and 7 K, measured with current 100 µA

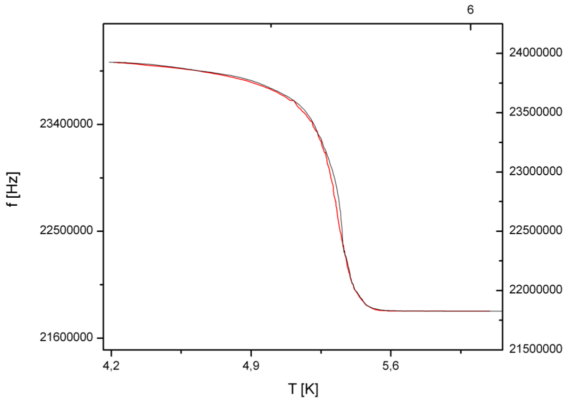

Fig. 3 Non-contact measurement of MoC layer, T_c at about 5.4 K

The T_c changes rapidly with concentration of carbide in MoC thin film. For better reproducibility we have decided to upgrade our system and replaced needle valve by high precision flow controllers. They should enable better control over the T_c and the roughness of the sample [5]. We expect to achieve maximal $T_c\approx8$ K. However, for the quantum phase slip devices the thin films with lower T_c can be more appropriate [3]. The most important properties required for quantum phase slip phenomena is smoothness and homogenity of the thin films.

CONCLUSIONS

We have prepared superconducting MoC thin film with very low average roughness <0.3 nm (Fig. 4) and $T_c\approx7$ K.

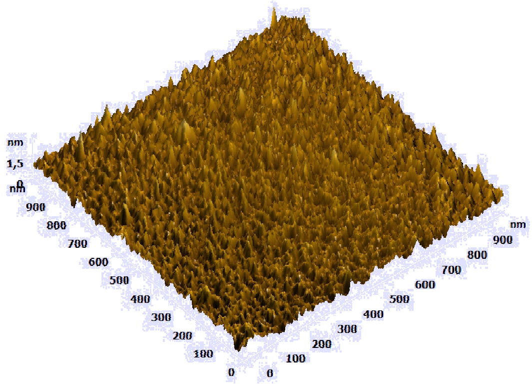

Fig. 4 1x1 µm AFM topography of an MoC thin film

Our results are promising and elaborated technology should enable us to produce superconducting structures which could exhibit quantum phenomena. The production of superconducting CPW resonators and superconducting phase slip qubits are in progress.

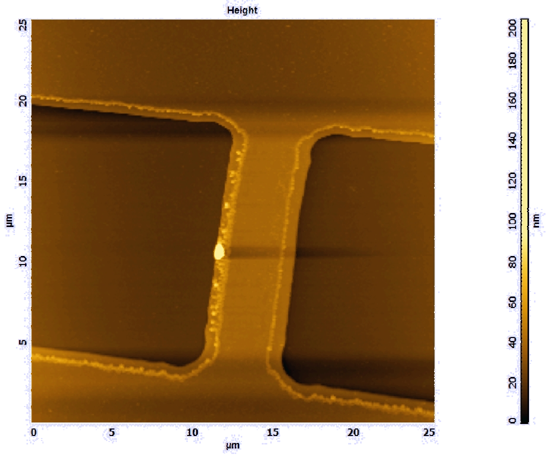

Fig. 5 AFM image of a MoC micro-bridge prepared by optical lithography

ACKNOWLEDGMENT: This work was supported by the Slovak Scientific Grant Agency Grant No. 1/0096/08, the Slovak Research and Development Agency under the contract No. APVV-0432-07 and No. VCCE-0058-07, ERDF OP R\&D, Project CE QUTE ITMS 262401022, and via CE SAS QUTE.

REFERENCES:

1. M.Göppl et al., J. Appl. Phys. 104, 113904 (2008).
2. J. Gao et al., Appl. Phys. Lett. 92, 152505 (2008).
3. J. E. Mooij, and C. J. P. M. Harmans, New Journal of Physics **7**, 219 (2005).
4. S. J. Lee and J. B. Ketterson, Phys. Rev. Lett. 64, 25 (1990).
5. J. Du et al., IEEE Trans. Appl. Supercnod. 17, 3520 (2007).

PREPARATION OF MgB_2 SUPERCONDUCTING THIN FILMS BY MAGNETRON SPUTTERING

J. Noskovic, jaroslav.noskovic@fmph.uniba.sk, Dpt. of Experimental Physics FMFI, Comenius University, 84215 Bratislava, A. Pidik, andrej.pidik@fmph.uniba.sk, Department of Experimental Physics FMFI, Comenius University, 84215 Bratislava, T. Roch, roch@fmph.uniba.sk, Dpt. of Experimental Physics FMFI, Comenius University, 842 15 Bratislava, M. Leporis, leporis@biont.sk, Dpt. of nanotechnology, BIONT, a.s., Karloveska 63, 84229 Bratislava, T. Plecenik, tomas.plecenik@fmph.uniba.sk, Dpt. of Experimental Physics FMFI, Comenius University, 84215 Bratislava, P. Kus, kus@fmph.uniba.sk, Dpt. of Experimental Physics FMFI, Comenius University, 84215 Bratislava, A. Plecenik, plecenik@fmph.uniba.sk, Dpt. of Experimental Physics FMFI, Comenius University, 84215 Bratislava

INTRODUCTION

Magnesium diboride (MgB_2) was found to be a superconductor with a critical temperature (T_c) of 39 K in January 2001 [1]. This discovery triggered an outburst of research on MgB_2 properties. Special hopes were associated with the fact that MgB_2 has possible utilization in microelectronic devices due to the relatively high T_c, simple crystal structure and the fairly high critical current density [2, 3].

Magnesium diboride is relatively stable substance, but metallic magnesium (Mg) is extremely reactive, easily oxidized and it has a low melting point of 650°C. On the other hand, the melting point of boron (B) is as high as 2550°C. The large difference in the characteristics of these two elements is considered to be the cause of the difficulties in fabrication of MgB_2 thin films. However, various methods have been used for the preparation of MgB_2 films, such as physical vapor deposition (PVD) [4], chemical vapor deposition (CVD) [5], and electrochemical plating [6]. Very good critical temperature (~ 39 K) has been achieved using pulsed laser deposition of B precursor, but this process requires ex situ annealing in magnesium vapor [7]. The direct deposition of Mg-B films with only minor finishing in the process of annealing is much more suitable for multilayer structures and complies with the standards of microelectronics. Samples that can be obtained in this way have lower critical temperature, but their surface is considerably smoother and also they have better uniformity.

This work is focused on preparation of MgB_2 thin films on Al_2O_3 substrates using magnetron sputtering and ex-situ annealing process in vacuum.

PREPARATION OF SUPERCONDUCTING THIN FILMS

Magnetron sputtering method is widely used for growing various types of thin films, partly because deposition is highly controllable, being dependent on an applied power involve and a working pressure. Fig. 1 shows a schematic diagram of our MgB_2 magnetron sputtering equipment used in magnetron sputtering method. The substrate holder rotates in the center and both targets are arranged in front of the holder to sequentially deposit Mg and B. For better process control shield with open apertures has been located between targets and holder.

Before carrying out the deposition, the chamber is usually evacuated to a vacuum level of at least $8x10^{-5}$ Pa and subsequently filled with argon to the working pressure $7.4x10^{-1}$ Pa. To deposit Mg-B precursor film, Mg and B are simultaneously sputtered using balanced magnetrons (ø 2”). Best results were obtained at DC (Mg target) 320 - 400 V and 85 – 95 mA and RF (B target) 200 or 225 W, respectively. After the deposition, samples are transferred quickly to another vacuum chamber, which includes annealing equipment. The heater is located horizontally above samples holder, which is cooled by flowing water (Fig. 2).

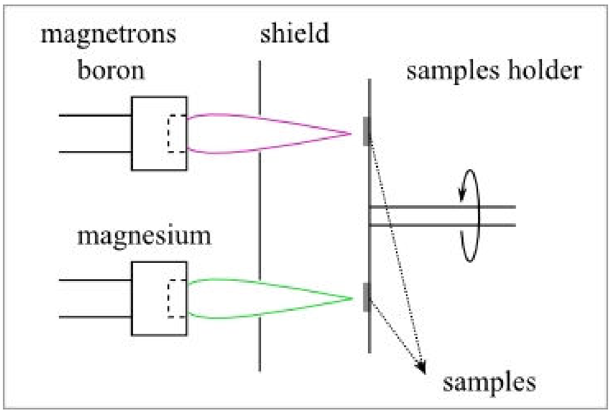

Fig. 1 Schematic diagram of Mg-B thin film equipment utilizing sputtering method.

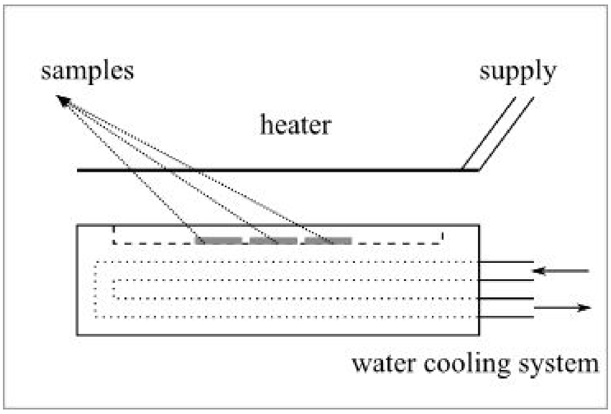

Fig. 2 Schematic diagram of annealing equipment.

The samples are quickly ramped in high vacuum to the temperature 600 – 720°C with a dwell time from 2 to 3 minutes and rapidly cooled down to room temperature.

Final films have dark brown color with goldish or silvery reflection and thickness abreast of several hundreds nanometers.

RESULTS AND CONCLUSION

In order to optimize our deposition process we have investigated electric transport properties (resistivity-temperature characteristics) and surface morphology of MgB_2 thin films. To obtain the optimum deposition conditions, the dependence of the thin film characteristics on the magnesium sputtering rate was studied, keeping boron sputtering rate fixed. Best results were obtain using parameters mentioned above. Our samples show critical temperature T_c from 29 to 34,7 K and transition width was usually less than 1,5 K (Fig. 3).

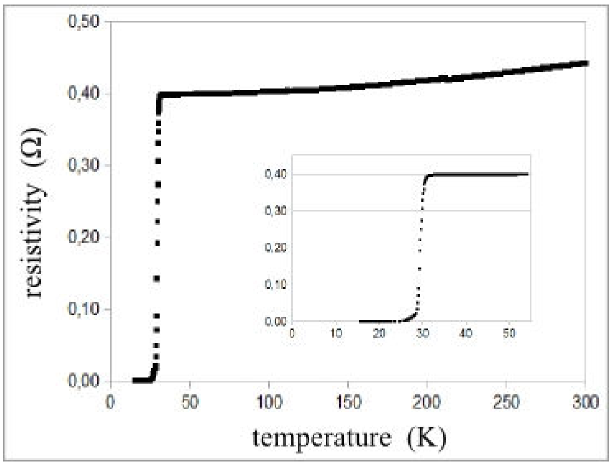

Fig. 3 Typical resistivity – temperature characteristics of a thin film produced by magnetron sputtering after ex-situ annealing process.

The surface morphology of MgB_2 films was investigated by AFM (Fig. 4). The sample was imaged at many different locations on the surface, in order to obtain an average value for the roughness (~ 10 nm). The images had area ranging from 200 nm up to 20 µm. The AFM makes use of a tip-moving scanning device. The microscope is driven by the Solver P47 - SPM electronic control data system from NT-MDT.

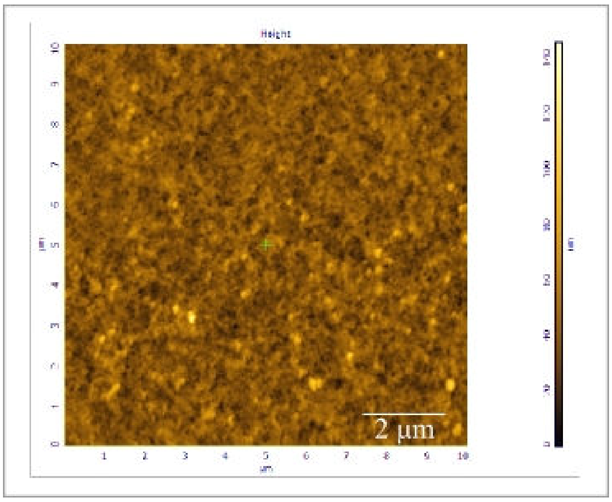

Fig. 4. AFM image with area of 10 µm x 10 µm of the MgB_2 thin film surface after 30 minutes of dry etching process.

Annealing process appears to be the most critical fabrication step. After several efforts, parameters mentioned above were found as the most suitable (640 – 710°C, 2 – 3 minutes). Quality of prepared samples varied considerably in dependence of temperature course during annealing process.

ACKNOWLEDGEMENT: This work was supported by the Slovak Research and Development Agency under the contract Nos. VVCE-0058-07, APVV-0034-07, APVV-0432-07 and LPP-0176-09.

REFERENCES

1. J. Nagamatsu, N. Nakagawa, T. Muranaka, Y. Zanitani, J. Akimitsu, Nature **410**, 63 (2001).
2. C.B. Eom, M.K. Lee, J.H. Choi, et all. Nature 411, 558 (2001).
3. H.J. Kim, W.N. Kang, E.M. Choi, M.S. Kim, K.H.P. Kim, S.I. Lee, Phys. Rev. Lett. 87, 087002 (2001).
4. R. Micunek, A. Plecenik, P. Kus, et all. Preparation of MgB_2 superconducting thin films by magnetron sputtering, Presented on Weak Superconductivity Symposium, Bratislava, September 2005.
5. X. H. Zeng, A. V. Pogrebnyakov, A. Kotcharov, et all., In-situ Epitaxial MgB_2 Thin Film for Superconducting Electronics, Nature Materials **1**, 35 (2002).
6. A. B. Jadhav, S. H. Pawar, Supercond. Sci. Techol. **16**, 752 (2003).
7. W. N. Kang, H.-J. Kim, E.-M. Choi, C. U. Jung, and S.-I. Lee, Science **292**, 1521 (2001).

USE OF CYLINDRICAL HPGe DETECTOR CANBERRA GX 4020 IN LOW-LEVEL RADIOACTIVITY MEASUREMENTS

J.Staníček, stanicek@fmph.uniba.sk, Department of Nuclear Physics and Biophysics, Faculty of Mathematics, Physics and Informatics, Comenius University, Mlynská dolina F1, 842 48 Bratislava 4

INTRODUCTION

The main problem in the experimental research in low-level gamma-ray spectrometry is that low intensity processes must be detected in the presence of the other higher intensity processes. For this reason for the successful experimental research of these processes must be used the high sensitivity spectrometer. The high sensitivity spectroscopic equipment must have a good-quality passive shield, because the crucial problem in low-level counting is the problem of background and besides the passive shield good-quality detectors must be used.

SEARCH OF FACTORS OF MERIT OF SINGLE SPECTROMETER

In our Low-level Gamma-ray Spectrometry Laboratory we studied the characteristics of the new cylindrical HPGe detector Canberra GX 4020. The detector has the crystal of dimension ø 61 x 62 mm, the relative efficiency 43.2 %, the ratio peak/Compton has the value 57 and the energy resolution for 1.33 MeV peak ^{60}Co is 2.0 keV. Electronic modules NIM fy Silena were used. The measured spectra were evaluated with the program EMCAPLUS made by fy Silena. We measured the values of the factors of merit in dependence on distances detector – source.

The value of the factor of merit, F, is characteristics for low-level gamma-ray spectrometers. Spectrometer with the highest value F has the highest sensitivity (the lowest limit of detection) for detecting gamma-rays of energy E in presence of interference radiation coming from the natural background of the spectrometer and from gamma-quanta higher energy of the emitters present in the measured sample. In our measurements the value of the factors of merit of spectrometer F was estimated from the equation

$$F = \frac{\varepsilon(E)}{\sqrt{B_N(E)}} \qquad (1)$$

where ε(E) is the peak efficiency for gamma rays of the energy E and $B_N(E)$ is the natural background of the spectrometer in the energy region E. The peak efficiency of spectrometer was estimated using point radioactive standards (^{241}Am, ^{133}Ba, ^{152}Eu, ^{22}Na, ^{137}Cs and ^{54}Mn). The standards were situated on the top of the detector, in the centre, in different distances detector – source (0, 5, 10, 15, 20 and 25 cm). The HPGe detector was located inside the simple lead shield (the layer of lead was 10 cm) and outside this shield.

From the obtained results it is evident that it is advantageous to use this single HPGe spectrometer for detection of single gamma-quanta in the measurements of low-level gamma-ray spectrometry.

RESULTS

Factors of merit of this single spectrometer were estimated with the point sources (gamma-rays) ^{241}Am, ^{133}Ba, ^{152}Eu, ^{22}Na, ^{137}Cs and ^{54}Mn also.

In Table 1 we list the factors of merit of the single HPGe spectrometer obtained in the measurements with 661.66 keV gamma-rays of ^{137}Cs located inside the shield (F_{Pb}) and outside the shield (F) that were obtained for different distances detector – source.

TAB. 1. Factors of merit of single HPGe spectrometer obtained for 661.66 keV gamma-rays of ^{137}Cs for various distances detector – source.

Distance detector-source [cm]	F [10^{-3}]	F_{Pb} [10^{-3}]
0	100.04 ± 3.02	343.70 ± 10.39
5	23.00 ± 0.49	78.80 ± 1.68
10	8.69 ± 0.18	29.80 ± 0.64
15	4.38 ± 0.09	15.00 ± 0.32
20	2.67 ± 0.06	9.20 ± 0.20
25	1.72 ± 0.03	5.92 ± 0.12

These factors of merit of single HPGe spectrometer in dependence on distances detector – source are shown in Figure1.

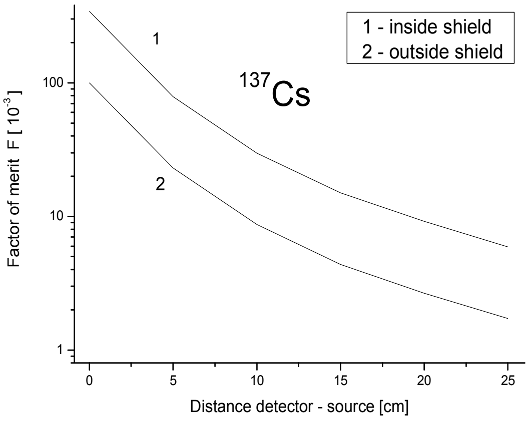

Fig. 1. Factors of merit of single HPGe spectrometer obtained with the measurement of ^{137}Cs inside and outside the simple lead shield in dependence on distances detector – source.

From the obtained results it is evident that simple shield improved factors of merit for all distances about 3.4 – times (the effect of the lower background).

The factors of merit of the single HPGe spectrometer obtained for ^{241}Am, ^{22}Na and ^{54}Mn sources when the detector was located inside the simple shield we list in Table 2.

Measured factors of merit of the single spectrometer in dependence on distances detector - source (detector was located inside the simple shield) obtained for three

TAB. 2. Factors of merit of single HPGe spectrometer obtained for gamma-rays of ^{241}Am, ^{22}Na and ^{54}Mn when the detector was located in simple shield.

Distance detector-source [cm]	Factor of merit [10^{-3}]		
	^{241}Am (59.54 keV)	^{22}Na (511 keV)	^{54}Mn (834.84 keV)
0	525.1±14.5	258.5±7.7	326.5±10.3
5	111.0±2.2	60.4±1.8	72.7±1.7
10	36.8±0.7	24.2±0.7	28.8±0.7
15	17.6±0.4	11.7±0.3	14.1±0.3
20	10.0±0.2	7.2±0.2	8.5±0.2
25	6.6±0.1	4.9±0.1	5.7±0.1

the most intensive gamma lines of ^{152}Eu: 121.78 keV (intensity 28.37 %), 344.28 keV (26.57 %) and 1408.01 keV (20.85 %) are shown in Figure 2. All errors of values of factors of merit were smaller then 3 %.

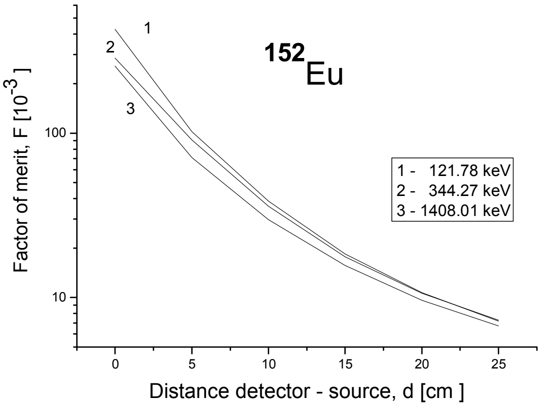

Fig. 2. Factors of merit in dependence on distances detector - source obtained in the measurements with ^{152}Eu. Detector was located inside the shield.

The dependences of factors of merit of the single spectrometer on distances detector – source (the detector was located inside and outside the shield) obtained for gamma lines 121.78 keV of ^{152}Eu are shown in Figure 3. The values of factors of merit obtained when HPGe detector was located inside the shield are about 4.6-times higher. For gamma rays of the energy 344.28 keV and 1408.01 keV of ^{152}Eu the values the factors of merit obtained with the detector located inside the shield were about 3.7 and 3.1-times higher than obtained when the detector was located outside the shield, respectively.

Only one obtained result can be compared with our earlier results – the value of the factor of merit of this spectrometer obtained for 511 keV gamma-rays when distance detector – source was zero (Tab.2). This value is higher than the factor of merit of the single spectrometer where we used the large-volume semiconductor coaxial HPGe detector with sensitive volume 280 cm^3 [1].

The obtained results show that the single spectrometer has good-quality and that this spectrometer is very suitable for the measurements of single gamma-rays in low-level gamma-ray spectrometry in generally.

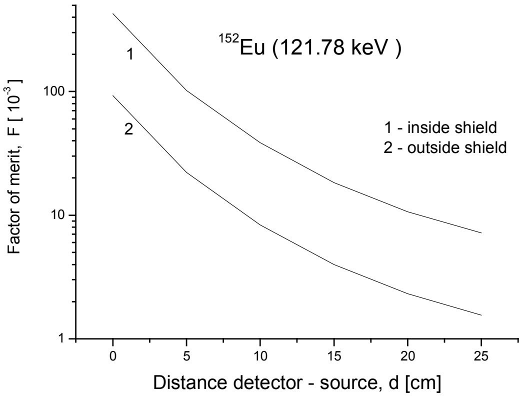

Fig. 3. Factors of merit in dependence on distances detector - source obtained in the measurements with ^{152}Eu for gamma line 121.78 keV.

CONCLUSION

Experimental determination of the factors of merit of single spectrometer containing the new cylindrical HPGe detector Canberra GX 4020 showed that this spectrometer is very suitable for the detection of single gamma-rays. In low-level gamma ray counting and spectrometry single HPGe spectrometers are used for estimating non-coincidence gamma rays emitted nuclei which are containing in measured samples. The single spectrometers we often use for estimating the radioactivity impurities of measured samples in which afterwards we are looking for some coincidence or anticoincidence gamma rays.

The obtained results showed that the new cylindrical HPGe detector Canberra GX 4020 will be very useful in experimental investigations in the field of low-level gamma rays counting and spectrometry.

REFERENCES

1. J. Staníček, Proceedings of the 16th Conference of Slovak Physicists, Žilina, 103 (2007).

MULTICOLOR PROBING OF FEMTOSECOND PULSE EXCITED SILVER NANOPARTICLES

A. Gaál, gaal@ilc.sk, Faculty of Mathematics, Physics and Informatics, Comenius University, Mlynská dolina, 842 48 Bratislava, Slovakia, I. Bugár, bugar@ilc.sk, M. Michalka, michalka@ilc.sk, A. Šatka, satka@ilc.sk, and F. Uherek, uherek@ilc.sk, International Laser Centre, Ilkovičova 3, 841 04 Bratislava, Slovakia, I. Capek, capek@upolign.savba.sk, L. Fialová, Polymer Institute, Slovak Academy of Scienses, Dúbravská cesta 9, 842 36 Bratislava, Slovakia, V. Szőcs, szocs@fns.uniba.sk, Faculty of Natural sciences, Comenius University, Mlynská Dolina, 842 15, Bratislava, Slovakia, T. Pálszegi, palszegi.tibor@savba.sk, Institute of Technology, Slovak Academy of Sciences, Dúbravská cesta 9, 845 13 Bratislava, Slovakia

INTRODUCTION

Surface plasmon resonance dynamics of metal nanoparticles (NP) is one of the most intensively investigated feature in the nanometer scale light-matter interaction in the last two decades [1-4]. NPs promising advanced applicability in the future memory units or photonic devices due to their special electron properties. In this paper colloidal silver solutions in toluene were investigated by femtosecond time-resolved absorption spectroscopy method to study electron-phonon interaction in confined conditions. The performed complex study allowed to compare the ultrafast relaxation processes experiments to computer simulations.

EXPERIMENTAL

Samples of silver nanoparticles with different sizes were synthesized on chemical way by inverse micelle technique described elsewhere [5]. Information about the NPs size was obtained from electron microscope analyse of monolayer films of colloidal samples. The particle diameters were determined according to the histogram analysis of scanning electron microscope images. The steady state absorption spectra of colloidal silver nanoparticles were recorded by classical UV-VIS spectrometer. Silver surface plasmon band causes the characteristic absorption maximum of samples at 400 nm.

The surface plasmon resonance dynamics were studied with femtosecond pump-probe technique in the VIS spectral region. After 400 nm excitation NPs were probed with broadband white light continuum pulses and recorded in range 400 – 600 nm to analyze the relaxation dynamics. The complex spectral-temporal information was obtained by detection of the time-resolved relative transmission reflecting the electron-phonon scattering in silver NPs. The registered data of time resolved absorbance were fitted by mono exponential function at selected wavelengths. Decay time dependence on probe wavelength was created in spectral range 460 – 600 nm.

RESULTS

The wavelength dependent decay times of silver NPs is shown on fig. 1a in case of 80 nm mean diameter NP and 0.4 mJ/cm^2 excitation energy flux.

The observed relaxation times were in range of 2 - 3.5 ps, which is related most probably to the electron-phonon scattering mechanism in silver NPs. The wavelength dependence was constructed in the region of induced absorption of silver NPs coated by organic surfactant. Monotonically decreasing relaxation time with increasing probe wavelength was the most often observed tendency. This finding has the role from the point of view of the determination of the relaxation process character. The changing relaxation time at increasing probe wavelength reveals different lifetime of the excited electrons at different energy levels. This observation suggests that the electron ensemble temperature is not equalized completely at the beginning of the electron-phonon relaxation process or the electron-phonon scattering process has different dynamics at different electron energies.

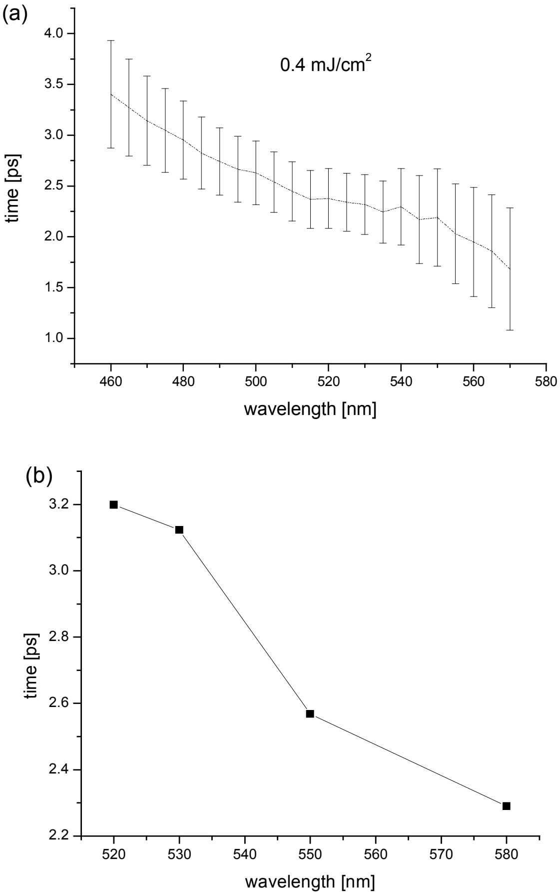

Fig. 1. Spectral characteristics of the induced absorption relaxation time in the case of sample of silver NPs with mean diameter 80 nm at excitation energy 0.4 mJ/cm^2 in the case of (a) experiment, and (b) computer simulation.

Computer simulations were based on two temperature model representing coupled electrons and phonons. The electron-phonon coupling coefficient was set as constant with value $g = 3.5 \times 10^{16}$ [W.m^{-3}.K^{-1}] [3]. In the fig. 1b is illustrated the computer simulation characteristics obtained at the same conditions that the experimental results revealing similar wavelength dependence. The performed computer simulation analysis revealed, that the observed wavelength dependence could be explained considering only the electron-phonon scattering. The second important finding is that the induced absorption lineshape is strongly dependent on the surrounding media dielectric constant and the excitation energy flux in correspondence to the experimental results.

CONCLUSIONS

Complex experimental study of transient absorption behavior in the case of colloidal silver NPs on the few picosecond time-scale was accomplished. The optical properties show size dependence due to electron confinement in range of small particle diameters comparable with lengths of visible wavelengths. The decay time of absorbance dynamics decrease with increasing probe wavelength in the case of majority of studied samples after 400 nm excitation. The performed simulation analysis resulted in reasonable correspondence with the experimental results both for the point of view of characteristic time and wavelength dependence tendency. The identified relaxation time values were in the 1 – 5 ps range for the whole set of samples. The clarification of the role and characteristic time of the electron-electron process needs further advanced study.

ACKNOWLEDGEMENT: We gratefully acknowledge the following organizations for their contribution: Slovak Research and Development Agency APVT-20-029804, APVV-0491-07, 20-0173-04, 0173-06, and Slovak scientific grant agency VEGA No. 1/0870/08, 2/7013/27, and 1/0046/08.

REFERENCES

1. U. Kreibig, M. Vollmer: Optical Properties of Metal Clusters, Springer-Verlag 1995.
2. J.-Y.Bigot, et al., Chem. Phys., 251 (2000) 181.
3. J. H. Hodak, et al., J. Chem. Phys., 111, 18 (1999) 8613.
4. Gaál, et al., Laser.Phys., 19, 5(2009) 961.
5. Capek, Advances in Colloid and Interface Science, 110 (2004) 49.

PHYSICS FOR SMALL KIDS

L.Ducárová, E.Bellová, Fakulta humanitných a prírodných vied, Prešovská Univerzita, ul 17. novembra, Prešov,
J.Víťazková, Ústav fyzikálnych vied , PF UPJŠ, Park Angelínum 9, Košice, M.Zentková, zentkova@saske.sk, IEP SAS, Watsonova 47, 040 01 Košice, Slovakia

MOTIVATION

Physics is a science with extremely high popularization potential. This fact is confirmed by commercial success of European science parks. The situation is however completely different in schools, where physics usually belongs to the less favourable subjects at all educational levels. The reason is hopefully related to the fact that within the standard curriculum there is no time enough to obtain personal experimental experience with physical laws and phenomena. The subject is very often reduced to the boring memorising of formulas without detailed information about its meaning. We thus proposed the Crayon Physics project for the small kids attending kindergarten (aged from 4 up to 6) or the first grade of elementary school (aged from 6 up to 10). The kindergarten kids can not read and write yet, one can therefore easily avoid mechanical learning of formulas and concentrate on the physics itself. Physics plays here the role of very efficient tool helping us to understand why and how the usual everyday processes are running around us. The main motivation for project is not popularization of the physics itself, but using physics for promoting the trust of the kids to the fact that the surrounding world is understandable on the rational basis and also that the physics and natural sciences in general do belong to the mankind's national heritage equally with the fine arts. The drawings of the scientific objects serve as the same source of beauty as paintings of people or countryside.

METHODOLOGY

The special methodology was developed for the Crayon physics course. Each cycle of experiments consists from 3 - 4 simple statements which should be attractive for the target group of kids. Each statement is proven by the series of simple experiments. As the kids can not read yet, the experiments are the only way how to prove validity of the statements. Experimental equipment is very simple and composed almost exclusively from the things everyone can find in its home. The kids can repeat the experiments at home in front of their family together with explanation of physical phenomena related. The total duration of the cycle should not exceed 60 minutes. It is impossible to keep the kindergarten kids attention for the longer time. The heart of each cycle is hands on experiments that means each kid, willing to do it so, should have the chance to try experiments itself, not only for reaching the skills, but for the psychologically very important personal experience with the topic.

The second phase of the cycle is coming the next day. The kids are drawing their impressions on the physical phenomena, they have studied yesterday. It is well known from psychology and psychiatry, that in this age category the drawing gives the most reliable information about kids emotions and thinking [1]. The painting is very often nothing more than mechanical record of experiments performed the day before. However, we got sometimes an authentic and very personal opinion of young researcher on the studied topic. The physical paintings serve to us as valuable information about the way, how the basic physical terms are understood by small kids. The painting phase is always supervised by professional painter, taking care about the artistic value of the drawings. The Crayon Physics is therefore an example of complex and integrated project combining sciences and arts.

EXAMPLE: SURFACE TENSION

Kids were playing games (Fig.1) to understand the difference between molecules from the bulk and those forming the surface layer and to understand the role of surfactants in washing process. The games were followed by simple experiments for example using.

Fig. 1. Molecules in action

Fig. 2. Painted molecules

spices for demonstrating the fact that the surface tension force is always acting perpendicularly to the surface and that water surface forms a membrane able to carry even small metal pieces. The most popular was however the part dealing with the physics of bubbles (Fig.3.).

The final phase was painting of physical projects. Some kids chose only one or two, most expressive experiments, while the others have drawn practically the whole program of experiments (Fig. 4, 5.).

Fig.3.How to make big bubbles

Fig.4. Physical painting. Making bubbles and water hill

Also this cycle of experiments has proven that the crucial thing for success of the cycle is choosing of the topics attractive for the target group. Once we started to speak about bubbles, the kids were very motivating to understand what is surface tension as they wanted to learn as much as possible about physics of bubbles.

CONCLUSIONS

The project of physics for small kids – Crayon Physics is running already more than 5 years. During that time we presented cycles of experiments on majority of interesting physical topics like: Motion, Force and gravity, Elasticity, Air, Sound, Light, Surface tension, Electricity and magnetism. Each cycle is prepared and realized by university students – future teachers as the part of their diploma thesis. Diploma thesis is written in the form of didactic material for teachers to enable them realization of the proposed physical cycles in the schools and kindergartens.

Fig.5. Overview of experiments

Our plans for close future are connected with adaptation of Crayon physics as effective methodology for physics coarse for kids with learning disabilities.

ACKNOWLEDGMENT: Presented work was supported by the projects LPP003006-Scientific incubator for pupils and students and LPP-0270-09- Science–user friendly .

REFERENCES

1. Davido R., La découverte de votre enfant par le dessin, L'Archipel, Paris, 1998.

ASSESSMENT OF SCHOLA LUDUS PROGRAM “SCIENCE BY PLAYING” AT SECONDARY SCHOOLS

D. Šimunová, simunova@fmph.uniba.sk, SCHOLA LUDUS – Centre for Support of Science Education and Non-formal Lifelong Science Education, Faculty of Mathematics, Physics and Informatics, Comenius University, Bratislava, Slovakia

INTRODUCTION

For many lower secondary pupils physics is just pointed out as the least preferred science subject. If you ask why their most common answers are “because it is stodgy, difficult and problematic to learn”, “we don´t understand formulas”, “we have to solve tasks only by inserting numbers”… and “Why to learn physics? What kind of profit can I gain for my future?”

But physics don’t have to be stodgy and scaring. The SCHOLA LUDUS Centre for Support of Science Education and Non-formal Lifelong Science Education at the Faculty of Mathematics, Physics and Informatics Comenius University in Bratislava is focused for long time on attractive ways of teaching science subjects, mostly physics.

PROJECT SCIENCE BY PLAYING

In years 2006 – 2008 the SCHOLA LUDUS Centre realized a complex educational, science-popularization program for lower secondary schools named “Science by playing”. The main goal of the program was to support long-term interest in science career among young people. The goal was filed through describing basic methods of scientific work to 12-15 years old pupils and through showing the science and specially one of science branch – physics – as a domain worth of their interest for everyday live and further learning.

Members of the SCHOLA LUDUS Project group realized wholly 5 mobile science-popularized modules. 47 lower secondary schools were involved in 3-5 day long programs in Nitra, Trnava and Trenčín region. Modules were prepared with emphasis on school physics’ themes and on attractive domain of modern science and technology. SCHOLA LUDUS strategies and tools for complex creative learning and teaching were used in development of particular modules.

1. Educational module „Kvap(k)aliny“ (the name combined words “Liquid” and “Drop”) focused on physical properties of liquids;
2. Educational module „Potápkaliny“ (the name combined words “Diver” and “Liquid”) focused on investigation of liquid properties linked with buoyancy (Archimedes' law) and hydrostatic pressure (Pascal’s law) with emphasize on untraditional applications in current science and technological research;
3. Educational module „How to draw it“ focused on deeper understanding of motion, (uniform, non-uniform), time, velocity, change and development concepts as well as on supporting visual thinking;
4. Educational module „What is this center point about?“ focused on the physical concept “center of mass”;
5. Educational module „Silence“ focused on acoustics – investigation of sound and its' properties with emphasize on untraditional and interesting application in current science and technology.

Each module consists of four educational parts:

1. Scientific theatre – shows with aim to engage pupils and motivate them for further learning the theme;
2. Interactive exhibition of simple physical demonstrations – each demonstration stimulate pupils to make their own hypothesis and to realize their own simple experiments;
3. Creative-discovery workshop focused on development of pupils' thinking and knowledge;
4. Educational game focused implicitly on verification and confirmation of new knowledge.

Totally 5648 pupils and 149 teachers involved in modules. Each school involved in program get a educational multimedia material include science theatre scenario, multimedia presentation used in program, methodic-didactical sheets for teachers and worksheets for pupils as well as photo- and video gallery from the modules realization.

CONCEPTUAL CHANGES

Summary conceptual changes are apparent from fulfilled activity sheets during CDW. For example, tasks from the CDW on droplets to gain preconceptions: “Draw and describe a water droplet. Consider your droplet in motion.... Where similar droplets occur?” – Pupils drew circles, tears and many tears. (Example of solution is shown on Fig. 1)

And at the end of CDW: “Try to sketch water droplet development by dripping from a faucet. Title the phases by short physical characteristics for each phase.” (Example of solution is shown in Fig.2) Pupils shifted their understanding from static droplets towards dynamic processes of fluids.

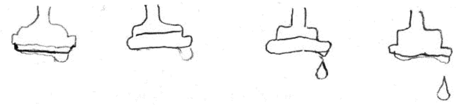

Fig. 1 Development of a droplet– preconception

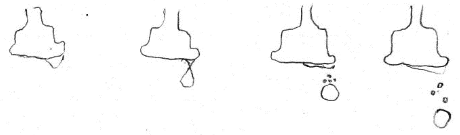

Fig. 2 Development of a droplet – changed conception

QUESTINNAIRES

A set of questionnaires was a component part of each realized module. Questionnaire A – we asked pupils before the realization of the module to fill introductory questionnaire focused on pupils' assertiveness to physics and scientific recognition, on pupils' conceptions about science and career in science and on pupils' interest to addict them to science in future. Questionnaire B – followed up the short-term effect of the educational module upon above mentioned factors. Pupils filled these questionnaires immediately after module realization. Questionnaire C – followed up the long-term effect of the educational module (approx. 3 months after realization). Questionnaire D – devoted to teachers, focused on identification the importance of the module to them and for their future pedagogical praxis. Questionnaires were prepared with simple statistical routine.

Program influenced pupils' look on physics and science in general. It drew attention to phenomena that pupils don't recognize before. Pupils want to look for more information about physics and about discovering in science and technology. They want to discover and investigate in future. Program changed also pupils' attitude to learning. They become aware of their right on their own conception about physical phenomena, of the right to change the conception and of the possibility and capability to ask questions and look for answers.

Particular educational parts were rated by pupils in numbers 1 - 5 (as in school). Exhibitions attained the best rating; they were followed by creative-discovery workshops, science theatres/shows and educational games. Particular parts attained "marks" 1,3 – 1,5. Most pupils expressed interest to take part in similar programs in future; they jump at such programs as component of school education.

On the basis of questionnaires we can allege that all parts of modules influenced pupils in positive way. One of positive assignments is active involving of pupils with less initial motivation (girls and slow pupils). Part of problematic subject matter becomes understandable and evident.

Most teachers adopt the program very positive as well. Some of them were inspired by program; some of them use particular parts in their lessons some will use obtained educational multimedia material in designing future lessons. Teachers observed positive change in pupils' behavior after modules realization. First of all pupils are more active - they ask more questions, discuss, involve imagination in etc..

One of the most valued teacher's statements is: The program influenced my view on teaching towards deeper and more effective learning/investigation of the real world, towards looking for connections, meaning of live, towards reverence of thinking and creativity. Gratifying is that even other subject (not physics) teachers rate the program focused on physics positively. As an illustration we can quote teacher of Hungarian language and literature and Slovak language and literature: „Program convinced me about necessity of concrete teaching. I will use it even on my lessons.

It is required that teachers will free of ossified ways of teaching and will be not afraid of bringing more creativity and invention to teaching process. Teachers have to give pupils more space to express their conceptions and confront these one another.

CONCLUSIONS

Results of realization and evaluation of the project SCHOLA LUDUS „Science by playing " are:

- Educational modules SCHOLA LUDUS as a educational form are effective means to show pupils that physics/science is interesting – educational modules free pupils from viewing physics obscure, modules show them physics charm and its attractiveness for future career.
- Educational modules SCHOLA LUDUS support learning, creativity, expression of pupils own opinions.
- Using educational modules with SCHOLA LUDUS strategies, forms and tools is universal – these tools allow preparing educational modules regarding any subject and any theme.
- Educational modules may be designed both - monothematic and interdisciplinary. This intensifies pupils' delight from learning.
- Educational modules SCHOLA LUDUS are means to change the way of teaching in harmony with school reform towards teaching attractive to pupils.

Success of the project SCIENCE BY PLAYING showed that educational modules are means to make physics more attractive to pupils and teachers. SCHOLA LUDUS department will continue to develop and realize educational modules also in the future. Should the physics be interesting and not frightening to pupils, it is necessary to introduce innovative educational approaches into everyday teaching praxis.

ACKNOWLEDGMENT: The program Science by playing was supported by European Social Fund. Our thanks belong to directors, teachers and pupils of all involved schools and to employees of local school authorities. Without them the project could not be realized.

REFERENCES

1. Monitoring reports 1 – 10 from the project "Science by playing" realization in years 2006-2008, Program was realized in frame of ESF project Nr. ITMS 2311230310150
2. K. Teplanová, M. Matejka, Selected Contributions from GIREP-EPEC Conference 2007 (ZLATNI REZ, Rijeka - 2008)

DIFFUSE COPLANAR SURFACE BARRIER DISCHARGE AND ITS APPLICATION FOR IN-LINE PLASMA TREATMENT

A. Zahoranová, zahoranova@fmph.uniba.sk, D. Kováčik, kovacik@fmph.uniba.sk, T. Homola, homola@fmph.uniba.sk, L.Bónová, bonova@fmph.uniba.sk, Department of Experimental Physics, Faculty of Mathematics, Physics and Informatics, Comenius University, Mlynská Dolina F2, 842 48 Bratislava, Slovakia, Ľ. Černáková, ludmila.cernakova@stuba.sk, Faculty of Chemical and Food Technology, Radlinského 9, 812 37, Bratislava, Slovakia, M.Černák, cernak@fmph.uniba.sk, Department of Experimental Physics, Faculty of Mathematics, Physics and Informatics, Comenius University, Mlynská Dolina F2, 842 48 Bratislava, Slovakia, Department of Physical Electronics, Faculty of Science, Masaryk University, Kotlářská 2, 611 37, Brno, Czech Republic

INTRODUCTION

Atmospheric-pressure non-thermal plasmas have recently received increased attention because of its use in „environmentally friendly" technology for various industrial applications. The development of atmospheric pressure plasma sources to replace plasma processing in vacuum system is a current trend in industrial plasma engineering [1].

Diffuse Coplanar Surface Barrier Discharge (DCSBD) developed at Comenius University in Bratislava and at Masaryk University in Brno [2] is an innovative plasma source, which was designed specifically for treating of web materials and planar workpieces, like flat glass, wooden materials, metal foils etc., fulfils the industrial requirements. For many surface treatment applications thin layer of atmospheric pressure plasma may be more useful like the large volume of plasma and can provide advantages in energy efficient, exposure time and technical simplicity.

This type of non-equilibrium plasma source was already successfully tested for on-line plasma activation and modification of surfaces of nonwoven textile [3, 4], wood [5], glass [6] and flat aluminium [7].

Some of the experimental results on in-line ambient air plasma polypropylene fabrics activation, glass, aluminium and wood surface plasma treatment will be presented.

DIFFUSE COPLANAR SURFACE BARRIER DISCHARGE

Atmospheric-pressure, non-equilibrium plasmas produced by dielectric barrier discharges (DBD) are very attractive for various industrial applications (pollution control, sterilization, ozone generation, surface modification) because of their low-cost, high operation speed and the ability to operate without vacuum systems. Unique type of DBD generator, the so called Diffuse Coplanar Surface Barrier Discharge (DCSBD), is able to produce a thin layer of non-equilibrium plasma with high power density (up to 100 W/cm^3) in practically any working gas (even in pure oxygen) [2]. Comparing to other surface DBD set-ups (as e.g. that invented by Masuda et al. [9]), major advantage of the DCSBD is that the surface micro-discharges are not in contact with metallic electrodes and thus the lifetime of the electrode system is not limited.

The above mentioned properties of the DCSBD designate it for surface treatment of wide scale of materials (e.g. polypropylene non-woven fabrics, polyester cords and wood).

NONWOVEN TEXTILE SURFACE PLASMA TREATMENT

The unique performance characteristics of DCSBD plasma source are illustrated by results on ambient air-plasma hydrophilization of light-weight spun-bonded polypropylene (PP) nonwoven textile, where the permanent hydrophilization was obtained at power consumption less than 1 kWh/kg. The efficiency of the hydrophilic character of treated PP textiles was verified by measurement of strike-through time as a function of treatment time and discharge power. After short plasma exposure (1 sec) the nonwoven samples became hydrophilic, and in addition the treated textiles were permanently hydrophilic even after 20 weeks without any washing out effect.

Surface modification of polypropylene non-woven fabrics by atmospheric-pressure plasma activation followed by acrylic acid grafting was successfully tested also [3, 4].

WOOD SURFACE PLASMA MODIFICATION

Two types of plasma processes were investigated using plasma generated by DCSBD at atmospheric pressure for treatment of wood surfaces [5]:

- increase hydrophilization on wood surface and so improvement adhesive properties of planar wood workpieces before their spray painting and finishing
- increase hydrophobization of wood surface of wood surface by plasma-polymerization.

Surface properties were characterized by several diagnostic methods: measurement of surface free energy, uptake time, ATR-FTIR spectra, adhesion test. The results have shown the most marked increase hydrophilization in pure oxygen.

Plasma-polymerization of hexamethyldisiloxane and hexamethyldisilazane was successfully tested for the hydrophobization of wood surface (see Fig. 1).

GLAS SURFACE PLASMA TREATMENT

The surface modification test of glass samples treated using DCSBD discharge was carried out in ambient air at atmospheric pressure (Simple experimen-

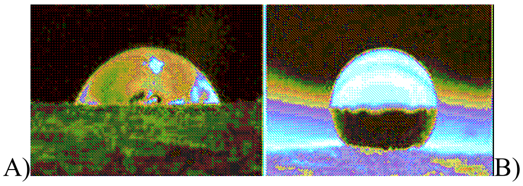

Fig. 1. Water droplet on the wood a) before coating b) after coating of hydrophobic layer at the concentration 0, 6 mmol/l HMDSO + N_2

tal set-up -see Fig. 2). Treated glass surfaces were characterized by the means of contact angle measurements, AFM, SIMS and MALDI TOF MS analyses [6]. The results illustrates an increase of the total surface energy due to cleaning and removing contaminants from the glass surface, what was proven for example by the contact angle decrease from 29.03° to 13.82° for treatment time 1 s in ambient air-plasma. Even short treatment times, on the order of seconds, were sufficient to make treated glass surfaces hydrophilic. By the means of the SIMS and MALDI TOF MS analyses it was shown, that the removing of the organic contamination from the treated surfaces by the action of DCSBD plasma plays important role in the improvement of the wettability of the glass surface. The energy consumption of the DCSBD system was estimated to ~ 5. 10^3 W s m^{-2} of the glass activated, which is 2 orders less than the energy consumption of the competing plasma jet systems.

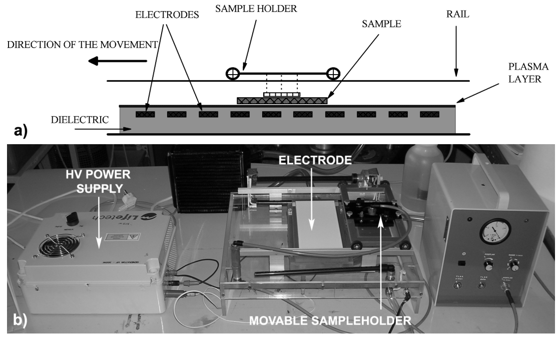

Fig. 2. Scheme a) and photo b) of the dynamic treatment mode device.

ALUMINIUM SURFACE PLASMA TREATMENT

Presented results of the plasma activation of aluminium surface demonstrate that the DCSBD plasma is an effective tool in enhancing the wettability (Fig. 3) of the treated surface [7]. The observed effect was assigned to the removal of the organic contamination from the treated surface with possible increase in the surface hydroxyl group density.

The ageing effect of the treatment was examined the wettability of the treated surface decreases with the storage time. This was assigned to the adsorption of the organic compounds from the surrounding ambient on the treated surface, which assumption was supported by the result of the vacuum storage experiment. The preliminary results indicate that this novel atmospheric-pressure plasma source may be useful for the activation and cleaning of aluminium surface

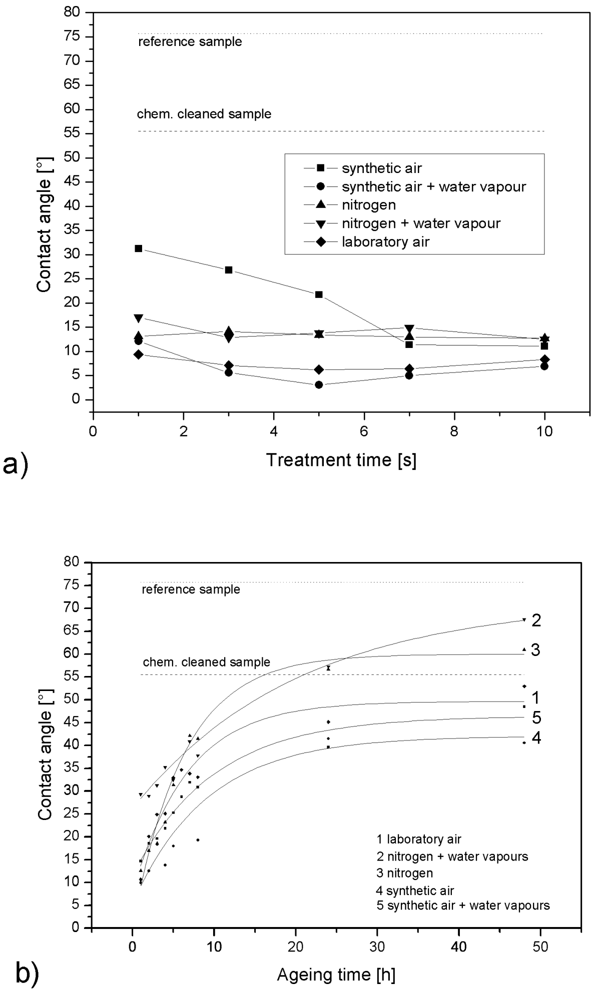

Fig. 3. Contact angle measurements of the plasma treated Al samples. Contact angle as a function of treatment time in various working gases (a) and the ageing effect of the plasma surface treatment (b)

ACKNOWLEDGMENT: This research has been supported by the Slovak Scientific Grant Agency, Project No. VEGA 1/4014/07, by the Slovak Research and Development Agency, Project No. APVV-0491-07.

REFERENCES

1. J. R. Roth, Industrial Plasma Engineering, Vol.2: Indt. Of Phys. Publishing, Bristol and Philadelphia, 2001
2. M. Šimor et al., Appl. Phys. Lett. **81** (2002) 2716.
3. M. Mikula et al., Journal of Adhesion Science and Technology, **17**, No. 15 (2003) 2097.
4. Ľ. Černáková, D. Kováčik, A. Zahoranová, M. Černák, M. Mazúr, Plasma Chemistry and Plasma Processsing. **25**, No. 4 (2005) 427.
5. Odrášková, M., Ráheľ J., Zahoranová, A., Tiňo, R., Černák, M.: Plasma Chem Plasma Process **28** (2008) 203.
6. A. Buček, T. Homola, M., Aranyosiová, D. Velič, T. Plecenik, J. Havel, P. Sťahel, A. Zahoranova. Chemické listy **102** (2008) 1459.
7. L. Bónová, A. Buček, T. Plecenik, A. Zahoranová, M. Černák, Chemické listy **102** (2008) 1452.
8. S. Masuda, K. Akutsu, M. Kuroda, Y. Awatsu, Y. Shibuya, IEEE Transactions on Industry Applications **24** (1988) 223.

COMPARISON OF PLASMA SURFACE TREATMENT EFFICIENCY OF NONWOVENS USING DIELECTRIC BARRIER DISCHARGES AS POTENTIALLY APPLICABLE PLASMA SOURCES

J. Kubincová, kubincova@gimmel.ip.fmph.uniba.sk, D. Kováčik, kovacik@fmph.uniba.sk, A. Zahoranová, zahoranova@fmph.uniba.sk, T. Homola, homola@gimmel.ip.fmph.uniba.sk, M. Černák, cernak@fmph.uniba.sk,
Department of Experimental Physics, Faculty of Mathematics, Physics and Informatics, Comenius University,
Mlynská dolina, 842 48 Bratislava, Slovakia

INTRODUCTION

Dielectric barrier discharges (DBDs), in which at least one of the electrodes is separated from the discharge area by dielectric, offer the simple way of avoiding plasma thermalization at atmospheric pressure. In general, the arrangement of the DBD electrodes system can be very various and depends on the specific application. Plasma of DBD consists of narrow filaments distributed statistically across the electrode area. Due to the current flowing through these filaments the electric charge is accumulated on the insulating dielectric barrier and consequently the externally alternating applied voltage is screened by this charge and the filaments extinguish. In the next half-periode of applied voltage the process goes further by contraries. This process is responsible for non-equilibrium plasma generated by DBDs.

EXPERIMETAL

In our experiment we tried to compare the applicability of volume DBD (VDBD), surface DBD (SDBD) and special designed coplanar DBD, so called Diffuse Coplanar Surface Barrier Discharge (DCSBD) [1, 2], for hydrophilic surface treatment of thin PP nonwoven textile (PPNW) - PEGAS Nonwovens, Czech Rep. - with the surface density 18 g/m^2.

Discharges were fed by sinusoidal high voltage and surface treatment was carried out in ambient air at different treatment time which was defined by the towing speed of textile. For the textile towing we used the mechanical part of plasma device for the continuous textile surface treatment *ZUP 200* [3, 4]. The particular dielectric barrier discharges used in our experiments are shown in Fig. 1 together with the schemes of their electrodes system.

The electrodes system of VDBD consists of two parallel Al_2O_3 (96% purity) dielectric plates with the screen-printed conductive area made of silver conductor paste, which were installed in relative distance approx. 0.7 - 1 mm (Fig. 1a). The difference in silver coated area inhibited the formation thermal microfilaments of the electrode boundaries.

In case of SDBD and DCSBD the dielectric is represented again by alumina of the same purity. The SDBD electrodes system is created by the inductive rectangle electrode on one side of alumina layer and discharge strips electrode on its upper side (Fig. 1b), whereas the DCSBD electrode consists of 19 pairs of silver strip electrodes embedded 0.5 mm below the surface of Al_2O_3 ceramics (Fig. 1c). Each of these electrodes systems were cooled by circulating insulation oil.

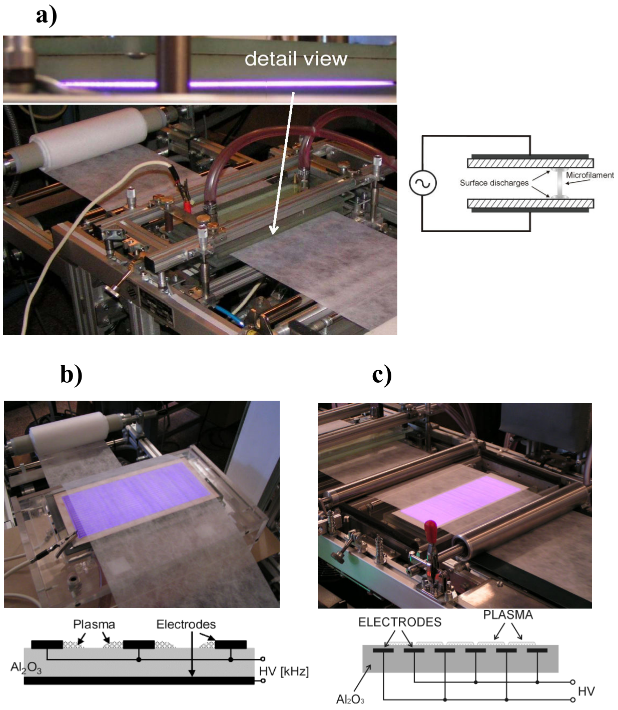

Fig. 1. The photos of volume DBD (a), surface DBD (b) and DCSBD (c) in experimental arrangement and the schemes of their electrodes system.

The quality and permanency of hydrophilic modification was tested by common strike-through time measurement and by critical wetting surface tension (CWST) measurement. Some of our results are summarized in TAB. 1 - 3 and presented by Fig. 2.

TAB. 1. Results of 18 g/m^2 PPNW treatment by VDBD at 250 W.

Fabric speed [m/min]	6 m/min	7 m/min	8 m/min
Treatment time [s]	0.8 s	0.7 s	0.6 s
Strike-through time [s]	14.9±7.4	7.9±1.2	7.8±3.4
Surface tension[mN/m]	70.3	80.3	81.2

The surface tension of untreated 18 g/m^2 PP nonwoven (PPNW) was 39 mN/m and corresponding strike-through time was greater than 100 sec, which is a conclusive evidence of hydrophobic nature of initial fabric surface.

Plasma treatment by VDBD for more than 0.9 sec resulted in a significant damage of rather thin material by some created localized discharge microfilaments. Plasma treatment for times shorter than 0.6 sec resulted in worse wettability improvement and higher statistic error of measured data. At low fabric speed is observed interesting phenomenon when wettability of PPNW is changed for worse. This is explained by the higher degree of spatial stabilization of discharge microfilaments, which will eventually result in the PPNW pinholing. Spatially localized microfilaments provide non-uniform fabrics treatment causing large statistical error of wettability characteristics.

TAB. 2. Results of 18 g/m^2 PPNW treatment by SDBD at 250 W.

Fabric speed [m/min]	1 m/min	2 m/min	3 m/min
Treatment time [s]	4.8 s	2.4 s	1.6 s
Strike-through time [s]	8.42±1.81	8.01±1.57	8.66±2.48
Surface tension[mN/m]	94	90.2	85.6

Air plasma of SDBD caused decrease of strike-through time only to the value approx. 8 sec. The disadvantage is that this surface discharge operating at high power densities above of 1 W/cm^2 is of limited value for industrial implementation because of a limited life-time of the discharge electrodes that are in a direct contact with the discharge plasma.

TAB. 3. Results of 18 g/m^2 PPNW treatment by DCSBD at 250 W.

Fabric speed [m/min]	1 m/min	2 m/min	3 m/min
Treatment time [s]	4.8 s	2.4 s	1.6 s
Strike-through time [s]	3.14±0.18	8.86±1.78	8.99±2.20
Surface tension[mN/m]	> 96.6	95.8	89.4

The treatment by DCSBD did not result in any pinholing damage. DCSBD plasma treatment for the time period shorter than 1.5 sec proved to be insufficient, with a large statistical error of wettability characteristics. Only the treatment time of 1.6 sec and more resulted in the improvement of wettability comparable to VDBD. Maximum improvement of wettability immediately after the treatment was obtained for 4.8 sec DCSBD treatment time. The samples of PPNW treated by DCSBD plasma for 4.8 sec were hydrophilic even after 20 weeks from treatment date with strike-through time approx. 5 sec [4] what indicates that only using DCSBD plasma it is possible to carry out permanent hydrophilic surface treatment of PP nonwovens. For illustration Fig. 2 shows how the strike-through time was changing within one month after treatment for samples exposured in DCSBD plasma at two different power values.

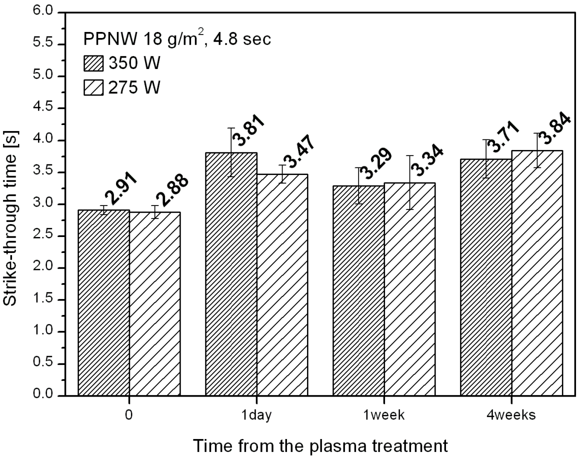

Fig. 2. The values of strike-through time for 18 g/m^2 PPNW measured at different time after DCSBD plasma treatment. The samples were treated 4.8 sec in ambient air at power a) 275 W, b) 350 W.

CONCLUSIONS

Presented results focused on hydrophilic surface plasma tretament of thin PP nonwovens using three different DBDs confirmed that plasma of DBDs is applicable for surface treatment of PPNW aiming to increase their initially low surface energy and make them hydrophilic. But from the industry applicability point of view we supposed that only DCSBD might be involved in continuous in-line surface treatment process [5] due to excellent properties of its plasma, unlimited life-time, robustness, safety and ability to operate in dusty ambient [6].

ACKNOWLEDGMENT: Authors would like to express thanks for financial support to Slovak research and development agency (grants No. APVV-0491-07 and APVV-0485-06) and Ministry of Education of the Slovak republic (grant No. AV-4/2033/08).

REFERENCES

1. M. Šimor, J. Ráheľ, P. Vojtek, M. Černák, Appl. Phys. Lett. **81**, 2716 (2002).
2. M. Černák, Ľ. Černáková, I. Hudec, D. Kováčik, A. Zahoranová, Eur. Phys. J. AP **47**, article number: 22806 (2009).
3. D. Kováčik, A. Zahoranová, A. Buček, J. Ráheľ, Ľ. Černáková, M. Černák, Proceedings: Contributed Papers of the 17th Symposium on Physics of Switching Arc, Vol. I., Nové Město na Moravě, September 10-13, 2007, Czech Republic, p. 129.
4. D. Kováčik, A. Zahoranová, A. Buček, M. Černák, Contributed Papers of HAKONE XI, Vol. 2, Oléron Island, September 7-12, 2008, France, p. 493.
5. M. Černák, D. Kováčik, A. Zahoranová, J. Kubincová, J. Ráheľ, P. Sťahel, Čs. Čas. Fyz. **59**, 250 (2009).
6. http://gimmel.ip.fmph.uniba.sk/treaters

APPLICATION OF DCSBD DISCHARGE FOR ALUMINIUM SURFACE

L. Bónová, bonova@fmph.uniba.sk, A. Zahoranova, M. Zahoran, and M. Černák, Katedra experimentálnej fyziky, Fakulta matematiky, fyziky a informatiky, Univerzita Komenského, Mlynská dolina F-2, 842 48 Bratislava

INTRODUCTION

Aluminium is a widely used material for many applications such as automobile industry, microelectronics, aerospace field and many others. In industry for temporary corrosion protection or lubrication sheet metals are coated by organic oils. This coatings need to be removed in advance of further metal manufacturing processes. Usually cleaning is performed in wet alkaline or acid baths so these chemical treatments are not environmentally friendly. Therefore the non-equilibrium atmospheric-pressure plasma treatment seems to be a suitable alternative to the wet chemical methods [1,2]. Another advantage of this environmentally safe treatment could be the activation of material surface.

The presented experimental results show the activation, cleaning of aluminium sheets using so-called Diffuse Coplanar Surface Barrier Discharge (DCSBD).

RESULTS AND DISCUSSION

The simple scheme of experimental apparatus is shown in the figure 1. Surface modification was carried out using the DCSBD generated in air at atmospheric pressure [3].

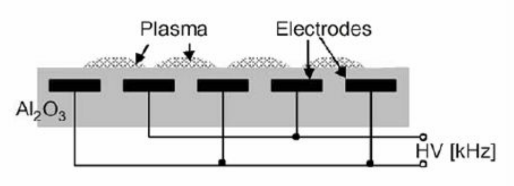

Fig. 1. Schematic drawing of the DCSBD electrode arrangement

As the samples aluminium plates (99.5% Al) and Al-coated Si-wafers were used. They were chemically cleaned. To obtain homogeneous treatment the samples were moved during the treatment process. By changing the movement speed it is possible to change the treatment time.

The DCSBD electrode geometry consists of stripline silver electrodes embedded 0.5 mm below the surface of 96 % Al_2O_3 ceramics. The discharge was powered by 14 kHz sinusoidal voltage supplied by HV generator. The active plasma area has the dimensions of 200 × 80 mm. The thickness of the plasma layer generated on the surface of the Al_2O_3 ceramics is approximately 0.5 mm. The power supplied to the reactor was approximately 320 W.

In general, a good wettability of metal surface is considered as a good indication that organic contamination was absent from the cleaned surfaces. As a consequence, the following surface energy measurement was used as an indication of the plasma surface cleaning efficiency. After the plasma cleaning the contact angle of one drop of distilled water (1 μl) on the treated surface was measured by the means of the Surface Energy Evaluation System. The surface of samples was analysed by AFM as well to see the effect of plasma treatment on its roughness. It was found out that the surface roughness remains unchanged.

The samples were spin coated by oil to see the cleaning effect of the plasma treatment. The treatment was done in air plasma. Then EDX analysis of the surface was done. The results showed that non-equilibrium plasma treatment results in a distinctive decrease of carbon and oxygen concentration.

In the figure 2 the dependence of contact angle on the treatment time is shown. After the treatment lasting for 1 s the contact angle changes dramatically.

In the figure 3 the ageing effect of the 3 s treatment is shown. The contact angles on the sample stored in ambient air are compared to the contact angle of an untreated sample. From the figure it is clear that the wettability of the treated surface decreases with the storage time.

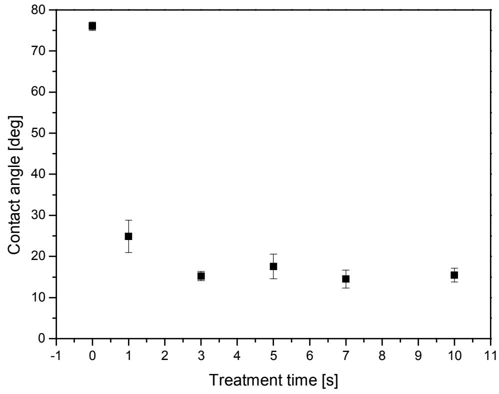

Fig. 2. Contact angle of distilled water droplets as a function of treatment time

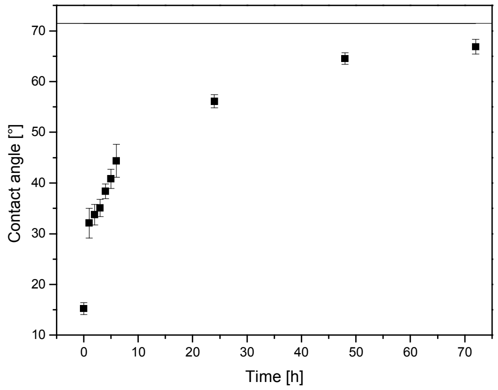

Fig. 3. Ageing effect of 3 s treated sample in air

CONCLUSIONS

The presented results of application of Diffuse

Coplanar Surface Barrier Discharge indicate that this novel type of atmospheric-pressure plasma source may be an effective tool in enhancing the wettability of treated aluminium surface. Treatment time of 3 s is sufficient enough to turn the treated aluminium surface hydrophilic.

ACKNOWLEDGMENT: This research has been supported by the Slovak Scientific Grant Agency, Project VEGA No. 1/4014/07 and Grant UK/415/2009.

REFERENCES

1. D.H. Shin, Ch.U. Bang, J.H. Kim, K.H. Han, Y.C. Hong, H.S. Uhm, D.K. Park, K.H. Kim: SurfCE AND Coatings Technology 2007, Vol..201, 4939-4942.
2. S.J.M. Pinson, J. Collins, G.E. Thompson, M.R. Alexander: ATB Metallurgie 2003, Vol.43, No. 1-2, pp 448-453.
3. M. Šimor. J. Raheľ, P. Vojtek, A. Brablec, M. Černak: Applied Physics Letters, 81, 2002, 2716-2718.

MODELLING OF CHEMICAL KINETICS OF NEGATIVE IONS IN NEGATIVE CORONA DISCHARGE IN N_2/O_2 MIXTURES

J. Páleník, jan.palenik@fmph.uniba.sk, J. Országh, P. Papp, Š. Matejčík, Department of Experimental Physics,
Faculty of Mathematics, Physics and Informatics, Comenius University, Mlynská dolina F2, 842 48 Bratislava

INTRODUCTION

This work is motivated with experimental studies of ion mobility of negative corona discharge in pure oxygen and in mixture of nitrogen/oxygen [1]. The aim of the study is to find a simple kinetic model that predicts relative concentrations of final products – negative ions. In present model we consider 171 chemical reactions; however, no reactions with transient or excited states are taken into account. Model does not count with spatial distribution, decomposition on walls, heat transfer, or interaction with photons, but focuses only on pure chemical kinetics. Such model is limited by rate constants available from previous experimental or theoretical papers.

MODEL

Main aim of this work is to find a set of chemical reactions that are the most important for modelling of negative corona discharge in pure O_2 and dry and wet mixtures of N_2/O_2. To achieve this, we have collected available rate constants. These rate constants were extracted from previous works (mostly [2-9]; other minor sources are not mentioned due to lack of space). Since the rate constants of some reactions with electrons are subject to change with the distribution function of electronic energy, we included the reactions for which the rate constant could be identified for fixed temperature at 300 K. Thus our final model includes 171 reactions.

Differential equation for the concentration of particle *i* in *j* chemical reactions with rate constants k_j is

$$\frac{dn_i}{dt} = \sum_j \pm k_j \prod_a n_a \qquad (1)$$

where $\Pi_a n_a$ is a product of concentrations of all reactants involved in reaction j. Sign of k_j depends if the concentration of element *i* is increasing or decreasing; for products the sign is positive while for reactants is negative. Right side represents change of concentration in infinitesimal time element. Such equation should be written for all elements involved. This leads to set of coupled differential equations. We used Radau5 method to solve the set of differential equations.

For model of pure oxygen we considered 7 reactants and 20 reactions. For model of dry mixture of N_2/O_2 we considered 16 reactants and 57 reactions. And for wet mixture of N_2/O_2 we considered 49 reactants (including water clusters) and 171 reactions.

INITIAL CONDITIONS

Approximate initial concentrations were needed for this model. Initial conditions were obtained by measuring IR absorption spectra in relevant mixtures of N_2/O_2 in negative corona discharge, comparison of bond strengths and estimate of authors.

RESULTS

Model is quite stable to slight variations of initial conditions. Ions O^-, O_2^-, NO_2^- in all cases fade away rapidly. In case of O^- the rate of decrease does not depend on initial ratio of N_2/O_2 nor on presence of water in model. We consider the most important channel for decomposition of O- this reaction

$$O^- + O_2 + O_2 \rightarrow O_3^- + O_2 \qquad (2)$$

Rate constant for this reaction is k_{66} = 1.1x10^{-30} cm^{6}s^{-1}. In case of O_2^- the situation is quite the same; the rate of decrease does not depend on initial ratio of N_2/O_2, nor on presence of water in model. However, it is more difficult to identify the most important channel of it's decomposition. Nevertheless, we assume that these reactions are responsible for rapid decomposition of O_2^-

$$O_2^- + H_2O + O_2 \rightarrow O_2^-(H_2O) + O_2 \qquad (3)$$

$$O_2^-(H_2O) + NO_2 \rightarrow NO_2^- + H_2O + O_2 \qquad (4)$$

with these rate constants k_{80} = 1.6x10^{-28} cm^{6}s^{-1} and k_{66} = 9.10^{10} cm^{6}s^{-1}. According to our model the only visible basic ions in experiment [1] should be O_3^- and NO_3^-. These results partly agree with results obtained by experiment [1]. If water is included, decrease of concentration of O_3^- is observed (Fig. 1). This decrease depends on amount of oxygen considered and influences the visibility (according to the rate of decrease) of ion in experiment [1] only if initial level of O_2 is smaller than 10% of total volume. The concentration of NO_3^- develops the same for every N_2/O_2 ratio, no matter whether with or without water (Fig. 2). Model also predicts that cluster O_3^- (H_2O) should be around noticeable level (Fig. 3). However, the experiment [1] does not give such results. Other water clusters should not be visible according to this model.

CONCLUSION

The output of this model corresponds with the results of work [1] for all basic ions. However results obtained for water clusters dos not as well as the effect of decrease of O_3^- in model with H_2O.The numerical model as well as the complete list of references used in this work are available on request for further development or for purpose of performing calculations with different initial conditions.

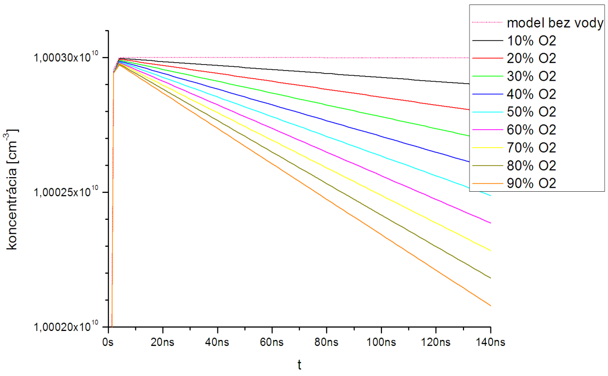

Fig. 1. Time development of concentration of O_3^- (every line except the first one represent model with water with different N_2/O_2 ratio).

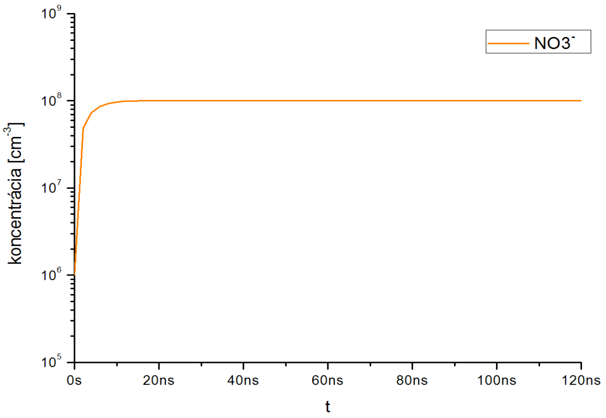

Fig. 2. Time development of concentration of NO_3^- ; the same for every ratio of N_2/O_2, no matter whether mixture was with or without water.

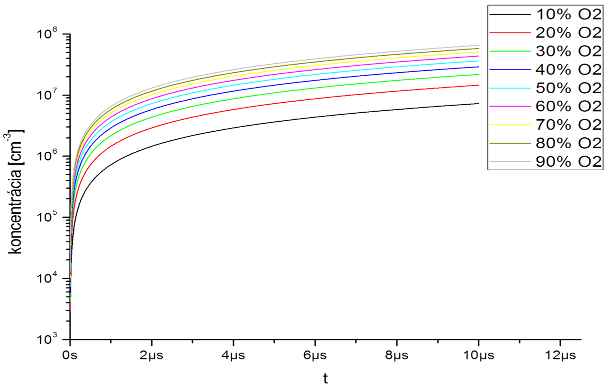

Fig. 2. Time development of concentration of NO_3^- ; the same for every ratio of N_2/O_2, no matter whether mixture was with or without water.

ACKNOWLEDGMENT: This work was supported by the Slovak grant agency VEGA project Nr. 1/0558/09. I would kindly like to thank RNDr. Juraj Országh for his generous help with experimental part.

REFERENCES

1. M. Stano, Chemické listy, **102**, 1414-1417 (2008)
2. C.Soria,F.Pontiga,A.Castellanos: Plasma Sources Sci. Technol. **13** 95-107 (2004)
3. R.Peyrous,P.Pignolet,B.Held: J. Phys. D: Appl. Phys. **22** 1658-1667 (1989)
4. K.Nagato,Y.Matsui,T.Miyata,T.Yamauchi: Int. J. of Mass Spectrometry **248** 142-147 (2006)
5. N.Bibinov,D.Dudek,P.Awakowicz,J.Engemann: J. Phys. D: Appl. Phys. **40** 7372-7378 (2007)
6. J.D.Skalny,T.Mikoviny,S.Matejcik,N.J.Mason: Int. J. of Mass Spectrometry **233** 317-324 (2004)
7. S.Mukkavilli,C.K.Lee,K.Varghese,L.L.Tavlarides: IEEE Trans. on Plasma Sci. vol **16** num 6 652-660 (1988)
8. B. Elliason, Electrical Discharge in Oxygen. Part 1. Basic Data,Rate Coefcients and Cross Sections, Report KLR 83/40 C, Brown Boveri Forschungszentrum, Baden-Dättwil, 1985
9. M.Huertas,J.Fontan,J.Gonzales: Atmospheric Environment **12** 2351 - 2362 (1978)

Sponzori konferencie

H TEST Slovakia spol. s r.o.
Zvolenská cesta 20
974 05 Banská Bystrica
tel: +421 484 324 350
fax: +421 484 324 353
e-mail: info@htest.sk
www.htest.sk

Fakulta matematiky, fyziky a informatiky UK
Mlynská dolina
842 48 Bratislava
tel: +421 2 6541 1353
fax: +421 2 6541 1344
e-mail: kvant@kvant.com
www.kvant.com

TESTOVACÍ TECHNIKA s.r.o.
Hakenova 1423/III
290 01 Poděbrady
tel: +420 325 610 123
fax: +420 325 610 134
e-mail: teste@teste.cz
www.teste.cz

Fakulta matematiky, fyziky a informatiky UK
Mlynská dolina
842 48 Bratislava
tel: 02/65429945
fax: 02/65412380
e-mail: asistent@topsoft.sk
www.topsoft.sk

Jánošíkova 1827/65
927 01 Šaľa
tel.: +421 31 770 7994,5
fax: +421 31 771 2155
e-mail: chromspec@chromspec.sk
www.chromspec.sk

Solartec, s.r.o.
Televizní 2618
756 61 Rožnov pod Radhoštěm
tel: +420 575 750 030
fax: +420 575 750 038
e-mail: obchod@solartec.cz
www.solartec.cz

KAMEA - Ing. Ladislav Kusenda
Nikola Teslu 17
921 01 Piešťany
tel: +421/33/796 61 11
Fax: +421/33/796 61 19
Email: kamea@kamea.sk
www.kamea.sk

CarniHerba
Na vrátkach 15
841 01 Bratislava
tel./fax: +421 2 644 644 11
e-mail: mmikulaj@nextra.sk
http://www.carniherba.sk/

Slovak RE Agency
Prepoštská 8
811 01 Bratislava
tel: +421 2 5443 5082
fax: +421 2 5443 3746
e-mail: info@skrea.sk
www.skrea.sk

ANAMET s.r.o.
Kováků 26
150 00 Praha 5 – Smíchov
tel: (+420) 257 328 175
fax: + 420 257 323 278
e-mail: sales@anamet.cz
www.anamet.cz

STATON s. r. o.

Staton s.r.o.
Sadova 1 148
038 53 TURANY
tel: +421 43 4292362
fax: +421 43 4292585
e-mail: staton@staton.sk
www.staton.sk

DIW Service s.r.o
Drobného 27
84102 Bratislava
tel: +421 2 6446 1440
fax: +421 2 6446 1289
e-mail: vibr.info@voith.com
www.diw.sk

Hetech Services a.s.
Mlynské nivy 61
827 11 Bratislava
tel : +421 2 5831 62 23
fax :+421 2 5341 36 10
e-mail: hetech-services@hetech-services.sk
www.hetech-services.sk

HP
Galvaniho 7, P.O. BOX 43
821 04 Bratislava 22
tel: 02 / 5752 5111
fax: 02 / 5752 5222
www.hp.sk

Linea SK, s.r.o.
Ružinovská 1/A
821 02 Bratislava
tel.: 02/4342 3707
fax.: 02/4333 7466
e-mail: linea@lineasro.sk
www.lineasro.sk

METRODAT s.r.o.
Beblavého 8
811 01 Bratislava
tel: +421 2 54430783
fax: +421 2 54411448
e-mail: metrodat@netax.sk
www.metrodat.sk

FEPA
Brezovská 448/20
907 01 Myjava
tel.: 034/6215 572
e-mail: obchod@fepa.sk, predajna@fepa.sk
www.fepa.sk

GASTROLine
areál EU
Dolnozemská cesta 1
852 35 Bratislava
tel.: 02/ 63 81 56 57
e-mail: gastroline@gastroline.sk
www.gastroline.sk

Malé centrum, kníhkupectvo a vydavateľstvo
P.O.Box 71/15
810 05 Bratislava 15
tel./fax: 02/52 49 98 26, 52 49 98 27
e-mail: zemlicka@malecentrum.sk
www.malecentrum.sk

ISBN 978-80-969124-7-6
EAN 9788096912476